The Geochemistry and Petrology of the Rodrigues Ridge (Western Indian Ocean).

By

Susan H. Mellor BSc. MSc. F.G.S.

A thesis submitted in partial fulfilment
of the requirements of the University of
Greenwich for a Doctorate in Philosophy

December 1998

Gravity Anomaly Map of the West Central Indian Ocean

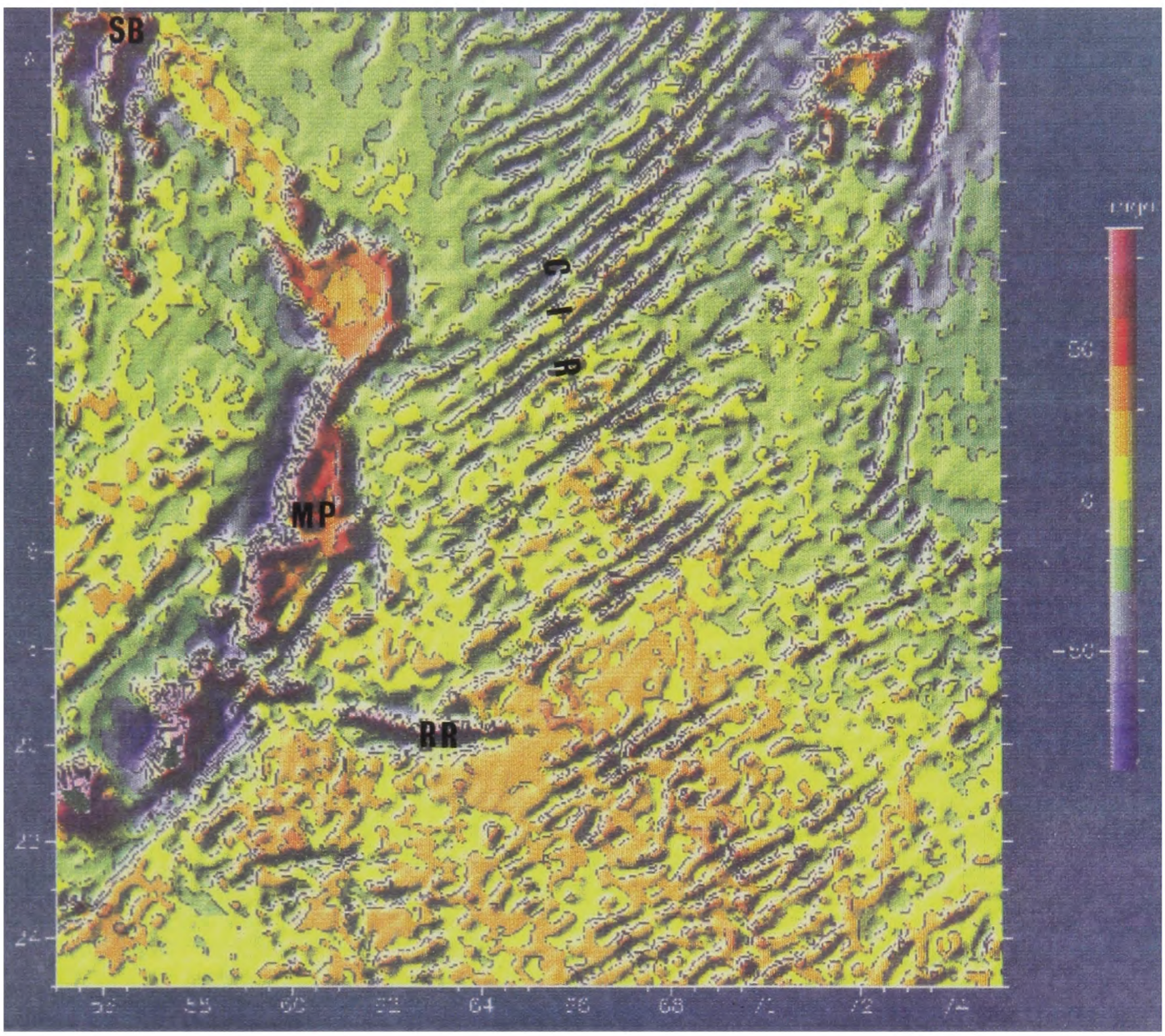

This false colour map covers 56° 00' E - 74° 00' E and 6° 00' S - 24° 00' S. False colour scale (red) +90 - -90 mgal (purple), colour bands are 15 mgal wide. Green - yellow boundary = 0 mgal.

The map clearly shows the fracture zones of the Central Indian Ridge (CIR), the Mascarene Plateau (MP), Seychelles Bank (SB) and the Rodrigues Ridge(RR).

Source: Scharroo R., No Date. Gravity Anomaly Atlas of the Indian Ocean [on line] Netherlands: DEOS. Available from: http://dutlru8.1r.tudelft.nl/img/indian.map?232,205.p.15. [Accessed 21 March 1997].

The Geochemistry, Petrology and Petrogenesis of the Rodrigues Ridge (Western Indian Ocean).

by

Susan H. Mellor BSc. MSc. F.G.S.

Abstract

The Rodrigues Ridge is a linear east-west trending volcanic ridge, located between 18°S and 20°S in the western Indian Ocean. The trend of the Rodrigues Ridge is contrary to the ocean floor fabric of the underlying crust, which formed on the Central Indian Ridge (CIR) between *ca.* 48 My and 10 My. Dating of dredged basalts from the Rodrigues Ridge showed them to be 8-10 My, with no systematic variations with longitude.

All samples recovered from the Rodrigues Ridge were olivine and plagioclase phyric with traces of chrome spinel. Only the most western site contained any phenocryst clinopyroxene. Phenocryst olivine was in the range Fo_{88-79} and plagioclase was in the range An_{79-60}. Where present the clinopyroxene was titaniferous (2.0-3.7% TiO_2) in the range $Ca_{48-52}Mg_{30-19}Fe_{19-33}$.

The Rodrigues Ridge lavas are transitional alkali basalts which display systematic geochemical variations with longitude. Most notably the trace elements Ba, Nb, Rb, Sr, Th, Y, Zr and the LREE increase from east to west, while Sc decreases. These variations may be described as ranging from depleted (in incompatible elements) MORB-like compositions in the east, to enriched OIB-like compositions in the west. This is manifested by at least a three-fold increase in the concentration of the incompatible elements. In accordance with the model presented by Ellam (1992) it is proposed that this behaviour is controlled by the depth to the base of the lithosphere, which acts as an upper limit to melting. In this model the upper limit on the melting is much deeper under the older thicker lithosphere than it is under the young lithosphere. Thus melt composition will increasingly be influenced by the presence of residual garnet under older ocean crust. Even in the absence of residual garnet clinopyroxene in the upper mantle may be capable of retaining the HREE and some trace elements such as Y and Zr. Furthermore shallow mantle is more likely to have been subjected to one or more previous melting episodes beneath spreading ridges, leading to melts depleted in incompatible elements being derived from beneath young ocean crust.

Rayleigh-type modelling for most sites along the Rodrigues Ridge produced only a poor correlation with the observed data. At several sites, notably RR3, some incompatible elements (*eg.*. Zr, Y, REE) show buffered or decreasing trends with decreasing MgO. Although the causes of this behaviour remain ambiguous, it is possible that these melts have not experienced significant high-level fractionation, and this unusual behaviour has its origin in melt-rock reactions within the upper mantle. At these depths the partition coefficients for Zr, Y and the mid-HREE in clinopyroxene have been shown to be greater than unity (Blundy *et al.*, 1998 and Vannucci *et al.*, 1998). Thus the reaction between the melt and coexisting clinopyroxene within the upper mantle, in conjunction with the crystallisation of olivine, may explain how these buffered and declining trends (with declining MgO) have developed.

To characterise their isotopic signature a subset of samples were analysed for Sr, Nd and Pb. Like the trace elements, the isotopes display clear linear trends with longitude. On paired isotope plots the Rodrigues Ridge lavas form similar linear trends between samples from the CIR (the Marie Celeste Fracture Zone) and the Réunion hotspot (notably Mauritius), suggesting that they are products of mixing between the mantle sources of the CIR and Réunion. It is proposed that the upper mantle has been passively contaminated by the Réunion plume (with *circa* $^{87}Sr/^{86}Sr = 0.7042$, $^{143}Nd/^{144}Nd = 0.51284$, $^{206}Pb/^{204}Pb = 18.788$, $^{207}Pb/^{204}Pb = 15.585$ and $^{208}Pb/^{204}Pb = 38.849$). At shallow levels, immediately below the lithosphere, the upper mantle is made up predominantly of a depleted MORB-like source, with *circa* $^{87}Sr/^{86}Sr = 0.7031$, $^{143}Nd/^{144}Nd = 0.51305$, $^{206}Pb/^{204}Pb = 18.354$,

$^{207}Pb/^{204}Pb$ = 15.517 and $^{208}Pb/^{204}Pb$ =38.214, while at greater depths more Réunion plume material is available. The observed linear array, on paired isotope plots, reflects the differing contributions made by these deep and shallow sources to the Rodrigues Ridge lavas.

It is proposed that the Rodrigues Ridge was formed due to a build up of stress, possibly resulting from its proximity to the Ridge-Ridge-Ridge triple junction (see Patriat &Ségoufin 1988), causing the rigid African plate to rupture parallel to the principal stress direction. This would have resulted in decompression melting in the upper mantle, so facilitating rapid but short-lived volcanism. Although volcanism has ceased, there is still elevated heat-flow within this area, suggesting that the upper mantle is still anomalously hot (von Herzen &Vacquier 1966). Isostatic readjustment could account for the magmatic reactivation at 1.5 My which formed Rodrigues island.

Acknowledgements

I would like to express my gratitude towards the following individuals for the help they have provided without which this work could not have been completed;

Dr. Ian Platten,
Dr. Matthew Thirlwall,
Dr. Dodie James,
Prof. Brian Upton,
Dr. Lindsay Parsons,
The Captain and crew of the RRS. Charles Darwin,
Mrs. Mildred Hall,
Mr. Barry Saunderson,
Mr. Pat Brown,
Mr. John Maddocks,
Mr. & Mrs. Donald Draper.

I would particularly like to thank the library staff at the University of Greenwich especially Mr. Nick Dobson and my supervisors Prof. Alistair Baxter and Dr. Andy Bussell. Lastly I would like to thank my husband Mr. Andrew Mellor for his patience while I have been working on this project.

Contents

List of Figures

List of Tables

Included On Disk

List of Plates

List of Appendices

Abbreviations Used in this Work

MIOR	Mid-Indian Ocean Ridge
CIR	Central Indian Ridge
SEIR	South East Indian Ridge
SWIR	South West Indian Ridge
MORB	Mid-Ocean Ridge Basalt
E-type MORB	Enriched type Mid-Ocean Ridge Basalt
N-type MORB	Normal type Mid-Ocean Ridge Basalt
HIMU	High In Mantle Uranium
OIB	Ocean Island Basalt
FZ	Fracture Zone
MFZ	Mauritius Fracture Zone
FZA	Fracture Zone A
mbsl	metres below sea level
MBL	Mechanical Boundary Layer
LMgO group	Low Magnesium Oxide group
HMgO group	High Magnesium Oxide group
ol.	olivine
cpx.	clinopyroxene
opx.	othopyroxene
pl.	plagioclase
sp.	spinel
Cr sp.	chrome spinel
D_X^Y	Partition coefficient of element X in mineral Y
K_{DX}	Bulk distribution coefficient of element X
Mc	Mass of Crystals
Ma	Assimilated Mass
Mz	Replenishment Mass

Abbreviations Used in this Work cont...

REE	Rare Earth Element
LREE	Light Rare Earth Element (La-Nd)
MREE	Mid-Rare Earth Elements (Sm-Tb)
HREE	Heavy Rare Earth Elements (Dy-Lu)
LILE	Large Ion Lithophile Element
HFSE	High Field Strength Element
LOI	Loss On Ignition
ppm	parts per million
ppb	parts per billion
XRF	X-Ray Fluorescence
XRD	X-Ray Diffraction
ICP-AES	Inductively Coupled Plasma Atomic Emission Spectrometry
ICP-MS	Inductively Coupled Plasma Mass Spectrometry
SSR	Sum of the squares of the residuals
PREMA	Prevalent mantle source
BSE	Bulk silicate earth source
HIMU	High in mantle Uranium source
EMI	Enriched mantle type 1 source
EMII	Enriched mantle type 2 source
DM	Depleted mantle

Chapter 1

1. The Rodrigues Ridge

1.1 Introduction

The Rodrigues Ridge is situated between 18°-20°S and 58°30'-64°45'E in the West-Central Indian Ocean. It is an east-west trending linear feature which lies at an oblique angle to the NNW-SSE trending fabric of the underlying ocean floor (fig. 1). The Ridge is surmounted towards its eastern end by the volcanic island of Rodrigues (fig. 1), whose lavas are dated at 1.5 my (McDougall *et al.*, 1965). This project originates from the CD21/87 cruise of the RRS. Charles Darwin to the West-Central Indian Ocean. During this cruise 15 sites were dredged (of which 9 yielded igneous specimens), and 3632 km of bathymetric, magnetic and gravity data, together with 950 km of seismic data were collected. Palaeontological and sedimentological samples were also collected as part of related projects on these aspects of the Rodrigues Ridge geology.

The aims of this work are :-

1. To provide a greater understanding of the geology, petrology, petrogenesis and geochemistry of the Rodrigues Ridge.
2. To explain the paradoxical relationship between the east-west trend of the Rodrigues Ridge and the underlying ocean floor which formed at the NNW-SSE trending Central Indian Ridge (CIR).
3. To examine the relationship between Rodrigues Island and the underlying Ridge.
4. To establish whether any relationship exists between the Rodrigues Ridge and other major volcanic features in the region, in particular the CIR and the Réunion hotspot.
5. To present an explanation of how and why the Rodrigues Ridge formed.

To achieve these aims, 15 dredges were undertaken on the Rodrigues Ridge, of which nine successfully yielded igneous samples. 76 basalts from these dredges were studied, of which 62 were subject to geochemical analysis.

The Rodrigues Ridge is built on a region of ocean floor formed on the present CIR between 8-30 my (Dyment 1999, pers comm.). At its western end it intersects the Mascarene Plateau, which, together with the Chagos-Laccadive Ridge, Mauritius and Réunion, forms the trace of the Réunion hotspot. West of this Plateau is older ocean crust formed at about 80 my on an extinct spreading ridge, the trace of which is situated south of Mauritius (Dyment 1999, pers comm.). During this chapter I shall outline the history and geochemistry of these surrounding areas, paying particular emphasis to those areas which may be related to the Rodrigues Ridge.

Figure 1 **Map Showing the Location of ODP Holes in the Western Indian Ocean and the Location of the Current Work.**

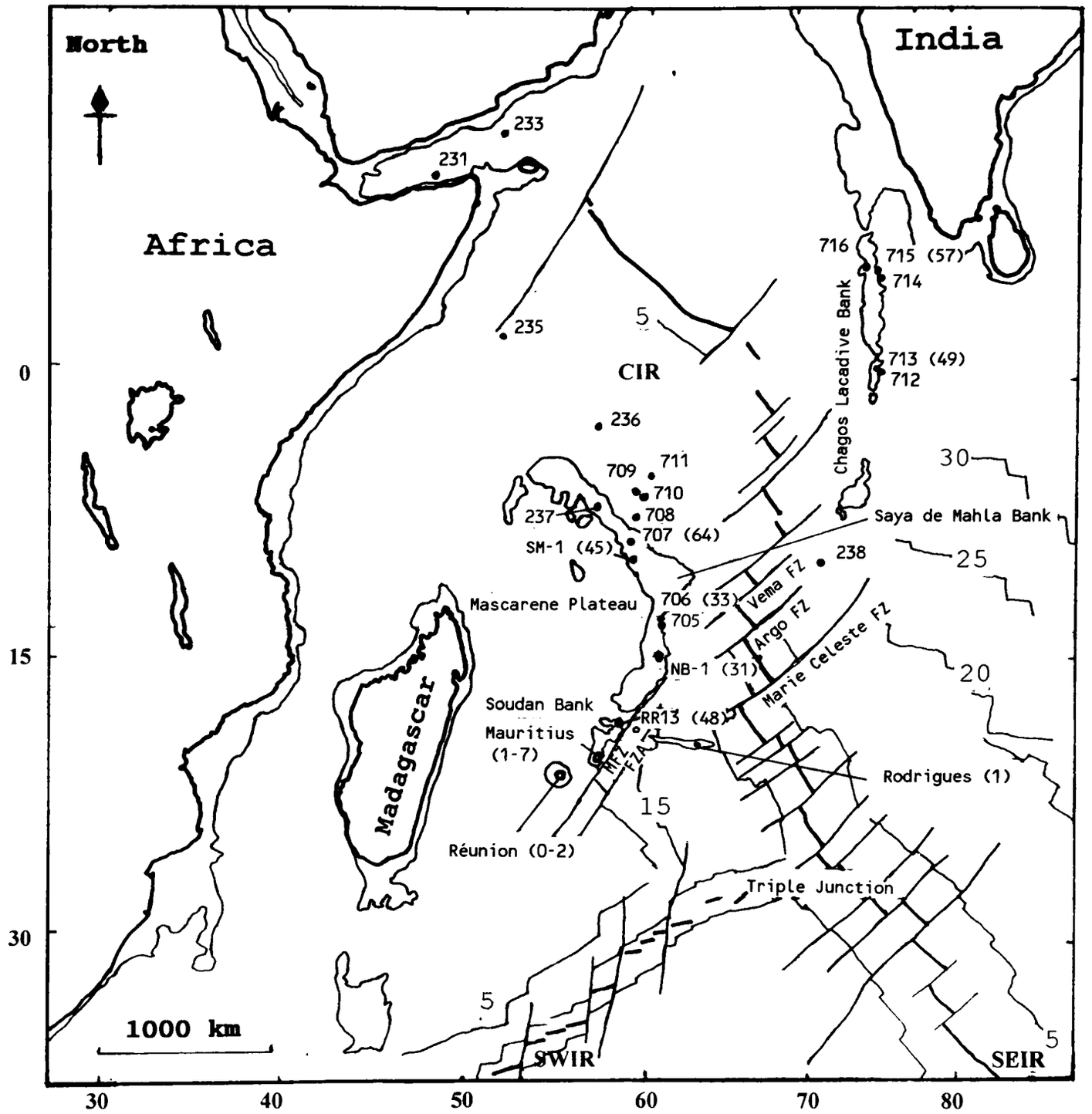

Key

. 713 (49)	ODP drill site (and age)
	2000 m bathymetric contour
25	Magnetic anomaly 25
	Coast
	CIR

References: Dmitriev (1974) and Duncan (1990).

1.2 The Evolution of the Indian Ocean

The earliest evidence for the existence of the Indian Ocean is found in the form of transgressive marine sediments of Permian age in northern Madagascar and East Africa (Kent, 1974). Open marine conditions are not recorded until the early Jurassic in Somalia and northern Madagascar and the late Jurassic in Mozambique (Kent, 1974). The earliest magnetic anomaly recorded in the Indian Ocean is M-22 in the Mozambique Basin (Ségoufin, 1978), which is dated as Kimmeridgian [147 my] (Couper, 1989). By the end of the Cretaceous (magnetic) Quiet Zone (85-111 my) the Indian Ocean was opening rapidly along a NW-SE trending spreading ridge, driving the Indian subcontinent quickly north east towards Eurasia. The record of this movement is preserved in magnetic anomalies 34-20 (85-45 my) found in the Madagascar-Mascarene Basins, the Crozet basin, the northern Central Indian Ocean Basin and the Arabian Basin (Couper, 1989). Between anomaly 20 and 18, the active spreading ridge jumped, forming a new NNW-SSE trending ridge (Patriat & Ségoufin, 1988). This ridge is the CIR, which has been active since anomaly 18 (44 my), forming the present central Indian Ocean floor, including the region which underlies the Rodrigues Ridge. Evidence for the Palaeocene (pre-anomaly 18) spreading ridge is preserved in the magnetic anomalies of the Mascarene Basin (fig. 1). In addition to the magnetic anomalies, the sub-parallel linear volcanic ridges and lines of islands which run across the Indian Ocean floor provide further evidence for this movement. These are the traces of both active and extinct hotspots [hot mantle plumes which result in increased magmatic activity on the sea floor (Morgan, 1971)]. Norton & Sclater (1979) and Mart (1988) speculated that the Mascarene Plateau-Chagos-Laccadive Ridge was the product of incipient volcanism associated with the Vishnu and other fracture zones situated on the Palaeocene spreading Ridge. Mart (*op. cit.*) suggested that Eocene subsidence (from shallow marine to abyssal depths) of the Northern Mascarene Plateau-Seychelles Bank was contemporaneous with the onset of spreading at the present CIR. This spreading resulted in the separation of the Chagos-Laccadive Ridge from the Mascarene Plateau. In contrast Morgan (1982) suggested that this 5000 km disrupted lineament was the trail of the Réunion hotspot, a view also expressed by Duncan & Hargraves (1990), Backman *et al.* (1988), Vandamme & Courtillot (1990), Duncan & Richards (1991) and Müller *et al.* (1993). The hotspot hypothesis implies that the youngest lavas on the Mascarene Plateau should be found in the south, at Réunion, and that the age of the lavas should serially increase northwards. Dating of the leg 115 sites of the Ocean Drilling Project (ODP) by Duncan & Hargraves (1990) and Müller *et al.* (1993) (fig. 1), together with data for Réunion, Mauritius, and the Deccan lavas (McDougall, 1971, McDougall & Chamalaun, 1969 and Duncan & Pyle, 1988) shows just such an age progression.

A hot mantle plume will continue to supply melt to the base of the lithosphere over a long time period. As the lithosphere drifts over this hotspot, new volcanoes will form while the older ones drift away from the source and eventually become extinct, resulting in an island chain or aseismic ridge, *e.g.* the Hawaiian chain. Experimental studies have demonstrated that, in order for mantle plumes to ascend

(initially) through the asthenosphere, they must have a large diapiric 'head' (Whitehead & Luther, 1975, Olson & Singer, 1985 and Richards *et al.,* 1989). In this model, once established, the plume can be sustained by a very much smaller conduit. Since Morgan (1981) first observed the relationship between hotspots and flood basalts, many authors have pointed to the Deccan Traps as the manifestation of the diapiric 'head' of the Réunion hotspot (Richards *et al.,* 1989, Duncan, 1990, Duncan & Richards, 1991 and Sleep, 1990).

The Deccan Province covers an area of about $5x10^5$ km^2 at the present day (Paul *et al.,* 1977), but may have covered $1.5x10^6$ km^2 at the time of its formation (Krishnan, 1953). The Traps reach a thickness in excess of 2000 m and consist predominantly of tholeiitic basalts (Beane *et al.,* 1986). Despite their volume, the Deccan lavas were all extruded during a very brief time period at the Cretaceous-Tertiary (K-T) boundary, fuelling speculation that this event was the cause of the mass extinction which also occurred at the K-T boundary (Courtillot, 1990). $^{40}Ar/^{39}Ar$ incremental heating gives ages in the range 67-68 my for the Deccan basalts (Duncan & Pyle, 1988).

The Réunion hotspot has an exceptionally well preserved history; from its dramatic onset in the Deccan Traps (67-68 my) (Duncan, 1990, Duncan & Hargraves, 1990 and Duncan & Pyle, 1988), through a period of steady magma flux (Chagos-Laccadive Ridge and Mascarene Plateau), to a waning stage producing the islands of Mauritius and Réunion. The initiation of Réunion also heralded the onset of spreading on the CIR (Patriat & Ségoufin, 1988). Despite this history, the combined processes of erosion and sedimentation have left no igneous material outcropping between Mauritius and the Deccan Traps on this substantial topographic feature. Prior to the onset of spreading on the CIR in the late Eocene, the Mascarene Plateau and the Chagos-Laccadive Ridge formed a single feature (Schlich, 1982, McKenzie & Sclater, 1971, Fisher *et al.,* 1967, Fisher *et al.,* 1971, Patriat & Ségoufin, 1988, Norton & Sclater, 1979 and Duncan, 1990).

Evidence for the origin and age of the basement between the Seychelles and the Saya de Malha Bank is very limited. Deep Sea Drilling Project (DSDP) hole 237 (fig. 1) failed to encounter igneous basement; but the oldest sediments recovered were dated as Palaeocene (57.6-60 my) (Mart, 1988). Basalts from ODP hole 707C (fig. I) were erupted at 63.7±1 my (Backman *et al.,* 1988, Duncan & Hargraves, 1990). Both of these dates suggest that the basement south-east of the Seychelles is related to the volcanicity of the Deccan Traps, rather than the 45 my Saya de Malha Bank (Duncan & Hargraves, 1990, White *et al.,* 1990 and Müller *et al.,* 1993).

1.3 The Physiography of the Rodrigues Ridge

The Rodrigues Ridge is a narrow (maximum width 50 km), east-west trending linear volcanic ridge 600 km long and dated at 8-10 my (Duncan, 1989 unpubl., see table 1). West of 62°30'E its trend changes from 090° to 110°. The Ridge is cut by two major fracture zones (at 60°30'E and at 59°30'E).

Figure 2

Bathymetric Map of the Rodrigues Ridge

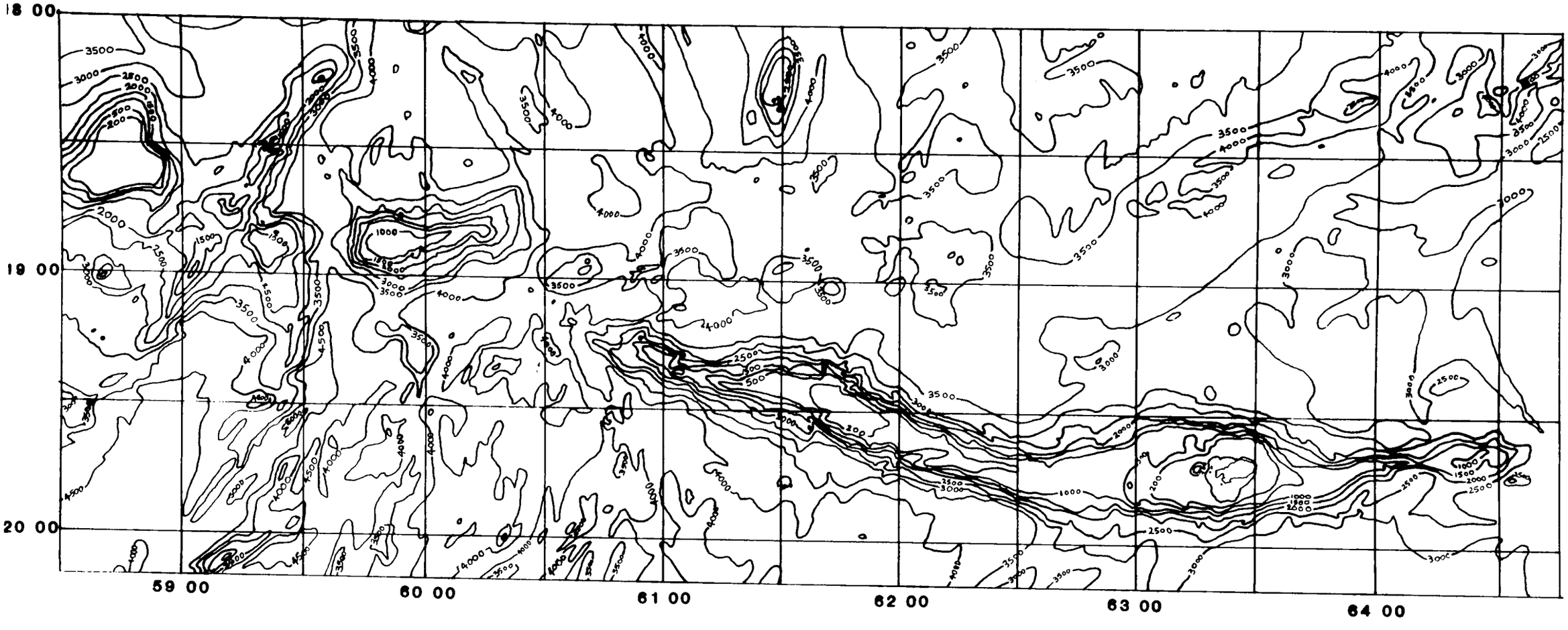

Mercator Projection

Contours in metres

Figure 3

Structural Map of the Rodrigues Ridge

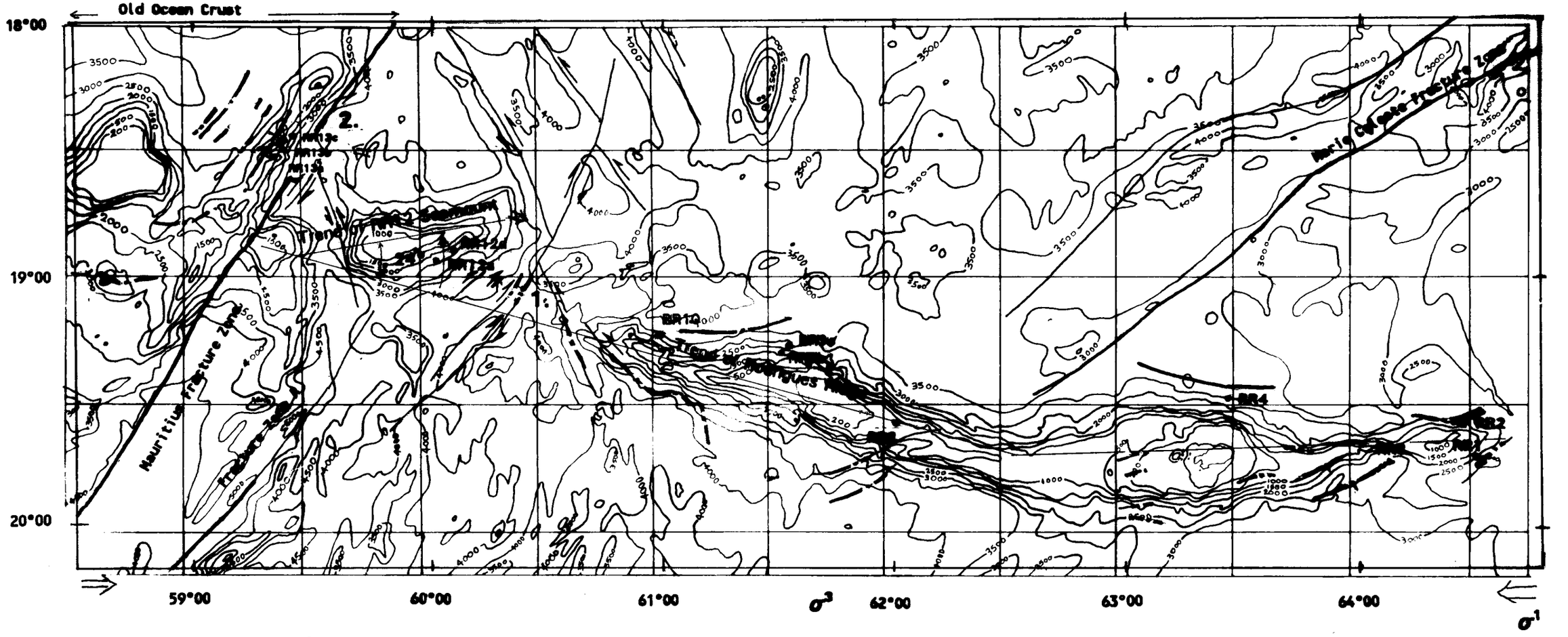

Fracture zones or faults identified on seismic lines

Fracture zone from previous work

Infered fault/fracture zone from bathymetry with throw where known

Infered fault movement

Overall diraction of movement

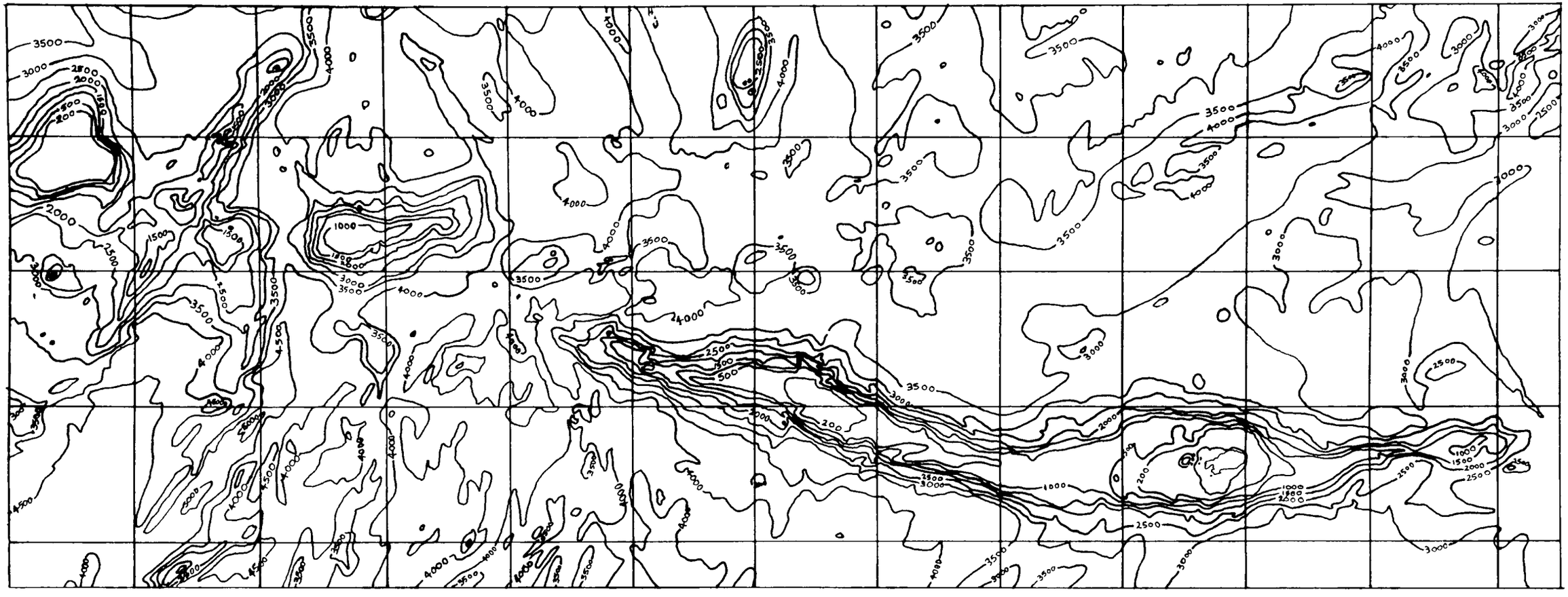

The first of these is the smaller feature and is un-named, but called FZA by de Ribet (1989), whereas the second is the 2000 km long Mauritius Fracture Zone (MFZ). The MFZ forms the eastern flank of the Mascarene Plateau (fig. 1). At the intersection of the Rodrigues Ridge and the Mascarene Plateau lies the prominent feature known as the Soudan Bank with a second un-named bank to the west of it. Though the affinities of these are uncertain, their bathymetry and trend suggest that they are related to the Rodrigues Ridge (figs. 1 & 2). Fig. 2 (see Ch. 2 for sources) also shows a NE-SW trending ridge on the western flank of the Mascarene Plateau from which the samples prefixed RR13 were dredged. This feature proved to be 48 my oceanic crust (table 1) from south of the Rodrigues Ridge and east of the MFZ which has been thrust up on to the Mascarene Plateau.

The Rodrigues Ridge rises from sea-floor depths of about 4 km in the west and 2.5 km in the east, to a flat wave-cut platform at about 50-60 metres below sea level (mbsl) along much of its length. This form suggests that at the time of its formation it had a subaerial expression as a chain of volcanic islands subsequently reduced by marine planation. It is capped by lithified or semi-lithified carbonates with occasional fossilised patch reefs. Most of the surface corals are dead (Heward, pers. comm.), suggesting that recent subsidence was in excess of coral growth rates. The steep slopes (≈30°) on the margins of the Ridge are largely devoid of sediment and are often associated with flanking normal faults and rotational slip planes (fig. 3). On the lower slopes extensive slump and re-sedimented carbonates, some containing basalt clasts, are present.

Table 1 ^{40}Ar-^{39}Ar Ages for Basaltic Rocks Dredged from the Rodrigues Ridge during the RRS Charles Darwin Cruise 21/87.

Sample Number	Description	% Radiogenic ^{40}Ar	Total Fusion Age (my)	Incremental Heating Age (my)
RR2.4	basalt	3.6	8.31±0.31	
RR4.1	basalt	7.8	7.53±0.23	
RR8.4	basalt	12.0	9.71±0.74	9.18±0.38*
				9.70±0.20**
RR9c.37	basalt	4.4	8.34±0.74	
RR10.1	basalt	16.1	9.77±0.55	8.06±0.49*
				11.1±0.50**
RR13c.3	basalt	11.8	48.5±0.5	

Ages calculated using the following abundance constants: $\lambda_e = 0.581 \times 10^{-10} yr^{-1}$; $\lambda_\beta = 4.962 \times 10^{-10} yr^{-1}$; $^{40}K/K = 1.167 \times 10^{-4}$mol/mol.
* isochron age
** plateau age

NB. RR12d.5 was reported to be 11my. (Duncan, 1989 pers. comm.)

It was established during the CD 21/87 cruise that the Rodrigues Ridge extends east beyond Rodrigues island, as suggested by Fisher *et al.* (1967), to at least 64° 45'E. Although the termination was not identified formally, it is not thought to be significantly further east than is shown in fig. 2 because the ocean crust beyond this point is younger than the 8-10 my of the Rodrigues Ridge. The termination lies within anomaly 5 (9-20 my, Patriat & Ségoufin, 1988), which indicates that the Rodrigues Ridge would have been on, or very close to, the CIR when it formed.

1.4 Rodrigues Island

Situated some 650 km northwest of Mauritius in the west-central Indian Ocean, the island of Rodrigues is the only subaerial exposure associated with the Rodrigues Ridge (fig. 1). With a surface area of 120 km^2, the island is dominated by a steep central ridge trending west-south-west, upon which the highest peaks, including the 396 m Mt. Limon, are situated.

The earliest reference to the geology of Rodrigues suggested that, like the Seychelles, the island was granitic (Higgin, 1848). Balfour (1879) and later Snell & Tams (1920), however, described, in some detail, the volcanic form of the island and also the limestones of the fringing reef. The petrology of the basalts and dolerites was first described by Maskelyne (1879) who, based on the appearance of both the lavas and the island, estimated that the island was formed during the Tertiary period. In practice $^{40}K/^{40}Ar$ dating of two lavas by McDougall *et al.* (1965) gives an age of 1.30-1.58 Ma.

The lavas are variably vesicular, olivine + hypersthene-normative, transitional basalts to nepheline-normative, alkali basalts (table 2) intruded by three small teschenite bodies (Baxter *et al.*, 1985). Olivine and plagioclase (labradorite) are the major phenocryst phases present. Within the Rodrigues lavas a megacryst suite is present, consisting of olivine, plagioclase, kaersutite, clinopyroxene (augite), apatite, magnetite and hercynitic-spinel. Either weathering or late-stage hydrothermal alteration has resulted in the decay of the groundmass plagioclase and augite, the replacement of the olivine phenocryst cores, indicating zoning, and the growth of secondary minerals such as aragonite, zeolites (Upton *et al.*, 1967) and quartz (Perroud, 1982 unpubl.).

The phenocryst assemblage is olivine (Fo_{88-68}), ± plagioclase (An_{73-50}) with rare clinopyroxenes ($Ca_{46-47}Mg_{45-38}Fe_{9-15}$). The anorthite content of plagioclases from these lavas overlaps that of the more anorthitic megacrysts. Matrix phases are olivine (Fo_{80-66}), plagioclase (An_{75-31}), pyroxene ($Ca_{47}Mg_{45-33}Fe_{8-20}$), titanomagnetite and analcime. Ilmenite (instead of titanomagnetite) and the more iron-rich pyroxenes are confined to the teschenites (Baxter *et al.*, 1985 and Upton *et al.*, 1967).

Xenoliths of troctolitic-anorthositic gabbro, often showing a layered fabric, are widely dispersed and locally common (Upton *et al.*, 1967 and Baxter *et al.*, 1985). These are often found as disaggregated and partially resorbed xenocrysts. High-level fractionation is invoked to explain the xenolith and xenocryst suites, but the lavas of Rodrigues Island cannot be directly related to those of the underlying

Rodrigues Ridge, which are at least 6 my older (table 1, Duncan, pers comm. and Duncan, 1990). Although quantitatively insignificant there are also a few small pyroclastic bodies, chiefly tuffs and agglomerates, in which the majority of the brown basaltic hornblende is found. There is also no evidence to suggest that the hornblende was stable during the initial crystallisation of the gabbro, at depth. It is suggested instead, that the localised development of hydrous magma, which led to the explosive eruption of pyroclastics, also allowed the replacement of pyroxene by hornblende. This high water-vapour pressure must have persisted for enough time to allow the complete replacement of the pyroxene within the pyroclastics (Upton *et al.,* 1967). Single broken crystals of brown basaltic hornblende, of uncertain origin, were found in limestones from RR13 on the Mascarene Plateau.

Among the lavas, clearly defined fractionation trends are found in SiO_2, Al_2O_3, TiO_2, CaO, P_2O_5, MnO, La, Zr, Sc, Nd, Ni, Cr, Cu, Ce, and Y. Broad, less well defined, fractionation trends can be found in Na_2O, K_2O, Ba, and Sr, and a general scatter with no discernible trends in Zn, Rb, V, Pb, and Th (Baxter *et al.,* 1985). Overall these patterns are consistent with Rayleigh modelling, which required *ca.* 45% crystallisation of the phenocryst phases; plagioclase, olivine, clinopyroxene and magnetite in the ratio 20:39:35:6 (Baxter *et al.,* 1985) to produce the most evolved lavas from the most primitive. Compared with the observed xenolith suite, this calculated assemblage is pyroxene-poor. This led to the conclusion that gabbros and/or ultrabasic rocks rich in clinopyroxene, must occur lower down in the layered complex (Baxter *et al.,* 1985). The high Al_2O_3/CaO ratio of the lavas suggests that there was a high clinopyroxene/garnet ratio in the remaining refractory residua after the extraction of these melts. Patterns of Ni, Cr, Sc and Cu content are consistent with this interpretation of the fractionation history of these lavas.

Scattered trends of K_2O, Rb, Ba and Sr with respect to MgO are probably the result of either deuteric alteration, or of tropical weathering (despite the samples being selected on the basis of their fresh appearance) and should be considered with some caution (Baxter *et al.,* 1985). The mobility of these elements has been investigated by Wood *et al.* (1976), Hart *et al.* (1974) and Cox & Hawkesworth (1985), and is discussed in chapter 4. The scattered distribution of V with MgO is strange, since Ti, Cr and Fe show consistent trends which V might be expected to follow. The partition coefficient for V in spinel (and presumably magnetite) is given as 38.0 by Ringwood (1970). Thus magnetite would be expected to show substantial control over V during its fractionation. The PhD work of Lindstrom (1976 unpubl.) shows that the partition coefficient of V in both clinopyroxene and magnetite varies substantially with oxygen fugacity. He suggests that with further research the partitioning of V could be used to estimate the oxygen fugacity of a melt. Rampone *et al.* (1993) suggest that a distribution coefficient of $D_V^{Sp} = 0.1$ would be more appropriate for terrestrial rocks. This is supported by the lack of correlation between V and the elements partitioned by magnetite (Fe, Cr and Ti).

The light rare earth elements (LREE) increase, as might be expected, with decreasing MgO, although within this generalisation there is substantial variation in the LREE/HREE ratio. The enrichment of heavy rare earth elements (HREE) in some samples suggests that they, at least, have a garnet-poor source. Only three samples were found which showed negative europium anomalies even though the

calculated extract has 39% plagioclase. The plagioclase/liquid partition coefficient for Eu (D_{Eu}) is strongly susceptible to variations in oxygen fugacity, since this controls the ratio Eu^{3+}/Eu^{2+} and hence the availability of Eu^{2+} capable of substituting for Ca^{2+} (Irving, 1978 and Drake, 1975). At low oxygen fugacity (1×10^{-13}) D_{Eu} is 1.2, whereas at high oxygen fugacity (0.1) it is 0.03 (fig. 4). Baxter *et al.* (1985) concluded that the lack of any significant Eu anomaly was the result of the lavas having an oxygen fugacity of around $10^{-7.1}$. This value is derived from the suggested value of 10^{-7} given for terrestrial basalts by Drake (1975), from which they seem not to vary significantly. At such oxygen fugacity D_{Eu} (in plag.) is 0.2 (see appendix 1) and the bulk distribution coefficient is about 0.137, *ie.* lying between the bulk distribution coefficients of Sm and Gd ($D_{Sm} = 0.084$, $D_{Gd} = 0.149$). Thus a substantial Eu anomaly would not be expected.

The lavas are unusually uniform in terms of their isotope composition (Baxter *et al.*, 1985). Sr and Nd isotopes ($^{87}Sr/^{86}Sr$ 0.70357-0.70406 and $^{143}Nd/^{144}Nd$ 0.51283-0.51289) are consistent with a mantle source depleted in LREE.

1.5 The Mascarene Plateau

The basalts recovered during ODP leg 115 are primarily vesicular, porphyritic tholeiites with plagioclase ≥ augite ≥ olivine at sites 706, 707 and 713, while site 715 is almost exclusively olivine-phyric (Baxter, 1990). None of these sites shows the evolved chemistry of the later series from the Mascarene islands. Indeed they can all be considered to be part of the shield-building phases of the respective volcanoes (Fisk *et al.*, 1989). Site 715 has a more evolved chemistry typical of ocean island basalts (OIB). Sites 706C, 707C and 713A have a mildly differentiated character in terms of their compatible elements, more akin to a mixed OIB-mid ocean ridge basalt (MORB). This should not be surprising in view of their proximity to the CIR at the time of their eruption (fig. 1) (Patriat & Ségoufin, 1988). This situation is analogous to the present tectonic setting of Iceland where the hotspot is on the mid-ocean ridge, and the resulting lavas show incompatible element characteristics indicative of mixed OIB-MORB (Fisk *et al.*, 1989). All sites are hypersthene-normative (10-24% at 706, 20-30% at 707, 7-19% at 713A and 0-25% at 715A), with only 715A having significant normative olivine (0-23%). All sites, except 715A, show major and trace element trends consistent with the fractionation of the observed phenocryst phases: plagioclase, augite and olivine (Baxter, 1990). The lavas of site 715A are more differentiated and resemble those of Mauritius and Réunion, which might be expected since they formed in a similar tectonic environment. They show major element fractionation trends controlled by olivine and plagioclase. This site has been subjected to greater amounts of seawater alteration than the other ODP sites.

The data for site 706C upper group, presented in table 3, shows the samples to have a clear affinity with Réunion. The source for these lavas must have been depleted in Ba relative to the current Réunion

Table 2. **CIPW norms for Rodrigues Island Lavas**

Sample	or	ab	an	ne/hy	di/C	ol	mt	il	ap	cc	An
Rd15	4.55	21.66	27.57	3.32 hy	18.35 di	16.70	1.89	2.94	0.53	0.71	56
Rd42	9.46	20.48	27.36	0.31 hy	13.36 di	20.01	1.68	3.21	0.74	0.89	57
Rd99	7.92	25.42	24.19	0.12 ne	11.24 di	24.65	2.03	2.85	0.83	0.48	49
Rd38	7.62	19.62	27.20	2.48 ne	16.98 di	18.69	1.71	3.23	0.79	0.36	58
Rd31	7.39	32.21	24.11	2.67 ne	11.47 di	14.73	1.73	3.36	1.20	0.52	43
Rd102	11.94	26.57	27.47	11.34 hy	5.70 di	8.15	1.95	3.15	1.20	0.34	51
Rd58	7.21	38.25	23.37	0.63 hy	6.23 di	14.97	1.78	3.32	1.51	0.84	38
Rd123	5.02	27.70	23.83	4.52 ne	15.37 di	15.61	1.68	3.11	1.07	0.61	46
Rd67	9.34	20.59	23.58	4.62 ne	14.27 di	19.48	1.86	3.53	0.90	0.41	53
Rd91	8.57	23.36	27.30	1.60 ne	12.55 di	19.28	1.69	3.49	0.88	0.48	54
Upton 1	8.57	18.61	26.03	6.70 ne	15.43 di	18.03	1.86	3.87	1.11	--	58
Upton 2	7.80	17.81	28.41	3.64 ne	16.47 di	19.13	1.68	3.51	1.16	--	61
Upton 3	13.42	21.04	21.59	9.00 ne	14.83 di	12.57	1.86	3.80	1.37	--	51
Upton 4	10.76	20.60	23.93	3.69 ne	16.01 di	16.52	1.72	3.87	1.18	--	54
Upton 5	9.75	29.01	23.81	0.97 ne	15.90 di	12.38	1.59	3.34	1.25	0.96	45
Upton 6	8.39	24.03	29.64	3.19 hy	9.54 di	16.11	1.79	3.34	1.14	0.84	55
Upton 7	22.81	29.80	8.49	10.31 ne	7.54 di	9.88	1.93	5.07	2.29	0.80	22
Upton 8	28.60	38.68	8.12	8.48 ne	0.96 C	7.93	1.15	2.60	1.32	0.18	17

All values are quoted as percentages; or orthoclase, ab albite, an anorthite, ne nepheline, hy hypersthene, di diopside, C corundum, ol olivine, mt magnetite, il ilmenite, ap apatite, cc calcite, An the calculated anorthite content of the plagioclase. CIPW Norm calculated using the *IGPET* program of based on the work of Wright & Doherty (1970) on the basis of $Fe_2O_3/Fe_2O_3+FeO = 0.13$ as suggested by Brooks 1976 and used here for consistency and compatibility with the Rodrigues Ridge data. Data sources:- Samples prefixed Rd from Baxter *et al.*, 1985, samples prefixed Upton from Upton *et al.*, 1967. Samples Upton 1-6 and all prefixed Rd except Rd15 are olivine basalts, Rd15 is a teschenite, Upton 7 is a pegmatite vein, Upton 8 is a fine-grained phonolite vein.

source, as evidenced by the Ba/Y and Ba/TiO_2 ratios (Baxter, 1990). The lower group, units 31 and 32, when compared with Réunion and the upper group, have low Ce/Y, Zr/Y, Nb/Y, Zr/Nb and Ba/Y ratios, with higher Ti/Zr and Ba/TiO_2. These lavas have closer affinities with the CIR (Baxter 1990), and are, like those from 707C, bracketed by the ratios for N-type MORB and E-type MORB (table 3). Baxter (1990) suggests that 706C-lower group, like the enriched lavas at site 707C-lower group and the lavas of 713A, may be related to the Ambenali Formation of the lower Deccan Traps. The Ambenali Formation lavas are relatively uncontaminated when compared to other Deccan lavas (Cox & Hawkesworth, 1985 and Lightfoot *et al.*, 1990), yet the 706C lower group lavas are depleted in incompatible elements when compared to Ambenali lavas of similar MgO content.

Figure 4 Plagioclase Liquid Distribution Coefficients

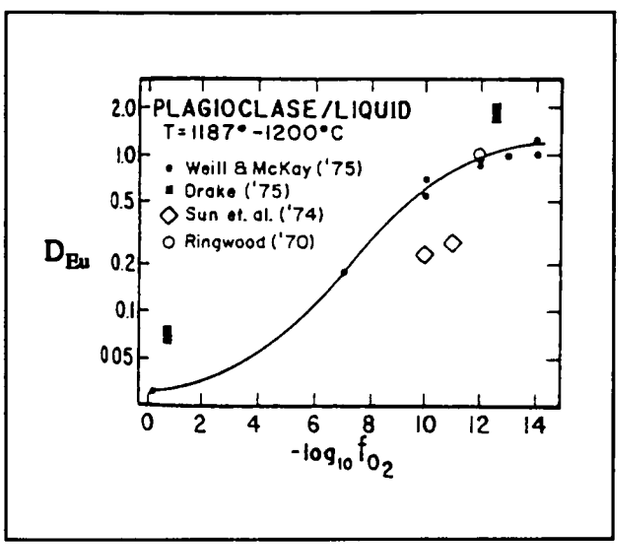

After Irving (1978)

The MORB-like affinities of the 706C lower group and the OIB-like affinities of the upper group can be explained by the close proximity of the CIR and Réunion hotspot at 33 my (Patriat & Ségoufin, 1988). The 706C upper group lavas were extruded during a period when a greater upwelling at the hotspot caused it to dominate the melting regime at/near the CIR crest. The resulting lavas have a greater Réunion component than those erupted during the period when the CIR dominated the melting regime, and therefore the chemistry. In this model, the depth and amount of partial melting would control the chemistry of the magma (Baxter, 1990). This model can also be used to explain the greater component of Deccan material found in the lower group at site 707C. In general site 713A is most like MORB, despite higher Nb/Zr ratios. This ratio is very sensitive to source enrichment (in highly incompatible elements), and appears to have declined over time for the Réunion hotspot (table 3).The significantly higher Ce/Y ratio for the upper group supports the view that the deeper Réunion source made a greater contribution to these lavas.

1.6 Réunion and Mauritius

Together with Mauritius, Réunion is the only subaerially exposed part of the hotspot trail south of the Deccan Traps. Réunion island, which rises from ocean floor depths of 4 km, is composed of two volcanic centres:- the extinct Piton de Neiges and the active Piton de la Fournaise. Piton de Neiges (3096 m) forms the two thirds of the island northwest of Piton de la Fournaise (2361 m), one of the world's most productive volcanoes, situated to the southwest. Piton de Neiges is now deeply dissected by erosion, resulting in the development of three large amphitheatre-headed valleys (Upton & Wadsworth, 1965). These deeply incised valleys expose a 2500 m succession of varied rock types, both intrusive and extrusive, detailing the history of this volcano over the last 2 my (Upton & Wadsworth, 1965, 1966, Zielinski, 1975, McDougall, 1971). The stratigraphy of Réunion is given in table 4, which shows the main extrusive rock types within each group.

The volcanic rocks of Mauritius can be divided into three distinct series, separated by two periods of quiescence. Younger Series rocks makes up the majority of the exposure on the island, whereas the volumetrically small Intermediate Series lavas are confined to the south-west of the island. The exposed remnants of the shield-forming Older Series form the mountains and the floors of deeply incised valleys.

Although the majority of the Réunion lavas lie to the hypersthene side of the 'critical plane of silica undersaturation' of Yoder & Tilley (1962) (Fisk *et al.*, 1988), some are quartz-normative (Upton, 1982). The shield lavas (older series) of both islands are transitional (between alkali and tholeiitic) olivine basalts (as defined by Macdonald & Katsura, 1964 for Hawaii) (Upton & Wadsworth, 1972a, Baxter, 1975).

The Mauritian Older Series are more alkaline compared with Réunion, straddling the critical plane of silica undersaturation, and have normative olivine with either hypersthene or nepheline. Since the critical plane of silica undersaturation approximates to the position of the basaltic thermal divide, these lavas must have acquired their transitional character at pressures in excess of 8 Kb, beyond which the thermal divide does not operate (Baxter, 1975). Transitional basalts are not uncommon among oceanic island lavas and have been recorded, for example, from Réunion (Upton & Wadsworth, 1972a), Rodrigues (Baxter *et al.*, 1985), Torfajökull volcano, Iceland (Macdonald *et al.*, 1990) and Anjouan in the Comores archipelago (Flower, 1973, Strong, 1972a, b). Like Rodrigues and Anjouan, the lavas of Mauritius plot on an evolutionary trend towards the more alkali compositions, whereas those of Réunion and Torfajökull adopt a trend towards the more silica-saturated compositions. For both islands the phenocrysts suites are olivine ± chrome spinel ± augite ± plagioclase. Additionally kaersutite is present as a phenocryst phase on Mauritius (and also in lavas from Piton de la Neiges and Rodrigues) in some of the more evolved compositions (Baxter, 1975; Upton, pers. comm.).

Table 3 **Incompatible Element Ratios for the Indian Ocean and Deccan Traps Including Average Results for the Rodrigues Ridge**

Lava Group	Zr/Y	Ba/Y	Zr/Ti	Ba/TiO_2	Nb/Y	Nb/Zr	Ce/Y
Leg 115							
706C Upper	5.5	2.7	0.0128	38	0.50	0.0909	1.084
706C Lower	2.6	1.9	0.0092	42	0.26	0.1031	0.417
707C Upper	1.42	0.72	0.0069	21	0.10	0.0833	0.005
707C Lower	2.39	0.99	0.0094	23	0.18	0.0714	0.220
713 Upper	2.50	1.35	0.0109	35	0.17	0.0714	0.251
713 Lower	2.10	1.03	0.0087	26	0.15	0.0714	0.147
715 low MgO	3.3	3.4	0.0100	62	0.39	0.1205	0.458
715 high MgO	3.0	3.4	0.0095	64	0.40	0.1333	0.407
General MORB	3	0.5	0.0125	20	0.06	0.0200	N/D
N-Type MORB	2.6	0.23	0.0097	5	0.08	0.0314	0.268
E-Type MORB	3.3	2.59	0.0122	57	0.38	0.1136	0.682
CIR							
Triple Junction	3.56	0.78	0.0133	19	0.09	0.0224	0.429
RR13	2.69	2.01	0.0117	48.9	0.11	0.0452	0.391
238 Argo FZ	1.2	0.18	0.0090	6	N/D	N/D	N/D
OIB	9.7	12.07	0.0164	122	1.66	0.1724	2.759
Seychelles	3.23	15.41	0.0078	227	0.45	0.0789	1.088
Réunion	6	5.6	0.0122	70	0.87	0.1333	1.582
Mauritius	5	8	0.0119	95	0.65	0.1351	
Rodrigues	6.0	18.01	0.0161	312	1.48	0.2439	1.889
Rodrigues Ridge:							
RR2 High MgO	3.01	0.62	0.0116	14.5	0.05	0.0174	0.343
Low MgO	2.64	0.66	0.0105	15.4	0.05	0.0179	0.354
RR3	2.75	1.31	0.0114	32.8	0.05	0.0183	0.309
RR4	3.75	3.83	0.0131	80.8	0.28	0.0740	0.659
RR8	4.55	5.42	0.0132	96.9	0.56	0.1225	1.211
RR9c	5.04	5.71	0.0137	92.5	0.51	0.1022	1.177
RR10	6.59	9.97	0.0117	104.9	1.10	0.1671	2.051
RR12	4.25	6.36	0.0218	196.9	0.59	0.1398	1.212
Deccan:							
Poladpur	4.0	3.9	0.0118	69	0.28	0.0714	N/D
Ambenali	3.8	2.0	0.0099	32	0.29	0.0833	N/D
Mahabaleshwar	4.5	4.3	0.0105	59	0.49	0.1075	N/D

Sources of data for table 3; Leg 24 lavas from Engel *et al.*, 1974, Rodrigues Island from Baxter *et al.*, 1985, Mauritius and general MORB from Baxter, 1990, Réunion from Upton & Wadsworth, 1972a and Fisk *et al.*, 1988, Deccan lavas from Cox & Hawkesworth, 1985, Seychelles from Devey & Stephens, 1991 and Devey & Stephens, 1992, E-type and N-type MORB and OIB from Sun & McDonough, 1989, Triple Junction lavas from Price *et al.*, 1986 and leg 115 lavas from Backman *et al.*, 1988.

Table 4. **Réunion Extrusive Rock Types**

Volcano and Series	Age	Rock Types
Réunion		
Piton de Neiges		
Differentiated Series	0.35-0.07 my.	Hawaiite, mugearite, rare trachytes and feldsparphyric basalts with interbedded pyroclastic deposits.
Younger Oceanite Series	2 my, 1.2-1 my and 0.55-0.43 my.	Olivine basalts with interbedded pyroclastics.
Older Oceanite Series	--	Zeolitized agglomerates, Porphyritic basalts.
Piton de la Fournaise		
Caldera Series	--	Olivine basalts and oceanites.
Primitive Shield	0.36 my.	Olivine basalts and oceanites, rare hawaiites, feldsparphyric basalts and ankaramites.
Mauritius		
Younger Series	0.7-0.2 my.	Mildly alkaline olivine basalt, some basanites.
Intermediate Series	3.5-2 my.	Alkali olivine basalts, Basanites and nephelinites.
Older Series	7.8-6.8 my.	Olivine basalt, oceanite and ankaramite intercalated with agglomerate, overlain by hawaiites, mugearites and feldsparphyric basalts.

Data from Upton & Wadsworth (1969 & 1972), McDougall (1971), McDougall & Chamalaun (1969) and Baxter (1972).

Figure 5 Major Element Variations for the Mauritian Older Series

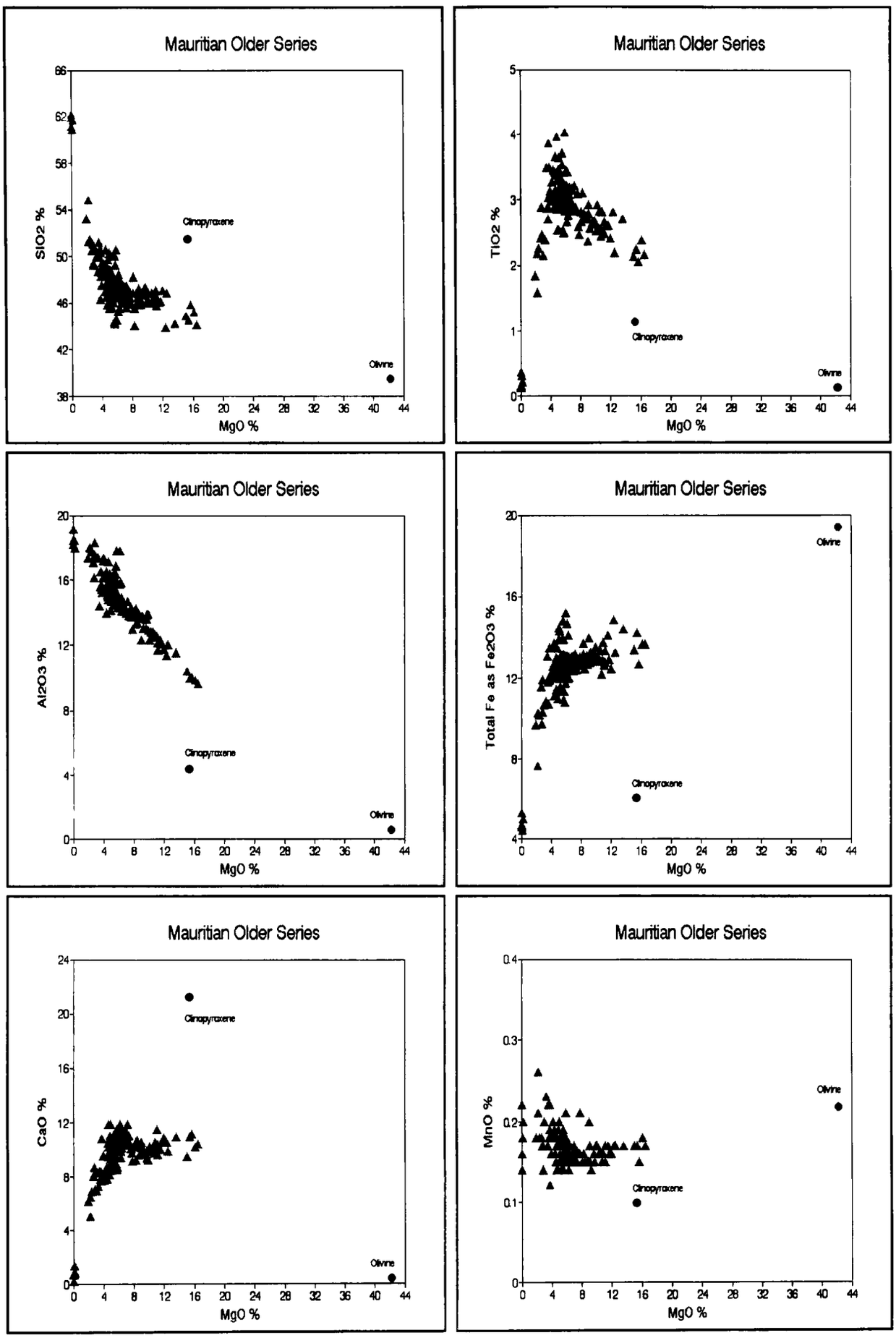

After Baxter (1975)

Figure 5 cont...

Major Element Variations for the Mauritian Older Series

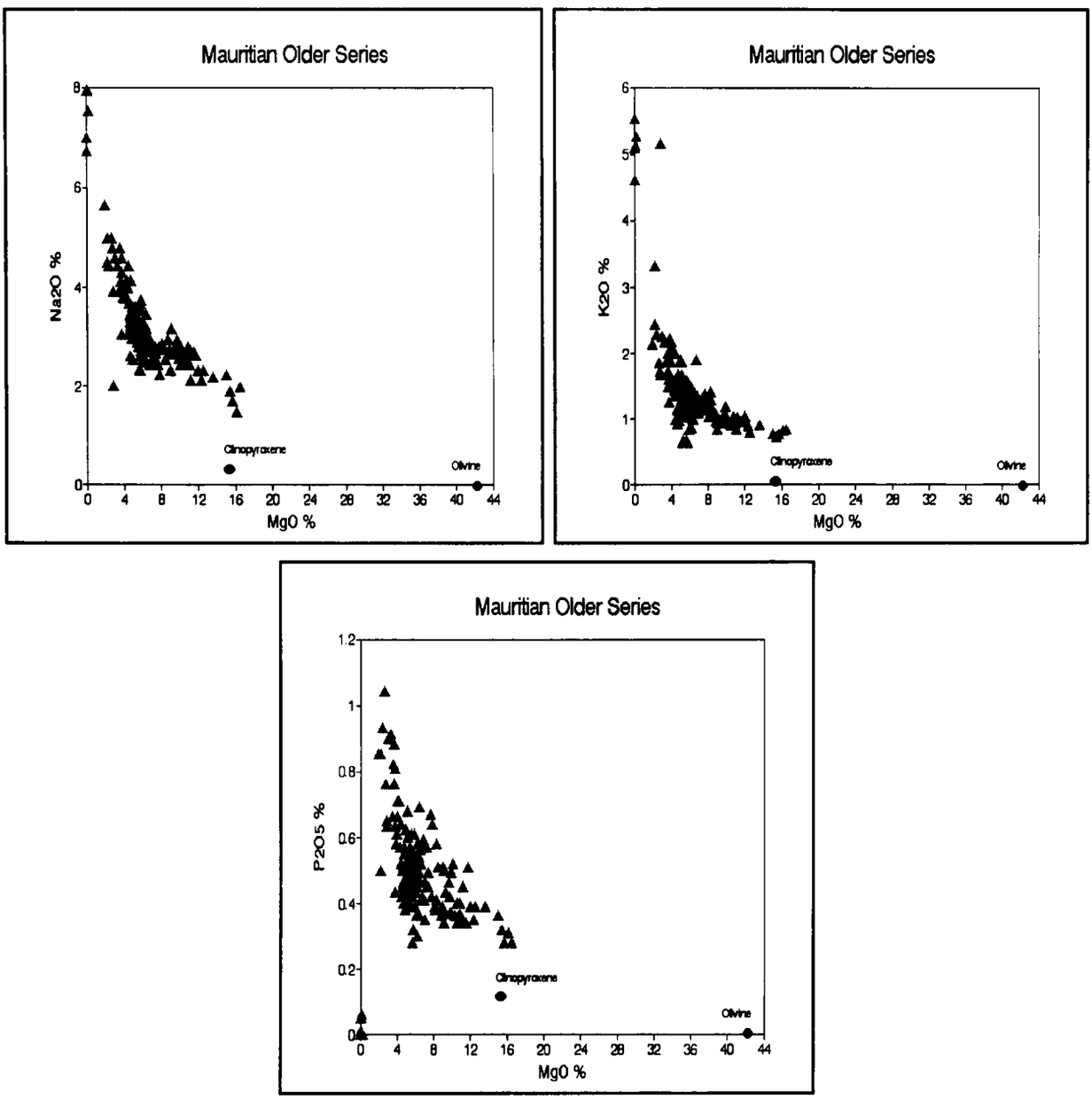

After Baxter (1975)

Figure 6 Trace Element Variation for the Mauritian Older Series

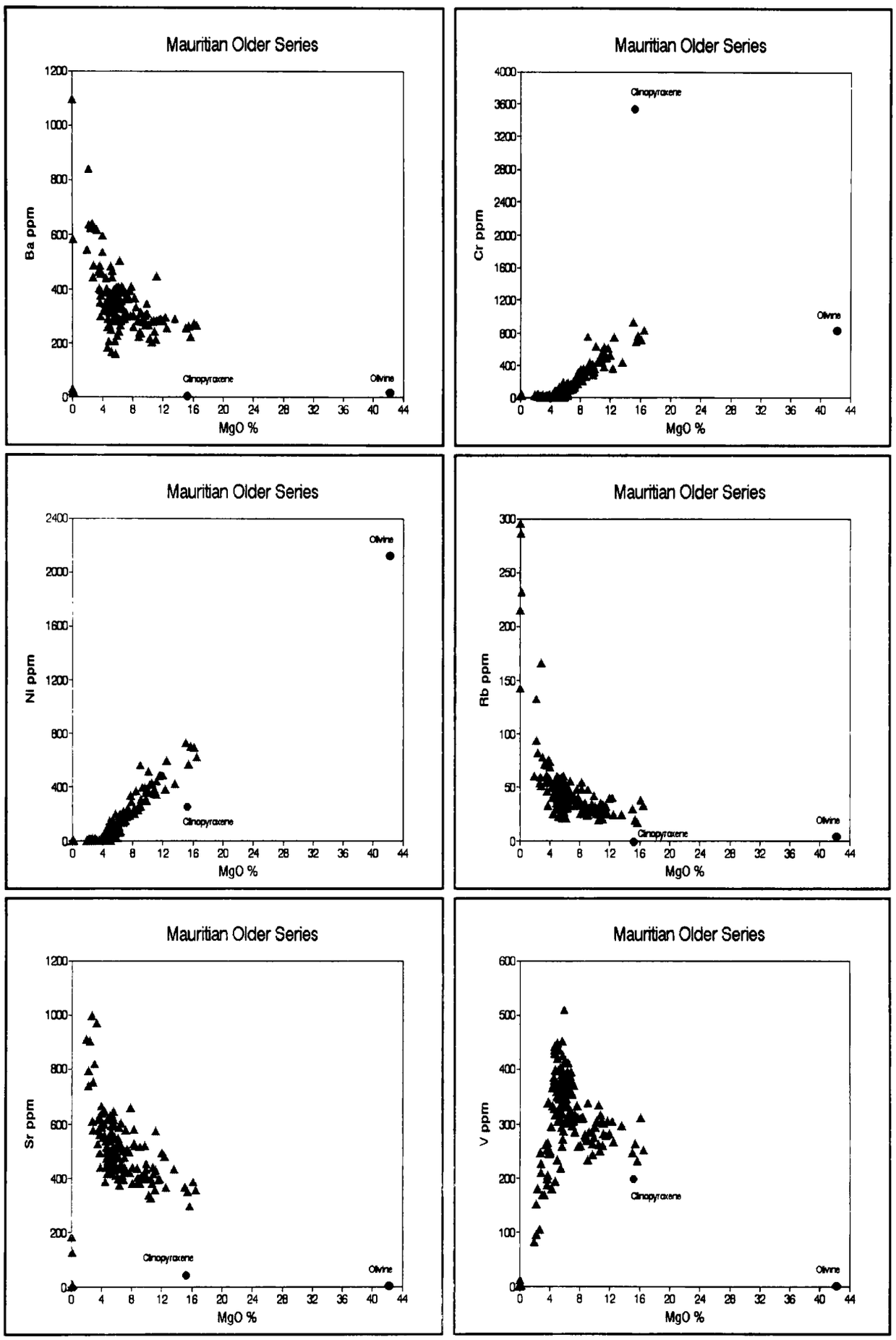

After Baxter (1975)

Figure 6 cont...

Trace Element Variation for the Mauritian Older Series

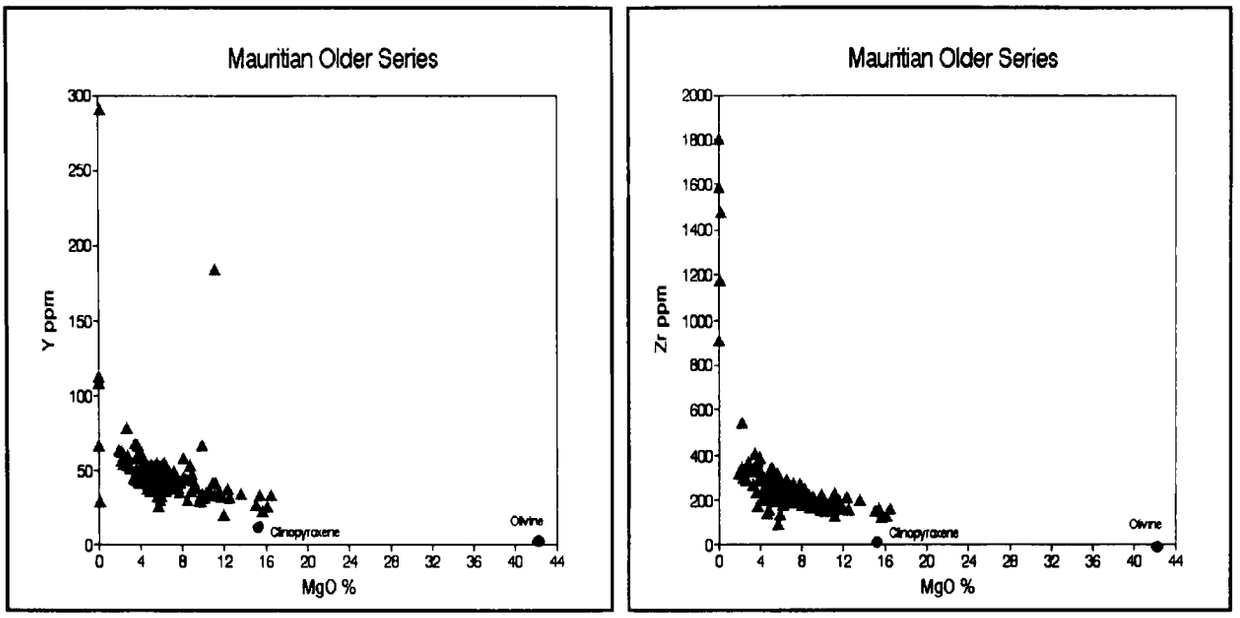

After Baxter (1975)

The major element chemistry of both Réunion and the Mauritian Older Series can be modelled by fractionation of olivine and clinopyroxene for those lavas with >5-6% MgO (Baxter, 1975 and Fisk *et al.*, 1988). For those lavas with lower MgO contents there is a change in trend coincident with the appearance of plagioclase and titanomagnetite as major phases in the phenocryst assemblage (fig. 5) (*op. cit.*). These conclusions are further reinforced by the trace element variation, particularly the compatible trace elements Cr and Ni. As would be expected, V mimics TiO_2 and FeO, *i.e.* with the onset of titanomagnetite fractionation it shows a sudden change from steadily increasing with declining MgO to sharply decreasing (fig. 6).

The Differentiated Series lavas of Piton de Neiges range from nepheline-normative basaltic compositions (Upton & Wadsworth, 1972a, Oversby, 1972, Upton & Wadsworth, 1966) to silica-saturated and oversaturated peralkaline rocks (Upton, 1982). The Differentiated Series can be separated from the more primitive Oceanite Series by a lower MgO content, usually <6%, whereas the Oceanite Series is usually >6%). These lavas show a pronounced deflection from the olivine control line resulting from the fractionation of the additional phenocryst phases plagioclase, augite and magnetite (Upton & Wadsworth, 1972a).

Chemically the Intermediate Series of Mauritius falls into a narrow compositional band for the major elements, except TiO_2 and K_2O. Clear major element trends are shown by CaO, P_2O_5, K_2O and TiO_2 which decrease with decreasing MgO, and by SiO_2 and Al_2O_3, which increase with decreasing MgO (Norry, 1973). The former trends are too steep to be the result of fractionation of the phenocryst olivine (fig. 7). [It should be noted here that the olivine composition used in fig. 7 is that of an Older Series olivine phenocryst, with a similar Fo content to those of the Intermediate Series.] Among the

Figure 7

Major Element Variation

for the Mauritian Intermediate Series

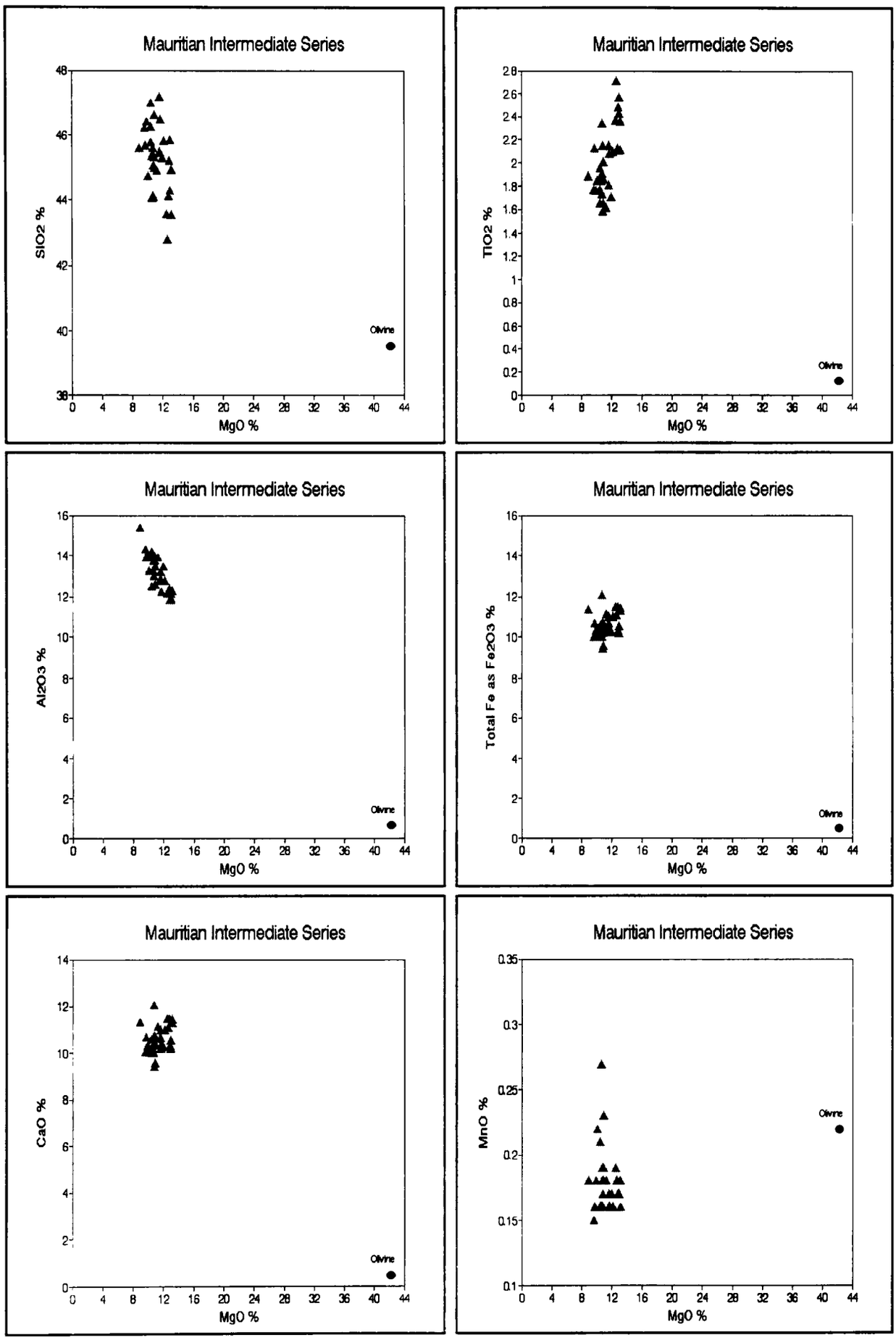

After Baxter (1976)

Figure 7 cont... Major Element Variation for the Mauritian Intermediate Series

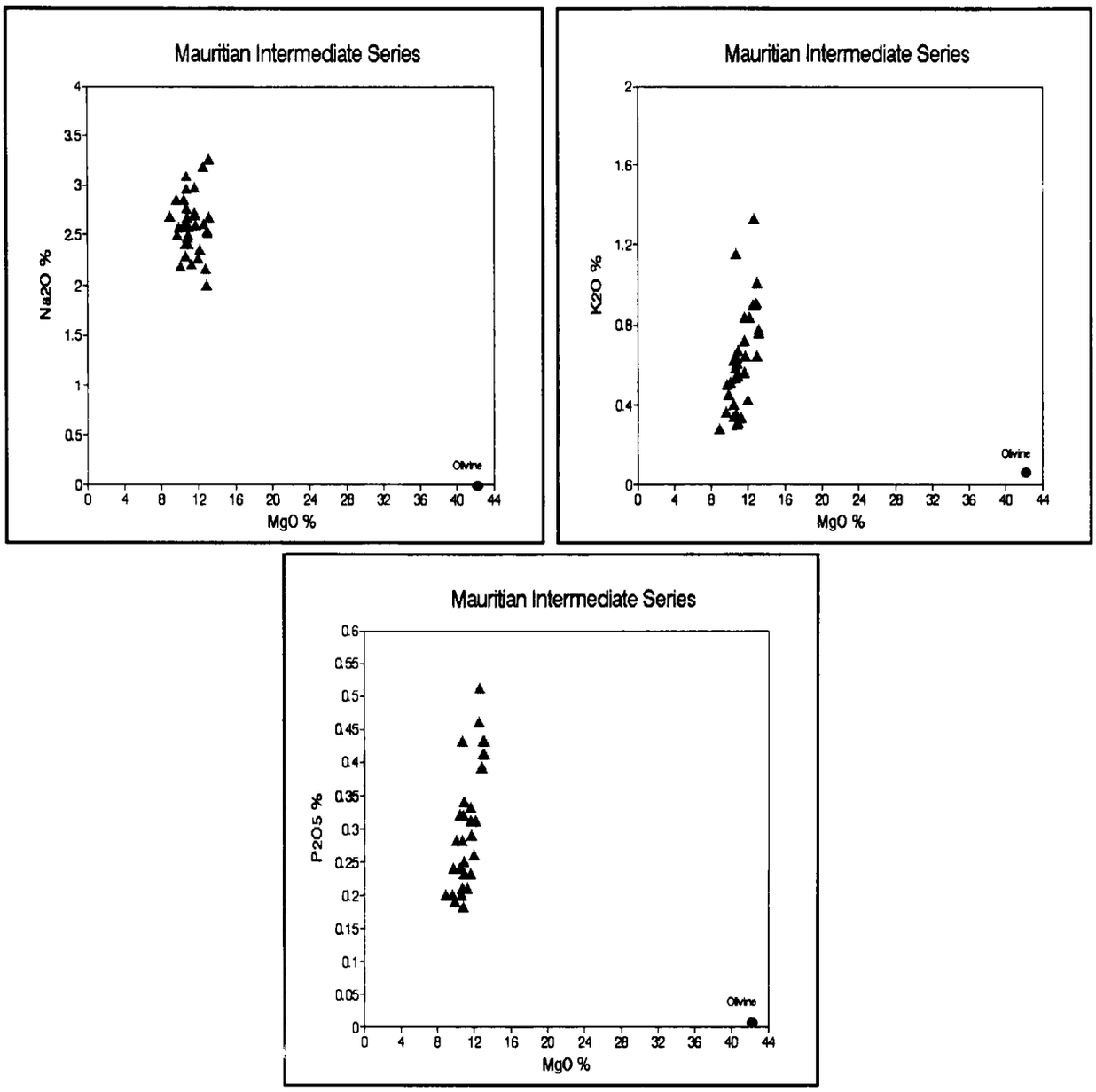

After Baxter (1976)

trace elements, a distinct positive correlation exists between Ba, Sr, Rb and Zr, and MgO. When considered in conjunction with the major element characteristics of these lavas it is concluded that they are the products of an earlier high pressure enrichment process (Baxter, 1976). These lavas form a rare suite of melts unmodified by high-level processes, which are apparently the products of variation in the degree of partial melting. The correlation between Rb and Rb/Sr is very significant in this respect since Rb should go in to the melt more readily than Sr during partial melting. Gradually increasing the small degree of melting should result in the observed positive linear correlation (Baxter, 1976).

Within the Younger Series, the oxidation and leaching of MgO and SiO_2, and the addition of water, lead to olivine phenocrysts frequently being pseudomorphed by iddingsite (Green pers. comm. and

Norry, 1973 unpubl.) as it does on Rodrigues and the Rodrigues Ridge. The Younger Series lavas have a transitional character with high-level fractionation of olivine controlling the majority of the major element chemical diversity. The evolutionary history of the Younger Series reflects that of the Intermediate Series (high pressure enrichment), with some low pressure olivine fractionation overprinting this (Baxter, 1976).

Figure 8 Experimental Phase Diagrams for Réunion

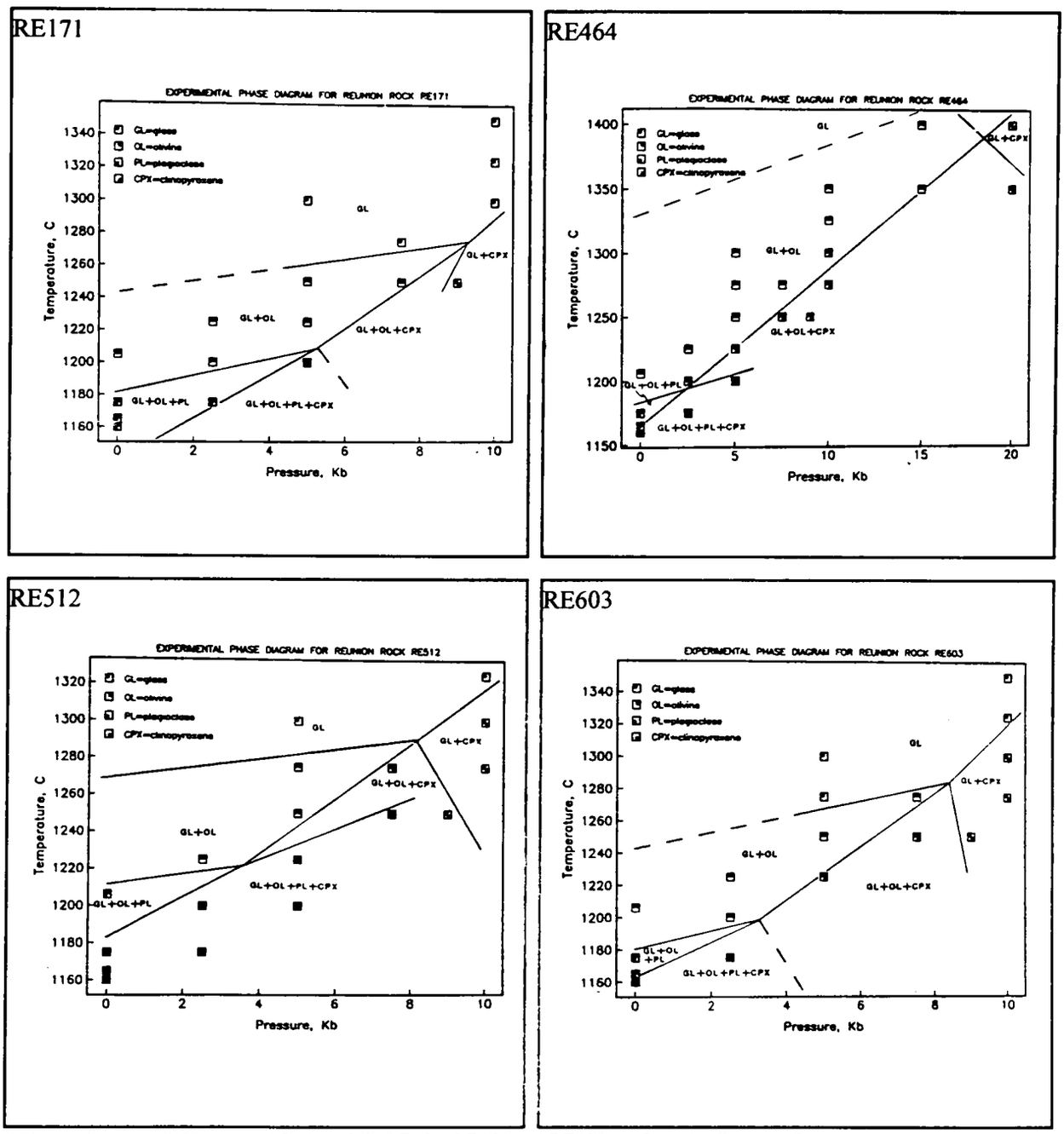

RE512 is from the Differentiated Series while RE171, RE464 and RE603 are from the Oceanite Series.

After Fisk *et al.* (1988)

Experimental studies on Piton de Neiges lavas showed that crystallisation sequences at low pressure

(0-5 kbar) was olivine→plagioclase→clinopyroxene. At higher pressure (5-8 kbar) the experimental sequence was olivine→clinopyroxene, whereas above 8 kbar augite was the only liquidus phase (Fisk *et al.*, 1988). The chemical evidence shows that olivine is the dominant liquidus phase at low pressure and that augite was the second most important, leading to the conclusion that fractionation of these lavas took place at pressures greater than 3-5 kbar (Fisk *et al.*, 1988) (fig. 8). For the Mauritian lavas the principal crystallisation sequences are:- olivine ± clinopyroxene ± plagioclase for the Older Series, ± chrome spinel + olivine ± clinopyroxene for the Intermediate Series and ± chrome spinel + olivine ± plagioclase in the Younger Series.

1.7 The Central Indian Ridge

Sampling of the Central Indian Ridge is limited to one drill hole - DSDP (Deep Sea Drilling Project) Site 238 in the Argo Fracture Zone. In addition to this there have been several dredges, principally concentrated around the triple junction and the Vema, Marie-Celeste and Argo fracture Zones (fig. 1 and table 5).

Lavas from the CIR are aphyric to porphyritic transitional basalts, with the majority being porphyritic olivine tholeiites. The phenocryst assemblage present in these lavas is plagioclase ≥ olivine ≥ augite ± Cr spinel ± magnetite, of which only plagioclase, in the range labradorite-bytownite (Bezrukov *et al.*, 1966), is common. At the triple junction plagioclase aggregates are often nucleated on the olivine phenocrysts and occasionally partially enclosed by them; a feature also seen in the Rodrigues Ridge samples. Plagioclase in MORB commonly shows extreme inter-site and intra-site variation ($An_{67.2}$-$An_{92.3}$ in a single specimen) (Price *et al.*, 1986). These samples are deficient in highly incompatible elements and have low Ti/Zr and high Hf/Zr ratios making these basalts distinct from those found in other ocean basins (Price *et al.*, 1986).

The primitive mantle-normalized rare earth element (REE) patterns of the Triple Junction basalts are flat or slightly LREE enriched when compared to N-type MORB, which shows marked LREE depletion (fig. 9). The Zr/Ti ratios for the Triple Junction samples are exceptionally high (0.011-0.013, table 3) as a result of the high Zr values.

Figure 9 REE's for Indian Ocean Samples

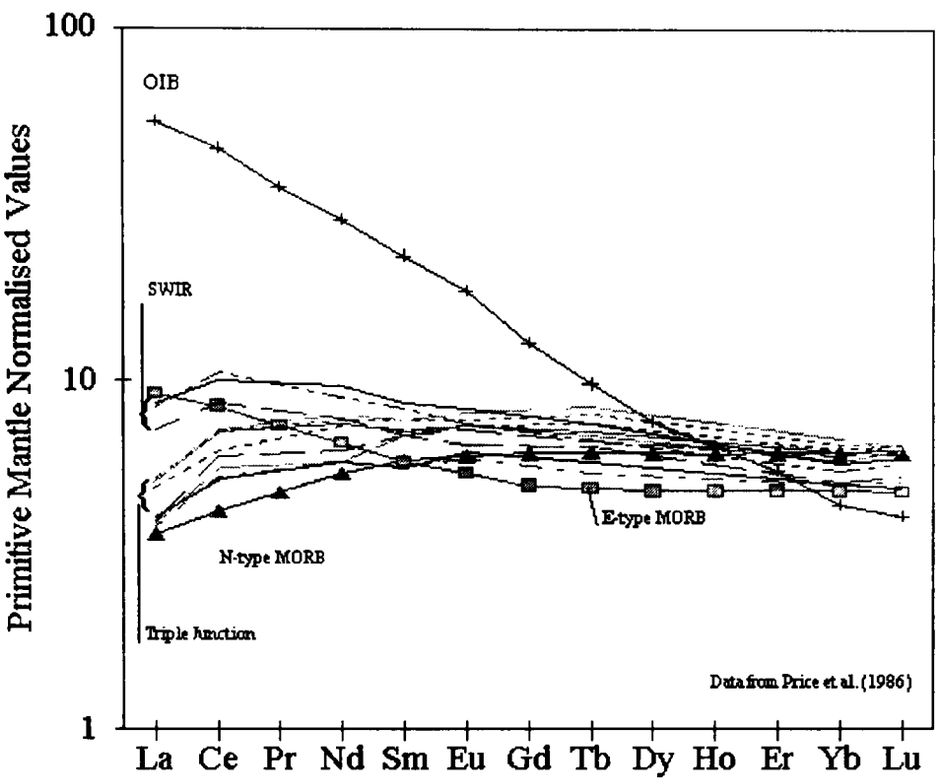

Primitive Mantle Normalising values used in fig.9 are those given by Sun & McDonough (1989)

Natland (1991) described three groups of Indian Ocean floor basalts, defined on the basis of their geochemistry and petrography. Type 1 formed on pre-Miocene spreading ridges, had low Na_2O and low TiO_2 for a given $Mg^{\#}$ (100MgO/MgO+FeO). Indeed these basalts have the lowest Na_2O values of any MORB so far analysed. Type 2 are more typical of oceanic tholeiites with respect to their Na_2O and TiO_2 contents. Type 3 basalts are found principally along the SWIR side of the Triple Junction. They have Na_2O values more typical of alkali basalts associated with high TiO_2 (Natland 1991). Mineralogically type 3 basalts have only olivine and Cr spinel phenocrysts, joined on the liquidus by plagioclase around An_{65} at $Mg^{\#}$ 0.65. In type 2 basalts both olivine and plagioclase are invariably on the liquidus with Cr spinel at higher $Mg^{\#}$. The type 1 samples have more fayalitic olivine with clinopyroxene, plagioclase (An_{85}) and bronzite (Natland, 1991 and Bloomer *et al.*, 1989). The presence of two high temperature (Mg) pyroxenes is generally uncommon among MORB's but has been reported in the North Atlantic (Sigurdson & Brown, 1970) and the East Pacific (Perfit & Fornari, 1983).

Table 5. **Analyses of Selected Lavas for the Indian Ocean and the Deccan Traps**

	Leg 115								Ambenali Formation	
	706C 6R-2 17-19	706C 9R-2 36-39	707C 23R-1 24-27	707C 26R-6 115-118	713A 13R-1 63-69	713A 20R-5 24-28	715A 24R-2 30-38	715A 29R-2 42-48	ABC12	ABC26
SiO_2	47.27	48.99	49.92	49.88	49.57	49.41	48.62	48.55	48.43	49.96
TiO_2	3.46	1.13	0.65	1.39	1.40	0.99	2.18	1.31	2.73	1.80
Al_2O_3	13.88	18.55	16.22	14.41	15.35	15.54	14.18	15.54	13.20	14.76
FeO^*	--	--	--	--	--	--	--	--	--	--
$Fe_2O_3^*$	16.16	9.94	10.18	14.27	12.07	10.88	15.84	12.12	16.34	13.52
MnO	0.23	0.13	0.10	0.19	0.19	0.19	0.21	0.17	0.25	0.20
MgO	5.55	5.52	8.72	6.92	6.46	7.68	6.33	9.68	5.88	5.88
CaO	10.30	13.10	12.24	11.32	13.10	13.21	10.28	10.90	10.27	11.33
Na_2O	2.67	2.21	1.88	2.10	2.24	1.94	2.24	1.93	2.41	2.28
K_2O	0.38	0.37	0.05	0.08	0.26	0.06	0.28	0.21	0.25	0.11
P_2O_5	0.36	0.11	0.03	0.10	0.11	0.06	0.23	0.14	0.23	0.15
CO_2	--	--	--	--	--	--	--	--	--	--
H_2O	--	--	--	--	--	--	--	--	--	--
LOI	0.22	1.01	0.87	-0.27	0.55	0.71	--	--	--	--
Total %	100.48	101.06	100.86	100.39	101.30	100.67	100.39	100.55	99.99	99.99

Table 5 cont...

Analyses of Selected Lavas for the Indian Ocean and the Deccan Traps

	Leg 115								Ambenali Formation	
	706C	706C	707C	707C	713A	713A	715A	715A	ABC12	ABC26
	6R-2	9R-2	23R-1	26R-6	13R-1	20R-5	24R-2	29R-2		
	17-19	36-39	24-27	115-118	63-69	24-28	30-38	42-48		
Ba	133	61	85	37.6	40.2	21.9	123.4	76.4	95	80
Cr	21.3	24.6	173.1	85.6	202.3	108.6	75.6	333.3	--	--
Cu	125.2	121.5	137.5	232.3	193.4	152.1	154.8	91.8	196	177
Nb	23.7	6.9	1.8	5.7	6.0	3.9	15.5	9.5	14	8
Ni	44.4	48.6	101.5	66.5	92.3	71.9	70.8	174.0	63	62
Rb	2.7	6.2	0.8	0.1	4.3	1.0	2.9	1.5	7	1
Sc	--	--	--	--	--	--	--	--	--	--
Sr	283.2	152.3	104.4	95.2	105.0	102.6	122.2	140.2	240	210
Th	--	--	--	--	--	--	--	--	--	--
U	--	--	--	--	--	--	--	--	--	--
V	432.9	255.3	297.7	422.1	391.4	327.4	474.0	243.0	--	--
Y	46.6	24.6	18.3	34.3	35.9	25.3	43.9	26.3	35	30
Zn	148.1	77.8	69.2	102.6	100.6	79.1	119.6	79.7	112	87
Zr	265.1	62.0	27.9	80.1	90.7	52.1	136.2	77.2	142	102

Table 5 cont...

Analyses of Selected Lavas for the Indian Ocean and the Deccan Traps

Leg 115

Ambenali Formation

	706C 6R-2 17-19	706C 9R-2 36-39	707C 23R-1 24-27	707C 26R-6 115-118	713A 13R-1 63-69	713A 20R-5 24-28	715A 24R-2 30-38	715A 29R-2 42-48	ABC12	ABC26
La	--	--	--	--	--	--	--	--	--	--
Ce	53.6	11.4	0.1	5.6	9.8	2.5	14.4	14.1	--	--
Pr	--	--	--	--	--	--	--	--	--	--
Nd	--	--	--	--	--	--	--	--	20.9	15.0
Sm	--	--	--	--	--	--	--	--	5.74	4.22
Eu	--	--	--	--	--	--	--	--	--	--
Gd	--	--	--	--	--	--	--	--	--	--
Tb	--	--	--	--	--	--	--	--	--	--
Dy	--	--	--	--	--	--	--	--	--	--
Ho	--	--	--	--	--	--	--	--	--	--
Er	--	--	--	--	--	--	--	--	--	--
Yb	--	--	--	--	--	--	--	--	--	--
Lu	--	--	--	--	--	--	--	--	--	--

Table 5 cont... **Analyses of Selected Lavas for the Indian Ocean and the Deccan Traps**

	Réunion Piton de Neiges	Réunion Piton de la Fournaise	Rodrigues Island	Rodrigues Island	Mauritius Older Series	Mauritius Younger Series	Rodrigues Ridge	Rodrigues Ridge	Triple Junction	DSDP Site 238	DSDP Site 238
	RE603	RE760	Rd67	Rd99	A91	C29	RR2.2	RR9c.36	12/16	57-3(7)	55-2(3)
SiO_2	48.55	47.02	47.29	48.62	47.58	46.48	47.41	47.20	50.82	48.60	48.50
TiO_2	2.35	2.38	1.86	1.50	3.00	1.83	1.29	1.49	1.42	1.30	1.10
Al_2O_3	13.18	12.23	16.01	15.74	14.81	15.70	17.20	16.05	15.77	14.75	14.45
FeO^*	--	--	--	--	6.09	10.13	--	--	7.24	7.90	5.57
$Fe_2O_3^*$	12.72	13.51	10.15	11.07	5.30	1.39	11.38	11.05	1.92	3.45	5.31
MnO	0.18	0.18	0.13	0.16	0.16	0.16	0.18	0.11	0.17	0.17	0.17
MgO	9.74	11.62	8.81	10.29	6.23	8.35	8.17	8.52	7.82	6.94	7.70
CaO	10.91	10.79	9.04	8.41	10.81	11.62	11.13	9.99	11.21	12.25	12.86
Na_2O	2.44	2.15	3.44	3.03	2.81	2.87	2.97	2.94	3.06	2.42	2.16
K_2O	0.62	0.70	1.58	1.34	1.37	0.33	0.11	0.69	0.10	0.06	0.22
P_2O_5	0.28	0.26	0.39	0.36	0.47	0.21	0.11	0.25	0.17	--	--
CO_2	--	--	0.18	0.21	--	--	0.22	0.77	0.04	--	--
H_2O	--	--	1.34	0.65	1.24	0.46	0.56	1.59	0.11	1.70	1.61
LOI	0.00	0.00	--	--	--	--	0.12	1.56	--	--	--
Total %	100.97	100.94	100.21	100.71	99.87	99.53	100.08	99.86	100.13	99.54	99.65

Table 5 cont... **Analyses of Selected Lavas for the Indian Ocean and the Deccan Traps**

	Réunion Piton de Neiges	Réunion Piton de la Fournaise	Rodrigues Island	Rodrigues Island	Mauritius Older Series	Mauritius Younger Series	Rodrigues Ridge	Rodrigues Ridge	Triple Junction	DSDP Site 238	DSDP Site 238
	RE603	RE760	Rd67	Rd99	A91	C29	RR2.2	RR9c.36	12/16	57-3(7)	55-2(3)
Ba	144	151	409	467	363	137	14.2	125.8	17	8	6
Cr	472	682	276	386	129	237	425.9	297.4	285	300	300
Cs	0.35	--	--	--	--	--	--	--	--	--	--
Cu	98	92	60	61	--	--	78.9	86.4	57	110	110
Nb	20	20	40	34	--	--	15.0	21.0	2.4	--	--
Ni	244	301	179	277	147	149	217.7	326.3	105	85	160
Pb	--	--	6.7	4.8	--	--	--	--	3.4	13	9
Rb	14	18	40	34	46	4	5.5	21.1	1.0	--	--
Sc	35	36	25	23	--	--	35.6	27.7	34.2	52	55
Sr	324	310	424	382	533	326	150.9	383.1	135	170	130
Th	3	2	4.6	2.8	--	--	0.12	1.08	--	--	--
U	--	--	--	--	--	--	0.08	0.37	--	--	--
V	321	319	170	161	346	261	222.6	206.1	279	240	210
Y	26	25	25	27	41	34	29.8	25.0	33.7	40	36
Zn	100	103	68	79	--	--	104.9	83.5	79	--	--
Zr	168	159	166	156	261	86	118.8	144.9	104	48	40

Table 5 cont... **Analyses of Selected Lavas for the Indian Ocean and the Deccan Traps**

	Réunion Piton de Neiges	Réunion Piton de la Fournaise	Rodrigues Island	Rodrigues Island	Mauritius Older Series	Mauritius Younger Series	Rodrigues Ridge	Rodrigues Ridge	Triple Junction	DSDP Site 238	DSDP Site 238
	RE603	RE760	Rd67	Rd99	A91	C29	RR2.2	RR9c.36	12/16	57-3(7)	55-2(3)
La	18	17	29	25	--	--	1.04	12.02	3.60	--	--
Ce	36	31	52	44	--	--	8.83	28.32	12.6	--	--
Pr	--	--	--	--	--	--	0.81	1.96	--	--	--
Nd	20	18	24	20	--	--	8.09	13.43	10.3	--	--
Sm	5.6	--	--	--	--	--	2.36	3.41	3.4	--	--
Eu	1.9	--	--	--	--	--	1.13	1.26	1.3	--	--
Gd	5.8	--	--	--	--	--	4.16	4.22	--	--	--
Tb	--	--	--	--	--	--	0.59	0.56	0.86	--	--
Dy	5.2	--	--	--	--	--	5.05	4.18	--	--	--
Ho	--	--	--	--	--	--	1.18	0.89	--	--	--
Er	2.6	--	--	--	--	--	3.01	2.33	--	--	--
Yb	2.1	--	--	--	--	--	3.37	2.33	3.27	4	3
Lu	0.31	--	--	--	--	--	0.38	0.32	0.49	--	--

References: Backman *et al.* (1988), Baxter (1975), Baxter (1976), Baxter *et al.* (1985), Dmitriev (1974), Engel *et al.* (1974) and Fisk *et al.* (1988).

Figure 10 **Olivine-Diopside-Quartz (Ol-Di-Q) triangular plot for Indian Ocean basalt glasses**

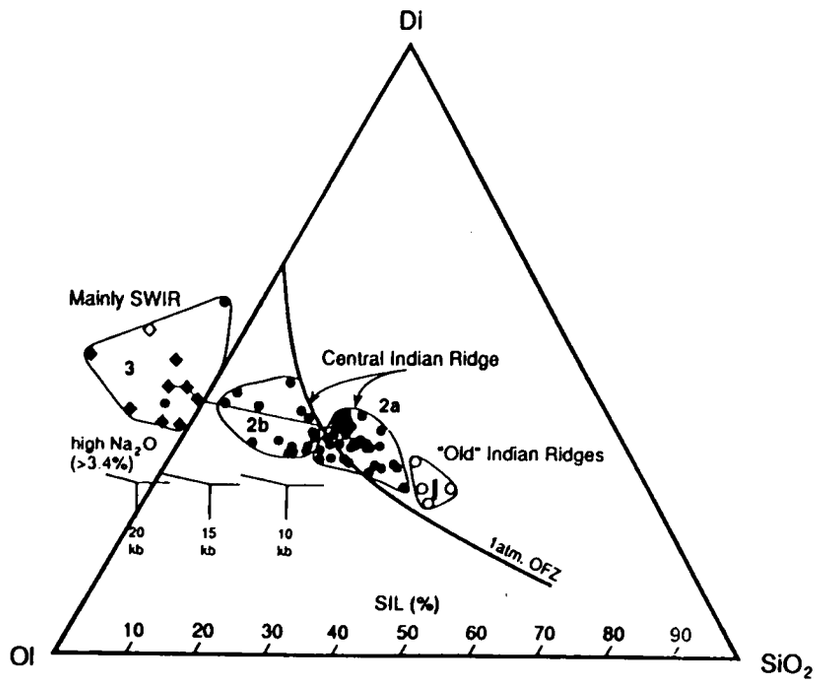

The bold line is the 1 atmosphere cotectic, the fine lines are the pseudo-invariant points for 10, 15 and 20 Kb, 1, 2 an 3 indicate the basalt type.

From Natland (1991).

On the Ol-Di-Q normative plot, type 3 lavas plot to the left of the Ol-Di join on the Ol side of the I atm cotectic, type 1 basalts plot on the Di side of the cotectic (in the centre of the diagram) and type 2 lavas fall between them (fig. 10). The three types form three distinct evolutionary paths, with the matrix plagioclases becoming increasingly sodic from type 1 to type 3, for a fixed $Mg^{\#}$ (Natland, 1991). On the basis of the liquidus mineralogy, Natland (1991) predicted the cumulates underlying the type 3 lavas of the SWIR would consist of two layers, one made up of dunites or possibly chromitites and troctolites, overlain by the second layer consisting of olivine gabbros and gabbro-norites. ODP hole 735B on the SWIR yielded a sequence of olivine and Fe-Ti gabbros underlain by olivine gabbros and troctolites (Robinson *et al.*, 1989). The crystallisation sequence for type 1 basalts is olivine→plagioclase→Mg-pyroxene suggesting that they represent shallow depths of partial melting. Types 2 and 3 basalts are derived from progressively deeper levels (Natland, 1991). Although not tested experimentally, low pressure crystallisation of similar refractory, silica-rich melts is thought to be responsible for some of the gabbros containing high-Mg pyroxene at the Mid-Indian Ocean Ridge (MIOR, this includes the CIR the Carlsberg Ridge and both Southeast and Southwest Indian Ridges) fracture zones (Bloomer *et al.*, 1989).

1.8 Previous Studies of the Rodrigues Ridge

In the mid-1960's it was suggested that the Rodrigues Ridge formed the southern flank of a major east-west trending `Rodrigues Fracture Zone,' (Heezen & Tharp, 1964, 1965 and 1966) [NB McKenzie & Sclater (1971) prefer to reserve this name for the larger fracture zone at 21°S]. The relationship between the Rodrigues Ridge and the fracture zone was apparently supported by an anomalously low heat flow north of 20-21°S (von Herzen & Vacquier, 1966) and high values immediately to the south of this (Fisher *et al.*, 1967). The fracture zone model was initially supported by several other authors (Fisher *et al.*, 1967, Le Pichon & Heirtzler, 1968 and Perroud, 1982 unpubl.). With the improved bathymetry available in the mid-1970s (Fisher *et al.*, 1971, Udintsev, 1975 and Hall, 1974) several authors (Fisher *et al.*, 1971, McKenzie & Sclater, 1971, and Schlich, 1982) raised objection to the fracture zone model, since the CIR fracture zones trend at 050° and not the 090° of the Rodrigues Ridge. Both Fisher *et al.* (1971) and McKenzie & Sclater (1971) had identified anomaly 5, east of the Rodrigues Ridge, which led Fisher (*op cit.*) to conclude that the Rodrigues Ridge was "a later feature not pertinent to the tectonics of the CIR." McKenzie & Sclater (1971) concluded that the Rodrigues Ridge was related by some complex mechanism to the triple junction, but were unable to elaborate any further on this.

Morgan (1978) proposed that magma was channelled away from the Réunion hotspot to the CIR as a consequence of their proximity to one another. In his model an asthenospheric jet or flow would be drawn from the hotspot (source) by the shortest route to the spreading ridge (sink). This would result in the development of a seamount on the CIR. Addition of the spreading vectors for the CIR and South West Indian Ridge (SWIR) gives a net east-west motion, hence the trace of such activity would also be east-west. According to this model the Rodrigues Ridge should be oldest in the west and should be of the same age as the ocean floor immediately alongside it. Bonneville *et al.* (1988), based on the age of the surrounding ocean floor, and supported by the Rodrigues Ridge's low rigidity ($<1x10^{+22}$ Nm) correctly suggested that the age of the Ridge was 10 my. Like Morgan, he, speculated that channelling of sublithospheric melt from the Réunion hotspot formed the Rodrigues Ridge. The dates in table 1 show no age progression along the Rodrigues Ridge and are therefore inconsistent with the views of Morgan (1978) and Bonneville *et al.* (1988). Several authors (Perroud, 1982, Morgan, 1978) have suggested that Rodrigues Island, whose lavas are dated at 1.5-1.3 my (McDougall *et al.*, 1965), is a rejuvenation of the `older guyot' (Rodrigues Ridge). Perroud also suggested a maximum age of 2 my for the island and an age of 7 my for the Rodrigues Ridge. This age for the island indicates simultaneous activity on all three Mascarene islands (Réunion, Mauritius and Rodrigues) (Schlich, 1982 and McDougall & Chamalaun, 1969). It should be noted, however, that the dates presented by McDougall *et al.* (1965) for Rodrigues island are bracketed by the quiescent period on Mauritius between the Intermediate and Younger Series.

Mahoney *et al.* (1989) show a pronounced Réunion-like spike in Pb, Sr and Nd isotope data along the

CIR, asymmetrically disposed about the Marie-Celeste Fracture Zone some 150 km north of the Rodrigues Ridge (fig. 11). Although they do not rule out Morgan's channelised asthenospheric flow model, they do point out that if such a channel exists then it must intersect the CIR at the Marie-Celeste Fracture Zone and not at the Rodrigues Ridge. Alternatively the isotopic spike, which they observed, may be the result of reduced partial melting and consequent enrichment of incompatible elements within the resulting magmas (Mahoney *et al.,* 1989 and Langmuir & Bender, 1984). Mahoney *et al.* (1989) suggested that if an asthenospheric 'channel' exists it is more likely to be a passive 'tongue' of Réunion-type mantle embedded in the asthenosphere, transported simply by convection parallel to the fracture zones of the CIR (*cf.* Schilling *et al.,* 1985 and Sleep, 1990). If the above hypothesis is true then the Réunion isotopic signature should be recognised in the lavas of the Rodrigues Ridge.

There are three other possible models for the formation of the Rodrigues Ridge:

(1.) the Ridge may be related to the reactivation of the north-north west trending Palaeocene spreading ridge at 18°50'N 55°00'E (fig. 1), by the Réunion hotspot. This model would produce a uniform age for the Rodrigues Ridge equivalent to the time of passage over the hotspot of about 16 my (Backman *et al.,* 1988 and Baxter *et al.,* 1989 unpubl.). As with other previously presented models this is inconsistent with the age data and with the evidence of a chemical trend from OIB-like lavas in the west to MORB-like lavas in the east (presented later). The reactivation of the Palaeocene spreading ridge might be expected to produce some mix of both OIB and MORB lavas along the length of the Ridge.

(2.) Backman *et al.* (1988) have suggested that the Rodrigues Ridge may be the trail of a younger and weaker hotspot than Réunion. They point out, however, that the trend of the Rodrigues Ridge seems somewhat inconsistent with a hotspot model. Furthermore, this model would require an age progression from young in the west to old in the east (opposite to that required by Morgan (1978)).

(3.) Baxter *et al.* (1989 unpubl). speculated on the presence of sublithospheric mixing of two magmatic sources or their products, one an Ocean Island Basalt (OIB) source (Réunion) and the other a Mid-Ocean Ridge Basalt (MORB) source (the CIR). Though the latter model fits the chemical evidence and does not negate the age data, the rheology of magmas is such that effective mixing of two such distant sources would require a magma body whose (three) dimensions were of similar size (see Bloomer & Meyer, 1992 and Oldenburg *et al.,* 1989). Such a magma body seems prohibitively large, and would be unlikely to produce a linear ridge.

The Rodrigues Ridge is then an anomalous feature, oblique to the tectonic fabric of the surrounding ocean floor. It represents a marked boundary between rugged ocean floor to the south, denuded of sediment by ocean bottom currents, and smooth sediment covered ocean floor to the north. To the east of the Rodrigues Ridge, the CIR is shallower than elsewhere along its crest (Morgan, 1978) and shown by GLORIA (Global Long Range Inclined Asdic) images to be of very regular morphology (Parsons pers. comm.). To the north the CIR is off-set by right lateral transforms and to the south by left lateral transforms, suggesting that it is still exerting an influence on the spreading ridge. Furthermore there is

Figure 11.

Sr, ϵ_{Nd} and Pb isotopes with latitude along the Indian Ocean Ridge System.

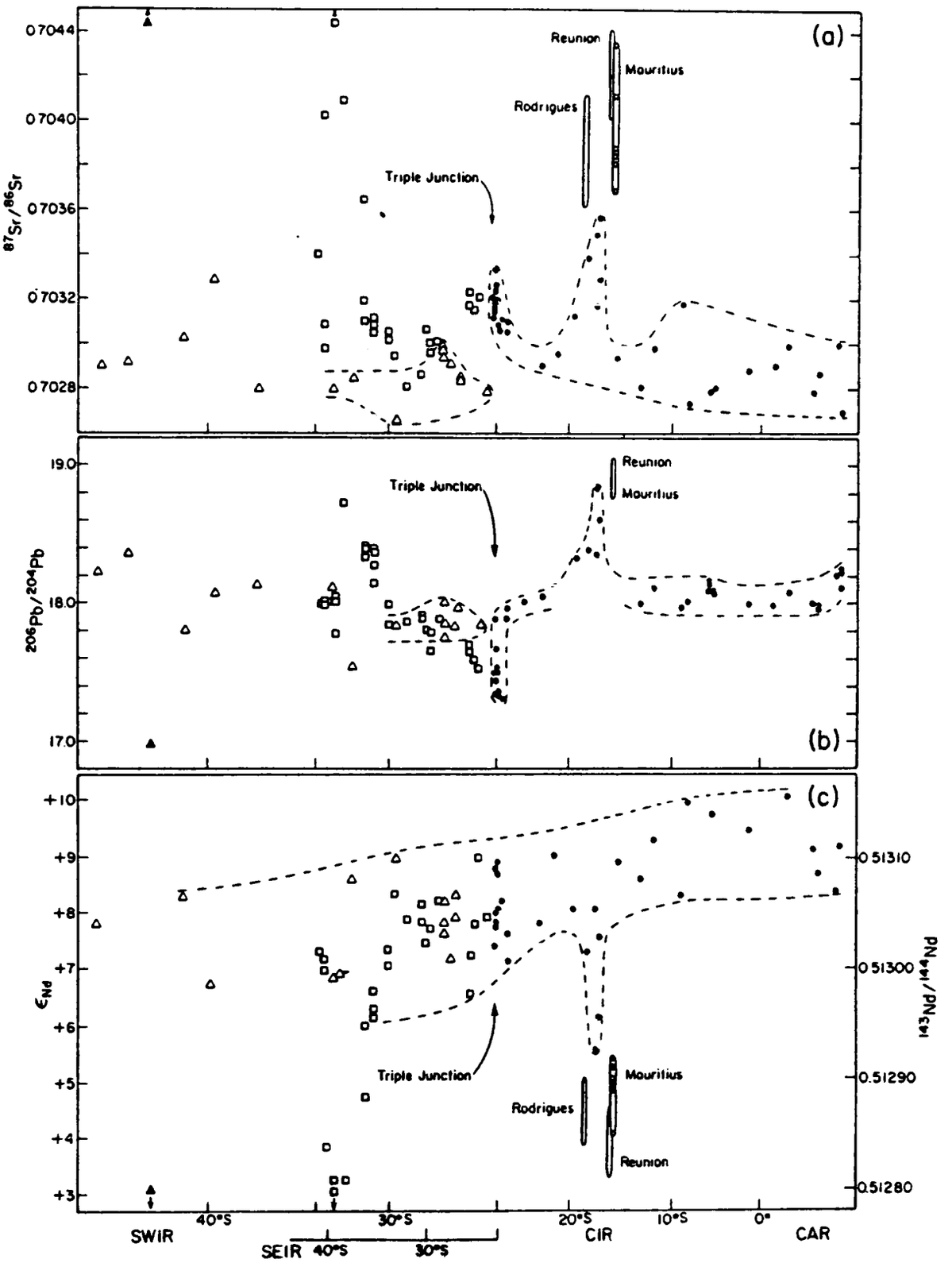

Variations of (a) $^{87}Sr/^{86}Sr$, (b) $^{206}Pb/^{204}Pb$ and (c) ϵ_{Nd} with distance along the Indian ridge crests from 5.5°N to 44°S. Triangles; South West Indian Ridge; squares, South East Indian Ridge; open circles, Mauritius; filled circles, Central Indian Ridge, Triple Junction and old deep sea drilling sites.

From Mahoney *et al.* (1989)

a localized gravimetric high situated immediately to the east of the Rodrigues Ridge on the Central Indian Ridge (Briais pers. comm.). Around 19°S 66°E the CIR is particularly shallow and is described as a "Rodrigues hotspot" by Parsons *et al.* (1993) and Briais (1994 unpubl.). This is the region where there is anomalously high heat flow (von Herzen & Vacquier, 1966) and a δ^3He spike (Jean-Baptiste *et al.*, 1992) which may be associate with hydrothermal activity.

1.9 Outline of Present Work

To understand the context of the mineralogical and geochemical data presented in chapters 3-6 it is necessary to first look at the Rodrigues Ridge as a whole, examining the seismic data collected during the 21/87 cruise in conjunction with the local bathymetry and the nature of the seabed geology. Once the physiography, mineralogy and geochemistry have been examined conclusions can then be drawn about the origins and evolution of the Rodrigues Ridge. Below is a brief outline of the content of the following chapters considering each of these aspects in tern.

Chapter 2 presents details of the local bathymetry, followed by an examination of the seismic profiles for ten transects of the Rodrigues Ridge. A local map is then constructed showing details of the seabed geology. Finally the locations of all the dredges which yielded igneous material are presented.

Chapter 3 examines the mineralogy of the samples recovered. This examination begins with an assessment of the alteration state of the suite as this is critical to the subsequent discussion. There follows an examination of the phenocryst mineralogy and then the matrix mineralogy. The chapter concludes with the presentation of representative analyses for the major minerals present in the suite as a whole.

Chapter 4 considers the geochemistry of the Rodrigues Ridge basalts. Initially their normative mineralogy is presented, then a complete list of the major, trace and rare earth elements, analysed for this work. The effects of alteration on the chemistry are examined in further detail, after which the geochemistry of each individual site is reviewed. Finally the relationships between each site are examined with particular emphasis on systematic variation with longitude.

Chapter 5 considers the radiogenic isotope characteristics of a subset of 21 samples.

Chapter 6 begins with an attempt to model the major and trace element characteristics of each site using the observed phenocryst minerals. The incompatible element ratios are then examined. These together with the isotope ratios for the Rodrigues Ridge are then compared with those of other near by volcanic features, including the Réunion hotspot trail, the CIR and Rodrigues Island. The lavas are then displayed in terms of the C-M-A-S quaternary system, and the nature of the melting regime is examined.

Finally chapter 7 presents a summary of the conclusions reached, together with a model for the formation of the structure.

Chapter 2

2. Bathymetry and Seismic Sections

2.1 Introduction

Having discussed the surrounding areas it is now appropriate to examine the bathymetry and seismic information available. Using data collected during the CD21/87 cruise and previously available data, a new bathymetric map has been constructed. This was used to locate the sampling sites (section 2.4) and the seismic lines described in sections 2.2 and 2.3.

2.2 Bathymetry

During the CD21/87 cruise of the RRS. Charles Darwin a total of 3632 km of bathymetric data were collected, together with 3.5 KHz sub-bottom profiles, gravity and magnetic data for most of this distance. In addition to this, 950 km of 48-channel seismic data were acquired in ten traverses across the Rodrigues Ridge.

The bathymetric chart of the Rodrigues Ridge (fig. 2) was constructed using data from the cruise CD21/87 with additional data from cruises A2015LO3, ANTIPO5MV, ANTIPO6MV, ANTIPO8MV, C1402, CIRCO6AR, CIRCO7AR, DME10, DSDP24GC, WI343728, MONSO3AR, ODP115JR, V2410, V2902, MONSO5, GGAL3, MMDNO, A2935 and A9311. All data were corrected to minimize the effects of variations in the speed of sound in sea water, resulting from regional variations in temperature and salinity, using the correction tables published by Carter (1980). Contours were added manually, assuming the more recent data to be more reliable. Only one major discrepancy was encountered; data from MONSO3AR deviated from other cruises between 19°31'S 58°30'E and 18°40'S 60°30'E, suggesting that the navigation on this track was suspect.

The new bathymetric chart has a number of modifications compared with those originally published by Fisher *et al.* (1967, 1971 and 1983 unpubl.) and Hall (1986). Most notable is the extension of the Rodrigues Ridge east by some 110 km to include the small seamounts reported by these authors. The eastern termination was not conclusively located but it was not thought to be significantly further east than shown in fig. 2. Other changes of note are the removal of the small pinnacle at 19°19'S 61°42'E and improved resolution of the NW-SE trending ridge bounding the Mascarene Plateau between 18°10'S and 18°40'S.

Figure 12

Rodrigues Ridge Site Location Map

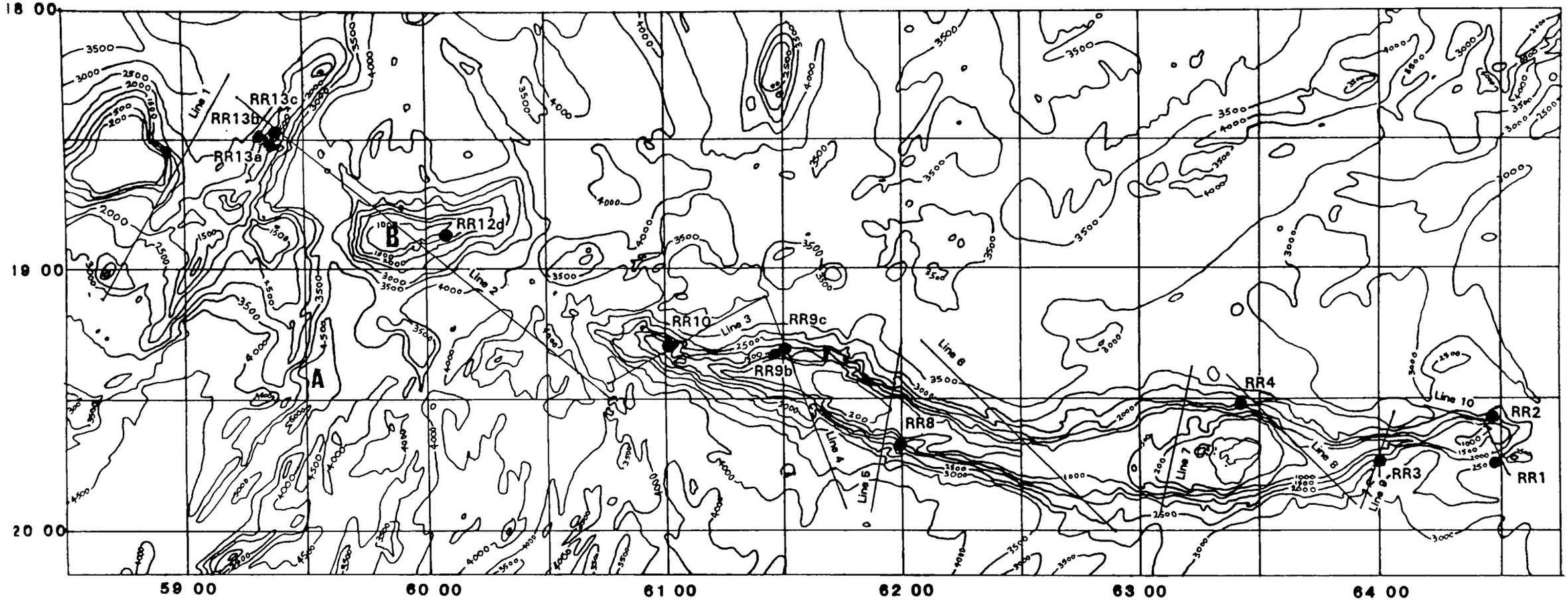

Mercator Projection

2.3 Seismic Sections

Ten lines of seismic data (fig. 12) totalling 8 days continuous recording over 48 channels were collected. Analogue records of channel 3 were used to make the preliminary interpretations discussed below. These interpretations have revealed several unconformities within the sedimentary sequence, indicating a complex history of post-volcanic movements, possibly associated with sea-level fluctuations. On all seismic lines an unconformity between 0.200 and 0.350 sec. 2-way time has been identified. Some tilting of the Ridge has taken place during this break in deposition, resulting in the development of an angular unconformity and the burying of a patch reef. In addition a second unconformity at 0.100 sec. is recognized in lines 1 and 4. Lines 1, 2, 9 and 10 show an unconformity at about >0.375 sec., with lines 6 and 9 showing one at about 0.500 sec. Line 9 also shows an unconformity at 0.475 sec. not seen on any of the other lines. The Ridge flanks show slump and slip units which have occasionally resulted in roll-over folding and chaotic units. The latter are very common and often obscure all other structures below them.

Numerous small en-echelon faults are present in the sediments on all lines; these seem to be facies-specific. Basement faults are also common, bounding the Ridge on both the north and the south on many of the lines. In addition there are at least two major fracture zones, as discussed by Bonneville *et al.* (1988).

The sediment-basement contact has been tentatively identified in those flank regions where slumping is not so extensive as to obscure all underlying reflectors; multiple reflections obscure it below the Ridge crest on most records. Also worthy of note is the tendency of some sedimentary units to dip gently towards the ridge (*eg.*. line 4) which may be due to isostatic readjustment as a result of the loading of the oceanic lithosphere in this area. It has been observed that the free air gravity anomalies do not show the large negative anomaly normally associated with aseismic ridges of this age (Heward. *pers. comm* 1989).

The discussions presented below represent the preliminary interpretations of the seismic data which forms the basis of a PhD thesis by G. Heward.

In the following discussion seafloor slopes, where mentioned, have been recalculated from the diagrams which show immense vertical exaggeration to give a true picture. Once vertical exaggeration had been removed, the technique described in appendix 2 was employed to assess the true slope.

LINE 1:- MASCARENE PLATEAU (Fig. 13)

The basement in both the southern and central parts of this line is fairly shallow or exposed at <1.000 sec. 2-way time. The overlying sediments are slumped and contain numerous small faults associated with the slumping. An unconformity is present throughout this section at about 0.250 sec. In the central sedimentary basin a second unconformity is also present at 0.100 sec.

Figure 13 Seismic Line 1

South North

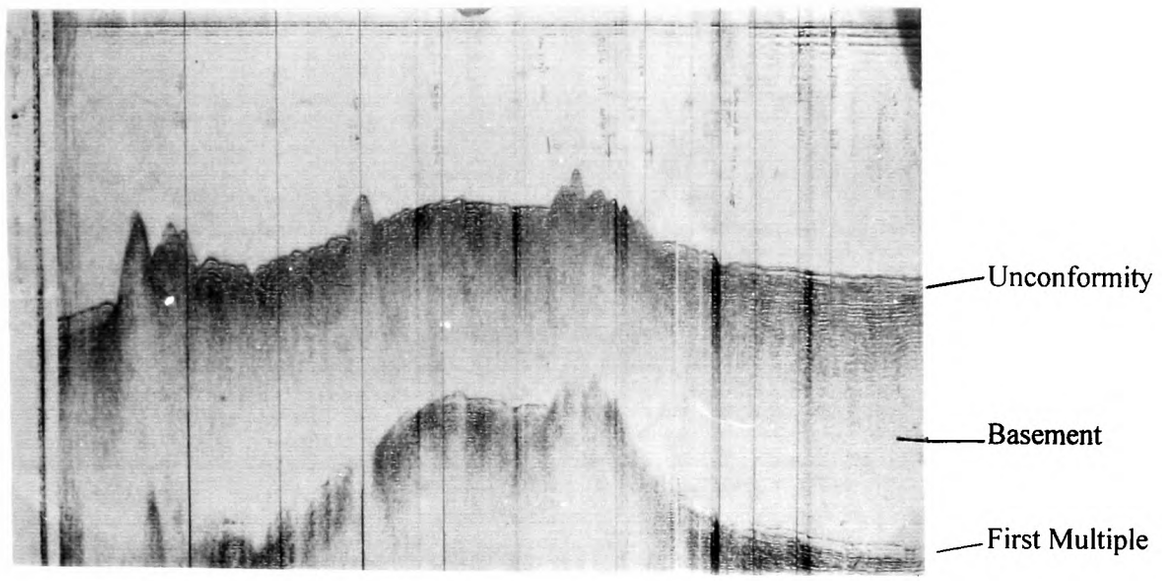

Figure 15 Seismic Line 3

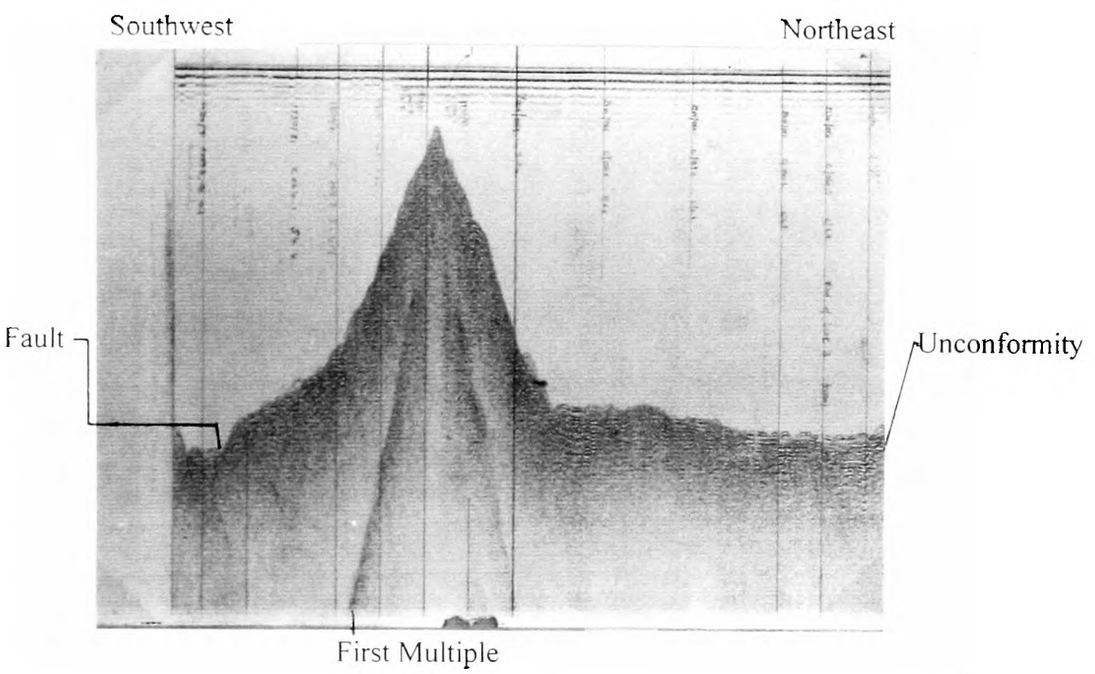

Figure 14

Seismic Line 2

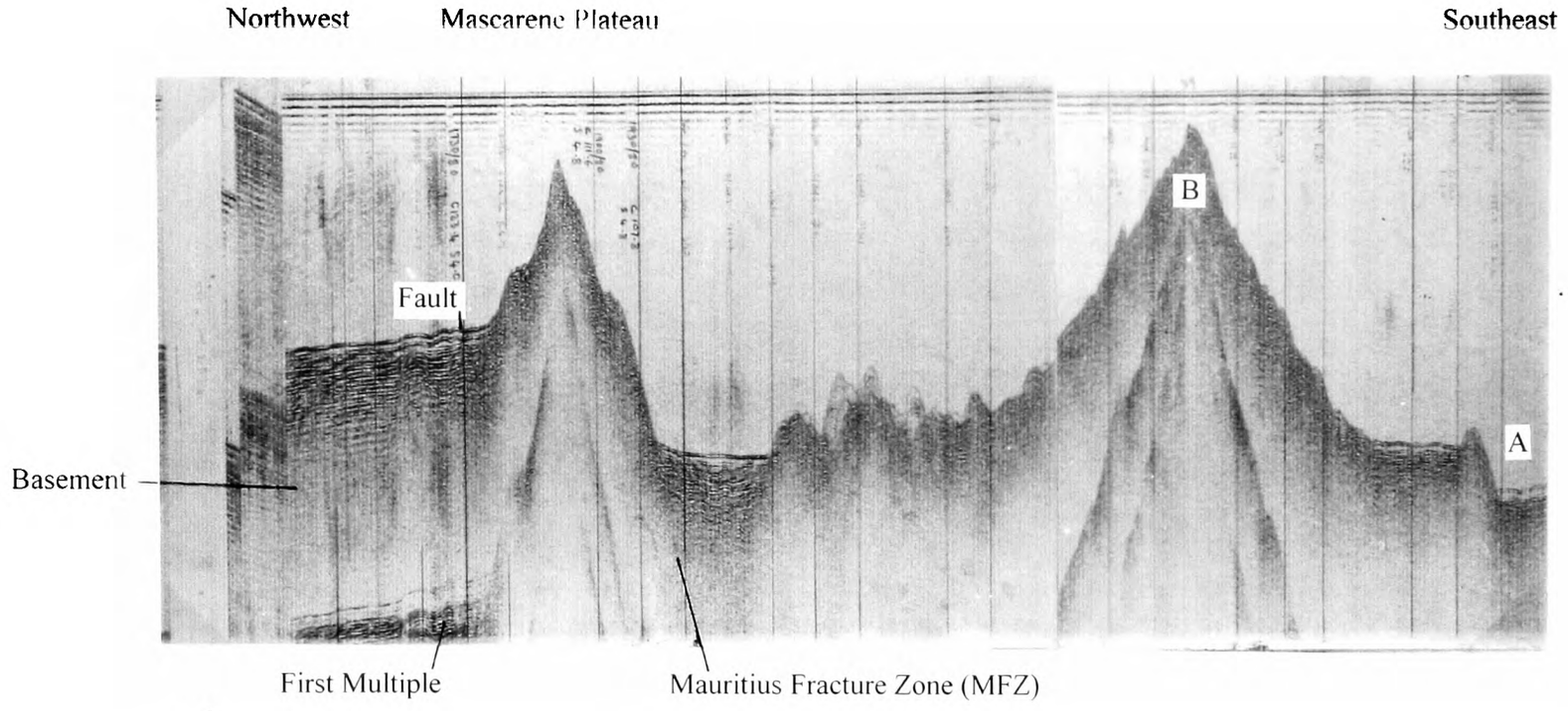

To the north there is a thicker sedimentary basin (about 2.000 sec.) which is the thickest sequence recognised on any of the sections from this cruise. This is disrupted by many small faults, some of which are associated with slumping. Listric normal faults are common and seem to be sensitive to seismic facies, often terminating against strong, apparently conformable, reflectors.

The basement has been marked in tentatively across this line though its precise location is unclear in places. It apparently surfaces as several irregular bodies in the south and central areas, usually capped with a veneer of chaotic slumped sediment. A single small fault is apparently present within the basement of the line, though its relationship with other structures cannot be demonstrated.

LINE 2 (Fig. 14)

This line (fig 12) forms an oblique traverse from the Mascarene Plateau in the northwest, running across the Mauritius Fracture Zone (MFZ) and the un-named isolated seamount (B, in fig. 12 at 18°50'S 60°00'E) which forms the most western extent of the Rodrigues Ridge, to an area of undisturbed seafloor at 19°30'S 60°48'E in the south. A second major fracture zone **(A)** southeast of the seamount **(B),** in a region of strongly faulted ocean floor, was crossed in addition to the MFZ,.

The sediment is thickest in the northwest, in the sedimentary basin seen at the end of line 1. A notable feature of this basin is a major basement growth fault with a normal component to its movement. The vertical throw of this fault is 0.400 sec. in the basement and 0.100 sec. at the sediment surface, down-thrown to the west, suggesting that it may be still active. Within the sediment this branching fault is accommodated by several en-echelon, low angle, listric normal faults.

The north western wall of the MFZ rises to about 750 metres below sea level and is covered by a thin layer of strongly disrupted sediment showing slump units on the north west flank. The MFZ is marked by a small sedimentary basin about 13 km wide, in which an unconformity at 0.250 sec. is observed. Unnamed seamount **(B)** is separated from the Mascarene Plateau by the MFZ. Like the north west wall of the MFZ, the seamount shows slump units on its flanks. Southeast of the seamount there is a small perched sedimentary basin (about 14 km across), containing some slumped sediments, whose southeast wall is made up of exposed basement, forming the northwest flank of a major fracture zone. This F.Z. (**A** in fig. 14) dips to the southeast as do numerous basement faults in the ocean floor southeast of it. The foot-wall (on the southeast side of the F.Z.) is tilted back in the direction of the fault, towards which the sediments diverge. The sea floor here is also slightly inclined suggesting that there may have been some recent movement. Slump and chaotic resedimented units are also common notably on the north sides of the relief, which is up to 1.400 sec., and made up primarily of exposed/thinly covered basement.

LINE 3 (Fig. 15)

This line crossed the westernmost end of the main part of the Ridge, which is bounded by a basement fault to the southwest. Chaotic slump units are present on both the north and south sides of the Ridge. These reflect the seismic signal in a chaotic manner and are consequently opaque to it. Thus it is

Figure 16 Seismic Line 4

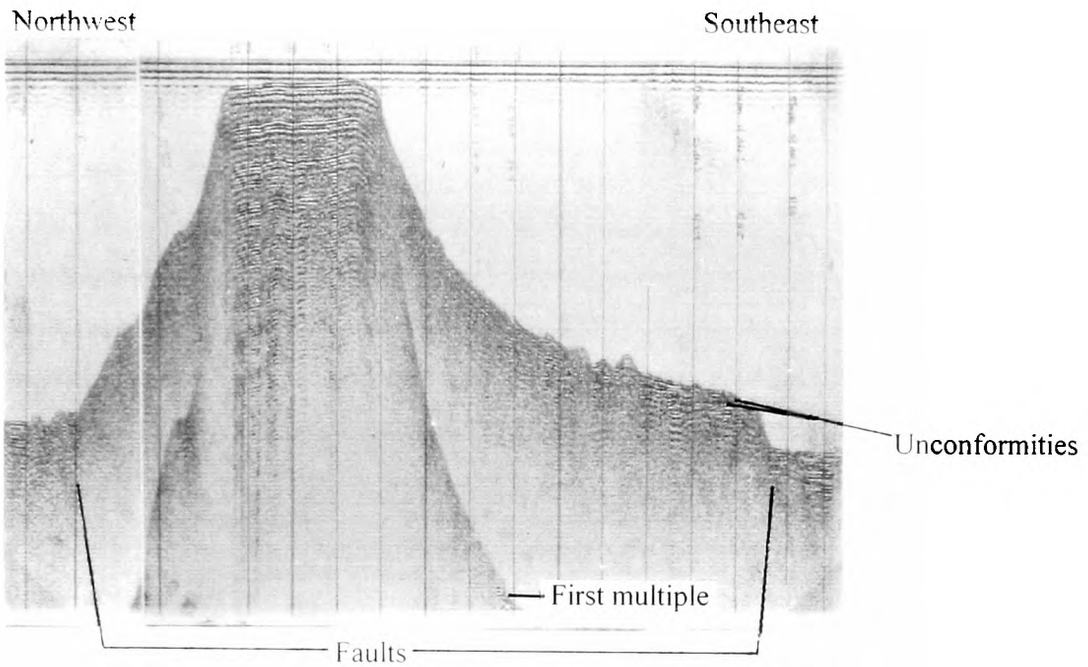

Figure 17 Seismic Line 5

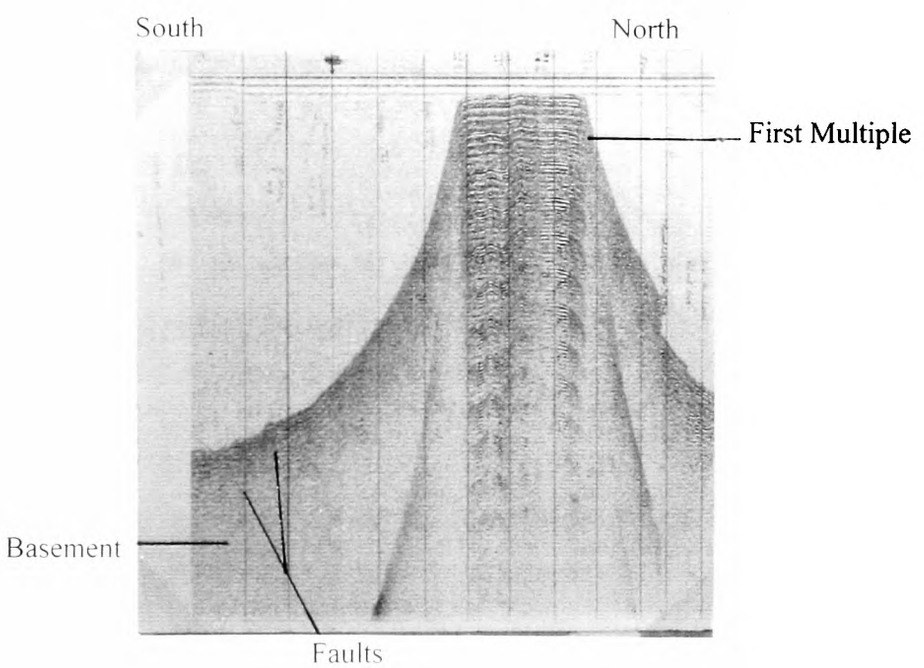

impossible to define the basement surface, though it appears that the Ridge in this area is made up of exposed/thinly covered rock. The unconformity at 0.250 sec. is once again present and is disrupted by numerous small, low angle, en-echelon normal faults, some of which are listric.

LINE 4 (Fig. 16)

The Ridge is seen in this line as a flat topped structure capped with sediment and bounded on both sides by major basement faults. Ocean floor sediments on the northwest show several small thrusts and associated roll-over folding, both features apparently associated with slope failures. Roll-over folding may also be seen on the southeast side of the Ridge, associated with small slumps. In addition to the unconformity at 0.250 sec. there is one at 0.100 sec. On the southeast flank both of these have been subject to tilting, possibly due to movement along small faults in the area. This has resulted in the units diverging as the ridge is approached.

LINE 5 (Fig. 17)

This line was abandoned after technical difficulties resulted in the loss of the record for part of the northern flank. Despite this the southern flank shows several faults apparently bounding the Ridge, though it is not known whether they penetrate basement. Slumping is again evident to the south as are several slope-parallel reflectors, possibly individual slope failure units. Basement is shown tentatively rising under the Ridge, which is again flat topped, with two strong apparently conformable reflectors which are cut by three small normal faults and one reverse fault.

LINE 6 (Fig. 18)

The Ridge has a much more irregular form along this line, with numerous slumps and rotational slip units on both flanks, resulting in a strong ocean floor relief to the north. The 0.250 sec. unconformity is recognized only on the north side, away from the slump/slip units. The strong reflectors on top of the Ridge (lines 4 and 5) are disrupted by faulting to the north. To the south they terminate against a small fringing reef, exposed on its upper surface.

LINE 7 (Fig. 19)

In this line there is a return to the flat-topped form of the Ridge. This however, has been subject to differential subsidence to the north, resulting in an inclined upper surface. Again there are numerous en-echelon basement faults bounding the Ridge on both sides. The 0.250 sec. unconformity of previous lines is present at this depth to the north, but is found at 0.300 sec. to the south, probably due to greater sedimentation. This is contrary to the expectation that sedimentation would be greater to the north since ocean floor circulation in the south, discussed by Stommel and Arons (1958, 1960a and 1960b) and more specifically by Kolla *et al.* (1976) and Draper unpubl. (1988), would be expected to scour the floor to the south, a feature apparent on the chart presented here and also on that of Fisher *et*

Figure 18 Seismic Line 6

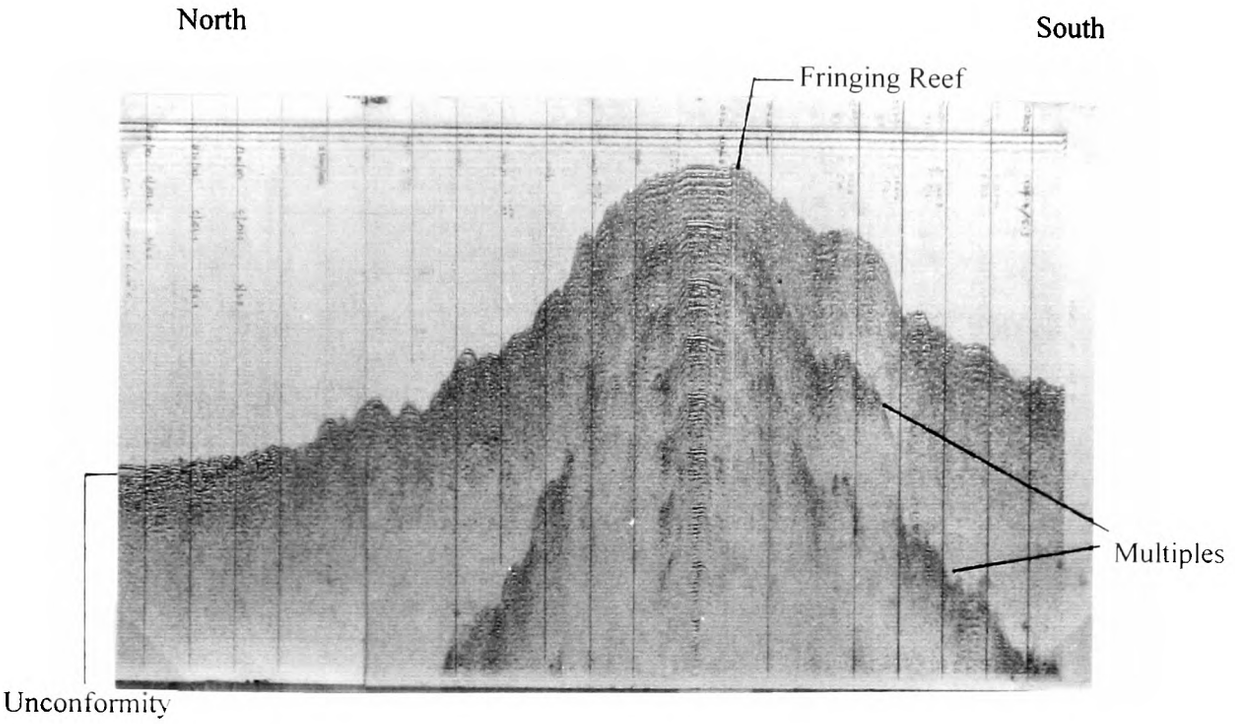

Figure 19 Seismic Line 7

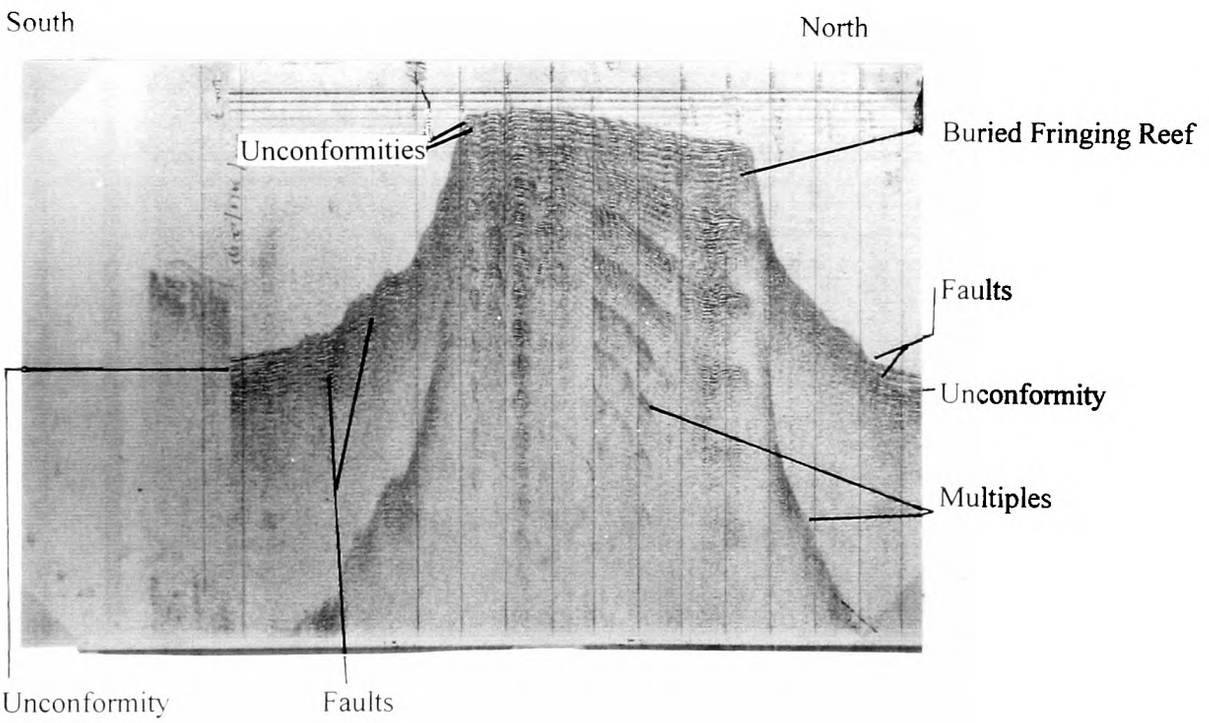

Figure 20 Seismic Line 8

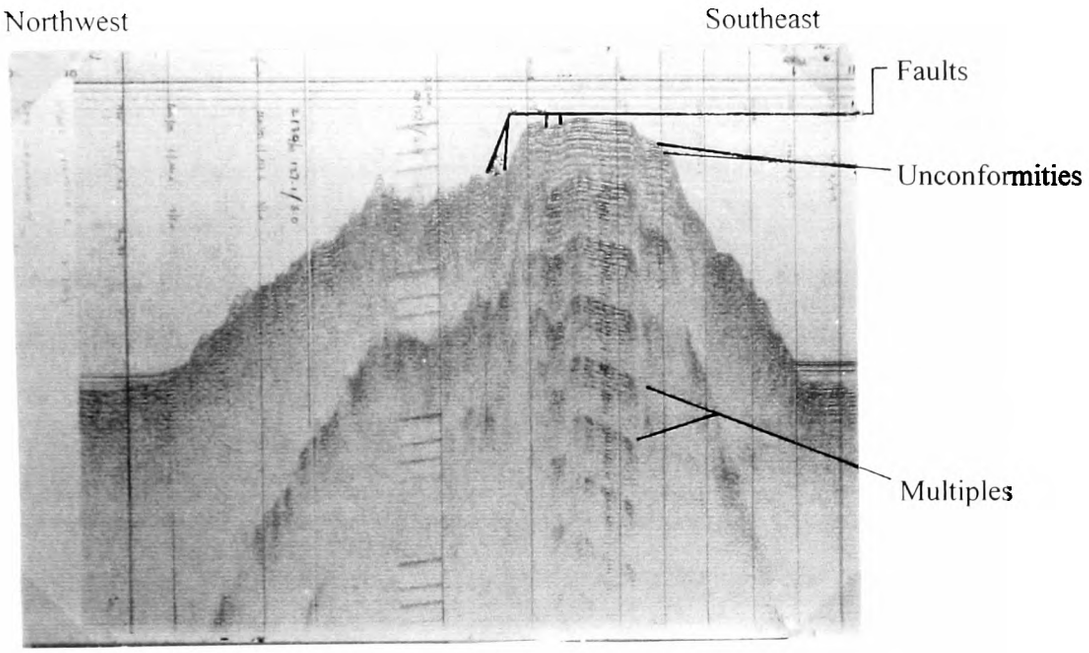

Figure 21 Seismic Line 9

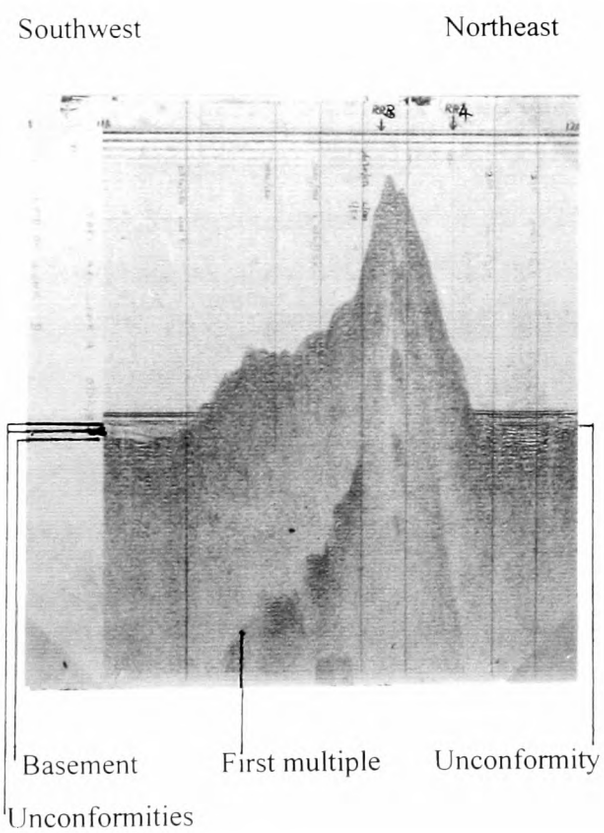

Figure 22 Seismic Line 10

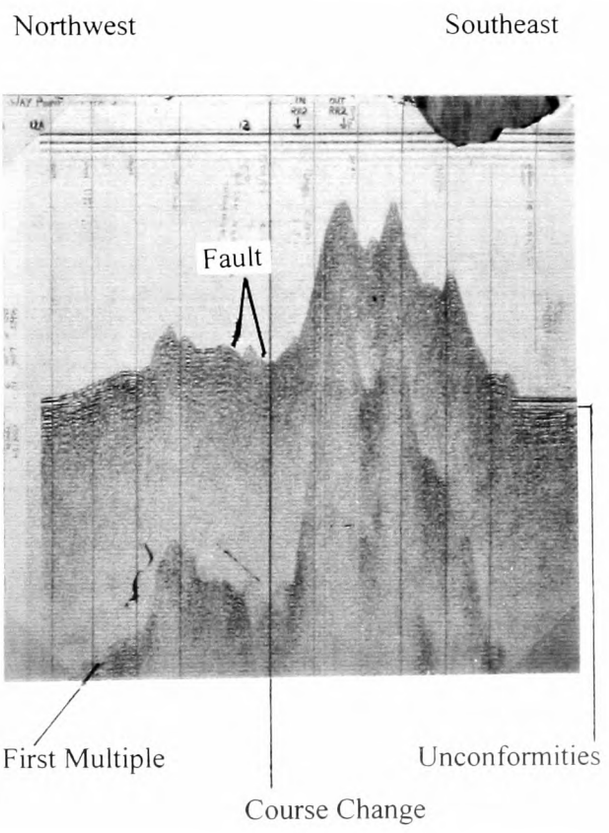

al. (1967, 1971 and 1983 unpubl.).

Two unconformities are present on top of the Ridge, one at 0.200 sec. and the other at 0.500 sec. The former is believed, to be that seen in other lines in the flank sediments at 0.250 sec. Here it is shallower due to the scouring effects of waves and circulation at this depth. It is clearly identified by a sequence of on-lapping reflectors in the north, below which there is a thick conformable layer, which overlies a buried fringing reef. This is a well developed structure which shows some internal reflectors.

Several slip units can be identified on the southern flank in this line though disturbance is minimal to the north.

LINE 8 (Fig. 20)

This line shows a major slope failure to the northwest, which has made depth to basement impossible to assess on this flank. The flat top of the Ridge (towards the southeast of the traverse) is cut by several steeply dipping normal faults probably associated with the failure. No unconformities are recognized in the central part. However, two are recognized in the faulted south east part the first at 0.100 sec., which converges with the second at 0.250 sec. before the edge of the Ridge platform. The Ridge is fault bounded on either side, more notably to the northwest. An unconformity is present in the surrounding ocean floor, which terminates against the bounding faults, at 0.350 sec. (to the SE) and 0.300 sec. (to the NW) which may be the same feature seen at 0.250 sec. in previous records.

LINE 9 (Fig. 21)

Lines 9 and 10 are somewhat shorter than previous lines as the Ridge is narrower here (30 km as opposed to 65 km in line 8). There are several bounding faults to the southwest and a major slope failure. The northern flank seems to be made up of exposed basement, possibly with a thin sediment cover. Ocean floor sediment reaches a maximum of 0.800 sec., and contains an unconformity at 0.225, sec. tentatively correlated with the 0.250 sec. unconformity of previous records. To the southwest four unconformities have been recognized at 0.225 sec., 0.350 sec., 0.475 sec. and 0.500 sec. The first of these has been correlated with that of the same depth on the other side of the Ridge. The other three are separated by several conformable reflectors, and dip gently (<1°) towards the Ridge.

LINE 10 (Fig. 22)

This is the most easterly of the lines and is the only one with a major change of course in it. Here the Ridge is made up of exposed basement with little sediment cover, and a deep valley (0.900 sec.) in the crest. The northwest side has apparently slipped possibly along the major basement fault, which dips north west at 11° and splits into two near the surface. West of this there is a major reverse fault which also penetrates the basement displacing it by about 0.250 sec.. To the south east two unconformities are present at 0.200 sec. and 0.375 sec.. The former is once again correlated with that at about 0.250 sec. on other lines.

Figure 23

Geological Map of the Rodrigues Ridge

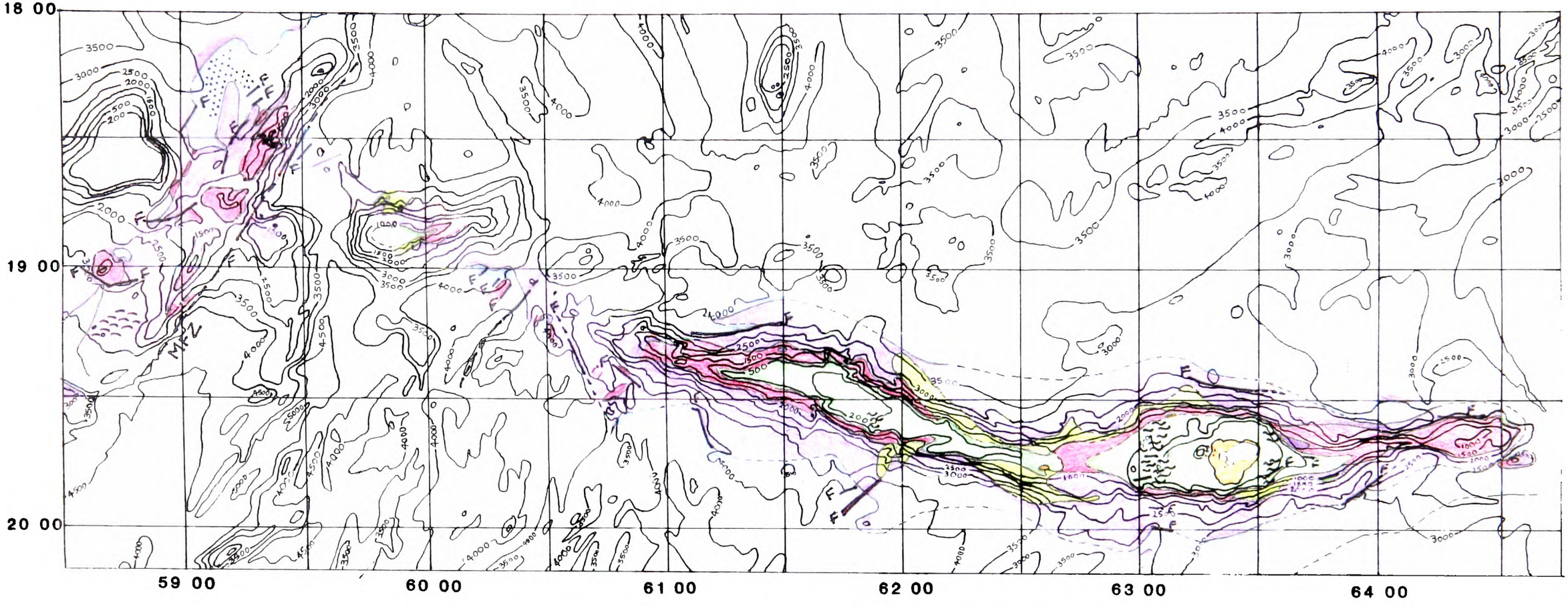

Mercator Projection

- Coral Reef
- Lithified Carbonates
- Resedimented Carbonates
- Exposed Basement
- Slumped Carbonate Sediment
- Undisturbed Carbonate Sediment

- Manganese Nodules
- Ripples
- Sand Waves
- Fault (F)
- MFZ — Mauritius Fracture Zone

2.4 Location of Dredge Sites

The CD12/87 cruise of the RRS. Charles Darwin successfully recovered igneous material from eight sites on the Rodrigues Ridge and one site on the flank of the Mascarene Plateau. The details of the location and depth of these dredges is give in table 6 and fig. 12. Several dredges were attempted in the 159.5 km between RR4 and RR8, but these snagged on the irregular bottom and were lost. Likewise dredges RR11, RR14 and RR15 all failed to recover any igneous material.

Table 6

Dredge Site Number	Location	Depth	Comment
Rodrigues Ridge			
RR1	19°44'S 64°29'E	1700 m	One small basalt specimen recovered
RR2	19°35'S 64°26'E	1000-1800 m	Good recovery
RR3	19°43'S 64°00'E	1000 m	Half pillow basalt recovered
RR4	19°33'S 63°25'E	1800 m	North of Rodrigues Island
RR8	19°38'S 61°59'E	1200 m	Limited number of samples recovered
RR9a	19°19'S 61°26'E	1880 m	Unsuccessful
RR9b	19°20'S 61°28'E	1450 m	Limited number of samples recovered
RR9c	19°19'S 61°30'E	1890 m	Good recovery
RR10	19°17'S 61°02'E	1050 m	Good recovery, but samples altered
RR12a	18°56'S 60°00'E	1790 m	Limited number of samples recovered
RR12d	18°52'S 60°07'E	1210 m	Good recovery
Mascarene Plateau			
RR13a	18°31'S 59°21'E	1460 m	Limited recovery, samples altered
RR13b	18°30'S 59°20'E	2215 m	Limited recovery, samples altered
RR13c	18°29'S 59°23'E	1620 m	Limited recovery, samples altered

The freshest igneous samples recovered from these eight sites were the subject of the petrographic and geochemical analysis which in conjunction with the seismic and bathymetric data, forms the basis of this work.

2.5 Discussion

The data from the seismic lines described above has been used in conjunction with the 3.5 KHz sub-bottom profiles and the 10 KHz echo sounder profiles to produce the map of the surface of the seabed shown in fig. 23. The map shows the structures also given in fig. 3 and the different seabed types identified by their seismic signatures. Figure 12 shows the dredge locations listed in table 7 on the bathymetric map presented in fig 2. Comparing fig. 12 with fig. 23 gives an indication of the type of seabed which was dredged at each site and thus an indication of the likely down-slope displacement of the recovered samples.

The Rodrigues Ridge is capped by a highly reflective flat carbonate platform. Attempts to recover core samples from this surface were unsuccessful. Dredged material revealed that the surface was lithified carbonate with the presence of dead corals, suggesting that the subsidence rate exceeded the coral growth rate. This lithified carbonate platform gives way at a depth of around 500-600 m to either exposed basement or carbonate turbidity current deposits. These units were sampled at sites SD1 and SD2 (19°26'S 61°58'E and 19°21'S 61°52'E, respectively). Geotechnical testing of these sediments confirmed them to be resedimented at substantially greater depths than they were first deposited (Draper 1988). Typically these turbidity current deposits occur as tongues stretching out over the apron of slumped sediments which in turn give way to undisturbed sediments at 3500-4000 m. Both of these deposits were cored on the Mascarene Plateau where they occur at the shallower depth of 2500-3000 m. These two cores, SD3 (18°32'S 59°00'E) and SD4 (18°31'S 59°03'E) together with SD1 and SD2 are discussed by Draper (1988). This study confirmed that the different seismic signatures depicted on fig. 23 were the result of varying degrees of disruption among the sediments. Also displayed on fig. 23 and on fig. 3 are the tectonic structures identified on the geophysical records.

The bathymetric map of the Rodrigues Ridge is given in fig. 2 while fig. 3 shows the location of faults identified on seismic sections or inferred from the bathymetry. Of particular note is the strike-slip faulting at the western end of the Ridge. Several major strike-slip faults occur in the region of the Mauritius Fracture Zone (MFZ). These separate the seamount **(B)**, from which samples prefixed RR12 were dredged from both the Mascarene Plateau and the Rodrigues Ridge. They also dislocate a series of CIR parallel valleys, some of which are fault controlled. West of the MFZ and parallel to it, a number of faults are identified, the first of which is the pronounced growth fault down-throwing west and discussed in the section on leg 2. East of the MFZ are a number of small listric normal faults down-throwing to the east. These faults bound a steep basement ridge, site RR13, from which basalts have been dated at 48 my (Duncan pers. comm. 1989). Geochemically these basalts are MORBs and not the OIBs of the Mascarene Plateau. Further east the long axis of the seamount at RR12 displays 24° of anticlockwise rotation from the line of the main body of the Rodrigues Ridge (fig. 3). These two observations imply that a region of oceanic lithosphere, bounded by a series of a major NW-SE trending sinistral and NE-SW trending dextral faults, has rotated, apparently due to compressive stress

approximately along the line of the Rodrigues Ridge. A consequence of this rotation is that the oceanic lithosphere near the MFZ (fig. 3) would be thrust up over the Mascarene Plateau. This movement rotated the RR12 seamount about a pole at 18°55'S 59°30'E. Although the motion is shown on one major NE-SW trending fault in fig. 3, several planes were recognised on the seismic profiles in this region suggesting that this model is an over simplification. A further problem with this is that recent information indicates that the ocean floor immediately east of the MFZ is only 30 my (Dyment 1999 *pers. comm.*). Thus the ocean floor material at RR13 must has been dislocated to the north as material of this age can only be found some distance south of the Rodrigues Ridge. This further emphasises the complexity of movements which have occurred in this region.

Chapter 3

3. Mineralogy

3.1 Introduction

In chapter 3 the mineralogy of the lavas recovered from the Rodrigues Ridge is examined in detail, considering their alteration state and the minerals present both as phenocrysts, and in the matrix. This information is then used to investigate the history of the melts and establish an order of crystallisation. At the end of this chapter examples of the chemistry of the glass phenocryst and matrix crystals are presented. For a more comprehensive list of analyses the accompanying disk may be consulted, this lists the analyses in tabulated form in either WordPerfect 7 format (*.wpd) or ASCII format.

Table 7 **Alteration Index**

Number	Description	Comment
1.	Fresh	The matrix has more fresh glass than palagonite. Major rock-forming minerals show no sign of alteration.
2.	Quite Fresh	At least a trace of fresh glass is present in the matrix and clean unaltered primary minerals are present.
3.	Slight	No glass in the matrix but fresh plagioclase and either no or slight alteration of the ferromagnesian minerals.
4.	Moderate	Secondary minerals present in the matrix. Olivine and/or plagioclase show clear traces of alteration *i.e.* olivine to iddingsite or serpentine.
5.	Severe	All major rock-forming minerals show significant alteration, *e.g.* plagioclase to albite, olivine to iddingsite and/or serpentine and clinopyroxene (where present) to clays.
6.	Total	All original rock-forming minerals altered, major new growth of secondary minerals. The rock appears porous.

This alteration scheme was constructed to allow a quick visual assessment of the alteration state of all the samples in the CD21/87 collection, and to permit comparison between samples and sites.

3.2 Mineralogy

RR1 yielded one small sample of holocrystaline, glomerophyric basalt which displayed moderate-severe (4-5) alteration according to the scheme, designed to differentiate these lavas, given in table 7. Owing to the small size of the single RR1 sample and its degree of alteration, the sample as not analysed. The remaining primary mineral suite consists of 4% (by volume) phenocryst olivine in a matrix of 25% plagioclase and 5% titanaugite. The secondary minerals are iddingsite, opaques and quartz, and these make up the remaining volume of the sample. The occurrence of secondary quartz in this sample is unique among the Rodrigues Ridge basalts. Many of the crystals are broken, this possibly having occurred during the extrusion process. The igneous samples from RR2, RR3, RR4, RR8, RR9b and RR9c were exclusively porphyritic basalts (olivine-plagioclase phyric, plates 1-4) many of which were glomerophyric (plate 1). Many of the samples recovered are clearly fragments of pillows. One half of a pillow (RR3.1) was recovered from RR3. Flow alignment of the plagioclase laths is observed at all the sites (*e.g.*. plate 1) but flow banding is only seen in samples from RR4, RR8, RR9 and RR12d. Many of the samples from RR9c were coated or loosely cemented together by carbonate sediments, collectively forming part of a debris flow deposit. Seismic data suggest that much of the flanks of the Rodrigues Ridge are cloaked by such gravity-flow deposits. Table 8 summarises the petrography of the Rodrigues Ridge basalts. The samples from RR10 are somewhat different to those found at the sites discussed so far. Here dredging recovered both basalts and tuffs. Many of the lavas are holocrystaline with pleochroic pink titanaugites within the matrix and numerous vesicles, some filled with zeolites. Phenocryst clinopyroxene is absent from all the observed samples except those of RR12d where rare laths of pleochroic pink titanaugite were observed (plate 4). Matrix glass no longer exists in RR10 samples, having been totally replaced where it once existed, principally by palagonite or secondary minerals. Many of the Rodrigues Ridge basalts are surrounded in a bright orange palagonitic rind with or without a 'manganese' coat, principally made up of Mn-Fe oxides and hydroxides with some organic material. The presence of 'manganese' both coating the lavas and as nodules in the dredges was notably greater at sites RR10 and RR12. Qualitatively alteration seems more extreme in the west; samples from RR10 and RR12 are considerably more altered than any of the more easterly sites. All of the samples studied were selected on the basis that they appeared to be the least altered of their particular dredge. Thus the higher level of alteration at RR10, which is the same age as samples collected from further east, must be related either to its location (*e.g.*. near the end of the Ridge; near several major fractures...) and/or to its chemistry.

Table 8 **Petrography of Rodrigues Ridge Basalts**

Site and location	Alteration	Texture	Primary minerals	Secondary minerals, and mineraloids
RR1 19°44'S 64°29'E	4-5	holocrystaline, glomerophyric	olivine, plagioclase, titanaugite	iddingsite, opaques, quartz
RR2 19°35'S 64°26'E	most 2-3 (1-4)	porphyritic, glomerophyric	olivine, plagioclase, Cr spinel	palagonite
RR3 19°43'S 64°00'E	3-4	porphyritic, glomerophyric	olivine, plagioclase, Cr spinel	palagonite
RR4 19°33S 63°25'E	1-3	porphyritic, flow banding, glomerophyric	olivine, plagioclase, Cr spinel, augite	palagonite
RR8 19°38'S 61°59'E	3-4	porphyritic, flow banding, glomerophyric	olivine, plagioclase, Cr spinel, augite	palagonite
RR9b 19°20'S 61°28'E	4	porphyritic, flow banding	olivine, plagioclase, Cr spinel, augite	palagonite
RR9c 19°19'S 61°30'E	1-4	porphyritic, flow banding, glomerophyric	olivine, plagioclase, Cr spinel, augite	carbonates, serpentine, palagonite
RR10 19°17'S 61°02'E	4-5	porphyritic, holocrystaline, porous	titanaugite, magnetite, Cr spinel, plagioclase	zeolites, iddingsite, palagonite, Mn-oxides, serpentine
RR12a	4	porphyritic, vesicular	plagioclase	iddingsite, zeolites. Palagonite
RR12d 18°52'S 60°07'E	4-5	porphyritic, vesicular	plagioclase, titanaugite	iddingsite, zeolites, serpentine, Mn-oxides

Plate 1 **Skeletal 'Hopper' Olivine at RR2**

Plane polarized light Chrome spinel

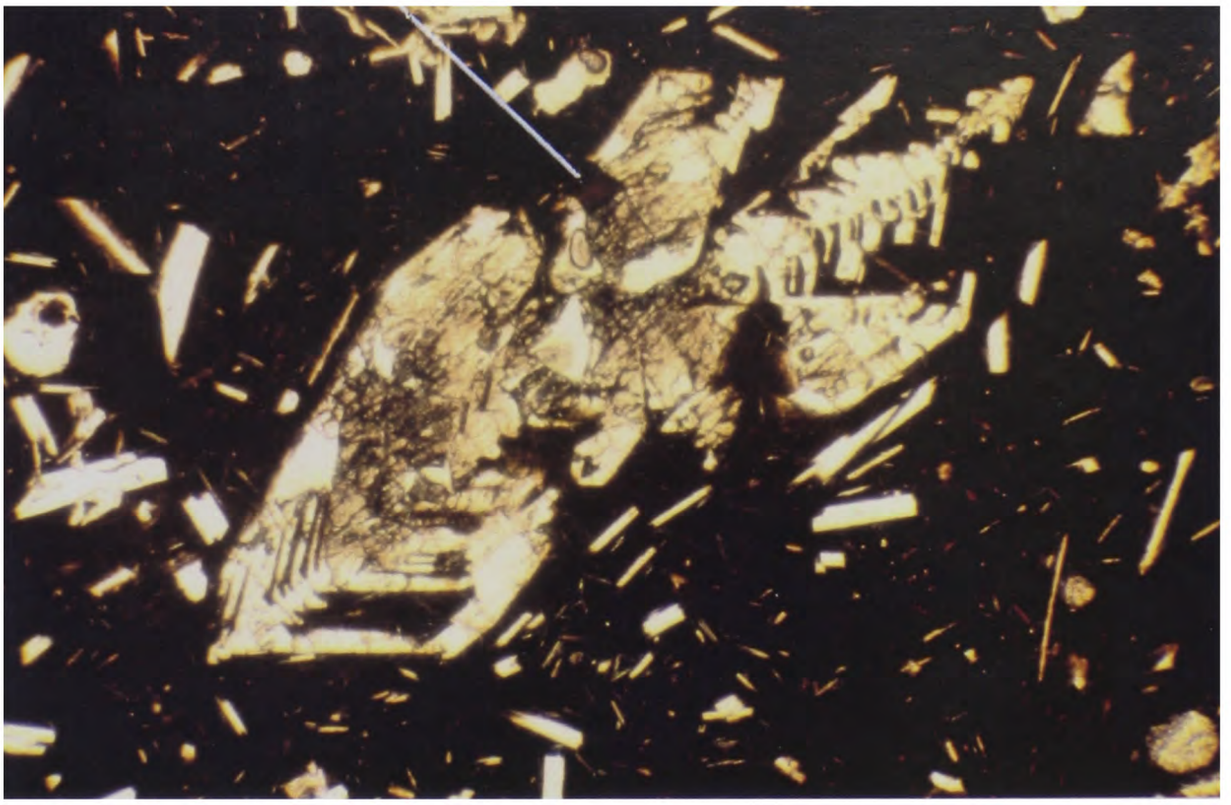

Cross polarized light Glomerophyric association of plagioclase and olivine

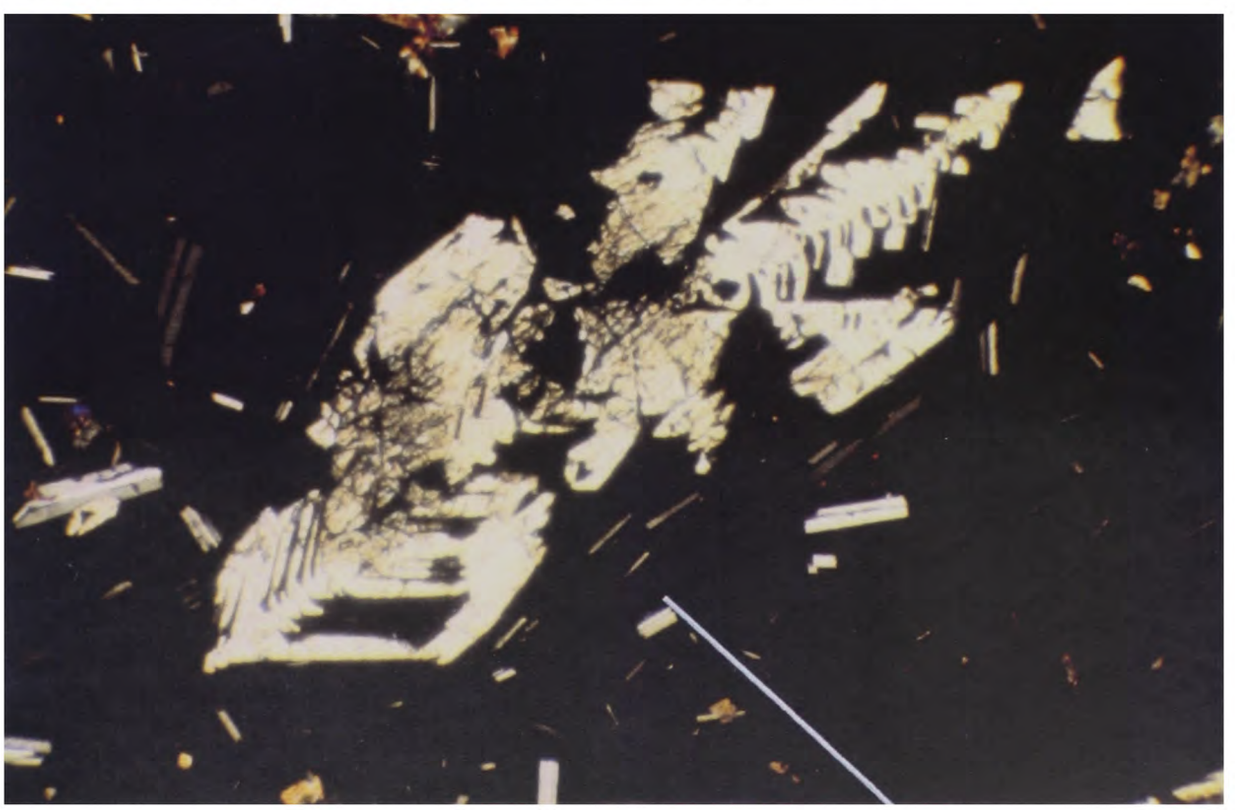

Flow aligned plagioclase

Skeletal crystals such as this olivine form during the rapid cooling of the melt when there is limited nucleation time and growth is very rapid. In such cases the crystals grow along their edges and corners preferentially resulting in spectacular but fragile crystal forms such as this. The lack of crystal nuclei also results in the glomerophyric associations such as is seen at the left-centre and top edge of this image. Here several crystals share one nuclei or the original crystal provides a nucleation site for later formed crystals as in this case. Here olivine was the first to form with plagioclase nucleating on it.

Plate 2 **Skeletal 'Hopper' Olivine at RR2**

Plane polarized light

Cross polarized light

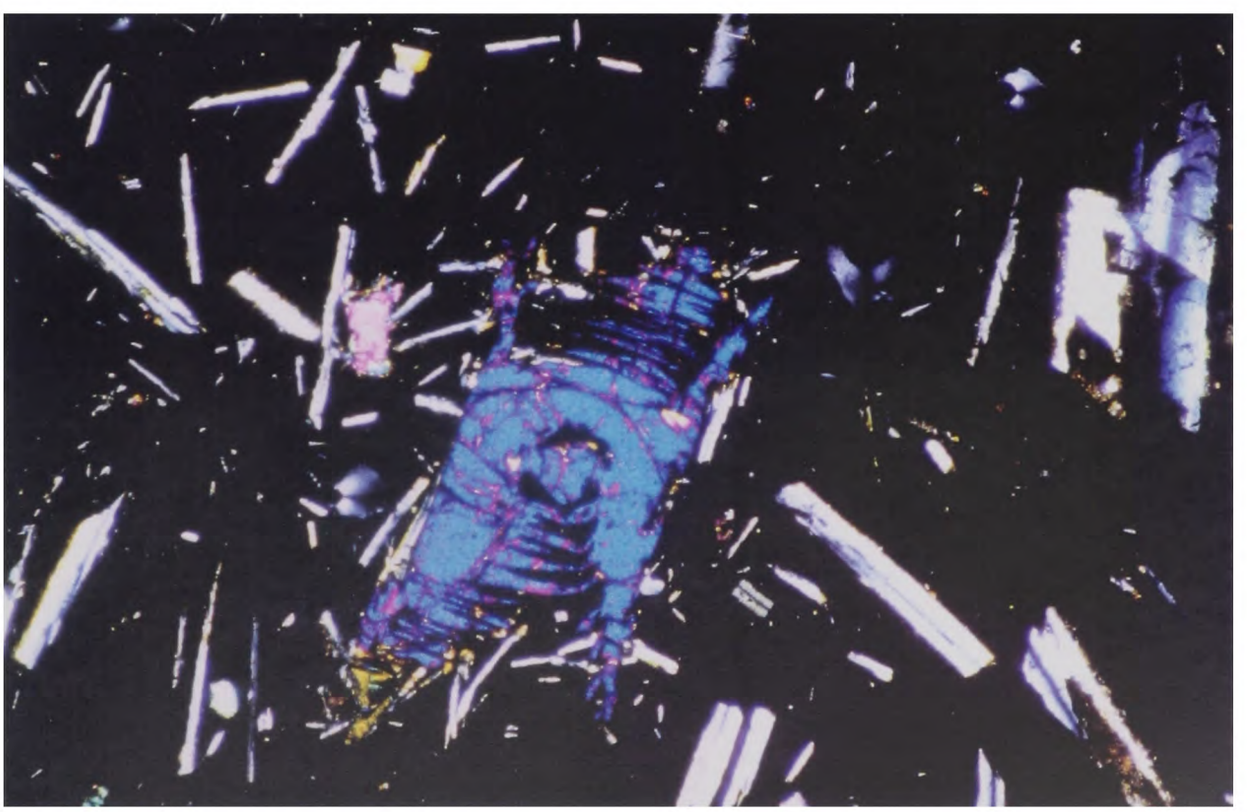

3.3 Phenocrysts

Representative electron microprobe analyses of the major phenocryst phases (olivine, plagioclase and chrome spinel) are given in tables 10-12. Further analyses are included in tables A1-A25 on the included disk.

Olivine

Olivine phenocrysts found in samples recovered from sites RR2-RR9c display mostly hopper (plate 1), or less commonly amoeboid skeletal, or embayed forms (plate 3). Small inclusions of either glass or altered glass were noted in olivines from RR9c. Olivine compositions are in the narrow range Fo_{87-82} at both RR2 and RR4, Fo_{88-86} at RR3, Fo_{86-75} at RR8 and Fo_{86-81} at RR9c (table 10). A single matrix olivine from RR4 had a composition of Fo_{49}, though others in this rock were around Fo_{83}. Matrix olivine at RR8 was in the range Fo_{64-58}, while at RR9c it was more forsteritic at Fo_{83-66}. No matrix olivines were analysed from either RR2 or RR3 where they were uncommon. At RR10 olivine phenocrysts are largely pseudomorphed by iddingsite. Where present, fresh olivine was in the range Fo_{88-80} with the lower forsterite values occurring near the edge of the crystals (see table A21). At RR12 skeletal olivine phenocrysts are largely replaced by iddingsite, which also occurs within the matrix (plate 4). No olivine analyses are available for this site since the few surviving crystals also proved to be altered to varying degrees. Microprobe analyses of these failed to produce good totals for the major element oxides, probably due to the alteration state of the crystals. Qualitatively these analyses showed crystals were less forsteritic than phenocryst olivine found at any of the other sites.

Plagioclase

Plagioclase at all of the sites forms glomerophyric associations with olivine (plates 1-3) and commonly has a skeletal 'bow-tie' form and/or ragged crystal terminations (plate 3). Only at RR12d do the larger plagioclases lack forked crystal terminations. Flow alignment of the plagioclase is common and the en echelon 'stacking' of plagioclase prisms in accordance with the flow direction was also observed in some RR3 and RR9c samples (plate 3). The anorthite content of the plagioclase was

Figure 24

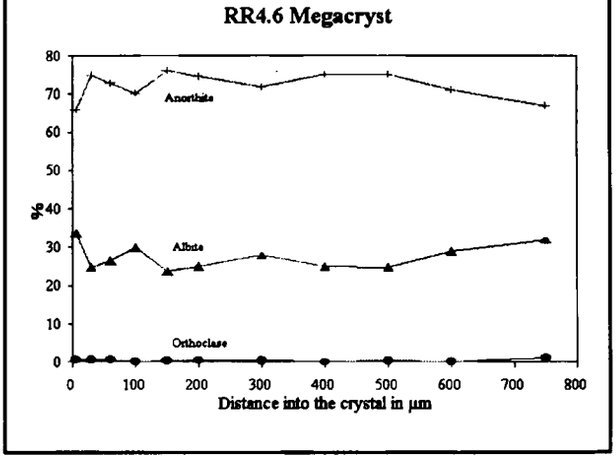

Figure 25

RR8, RR10 and RR12d

An-Ab-Or triangular diagram.

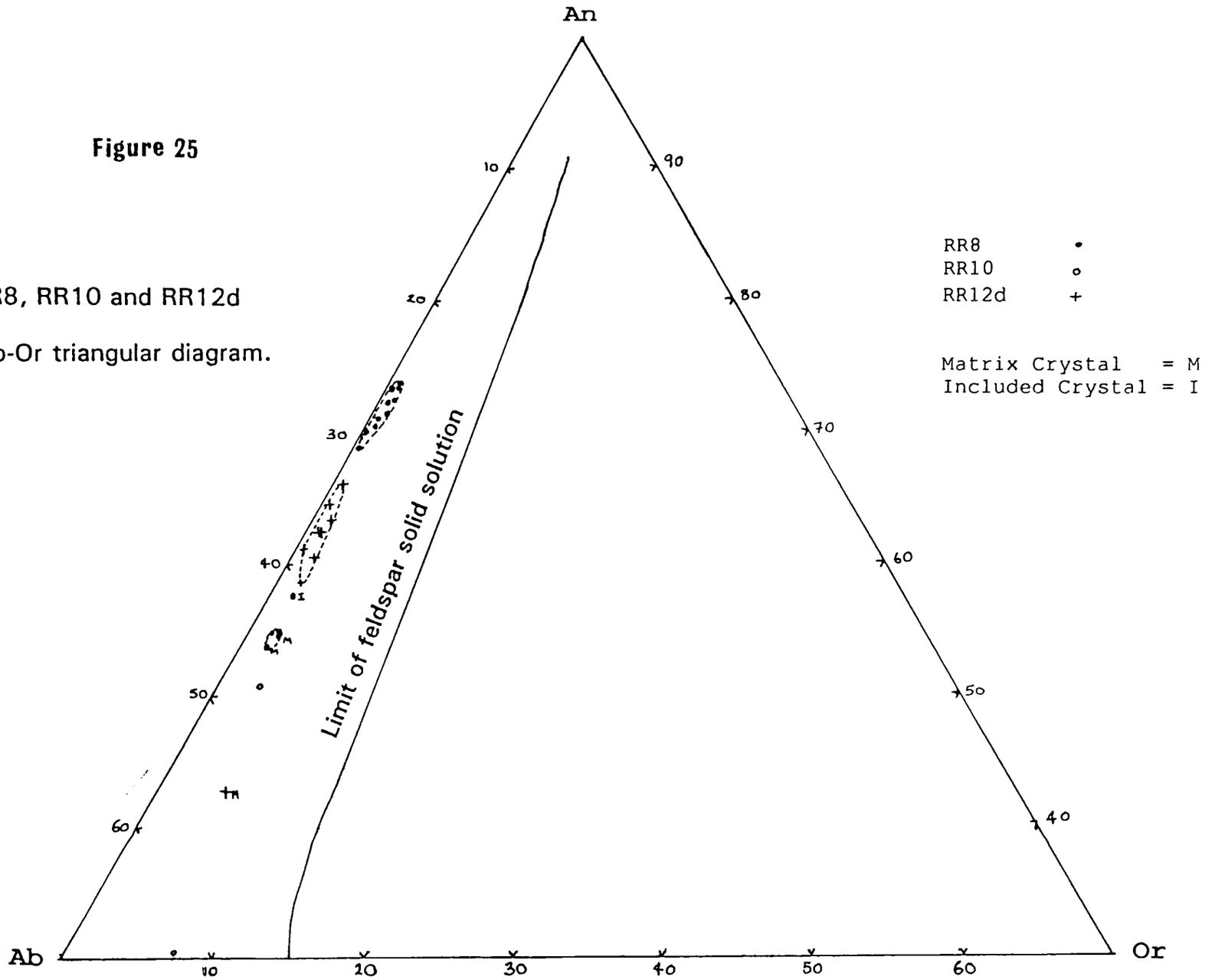

Figure 26

RR2 Or-An-Ab triangular diagram.

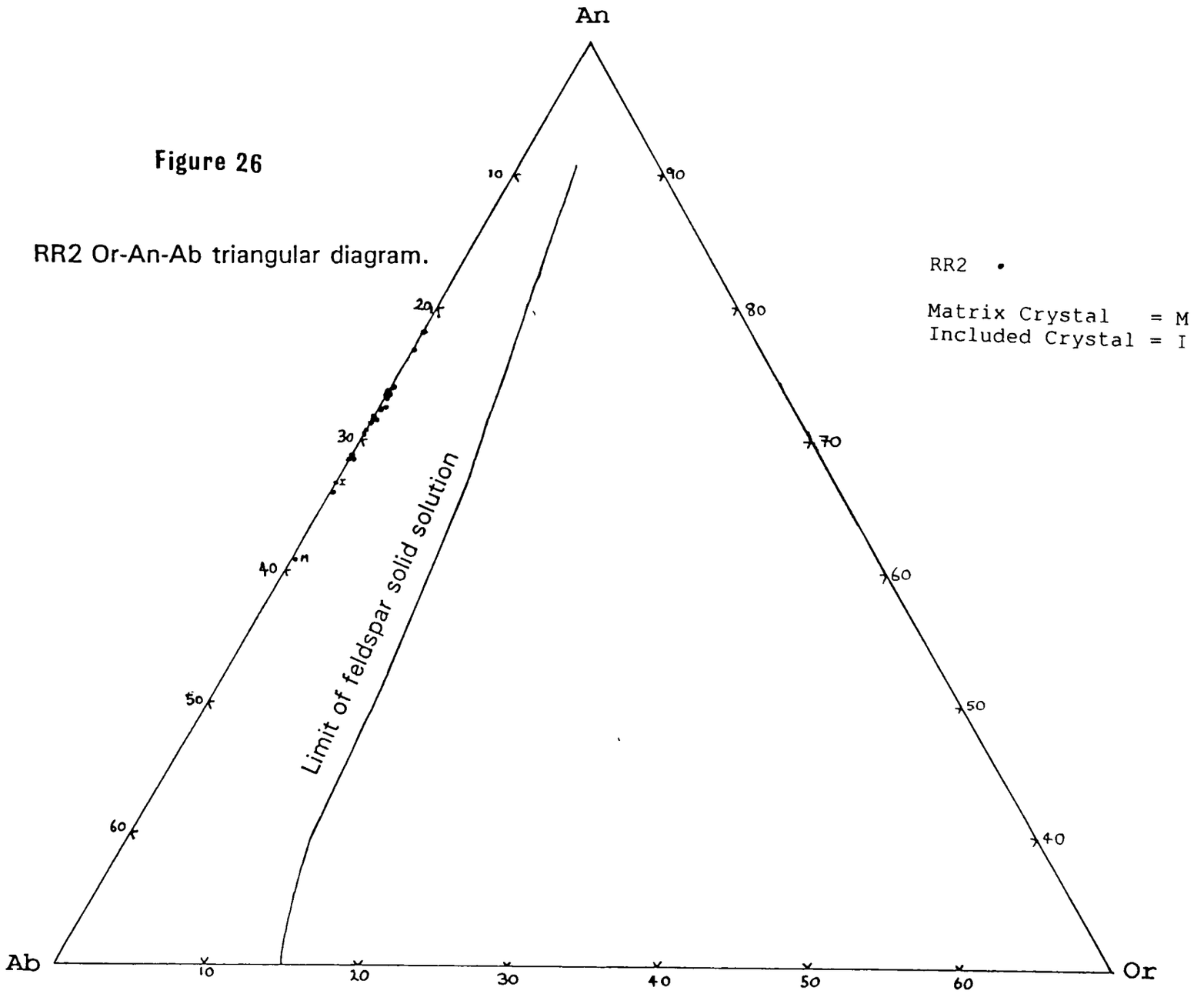

Figure 27

RR3 Or-An-Ab triangular plot.

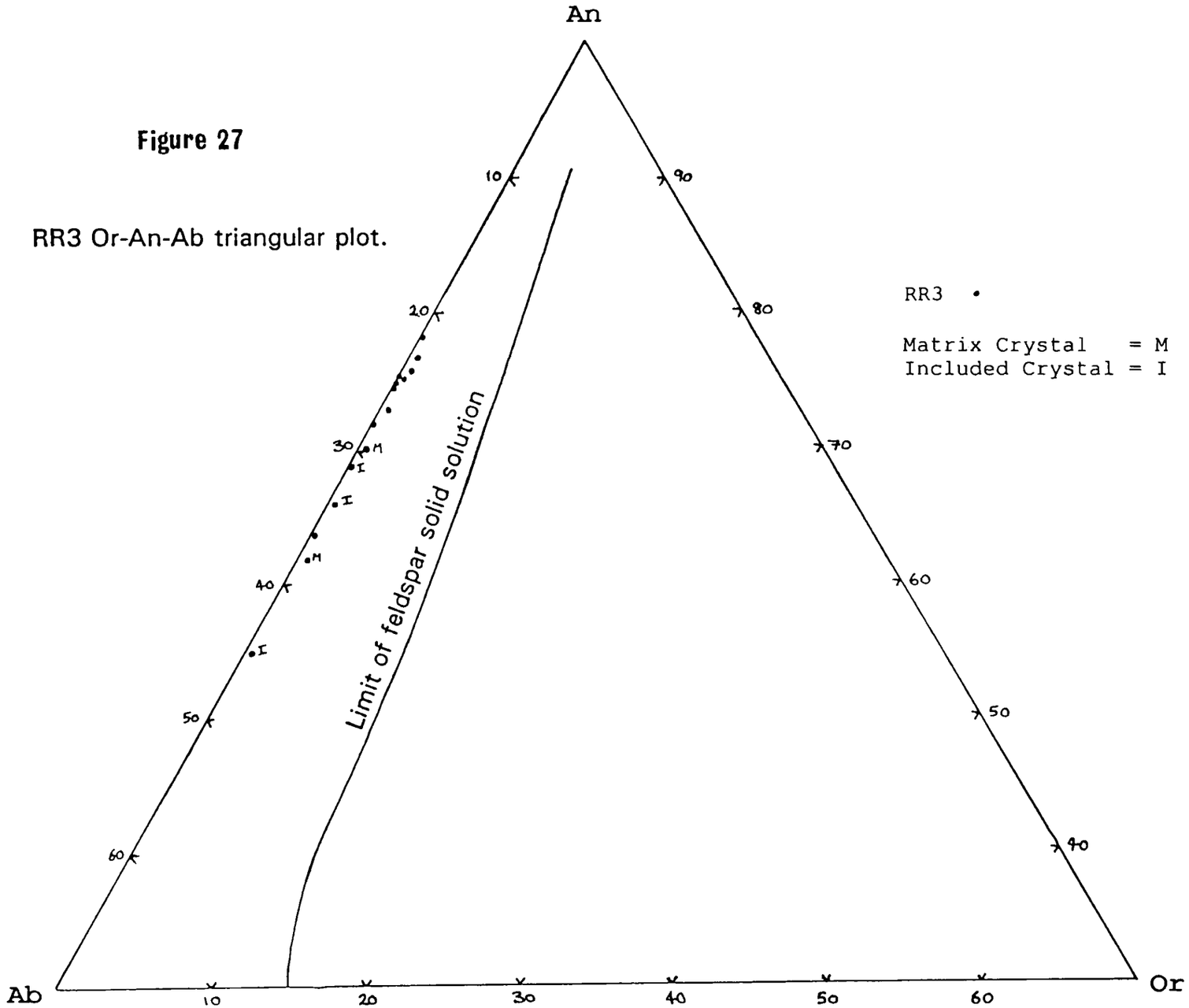

Figure 28

RR4 An-Ab-Or triangular diagram.

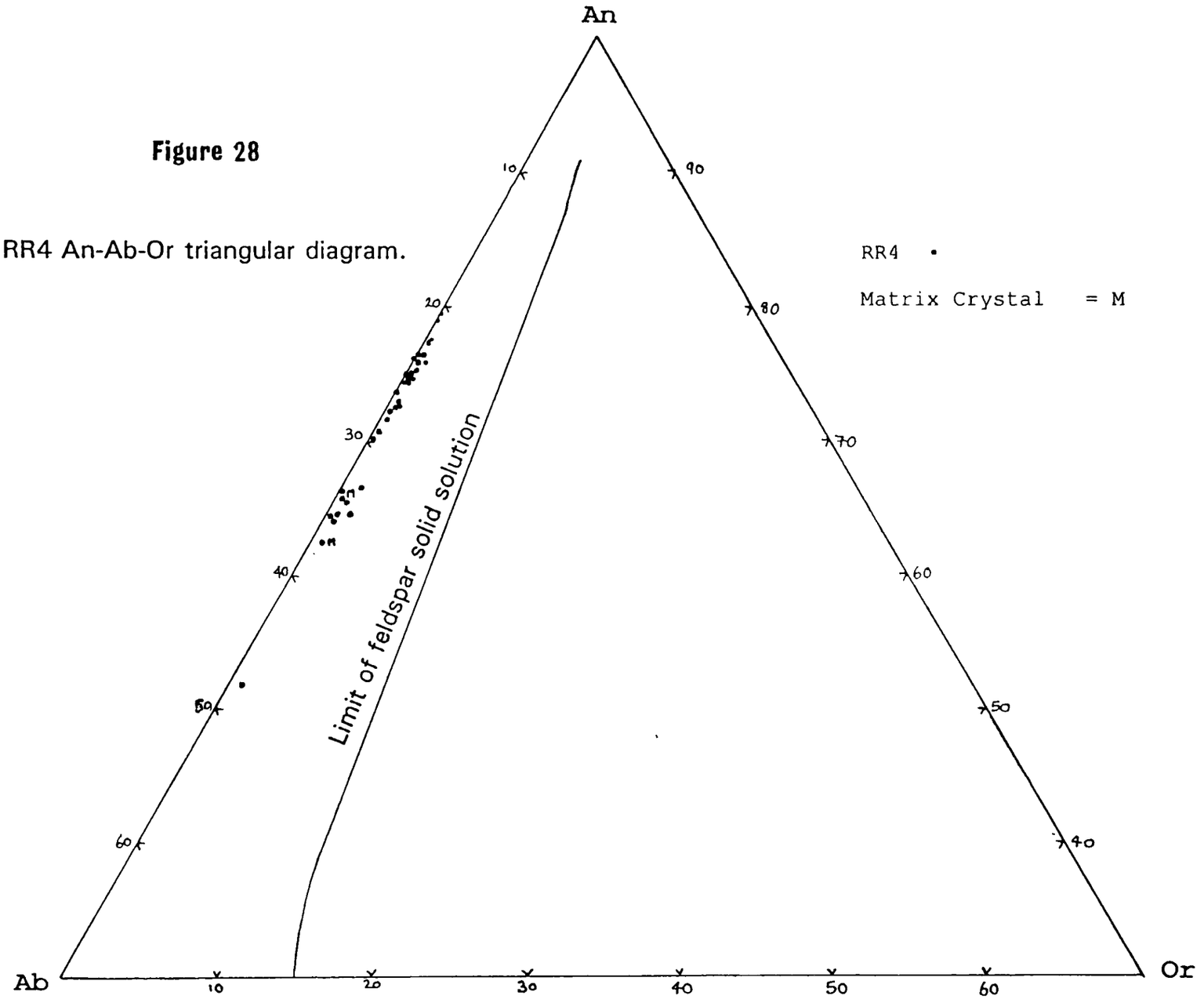

Figure 29

RR9c An-Ab-Or triangular diagram.

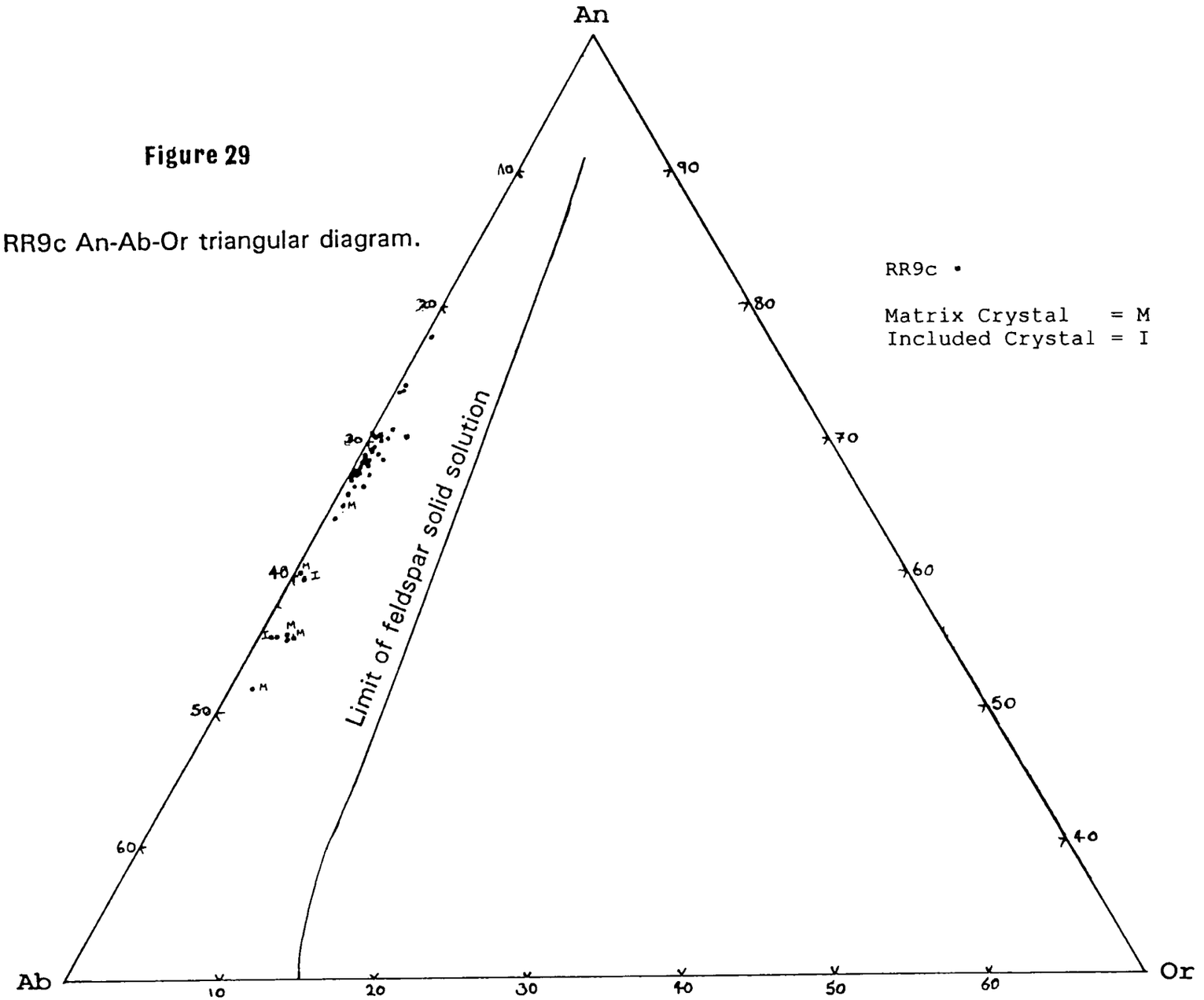

Plate 3 Embayed Olivine Phenocryst in Glassy Matrix at RR9c

Plane polarized light

Serpentine vein, note increased alteration of glass matrix around vein

Cross polarized light Vesicle with serpentine lining

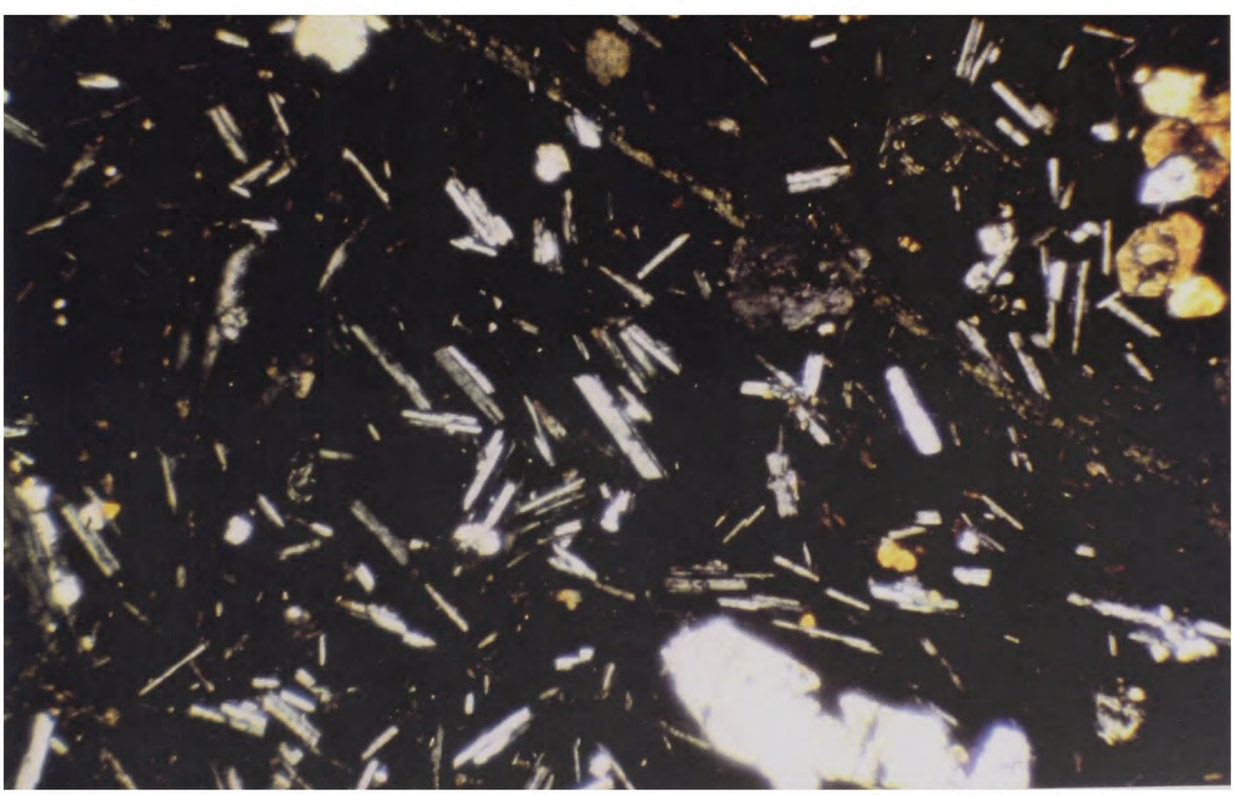

Embayed olivine phenocryst

Note the *en echelon* stacking of plagioclase in the centre of the slide.

Plate 4 **Vesiculation at RR12d**

Plane polarized light

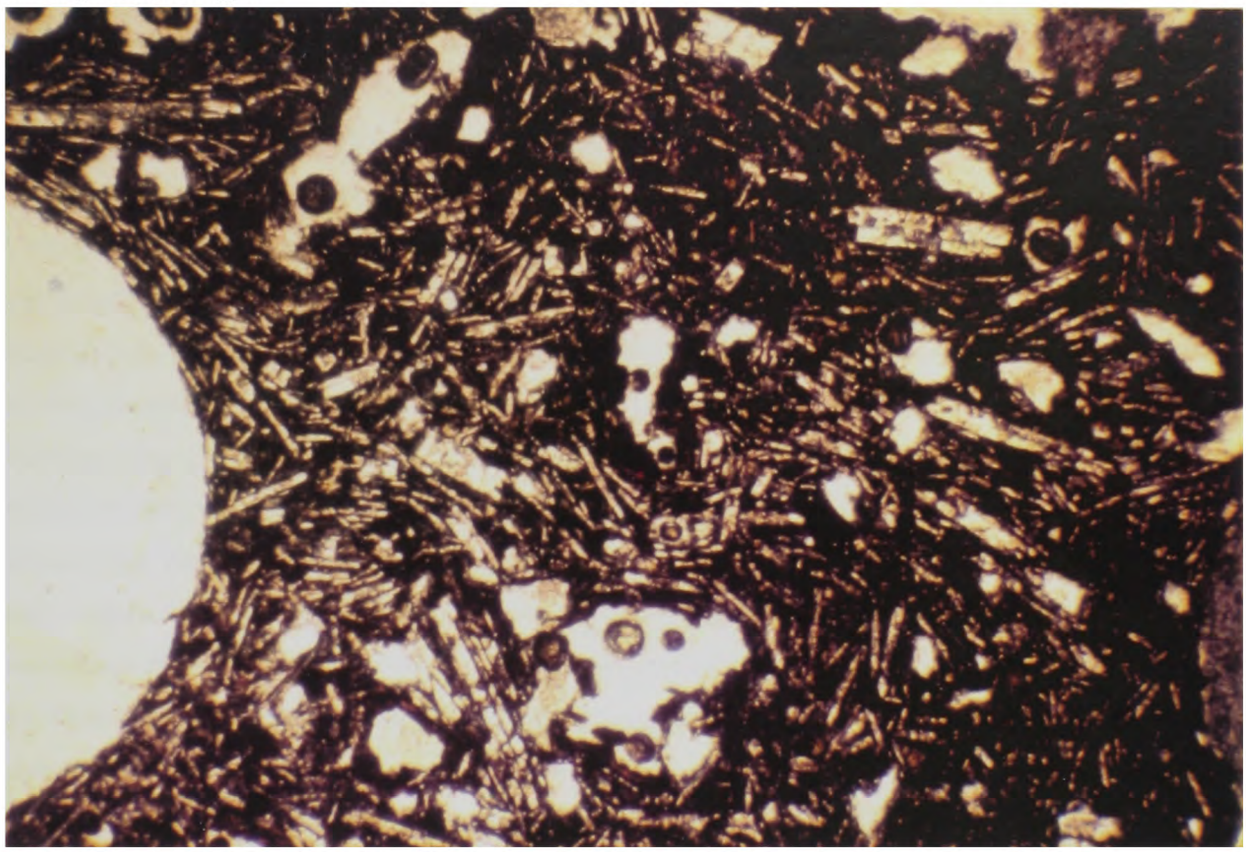

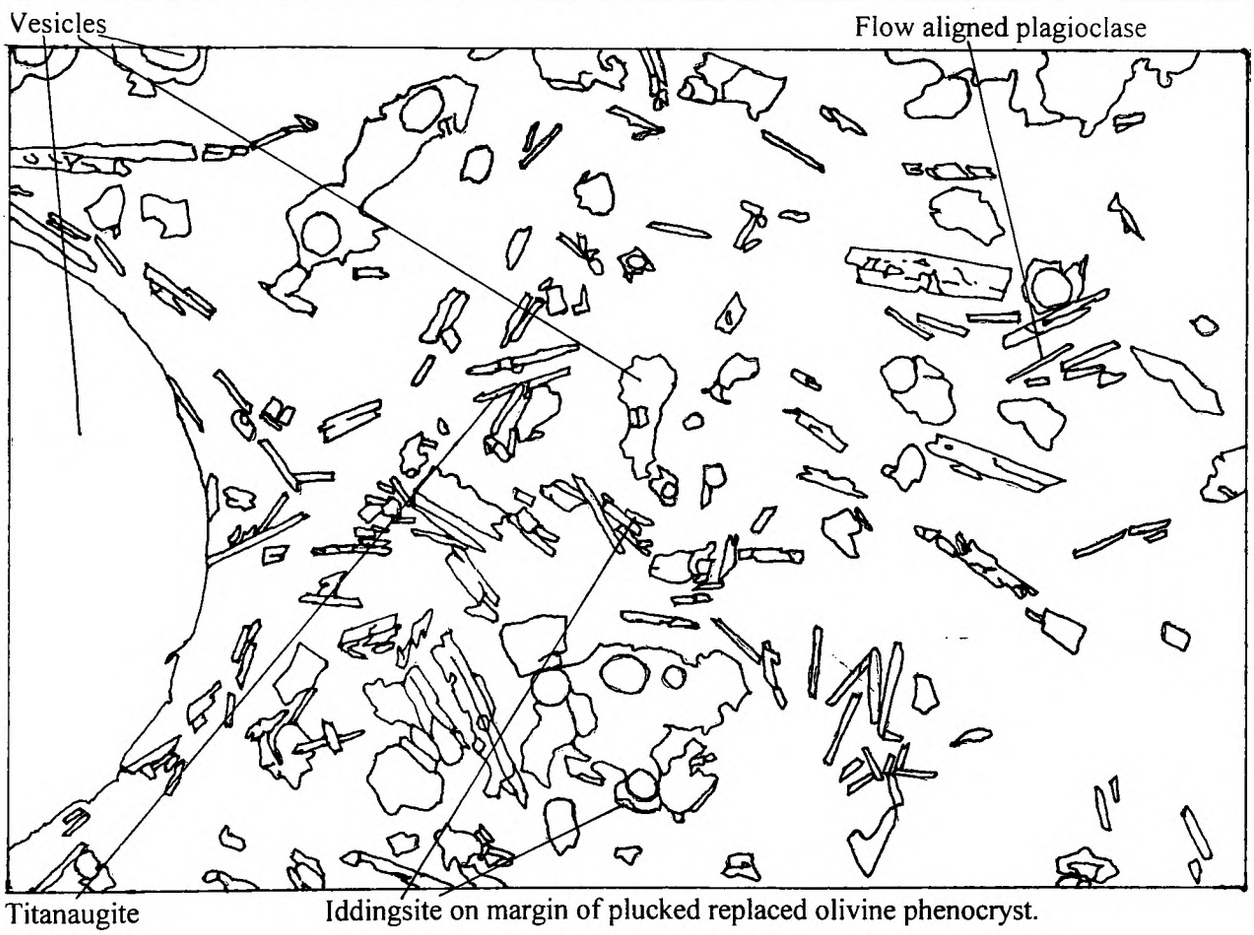

estimated using optical techniques to be in the labradorite range at RR3, labradorite-bytownite (An_{77-59}) at RR2, bytownite (An_{72}) at RR4 and labradorite-bytownite (An_{72-60}) at RR9c. At RR8 only one sample was tested optically but this gave a value of An_{68}. Optically the unaltered plagioclase at RR12d gave an anorthite value of An_{63} though the larger crystals were noted to be zoned. Microprobe analysis revealed the phenocrysts at RR2 to have anorthite contents of An_{78-66} while the matrix crystals were around An_{60} (table 8 and table A2). At RR3 the phenocrysts occupy a slightly broader range An_{78-63} while the matrix crystals are An_{68-54} (table 11 and table A6). At RR4 the anorthite content of the plagioclase phenocrysts is higher at An_{80-73} with the margins as low as An_{52} (table A10). Phenocrysts from sample RR4.6, which is chemically more evolved (lower in MgO, CaO, Al_2O_3 and Ni higher in TiO_2 and incompatible elements *e.g.*. Zr, Th, REE), are notably less anorthitic at An_{65-64}. This sample also includes one large rounded, possibly resorbed, plagioclase megacryst, with a marginal composition of An_{66} and core in the range An_{76-69}. Fig. 24 shows the variation in anorthite content with distance into this crystal. This crystal, the only megacryst to have been identified in any of the Rodrigues Ridge lavas, may have been derived from the other lavas at this site which have similar anorthite contents. Microprobe analyses of plagioclase at RR8 revealed that phenocryst plagioclase falls in the range An_{74-69} whereas the matrix crystals are around An_{57-54} (table A14). These values are similar to both RR2 and RR3. Analytical data for RR9c displayed matrix plagioclase between An_{65-52}; this includes two crystals included in olivine phenocrysts, both of which are around An_{56}. Phenocrysts compositions range from An_{55} near the edge of crystals, to An_{78} near the core; this is consistent with the values obtained optically. At RR10 plagioclase appeared albitised in thin section; analysis confirmed this, giving anorthite contents of An_{51} and An_{30} for the two crystals examined, which is somewhat less than at the previously discussed sites (fig. 25). At RR12d the plagioclase phenocrysts are in the range An_{66-52} with matrix crystals around An_{43} (table A24 and fig. 25). This observation, in conjunction with the qualitative observation that the olivines are less forsteritic (than at RR2-10), is consistent with the geochemistry in showing that the RR12d lavas are more evolved.

Plagioclase at RR2-9c is very low in K_2O (0-0.40%), plotting along the An-Ab margin of the Ab-An-Or triangular diagram (figs. 26, 27, 28, 25, 29). At RR10 there is significantly more K_2O (0.49-1.28%), and Na_2O (5.25-7.23% compared with 2.18-5.28% at RR2-9c), probably as a result of albitisation. Two groups can be distinguished at sites RR2-9; the phenocrysts and the matrix/included crystals, the latter being substantially higher in Ab than the former. At RR2 the matrix crystals are generally narrower than the 3 μm spot size of the microprobe beam. This resulted in insufficient data to establish the range of anorthite contents among the matrix plagioclase in these samples. In tables 16-22 the left-hand column indicates the normative anorthite content of plagioclase which is similar to the An content of the matrix crystals for both sites. The quenched (skeletal) crystal forms, and this chemical difference between the matrix and phenocryst plagioclase, both indicate that the final cooling stage of these melts was very rapid, as would be expected for a lava erupted into seawater.

Chrome Spinel

Chocolate brown chrome spinel occurs either included in the olivine phenocrysts, or in the matrix, often associated with broken skeletal olivines, or away from any olivine but surrounded in a magnetite coating. In extreme cases (at the more western sites) chrome spinel is apparently replaced by opaque magnetite. This is probably due to the early formed Cr spinels reacting with the final stages of the melt, in which they would no longer be in equilibrium. Microprobe analyses of these minerals reveal 20-30% Cr_2O_3, typical of chrome spinel in Rodrigues Ridge lavas (table 12). At RR10 magnetite is present within the matrix together with occasional chrome spinels. These occur as opaque crystals whose identity was only confirmed by microprobe analysis. As will be demonstrated in ch.6 two geochemically distinct groups exist; one with low MgO, TiO_2 and Zr, the other with high MgO, TiO_2 and Zr. Within the high MgO group, chrome spinel is present within the matrix without any obvious reaction rim. In the low MgO group it is generally less common and is either contained within olivine phenocrysts or, if present in the matrix, with a magnetite reaction rim. This subtle variation in the chrome spinel content of the two groups is reflected in slightly higher absolute values of Cr in the high MgO group. Chrome spinel at RR8 is less common than at the more easterly sites, it is enclosed in olivine and often coated or partially replaced by magnetite.

3.4 Chemical Zoning

All three major mineral phases show subtle chemical zonations which do not affect their optical properties. This zoning is the result of failure to maintain equilibrium with the rapidly evolving melt composition. Where crystal size and the state of the polishing permitted, multiple analysis of individual crystals revealed this zoning. (In all cases the spot diameter was 3 μm). The olivine phenocrysts in RR2 show chemical zoning which is displayed graphically in figs. 30-31. With the exception of crystal 6 in RR2.3, all the phenocrysts sampled show similar trends towards decreasing MgO and increasing FeO^* content away from the centre of the crystal, towards the rim (fig. 31). Broadly similar olivine behaviour is observed at all the sites (figs. 32-33, 34-35, 36-37, 38-39 and 40-41). The olivine samples studied from RR9c display a more complex pattern than those from the more easterly sites. Here the MgO content declines sharply close to the margin and is accompanied by a rise in the FeO^* content (figs. 38-39). The MgO content levels off around 50-80 μm from the margin, rises again to a peak between 100 μm and 250 μm, after which it declines to 400 μm before climbing again (fig. 38). The rise in MgO content between 250-400 μm suggests reinjection of a more magnesian melt causing a rise in the MgO content of the magma and hence of the fractionating olivine. Continued fractionation results in the MgO content declining as the crystal continued to grow. The levelling off of the curve between about 50 μm and 100 μm may indicate a further injection of melt immediately prior to the

Figure 30 MgO Content of RR2 Olivines plotted against distance into the crystal

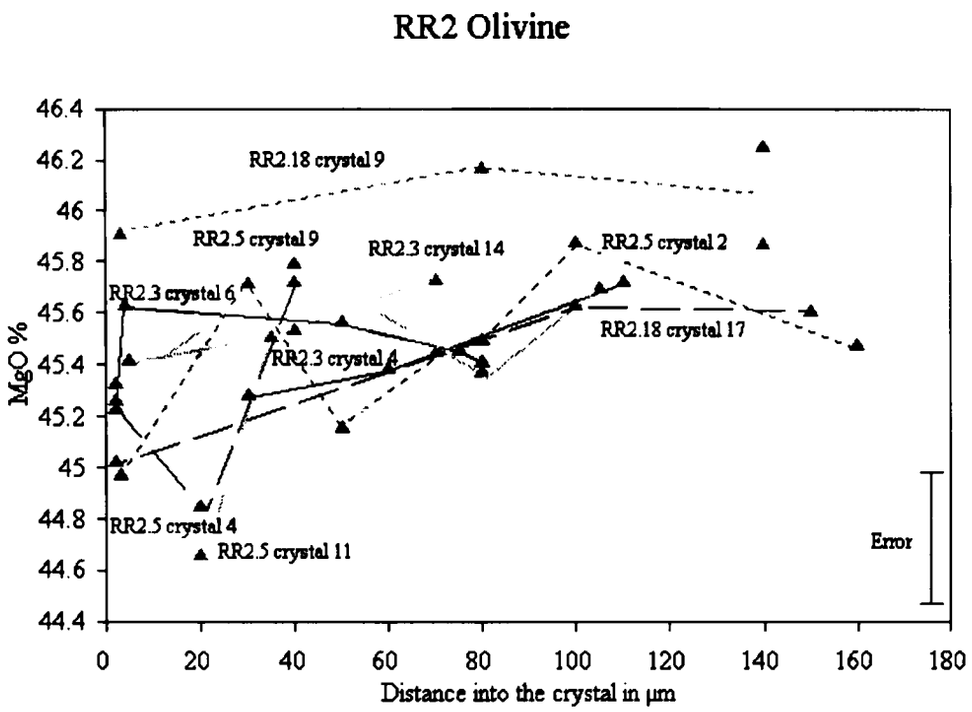

Figure 31 FeO content of RR2 olivines plotted against distance into the crystal

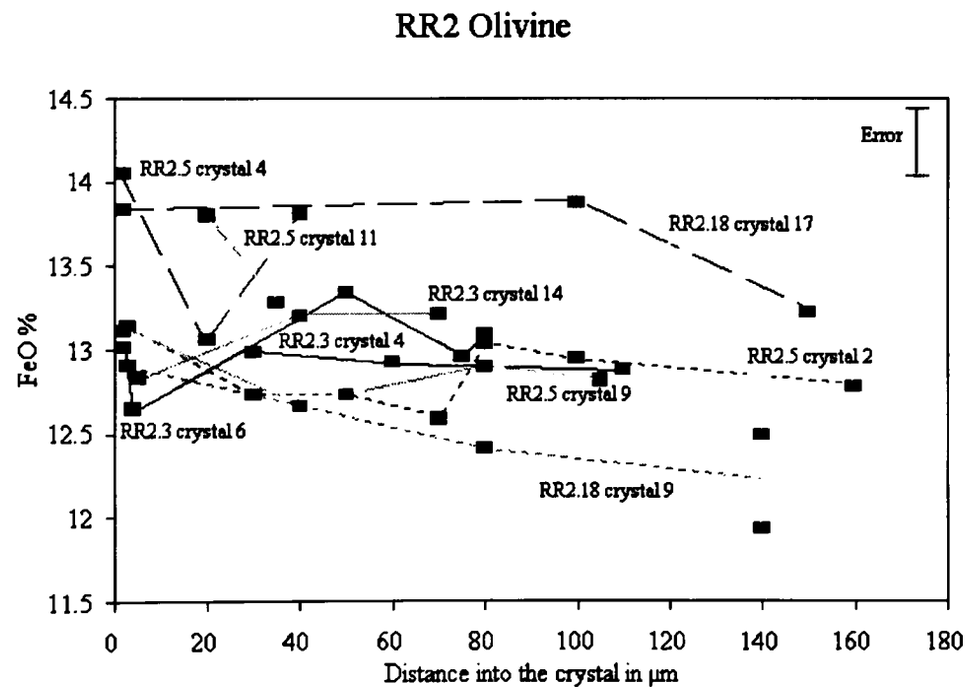

Figure 32 **MgO content of RR3 olivines plotted against distance into the crystal**

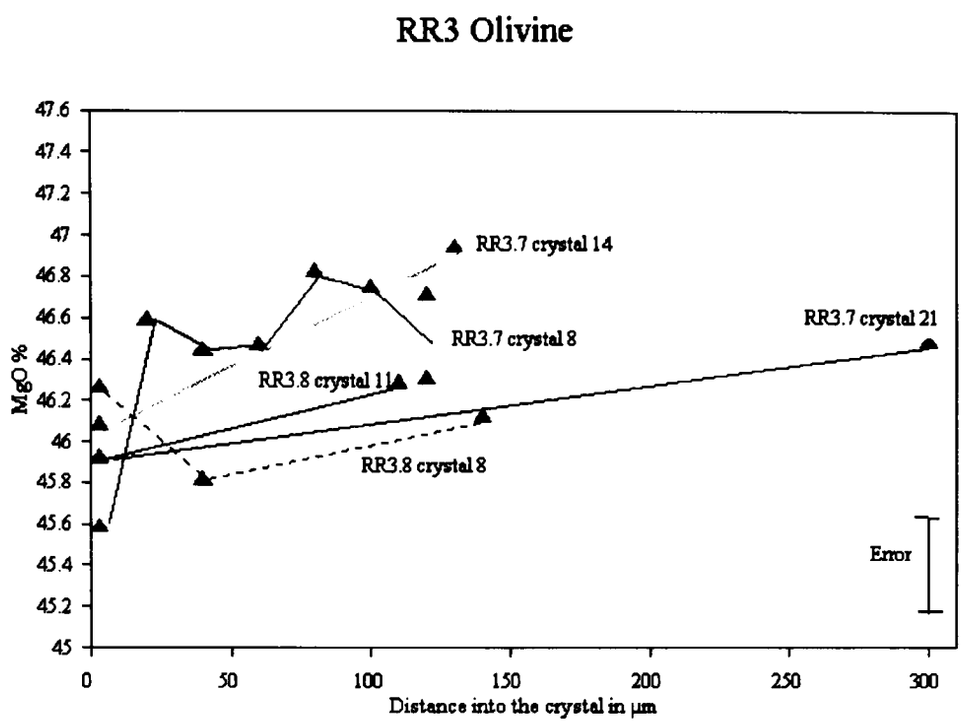

Figure 33 **FeO content of RR3 olivines plotted against distance into the crystal**

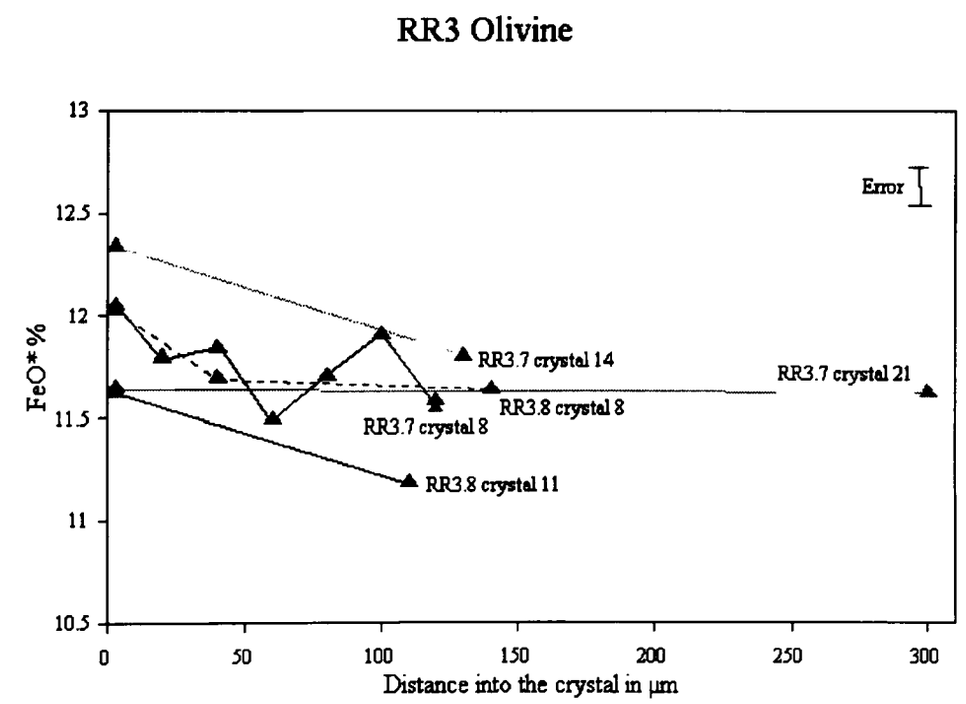

Figure 34 **MgO content of RR4 olivines plotted against distance into the crystal**

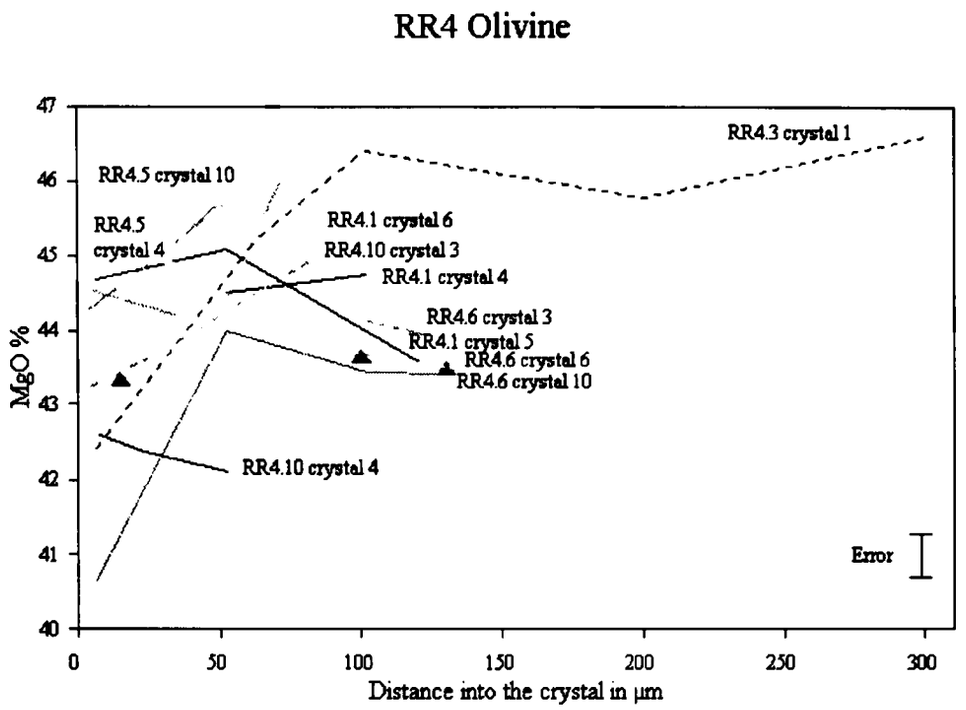

Figure 35 **FeO content of RR4 olivines plotted against distance into the crystal**

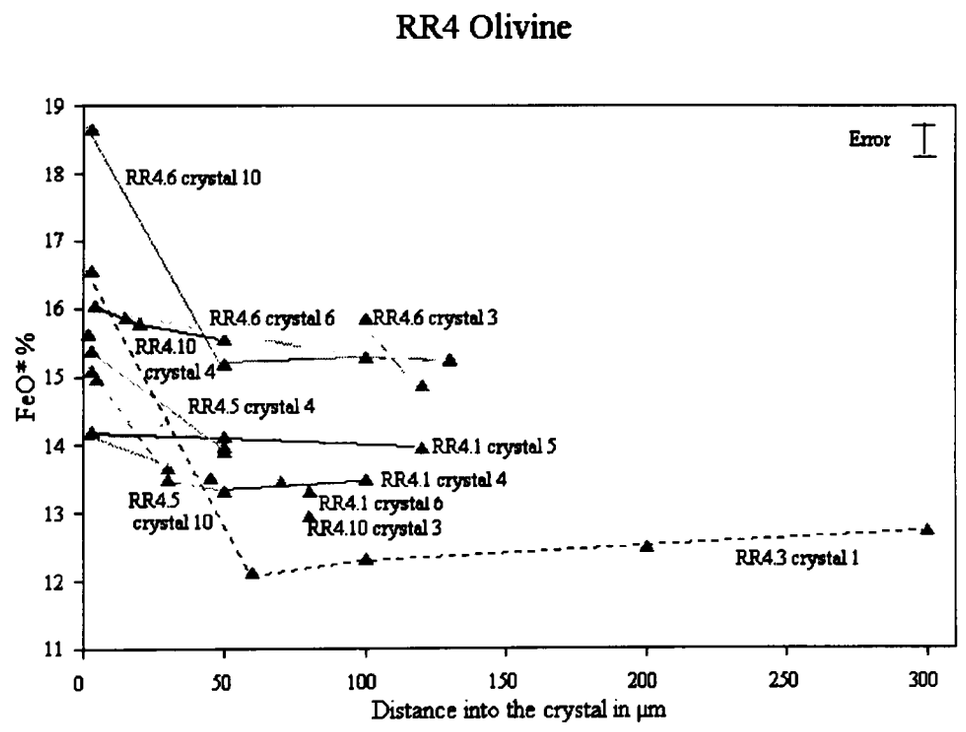

Figure 36 **MgO content of RR8 olivines plotted against distance into the crystal**

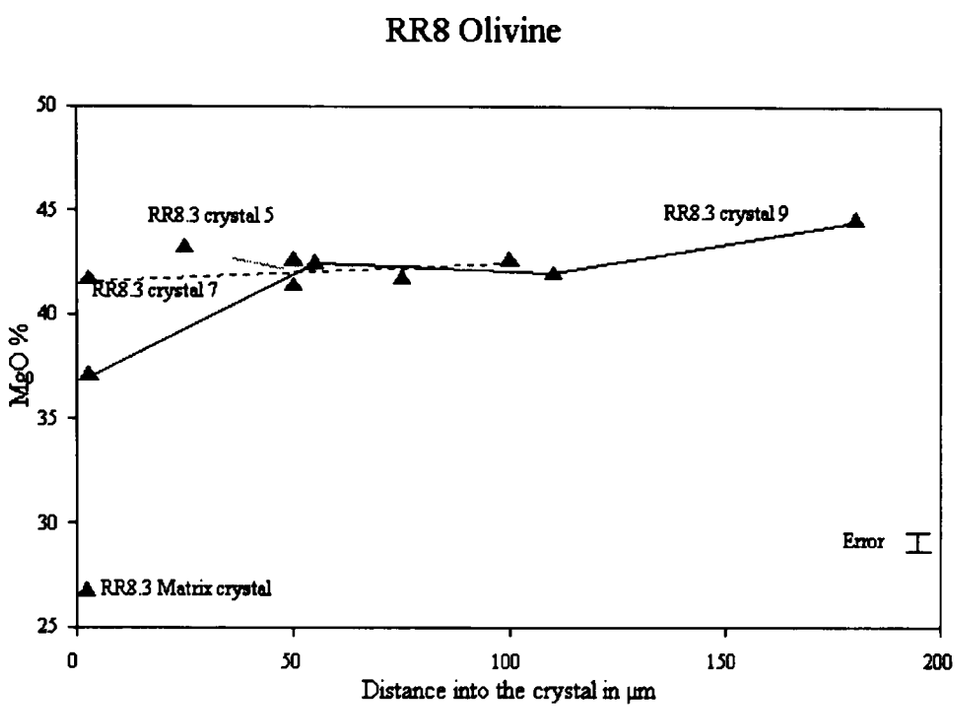

Figure 37 **FeO content of RR8 olivines plotted against distance into the crystal**

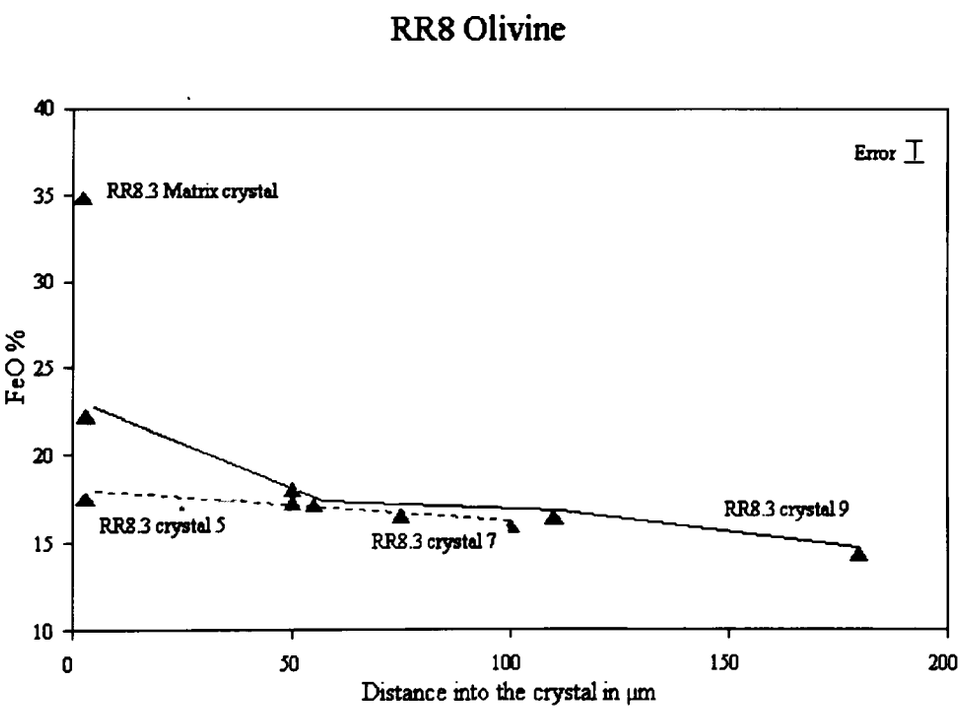

Figure 38 MgO content of RR9c olivines plotted against distance into the crystal

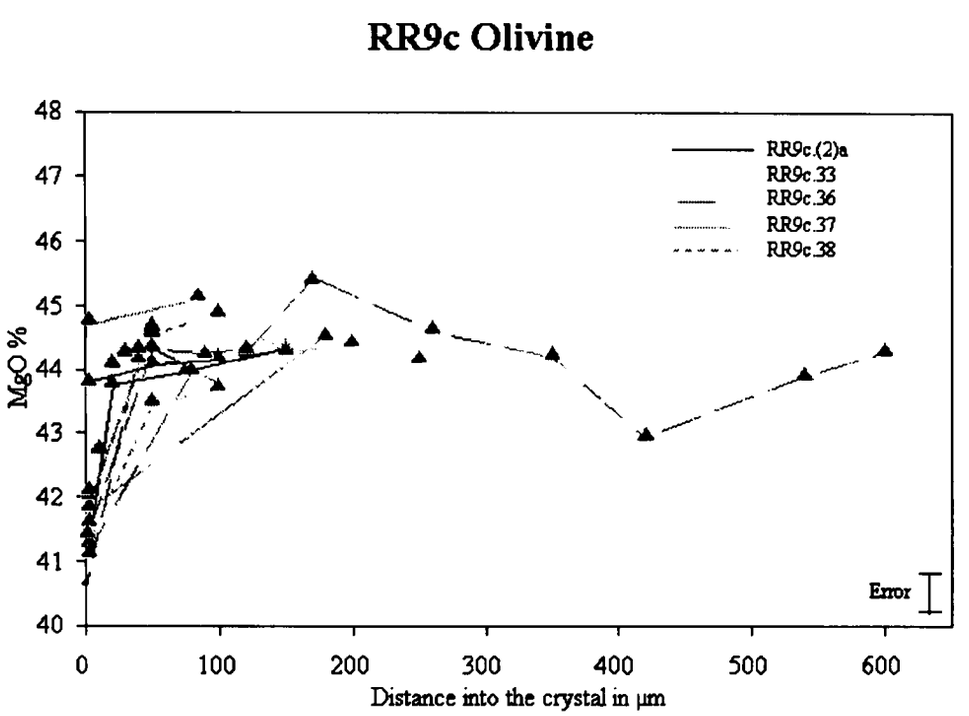

Figure 39 FeO content of RR9c olivines plotted against distance into the crystal

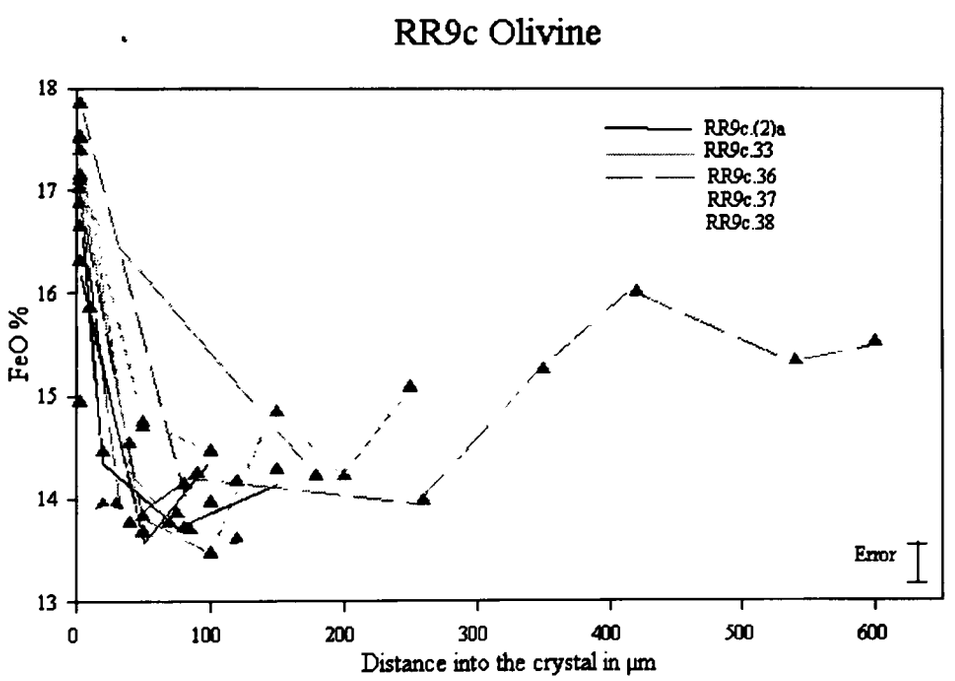

Figure 40 MgO content of RR10 olivines plotted against distance into the crystal

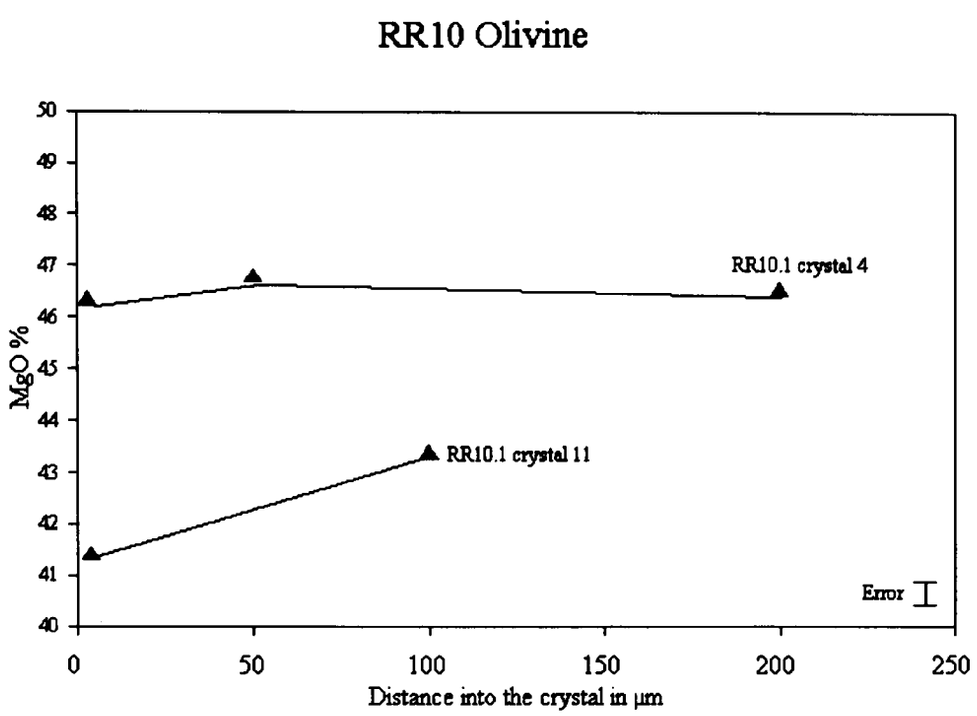

Figure 41 FeO content of RR10 olivines plotted against distance into the crystal

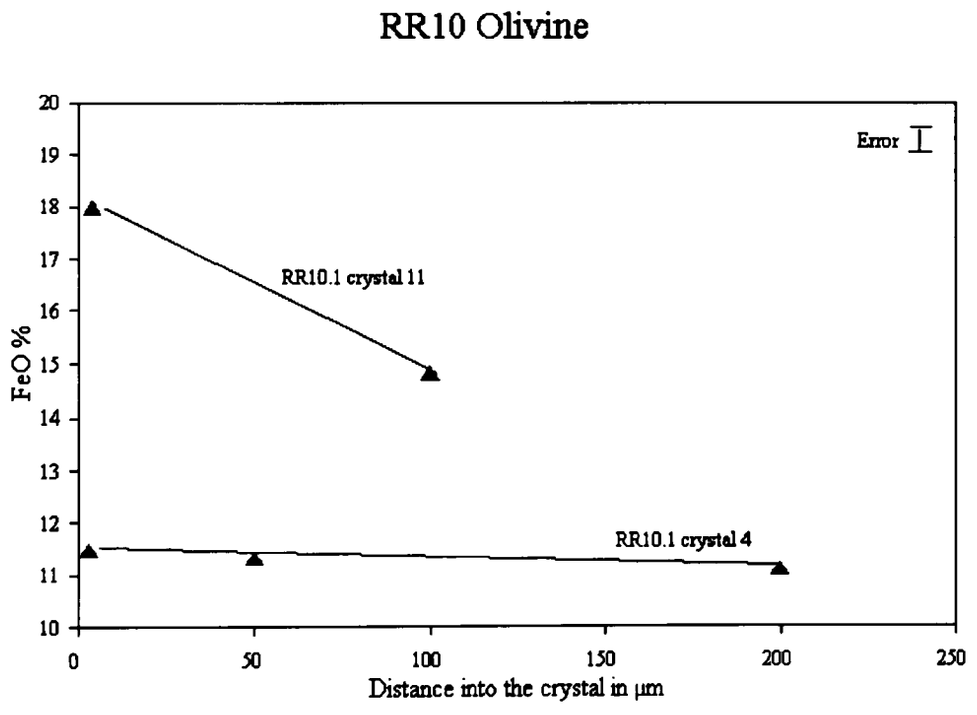

Figure 42 An content of RR9c plagioclase plotted against distance into the crystal

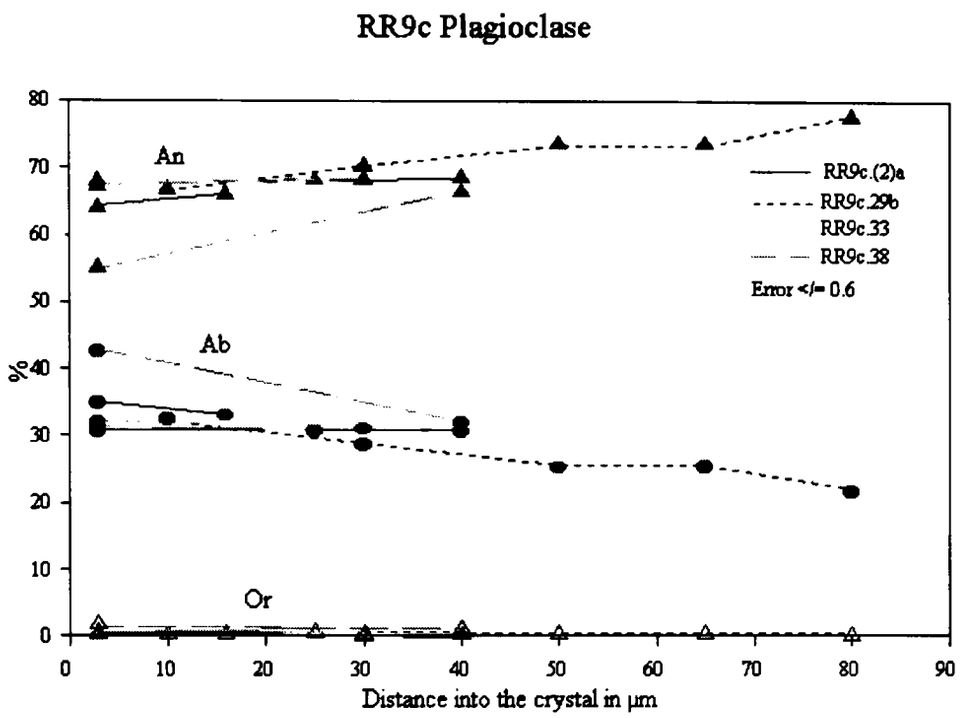

eruption of these lavas. [Two crystals in figs. 38-39 do not show the sharp fall in MgO near the margin of the crystal; this may be due to sampling (the form of the crystal and the angle it is cut), or to the crystal being broken during eruption, or to difficulties in measuring the distance into the crystal accurately.] In plagioclase, the Na_2O content increases towards the margins of the phenocrysts and is always higher in the matrix crystals. Plotting anorthite content as a function of distance into the phenocryst for RR9c clearly displays the zonation in the plagioclase phenocrysts (fig. 42).

The variation in chemistry with distance into the crystal, although evident, is difficult to quantify for chrome spinel as the crystals rarely exceed 40 μm diameter. The FeO^* contents invariably increase from core to margin, MgO and Al_2O_3 both decrease while chromium behaves in a less predictable manner. In all cases the greatest change occurs close to the edge of the crystal.

3.5 Matrix Mineralogy

Clinopyroxene is clearly present within the matrix of the more westerly sites where microlites are slightly larger than at the easterly sites. At both RR2 and RR3 clinopyroxene was identified as a matrix phase in some samples. It does not exceed 2% by volume in any of the RR3 samples, whereas at RR2 microlites of clinopyroxene may represent 4-5% of some samples. All the samples in this collection

display some matrix alteration, where microlites form the nucleation sites for the growth of palagonite[1] minerals. The principal microlite phase present is clinopyroxene at sites RR2-9c, with magnetite becoming increasingly important in the matrix from RR8 westwards. The heavy body colour of the alteration minerals severely hampers both the identification and estimation of concentration of such microlites (see for example plate 1 and 2 plane polarized light images). Consequently, estimates of the concentration of clinopyroxene in samples from RR2, and to a lesser extent from other eastern sites, should be considered with some caution. Microprobe compositions from the slightly larger matrix crystals of clinopyroxene at RR3 are given in table 13 (and table A8). Three samples from RR4 contained matrix clinopyroxene crystals large enough to be analysed (*ca.* 3 μm); the results are listed in table 13 (and table A12). The matrix crystals show widely varying chemistry between the three rocks, probably reflecting the variation in the chemistry of the final melts from which they crystallised. In all cases clinopyroxene is Ca- and Ti-rich and falls into the augite or salite fields of the pyroxene tetrahedron. Clinopyroxenes at RR12d are typically titaniferous salite-ferrosalite in the range $Ca_{52}Mg_{30}Fe_{18}$-$Ca_{48}Mg_{19}Fe_{33}$ (though no good quality analyses were obtained due to their slight alteration). They are lower in Mg and higher in Ca and Fe than the matrix clinopyroxene recorded from Rodrigues island which was in the range $Ca_{47}Mg_{45}Fe_{8}$-$Ca_{47}Mg_{33}Fe_{20}$ (Baxter *et al.*, 1985). They are however, contained within the broad range displayed by the matrix clinopyroxenes from other sites on the Rodrigues Ridge ($Ca_{52\text{-}34}Mg_{46\text{-}7}Fe_{18\text{-}46}$).

Magnetite occurs as a fine dust within the matrix, and as a pseudomorph after the rare chrome spinels in RR12d. At this site some other opaques, possibly skeletal ilmenite, were also noted within the matrix, although no analytical data are available for these. At all of the sites the magnetite in the matrix is invariably skeletal and generally too small (<3 μm diameter) for quantitative analysis although a qualitative analysis is given in table 14.

3.6 Vesicles and Alteration

The lavas of the Rodrigues Ridge as a whole, show an increase in the amount of vesiculation and in the quantity of alteration products, from east to west. Typically zeolites are more common in RR10 and RR12d lavas than in those of the more eastern sites. The lavas of RR10 and RR12 also show a greater degree of vesiculation and a higher degree of porosity caused by changes in volume associated with formation of alteration minerals.

Lavas from RR2 have between 2-10% (by volume) of vesicles, occasionally infilled by calcite. At RR3, RR4 and RR8 vesicles make up no more than 6% of the samples by volume, and are occasionally

---

1

Palagonite is actually a mineraloid devitrification product of volcanic glass, which itself is replaced principally by chlorite, serpentine and clay minerals. The term 'palagonite' is used here for the yellow orange or brown amorphous replacement product of volcanic glass. The precise nature of this material is beyond the scope of this thesis and is the subject of research currently being undertaken by M. M. Hall.

partially infilled by either palagonite[1] (RR3 and RR8 only), serpentine (RR8 only) or calcite. Some samples from RR4 display partially infilled vesicles with parallel surfaces, one side of which is filled. These 'geopetal' infills are the result of calcite filling the lower part of the vesicle and indicate the orientation of the sample on the sea floor. One sample from RR12d was also noted to contain a limestone clast with its own manganese coat and geopetal infills. At both RR8 and RR12d some samples were noted to have foraminifera within the vesicles, indicating that the vesicles had been open to the surrounding sea water. It is likely that these foraminifera, which are invariably juveniles (Heward pers. comm.), are drawn into the vesicles during the cooling process. The occurrence of microfossils in submarine basalts is not uncommon and has been related to the disruption and reworking of sediments during the eruptive process (Nayudu 1972). At RR9c vesicles and amygdales, do not exceed 8% by volume; they are lined or partially infilled by serpentine, zeolite, palagonite, calcite, opaques and the red-brown pleochroic mineraloid, iddingsite. There is an increase in the number of secondary mineral species from east to west along the Rodrigues Ridge between RR2 and RR10, which is reflected in the greater variety of vesicle linings. Like RR10 the lavas of RR12d are highly vesicular ranging from 12-38% by volume of the thin sections. At RR10 in particular, the severe alteration makes the degree of vesiculation difficult to estimate. The replacement of original minerals such as olivine, plagioclase or clinopyroxene by secondary minerals like serpentine, albite or the mineraloid iddingsite results in slight volume changes, which in turn opens up fractures allowing more seawater into the rock. Further secondary minerals like zeolites, which may reach 35% by volume, grow in the vesicles and in the spaces left by the alteration and leaching of the matrix. Voids reached 20% in the RR12 lavas while in the single tuff studied they compose 65% of the volume. The major element analyses display very high LOI (loss on ignition) values in conjunction with high levels of K_2O, H_2O and CO_2. The high level of alteration minerals in these samples resulted in one sample actually melting during ignition! The zeolites in the two RR10 lavas studied show consistently low Ca contents with high K contents (see table 14). At RR10.1 the zeolites show the highest K, Si and Al contents associated with lower Na and higher totals *i.e.*. lower unanalysed volatiles when compared to the other Rodrigues Ridge sites. Calcite has been observed within the vesicles of some RR10 lavas, suggesting that the CaO content (*ca.* 11-13%) of some RR10 lavas, although apparently typical of basalt, is the result of secondary mineral growth and is not original. This demonstrates how the presence of secondary minerals significantly affects the chemistry.

1

Palagonite is actually a mineraloid devitrification product of volcanic glass, which itself is replaced principally by clay minerals, chlorite and serpentine. The term 'palagonite' is used here for the yellow orange or brown amorphous replacement product of volcanic glass. The precise nature of this material is beyond the scope of this thesis and is the subject of research currently being undertaken by M. M. Hall.

3.7 Discussion

This suite of porphyritic basalts was sufficiently fresh to permit the chemical characterisation of the phenocryst and matrix mineral suites. Only RR10 displayed substantial replacement of the original basaltic minerals. The phenocryst assemblage indicates that the liquidus phases were olivine + chrome spinel + plagioclase. Skeletal textures are very common with phenocryst olivine displaying hopper or less commonly ameboid forms. Plagioclase displays forked or ragged terminations in samples from all sites except RR12d. These skeletal forms are consistent with the lavas having been rapidly cooled on extrusion. The mineralogy of these lavas is typical of basaltic compositions although clinopyroxene does not occur as a phenocryst in the lavas from sites RR2-RR10. At RR12d, where rare phenocrysts of pink titanaugite were observed, no quantitative analyses were possible due to the effects of seawater alteration. These crystals showed flow alignment, like the plagioclase at this site. Based on the observed crystal relationships, the crystallisation sequence was; chrome spinel → olivine → plagioclase (→ clinopyroxene). Crystallisation of clinopyroxene phenocrysts only occurred at the western most site RR12, which was significantly more evolved than the other sites.

There is a general increase in the upper values for Cr# = 100Cr/(Cr + Al) of the chrome spinel crystals present from RR2 to RR10 (table 9). This trend is apparently reversed at RR12 but the limited number of crystals (and of successful analyses) makes this conclusion uncertain. The lower values at each site vary in a less consistent manner. At RR2 the low MgO group has spinels which have higher Al_2O_3 contents and lower Cr# than the high MgO group. These spinels display opaque reaction rims where they occur in the matrix, whereas the spinels observed in the matrix of the high MgO group do not. Behaviour, such as that of the low MgO group, is indicative of crystallisation at higher pressure where the Cr distribution coefficient is reduced (Dick & Bullen 1984). This would also account for the apparent disequilibrium of these spinels. All the analysed chrome spinels from Rodrigues Ridge basalts fall in to type 1 (Cr# <0.60) of Dick & Bullen (1984), *i.e.* they are typical of ocean ridges. Lavas from this group have been derived from the melting of comparatively dry mantle where the phase boundary Ol - En - Di - Sp + melt ⇌ Ol - En - Sp + melt (Ol = olivine, En = enstatite, Di = diopside and Sp = spinel) has limited the degree of melting (*op. cit.*).

Table 9 **Cr# and Al_2O_3 for Chrome Spinel**

Site	Cr#	Al_2O_3 %	Site	Cr#	Al_2O_3 %
RR2 Low MgO Group	0.22 - 0.34	37.0-46.1	RR8	0.27 - 0.52	22.4-40.3
RR2 High MgO Group	0.26 - 0.36	33.3-42.8	RR9c	0.23 - 0.41	27.0-41.3
RR3	0.19 - 0.30	41.0-48.6	RR10	0.48	21.7
RR4	0.20 - 0.40	26.6-47.8	RR12d	0.37	29.8

Table 10

Representative Olivine Analyses

Rock	RR2.3	RR3.7	RR4.6	RR8.2	RR9c.36	RR10.1
Distance	100 μm	Centre	15 μm	Centre	540 μm	4 μm
SiO_2	39.53	40.22	39.61	39.12	39.04	37.99
TiO_2	0.05	0.00	0.05	0.00	0.05	0.22
Al_2O_3	0.21	0.57	0.25	0.00	0.19	1.00
MgO	45.73	46.72	43.35	43.98	43.96	41.43
FeO*	12.88	11.55	15.89	16.03	15.35	17.99
Na_2O	0.51	0.12	0.42	0.26	0.49	0.05
CaO	0.35	0.37	0.23	0.10	0.39	0.39
K_2O	0.00	0.03	0.02	0.00	0.00	0.03
MnO	0.17	0.04	0.11	0.07	0.15	0.23
P_2O_5	0.03	0.24	0.00	0.00	0.04	0.14
Cl	0.01	0.01	0.02	0.00	0.00	0.00
Cr_2O_3	0.00	0.11	0.00	0.14	0.15	0.09
S	0.04	0.02	0.04	0.00	0.00	0.00
Total %	99.51	100.00	99.99	99.70	99.81	99.56
Fo %	86.36	87.82	82.94	83.02	83.62	80.42

NB. Olivine phenocrysts in RR12d samples was rare and generally partially altered, hence no satisfactory analyses were obtained.

---

* Total Fe is calculated as FeO

All measurements take from edge of crystal. 'Centre' indicates that the analysis is from the centre of the phenocryst. Fo = forsterite content, *ie.* 100Mg/(Mg + Fe).

Table 11

Representative Plagioclase Analyses

Rock	RR2.18	RR3.3	RR4.1	RR8.2	RR9c.29b	RR10.1	RR12d.1
Distance	55 μm	Centre	Centre	Centre	50 μm	Centre	Centre
SiO_2	50.08	49.58	48.89	48.95	48.73	57.91	51.11
TiO_2	0.08	0.07	0.11	0.22	0.09	0.28	0.16
Al_2O_3	31.14	31.31	32.37	31.81	31.42	24.34	30.08
MgO	0.00	0.00	0.00	0.06	0.31	0.00	0.19
FeO*	0.51	0.45	0.38	0.33	0.70	1.22	0.75
Na_2O	3.28	2.72	2.64	2.80	2.90	7.23	3.69
CaO	14.33	15.70	15.42	14.90	15.34	6.34	13.32
K_2O	0.00	0.04	0.00	0.16	0.13	1.28	0.10
MnO	0.06	0.05	0.00	0.06	0.04	0.01	0.18
P_2O_5	0.00	0.02	0.05	0.00	0.00	0.02	0.00
Cl	0.06	0.03	0.02	0.02	0.04	0.00	0.00
Cr_2O_3	0.00	0.06	0.07	--	0.14	0.21	0.03
S	0.00	0.00	0.00	0.00	--	0.00	0.00
Total %	99.54	100.03	99.95	99.31	99.84	98.84	99.61
Ab %	29.30	23.79	23.63	25.11	25.31	62.45	33.22
An %	70.70	75.97	76.37	73.96	73.98	30.28	66.18
Or %	0.00	0.25	0.00	0.93	0.71	7.27	0.61

* Total Fe is calculated as FeO

All measurements take from edge of crystal. 'Centre' indicates that the analysis is from the centre of the phenocryst. Ab = Albite content, *ie.* 100Na/(Na+Ca+K), An = Anorthite content, *ie.* 100Ca/(Ca+Na+K), Or = Orthoclase content, *ie.* 100K/(K+Na+Ca).

Table 12

Representative Chrome Spinel Analyses

Rock	RR2.18	RR3.7	RR4.3	RR8.7	RR9c.38	RR10.1	RR12d.4
Distance	10 μm	65 μm	Centre	Centre	28 μm	Centre	Centre
SiO_2	0.42	0.32	4.35	0.62	0.55	0.45	0.51
TiO_2	0.42	0.44	1.00	1.21	0.59	2.90	1.41
Al_2O_3	38.74	46.09	35.61	28.12	39.27	21.66	29.84
MgO	15.84	18.06	13.65	13.48	15.51	11.26	11.24
FeO*	18.63	14.57	20.83	22.50	20.05	31.43	29.74
Na_2O	0.09	0.00	0.59	0.15	0.00	0.37	0.45
CaO	0.11	0.08	0.51	0.05	0.00	0.14	0.13
K_2O	0.05	0.00	0.15	0.01	0.00	0.01	0.01
MnO	0.03	0.12	0.31	0.17	0.13	0.38	0.35
P_2O_5	0.06	0.00	0.00	0.00	0.00	0.00	0.00
Cl	0.06	0.10	0.11	0.02	0.07	0.02	0.06
Cr_2O_3	25.48	20.20	23.29	33.47	23.78	30.34	26.15
S	0.03	0.00	0.00	0.08	0.00	0.00	0.01
Total %	99.96	99.98	100.40	99.88	99.95	98.96	99.90
Cr #	30.61	22.72	30.50	44.40	28.89	48.45	37.02

* Total Fe is calculated as FeO

All measurements take from edge of crystal. 'Centre' indicates that the analysis is from the centre of the phenocryst. Cr # = 100Cr/(Cr+Al)

Table 13

Representative Clinopyroxene Analyses

Rock	RR3.3 Matrix	RR4.1 Matrix	RR8.7 Matrix	RR9c.(2)a Matrix
SiO_2	48.77	44.70	50.30	48.84
TiO_2	2.36	3.72	1.99	1.97
Al_2O_3	9.18	6.46	13.17	4.97
MgO	3.59	9.85	7.98	12.85
FeO*	14.53	11.97	9.61	8.84
Na_2O	3.50	0.67	2.88	0.65
CaO	16.25	20.27	12.34	20.24
K_2O	0.12	0.00	0.16	0.06
MnO	0.18	0.27	0.18	0.11
P_2O_5	0.12	0.33	0.56	0.20
Cl	0.00	0.05	0.10	0.00
Cr_2O_3	0.04	0.15	0.00	0.34
S	0.05	0.00	0.01	0.00
Total %	98.69	98.44	99.28	99.07
Ca	47.28	48.16	41.79	48.27
Mg	10.45	23.40	22.81	30.65
Fe	42.27	28.44	35.40	21.08

* Total Fe is calculated as FeO

All measurements take from edge of crystal. 'Centre' indicates that the analysis is from the centre of the phenocryst. Ca = 100Ca/(Ca+Fe+Mg), Mg = 100Mg/(Mg+Fe+Ca) and Fe = 100Fe/(Fe+Mg+Ca)

Table 14

Representative Analyses of Other Minerals

Rock	RR10.1	RR12d.1	RR10.1	RR10.1
Mineral	Zeolite[1]	Zeolite[1]	Calcite[2]	Matrix Magnetite[3]
SiO_2	50.37	52.85	0.23	0.93
TiO_2	0.05	0.10	0.00	21.39
Al_2O_3	21.49	22.26	0.08	2.17
MgO	0.00	0.01	NA	1.45
$MgCO_3$	NA	NA	6.12	NA
FeO*	0.35	0.36	0.04	NA
Fe_2O_3	NA	NA	NA	66.79
Na_2O	3.26	7.12	0.21	0.35
CaO	0.28	0.26	NA	0.52
$CaCO_3$	NA	NA	91.63	NA
K_2O	13.95	8.76	0.02	0.13
MnO	0.00	0.00	0.03	0.67
P_2O_5	0.08	0.05	0.00	0.02
Cl	0.00	0.01	0.01	0.05
Cr_2O_3	0.05	0.00	0.05	0.00
S	0.00	0.06	0.17	0.02
Total %	89.88	91.84	98.59	94.49

[1] Zeolites contain significant amounts of water, typically 9-25% (Deer *et al.*, 1966) which is not detected by the electron microprobe. This has resulted in consistently low totals for analyses of this mineral.

[2] The carbonates in the calcite were calculated assuming stochiometry.

[3] Matrix magnetite crystals rarely exceed 3 μm in any of these rocks and are often skeletal and/or associated with ilmenite consequently some difficulty has been experienced in analysing these. This result is presented here to demonstrate the titaniferous nature of the matrix minerals. Total iron is shown as Fe_2O_3.

* Total Fe is calculated as FeO

Table 15

Representative Glass Analyses

	RR2.11	RR2.18 Point A	RR2.18 Point B	RR9c.15	RR9c.32	RR9c.15
SiO_2	46.93	48.42	48.66	48.37	49.53	48.18
TiO_2	0.74	1.82	1.67	1.78	2.06	1.82
Al_2O_3	16.31	16.60	16.80	16.20	17.01	16.18
MgO	11.25	7.48	7.36	6.40	4.44	6.36
FeO*	11.85	10.29	10.41	10.18	11.04	10.12
Na_2O	3.56	3.50	3.13	3.87	3.90	3.97
CaO	7.60	11.09	11.10	9.99	9.84	10.22
K_2O	0.02	0.02	0.06	0.77	0.80	0.83
MnO	0.32	0.12	0.11	0.24	0.12	0.03
P_2O_5	0.17	0.00	0.15	0.46	0.66	0.27
Cl	0.08	0.00	0.01	--	0.14	--
Cr_2O_3	0.05	0.03	0.00	0.06	0.14	0.28
S	0.27	0.13	0.17	--	0.08	--
Total %	99.15	99.50	99.63	98.32	99.76	98.26

* Total Fe is calculated as FeO

Chapter 4

4. Geochemistry

4.1 Introduction

In chapter 4 the chemistry of 62 Rodrigues Ridge samples is examined in detail beginning with general characteristics, alteration and then examining the samples for each individual site. After the inter-site characteristics have been considered, C-M-A-S diagrams are drawn to examine the fractionation history of the lavas. The results are then discussed and the along-ridge variation considered.

4.2 Geochemistry

A total of one tuff and 61 lava samples were selected for analysis from seven dredge sites along the Rodrigues Ridge (localities of which are given on fig. 2). Sixty of these samples were selected on the basis of their fresh appearance in hand specimen and thin section. Additionally two altered samples, one from RR12d and one from RR10 were analysed to observe the effects of alteration on their primary chemistry. XRF techniques were used to provide analyses of twelve major and minor element oxides namely; SiO_2, TiO_2, Al_2O_3, $Fe_2O_3^*$ (* total iron as Fe_2O_3), MgO, CaO, MnO, Na_2O, K_2O and P_2O_5. 47 samples were analysed for the volatiles H_2O and CO_2 using an elemental analyser. 14 trace elements; Ba, Cr, Cu, Nb, Ni, Rb, Sc, Sr, Th, U, V, Y, Zn and Zr. were analysed for all samples by either ICP-AES or ICP-MS techniques. Hf was analysed in 25 samples across the suite by ICP-MS. All 62 samples were also analysed for the rare earth elements (REE); La, Ce, Pr, Nd, Sm, Eu, Gd, Tb, Dy, Ho, Er, Yb and Lu either using the ion exchange separation technique of Jarvis & Jarvis (1985) followed by ICP-AES determination, or by ICP-MS directly on whole rock solutions. The results are given in table 16, while details of the analytical techniques used can be found in appendix 3.

4.3 General Characteristics

Collectively the lavas of the Rodrigues Ridge are transitional alkali basalts in the range 8.37% ne (normative nepheline)-7.47% hy (normative hypersthene) (tables 17-23), [NB. due to their severe alteration the six samples from RR10 and one from RR12d have been excluded from this discussion]. Plotted on the normative basalt tetrahedron, they straddle the plane Fo-Ab-Di (olivine-albite-diopside), which approximates to the thermal divide and separates alkaline and tholeiitic compositions (Yoder &

Table 16

Analytical Data for the Rodrigues Ridge

Sample	SiO_2	TiO_2	Al_2O_3	$Fe_2O_3^*$	MgO	CaO	Na_2O	K_2O	MnO	P_2O_5	LOI	Total %	CO_2	H_2O
RR2.2	47.41	I.285	17.20	11.38	8.17	11.13	2.97	0.113	0.180	0.112	0.12	100.070	0.22	0.56
RR2.3	46.76	1.082	19.41	11.84	4.52	11.96	3.14	0.158	0.156	0.162	0.72	99.908	0.33	1.03
RR2.4	47.68	1.024	18.20	10.94	7.60	11.59	2.95	0.157	0.153	0.076	-0.07	100.300	0.29	0.56
RR2.5	46.74	1.052	19.00	11.54	5.30	11.75	3.03	0.159	0.148	0.141	0.72	99.580	0.26	0.87
RR2.6	46.41	1.036	18.63	11.41	6.38	11.53	2.90	0.103	0.165	0.142	0.72	99.426	0.40	0.95
RR2.7	47.18	1.271	16.82	11.25	8.52	11.01	2.97	0.127	0.168	0.097	0.00	99.413	0.22	0.48
RR2.8	47.33	1.256	16.97	11.29	8.51	11.02	2.99	0.141	0.179	0.100	0.13	99.916	0.18	0.56
RR2.9	47.12	1.260	16.57	11.20	8.70	10.72	2.85	0.180	0.286	0.098	0.66	99.644	--	--
RR2.10	47.82	1.271	17.08	11.23	8.62	10.93	2.99	0.128	0.174	0.096	0.05	100.389	0.18	0.56
RR2.11	47.61	1.248	16.83	11.22	9.00	10.81	2.97	0.121	0.203	0.092	-0.18	99.924	0.15	0.48
RR2.12b	47.34	0.917	17.60	10.92	8.40	10.84	2.85	0.281	0.161	0.081	0.28	99.670	--	--
RR2.16	46.15	1.096	19.50	12.25	3.92	12.18	3.15	0.077	0.162	0.235	0.97	99.690	0.35	1.07
RR2.17	47.52	1.233	16.78	11.11	8.76	10.67	2.92	0.124	0.176	0.090	-0.08	99.303	0.29	0.56
RR2.18	47.46	1.255	16.97	11.31	8.62	10.86	2.98	0.115	0.175	0.108	0.07	99.923	0.33	0.56
RR3.1	44.65	0.992	18.85	10.67	3.03	15.06	3.01	0.123	0.153	0.135	3.27	99.943	2.60	0.87
RR3.2	45.80	0.971	19.16	11.67	5.35	11.97	3.02	0.131	0.181	0.192	1.34	99.785	0.37	1.19
RR3.3	45.49	1.017	19.54	11.85	5.03	11.59	3.12	0.134	0.191	0.280	1.42	99.662	0.15	1.27
RR3.5	44.40	0.977	18.94	12.33	8.22	10.42	2.87	0.079	0.125	0.407	1.53	100.298	0.37	1.51
RR3.6	45.15	0.998	19.21	11.72	5.91	11.55	3.00	0.116	0.134	0.360	1.32	99.468	0.26	1.35
RR3.7	44.40	0.947	19.58	11.86	7.55	10.83	2.89	0.111	0.142	0.381	1.49	100.181	0.44	1.43
RR3.8	44.07	0.983	19.32	12.03	7.30	10.07	2.91	0.095	0.218	0.350	1.44	98.786	0.33	1.67
RR3.11	45.74	1.154	20.22	12.07	3.09	11.93	3.33	0.092	0.163	0.279	1.57	99.638	--	--

Table 16 cont... **Analytical Data for the Rodrigues Ridge**

Sample	SiO_2	TiO_2	Al_2O_3	$Fe_2O_3^*$	MgO	CaO	Na_2O	K_2O	MnO	P_2O_5	LOI	Total %	CO_2	H_2O
RR4.1	47.27	0.861	17.56	10.94	8.97	11.02	2.84	0.225	0.159	0.067	0.30	100.212	0.66	0.32
RR4.2	47.50	0.882	17.70	10.89	8.71	10.80	2.86	0.242	0.161	0.076	-0.17	99.651	0.26	0.40
RR4.3	47.78	0.962	17.73	10.90	8.68	10.71	2.94	0.314	0.160	0.098	-0.25	100.024	0.37	0.48
RR4.4	46.53	0.958	17.21	10.70	8.92	10.49	2.92	0.336	0.163	0.096	-0.10	98.223	--	--
RR4.6	47.96	1.814	16.95	11.90	7.52	9.44	3.48	0.631	0.185	0.247	0.09	100.217	0.22	0.64
RR4.8	47.28	1.283	16.91	11.25	8.48	11.00	2.95	0.123	0.175	0.112	-0.04	99.523	--	--
RR4.10	47.41	0.866	17.62	10.85	8.95	10.76	2.84	0.244	0.159	0.073	-0.04	99.732	0.40	0.56
RR4.12	47.58	0.895	17.61	10.88	8.73	10.87	2.82	0.252	0.163	0.074	-0.08	99.794	--	--
RR8.1	45.32	1.484	15.52	12.06	11.67	9.90	2.63	0.622	0.174	0.311	0.67	100.361	0.37	1.03
RR8.2	45.72	1.433	15.20	11.99	12.13	9.63	2.64	0.663	0.170	0.240	0.26	100.076	0.37	0.79
RR8.3	43.89	1.503	15.24	13.42	9.89	10.20	2.46	0.463	0.335	0.395	1.94	99.736	--	--
RR8.4	45.68	1.348	15.08	11.97	12.06	9.18	2.62	0.552	0.168	0.230	0.51	99.398	0.29	1.03
RR8.5	48.56	1.525	17.55	10.01	6.21	10.30	3.04	0.869	0.079	0.377	1.27	99.880	--	--
RR8.7	47.15	1.502	17.30	11.80	8.10	9.33	3.19	0.362	0.125	0.149	1.44	100.448	0.73	1.43
RR9c.6	47.41	1.518	16.23	11.45	9.70	8.95	3.00	0.714	0.129	0.232	0.97	100.303	0.15	1.35
RR9c.11	44.00	1.458	16.69	13.80	8.39	9.98	2.99	0.321	0.169	0.903	1.28	99.981	0.37	1.43
RR9c.14	46.98	1.503	16.18	11.13	9.20	9.48	2.94	0.712	0.118	0.330	1.25	99.823	0.40	1.43
RR9c.15	47.32	1.425	15.56	11.63	10.41	8.84	3.01	0.744	0.154	0.207	0.53	99.830	0.33	0.95
RR9c.18	47.29	1.498	16.09	11.17	7.85	10.08	2.97	0.726	0.113	0.258	1.63	99.675	0.59	1.59
RR9c.20	48.35	1.531	17.95	9.96	6.19	10.32	3.19	0.865	0.082	0.375	1.49	100.303	0.29	1.51
RR9c.21	46.36	1.494	15.71	11.60	10.18	8.91	2.98	0.720	0.132	0.228	1.05	99.364	--	--

Table 16 cont... **Analytical Data for the Rodrigues Ridge**

Sample	SiO_2	TiO_2	Al_2O_3	$Fe_2O_3^*$	MgO	CaO	Na_2O	K_2O	MnO	P_2O_5	LOI	Total %	CO_2	H_2O
RR9c.32	47.65	1.557	16.55	10.89	8.61	9.37	3.09	0.734	0.111	0.337	1.12	100.019	0.29	1.35
RR9c.33	47.57	1.451	16.37	10.99	8.97	9.65	2.90	0.715	0.109	0.326	1.21	100.261	0.22	1.35
RR9c.35	47.84	1.617	17.50	10.75	6.65	10.29	3.19	0.704	0.110	0.28	1.01	99.941	0.29	1.43
RR9c.36	47.20	1.488	16.05	11.05	8.52	9.99	2.94	0.685	0.114	0.251	1.56	99.848	0.77	1.59
RR9c.37	47.30	1.437	15.59	10.86	9.44	9.68	2.89	0.618	0.118	0.214	1.54	99.687	0.48	1.59
RR9c.38	47.82	1.539	16.81	11.19	7.35	10.06	3.08	0.769	0.098	0.321	1.56	100.597	0.33	1.75
RR9c.39	47.30	1.534	16.41	10.44	6.87	11.25	3.07	0.803	0.105	0.400	2.17	100.352	0.36	1.59
RR10.1	31.27	2.744	14.62	13.59	9.75	12.86	2.47	0.410	0.180	1.039	10.12	99.053	3.33	5.16
RR10.6	30.71	2.363	13.39	12.35	8.31	16.45	2.30	0.497	0.176	0.713	11.68	99.939	7.44	3.97
RR10.7	27.58	2.337	17.07	13.05	13.72	2.56	3.32	1.356	0.198	2.404	13.61	97.205	--	--
RR10.8	39.86	2.918	16.13	14.67	5.86	1.37	5.43	3.904	0.221	0.353	8.87	99.586	--	--
RR10.19	39.43	2.735	16.32	13.74	5.25	2.50	5.68	3.733	0.217	0.373	10.05	100.028	--	--
RR10.23	40.34	2.951	15.47	14.87	8.26	7.78	3.39	1.514	0.267	0.932	4.02	99.794	0.55	4.29
RR12d.1	46.55	1.916	17.84	13.57	3.00	8.30	4.23	1.423	0.405	1.052	2.35	100.636	--	--
RR12d.2	46.46	1.868	17.94	12.23	3.18	8.61	4.40	1.412	0.214	1.428	2.41	100.152	--	--
RR12d.4	46.33	1.903	17.67	12.23	2.91	8.24	4.29	1.492	0.257	1.104	2.05	98.476	0.40	1.98
RR12d.5	48.55	1.884	17.97	12.20	3.09	7.86	4.35	1.770	0.157	0.694	1.66	100.185	0.22	1.59
RR12d.8	41.60	2.076	17.41	13.72	4.30	8.01	3.74	1.634	0.238	0.448	6.53	99.706	--	--
RR12d.9	48.56	2.176	18.31	14.09	2.92	8.413	4.35	1.160	0.561	0.964	--	101.501	0.57	1.91

Major elements were achieved by XRF except for RR12d.9 which was analysed on the ICP-AES. Water and CO_2 were obtained by elemental analyser.

Table 16 cont... **Analytical Data for the Rodrigues Ridge**

Sample	Ba	Cr	Cu	Hf	Nb	Ni	Rb	Sc	Sr	Th	U	V	Y	Zn	Zr
RR2.2	14.15	425.9	78.87	--	1.37	217.73	0.74	35.59	150.9	0.12	0.08	222.6	28.88	104.91	88.8
RR2.3	13.31	264.2	105.89	--	1.30	152.40	2.91	33.56	165.8	0.08	0.35	241.3	25.61	104.30	60.0
RR2.4	9.64	361.3	114.21	1.27	0.83	188.76	3.04	31.05	152.0	0.28	0.51	202.3	20.09	117.99	57.1
RR2.5	15.28	249.6	122.13	--	0.87	145.35	3.65	32.86	161.6	0.17	0.31	230.9	22.80	84.31	59.4
RR2.6	14.23	235.9	102.12	2.70	0.93	171.13	1.45	32.80	159.5	0.17	0.33	221.61	21.73	78.09	57.4
RR2.7	19.85	401.7	83.80	--	1.76	213.97	2.46	34.78	158.2	0.18	0.08	216.98	30.03	87.30	88.2
RR2.8	24.02	388.4	82.90	--	1.66	211.31	4.94	34.81	158.7	0.08	0.07	218.87	29.55	84.30	89.1
RR2.9	17.49	325.0	82.32	1.67	1.08	246.28	1.11	35.85	162.7*	0.24	0.10	224.0*	28.33	116.93	89.8
RR2.10	28.81	387.8	75.80	--	--	215.80	--	35.43	160.4	0.16	0.05	217.56	39.84	98.20	87.2
RR2.11	13.90	384.2	97.26	2.26	1.35	247.86	1.83	34.81	148.8	0.24	0.06	205.8	28.51	94.71	88.5
RR2.12b	11.88	370.0	104.68	2.41	1.14	245.24	4.23	39.85	158.6*	0.12	0.08	236.2*	29.24	134.19	89.1
RR2.16	32.52	193.2¶	102.80	--	1.73	83.19	0.76	34.09	173.1	0.24	0.66	295.8	26.60	125.70	--
RR2.17	14.93	352.2	91.41	1.65	1.83	214.09	5.73	34.95	161.0	0.66	0.79	206.27	28.58	108.86	--
RR2.18	12.76	296.0	85.11	--	--	221.28	--	34.68	148.3	0.21	0.10	216.2	29.00	109.35	89.1
RR3.1	12.35	243.5	124.61	0.99	1.39	127.55	3.30	32.68	171.9	0.19	0.31	224.1	24.17	71.17	65.6
RR3.2	27.83	562.1	122.85	--	0.82	295.78	0.90	34.91	160.5	0.92	0.39	240.2	22.93	83.64	65.4
RR3.3	47.79	300.2	122.90	--	0.98	205.00	2.12	35.40	177.2	0.39	1.18	248.29	25.30	102.10	68.6
RR3.5	46.17	554.5	115.70	--	2.32	302.73	6.58	33.12	166.0	0.36	2.64	232.31	25.51	120.30	--
RR3.6	56.15	520.0	116.80	--	1.94	211.58	6.40	35.78	162.3	0.43	2.65	244.0	25.12	101.40	68.5
RR3.7	16.59	530.3	122.85	--	1.14	307.80	2.42	35.18	149.5	0.16	2.69	240.1	27.35	94.27	--
RR3.8	37.17	503.9	132.97	--	0.54	296.6	<0.19	33.94	181.2	0.40	2.11	225.0	24.23	136.70	--
RR3.11	17.67	238.5	114.50	1.71	0.81	138.77	2.35	37.85	186.7*	0.07	1.03	289.9*	25.26	123.83	77.8

Table 16 cont... **Analytical Data for the Rodrigues Ridge**

Sample	Ba	Cr	Cu	Hf	Nb	Ni	Rb	Sc	Sr	Th	U	V	Y	Zn	Zr
RR4.1	52.41	256.6	89.26	--	4.86	198.99	4.87	29.72	189.0	0.46	0.11	180.6	19.21	71.00	67.7
RR4.2	57.78	220.5	103.82	--	5.12	194.73	10.07	29.95	188.1	0.63	0.13	173.2	19.72	64.64	68.9
RR4.3	97.80	252.0	92.31	--	6.83	191.95	11.79	30.00	210.8	0.58	0.17	177.64	23.24	72.85	82.4
RR4.4	69.41	216.7	95.21	1.72	8.14	210.52	7.96	30.55	213.9*	1.16	0.24	178.2*	20.45	94.81	82.6
RR4.6	292.6	171.1	70.49	--	15.79	171.73	12.95	29.34	233.9	1.32	0.39	230.11	36.71	93.60	176.5
RR4.8	57.88	268.3	83.18	1.57	4.20	188.95	4.29	28.59	214.0*	1.02	0.14	187.8*	18.06	92.92	74.4
RR4.10	72.56	232.1	96.80	0.98	3.82	200.12	4.85	29.71	194.2	0.82	0.18	175.65	20.02	77.10	--
RR4.12	49.51	187.4	96.79	1.40	3.07	203.87	3.11	30.66	197.5*	1.07	0.25	177.2*	19.40	96.50	69.5
RR8.1	205.90	509.9	68.15	--	15.20	365.40	8.75	28.59	360.3	1.48	0.42	231.5	28.77	95.00	--
RR8.2	193.10	481.4	77.70	0.51	15.98	367.89	12.62	27.65	341.7	1.16	0.33	206.94	23.51	88.90	123.4
RR8.3	152.93	624.3	90.93	3.06	17.43	348.82	11.64	29.52	357.6*	2.56	1.05	326.3*	39.77	169.72	128.9
RR8.4	135.96	453.4	85.11	--	14.69	397.60	14.13	28.32	306.7	1.25	0.44	208.7	22.60	90.00	--
RR8.5	115.22	550.5	171.23	2.52	16.65	479.95	12.87	25.74	302.5*	2.03	0.72	202.2*	21.86	236.47	141.6
RR8.7	44.61	491.7	58.08	--	6.19	202.30	16.62	24.30	234.3	0.54	0.45	179.9	22.25	117.60	87.9
RR9c.6	171.45	481.9	91.34	--	13.66	340.83	13.67	26.80	334.7	1.43	0.42	189.8	22.96	91.27	128.2
RR9c.11	112.53	343.3	83.03	--	11.01	325.33	3.11	29.01	411.2	0.87	1.37	242.4	28.03	117.00	109.7
RR9c.14	130.60	340.9	78.70	--	9.11	300.50	16.50	28.23	350.7	1.24	0.38	200.47	27.67	91.20	--
RR9c.15	144.50	431.6	78.10	--	12.13	331.83	13.99	26.97	326.5	0.99	0.29	192.0	22.11	77.80	123.0
RR9c.18	148.27	410.6	78.87	--	13.14	291.30	15.29	27.99	403.0	1.04	0.37	209.8	23.99	94.00	130.4
RR9c.20	126.84	498.2	80.95	--	--	219.40	--	29.46	351.6	1.38	0.49	195.2	23.57	91.18	--
RR9c.21	--	471.7*	81.7*	--	15.82	322.6*	21.89	--	340.5*	--	--	199.9*	24.20*	99.9*	128.7

Table 16 cont... **Analytical Data for the Rodrigues Ridge**

Sample	Ba	Cr	Cu	Hf	Nb	Ni	Rb	Sc	Sr	Th	U	V	Y	Zn	Zr
RR9c.32	175.30	440.5	78.70	--	--	300.14	--	27.98	362.2	1.56	0.41	201.39	25.01	98.80	134.4
RR9c.33	110.80	476.9	90.40	--	12.34	311.59	19.35	28.22	322.3	0.98	0.31	202.22	23.88	97.40	118.1
RR9c.35	136.47	242.1	90.44	--	10.69	186.25	18.03	29.53	368.0	1.30	0.30	216.5	26.09	88.14	138.4
RR9c.36	125.84	297.4	86.38	--	11.55	326.33	15.42	27.70	383.1	1.08	0.37	206.1	23.56	83.17	127.2
RR9c.37	148.47	418.6	78.87	--	12.09	382.32	11.07	27.17	364.0	0.96	0.30	195.9	23.17	76.19	122.3
RR9c.38	125.14	348.2	83.03	0.16	13.51	285.30	23.46	28.62	364.0	1.05	0.33	220.3	24.95	105.90	129.9
RR9c.39	151.18	418.5	82.33	--	13.44	262.25	21.17	27.84	400.3	1.13	0.45	212.1	23.56	82.54	127.2
RR10.1	294.06	549.3	72.63	0.68	30.56	333.35	3.70	22.12	529.4	2.02	1.91	289.0	28.72	94.04	187.1
RR10.6	274.90	352.4	61.57	--	26.07	316.64	4.80	22.07	475.1	2.72	2.20	261.0	22.80	108.10	156.3
RR10.7	153.18	304.0	79.88	1.80	26.51	390.51	15.03	18.72	9487*	2.57	3.39	142.2*	31.39	119.42	201.5
RR10.8	274.18	585.6	115.23	1.89	35.28	365.29	44.97	24.23	189.2*	4.48	4.37	147.5*	24.28	185.90	191.0
RR10.19	306.61	593.8	110.49	2.46	31.99	325.47	43.22	22.73	208.2*	4.66	7.80	162.5*	27.10	214.24	181.9
RR10.23	395.85	666.0	87.18	--	36.94	314.70	11.02	23.25	513.6	3.74	4.17	296.1	39.52	112.70	--
RR12d.1	413.61	297.2	81.25	5.50	39.59	91.23	17.41	21.28	569.3*	6.37	2.29	279.8*	68.87	178.83	291.4
RR12d.2	388.75	304.7	72.58	5.24	42.79	69.32	19.19	20.07	593.0*	5.94	2.95	256.2*	68.52	160.71	280.1
RR12d.4	442.41	292.7	80.95	3.29	30.44	63.83	19.38	20.70	540.8	3.41	1.60	236.6	68.55	146.10	284.3
RR12d.5	383.90	330.7	84.26	--	36.36	47.54	34.70	21.17	512.1	3.17	1.64	243.88	40.86	147.55	274.8
RR12d.8	198.22	358.6	127.02	3.24	21.05	142.81	26.73	29.66	405.7*	2.30	1.96	338.9*	46.64	190.23	131.6
RR12d.9	490.49	339.7	74.71	--	40.56	69.92	25.64	20.89	542.8	3.67	1.47	249.2	76.81	160.00	--

Zr was achieved by XRF, U and Th by ICP-MS. All other trace elements were achieved by ICP-AES except for RR2.9, RR2.12b, RR3.11, RR4.4, RR4.8, RR4.12, RR8.3, RR8.5, RR9c.21, RR10.7 RR10.8, RR10.19, RR12d.1, RR12d.2 and RR12d.8 where ICP-MS was used. * Indicates those samples where XRF results were used. ¶ This result has not been confirmed by any other technique.

Table 16 cont... **Analytical Data for the Rodrigues Ridge**

Sample	La	Ce	Pr	Nd	Sm	Eu	Gd	Tb	Dy	Ho	Er	Yb	Lu
RR2.2	1.037	8.833	0.807	8.087	2.355	1.126	4.164	0.590	5.050	1.181	3.009	3.366	0.384
RR2.3	3.185	11.848	0.591	8.558	2.613	1.323	5.126	0.471	5.806	1.290	3.552	3.697	0.248
RR2.4	1.69	6.169	0.601	5.325	1.672	0.803	2.837	0.433	3.399	0.731	2.083	2.119	0.288
RR2.5	3.497	9.103	0.615	6.267	1.767	0.980	3.680	0.443	4.109	0.937	2.521	2.653	0.297
RR2.6	4.853	6.163	0.544	11.168	1.894	0.768	2.555	0.485	3.490	0.676	1.980	2.042	0.282
RR2.7	2.903	8.430	0.913	8.046	2.555	1.158	4.190	0.510	5.051	1.227	3.138	3.191	0.389
RR2.8	5.858	8.339	0.669	13.765	3.000	0.998	3.733	0.565	4.884	0.993	2.838	2.817	0.401
RR2.9	4.673	12.613	1.242	7.966	2.772	0.994	3.516	0.620	3.696	0.960	2.476	2.579	0.447
RR2.10	2.203	9.676	0.812	8.347	2.619	1.086	3.844	0.606	4.918	0.966	3.062	2.976	0.344
RR2.11	2.122	10.521	0.767	8.745	2.520	1.215	4.549	0.682	5.245	0.993	3.250	3.460	0.421
RR2.12b	3.858	9.61	0.996	7.681	2.657	1.179	3.202	0.554	3.715	1.015	2.775	2.591	0.392
RR2.16	4.441	9.051	0.704	7.921	2.392	1.076	4.040	0.508	4.640	1.111	3.100	3.190	0.340
RR2.17	10.324	11.711	0.904	9.392	3.190	1.370	4.953	0.576	5.708	1.327	3.563	3.669	0.413
RR2.18	2.651	9.486	0.792	7.570	2.508	1.147	4.372	0.698	5.025	1.143	3.005	3.196	0.379
RR3.1	4.77	7.236	0.578	10.991	1.950	0.870	3.015	0.440	4.127	0.823	2.439	2.380	0.303
RR3.2	0.781	7.229	0.584	6.052	1.722	0.859	3.042	0.416	3.852	0.807	2.440	2.409	0.335
RR3.3	5.384	6.088	1.006	5.793	2.029	0.914	3.172	0.642	3.996	0.887	2.447	2.634	0.467
RR3.5	4.999	7.622	0.799	7.507	1.886	0.922	3.476	0.470	4.080	0.873	2.523	2.875	0.348
RR3.6	7.406	7.849	0.967	6.076	1.541	0.691	3.497	0.508	3.673	0.768	2.363	2.532	0.385
RR3.7	4.165	9.827	0.638	8.013	1.923	1.089	4.152	0.418	5.122	1.135	3.210	3.627	0.359
RR3.8	4.175	8.462	0.946	6.915	1.721	0.992	3.671	0.658	4.268	0.958	2.659	2.746	0.365
RR3.11	4.041	7.492	0.847	6.589	2.508	0.964	2.853	0.480	3.122	0.854	2.458	2.244	0.379

Table 16 cont... **Analytical Data for the Rodrigues Ridge**

Sample	La	Ce	Pr	Nd	Sm	Eu	Gd	Tb	Dy	Ho	Er	Yb	Lu
RR4.1	3.421	11.399	0.722	6.218	1.651	0.753	2.615	0.397	3.333	0.678	2.060	2.208	0.306
RR4.2	4.297	9.398	0.757	5.464	1.462	0.747	2.514	0.417	3.185	0.738	1.972	2.044	0.270
RR4.3	7.394	17.23	0.844	9.249	2.086	1.051	3.806	0.400	4.435	0.938	2.703	2.786	0.255
RR4.4	7.207	13.395	1.175	6.442	2.142	0.773	2.648	0.338	2.382	0.676	1.939	1.833	0.312
RR4.6	13.167	36.117	2.154	18.493	4.487	1.611	6.925	0.776	6.316	1.297	4.027	3.921	0.483
RR4.8	6.356	12.545	0.981	5.798	1.904	0.786	2.521	0.339	2.402	0.689	1.761	1.747	0.273
RR4.10	6.932	11.37	1.264	6.016	1.688	0.794	2.912	0.531	3.411	0.630	2.051	2.211	0.336
RR4.12	5.77	10.807	0.880	5.550	1.869	0.839	2.490	0.370	2.420	0.652	1.878	1.768	0.289
RR8.1	18.752	42.109	2.249	20.489	4.153	1.528	5.036	0.690	5.040	0.903	2.851	2.752	0.342
RR8.2	1.465	35.172	1.865	19.145	4.109	1.308	4.320	0.484	4.250	0.917	3.472	2.267	0.275
RR8.3	21.75	37.657	3.735	18.611	4.228	1.448	5.572	0.698	4.131	1.182	3.188	2.665	0.477
RR8.4	12.77	28.64	1.854	13.130	3.471	1.108	4.128	0.600	4.009	0.818	2.442	2.270	0.383
RR8.5	14.229	31.688	2.508	13.055	3.096	1.003	3.778	0.505	2.992	0.843	2.146	2.114	0.313
RR8.7	9.822	14.24	1.121	11.430	3.239	1.429	4.603	0.547	4.955	1.020	2.572	2.439	0.261
RR9c.6	9.44	28.025	2.359	13.824	3.097	1.221	3.799	0.747	3.665	0.765	2.204	2.188	0.414
RR9c.11	11.109	26.264	1.684	12.740	3.445	1.252	4.620	0.686	4.539	1.069	2.585	2.616	0.337
RR9c.14	15.825	34.929	2.219	17.466	4.148	1.541	4.899	0.696	5.130	0.993	2.931	2.802	0.381
RR9c.15	12.031	29.36	1.610	13.526	2.941	1.223	4.324	0.481	4.083	0.825	2.284	2.325	0.224
RR9c.18	14.849	29.85	2.007	17.868	3.509	1.183	3.901	0.637	4.223	0.750	2.213	2.114	0.323
RR9c.20	15.91	24.23	2.381	11.930	3.007	1.154	3.726	0.761	3.796	0.856	2.120	2.124	0.395
RR9c.21	--	--	--	--	--	--	--	--	--	--	--	--	--

Table 16 cont... **Analytical Data for the Rodrigues Ridge**

Sample	La	Ce	Pr	Nd	Sm	Eu	Gd	Tb	Dy	Ho	Er	Yb	Lu
RR9c.32	13.03	28.61	2.605	14.480	3.424	1.241	4.091	0.643	4.164	0.852	2.319	2.478	0.403
RR9c.33	11.29	26.53	1.507	12.910	3.070	1.260	4.003	0.525	4.154	0.885	2.278	2.298	0.287
RR9c.35	13.55	31.684	2.058	15.408	3.470	1.331	4.411	0.553	4.506	0.967	2.475	2.545	0.266
RR9c.36	12.02	28.32	1.956	13.430	3.409	1.264	4.216	0.559	4.183	0.893	2.325	2.331	0.315
RR9c.37	14.799	26.03	1.715	19.138	3.489	1.178	3.703	0.510	4.086	0.813	2.137	2.043	0.295
RR9c.38	11.96	26.82	1.843	13.180	3.238	1.207	4.192	0.309	4.087	0.832	2.278	2.298	0.609
RR9c.39	14.799	27.52	2.083	17.978	3.540	1.227	3.909	0.642	4.311	0.776	2.273	2.138	0.339
RR10.1	34.733	83.792	3.143	38.607	8.673	2.858	8.975	0.792	7.201	0.790	3.222	2.836	0.214
RR10.6	17.878	47.696	2.749	22.503	4.823	1.675	4.980	0.630	4.480	0.770	2.100	1.763	0.257
RR10.7	31.769	40.417	5.766	27.628	5.887	1.997	6.983	0.810	3.663	0.932	2.095	1.580	0.276
RR10.8	27.042	59.472	5.445	25.818	5.858	1.743	7.033	0.746	4.106	0.940	2.314	1.897	0.293
RR10.19	24.44	51.868	4.684	22.479	5.423	1.583	6.537	0.705	3.406	0.931	2.340	1.912	0.281
RR10.23	51.218	64.992	4.390	28.557	6.802	2.128	7.329	1.046	5.868	1.129	3.316	2.786	0.461
RR12d.1	50.636	84.147	8.674	38.716	7.673	2.425	10.315	1.176	6.333	1.676	4.800	4.112	0.698
RR12d.2	46.596	71.851	7.627	34.404	6.915	2.218	9.146	1.000	5.371	1.487	4.361	3.882	0.693
RR12d.4	41.380	73.90	4.932	32.990	6.497	2.168	7.862	1.054	7.111	1.643	4.636	4.637	0.703
RR12d.5	40.823	75.088	4.242	33.333	7.129	2.202	7.238	0.857	6.396	1.326	3.443	3.487	0.488
RR12d.8	25.988	35.874	4.514	23.648	5.446	1.858	6.695	0.843	4.890	1.340	3.608	2.979	0.524
RR12d.9	63.210	101.2	5.618	43.390	9.107	2.991	11.380	1.255	9.956	2.335	6.112	5.706	0.734

Rare earth elements were achieved by ICP-MS for RR2.9, RR2.12b, RR3.11, RR4.4, RR4.8, RR4.12, RR8.3, RR8.5, RR9c.21, RR10.7, RR10.8, RR10.19, RR12d.1, RR12d.2 and RR12d.8.

For all other samples an ion exchange column separation followed by ICP-AES was used for all REE except Pr, Tb and Lu for which ICP-MS was used for all samples.

Table 17 **CIPW norms for RR2**

Sample	or	ab	an	ne/hy	di	ol	mt	il	ap	cc	An
RR2.2	0.67	24.50	33.27	0.34 ne	16.19	19.04	1.96	2.44	0.26	0.50	58
RR2.3	0.93	24.04	38.40	1.37 ne	14.88	13.63	2.04	2.05	0.36	0.75	62
RR2.4	0.93	23.75	35.96	0.66 ne	15.70	18.03	1.89	1.94	0.18	0.67	60
RR2.5	0.94	23.85	37.78	0.97 ne	14.91	14.76	1.99	2.00	0.33	0.58	61
RR2.6	0.61	23.95	37.51	0.32 ne	13.36	17.17	1.97	1.97	0.33	0.92	61
RR2.7	0.75	24.00	32.19	0.61 ne	16.64	19.37	1.94	2.41	0.22	0.50	57
RR2.8	0.83	23.84	32.47	0.79 ne	16.63	19.43	1.95	2.39	0.23	0.42	58
RR2.9*	1.06	24.12	31.89	1.50 hy	15.29	19.20	1.93	2.39	0.23	0.68	57
RR2.10	0.76	25.11	32.81	0.10 ne	16.00	19.76	1.94	2.41	0.22	0.42	57
RR2.11	0.72	24.52	32.24	0.33 ne	16.17	20.44	1.93	2.37	0.21	0.33	57
RR2.12b*	1.66	24.06	34.40	0.03 ne	13.83	20.25	1.88	1.74	0.19	0.68	59
RR2.16	0.46	23.61	38.84	1.65 ne	14.99	12.91	2.11	2.08	0.54	0.79	62
RR2.17	0.73	24.71	32.31	2.35 hy	14.81	18.65	1.92	2.34	0.21	0.67	57
RR2.18	0.68	25.22	32.59	0.35 hy	15.08	19.94	1.95	2.38	0.25	0.75	56

All values are quoted as percentages; or orthoclase, ab albite, an anorthite, ne nepheline, hy hypersthene, di diopside, ol olivine, mt magnetite, il ilmenite, ap apatite, cc calcite, An the calculated anorthite content of the plagioclase. CIPW Norm calculated on the basis of $Fe_2O_3/Fe_2O_3+FeO = 0.13$ *as suggested by* ***Brooks 1976.***

* indicates samples where no CO_2 data were available and CO_2 was assumed to be 0.3%.

Table 18 **CIPW norms for RR3**

Sample	or	ab	an	ne/hy	di	ol	mt	il	ap	cc	An
RR3.1	0.73	22.79	37.56	1.45 ne	16.72	9.13	1.84	1.88	0.31	5.92	62
RR3.2	0.77	21.64	38.34	2.12 ne	14.50	15.26	2.01	1.86	0.44	0.83	64
RR3.3	0.79	21.78	38.92	2.50 ne	13.16	15.33	2.04	1.93	0.65	0.33	64
RR3.5	0.47	20.97	38.57	1.80 ne	6.69	23.81	2.13	1.86	0.94	0.83	65
RR3.6	0.69	21.24	38.61	2.25 ne	12.17	17.08	2.02	1.90	0.83	0.58	65
RR3.7	0.66	20.39	40.13	2.20 ne	6.84	22.15	2.04	1.80	0.88	1.00	66
RR3.8	0.56	22.17	39.38	1.33 ne	5.11	22.57	2.07	1.87	0.81	0.75	64
RR3.11*	0.54	23.95	39.96	2.29 ne	13.12	11.84	2.08	2.19	0.65	0.68	63

All values are quoted as percentages; or orthoclase, ab albite, an anorthite, ne nepheline, hy hypersthene, di diopside, ol olivine, mt magnetite, il ilmenite, ap apatite, cc calcite, An the calculated anorthite content of the plagioclase. CIPW Norm calculated on the basis of $Fe_2O_3/Fe_2O_3+FeO = 0.13$ *as suggested by* ***Brooks 1976.***

* RR3.11 norm was calculated assuming $CO_2 = 0.3$ since no actual data were available.

Table 19 **CIPW norms for RR4**

Sample	or	ab	an	ne/hy	di	ol	mt	il	ap	cc	An
RR4.1	1.33	24.03	34.50	0.50 hy	12.67	21.40	1.89	1.64	0.16	1.50	59
RR4.2	1.43	24.02	34.75	0.10 ne	13.63	20.88	1.88	1.68	0.18	0.58	59
RR4.3	1.86	24.83	34.26	0.03 ne	12.98	20.97	1.88	1.83	0.23	0.83	58
RR4.4*	1.99	22.53	32.86	1.18 ne	13.56	21.00	1.84	1.82	0.22	0.68	59
RR4.6	3.73	27.96	28.77	0.81 ne	12.33	19.14	2.05	3.45	0.57	0.50	51
RR4.8	0.73	24.96	32.54	0.46 hy	15.31	19.43	1.94	2.44	0.26	0.91	57
RR4.10	1.44	24.03	34.61	0.51 hy	12.82	21.20	1.87	1.64	0.17	0.92	59
RR4.12*	1.49	23.86	34.65	0.62 hy	13.77	20.39	1.88	1.70	0.17	0.68	59

All values are quoted as percentages; or orthoclase, ab albite, an anorthite, ne nepheline, hy hypersthene, di diopside, ol olivine, mt magnetite, il ilmenite, ap apatite, cc calcite, An the calculated anorthite content of the plagioclase. CIPW Norm calculated on the basis of $Fe_2O_3/Fe_2O_3+FeO = 0.13$ *as suggested by* ***Brooks 1976.***

* Calculated using an estimated CO_2 content of 0.3%

Table 20 **CIPW norms for RR8**

Sample	or	ab	an	ne/hy	di	ol	mt	il	ap	cc	An
RR8.1	3.68	18.10	28.71	2.25 ne	13.00	26.81	2.08	2.82	0.72	0.83	61
RR8.2	3.92	18.71	27.67	1.96 ne	13.12	27.57	2.07	2.72	0.56	0.83	60
RR8.3*	2.74	18.25	29.18	1.39 ne	13.32	25.15	2.31	2.85	0.92	0.91	62
RR8.4	3.26	20.88	27.76	0.70 ne	11.67	28.03	2.06	2.56	0.53	0.67	57
RR8.5*	5.14	25.72	31.68	7.47 hy	11.82	9.81	1.73	2.90	0.87	0.91	55
RR8.7	2.14	26.99	31.82	5.26 hy	7.24	18.35	2.03	2.85	0.35	1.67	54

All values are quoted as percentages; or orthoclase, ab albite, an anorthite, ne nepheline, hy hypersthene, di diopside, ol olivine, mt magnetite, il ilmenite, ap apatite, cc calcite, An the calculated anorthite content of the plagioclase. CIPW Norm calculated on the basis of $Fe_2O_3/Fe_2O_3+FeO = 0.13$ *as suggested by* ***Brooks 1976.***

* These samples were calculated assuming 0.4% CO_2 as no analytical data were available.

Table 21 **CIPW norms for RR9c**

Sample	or	ab	an	ne/hy	di	ol	mt	il	ap	cc	An
RR9c.6	4.22	25.39	28.71	1.03 hy	10.75	22.64	1.97	2.88	0.54	0.33	53
RR9c.11	1.90	22.21	31.17	1.67 ne	8.32	24.53	2.38	2.73	2.09	0.83	58
RR9c.14	4.21	24.88	28.85	1.99 hy	10.95	20.67	1.92	2.85	0.76	0.92	54
RR9c.15	4.40	25.47	26.75	0.36 hy	11.08	24.60	2.01	2.71	0.48	0.75	51
RR9c.18	4.29	25.13	28.43	3.41 hy	13.22	16.47	1.93	2.85	0.60	1.33	53
RR9c.20	5.11	26.99	32.11	2.50 hy	12.11	13.25	1.72	2.91	0.87	0.67	54
RR9c.21*	4.26	23.96	27.37	0.68 ne	10.91	24.37	2.00	2.84	0.53	0.68	53
RR9c.32	4.34	26.15	29.12	2.68 hy	10.82	18.84	1.88	2.96	0.78	0.67	53
RR9c.33	4.23	24.54	29.54	3.01 hy	12.04	19.04	1.90	2.76	0.76	0.50	55
RR9c.35	4.16	26.99	31.35	0.52 hy	13.12	15.89	1.85	3.07	0.65	0.67	54
RR9c.36	4.05	24.88	28.58	4.36 hy	11.79	17.37	1.91	2.83	0.58	1.75	53
RR9c.37	3.65	24.45	27.74	4.00 hy	12.88	18.76	1.87	2.73	0.50	1.08	53
RR9c.38	4.54	26.06	29.77	1.97 hy	13.05	16.63	1.93	2.92	0.74	0.75	53
RR9c.39	4.75	25.98	28.63	3.72 hy	13.08	13.74	1.80	2.91	0.93	3.08	52

All values are quoted as percentages; or orthoclase, ab albite, an anorthite, ne nepheline, hy hypersthene, di diopside, ol olivine, mt magnetite, il ilmenite, ap apatite, cc calcite, An the calculated anorthite content of the plagioclase. CIPW Norm calculated on the basis of $Fe_2O_3/Fe_2O_3+FeO = 0.13$ *as suggested by* ***Brooks 1976.***

* Calculated assuming 0.3% CO_2 since no value were available for this sample.

Table 22

CIPW norms for RR10

Sample	or	ab/lc	an	ne/hy	di/C	ol	mt	il	ap	cc	An
RR10.1	1.40	0.81 lc	27.60	11.32 ne	6.78 di	25.62	2.34	5.21	2.41	7.58	100
RR10.6	2.94	6.07 ab	24.75	7.25 ne	4.23 di	23.19	2.13	4.49	1.65	16.92	80
*RR10.7	8.01	28.09 ab	0.00	39.97 hy	28.39 C	6.08	2.25	4.44	5.57	16.83	0
°RR10.8	23.07	11.72 ab	2.59	18.54 ne	2.02 C	22.20	2.53	5.54	0.82	0.68	18
°RR10.19	22.06	25.34 ab	0.00	12.31 ne	6.93 C	20.39	2.37	5.19	0.86	7.50	-75
RR10.23	8.95	13.92 ab	22.52	8.00 ne	5.34 di	24.71	2.56	5.60	2.16	1.25	62

All values are quoted as percentages; or orthoclase, ab albite, lc lucite, an anorthite, C corundum, ne nepheline, hy hypersthene, di diopside, ol olivine, mt magnetite, il ilmenite, ap apatite, cc calcite, An the calculated anorthite content of the plagioclase. CIPW Norm calculated on the basis of $Fe_2O_3/Fe_2O_3+FeO = 0.13$ *as suggested by* ***Brooks 1976****.*

* Calculated assuming 7.4% CO_2 like RR10.6 which has the nearest LOI to this sample.

° Calculated assuming 3.3% CO_2 like RR10.1 which has the nearest LOI to these samples.

Table 23

CIPW norms for RR12d

Sample	or	ab	an	ne/hy	di	ol	mt	il	ap	cc	An
RR12d.1*	8.41	31.16	25.49	2.51 ne	5.32	14.54	2.17	3.64	2.44	0.91	45
RR12d.2*	8.34	31.17	25.03	3.28 ne	4.91	14.45	2.11	3.55	3.31	0.91	45
RR12d.4	8.82	31.04	24.55	2.85 ne	5.55	13.74	2.11	3.61	2.56	0.92	44
RR12d.5	10.46	31.80	24.28	2.71 ne	7.41	13.21	2.10	3.58	1.61	0.50	43
RR12d.8*	9.66	16.20	25.89	8.37 ne	7.03	16.96	2.37	3.94	1.04	0.91	62
RR12d.9	6.86	35.40	27.01	0.76 ne	4.12	17.26	2.58	4.13	2.23	1.29	43

All values are quoted as percentages; or orthoclase, ab albite, an anorthite, ne nepheline, hy hypersthene, di diopside, ol olivine, mt magnetite, il ilmenite, ap apatite, cc calcite, An the calculated anorthite content of the plagioclase. CIPW Norm calculated on the basis of $Fe_2O_3/Fe_2O_3+FeO = 0.13$ *as suggested by* ***Brooks (1976)***.

* CO_2 content estimated as 0.4% as no analytical data were available.

Tilley 1962). This characteristic must have been acquired above *ca.* 8 kb (25 km) where the thermal divide is absent. On the alkali-silica diagram of Macdonald & Katsura (1964) they straddle the divide between tholeiitic and alkali basalts, with the majority of the samples being mildly alkaline (figs. 43-49).

The Rodrigues Ridge lavas span a wide compositional range, with SiO_2 43.9-48.6%, MgO 2.9-12.1%, Al_2O_3 15.1-20.2%, CaO 7.8-15.1% and $Na_2O + K_2O$ (alkalis) 2.9-6.1%. These ranges are similar to those observed among basalts from Réunion (SiO_2 45.2-48.1%, MgO 1.9-23.7%, Al_2O_3 7.9-21.4 and alkalis 1.7-8.0%). Other oceanic basalts show some overlap with the Rodrigues Ridge but do not display;

1. such low SiO_2 values, *e.g.* Rodrigues Island (46.7-50.1%), the CIR (47.5-51.4%), while the Leg 115 samples from Mascarene Plateau and Chagos-Laccadive Ridge (*i.e.* the trace of the Réunion hotspot) has 45.6-51.5% (Fisk *et al.*, 1988, Baxter *et al.*, 1985, Erlank & Reed 1974, Hekinian 1982 and Backman *et al.*, 1988).
2. such high CaO values, *e.g.* Rodrigues Island (7.6-10.8%), the CIR (10.9-12.9%), Leg 115 (8.3-11.9%), or Mauritius (0.7-11.8%) (*op. cit.*). Furthermore there is a progressive decrease in CaO from east to west along the Rodrigues Ridge.
3. such high Al_2O_3, *e.g.* Rodrigues Island (15.3-17.4%), the CIR (13.8-17.0%), Leg 115 (13.11-18.55%) or Mauritius (9.6-19.1%) (*op. cit.*).
4. Such a broad range of alkali values, *e.g.* Rodrigues Island (3.33-5.74%), the CIR (2.38-3.12%) or Leg 115 (1.68-4.14%) (*op. cit.*).

Like Réunion the lavas of Mauritius display considerable ranges in some of these elements, notably MgO (0-16.1%) and alkalis (2.27-13.4%), which both encompass the values displayed by the Rodrigues Ridge. Similarly the Older Series lavas of Mauritius display lower silica values (43.9-62.2%)(Baxter 1972) like those of the Rodrigues Ridge. Such broad ranges for these two islands probably reflects both the more complete sampling that has been possible here (as well as the wider chemical variation. On the Rodrigues Ridge the sampling of individual sites (volcanic centres) is limited and the broad chemical range reflects the variations between the different volcanic centres sampled along the Ridge. It is notable that for many elements such as Na_2O and K_2O, the lavas from RR2 and RR3 in the east have ranges similar to those of mid-ocean ridges, while the lavas from RR10 and RR12d in the west have ranges more like ocean islands.

Trace element ranges are as follows; Ba 11.9-490.5 ppm, Cr 171-624 ppm, Cu 58.1-171.2 ppm, Hf 0.16-5.50 ppm, Nb 0.8-42.8 ppm, Ni 47.5-480.0 ppm, Rb <0.19-44.97 ppm, Sc 18.7-39.85 ppm, Sr 148.3-593.0 ppm, Th 0.07-6.37 ppm, U 0.06-4.80 ppm, V 173-339 ppm, Y 18.1-68.9 ppm, Zn 70.5-196.0 ppm and Zr 57.1-291.4 ppm. The lavas display a broad range of trace element values, often changing systematically with progression east to west along the Ridge. Despite this, single element plots with MgO show no clear unifying trends linking all the dredge sites. Thus, the systematic trace element variation along the Ridge cannot be explained by high-level processes. In general the incompatible trace elements and Cr increase from east to west, *i.e.* from RR2-RR12d. For each of the

above trace elements the range described by the Rodrigues Ridge is greater than that of Rodrigues Island, the CIR or Leg 115. Only the well sampled and differentiated islands of Mauritius and Réunion have wider ranges for Cr, Ni, V, Y and Zr. On these islands Ba and Nb are similar to the western sites on the Rodrigues Ridge, but higher than at the eastern sites, where Ba and Nb values resemble those of the CIR [8.5-180.3 ppm Ba and 1.2-2.4 ppm Nb (triple junction only)].

Although single element plots with MgO show no clear trends along the Ridge as a whole (see section 6.1), olivine ± plagioclase fractionation trends can be recognised within individual sites, perhaps indicating that the Ridge lavas were derived from several independently evolving volcanic centres. In this model the Ridge results from the coalescence of a number of distinct volcanoes (islands or seamounts). As a result of high-level processes each centre has its own unique geochemical signature, which overprint the signature of the suite as a whole. The suite displays a clear progression from depleted, MORB-like signatures in the east to OIB-like signatures in the west (compare figs. 51-52 with fig. 58, see also section 6.6).

Figure 43

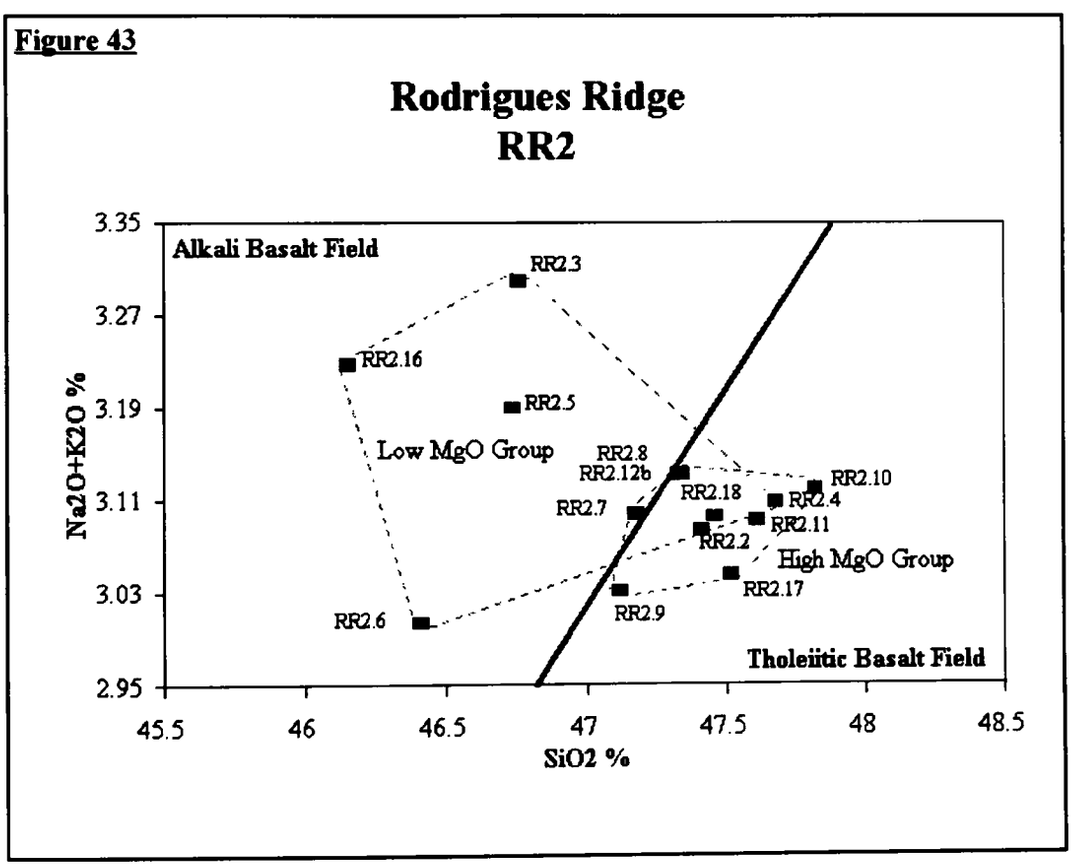

Silica-alkali diagram for the Rodrigues Ridge showing the position of RR2 samples relative to the fields of tholeiites and alkali basalts (Macdonald & Katsura 1964).
Similar diagrams for the other Rodrigues Ridge sites are given over the page.

$Na2O+K_2O$ Plotted Against SiO_2 for Sites West of RR2

Figure 44

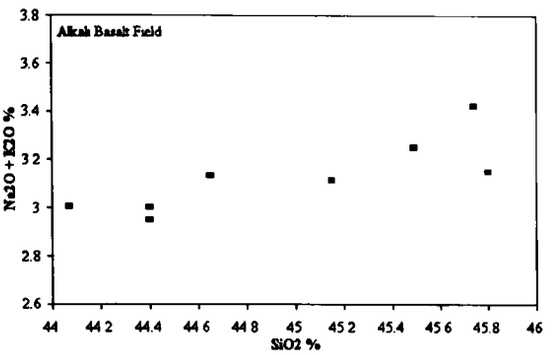

Figure 45

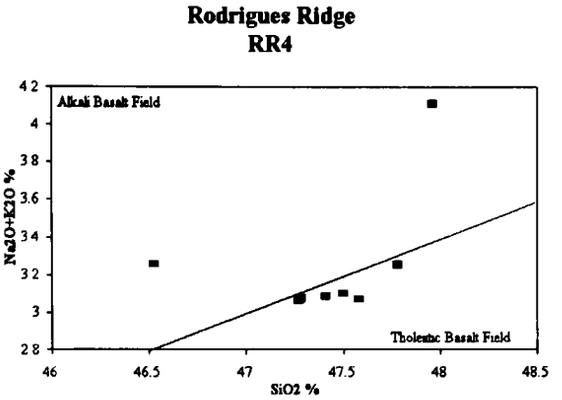

Figure 46

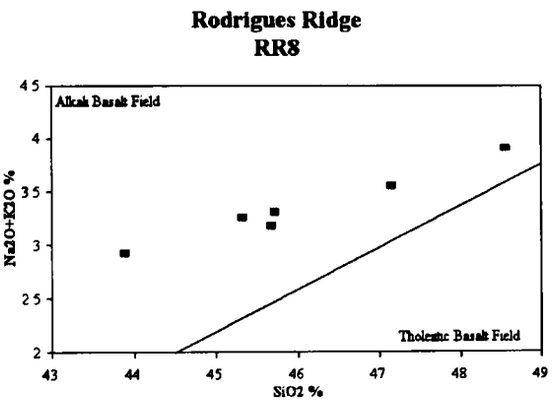

Figure 47

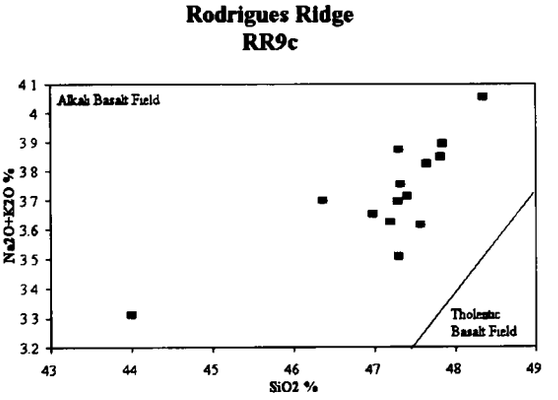

Figure 48

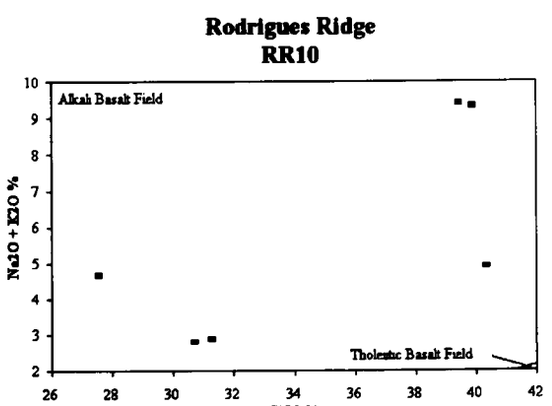

Figure 49

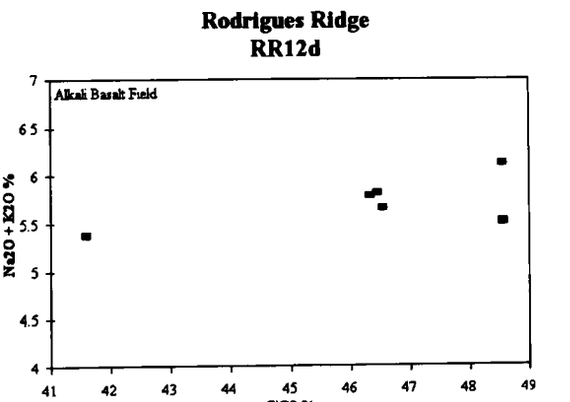

4.4 Alteration

All the Rodrigues Ridge lavas have been subject to some incipient seawater alteration. This is manifested both as yellow/orange palagonite alteration of matrix glass, and by the growth of secondary minerals such as serpentine, calcite and zeolites. The least altered samples still retain some matrix glass, have clear olivine and plagioclase phenocrysts and do not have any secondary minerals (other than palagonite). No matrix glass remained at RR3, RR8, RR10 or RR12d; secondary minerals were observed in all the samples from sites RR10 and RR12d.

Studies of the chemical effects of seawater alteration (Hart *et al.*, 1974, Wood *et al.*, 1976 and Cox & Hawkesworth 1985) suggest that, under zeolite facies alteration, Si, Mg, K, Rb, Ba, Sr and LREE are mobile (Wood *et al.*, 1976 and Cox & Hawkesworth 1985), whereas under even lower temperature alteration (seawater weathering) Si, Al, Ca, S and Ga are lost and Fe^{3+}, Fe^{2+}, Mn, K, H_2O, Cl, B, Rb and Cs increase. Other elements which are mobile to a lesser degree, and in a less consistent manner, are Mg, Na, P, Ba, Ni, and Cu (Hart *et al.*, 1974).

The alkalis K_2O and Na_2O and the volatiles H_2O and CO_2 are sensitive to the effects of seawater alteration (Hekinian 1982 and Tlig 1991). For example on the CIR, low SiO_2, with high K and Rb but low K/Rb, were used to indicate alteration (Erlank & Reed 1974). Qualitatively these authors observed that, under the electron microprobe, the most altered areas of the MORB's recovered on DSDP leg 25 showed even higher K values than the surrounding rock. Fig. 50a shows a plot of $100K_2O/K_2O+Na_2O$ against water used to distinguish between unaltered, metamorphosed and weathered ocean floor volcanics (Hekinian 1982). For reference the fields of Rodrigues island (solid line) and the weathered MORB volcanics of RR13 (dashed line) are shown on this figure. Hekinian (1982) suggests that lavas with greater than 2% H_2O (vertical line on fig. 50a) have been subject to either seawater weathering and/or metamorphism. Since H_2O (and CO_2) data are only available for 47 of the 62 Rodrigues Ridge samples, $100K_2O/K_2O+Na_2O$ was also plotted against LOI (fig. 50b). Loss on ignition (LOI) is the change in weight which occurs when the sample is placed in a furnace at 800°C for 20 minutes. This weight change is principally made up of three components;- 1. loss of water, 2. loss of CO_2, and 3. gain in oxygen due to oxidation of the ferric iron. Since both water and CO_2

Figure 50a Plot of $100K_2O/K_2O+Na_2O$ against H_2O for the Rodrigues Ridge lavas.

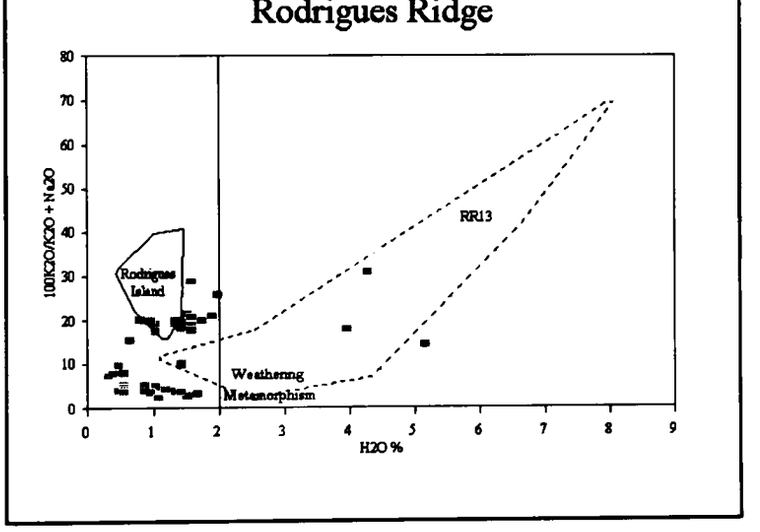

increase during alteration (Tlig 1991), high LOI is probably indicative of alteration. Fig. 50b shows all the samples from RR10, RR12d.8 and RR3.1 plot to the right of a line drawn through 2.5% LOI. The value of 2.5% LOI was selected to fit with the petrographic descriptions of moderate to severe alteration (4-5). Petrographic data show that RR10 and to a lesser degree RR12d have been subject to alteration and secondary mineral growth. RR3.1 contains calcite in some vesicles and consequently has high CO_2 and therefore high LOI.

Figure 50b Plot of $100K_2O/K_2O+Na_2O$ against LOI for the Rodrigues Ridge lavas.

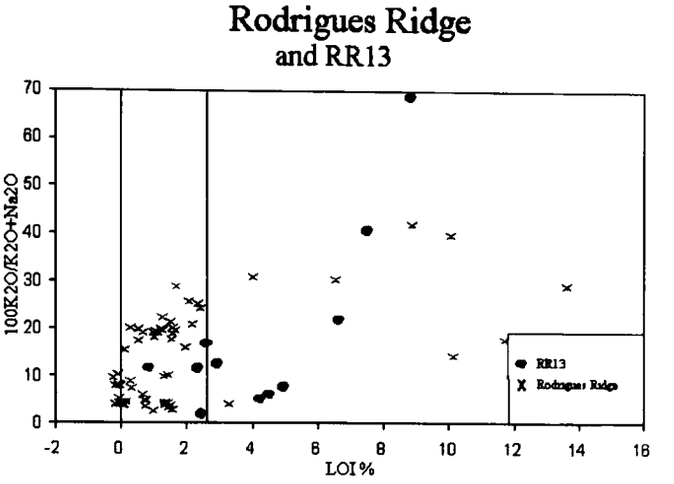

The lavas of RR10 and RR3, together with RR9c.11, RR8.3 and RR12d.8, are all low in SiO_2. Backman *et al.* (1988) observed that low silica lavas from site 715 (ODP leg 115) have been subject to alteration. High $^{87}Sr/^{86}Sr$ is used to identify seawater alteration (Backman *et al.*, 1988). Of the Rodrigues Ridge lavas already mentioned as possibly altered, the samples from RR10 for which isotopes are available (RR10.1 and RR10.8) both show elevated $^{87}Sr/^{86}Sr$, as does RR9c.11. None of the lavas from RR3 or RR12d show enrichment in radiogenic Sr, suggesting that if these lavas are altered they have not been contaminated by radiogenic Sr from seawater.

Primitive mantle-normalised trace element plots for the Rodrigues Ridge (figs. 51-58) clearly demonstrate the erratic behaviour of Ba and Rb, probably indicating that these elements have been mobilised. A number of Rodrigues Ridge lavas display elevated U and P on these plots, notably all RR3, RR10 lavas and the low MgO group lavas of RR2, RR2.17 and RR9c.11. Slight enrichment of these elements is also observed at RR12d. In contrast to U, Th remains low.

Since U and Th have very similar partition coefficients (table 2), partial melting and/or mineral fractionation are unlikely to be effective mechanisms for their separation. However U, unlike Th, has several different oxidation states and is strongly enriched during oxidation of crystalline MORB (Verma 1992). Th is lost during palagonitization, but it remains more or less constant during oxidation (Verma 1992), hence anomalously high U with normal or low Th can be developed. Faure (1991) observed that there are a number of natural UO_2^{2+} phosphates which develop in aqueous solutions but which are insoluble. This may explain the apparent relationship between U and P during the oxidation of these lavas.

Figure 51

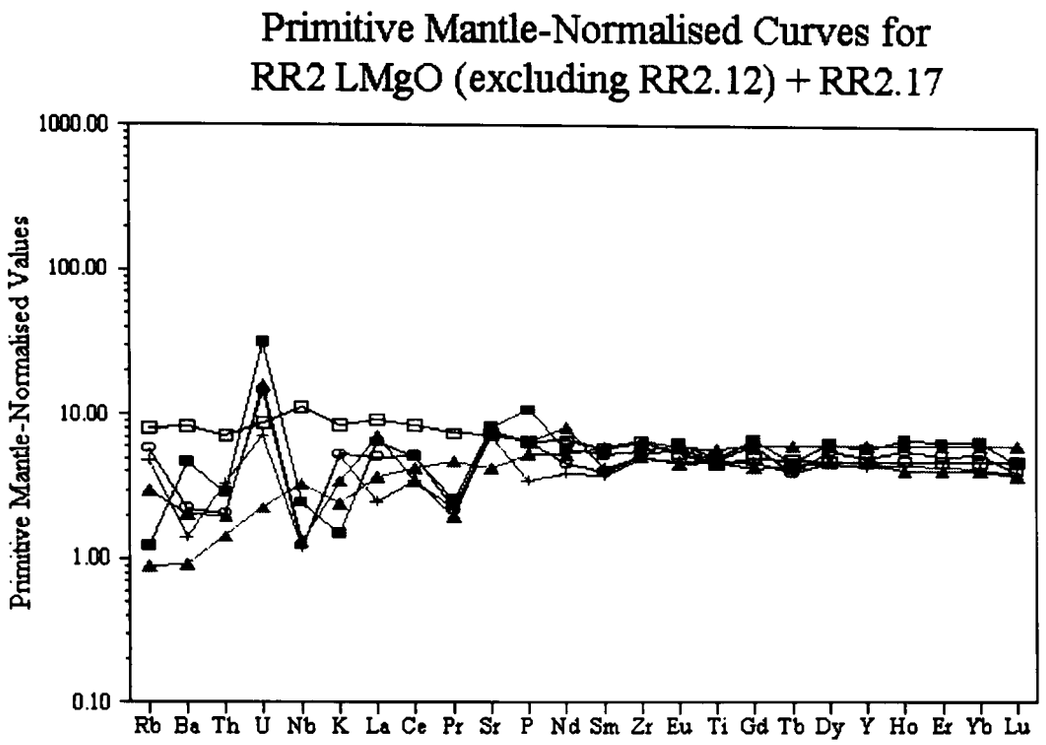

Figure 52

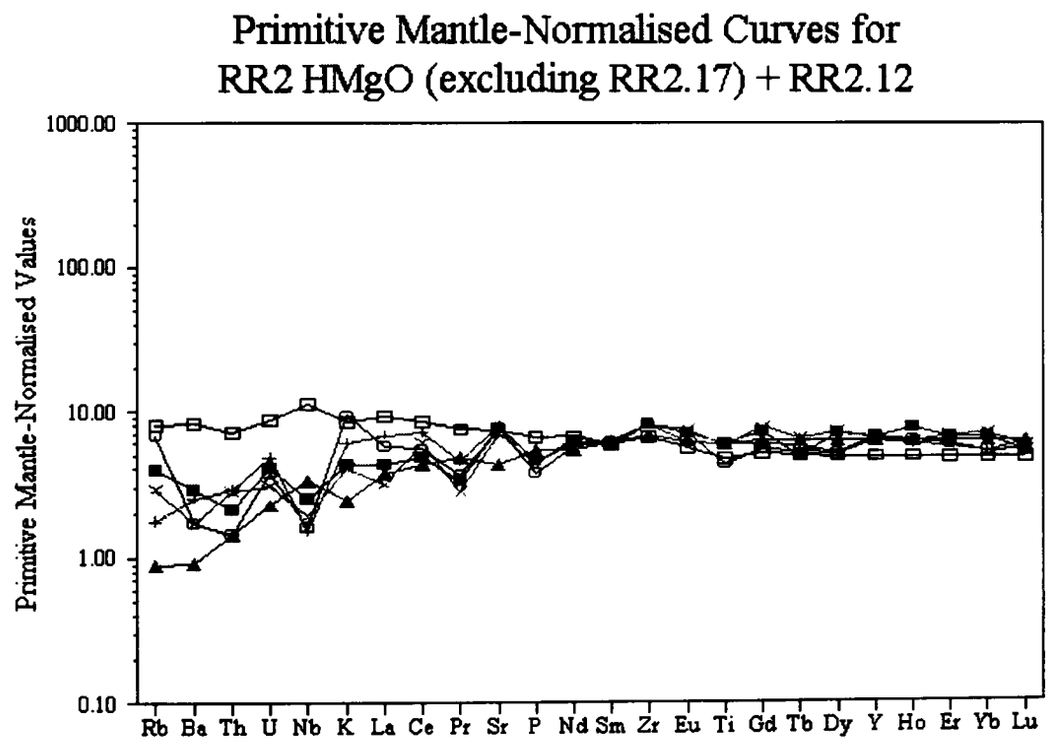

N-type MORB is indicated by filled triangles and E-type MORB by open squares. Primitive mantle, N-type MORB and E-type MORB are from Sun & McDonough (1989).

Figure 53

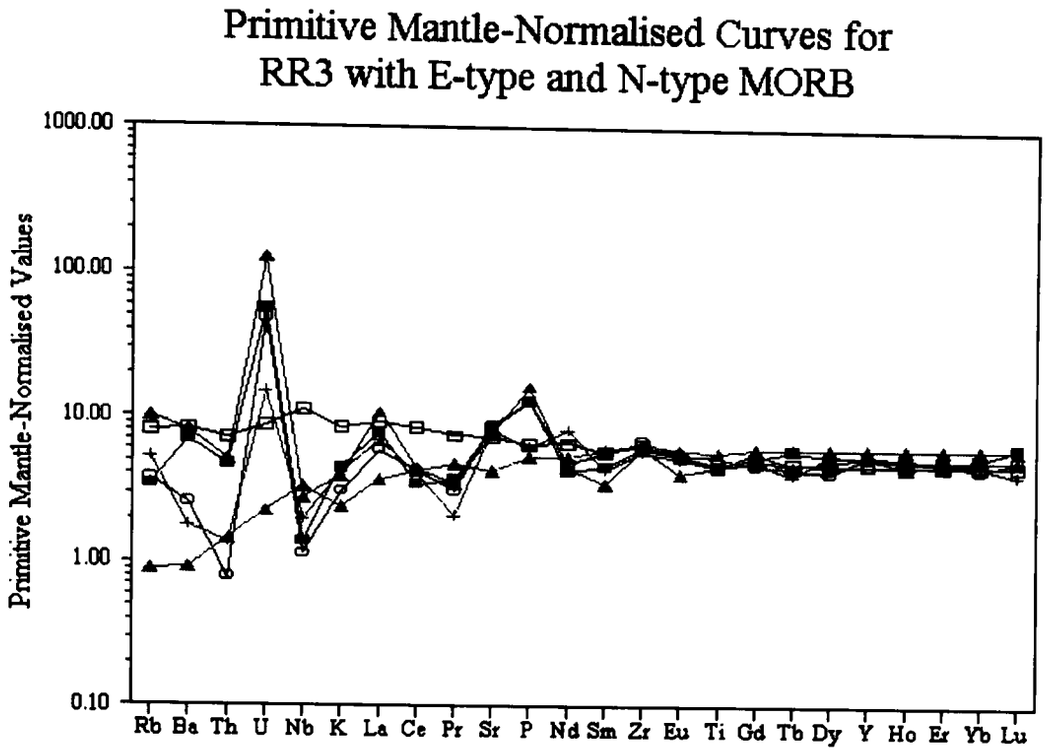

Figure 54

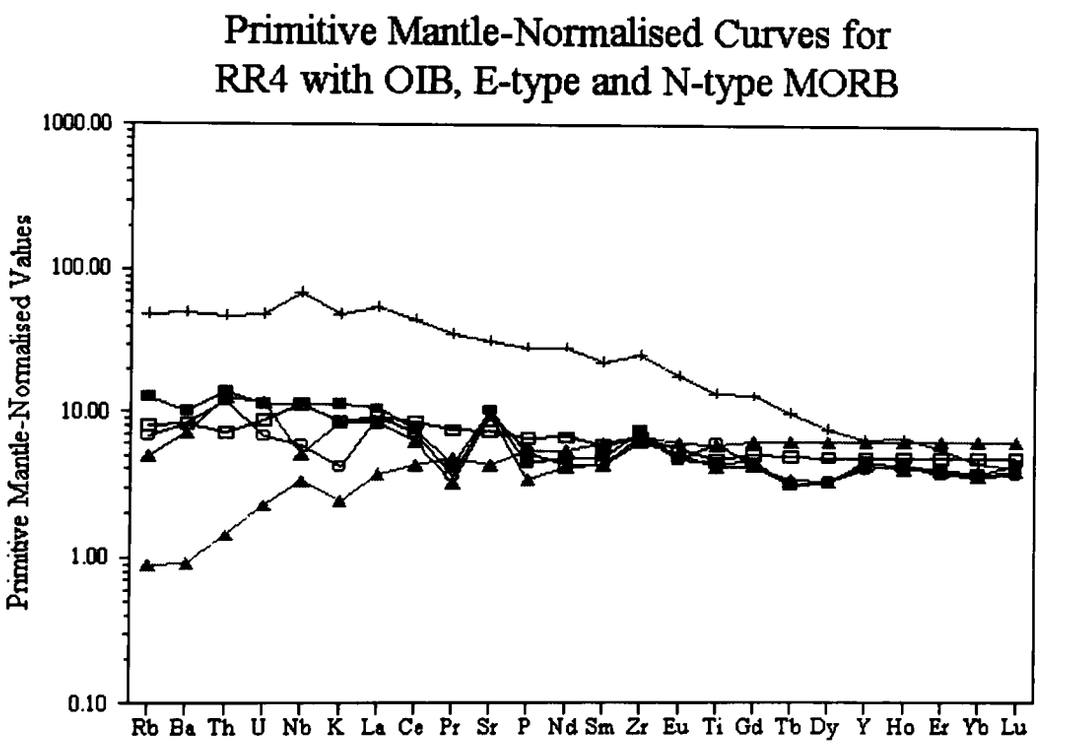

N-type MORB is indicated by filled triangles, E-type MORB by open squares and OIB by crosses (fig. 54 only). Primitive mantle, N-type MORB, E-type MORB and OIB are from Sun & McDonough (1989).

Figure 55

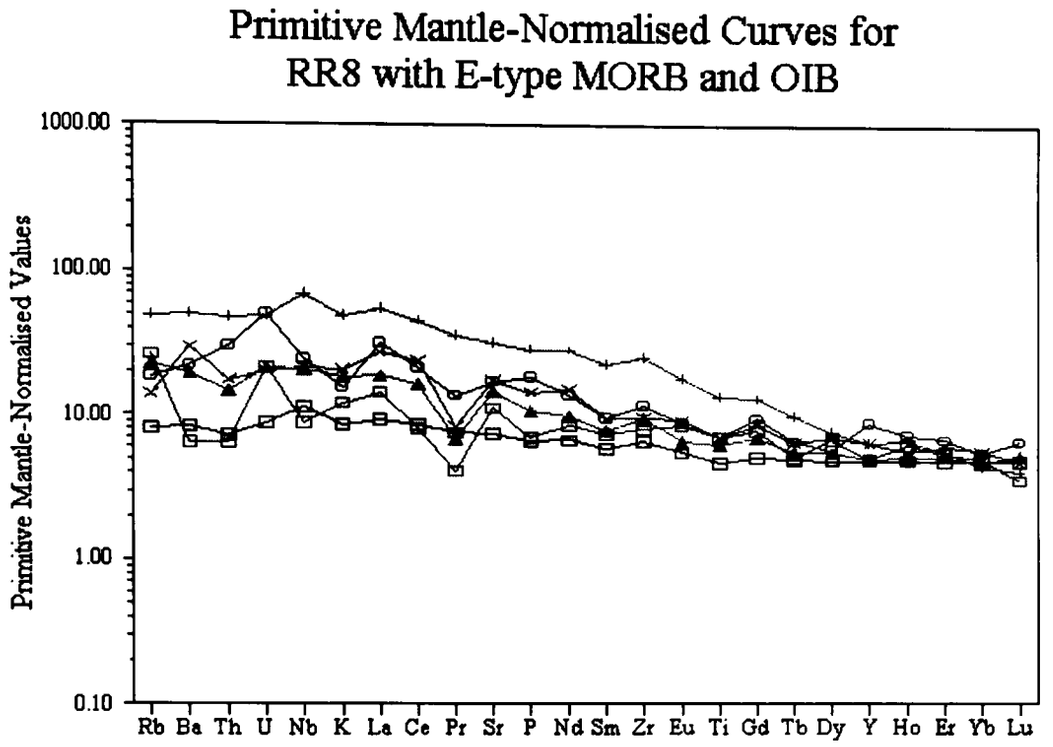

Figure 56a

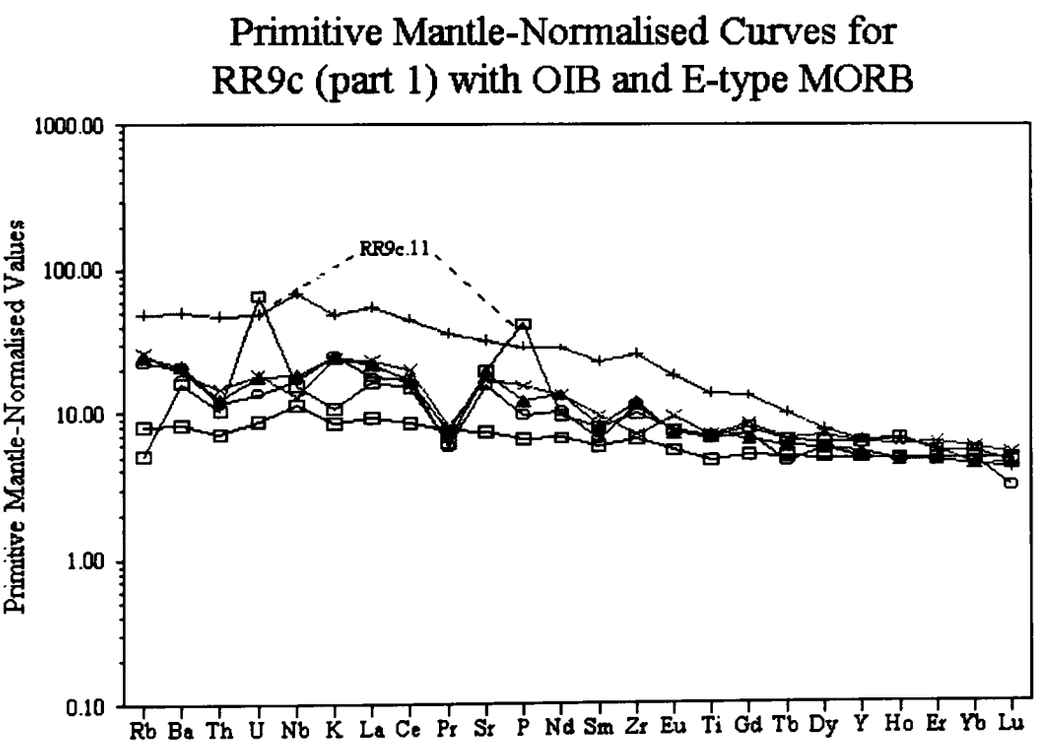

E-type MORB by open squares and OIB by crosses. Primitive mantle, E-type MORB and OIB are from Sun & McDonough (1989).

Figure 56b

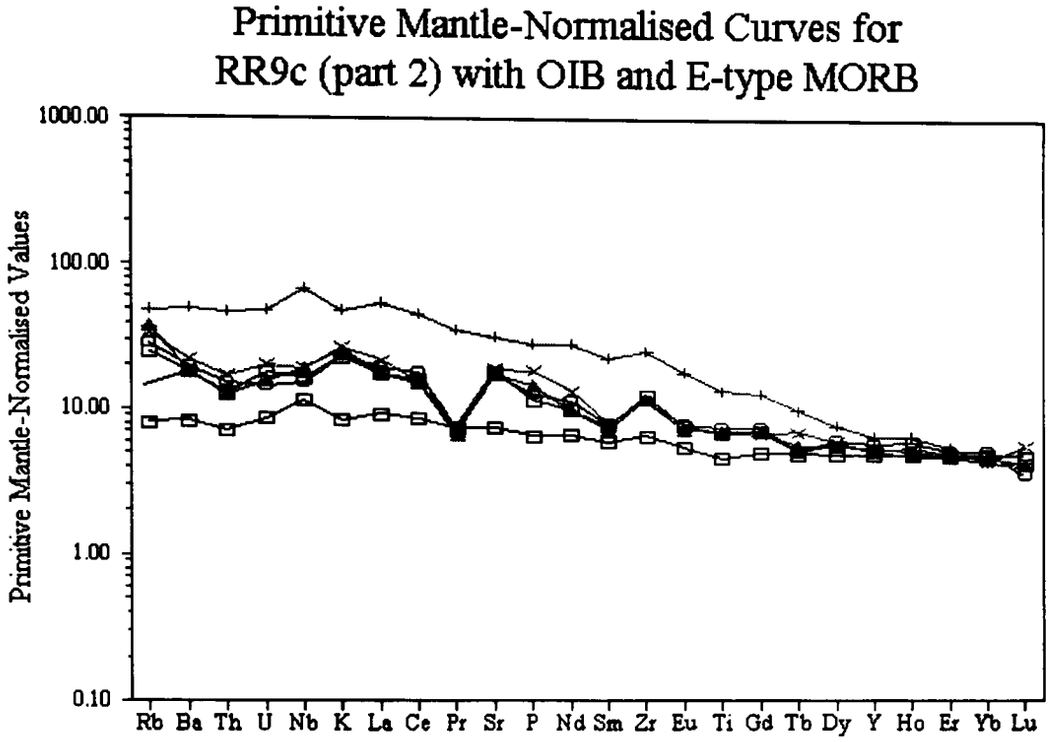

Figure 57

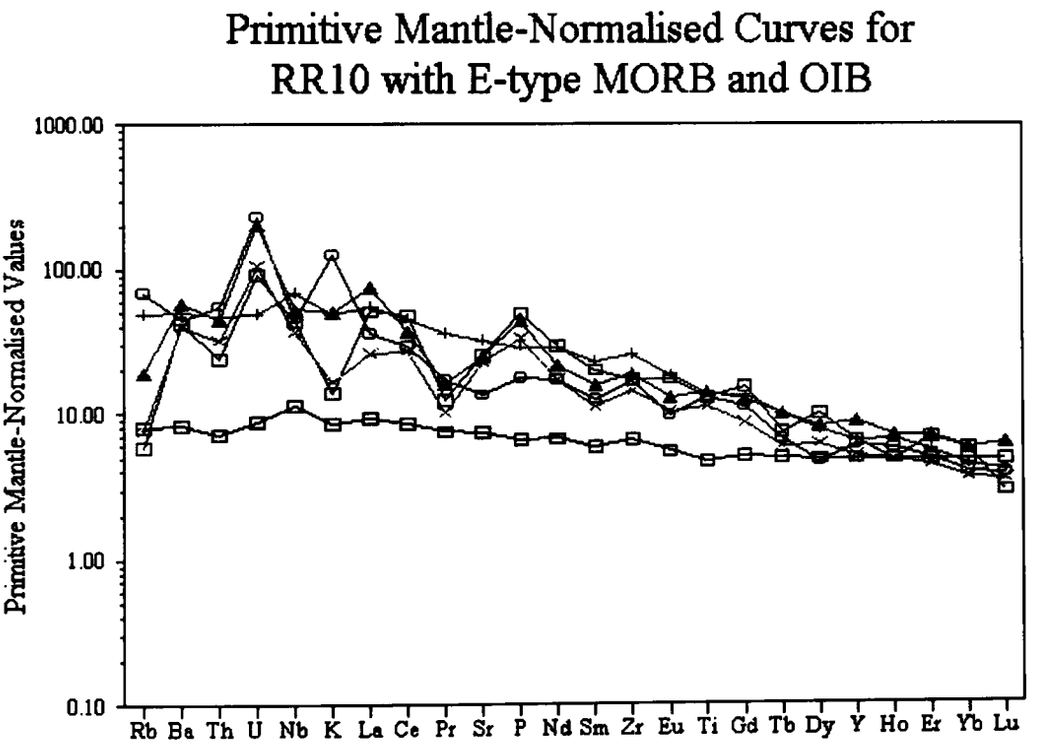

E-type MORB by open squares and OIB by crosses. Primitive mantle, E-type MORB and OIB are from Sun & McDonough (1989).

Figure 58

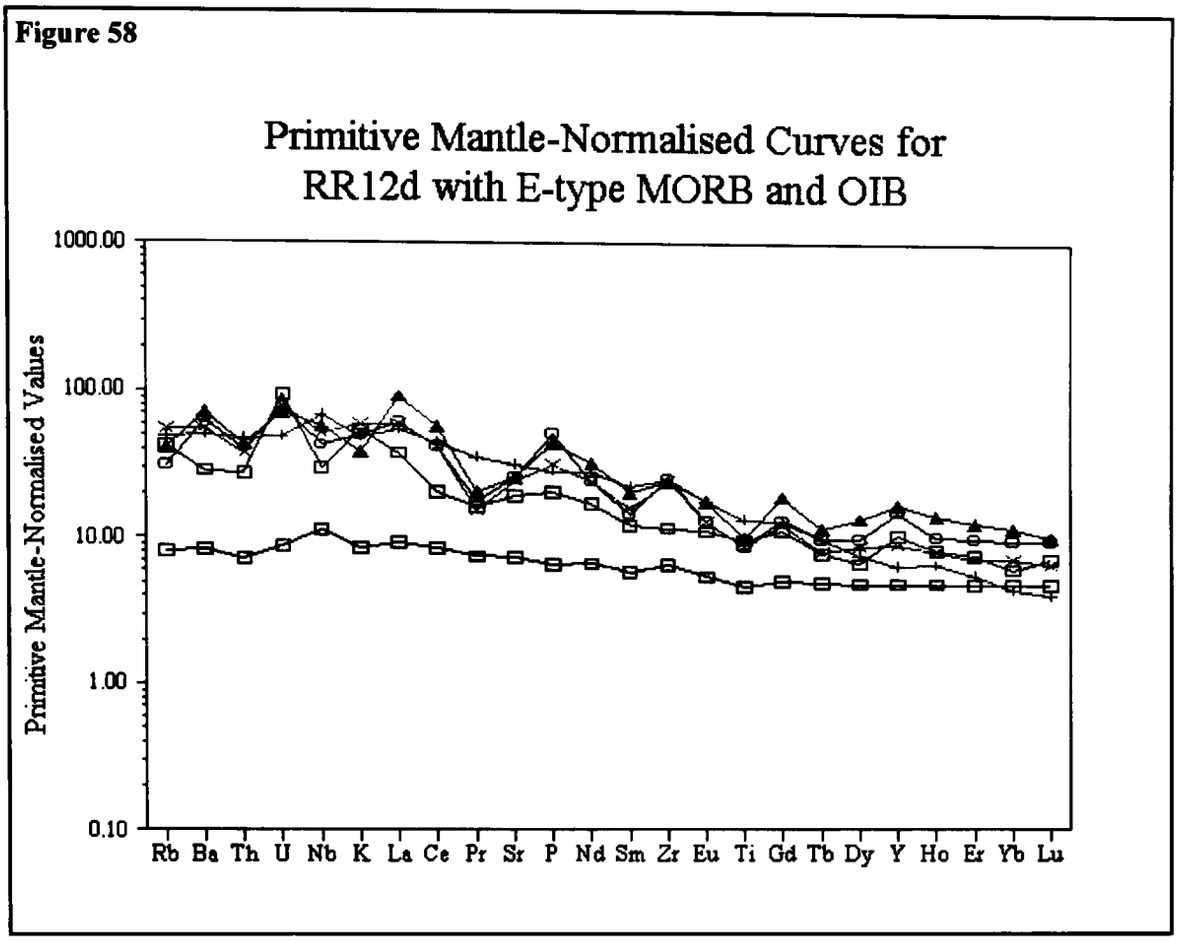

E-type MORB by open squares and OIB by crosses. Primitive mantle, E-type MORB and OIB are from Sun & McDonough (1989).

4.5 Site Characteristics

RR2

Fourteen samples from RR2 were selected for analysis. These are transitional alkali basalts as defined by Macdonald & Katsura (1964) on an alkali-silica plot (fig. 43 page 100). On fig. 43 samples from RR2 divide into two groups; one predominantly on the alkali side of the divide (the low MgO group, see below), the other just on the tholeiitic side (the high MgO group). The normative mineralogy of these lavas is given in table 17. The high MgO group were found to straddle the thermal divide having 2.35% hy-0.79% ne, implying that they last equilibrated above 8 kb. The low MgO group are all nepheline normative (0.03-1.65% ne). These two groups at RR2 can best be distinguished on a plot of TiO_2 with Zr (fig. 59) although, as will be discussed later, one sample does not fall clearly into either group.

Variation diagrams for RR2 are given in figs. 60-80. Clear geochemical trends are observed for TiO_2, Al_2O_3, $Fe_2O_3^*$, CaO, P_2O_5, H_2O, Ni, Sc, Sr, V, Y and Zr (figs. 61-64, 68-9, 73, 74-5, 76-7, and 78,) while curved or diffuse trends are displayed by MnO, Cr, Nb, (figs. 67, 70 and 72), Rb, Th, U and Zn,

(not shown); most diagrams show two groups. On the basis of these variation diagrams, RR2 can be divided into two distinct geochemical groups. One (the low MgO group) with MgO <8.5%, TiO_2 0.9-1.1%, Al_2O_3 17.6-19.5%, CaO 10.8-12.2% and Zr 55-65 ppm (samples RR2.3-RR2.6, RR2.12b and RR2.16). The second (the high MgO group) has MgO >8.1%, TiO_2 1.2-1.3%, Al_2O_3 16.6-17.2%, CaO 10.7-11.1% and Zr 85-90 ppm. These two groups cannot be related by high-level fractionation of any of the phenocryst phases present. The low MgO group displays clear olivine fractionation trends whereas the high MgO group displays a weakly defined olivine trend. Some elements, however, notably Y and the REE, show buffered trends which cannot be attributed to the fractionation of any observed mineral phase. Fractionation trends based on Rayleigh modelling of the two groups are shown on the variation diagrams. These models, discussed in chapter 6, are based on the fractionation of the phenocryst phases olivine and plagioclase. Three samples (RR2.12b, RR2.4 and RR2.17) show some characteristics associated with both groups. RR2.12b has 8.4% MgO, 0.917% TiO_2 but 89.1 ppm Zr. It plots with the low MgO group for total Fe, Ti and Al_2O_3 but not for any of the trace elements. Furthermore this sample is enriched in radiogenic Pb compared to the other Rodrigues Ridge samples. In short this lava appears to have acquired its trace element signature from the high MgO group but its major element signature from the low MgO group (fig. 59). RR2.4, with 7.60% MgO, while falling into the low MgO group in terms of its TiO_2, Al_2O_3, total Fe, Sc, U (not shown), V, Y and Zr values (figs. 61-3, 74, 76-7, & 78), plots with the high MgO group in terms of SiO_2, Na_2O, H_2O, Cr and Nb (figs. 60, 65, 69, 70 & 72). RR2.4 is also the only tholeiitic basalt in the low MgO group and the only low MgO group lava to plot within the field of the high MgO group on the alkali-silica diagram (fig 43). RR2.17 plots firmly within the field of the high MgO group for most elements but shows U enrichment characteristic of the low MgO group (excluding RR2.12b). This U enrichment is probably the result of oxidation as discussed earlier.

Figure 59

TiO_2 against Zr for RR2

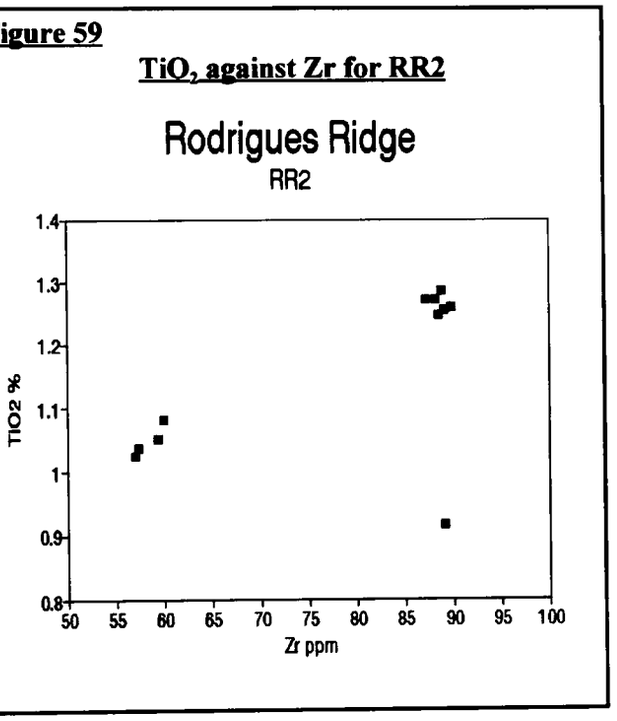

SiO_2, Na_2O, K_2O, CO_2 (not shown), Ba (not shown), and Cu show no discernible geochemical correlation with MgO (figs. 61, 65-6, and 71). Elements such as K_2O, Na_2O, H_2O, CO_2, Ba and Rb, which are susceptible to seawater alteration, often lack any correlation with MgO along the Rodrigues Ridge, probably due to the incipient seawater alteration. The lack of correlation between Cu, which is not particularly mobile, and MgO may reflect the formation of trace amounts of Cu bearing sulphides. Most thin sections studied contained numerous tiny opaques, too small for meaningful analysis with the electron microprobe. Most of these were apparently iron oxides, though some contained significant levels of sulphide, suggesting that iron and/or copper sulphides were present in trace amounts.

Primitive mantle-normalised trace element plots for RR2 (figs. 51-2) display slightly light REE depleted trends similar to N-type MORB. On these figures an average N-type MORB and E-type MORB (Sun & McDonough 1989) are shown. Some variation is observed among the most mobile elements (Rb, Ba, Th, U and K) particularly among the low MgO group samples. Marked enrichment of U is also observed in these lavas (and RR2.17). Despite this there is no obvious enrichment in radiogenic Pb. The $^{87}Sr/^{86}Sr$ ratios, which are sensitive to seawater alteration, remain very low. These observations suggest that these lavas have been subject to only limited alteration. The C1 chondrite normalised plots for RR2 show slight LREE depletion, with the high MgO group showing greater scatter among the LREE (figs. 81-2).

Variation Diagrams for RR2

Figure 60

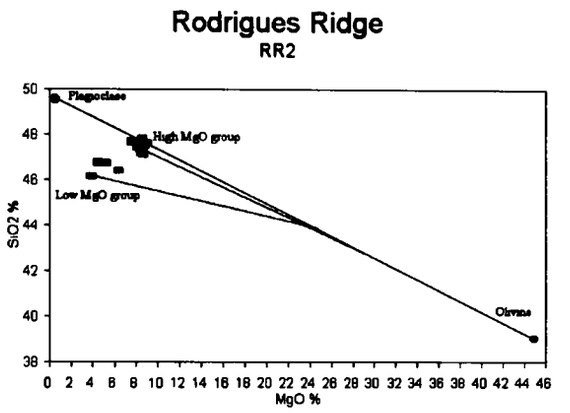

Figure 61

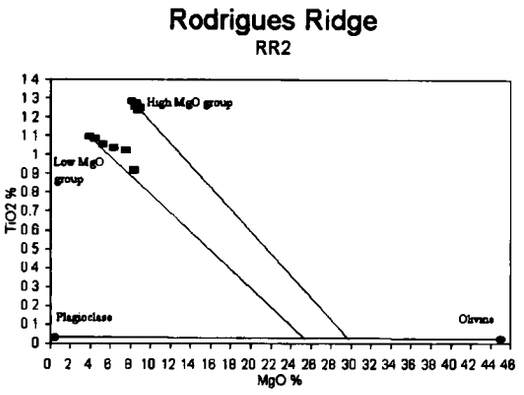

Figure 62

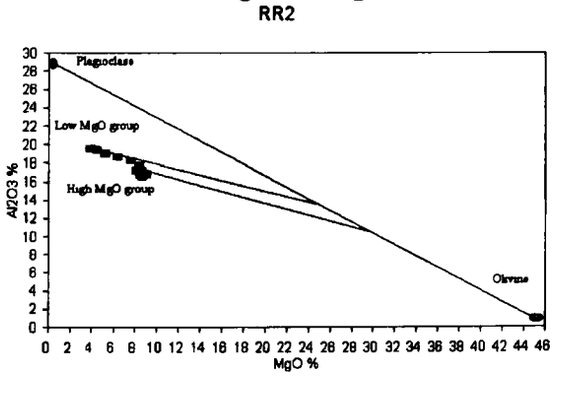

Figure 63

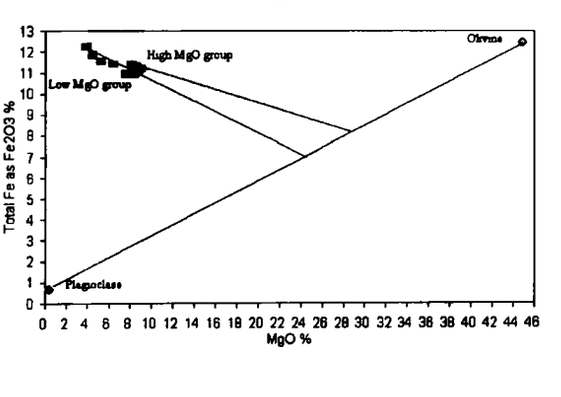

In figs 60-68, the compositional fields for plagioclase and olivine phenocrysts are shown joined. The modelled fractionation paths for both the high and low MgO group are also shown, linking the parent and daughter to the proposed fractionating assemblage. A full discussion of how these models were produced can be found in chapter 6.

Variation Diagrams for RR2

Figure 64

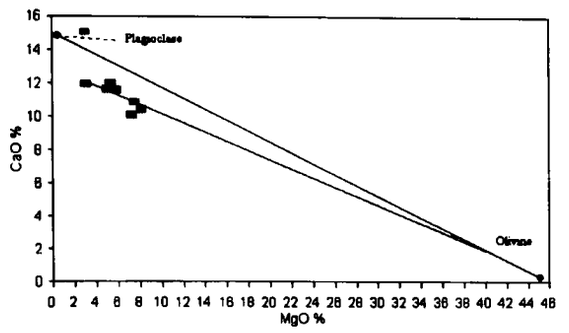

Figure 65

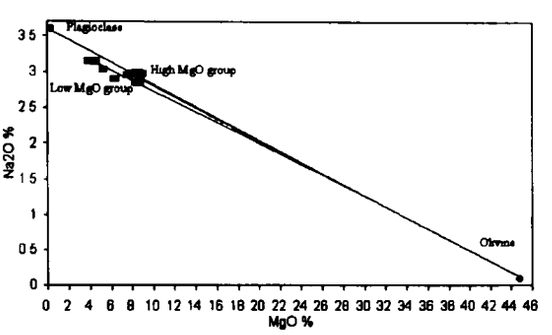

Figure 66

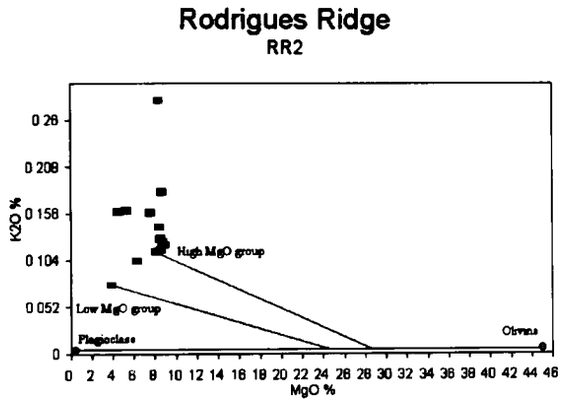

Figure 67

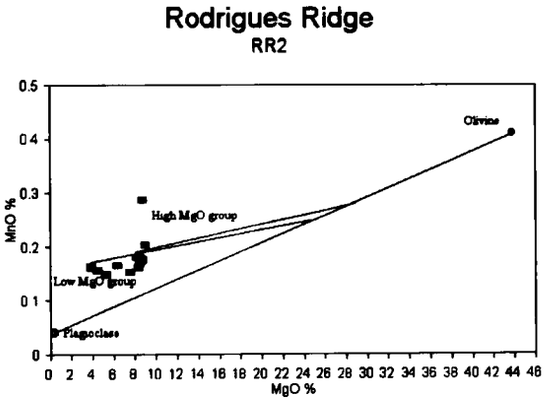

Figure 68

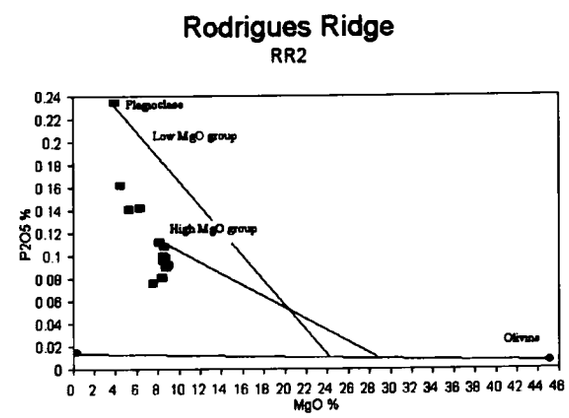

Figure 69

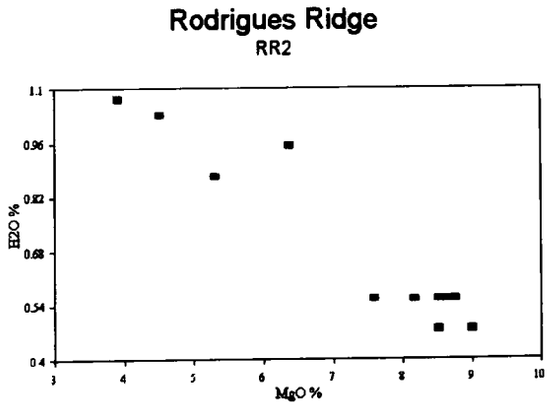

Variation Diagrams for RR2

Figure 70

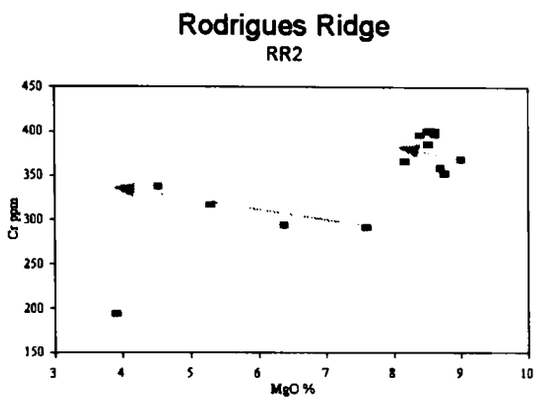

Figure 71

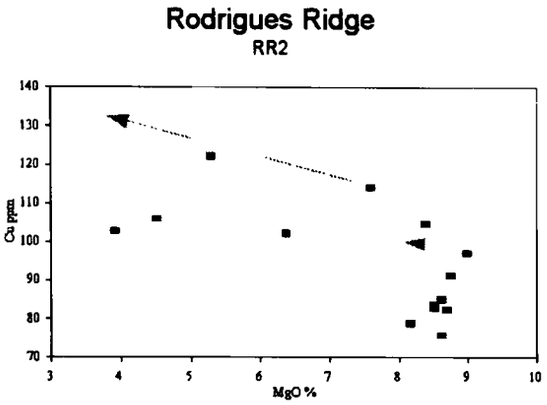

Figure 72

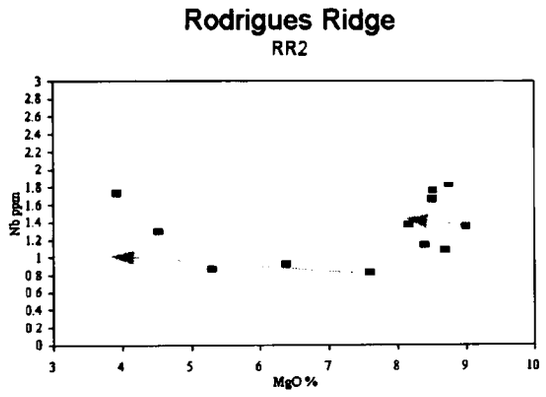

Figure 73

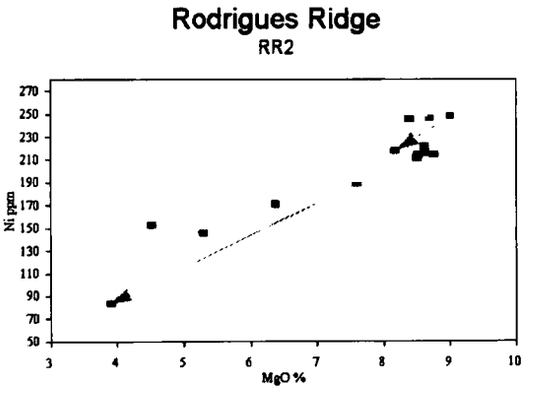

Figure 74

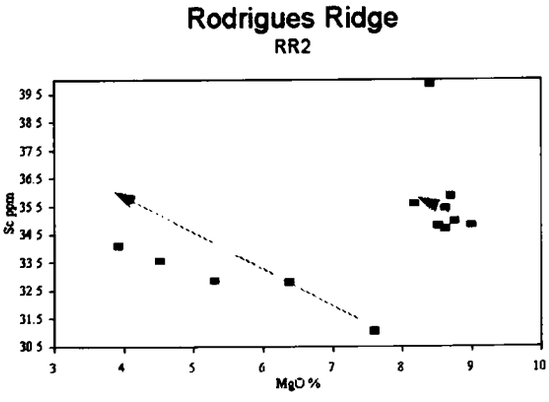

Figure 75

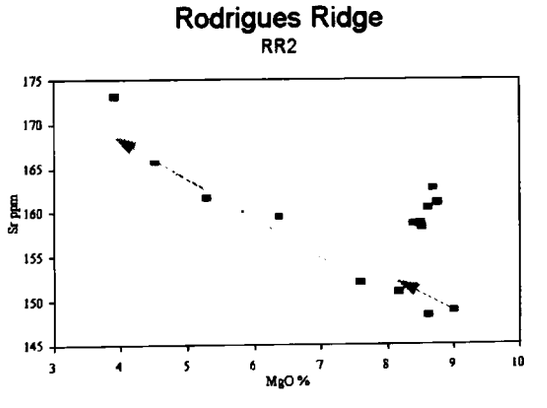

Variation Diagrams for RR2

Figure 76

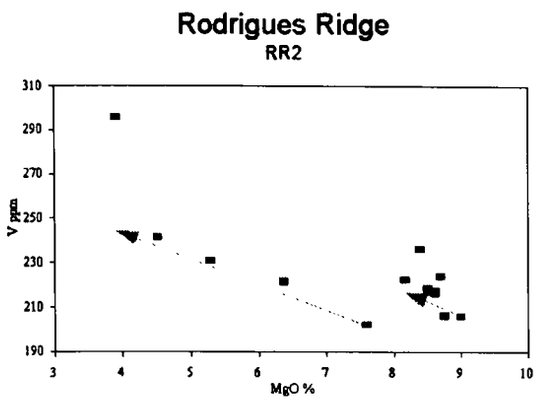

Figure 77

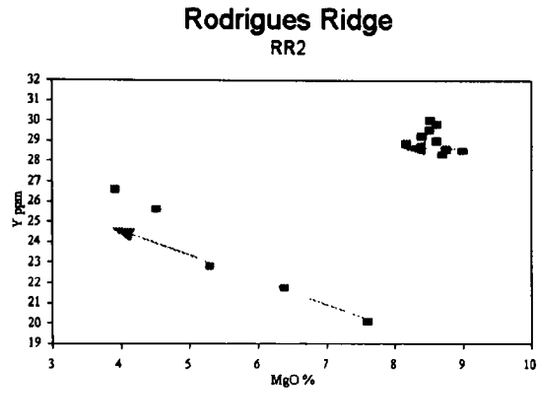

Figure 78

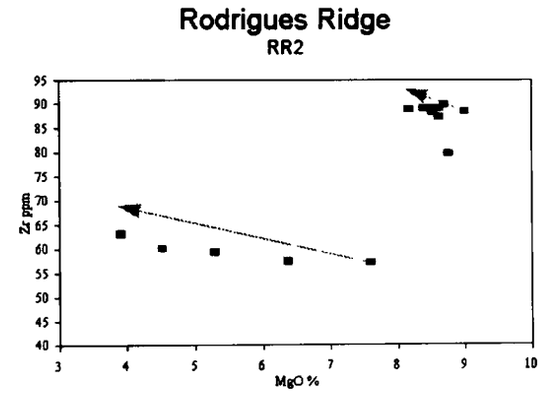

Figure 79

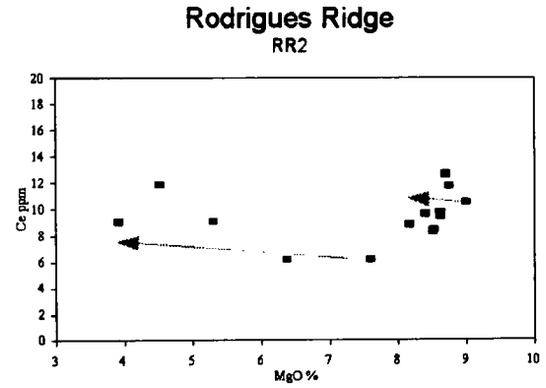

Figure 80

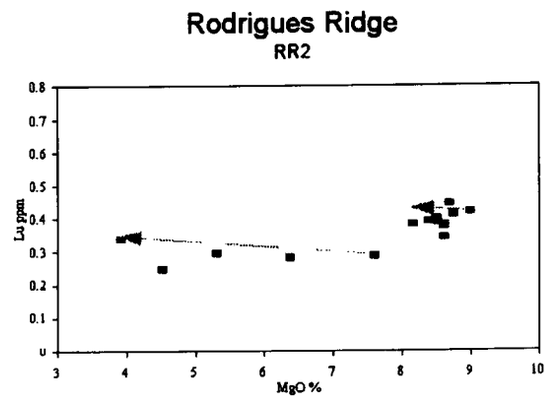

Arrows shown on figs. 70-80 indicate the modelled fractionation trend described in chapter 6.

Figure 81

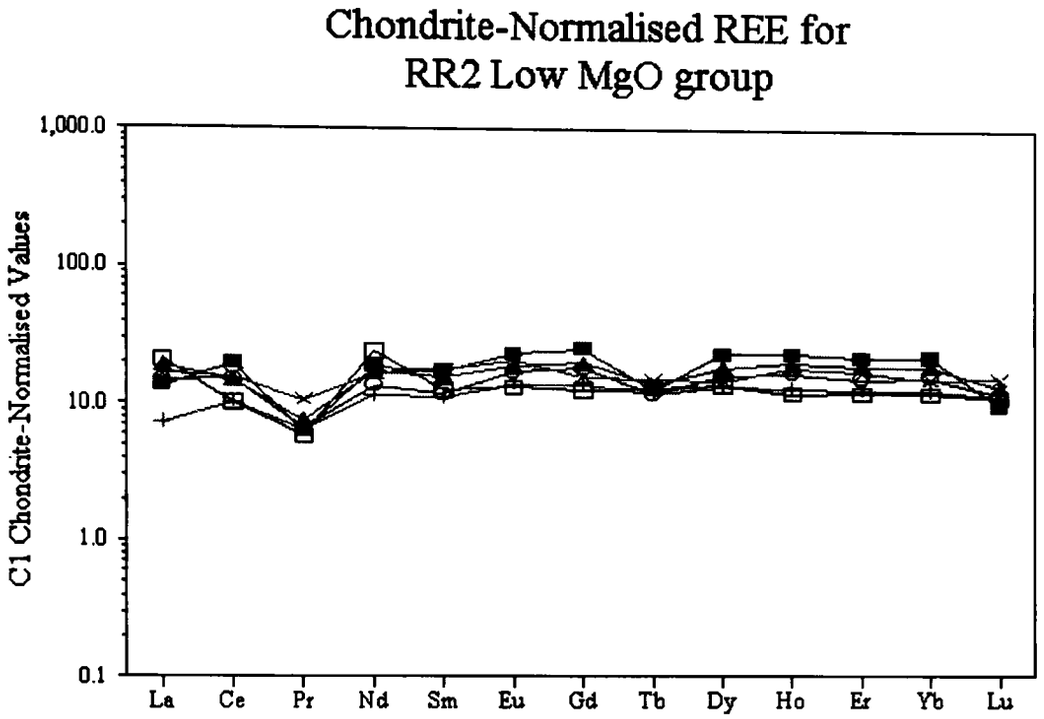

Figure 82

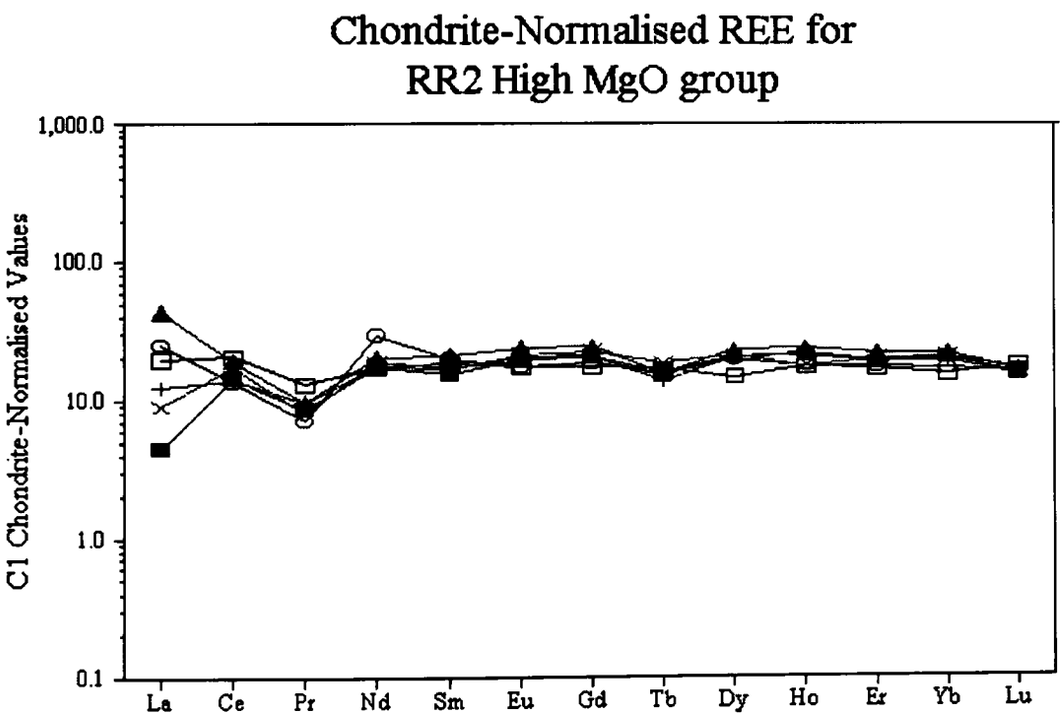

Chondrite values from Sun & McDonough (1989).

RR3

Eight samples (fig. 44 page 101) were analysed from this site. Samples from RR3 are all nepheline normative having 1.33-2.50% ne (table 18) and are mildly alkaline basalts. Variation diagrams for RR3 are given in figs. 83-106. These diagrams show fractionation trends based on the fractionation of the phenocryst phases olivine and plagioclase. These models are described in more detail in chapter 6. In general, the lavas of RR3 are somewhat different from those of the surrounding sites. The ranges of Al_2O_3 (15.08-19.41%) and CaO (7.86-11.96) for RR2, RR4, RR8, RR9c and RR12d (excluding RR9c.11 and RR12d.8) show some overlap with those of RR3 (Al_2O_3 18.85-20.22% and CaO 10.07-15.06%), but do not encompass them. Clear geochemical trends exist in plots of SiO_2, TiO_2, $Fe_2O_3^*$, CaO, Na_2O, K_2O, H_2O, Eu, Yb, Gd, Nb, Ni, Sc, V and Y against MgO. Less well defined trends are also found with Al_2O_3, P_2O_5, CO_2, MnO, Cr, La, Ce, Nd, Sm, Dy, Lu, U, Zn and Zr. RR3 displays anomalous behaviour among many of the major, trace and REE, critically among elements such as Zr and Ti which are not affected by alteration. TiO_2, Nb and Zr display buffered trends with decreasing MgO. $Fe_2O_3^*$, CaO, P_2O_5, H_2O, Cr, Ni, U, Y and the REE all show decreasing trends with decreasing MgO, many of which cannot be explained by fractionation of basaltic minerals or by secondary processes. No discernible trends exist for Ba, Cu, Rb, Sr, Th.

A number of unifying characteristics have been observed among the RR3 lavas; they are all low in silica (44.07-45.80%) and high in Al_2O_3 (18.85-20.22%). TiO_2 (0.95-1.15%) is lower than in the high MgO group at RR2 (1.23-1.29%), similar to the low MgO group (0.92-1.10%), while K_2O (0.08-0.13%) is similar to RR2 (0.08-0.28%) but lower than RR4 (0.12-0.63%). They display low absolute values for LREE. Ce falls in the range 6.09-9.83 ppm compared to 6.16-12.61 ppm for RR2 and 9.40-36.12 ppm for RR4. RR3 also displays the highest $^{143}Nd/^{144}Nd$ associated with the lowest levels of radiogenic Sr and Pb found on the Rodrigues Ridge.

The half-pillow, RR3.1 (with 3.03% MgO) plotted significantly off the trend described by the other samples for SiO_2, Al_2O_3, $Fe_2O_3^*$, Na_2O, P_2O_5, CO_2, Nd and Sc. This behaviour cannot be solely attributed to the alteration state of this lava. Some compositional zoning across the pillow has been observed (Hall pers. comm.) suggesting that the aberrant behaviour of this sample may have its origins in post eruptive processes.

RR3 samples all have high P and U as a consequence of their oxidation. Like RR2, they show primitive mantle-normalised trends similar to N-type MORB (fig. 53). Like RR2, RR3 plots between these two MORB types, but with somewhat greater scatter among the more mobile elements. The chondrite-normalised REE signatures show a slight LREE depletion associated with low overall REE concentrations (fig. 107 page 120).

In figs 83-91, the compositional fields for plagioclase and olivine phenocrysts are shown joined. The modelled fractionation path is shown, linking the parent and daughter to the proposed fractionating assemblage. A full discussion of how this model was produced can be found in chapter 6. Arrows shown on figs. 93-106 indicate the modelled fractionation trend for the trace elements, also described in chapter 6.

Variation Diagrams for RR3

Figure 83

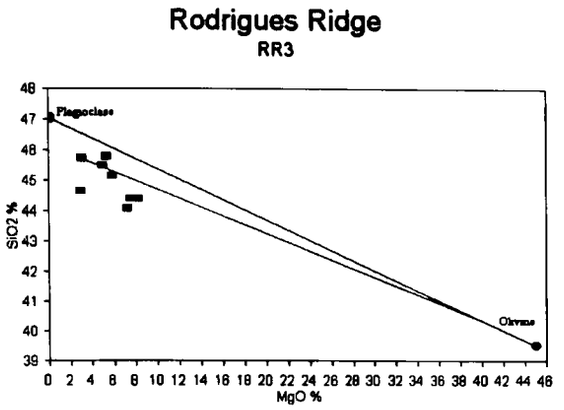

Figure 84

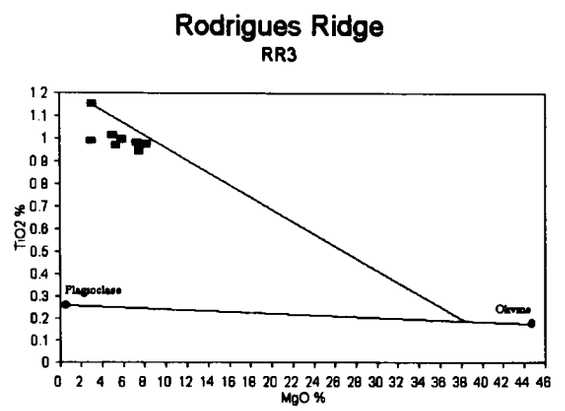

Figure 85

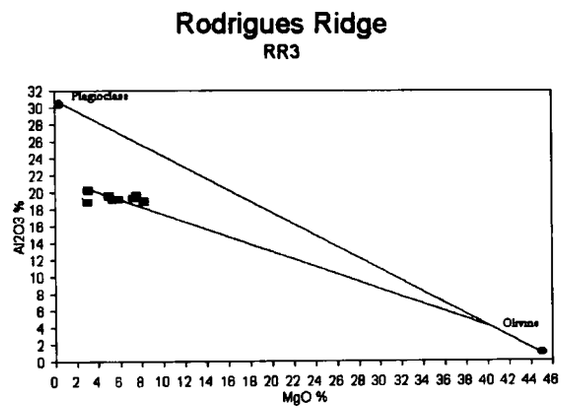

Figure 86

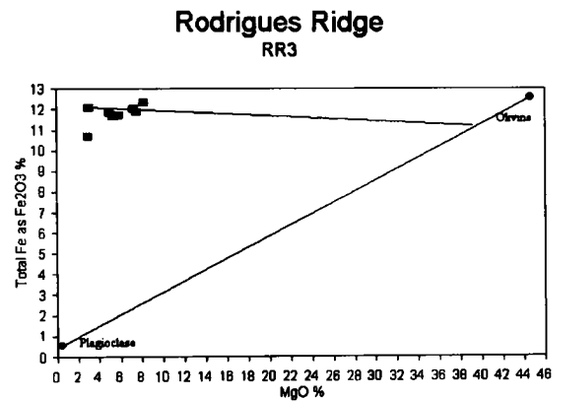

Figure 87

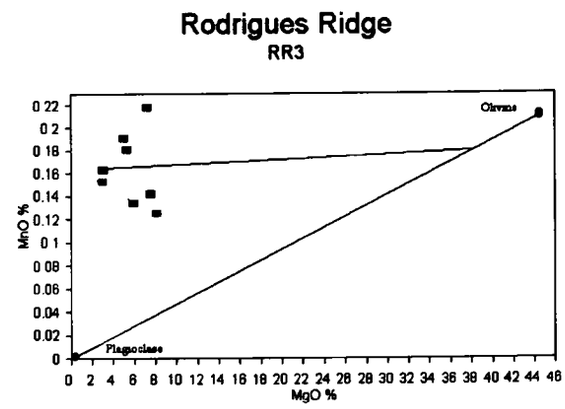

Figure 88

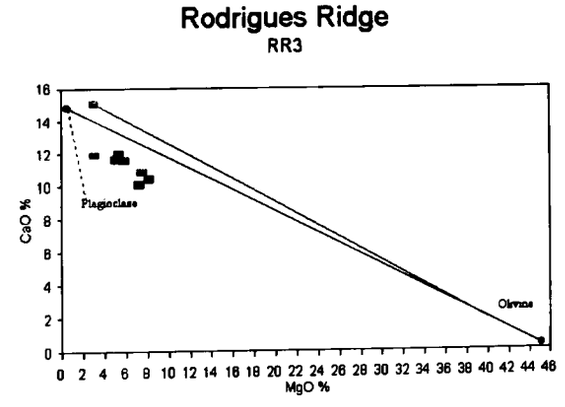

Variation Diagrams for RR3

Figure 89

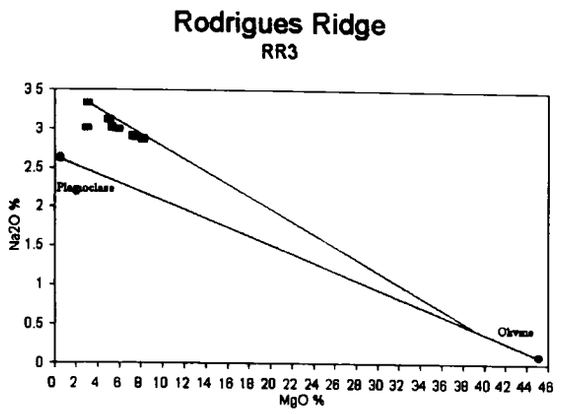

Figure 90

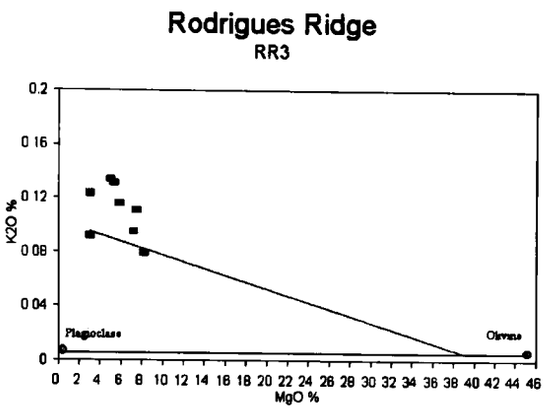

Figure 91

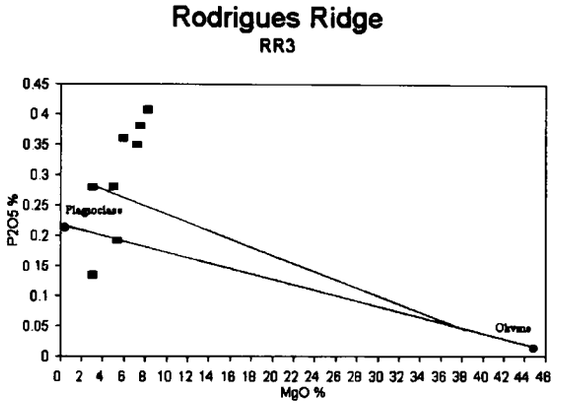

Figure 92

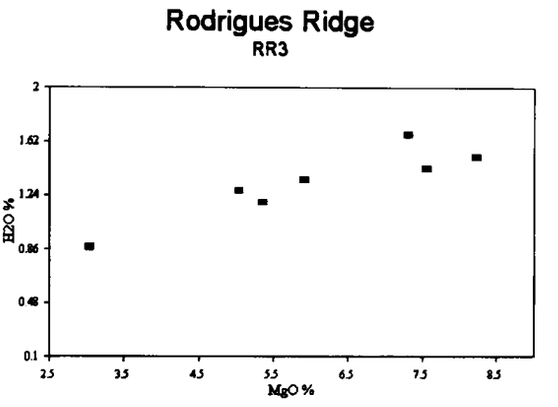

Figure 93

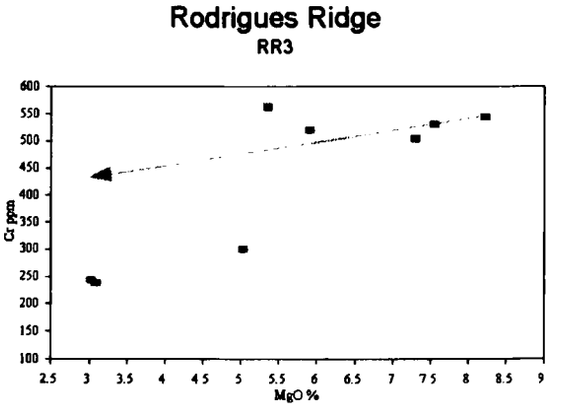

Figure 94

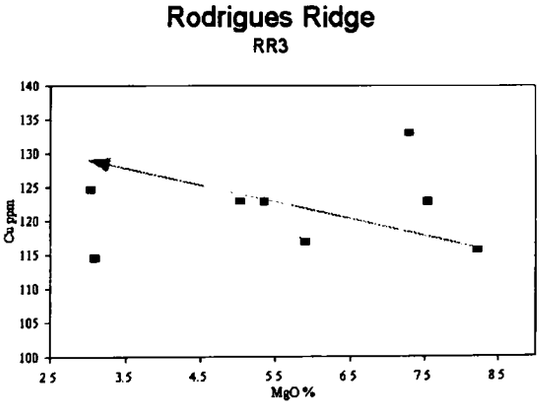

Variation Diagrams for RR3

Figure 95

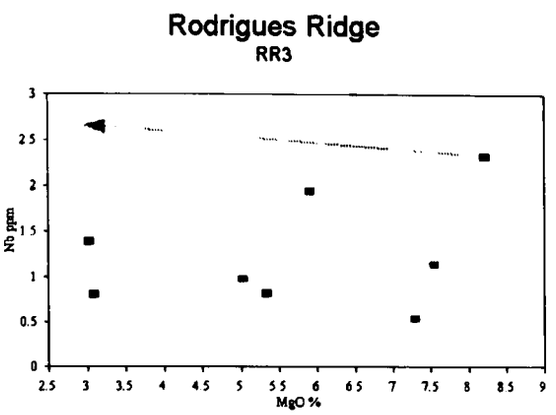

Figure 96

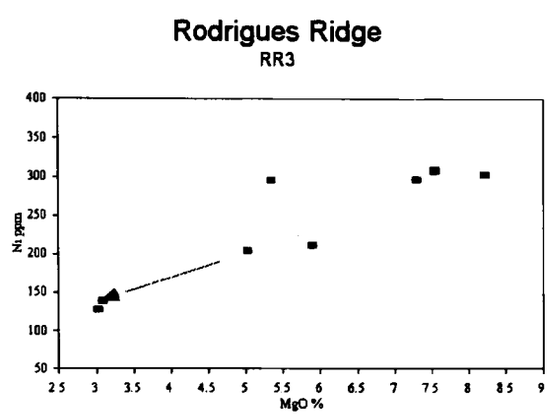

Figure 97

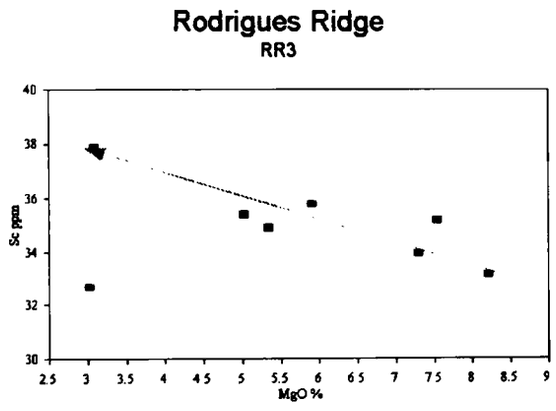

Figure 98

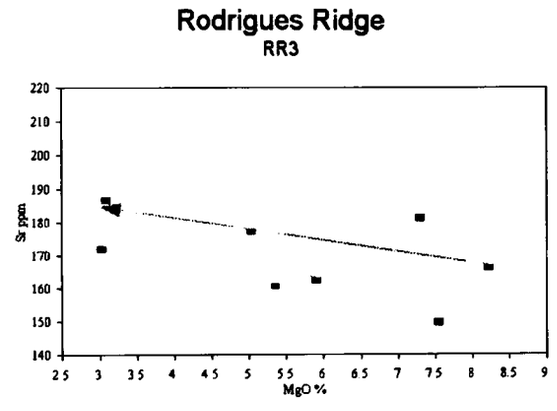

Figure 99

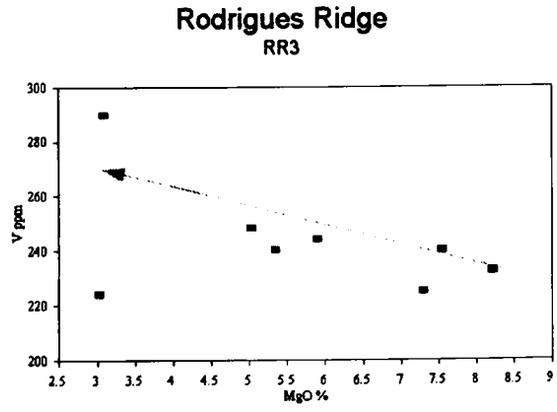

Figure 100

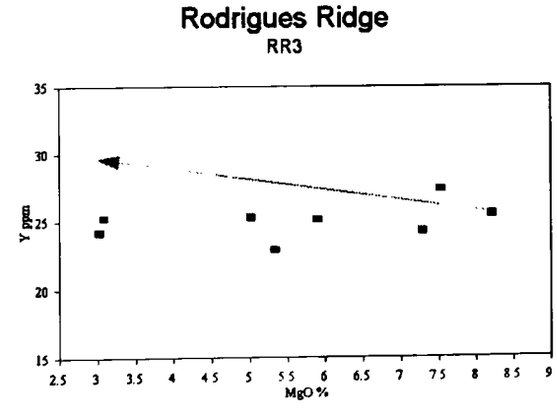

Variation Diagrams for RR3

Figure 101

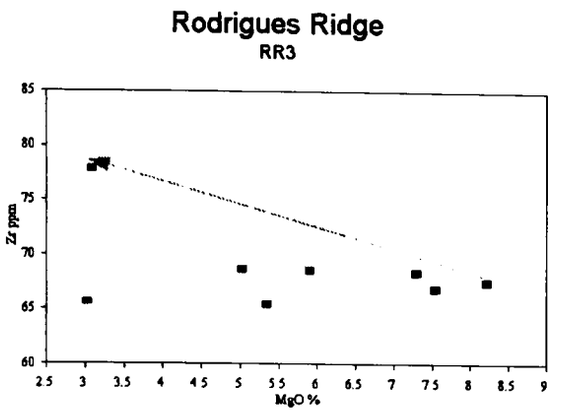

Figure 102

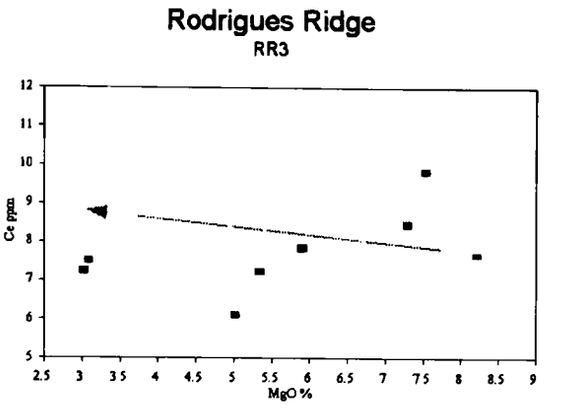

Figure 103

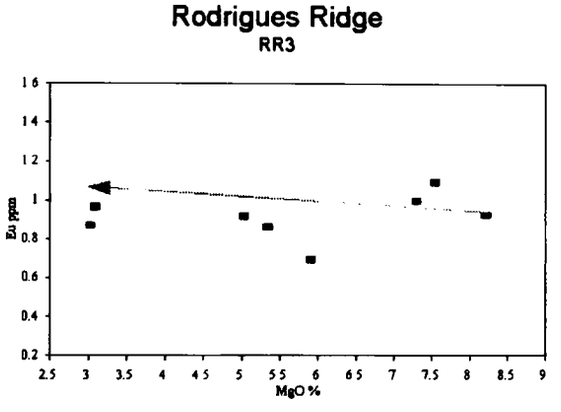

Figure 104

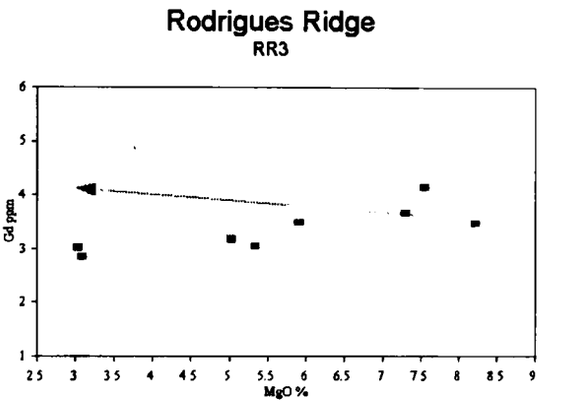

Figure 105

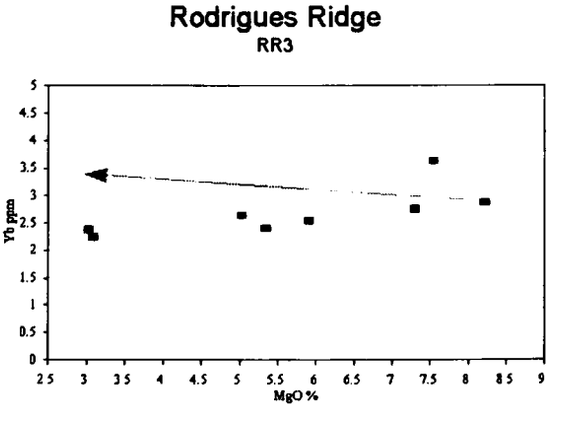

Figure 106

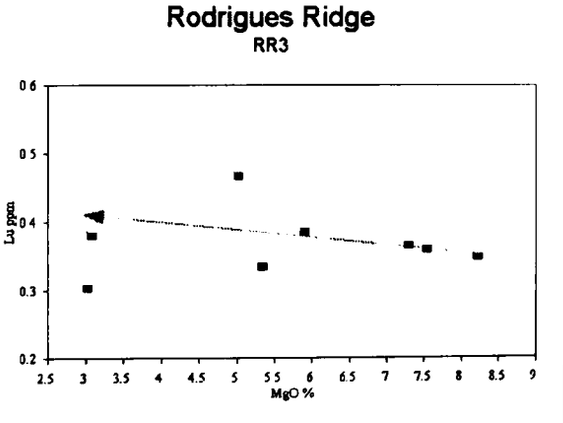

Figure 107

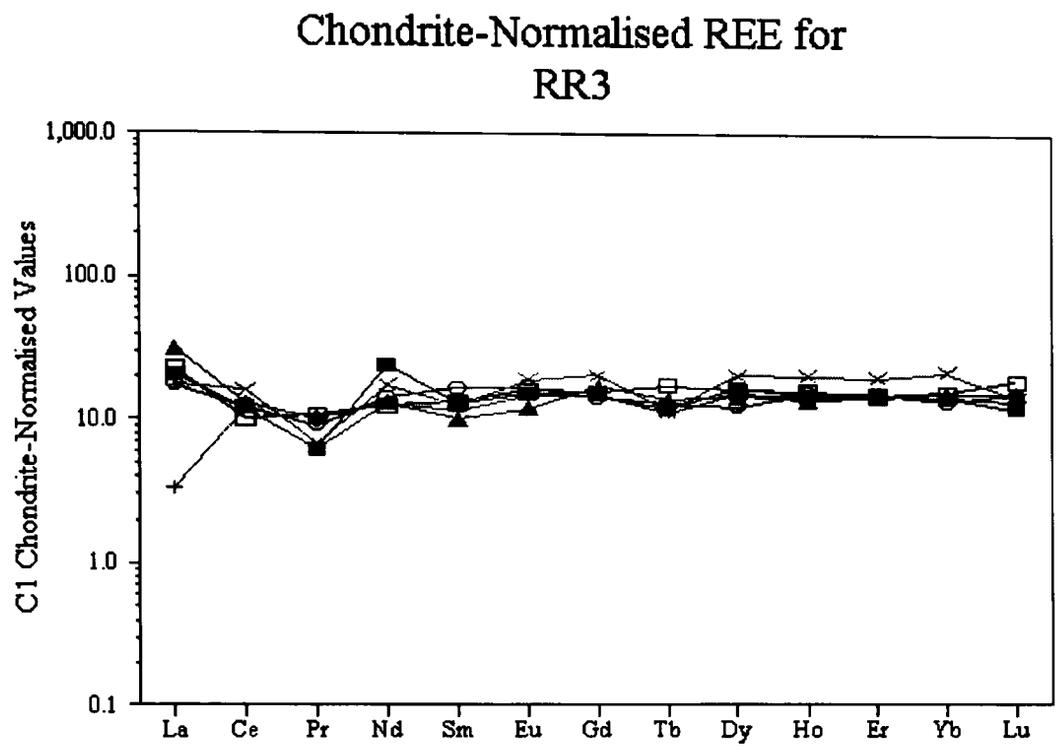

Chondrite values from Sun & McDonough (1989)

RR4

Eight samples from site RR4 were analysed. Like the lavas of RR2, they straddle the thermal divide (fig. 45 page 101) having 0.62% hy-1.18% ne (table 19). Variation diagrams for RR4 are given in figs. 108-125. Clear geochemical trends exist for SiO_2, TiO_2, $Fe_2O_3^*$, P_2O_5, Ni and V with MgO (figs. 108-9, 111, 116, 119 and 122). Less well defined trends are present for Al_2O_3, MnO, Na_2O, CO_2 (not shown), Rb (not shown) and Y (figs. 110, 112, 114, and 123). At RR4, the narrow range of MgO (7.52-8.97%) reflects the reduced role of olivine during its fractionation history. Qualitatively the role of plagioclase and possibly clinopyroxene fractionation (see ch. 6) must be greater than at other sites to explain the wide ranges found in elements like TiO_2 (0.861-1.814%) $Fe_2O_3^*$ (8.63-9.43%) and CaO (9.44-11.02%). Similar wide ranges can be found in the other incompatible elements notably P_2O_5 (0.07-0.25%), Y (18.06-36.71 ppm) and Zr (51.1-165.3 ppm) (table 16), confirming that these lavas have undergone substantial fractionation (see ch. 6 for discussion of fractionation models). The fractionation models described in chapter 6 which require the fractionation of the phenocryst phases olivine and plagioclase are shown on these variation diagrams. The water content at RR4 is the lowest of all the sites (0.3-0.6%), implying that these lavas were derived from relatively dry melts. No obvious trends exist for CaO, K_2O, H_2O (not shown), Ba (not shown), Cr, Cu, Hf (not shown), Nb (not shown),

Sc, Sr, Th (not shown), U (not shown), Zn (not shown) and Zr (figs. 113, 115, 117-8, 120-1, and 124). On a plot of primitive mantle-normalised trace elements, the overall trace is most like E-type MORB (fig. 54). The peaks in U and P, seen in the RR2 low MgO group and at RR3, are not found. The only sample to plot above the E-type MORB line for all elements is RR4.6 which has a more evolved chemistry. In general the lavas of RR4 are enriched in the most incompatible elements (Rb-Sm) when compared to the more easterly sites. The lavas also show a small peak in Sr about which they are tightly grouped with only RR4.6 being significantly higher. The cause of this grouping is not clear. The range of Sr is narrow at 188-214 ppm, excluding RR4.6 which has 234 ppm. Similarly the chondrite-normalized REE (fig. 126) show level or slightly LREE enriched traces.

In figs 108-116, the compositional fields for plagioclase and olivine phenocrysts are shown joined. The modelled fractionation path is shown, linking the parent and daughter to the proposed fractionating assemblage. A full discussion of how this model was produced can be found in chapter 6.

Variation Diagrams for RR4

Figure 108

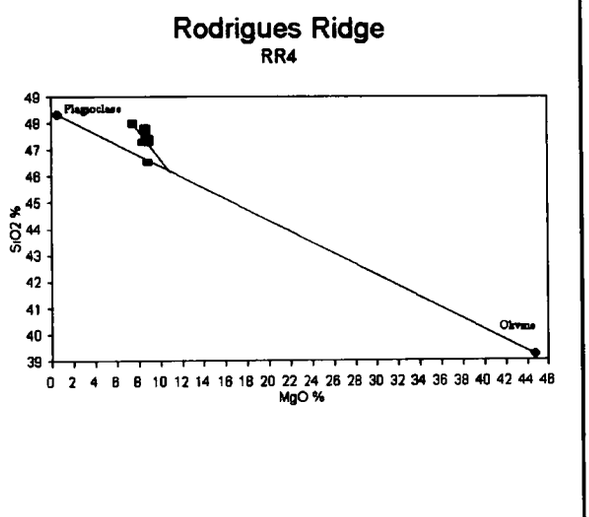

Figure 109

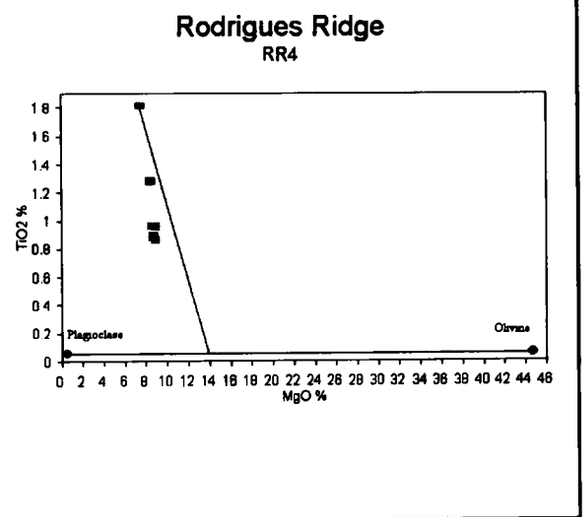

Figure 110

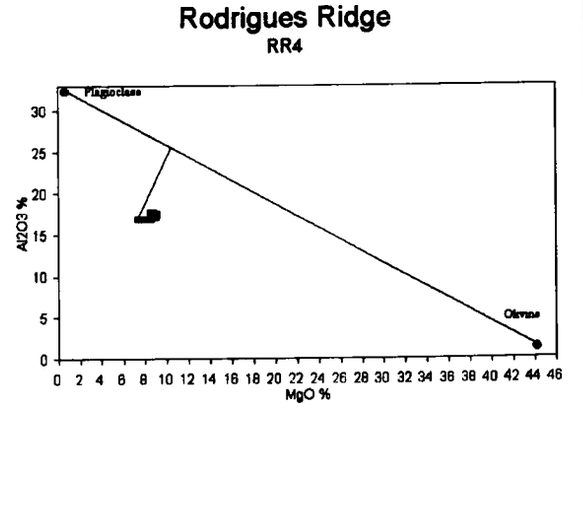

Figure 111

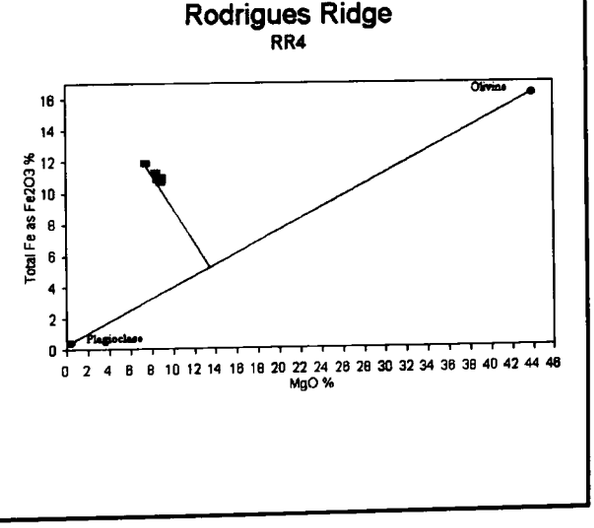

Variation Diagrams for RR4

Figure 112

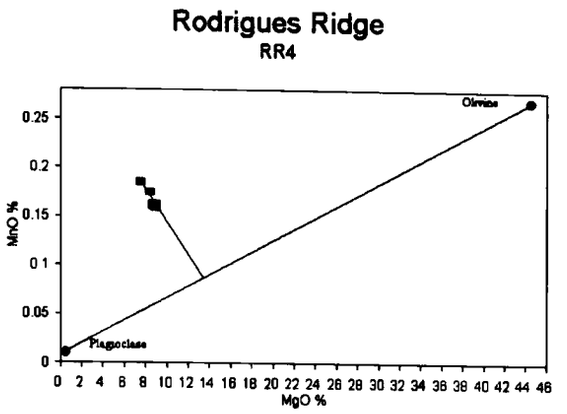

Figure 113

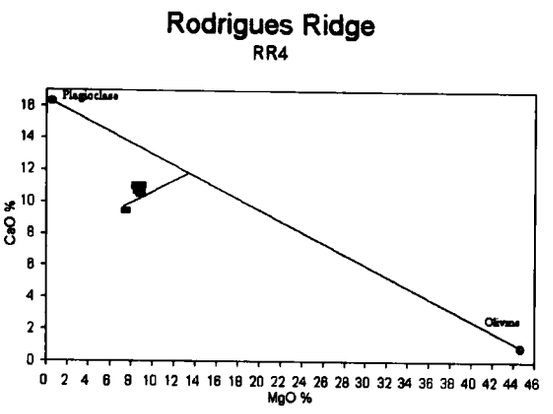

Figure 114

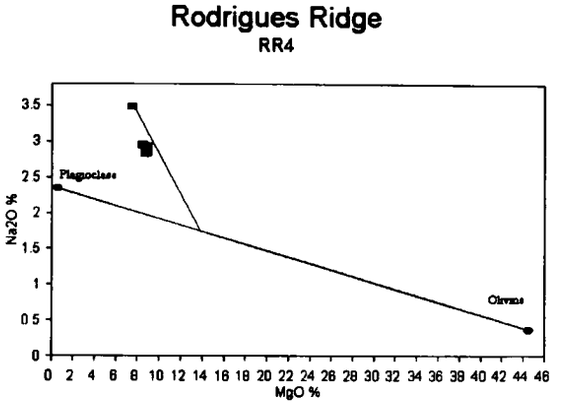

Figure 115

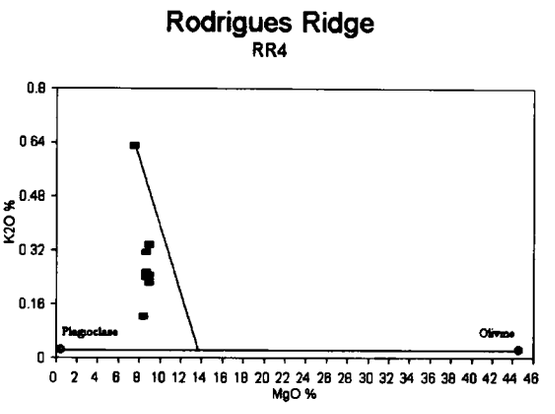

Figure 116

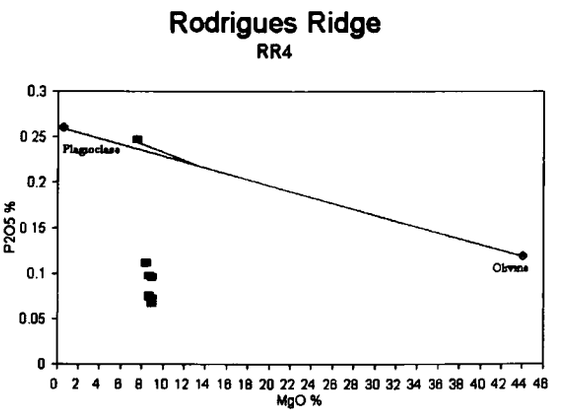

Figure 117

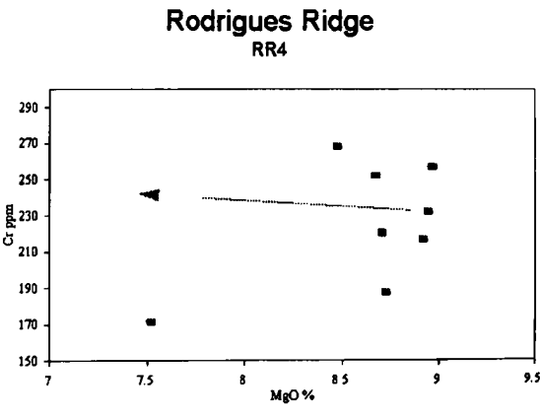

Variation Diagrams for RR4

Figure 118

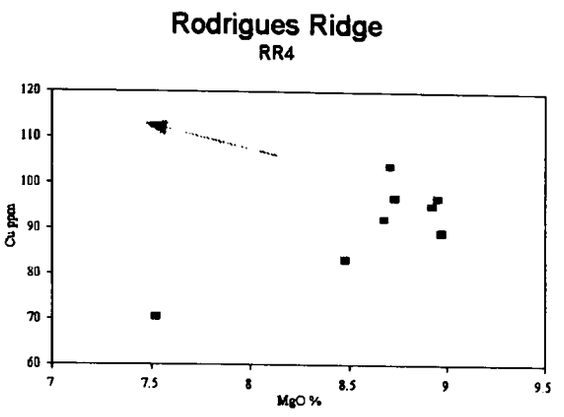

Figure 119

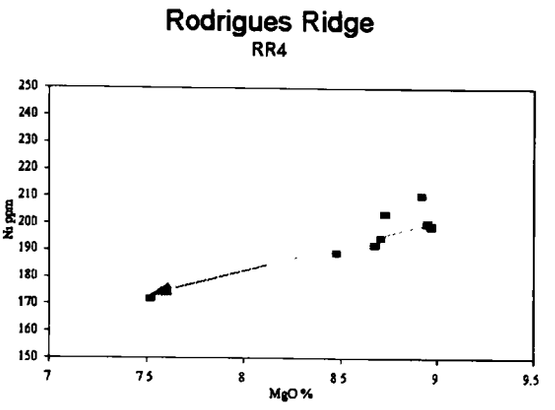

Figure 120

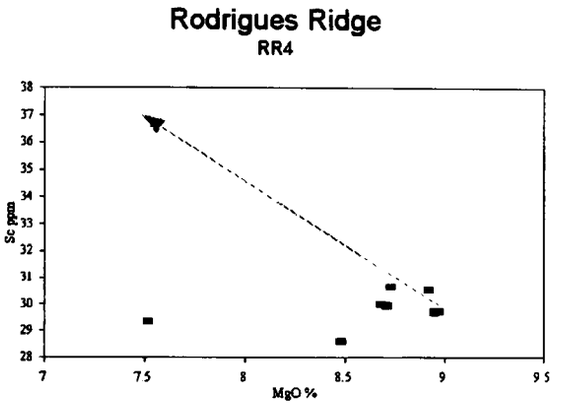

Figure 121

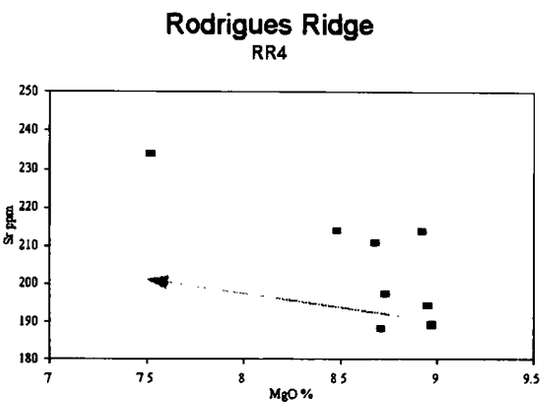

Figure 122

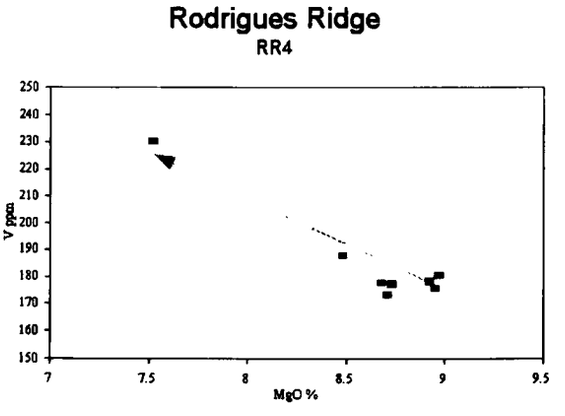

Figure 123

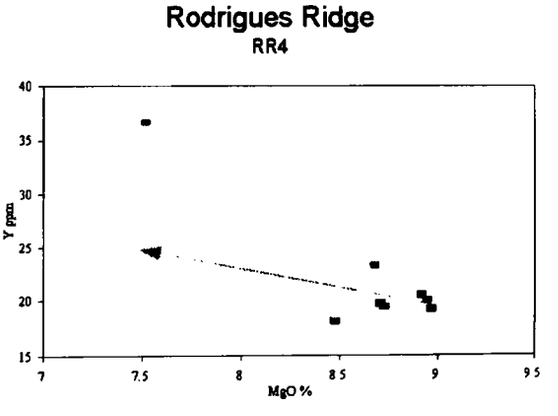

Variation Diagrams for RR4

Figure 124

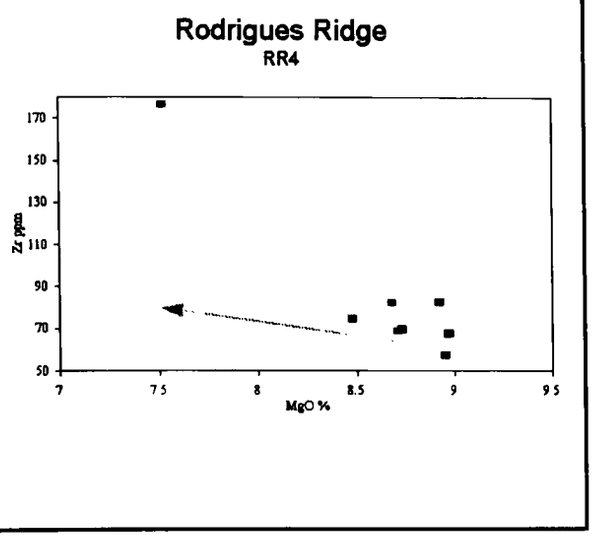

Figure 125

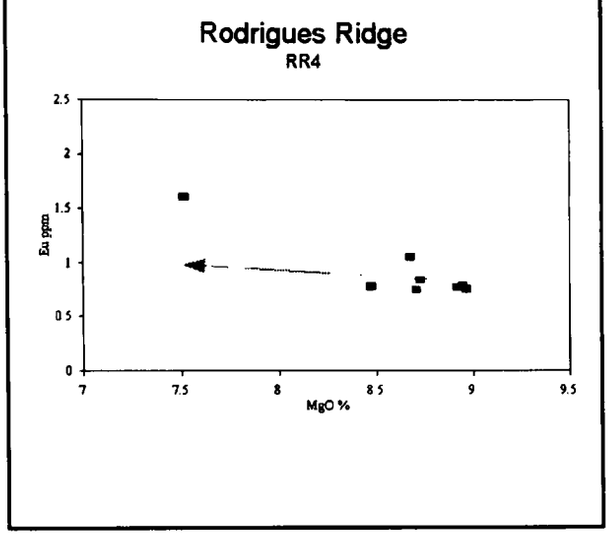

Arrows shown on figs. 117-125 indicate the modelled fractionation trend for the trace elements, described in chapter 6.

Figure 126

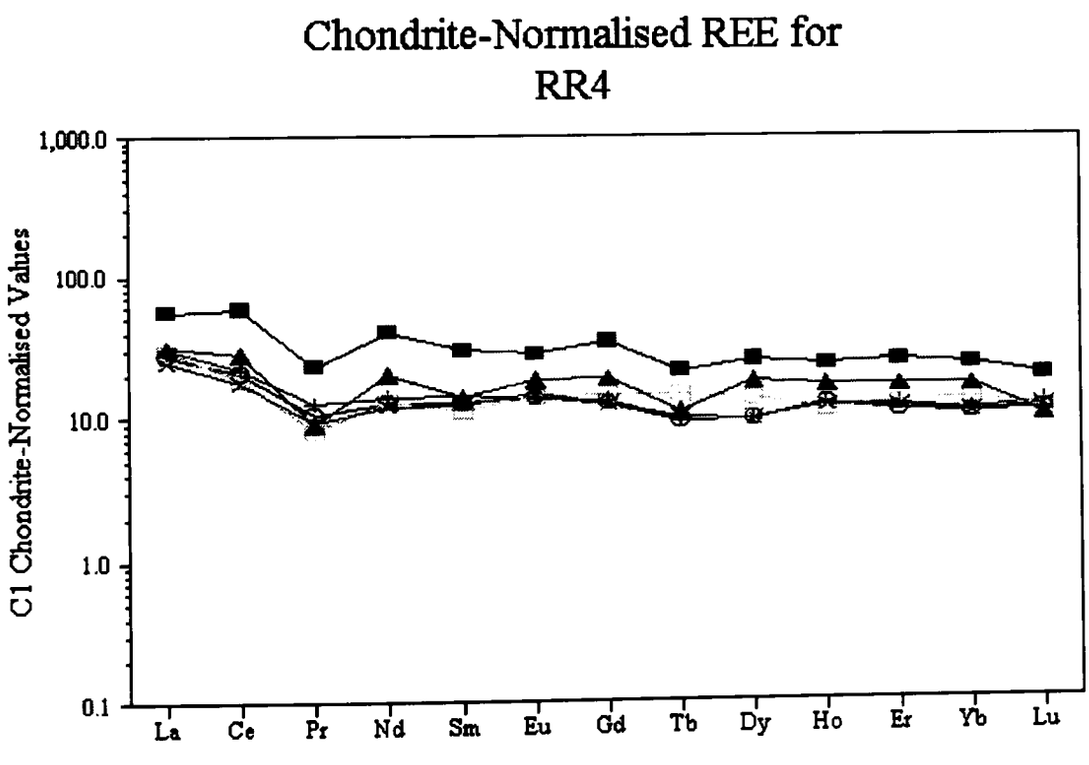

Chondrite values from Sun & McDonough (1989).

RR8

Six lavas were analysed from this site. These plot along a linear trend on the alkali side of the alkali-silica divide in fig. 46 (page 101). Although all the samples from RR8 plot in the field of alkali basalts they straddle the Ol-Ab (olivine-albite) join in the system Ol-Ne-Q (olivine-nepheline-quartz) *i.e.* the critical plane of silica undersaturation. They have between 7.47% hy and 2.25% ne (table 20). Variation diagrams for RR8 are given in figs. 127-147. The major, trace and REE variation diagrams show linear relationships between Al_2O_3, H_2O, CO_2, Zn, Yb and MgO. Additionally SiO_2, TiO_2, $Fe_2O_3^*$, MnO, Cr, Rb, Y, La, Gd and Sm, show a consistent change in trend at about 10% MgO, although the limited data set makes this a rather tentative observation. The olivine-plagioclase fractionation trends shown on the variation diagrams are based on models described in chapter 6.

The basalts from RR8 include some of the most magnesian samples recovered from the Rodrigues Ridge, with the MgO content ranging from 12.13-6.21%. Generally the more magnesian samples at this site have higher olivine contents. TiO_2 at RR8 is slightly higher than at the more easterly sites (1.35-1.53%), similar to RR9c (1.43-1.62%) but substantially lower than at RR10 (2.33-3.00%), reflecting the tendency for this element to increases from east to west along the Rodrigues Ridge. Al_2O_3 (15.08-17.55%) and CaO (9.18-10.30%) are lower than at RR4 (16.91-17.73% and 9.44-11.02%), while SiO_2 has a much wider range (43.89-48.56%) encompassing that of all the other unaltered lavas from the Rodrigues Ridge. RR8 is richer in Cr, Nb, V and Y (453-624 ppm, 6.19-17.43 ppm, 180-326 ppm and 21.86-39.77 ppm) than RR4 (171-268 ppm, 3.61-15.79 ppm 173-230 ppm and 18.06-36.71 ppm respectively).

At RR8, clear enrichment of the more incompatible elements is observed on a plot of the primitive mantle-normalised trace elements (fig. 55). These elements (Rb-P) also show greater variation between the individual samples. Two traces (RR8.5 and RR8.3) show a slight peak in U and to a lesser extent in P and Zr, similar to the behaviour observed at RR3. The trace element patterns for RR8 (including any enrichment in U) are confined between the patterns for E-type MORB and OIB. Similarly the C1 chondrite-normalised REE (fig. 148) show clear LREE enrichment while the HREE are broadly similar to those of the more easterly sites and also RR9c.

In figs 127-135, the compositional fields for plagioclase and olivine phenocrysts are shown joined. The modelled fractionation path is shown, linking the parent and daughter to the proposed fractionating assemblage. A full discussion of how this model was produced can be found in chapter 6. Arrows shown on figs. 136-147 indicate the modelled fractionation trend for the trace elements, also described in chapter 6.

Variation Diagrams for RR8

Figure 127

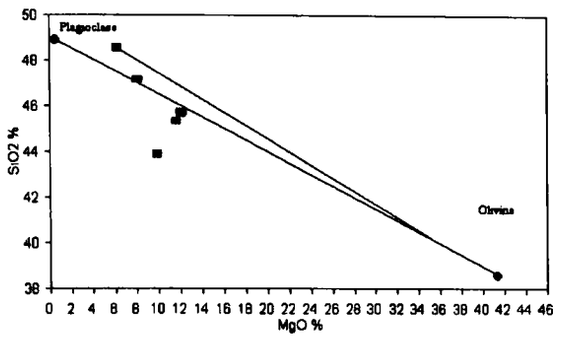

Figure 128

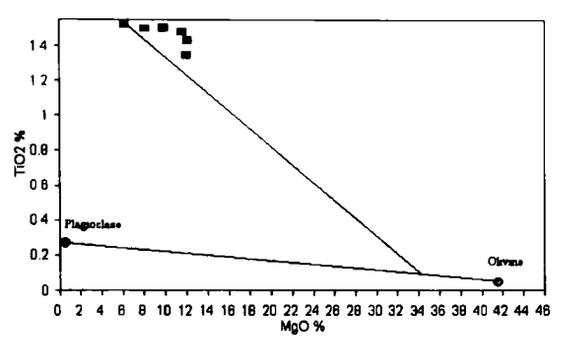

Figure 129

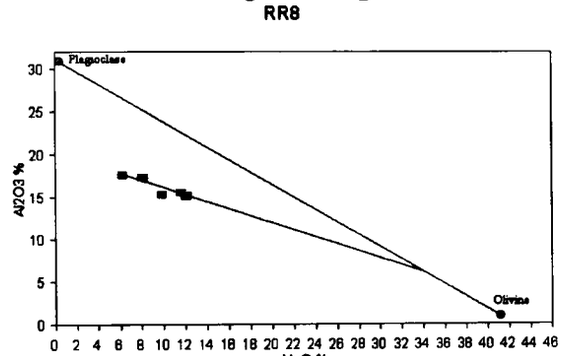

Figure 130

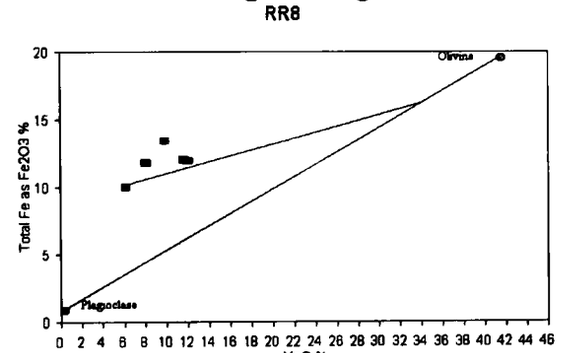

Figure 131

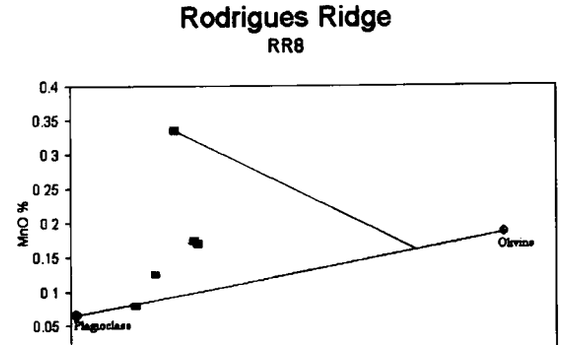

Figure 132

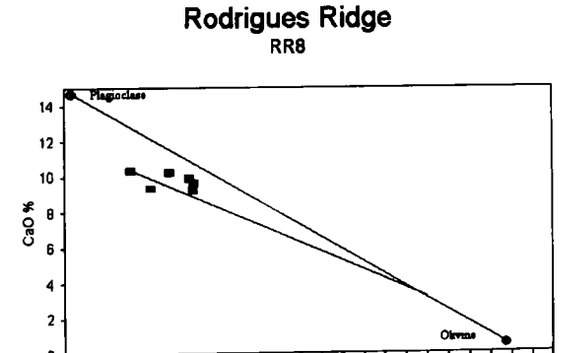

Variation Diagrams for RR8

Figure 133

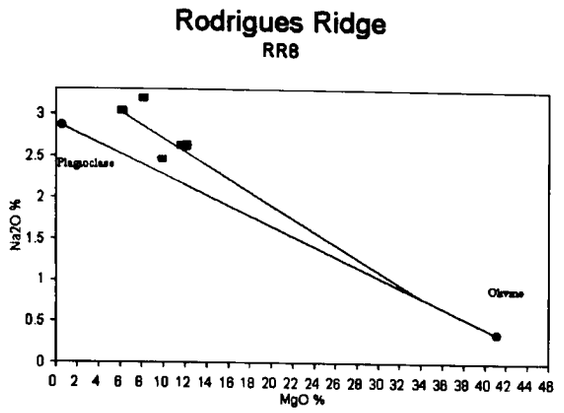

Figure 134

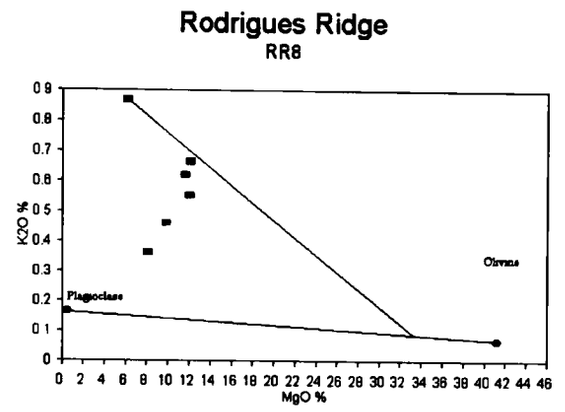

Figure 135

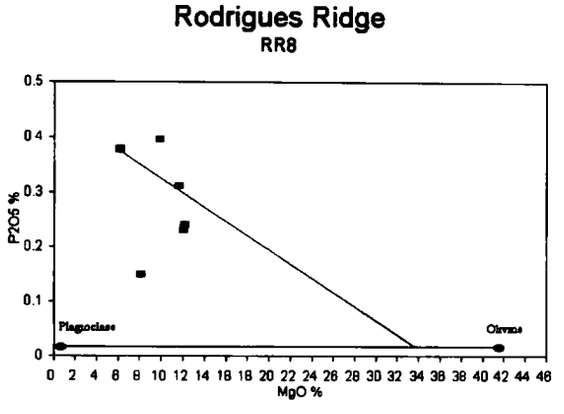

Figure 136

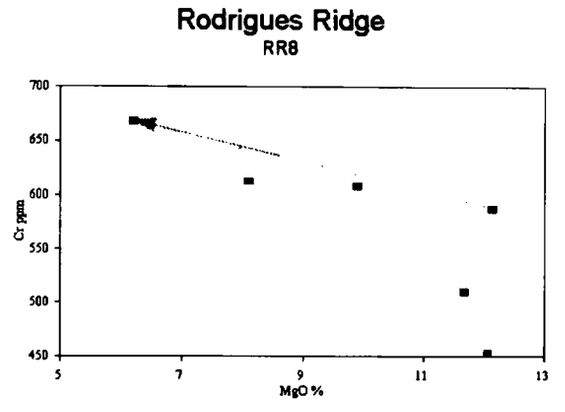

Figure 137

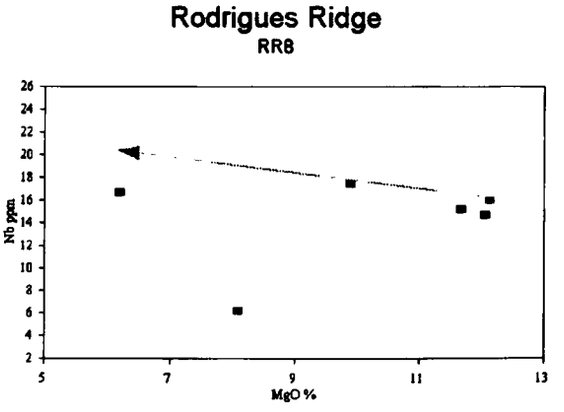

Figure 138

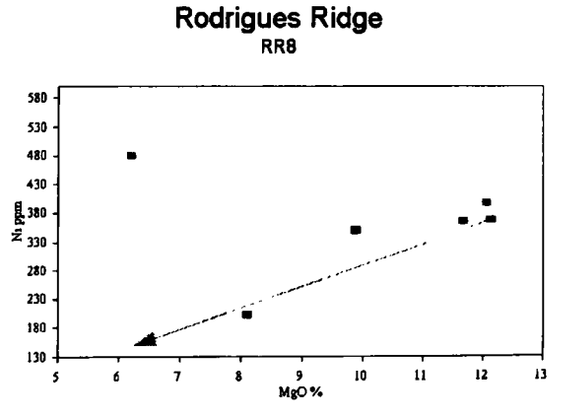

Variation Diagrams for RR8

Figure 139

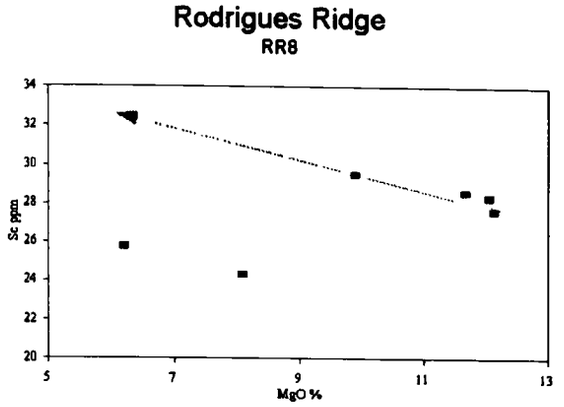

Figure 140

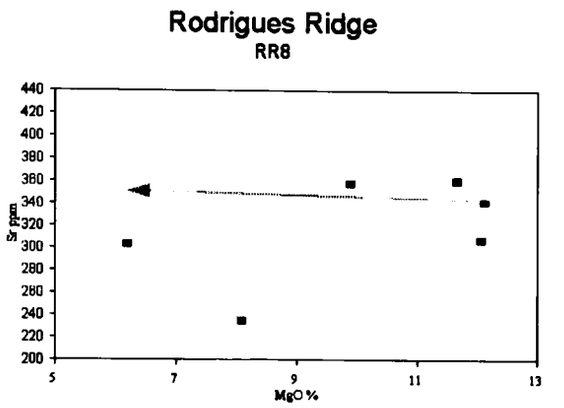

Figure 141

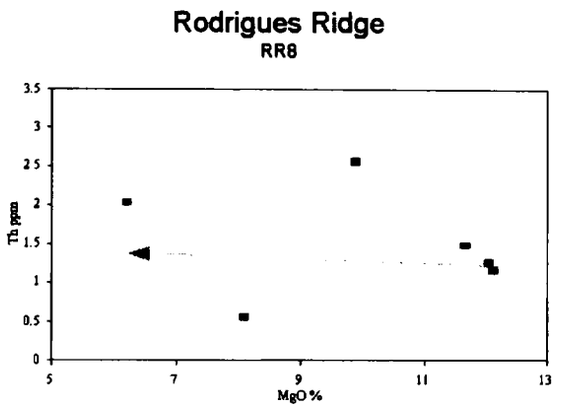

Figure 142

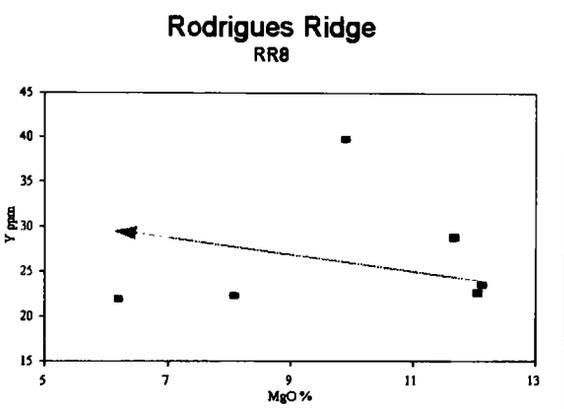

Figure 143

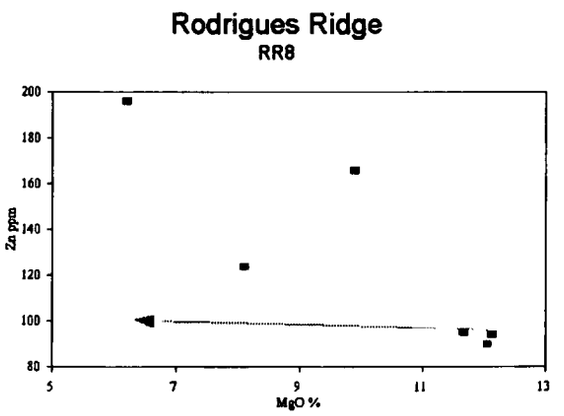

Figure 144

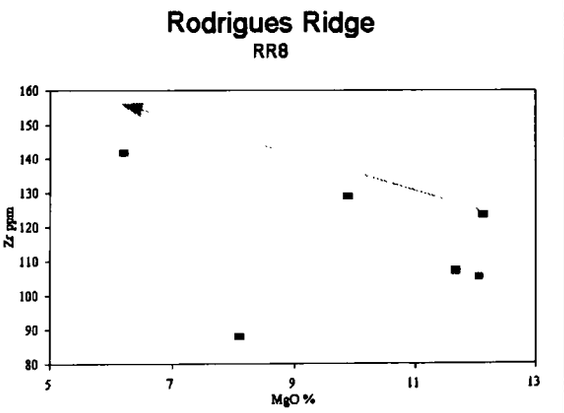

Variation Diagrams for RR8

Figure 145

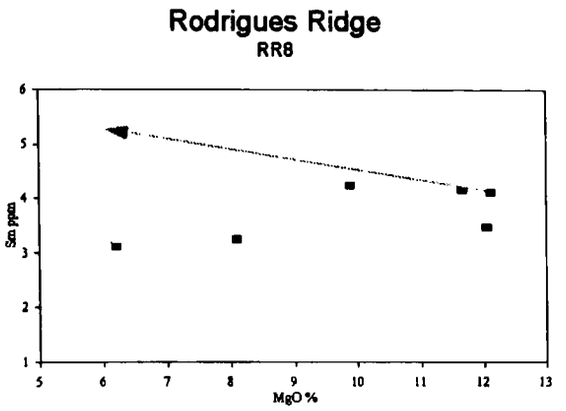

Figure 146

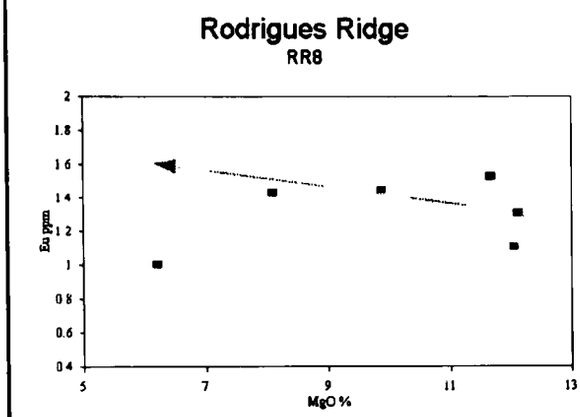

Figure 147

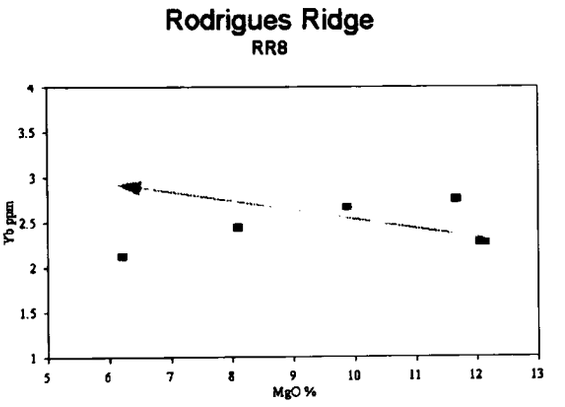

Figure 148

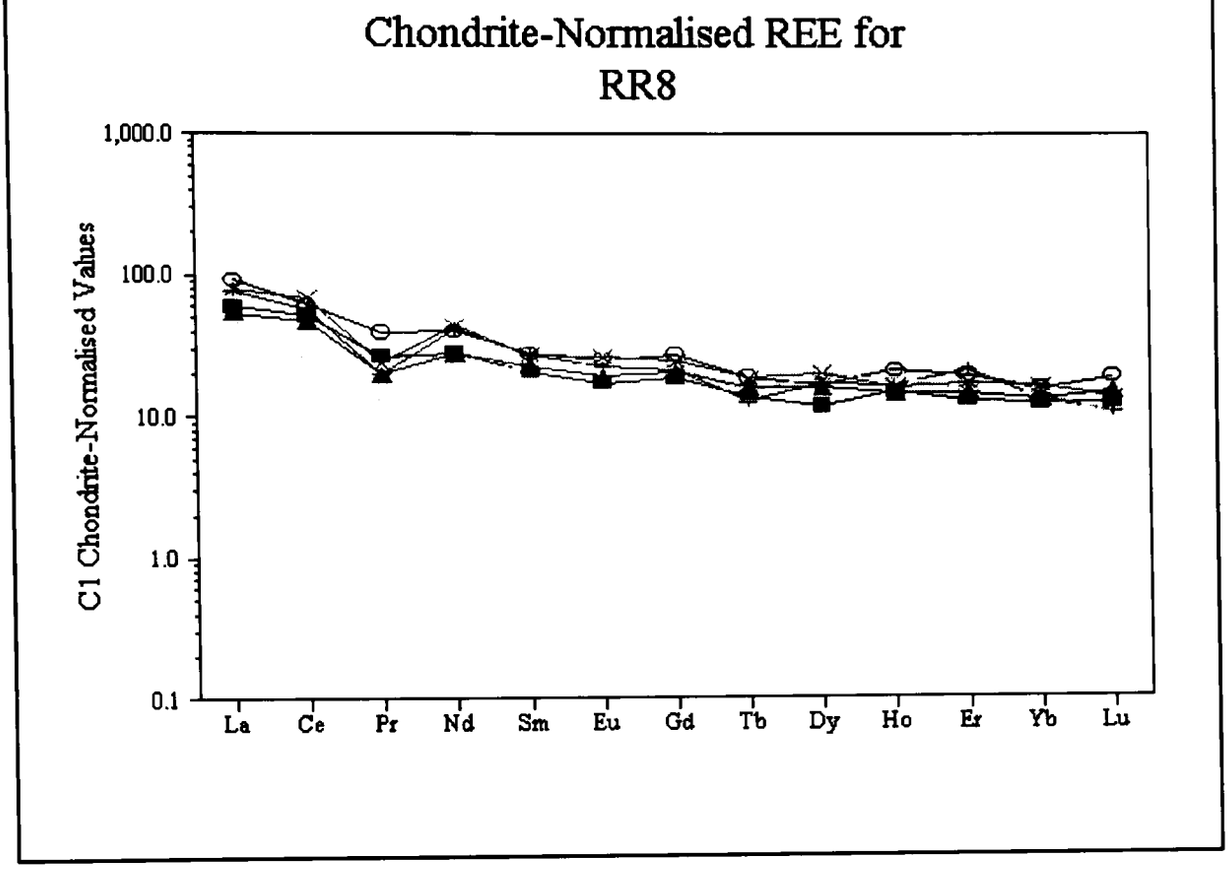

Chondrite values from Sun & McDonough (1989).

RR9c

The fourteen samples from RR9c all plot on the alkali side of the divide on the alkali-silica diagram (fig. 47 page 101). Of these, only RR9c.11 is nepheline normative. This sample can been seen as anomalous on many of the variation diagrams. Collectively the lavas fall into a narrow range in terms of their normative mineralogy (4.36% hy-1.67% ne see table 21). At this site SiO_2 is in the range (46.36-48.35%) for all but RR9c.11, which may be altered and is excluded from all the ranges quoted here. CaO, FeO^*, MgO and Al_2O_3 are in the ranges 8.84-11.25%, 7.90-9.22%, 6.19-10.41% and 15.56-17.95%. Variation diagrams for RR9c are given in figs. 149-171. When plotted against MgO, clear olivine controlled fractionation curves are expressed by; SiO_2, Al_2O_3, TiO_2, $Fe_2O_3^*$, CaO, K_2O, MnO, P_2O_5, Cr, Ni, Sc, U (not shown), V, Y, Zr, (figs. 149-153, 156-7, 158, 160, 162, 164-5, 166) Sm, Gd, Dy (not shown), Eu and Yb (figs. 167-69). Fractionation trends shown on all diagrams were based on modelling described in chapter 6, of olivine fractionation only. Scattered trends are also expressed by; Na_2O (fig.154), H_2O (not shown), Nb, Rb, Sr, (figs. 159, 161, 163) Th , La, Ce and Lu (not shown). CO_2, Ba, Cu, Zn and Nd show no obvious trends (not shown).

At RR9c, K_2O is in the range 0.32-0.87%, the lower value being that of RR9c.11 which shows anomalous behaviour which cannot be attributed solely to alteration processes for; SiO_2, $Fe_2O_3^*$, MnO,

K_2O, P_2O_5, Cr, Th, U, V, Nb and Zn. Some trace elements at RR9c show a broad spread of points, apparently forming independent trends crossing the olivine control line. Most notable of these are K_2O, Nb, Rb, Sr, V and Zr (figs. 155, 159, 161, 163-4 & 166). RR9c.11 falls on the extremity of one of these trends. This unusual behaviour was noted on data obtained from several different instruments and on replicate preparations, negating the possibility of analytical error as a cause (see appendix 4).

The primitive mantle-normalized trace element pattern (figs. 56a & b) for the anomalous sample, RR9c.11, displays the peaks over U and P which were seen at RR2-low MgO group and RR3. Another smaller peak is also present over Zr in this and the other RR9c samples. The RR9c lavas also show some elevation of Rb, K_2O and Sr values. In short, the RR9c lavas show peaks on these primitive mantle-normalised traces for those elements which show a spread of data on the variation diagrams. The C1 chondrite-normalised REE curves (figs. 172a & b) for RR9c show smooth mildly LREE enriched patterns.

Variation Diagrams for RR9c

Figure 149

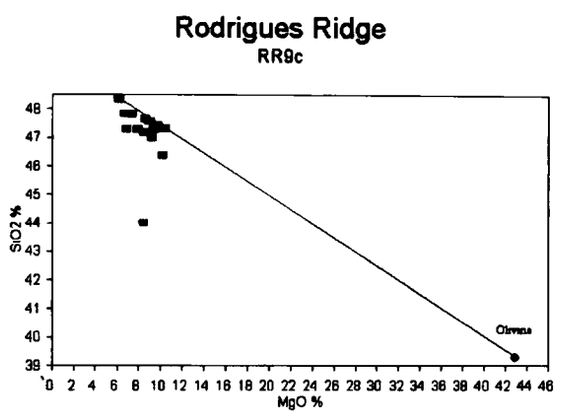

Figure 150

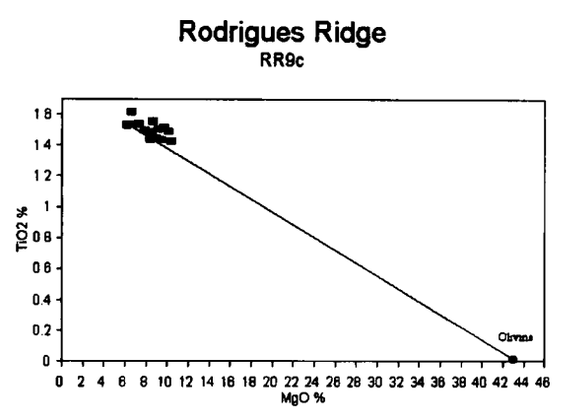

Figure 151

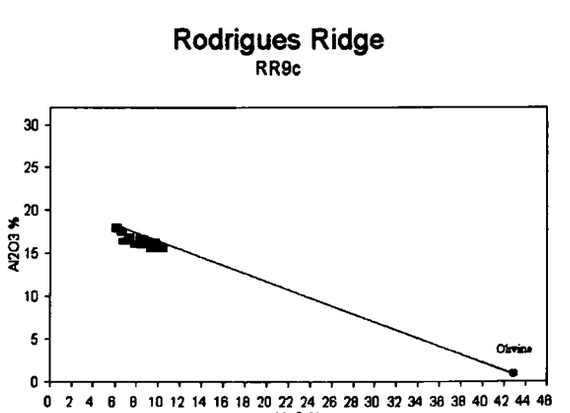

Figure 152

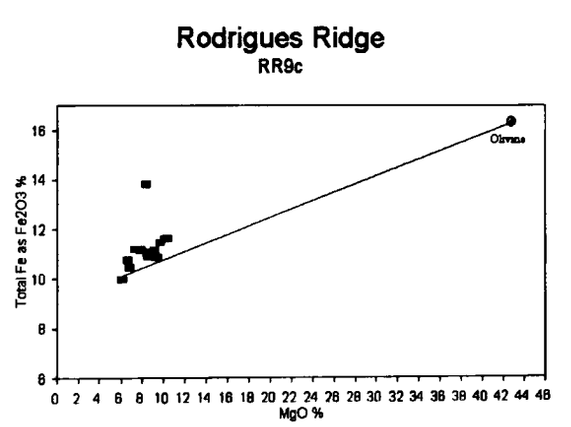

Variation Diagrams for RR9c

Figure 153

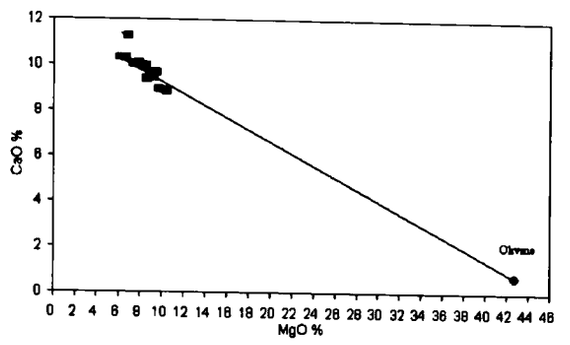

Figure 154

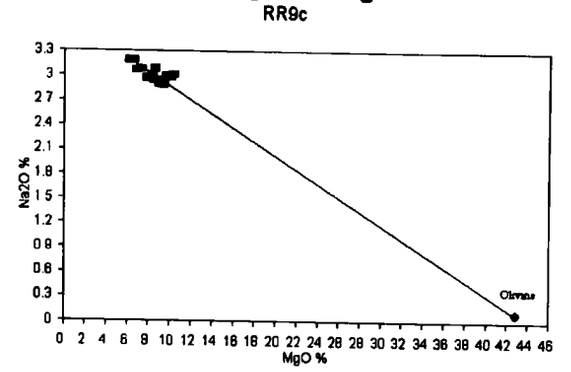

Figure 155

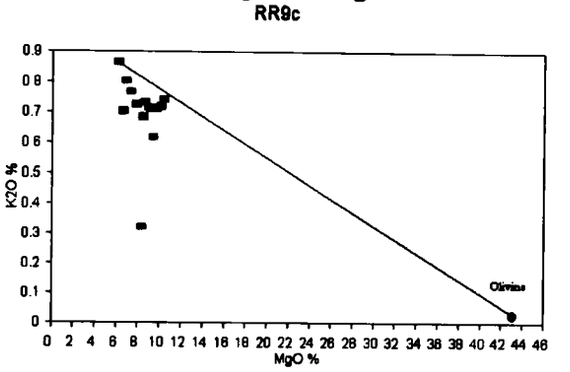

Figure 156

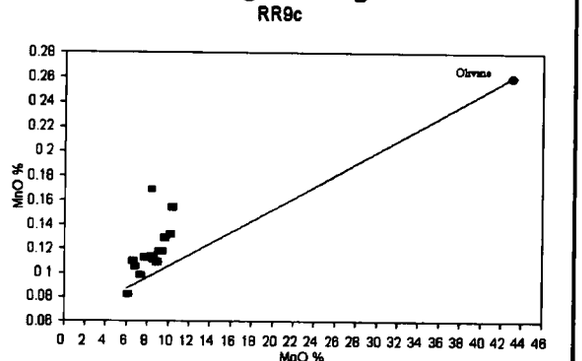

Figure 157

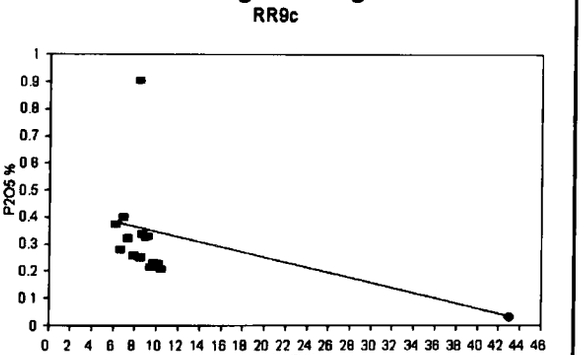

Figure 158

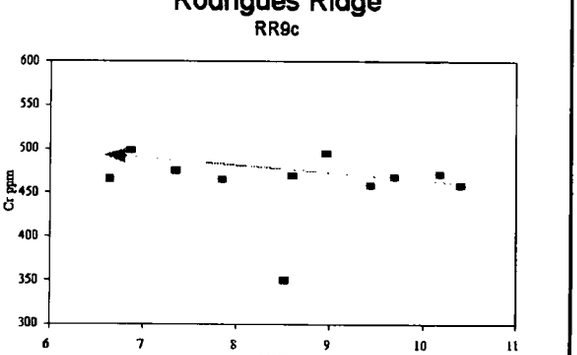

Variation Diagrams for RR9c

Figure 159

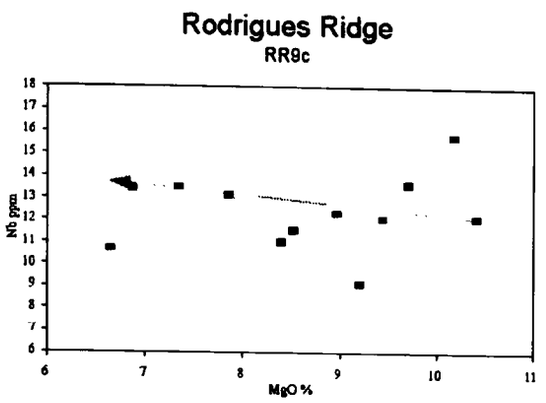

Figure 160

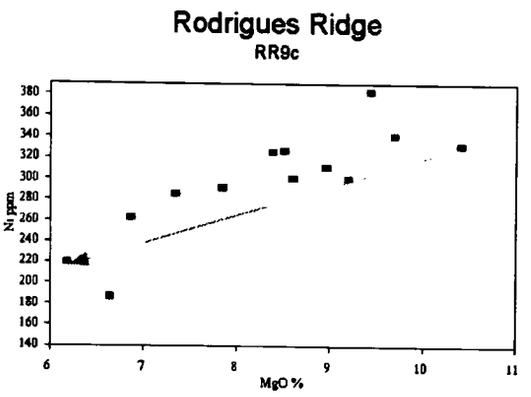

Figure 161

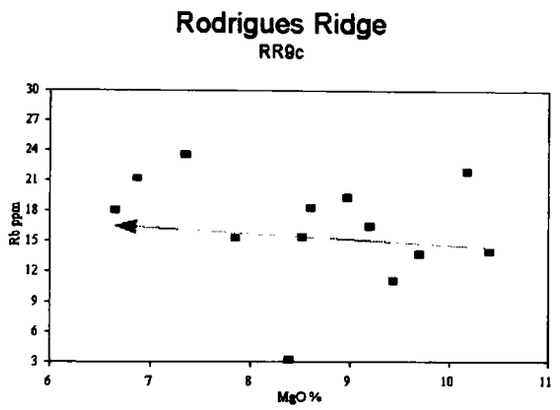

Figure 162

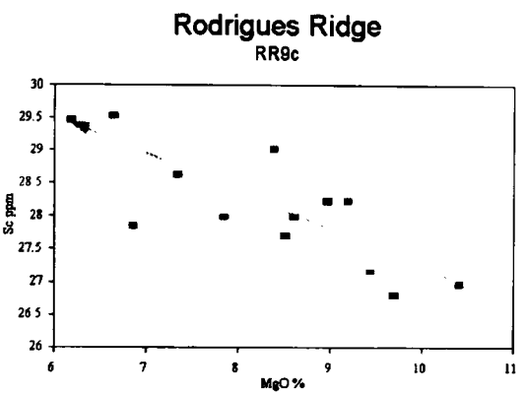

Figure 163

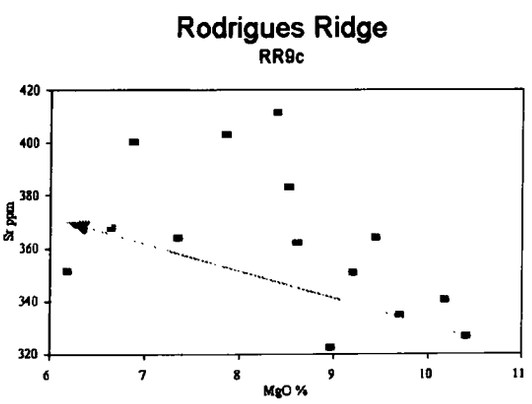

Figure 164

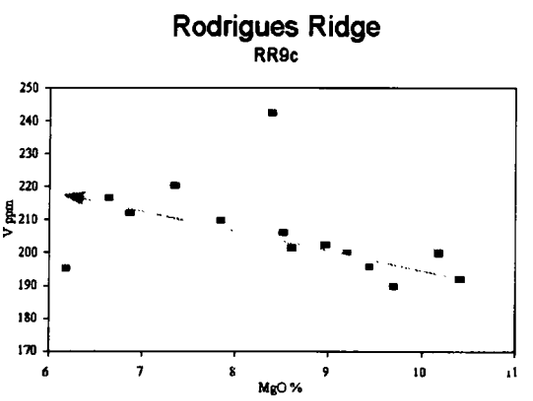

Variation Diagrams for RR9c

Figure 165

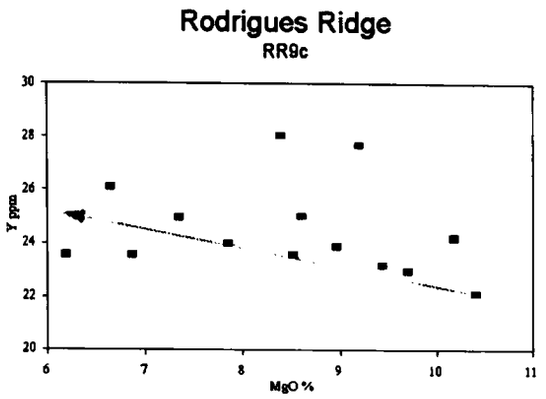

Figure 166

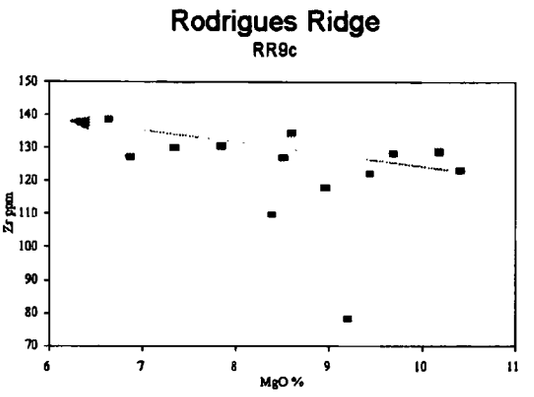

Figure 167

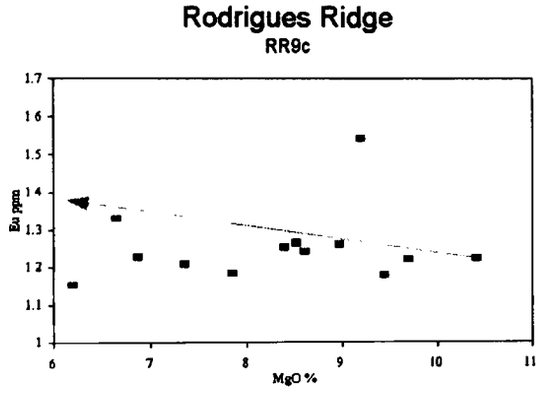

Figure 168

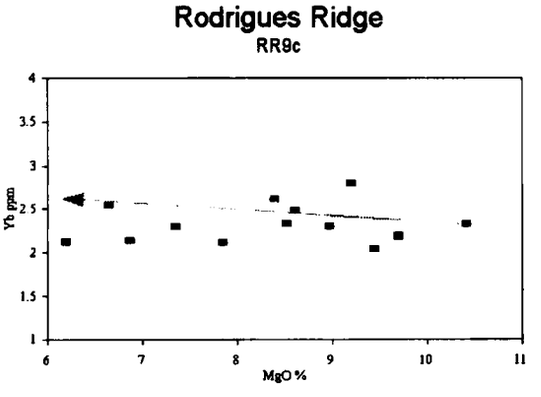

In figs 149-157, the compositional field for the olivine phenocrysts is shown. The modelled fractionation path is shown, linking the parent and daughter to the proposed fractionating assemblage. A full discussion of how this model was produced can be found in chapter 6. Arrows shown on figs. 158-168 indicate the modelled fractionation trend for the trace elements, also described in chapter 6.

Figure 169a

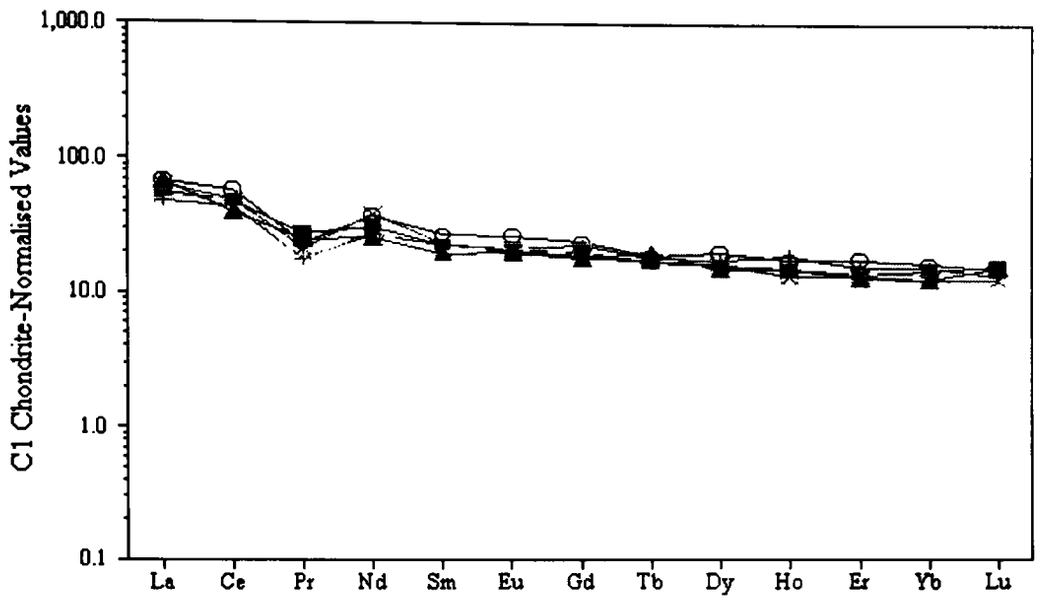

Figure 169b

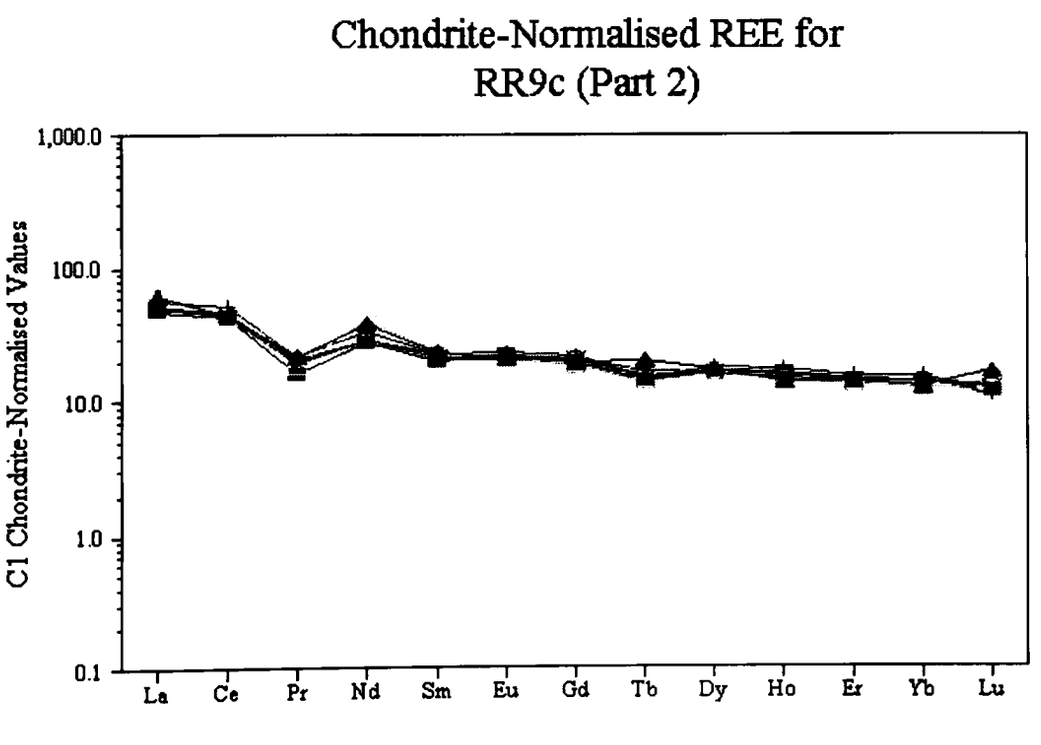

Chondrite values from Sun & McDonough (1989).

RR10

Five basalts and one tuff (RR10.19) from RR10 were analysed. Like the lavas of RR3, RR8 RR9c and RR12d they are all mildly alkali basalts (fig. 48 page 101). RR10.8 was selected to study the effects of alteration, however all the lavas analysed from this site were subsequently found to be altered. They contain significant quantities of zeolites and calcite which have radically affected the whole rock chemistry. For most Rodrigues Ridge sites Al_2O_3 is in the range 15.08-19.41%, SiO_2 is 43.89-48.56%, TiO_2 is 0.87-2.08% and alkalis ($K_2O + Na_2O$) are 2.92-6.12%, whereas at RR10 Al_2O_3 is 13.39-17.07%, SiO_2 is 27.58-40.34%, TiO_2 is 2.34-2.95% and alkalis are 2.80-9.41%. This selection of major elements demonstrates the extreme deviation of RR10 from the fields defined at the other Rodrigues Ridge sites. The lavas from RR10 show enrichment of the alkalis and depletion in SiO_2, probably as a consequence of alteration and zeolite growth. This causes them to display unusual normative mineralogies (table 22). The lavas of RR10 also show enrichment of (immobile) incompatible elements such as Nb, Zr and Ti.

Variation diagrams for RR10 are given in figs. 170-191. Major and trace element plots with MgO reveal clear trends in TiO_2, P_2O_5, Sc and Sr (excepting RR10.7 which shows exceptionally high Sr values) (figs. 171, 178, 182 and 183). Less distinct trend can also be recognised in SiO_2, $Fe_2O_3^*$, MnO, Cu (not shown), Hf (not shown), Nb, Rb, Th, Zr and the REE (figs. 170, 173, 175, 180-1, 184, 188-91). RR10.7 was observed to have very low CaO (2.56%) in conjunction with very high Sr (6975 ppm). This sample appeared relatively fresh in hand specimen but in thin section it was apparent that the vesicles were filled by zeolites. In zeolites Sr, derived from sea water, may substitute for Ca (Deer *et al.*, 1971). On the major element variation diagrams the compositional fields are shown, for the most likely fractionating phases; olivine, plagioclase and clinopyroxene. These fields are based on the composition of these minerals at this and/or surrounding sites. Since the degree of alteration of these rocks prevented the development of sensible fractionation models, no attempt has been made to show possible fractionation paths at this site.

The primitive mantle-normalised trace element (fig. 57) curves for RR10 clearly show that the strongly incompatible elements (Rb-P) excluding Nb, La and Ce, show substantial scatter between these samples, whereas Nb, La, Ce and Nd-Lu still plot along the typical OIB curve. The C1 chondrite-normalised traces for RR10 (fig. 192) are strongly LREE enriched, as would be expected for a typical OIB although the HREE tend to plot below those of typical OIB.

In figs 170-178, the compositional fields for plagioclase, olivine and clinopyroxene phenocrysts are shown. No modelling was attempted at this site due to the alteration state of the lavas. Further discussion can be found in chapter 6.

Variation Diagrams for RR10

Figure 170

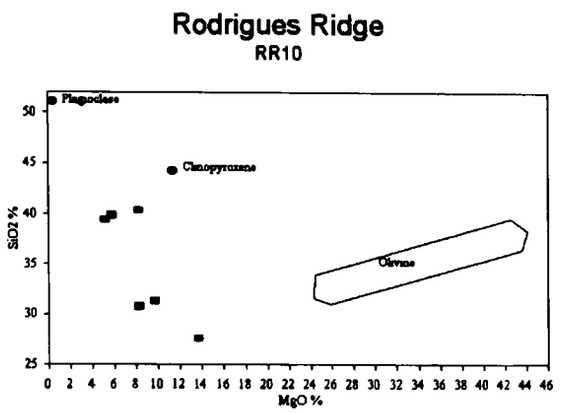

Figure 171

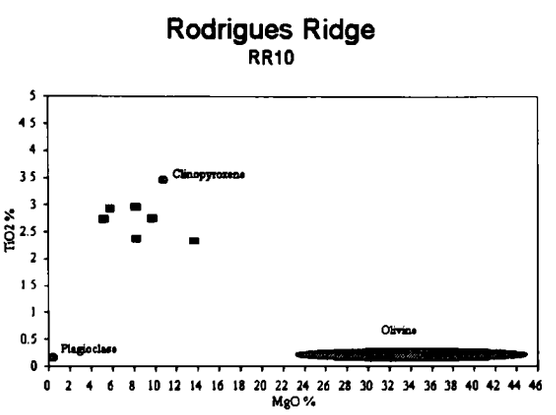

Figure 172

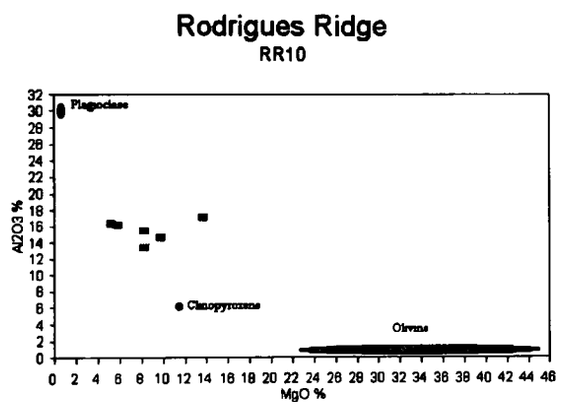

Figure 173

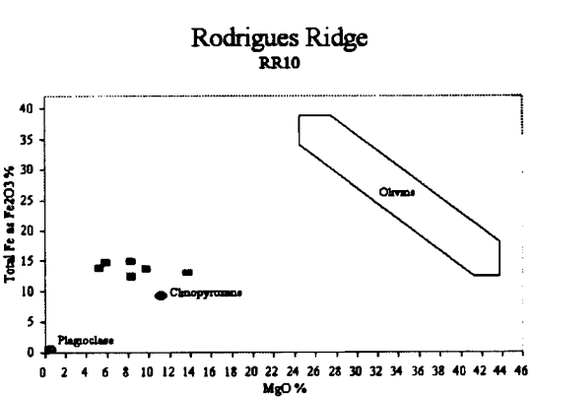

Figure 174

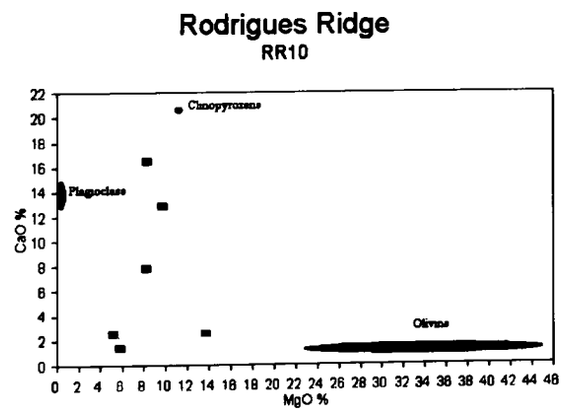

Figure 175

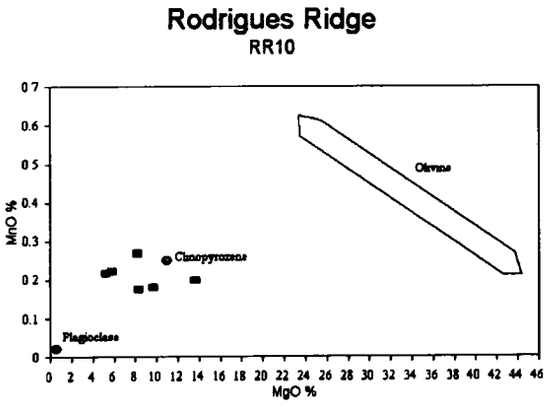

Variation Diagrams for RR10

Figure 176

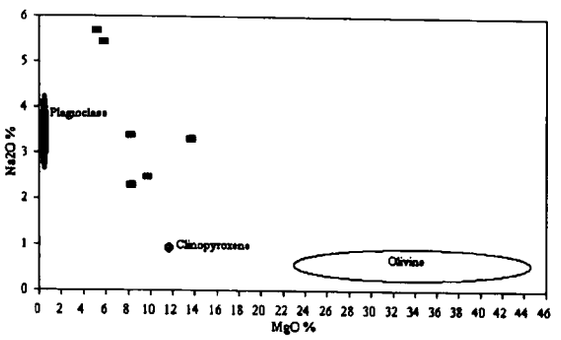

Figure 177

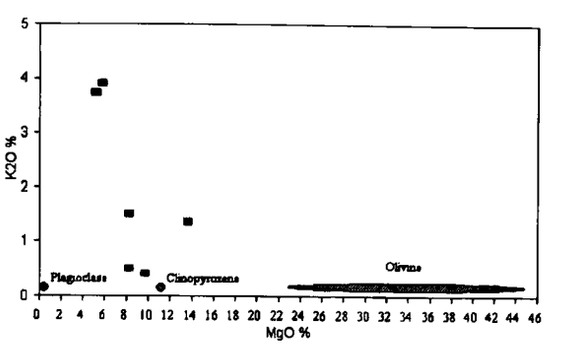

Figure 178

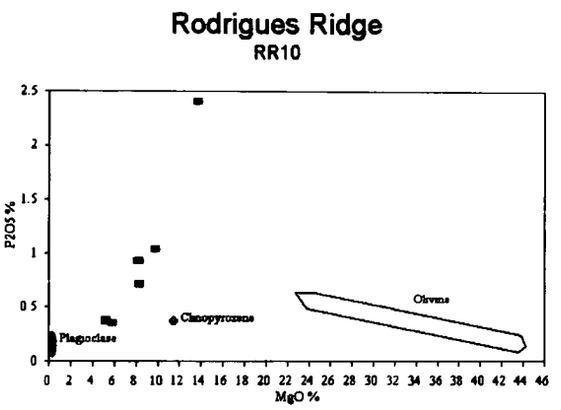

Figure 179

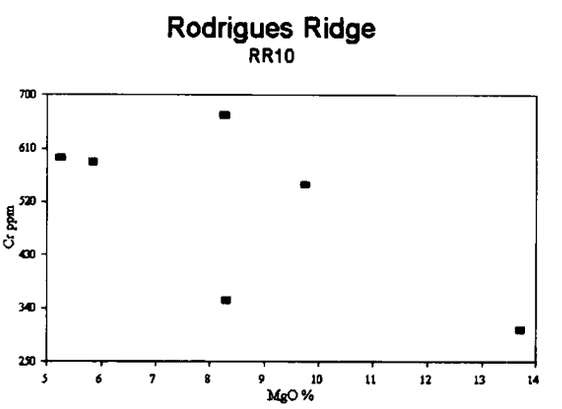

Figure 180

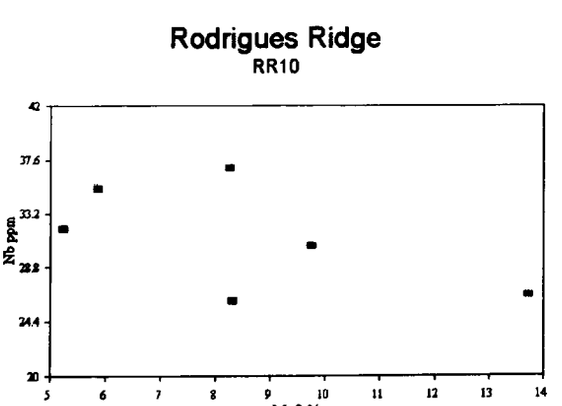

Figure 181

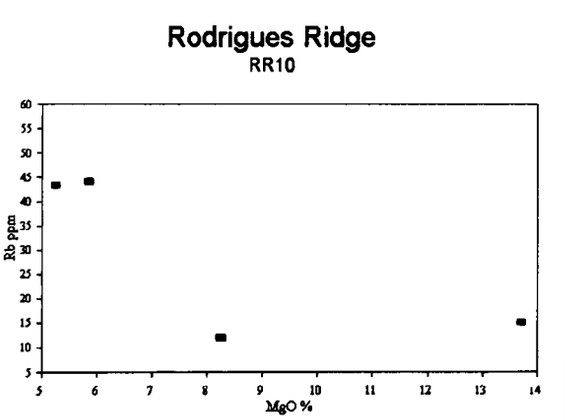

Variation Diagrams for RR10

Figure 182

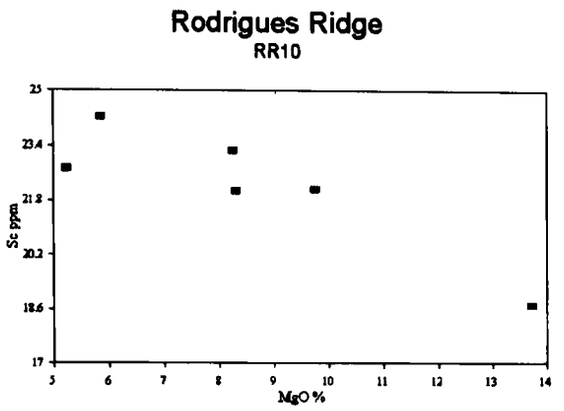

Figure 183

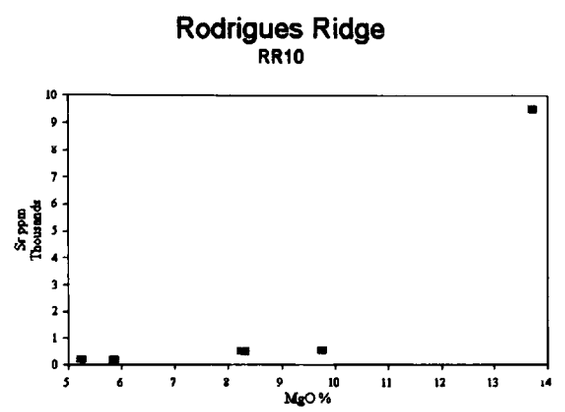

Figure 184

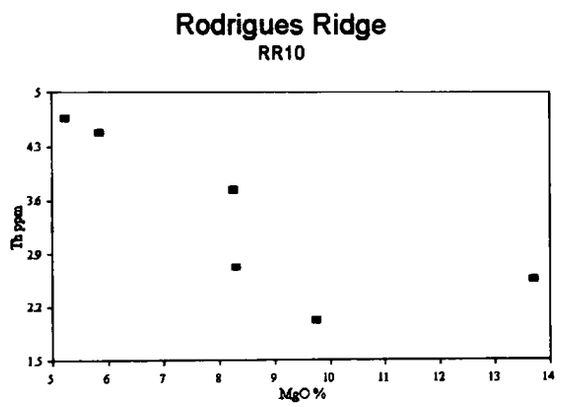

Figure 185

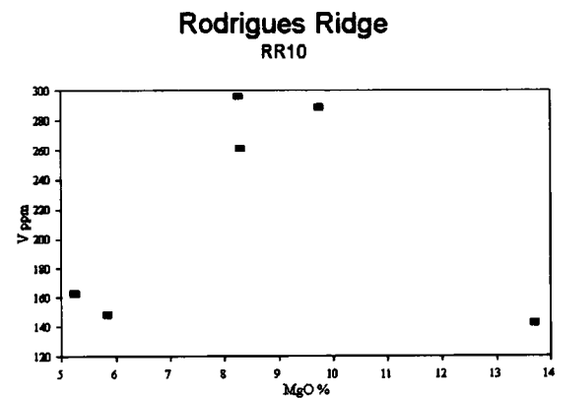

Figure 186

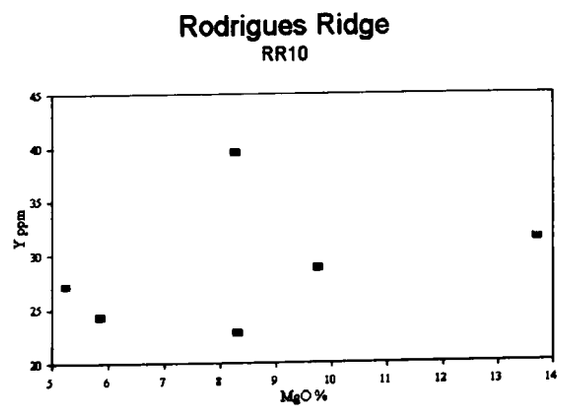

Figure 187

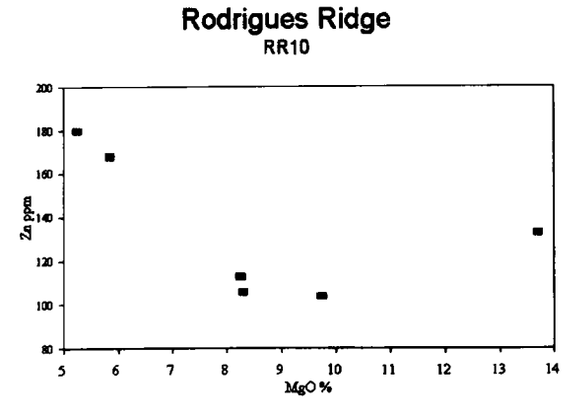

Variation Diagrams for RR10

Figure 188

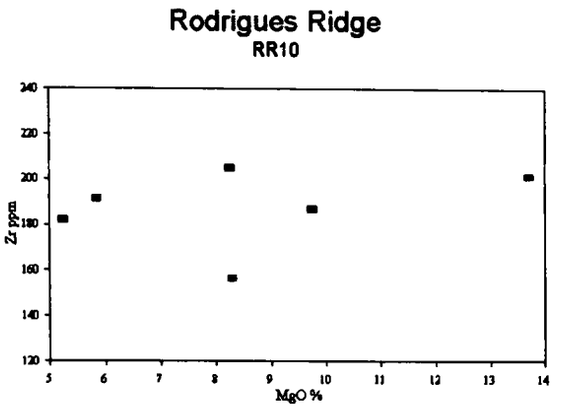

Figure 189

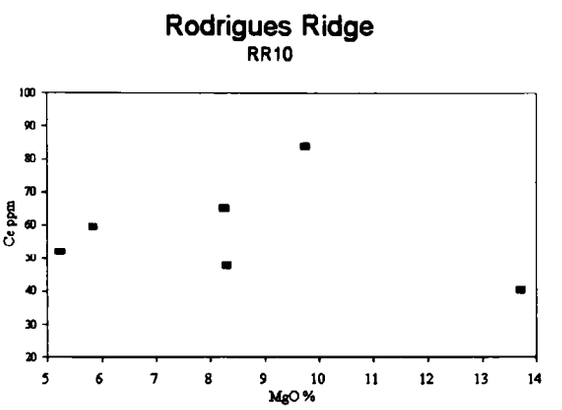

Figure 190

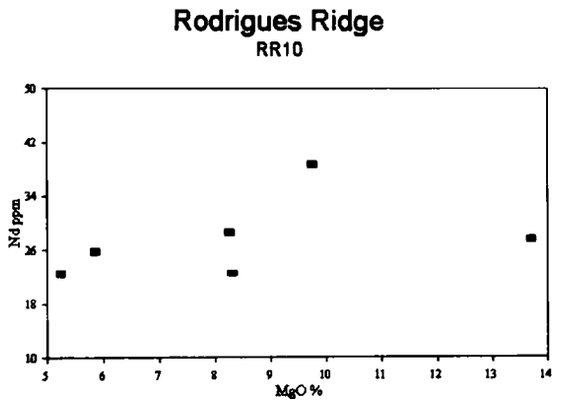

Figure 191

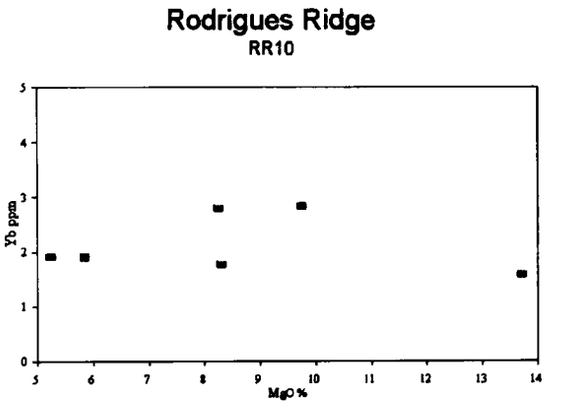

Figure 192

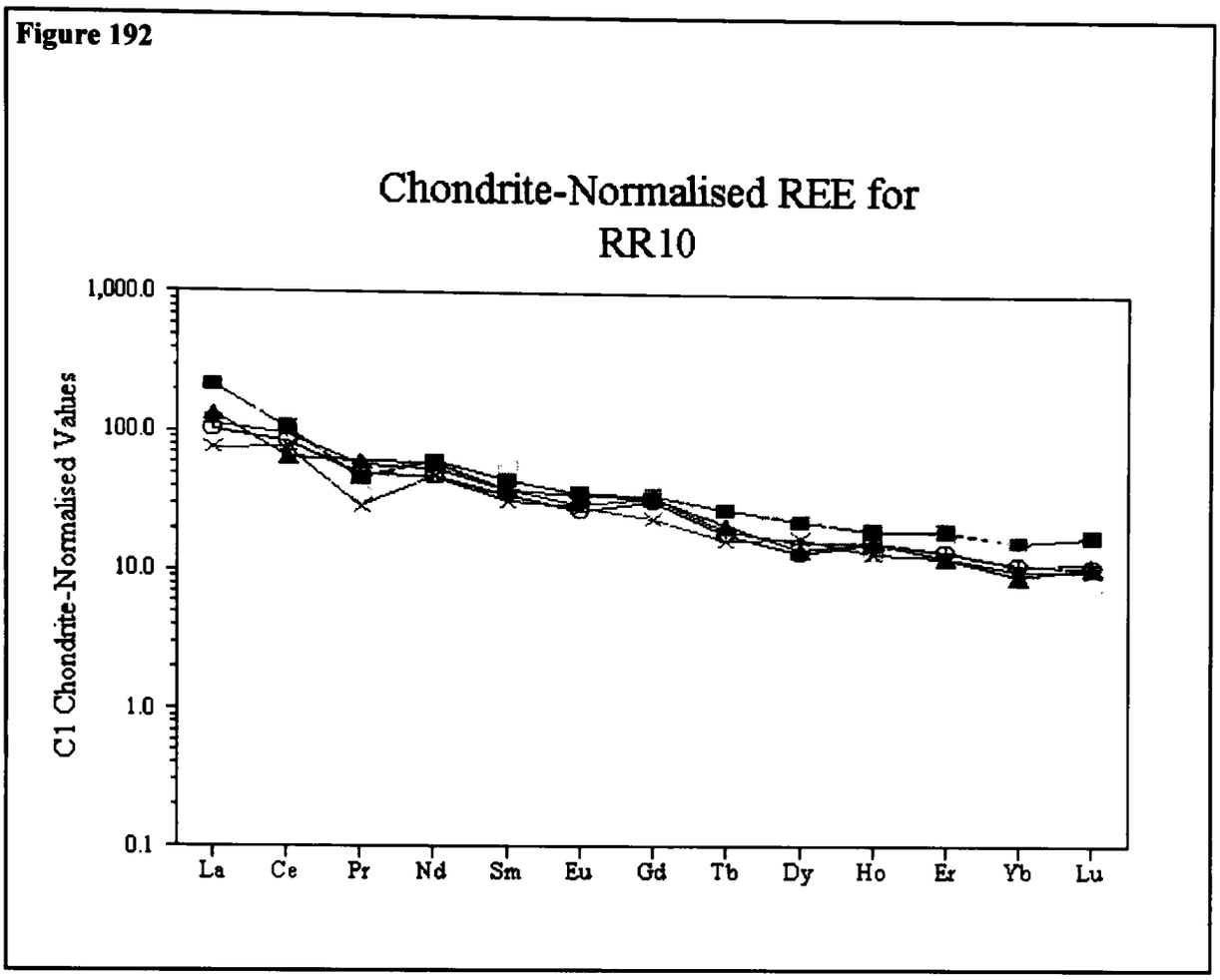

Chondrite values from Sun & McDonough (1989)

RR12d

Five samples from RR12d were selected for geochemical analysis on a visual assessment of their freshness. One further sample RR12d.8 was altered and was selected to see what effects alteration had on the lavas. All the RR12d lavas are mildly alkali basalts on fig. 49 (page 101). All samples from RR12d were found to be nepheline normative (table 23). RR12d.8 had 8.37% ne, whereas the other RR12d samples were in the range 0.76-3.28% ne, suggesting that, in this case, severe alteration has caused the sample to become progressively more ne normative (silica poor). Seawater alteration results in the loss of SiO_2 (Hart *et al.*, 1974) as has been observed at RR10. Variation diagrams for RR12d are given in figs. 193-211. Geochemical trends with MgO are difficult to recognize at this site as the samples display a narrow range of MgO. Scattered trends are found for TiO_2, Al_2O_3, Na_2O, Ba, V, Zr, (figs. 194-5, 199, 202, 206 and 208) and the REE (if the most magnesian sample RR12d.8 is ignored) (figs 209-11). The six RR12d samples studied are all low in MgO, with a narrow range (2.91-4.30%) compared to the other Rodrigues Ridge sites. Only the more evolved compositions from RR2 and RR3 have similar MgO contents (2.91-4.30% at RR12d compared to 3.9-8.8% at RR2 and 3.0-8.3% at RR3). Comparing them with the evolved lavas from the eastern end of the Rodrigues Ridge only serves to underline the dramatic change in basalt chemistry which takes place along this structure (compare

RR3.11 with RR12d.5 both of which have 3.09% MgO in table 16). In addition to the MgO content, the more evolved character of these lavas is also demonstrated by Ni, Y and Zr which are in the range 139-480 ppm, 18.06-39.77 ppm and 57.1-205.1 ppm for all the other sites, but from 48-143 ppm, 40.86-76.81 ppm and 131.6-291.4 ppm at RR12d. Major element fractionation models are described in chapter 6 and are shown on the variation diagrams. The fractionation paths shown on the trace element plots are based on the same model which requires the fractionation of olivine, plagioclase and clinopyroxene, however since the absolute amount of fractionation is very low the observed variation between parent and daughter is often close to instrumental detection limits. For this reason these models are presented on these diagram only as a guide to the expected fractionation paths.

At RR12d primitive mantle-normalised trace element plots (fig. 58) show curves similar to typical OIB, but unlike RR10 they are enriched in the HREE. Ce/Yb ratios for RR12d are 12.04-21.53 compared to 2.62-4.89 for RR2 and 23.33-31.35 at RR10 (typical values for MORB are 2.5 while for OIB they are 37.0). The decrease in Ce/Yb between RR10 and RR12d reflects the increase in the concentrations of HREE at RR12d compared to RR10 (Yb = 2.98-5.71 ppm at RR12d compared with 1.58-2.84 ppm at RR10). RR12d basalts display peaks over P, Zr, U, and Y similar to RR2-low MgO group, RR3, RR8.3, RR8.5, RR9c.11 and RR10. Two other peaks are also observed over La and Gd in both figs. 212 and 58.

Variation Diagrams for RR12d

Figure 193

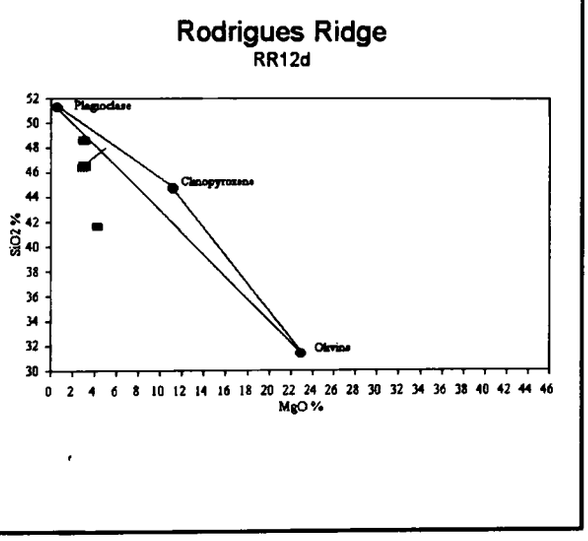

Figure 194

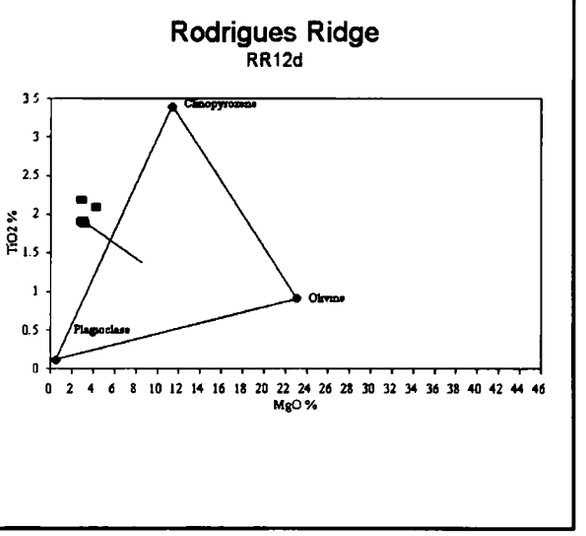

In figs 193-201, the compositional fields for plagioclase, olivine and clinopyroxene phenocrysts are shown joined. The modelled fractionation path is shown, linking the parent and daughter to the proposed fractionating assemblage. A full discussion of how this model was produced can be found in chapter 6. Arrows shown on figs. 202-211 indicate the modelled fractionation trend for the trace elements. The reader should take note of the discussion in chapter 6 regarding the difficulty in modelling very small amounts of fractionation.

Variation Diagrams for RR12d

Figure 195

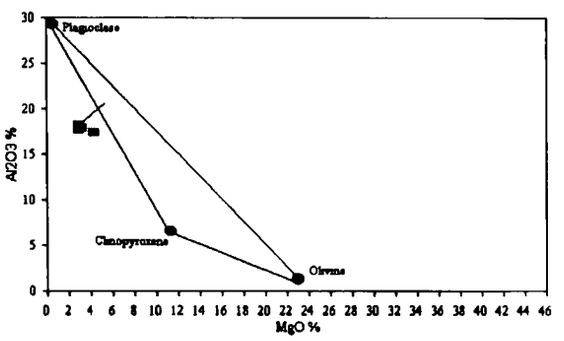

Figure 196

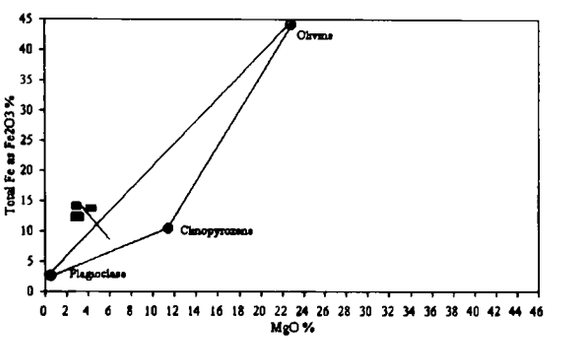

Figure 197

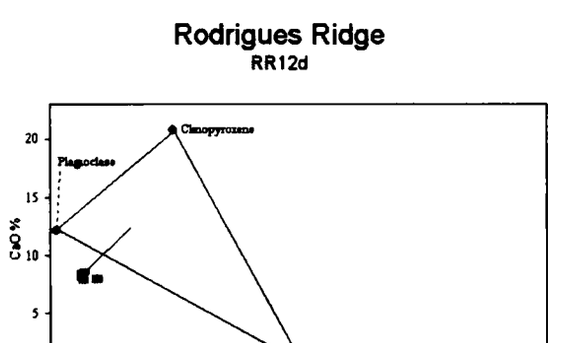

Figure 198

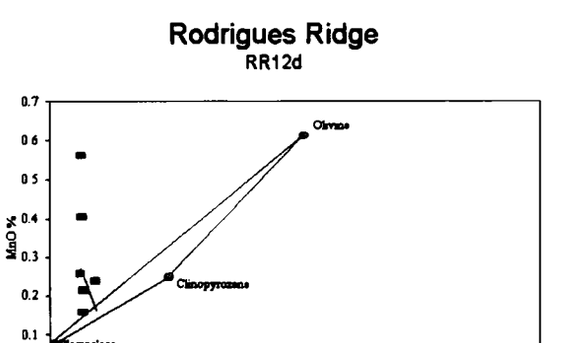

Figure 199

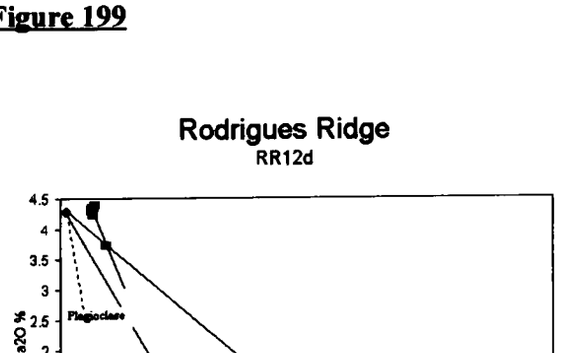

Figure 200

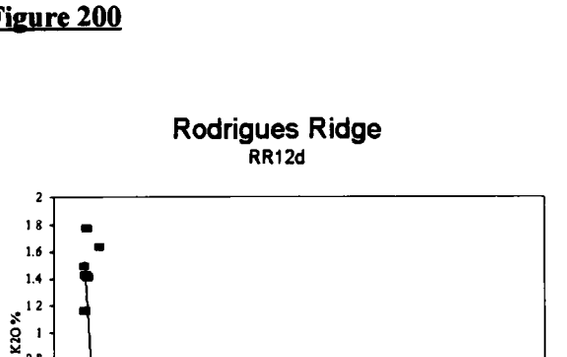

Variation Diagrams for RR12d

Figure 201

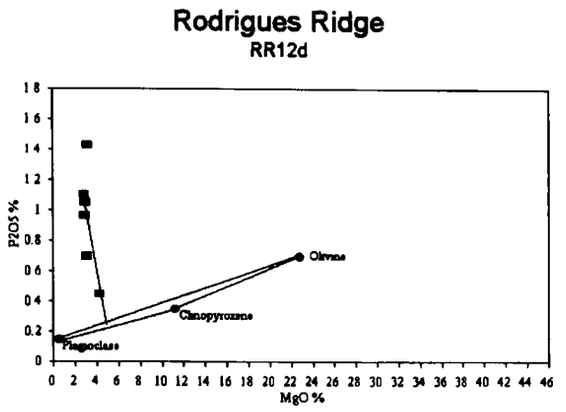

Figure 202

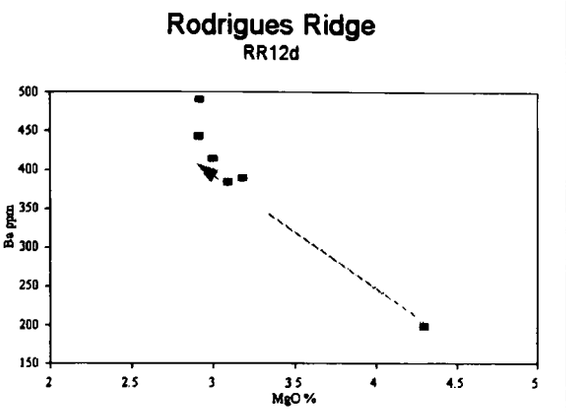

Figure 203

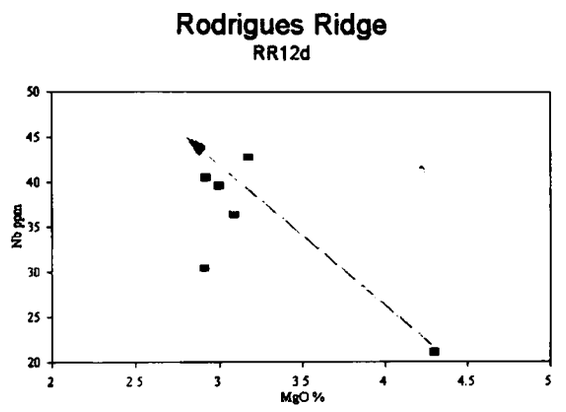

Figure 204

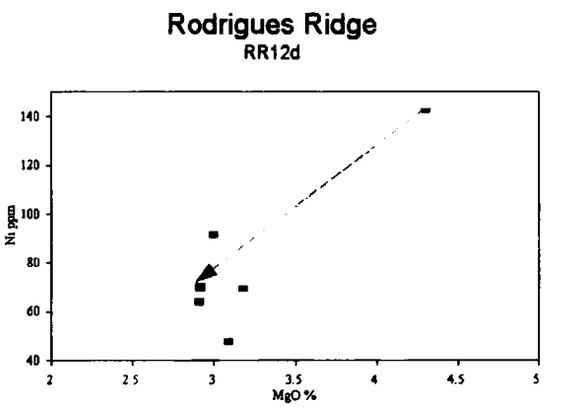

Figure 205

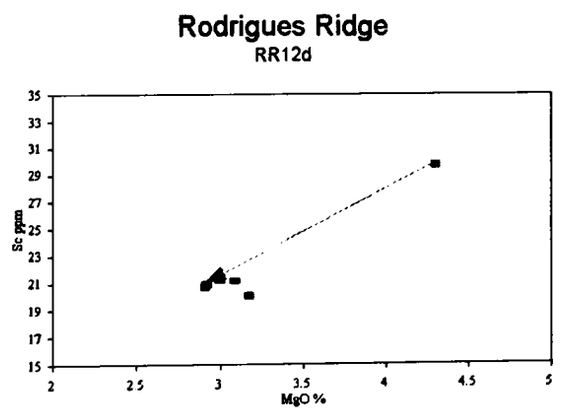

Figure 206

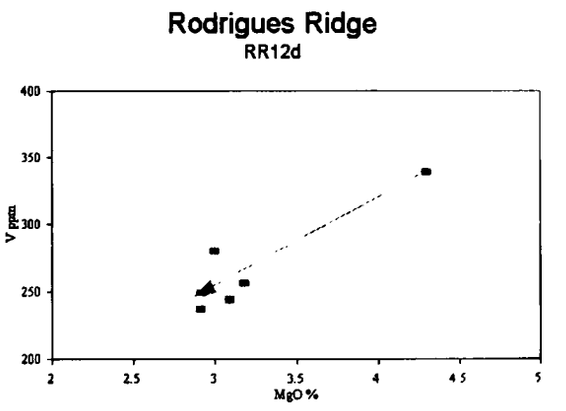

Variation Diagrams for RR12d

Figure 207

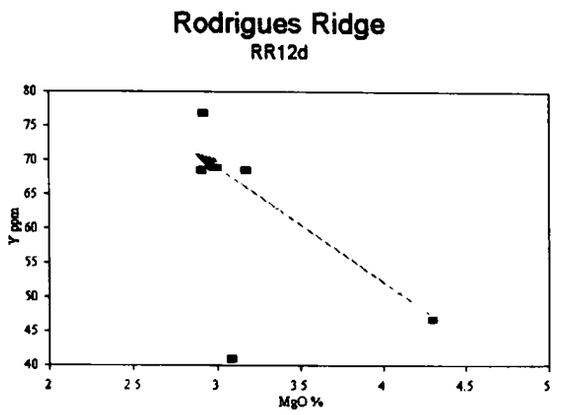

Figure 208

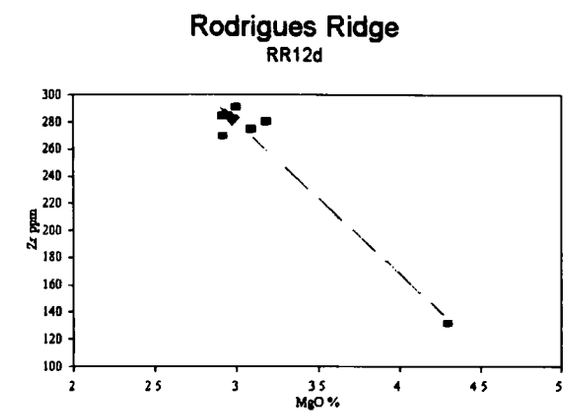

Figure 209

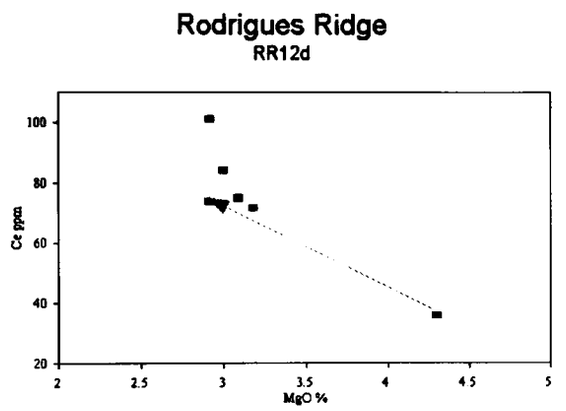

Figure 210

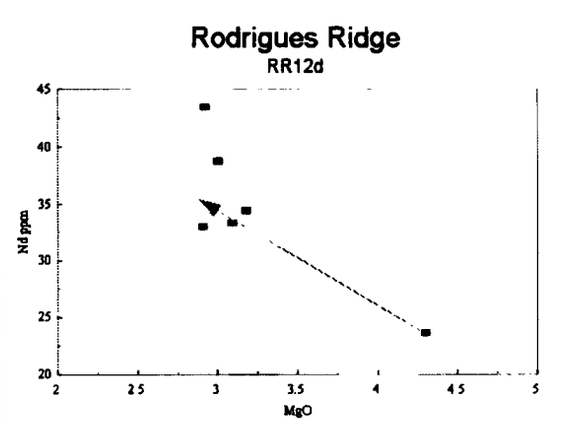

Figure 211

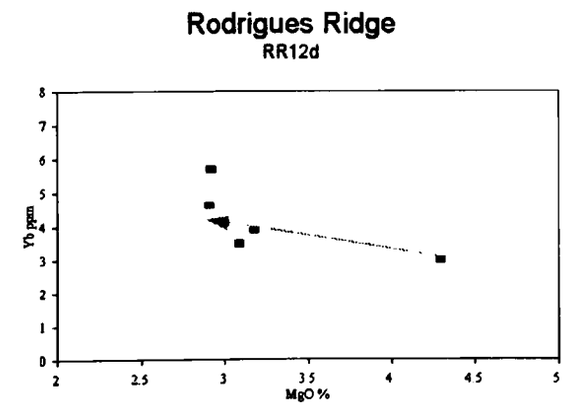

Figure 212

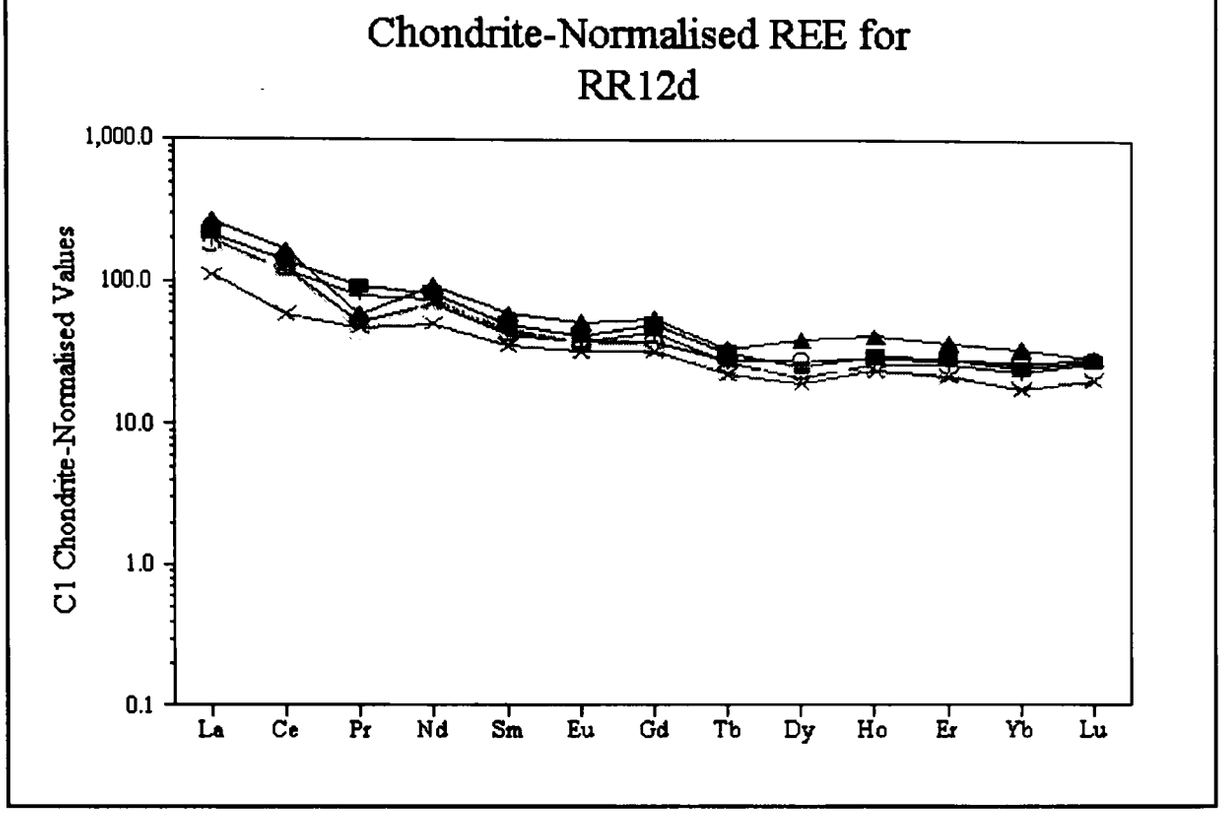

Chondrite values from Sun & McDonough (1989)

4.6 The C-M-A-S Quaternary System

One of the primary difficulties in handling a natural multi-component system such as the basaltic system is relating experimental data from much simpler chemical analogues and visually imaging the data in a way which can be readily interpreted. In 1968 O'Hara devised the C.M.A.S ternary system for displaying phase relationships in a suite of lavas. In this ternary system (molecular proportions);

$C = 56.08(CaO - 3⅓\ P_2O_5 + 2Na_2O + 2K_2O)$

$M = 40.31(FeO + MnO + NiO + MgO - TiO_2)$

$A = 101.96(Al_2O_3 + Cr_2O_3 + Fe_2O_3 + Na_2O + K_2O + TiO_2)$

$S = 60.09(SiO_2 - 2Na_2O - 2K_2O)$

Whole rock analyses and mineral compositions can be expressed in terms of these four components and plotted, along with phase boundaries, in the volume described by the tetrahedron. In interpreting triangular diagrams (two dimensional expressions of this three dimensional system) it is important to bear in mind; (1). The possibility that the data may plot above, below or on the plane being viewed,

(2). the possibility that the data may be distorted by the angle from which it is viewed, this causes spurious trends such as the trend towards MS (enstatite) on the plane CS-MS-A when viewed from M_2S (forsterite). (3). Increasing the (Na + K)/Ca ratio results in the projection scheme breaking down, hence evolved compositions should be avoided. When selecting which projection to use, it is best to use the primary crystallising phase to ensure correct reading of crystallisation sequences. The primary crystallising phase in the Rodrigues Ridge lavas is olivine (*i.e.* M_2S). The Rodrigues Ridge lavas are shown in figs. 213-215 using the M_2S (forsterite) projection on to the plane CS-MS-A, the CMS_2 (diopside) projection on to the plane C_3A-S-M and the MS (enstatite) projection on to the plane C_2S_3-A_2S_3-M_2S. Included on these diagrams are the 1 atmosphere and 10 Kb phase boundaries; additional phase boundaries can be found on figs. 216-218 (O'Hara 1968).

On the plane CS-MS-A (projection from olivine) (fig. 213), the lavas of RR2 plot along 1 atm plagioclase-clinopyroxene cotectic, whereas the majority of the remaining sites plot between this and the 10 Kb plagioclase-spinel-clinopyroxene cotectic. This suggests that they may have begun to fractionate at greater depths, where clinopyroxene was stable, before rising into the plagioclase stability field. It is notable that all the RR12d lavas plot on the 10 Kb plagioclase-clinopyroxene cotectic in a group distinct from the rest of the Rodrigues Ridge.

On the plane C_3A-S-M (projecting from diopside) (fig. 214) the entire Rodrigues Ridge lava suite plots in a narrow band close to the olivine-gabbro plane straddling the 1 atm, 5 Kb and 10 Kb cotectics in the fields of olivine and plagioclase ± spinel. These two projections suggest that the lavas have experienced some polybaric fractionation. Using the enstatite projection onto the plane C_2S_3-A_2S_3-M_2S, separates further the I atm and 10 Kb phase boundaries. On this diagram, all the Rodrigues Ridge lavas plot in a tight group around the 10 Kb cotectics of olivine, plagioclase, clinopyroxene and spinel (fig. 215). Collectively the lavas plot either on the eutectic or they plot along a line from the plagioclase-clinopyroxene cotectic across the field of clinopyroxene into that of olivine. The mechanism controlling this trend is not clear.

RR3.1 and RR12d.8, the two samples noted for their unusual chemistry and behaviour inconsistent with their site, have been omitted from these diagrams. RR3.1 was taken from the half pillow recovered from site RR3. It has substantially high CaO (15.06 compared to 10.07-11.97) and has the lowest MgO value. It plots notably off the evolutionary path for SiO_2, Al_2O_3, Fe_2O_3, CaO, Na_2O, CO_2 (not shown), Sc and V (figs. 83, 85-86, 88-89, 97 and 99) and has substantially less normative olivine than the other RR3 samples (9.13% compared with 11.84-23.81%). RR12d.8 was known to have been affected by seawater alteration and was found to plot well outside the field described by the other Rodrigues Ridge lavas. Clearly both these samples are distinct from the others at their site; they were therefore omitted.

The more evolved lavas from RR12d plotted on the olivine-plagioclase-clinopyroxene cotectic at 10 Kb on all three diagrams presented, whereas plagioclase does not feature on the liquidus for most other samples. This reflects the greater importance of plagioclase in the thin sections from this site and its dominant role in the modelled fractionating assemblage (shown on the variation diagrams).

Figure 213

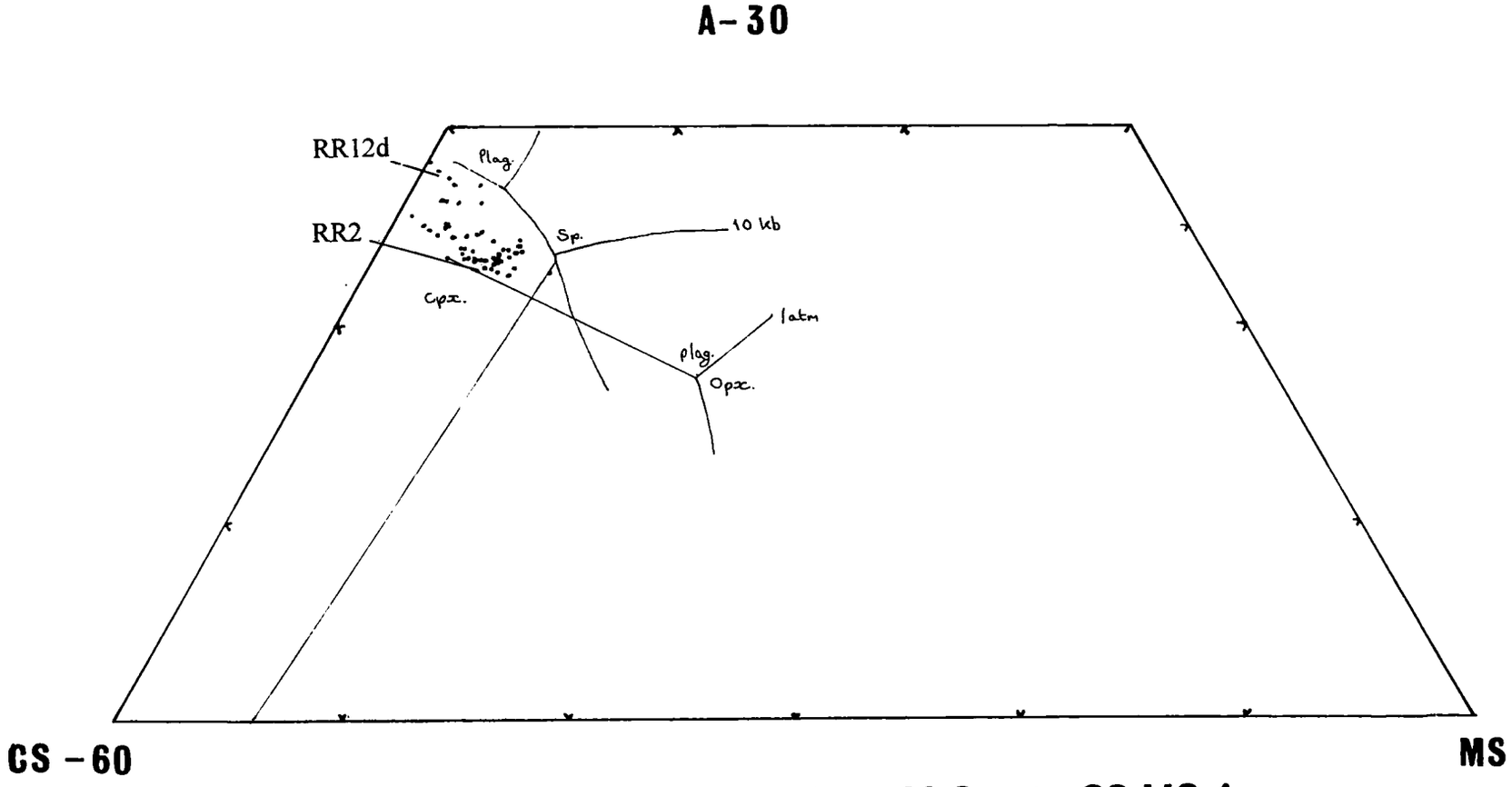

All Rodrigues Ridge samples from M_2S onto CS-MS-A

Figure 214

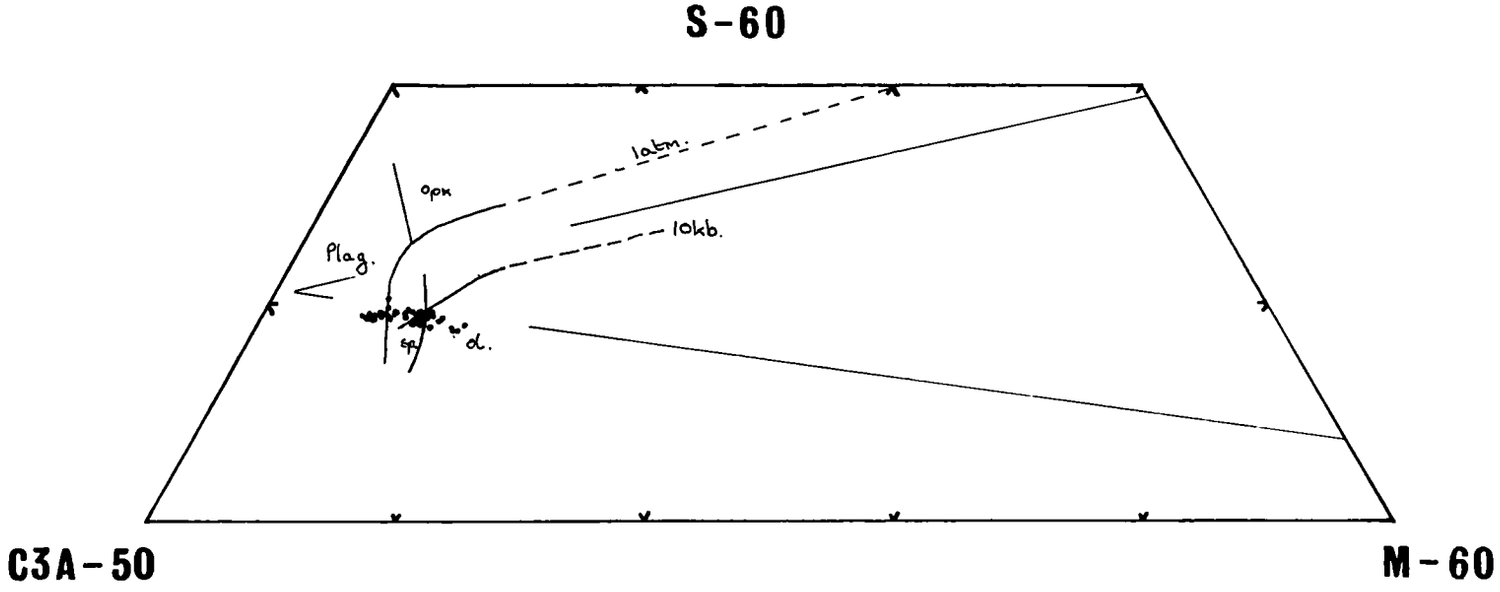

All Rodrigues Ridge samples from CMS_2 onto C_3A-S-M

A2S3 - 50

Figure 215

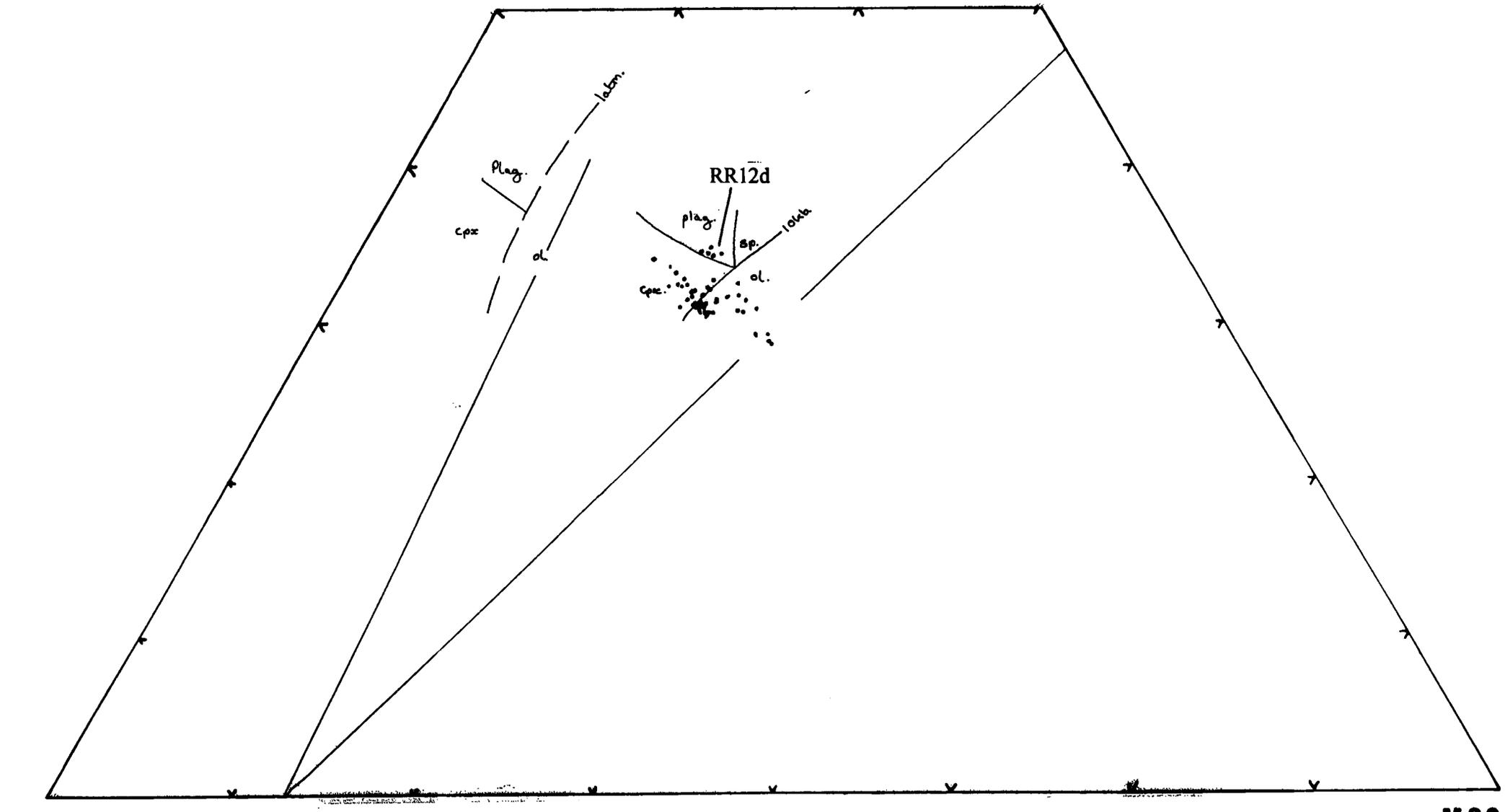

C2S3 - 80

M2S

All Rodrigues Ridge samples from MS onto C_2S_3-A_2S_3-M_2S

Figure 216

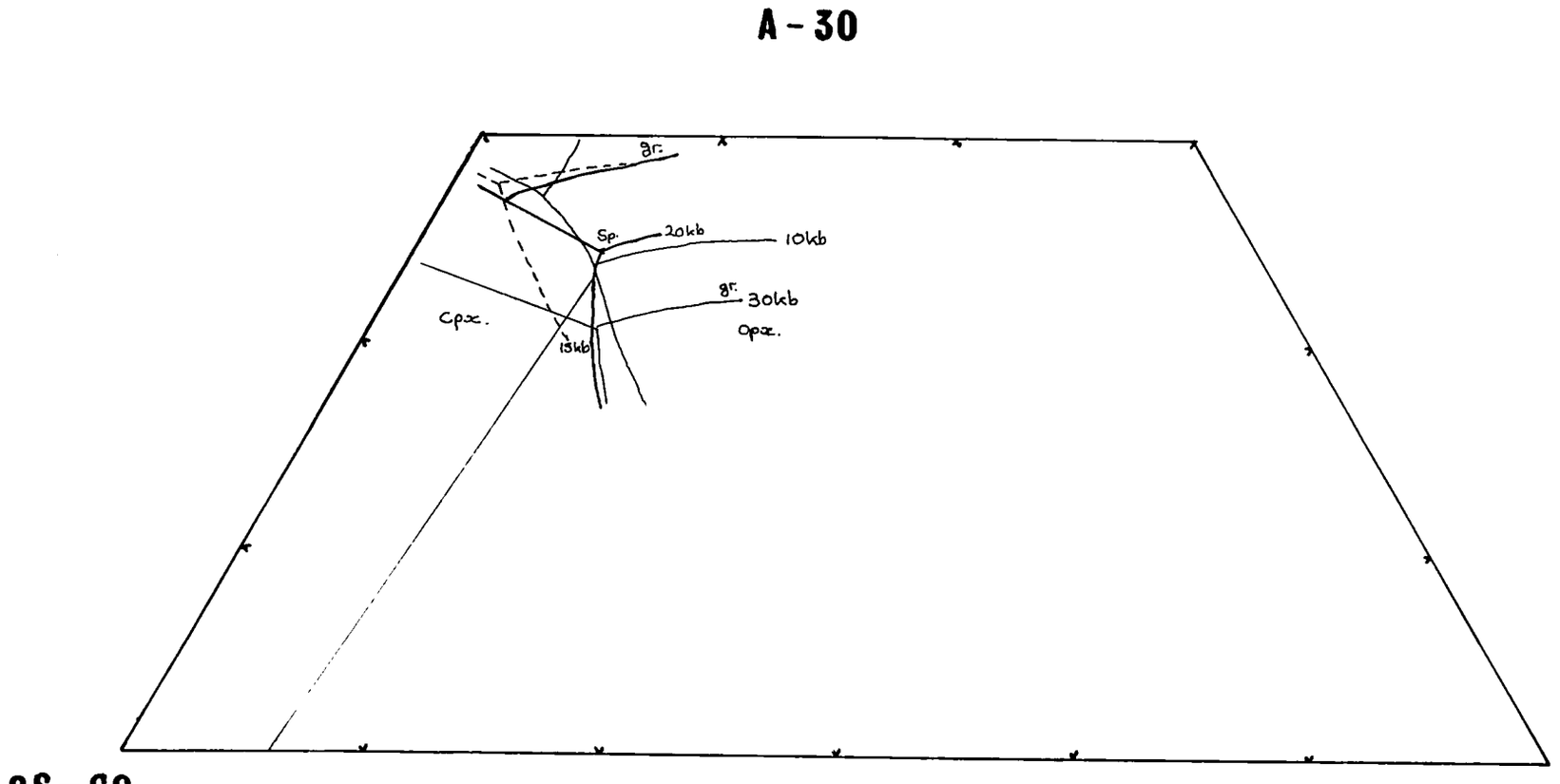

CS-MS-A viewed from M_2S Showing the Positions of the Phase Boundaries at 10Kb, 15Kb, 20Kb and 30Kb

Figure 217

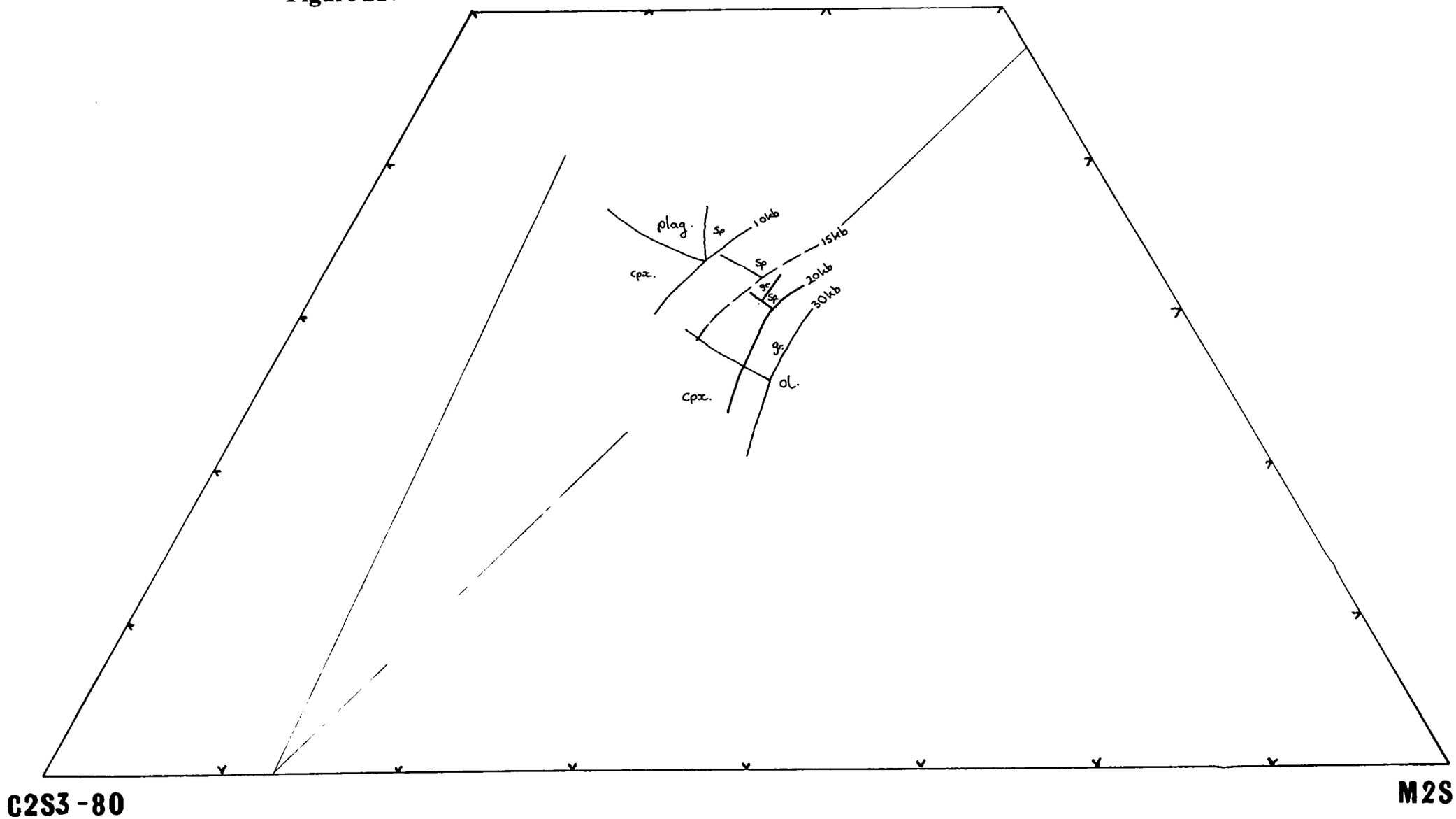

C_2S_3-A_2S_3-M_2S viewed from MS Showing the Positions of the Phase Boundaries at 10Kb, 15Kb, 20Kb and 30Kb

Figure 218

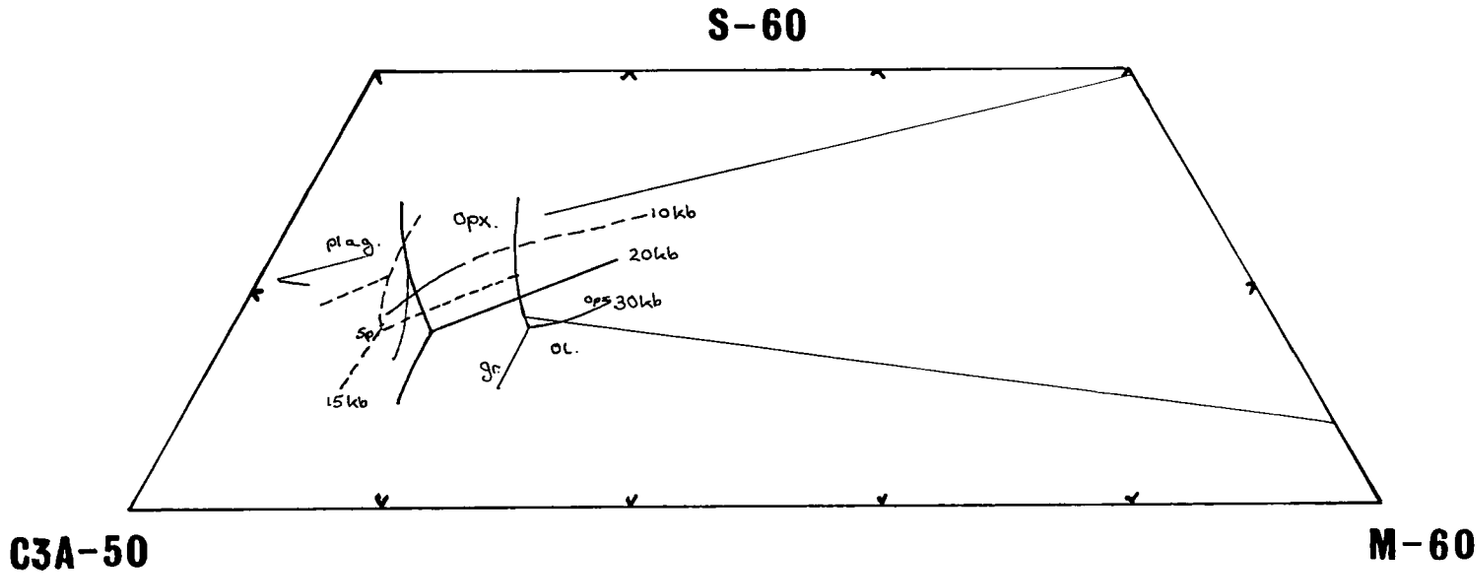

C_3A-S-M viewed from CMS_2 Showing the Positions of the Phase Boundaries at 10Kb, 15Kb, 20Kb and 30Kb

4.7 Discussion

On the variation diagrams presented in this chapter, clear olivine-plagioclase controlled fractionation trends can be seen at sites RR2, RR3, RR4 and RR8, while RR12d with its limited range of MgO shows evidence of olivine, plagioclase and clinopyroxene fractionation. At RR9c, olivine alone seems to be controlling the evolution of the lavas. At RR9c, the modelled fractionation is able to reproduce the observed trends well, whereas at the other sites, notably RR3, the model trends often seem to show a mismatch with the observed trends. At some sites, models involving clinopyroxene produce better matches with the data (see appendix 5), although this cannot explain the REE trends observed at RR3 and some other sites. On C-A-M-S plots (section 4.6) sites RR3-RR9 all plot between the 1 atm and 10 Kb cotectic on the plane CS-MS-A (projection from olivine), whereas RR2 plots close to the 1 atm cotectic and RR12d close to the 10 Kb cotectic. On the plane C_3A-S-M (projecting from diopside) the entire suite straddles the 1 atm, 5 Kb and 10 Kb cotectics whereas on the plane C_2S_3-A_2S_3-M_2S (projection from enstatite) the sites all plot around the 10 Kb cotectic. This implies that the lavas have had a polybaric fractionation history, in which the final fractionating phases were olivine + plagioclase for RR2-RR8, olivine for RR9c and olivine + plagioclase + clinopyroxene for RR12d. Although the role clinopyroxene in the fractionation history of these lavas is uncertain, the C-A-M-S diagrams it imply that clinopyroxene may have been an important phase in the early part of the fractionation history of the lavas from all sites and not just RR12d. Unlike the lavas of Rodrigues Island, the Rodrigues Ridge lavas do not contain any xenocrysts or xenoliths to provide an insight in to the fractionating assemblage. However the observed phenocryst phases at some sites, such as RR9c, seem good candidates for the fractionating phases. The curious REE behaviour at RR3 and others may be reflecting processes which took place during the melting and early history of the melt and which has not been significantly overprinted by later events. The history of these lavas may be summarised as follows:

1. Melting in the upper mantle within the field Ol + En + Di + Sp, but constrained by the phase boundary Ol - En - Di - Sp - melt ⇌ Ol - En - Sp - melt (Dick & Bullen 1984). *ie...* diopside remains in the residue after melting.
2. Polybaric fractionation between 10 Kb and 1 atm involving olivine, spinel, (clinopyroxene), and plagioclase.
3. Eruption on to sea floor.

Along-Ridge Variation

The incompatible elements increase from east to west. Distinct increasing trends can be observed for K_2O, Ba, Nb, Rb, Sr, Th, U, Zr and the REE, notably the LREE. This is exemplified by Zr at RR8

which is higher than at RR2, RR3 and at RR4, though not RR4.6. At RR9c Zr is slightly lower though the overall upward trend continues from RR10 to RR12d (fig. 219a). Coincident with this increase from east to west is the broadening of the ranges displayed at individual sites. Furthermore, when samples from the CIR, RR13 (old MORB), Réunion, Mauritius and Rodrigues Island are included, the general trend remains (fig.219b), although it is more diffuse. Rodrigues Island and RR13 are the two sites which deviate the most from the trend. RR13 is old (48 my), altered ocean crust, thrust up on to

Figure 219a

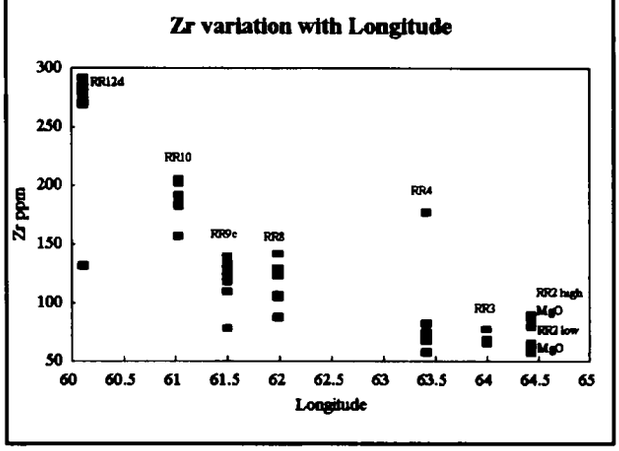

Figure 219b

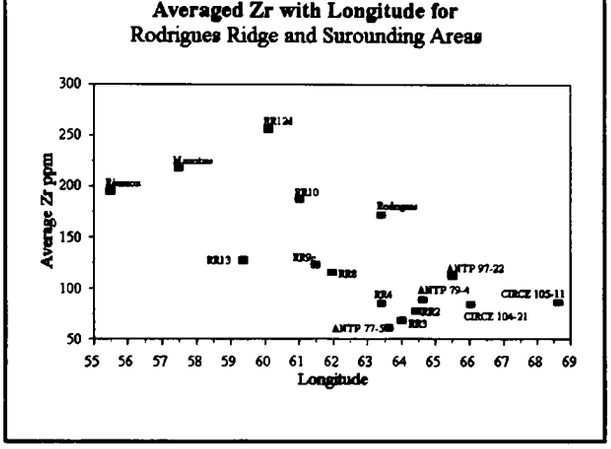

Sources of data: Rodrigues Island from Baxter *et al.* (1985); Mauritius from Baxter (1990); Réunion from Upton & Wadsworth (1972) and Fisk *et al.* (1988); CIR from Mahoney *et al.* (1989).

the Mascarene Plateau, and would more appropriately be plotted close to the CIR. But it now has more Zr than other CIR lavas, as a result of alteration (in this case the leaching out of mobile elements, concentrating the remaining immobile elements). Rodrigues Island is, as has been mentioned in ch.1, younger than the Rodrigues Ridge. Its lavas show enrichment in incompatible elements like Zr, typical of OIB, hence it would not be unreasonable to move it closer to the position of Mauritius and Réunion on this diagram. Also notable on fig. 219b is the very high absolute values for Zr at RR12d. This site has been subject to much greater degrees of fractionation than the other Rodrigues Ridge sites, reducing the concentration of the compatible elements like Ni (fig. 220), but enriching that of the incompatible elements like Zr.

The enrichment in REE, particularly the LREE, is highlighted by Ce in the range 24.23-34.92 ppm at RR9c compared with 14.24-42.11 ppm at RR8 and 6.16-12.61 ppm at RR2. Yb shows little change, from RR2 (2.04-3.70 ppm) to RR9c (2.04-2.80 ppm),

Figure 220

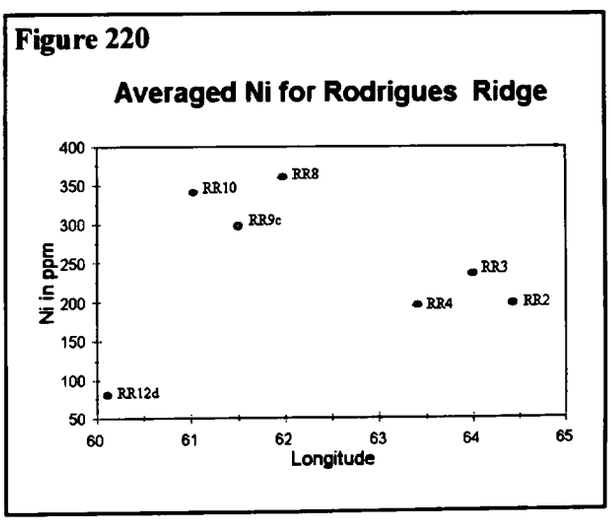

Figure 221

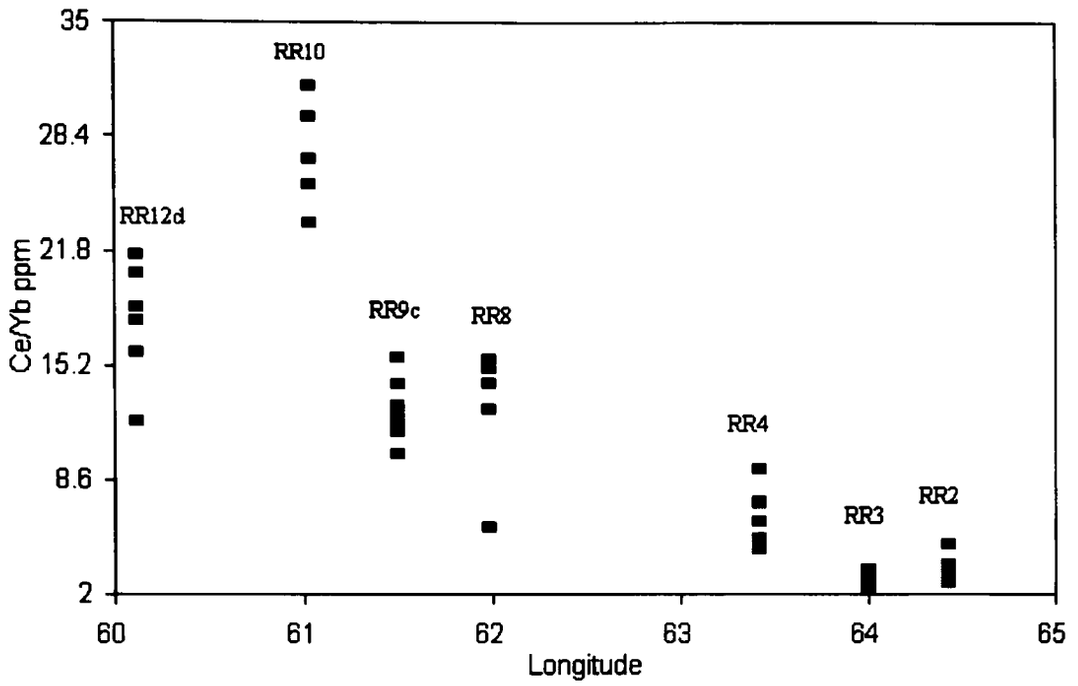

Figure 222a

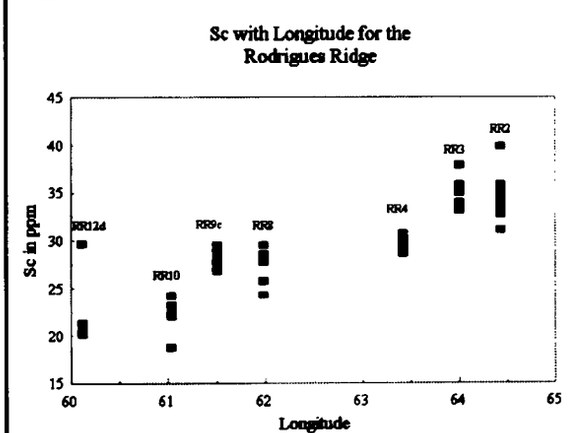

Figure 222b

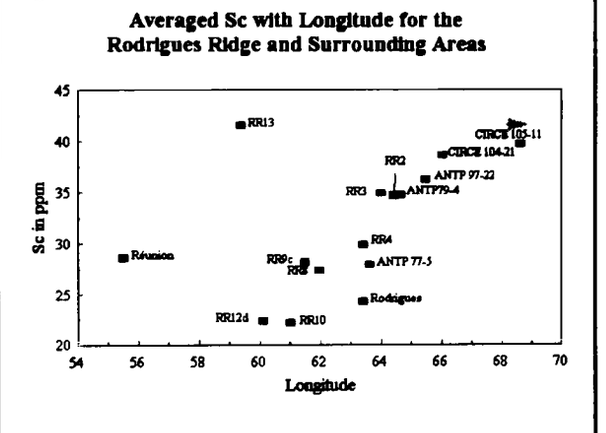

On Figure 222b arrow indicates where RR13 would have formed and hence where it would more appropriately be plotted.

---

despite (at least) a two fold increase in Ce (fig. 221). A systematic increasing trend was also observed for Ni (fig. 220), while Sc decreased from east to west (fig. 222a & b). The decline in Sc must either reflect a smaller amount of partial melting, or the increased role of garnet or/and clinopyroxene in the upper mantle, or a reduced partition coefficient for Sc in diopside at mantle temperatures and pressures. As has been discussed in chapter 3, the presence chrome spinels with Cr# <0.60 indicates that all the Rodrigues Ridge lavas fall into type 1 of Dick & Bullen (1984). This group are all of

oceanic origin, having formed on oceanic ridges where the degree of partial melting is restricted by the phase boundary Ol - En - Di - Sp ⇌ Ol - En - Sp (Dick & Bullen 1984). In short, diopside remains in the residue after melting for all type 1 lavas, including the Rodrigues Ridge sites. Irving (1978) suggests that, as temperature increases, the partition coefficient of Sc in diopside declines, although he does not give any information on the behaviour of Sc at mantle pressures. If, as suggested by these experiments, the partition coefficient of Sc in diopside is much reduced at upper mantle temperatures (and pressures), the observed behaviour may be controlled by another phase such as garnet. Both diopside and garnet partition Sc, but garnet will only be present at depths below 60-80 km (Ellam 1992). The contribution of some melt from depths where garnet is present, may also help explain the marked decline in Sc which has been observed. Close to the base of the crust, the upper mantle (in oceanic environments) tends to be depleted by repeated cycles of melting at mid-ocean ridge systems. At greater depths this is not the case, hence melt derived from lower in the mantle tends to be enriched in trace elements like Zr, Sc and LREE. HREE are strongly partitioned by garnet and thus remain low in melts where garnet is present in the residue.

The change in the chemistry from east to west can also be seen by comparing the primitive mantle-normalised trace element patterns and the chondrite-normalised REE for each site (figs. 51-52, 81-82, 53, 107, 54, 127, 55, 150, 56a & b, 172a & b, 57, 195, 58 & 212). On these diagrams the easterly sites RR2 and RR3 show LREE depleted patterns similar to those of N-type MORB. The westerly sites RR10 and RR12d show patterns similar to Réunion or typical OIB. Sites RR4 and RR8 are most like E-type MORB, while RR9c has an intermediate character between E-type MORB and OIB.

In addition to the trends described above, some elements show sharp increases or decreases at RR10 and/or RR12d *i.e.* TiO_2, CaO, Na_2O, Hf, Y and Zn. These two sites were also noted to display distinct differences in their mineralogy. RR10 showed significantly greater levels of alteration while RR12d was the only site where clinopyroxene microphenocrysts were observed. Both of these two sites showed significantly greater levels of vesiculation, indicating that, unlike the lavas from sites RR2-RR9c which were erupted at ocean floor depths, these lavas were erupted close to the sea surface.

Chapter 5

5. Radiogenic Isotopes

5.1 Introduction

In chapter 5, the radiogenic isotope ratios of Sr, Nd and Pb are examined for a selection of samples, for which the geochemistry is available, in order to characterise the isotope geochemistry for each site, and thus for the structure as a whole. The isotopic variation with longitude is considered before paired isotope plots are used to investigate the detail of the mantle source from which these rocks were derived, and to consider the relationship between the Rodrigues Ridge and other related features.

5.2 Isotope Geochemistry

Of the sixty two samples analysed for major, trace and rare earth elements, 21 basalts were selected to study the radiogenic isotopes of Sr, Pb and Nd. This group was made up of 5 samples from RR2, 3 from each of RR3 and RR12d, 2 from each of RR4, RR8 and RR10 and 4 from RR9c. All 21 samples were analysed for $^{87}Sr/^{86}Sr$, ten were analysed for $^{143}Nd/^{144}Nd$ and eight for $^{206}Pb/^{204}Pb$, $^{207}Pb/^{204}Pb$ and $^{208}Pb/^{204}Pb$. The principal criteria used when selecting the samples were their freshness and the amount of material available. To limit the effects of fractionation on the plots of radiogenic isotopes with trace element ratios, samples with around 8% MgO were selected. The small size of some samples from RR8 and RR3 meant that this was impossible at these sites. At RR12d, the limited range of MgO precluded the use of such magnesian samples. The two samples selected to study alteration (RR10.8 and RR12d.8) were analysed for $^{87}Sr/^{86}Sr$ as this ratio is sensitive to seawater alteration (White *et al.*, 1990).

The radiogenic isotopes were analysed at Royal Holloway and Bedford New College's isotope laboratory using a VG354 Mass Spectrometer. Details of the analytical techniques used are given in appendix 3. The results are given in table 24a. Also shown in table 24a are the isotopic data for dredged basalts from the CIR, site RR13 (old MORB) and the Marie Celeste F.Z. Table 24b shows averaged data for other Indian Ocean areas which may be relevant to the Rodrigues Ridge.

5.3 Variation in $^{87}Sr/^{86}Sr$

For the Rodrigues Ridge as a whole, $^{87}Sr/^{86}Sr$ is in the range 0.703419-0.703946, excluding RR10.8 and RR9c.11 (discussed below). The lowest $^{87}Sr/^{86}Sr$ ratio on the Rodrigues Ridge is found at RR3 in the east, from where there is a systematic increase westward to RR10. Dredged lavas from the west side of the Marie Celeste F.Z. and the CIR segment immediately due east of the Rodrigues Ridge both

Figure 223

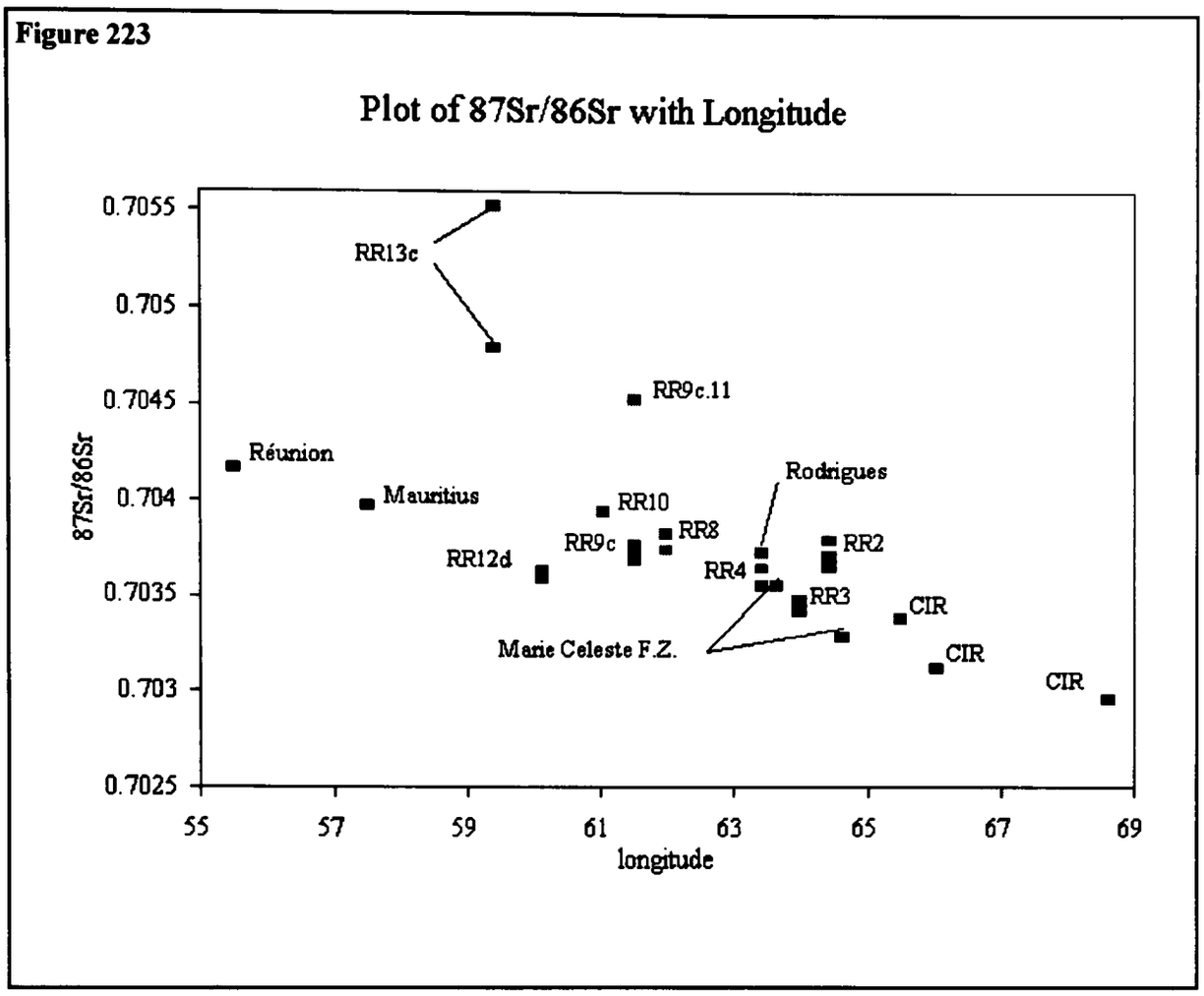

Sources of data: Réunion from Fisk *et al.* (1988), Rodrigues from Baxter *et al.* (1985), CIR, Mauritius and the Marie Celeste F.Z. from Mahoney *et al.* (1989).

show elevated levels of radiogenic Sr in the range 0.70266-0.70356 (Mahoney *et al.*, 1989). While higher than the rest of the CIR, these ratios are lower than for most sites on the Rodrigues Ridge except RR3, which overlaps their range. Mauritius, Rodrigues Island and Réunion have $^{87}Sr/^{86}Sr$ between 0.70369-0.70433, 0.703569-0.704057 and 0.70397-0.70436, respectively (Mahoney *et al.*, 1989, Baxter *et al.*, 1985 and Fisk *et al.*, 1988). In general, the Sr isotope ratios of these three islands are higher than those of the Rodrigues Ridge. Notably the values for Réunion are higher than any of the unaltered Rodrigues Ridge lavas. Fig. 223 shows the increase in $^{87}Sr/^{86}Sr$ with decreasing longitude along the Rodrigues Ridge. For reference, data for the three Mascarene Islands, site RR13, the west side of the Marie Celeste F.Z. and the CIR (due east of the Rodrigues Ridge) have also been included on this diagram. Only data from the west side of the Marie Celeste F.Z. have been used as $^{87}Sr/^{86}Sr$ ratios increase in both directions away from the active spreading ridge. This symmetry suggests that the melt source has changed over time. Using the data from the west only means that on the figure longitude can be related to distance from the spreading ridge or age of the basement. For simplicity, averaged data for Réunion, Mauritius and Rodrigues (given in table 24b) are used in this diagram. In

fig. 223, there is a clear linear progression of increasing $^{87}Sr/^{86}Sr$ from the CIR to Réunion along the Rodrigues Ridge. Two sites show slight deviation from this relationship; RR12d and RR2. RR12d plots lower that would be expected for its longitude whereas RR2 is slightly higher.

Alteration

To confirm that the whole suite of lavas was not affected by incipient alteration, samples were processed to extract plagioclase crystals. These were then analysed to ascertain their $^{87}Sr/^{86}Sr$ values. Unfortunately serious difficulties were encountered in separating the plagioclase from the matrix. Consequently only one sample RR2.2 yielded meaningful results. In this sample $^{87}Sr/^{86}Sr$ was 0.70366±5 while in the plagioclase it was 0.70358±2, a discrepancy only just above the analytical error. Very high Sr isotope ratios in oceanic environments, such as that shown by RR10.8 (0.707861±17), are generally the result of contamination by seawater, during alteration. Seawater has an $^{87}Sr/^{86}Sr$ ratio of 0.7092 (Faure, 1977, Cox *et al.*, 1987 and Rollinson, 1993) considerably higher than fresh basaltic rocks. It is therefore concluded that RR10.8 has been severely affected by seawater alteration, a conclusion consistent with the petrographic and geochemical observations and consequently this lava will not be considered further in this discussion. Sample RR12d.8, was also selected to study alteration, but does not show elevated Sr ratios (table 24a). This implies that the preparation techniques used to remove any contaminated material was successful (see appendix 3). RR9c.11 has also been excluded as this sample has $^{87}Sr/^{86}Sr = 0.704530$, which is considerably higher than the other RR9c samples ($^{87}Sr/^{86}Sr = 0.703689$-$0.703770$). RR9c.11 is anomalous in terms of both its major and trace element chemistry, (*e.g.* $SiO_2 = 44.00\%$, U = 1.37 ppm and V = 242.4 ppm compared to 46.36-48.35%, 0.29-0.49 ppm and 189.8-220.2 ppm for the remaining samples from site RR9c). The high $^{87}Sr/^{86}Sr$ data would suggest that this sample has suffered some seawater contamination but this was not evident from the petrography. Hence the only conclusion which can be reached is that this sample is anomalous and that more data is required in order to explain the reasons for this. Clearly the 48 my ocean floor samples from RR13 have been altered (fig. 223).

5.4 Variation in $^{143}Nd/^{144}Nd$

$^{143}Nd/^{144}Nd$ ratios for the Rodrigues Ridge lie in the range 0.512882-0.512952. The highest ratio was obtained from RR3 where the lowest levels of radiogenic Sr were observed. As with Sr, this value is closest to the range observed on the CIR (0.512925-0.513150) (Mahoney *et al.*, 1989). By comparison, the range of $^{143}Nd/^{144}Nd$ ratios for Rodrigues Island, Mauritius and Réunion are;- 0.512837-0.512886, 0.512850-0.512909 and 0.512823-0.512861 (Baxter *et al.*, 1985, Mahoney *et al.*, 1989 and Fisk *et al.*, 1988). Unlike Sr, Nd isotopic ratios are not significantly affected by seawater alteration (Cox *et al.*, 1987). There is a good correlation between longitude and $^{143}Nd/^{144}Nd$. The CIR (close to the Rodrigues

Table 24a **Isotope data for the Rodrigues Ridge and Related Localities**

Site	$^{87}Sr/^{86}Sr$	$^{143}Nd/^{144}Nd$	ϵ_{Nd}	$^{206}Pb/^{204}Pb$	$^{207}Pb/^{204}Pb$	$^{208}Pb/^{204}Pb$
Rodrigues Ridge						
RR2.2	0.703659±49	0.512939±5	5.87	18.684	15.611	38.705
RR2.3	0.703707±14					
RR2.4	0.703796±11	0.512913±4	5.36	18.720	15.586	38.728
RR2.9	0.703710±41	0.512935±5	5.79			
RR2.12b	0.703649±11	0.512927±5	5.64	19.020	15.620	39.091
RR3.1	0.703439±16					
RR3.2	0.703485±14	0.512952±4	6.13	18.471	15.556	38.382
RR3.3	0.703419±20					
RR4.1	0.703651±15	0.512919±5	5.48	18.724	15.566	38.820
RR4.12	0.703594±18					
RR8.2	0.703832±12	0.512882±5	4.76			
RR8.4	0.703747±16					
RR9c.11	0.704530±27					
RR9c.18	0.703735±14					
RR9c.36	0.703770±17	0.512907±4	5.25	18.605	15.590	38.745
RR9c.37	0.703689±13					
RR10.1	0.703946±11	0.512899±5	5.09	18.904	15.623	39.092
RR10.8	0.707861±17					
RR12d.2	0.703604±9					
RR12d.5	0.703637±15	0.512932±5	5.74			
RR12d.8	0.703598±15					
Old MORB						
RR13c.1	0.704795±13	0.512906±5	5.23	18.617	15.705	39.399
RR13c.2	0.705527±11					
Marie Celeste F.Z.						
ANTP 79-4	0.70329±3	0.513029±16	7.63			
ANTP 77-5	0.70356±3	0.512957±22	6.22	18.602	15.572	38.663
CIR						
ANTP 97-22	0.70338±3	0.513016±14	7.37	18.392	15.490	38.308
CIRCE 104-21	0.70312±3	0.513054±14	8.11	18.354	15.517	38.214
CIRCE 105-11	0.70296±3	0.513101±22	9.03			

Data for Marie Celeste F.Z. and CIR from Mahoney *et al.*, 1989

Figure 224

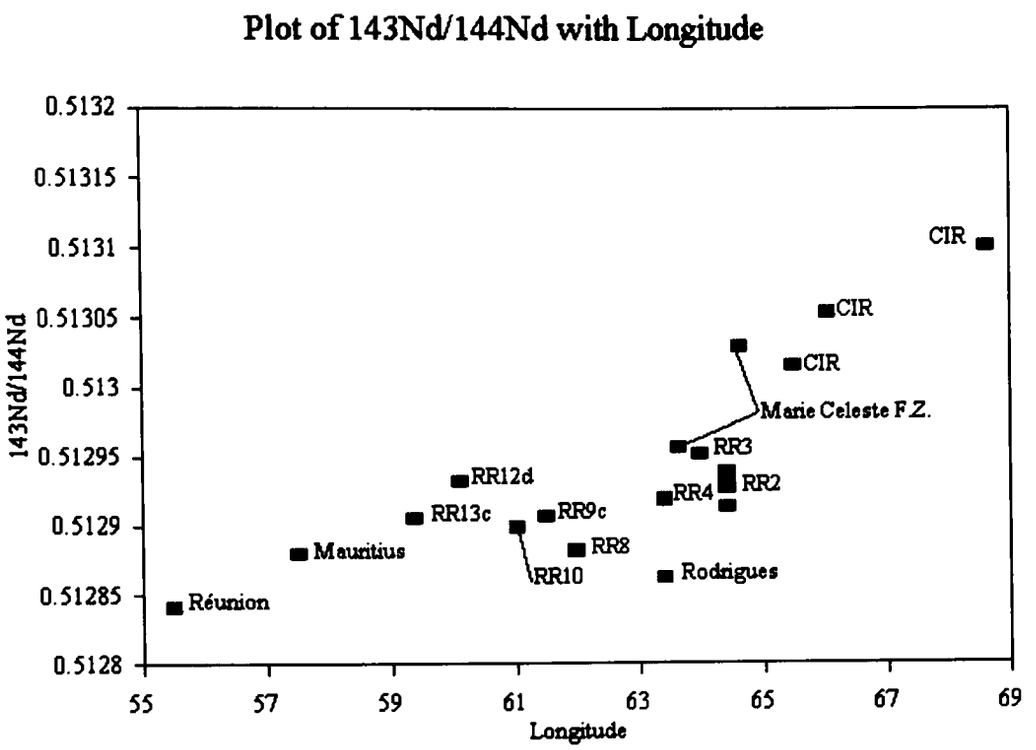

Figure 225

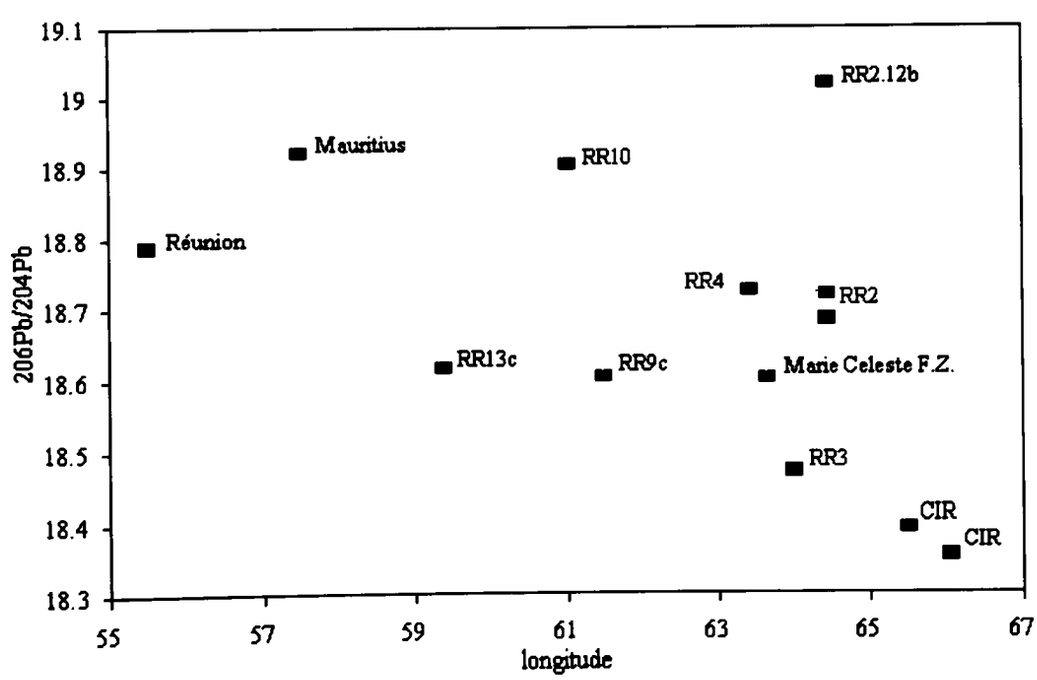

Sources of Nd data: Réunion Nd from Fisk *et al.* (1988), Pb from Oversby (1972); Rodrigues Nd from Baxter *et al.* (1985), Mauritius Pb from Peng & Mahoney (1995), Mauritius Nd, the CIR, and the Marie Celeste F.Z. from Mahoney *et al.* (1989).

Table 24b **Averaged Isotope data for the Réunion hotspot in order of site age.**

Site	$^{87}Sr/^{86}Sr$	$^{143}Nd/^{144}Nd$	ϵ_{Nd}	$^{206}Pb/^{204}Pb$	$^{207}Pb/^{204}Pb$	$^{208}Pb/^{204}Pb$
Rodrigues	0.70373	0.512862	4.37			
Réunion	0.70417	0.512841	3.96	18.788	15.585	38.849
Mauritius	0.70402	0.512877	4.65	18.922	15.602	38.979
Leg 115- 706	0.70370	0.512939	5.88	18.749	15.595	38.896
SM-1	0.70437	0.512936	5.80	18.760	15.588	38.792
Leg 115-713	0.70376	0.512971	6.50	18.608	15.569	38.645
Leg 115-715	0.70346	0.512989	6.84	18.496	15.543	38.388
Leg 115-707	0.70345	0.513006	7.17	18.668	15.576	38.596
Ambenali	0.70433	0.512856	2.97	17.977	15.440	38.270

Sources of data: Lead isotopes for the Ambenali Formation Lightfoot *et al.*, 1990, other Ambenali isotopes from Cox & Hawkesworth, 1985, Leg 115 and SM-1 isotopes White *et al.*, 1990, for Réunion Sr and Nd from Fisk *et al.*, 1988, and Pb from Oversby, 1972, for Mauritius Sr and Nd from Mahoney *et al.*, 1989, Pb from Peng & Mahoney, 1995, for Rodrigues Sr and Nd from Baxter *et al.*, 1985.

Ridge) forms one end of this trend while Réunion forms the other (fig. 224). As with $^{87}Sr/^{86}Sr$, (fig. 223) most Rodrigues Ridge sites plot off the overall trend. Similarly the $^{143}Nd/^{144}Nd$ ratios for Rodrigues Island plot off the CIR-Réunion trend.

5.5 Pb isotope ratios.

Pb isotope ratios for the Rodrigues Ridge, fall into the following ranges; $^{206}Pb/^{204}Pb$ 18.471-19.020, $^{207}Pb/^{204}Pb$ 15.556-15.623 and $^{208}Pb/^{204}Pb$ 38.382-39.092. The lowest value for all three isotopes of Pb was from site RR3. The highest values were obtained either from RR10 or from RR2.12b. As has already been observed the major and trace element characteristic of RR2.12b are anomalous (fig. 80). No Pb data are available for Rodrigues Island, but for Mauritius (Older Series) and Réunion $^{206}Pb/^{204}Pb$ are 18.888-18.956 and 18.654-19.000, $^{207}Pb/^{204}Pb$ are 15.600-15.603 and 15.532-15.645 and $^{208}Pb/^{204}Pb$ are 38.954-39.003 and 2.0520-2.0758 (Peng & Mahoney, 1995 and Oversby, 1972). The ranges given for Mauritius are based on only two samples. This limited data set is contained within the broad range described by the Rodrigues Ridge. Plots of the three isotopic ratios of Pb against longitude are given in figs. 225-227. Unlike Sr and Nd, any trend with longitude observed for Pb is somewhat scattered. Only

Figure 226

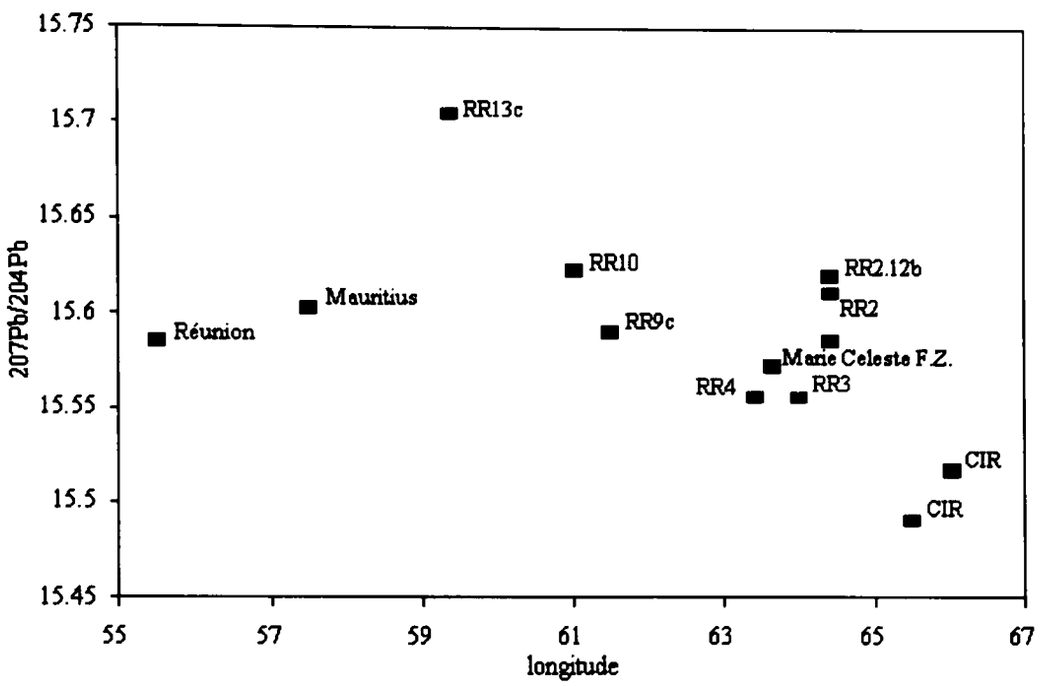

Figure 227

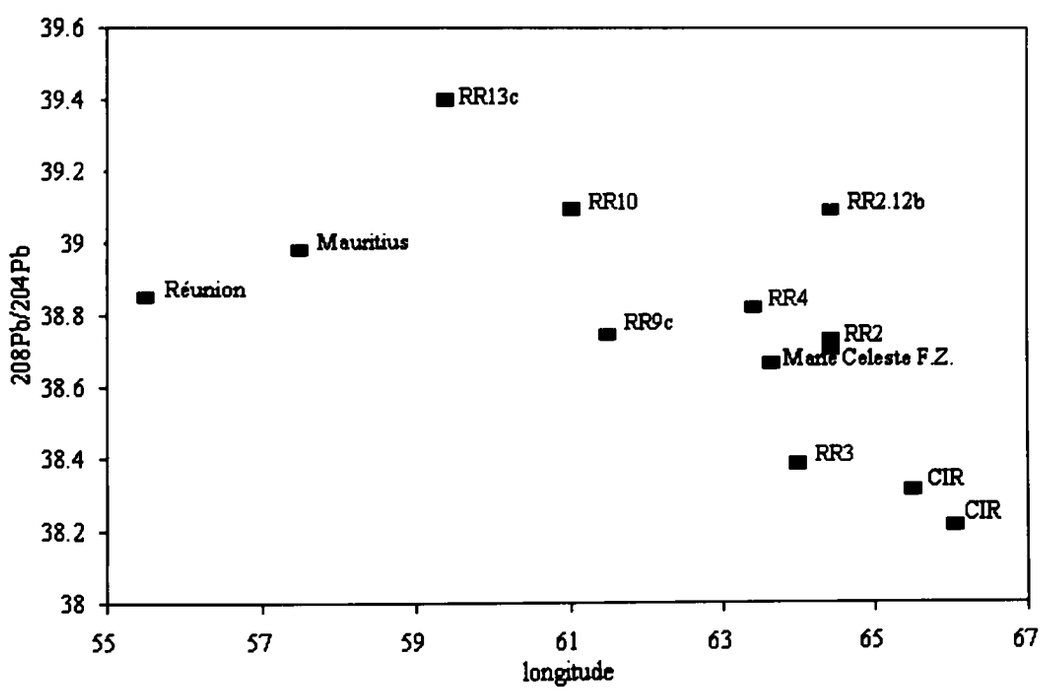

Sources of data: Réunion from Oversby (1972), Mauritius from Peng & Mahoney (1995) and the CIR and the Marie Celeste F.Z. from Mahoney *et al.* (1989).

$^{206}Pb/^{204}Pb$ (excluding RR2.12b) shows a broad, linear, increasing trend with decreasing longitude from the CIR to Réunion and Mauritius. The ratios $^{207}Pb/^{204}Pb$ and $^{208}Pb/^{204}Pb$ both show an increase with decreasing longitude, but are generally rather scattered (figs. 226-227).

When compared with Icelandic lavas, the Rodrigues Ridge lavas are enriched in $^{207}Pb/^{204}Pb$ but depleted in $^{206}Pb/^{204}Pb$ for a given $^{208}Pb/^{204}Pb$ value. For all Pb isotopes Iceland displays a much greater range of values typically spanning the full range of values displayed by the spreading ridges of the Indian Ocean and the oceanic islands of Mauritius and Réunion.

5.6 Radiogenic Isotopes - Discussion

Paired isotope plots for the Rodrigues Ridge and surrounding areas ($^{87}Sr/^{86}Sr$ with $^{206}Pb/^{204}Pb$, $^{207}Pb/^{204}Pb$ or $^{208}Pb/^{204}Pb$ or $^{143}Nd/^{144}Nd$, $^{143}Nd/^{144}Nd$ with $^{206}Pb/^{204}Pb$, $^{207}Pb/^{204}Pb$ or $^{208}Pb/^{204}Pb$ or $^{207}Pb/^{204}Pb$ or $^{208}Pb/^{204}Pb$ with $^{206}Pb/^{204}Pb$), all show pronounced linear trends. For all the paired isotope plots (figs. 228-232) the CIR forms one end member, while the other end member is made up of a tight group comprising of Mauritius, Réunion and RR10 on all plots involving Sr or Nd ratios, or RR2.12b on plots of $^{207}/^{204}Pb$ or $^{208}Pb/^{204}Pb$ against $^{206}Pb/^{204}Pb$. On most of the paired isotope diagrams, RR2.12b plots on the trend described by the Rodrigues Ridge, Mascarene Islands, CIR and Marie Celeste F.Z. However, on plots of $^{87}Sr/^{86}Sr$ and $^{143}Nd/^{144}Nd$ against $^{206}Pb/^{204}Pb$ (figs. 231-232) this sample displays higher Nd and lower Sr ratios for a given value of $^{206}Pb/^{204}Pb$.

The data clearly implicates at least two mantle sources in the formation of the Rodrigues Ridge lava suite, with progressive along-ridge mixing between them. The position of the CIR and Marie Celeste F.Z. samples on all these plots clearly indicates that they are related to the Rodrigues Ridge. The CIR samples with their low $^{87}Sr/^{86}Sr$, high $^{143}Nd/^{144}Nd$ and low radiogenic Pb are representative of one end-member mantle source (MORB-type) while Mauritius and Réunion together represents the other end-member (OIB-type) in a mixing trend which has been sampled at different points along its length. Variable amounts of mixing of these sources could account for the progression both in the geochemistry and in the isotope ratios observed along the Rodrigues Ridge. Source mixing at depth is preferred to mixing of melts, as this would require a single large magma chamber which would be unlikely to produce a linear volcanic ridge made up of coalesced volcanic centres. Along axis melt migration from two distant sources would, as a consequence of the rheology of the melt and the linear form of the magma chamber, tend to produce an abrupt change in chemistry where the two melts met, rather than the observed gradual change (see Bloomer & Meyer, 1992 and Oldenburg *et al.*, 1989). Linear mixing cannot be ruled out as a coincident process, occurring along side source mixing over short (*circa* $\leq$ 50 km) distances less than or equal to the width of the structure. In such a model linear mixing would allow localised homogenisation while source mixing would produce the overall gradual change. The sampling density is such that this process cannot be quantified and further sampling would be required.

Figure 228

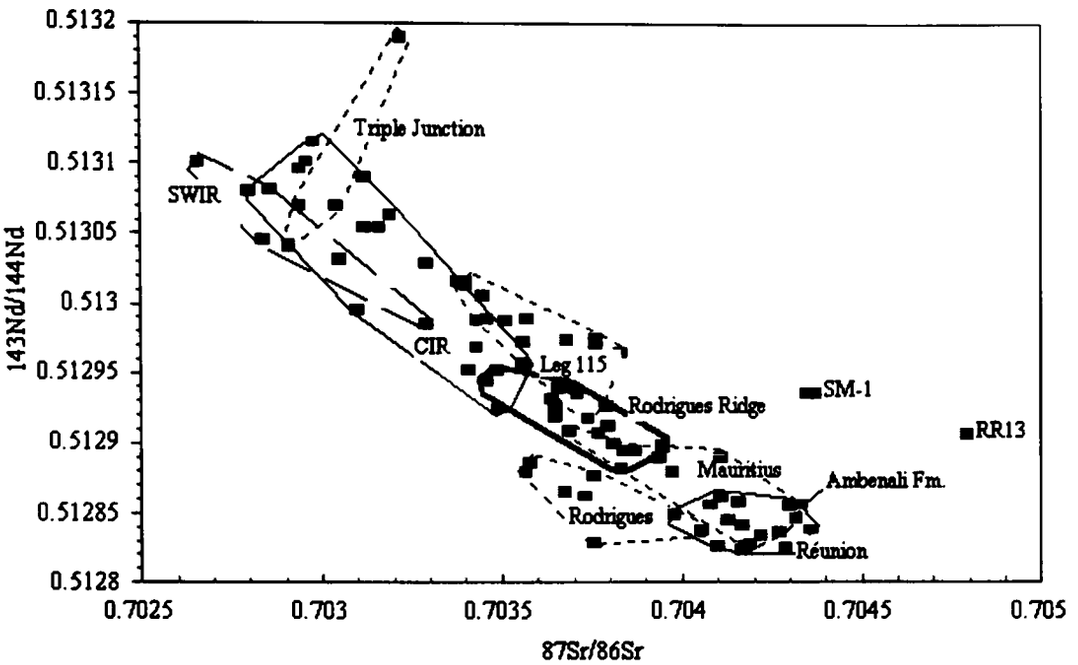

Figure 229

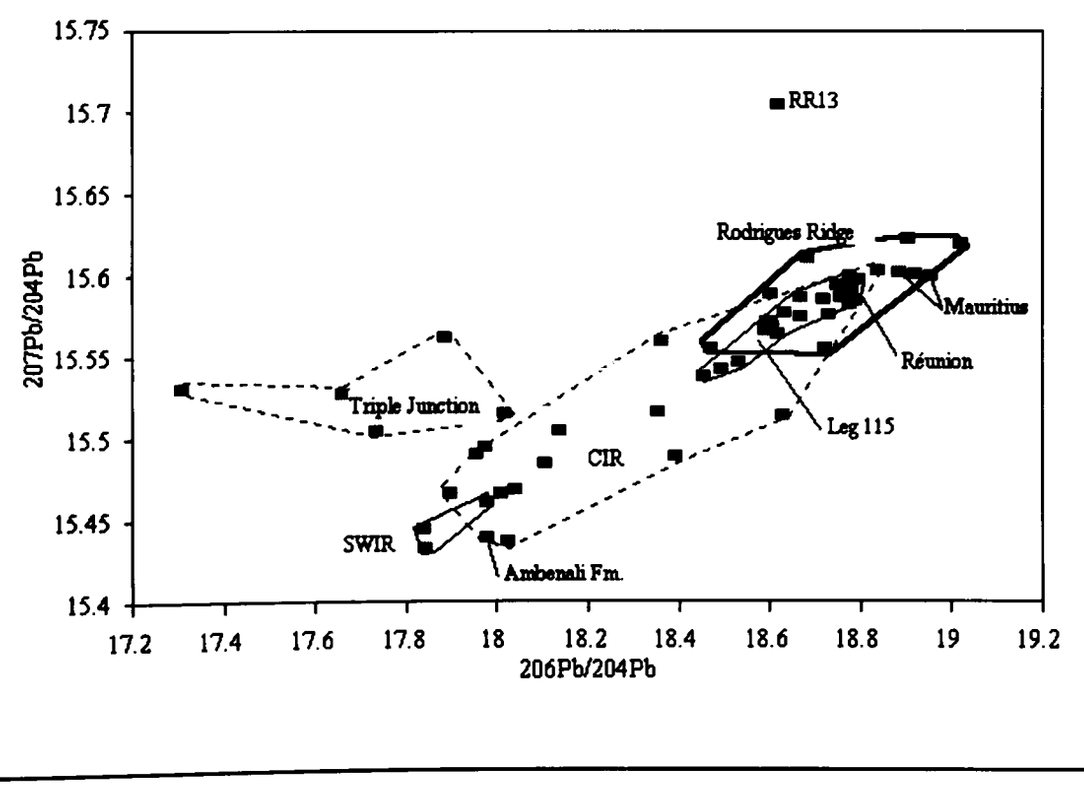

Sources of data: SWIR from Mahoney *et al.* (1989), Triple Junction from Price *et al.* (1986) all other data sources as in table 24b.

Figure 230

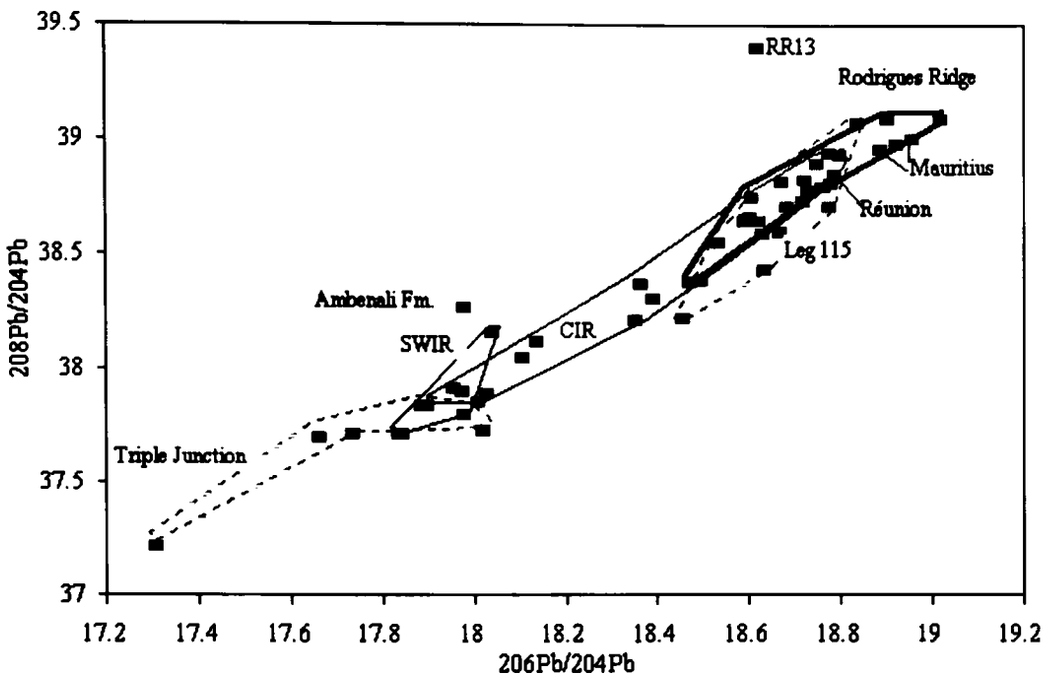

Figure 231a

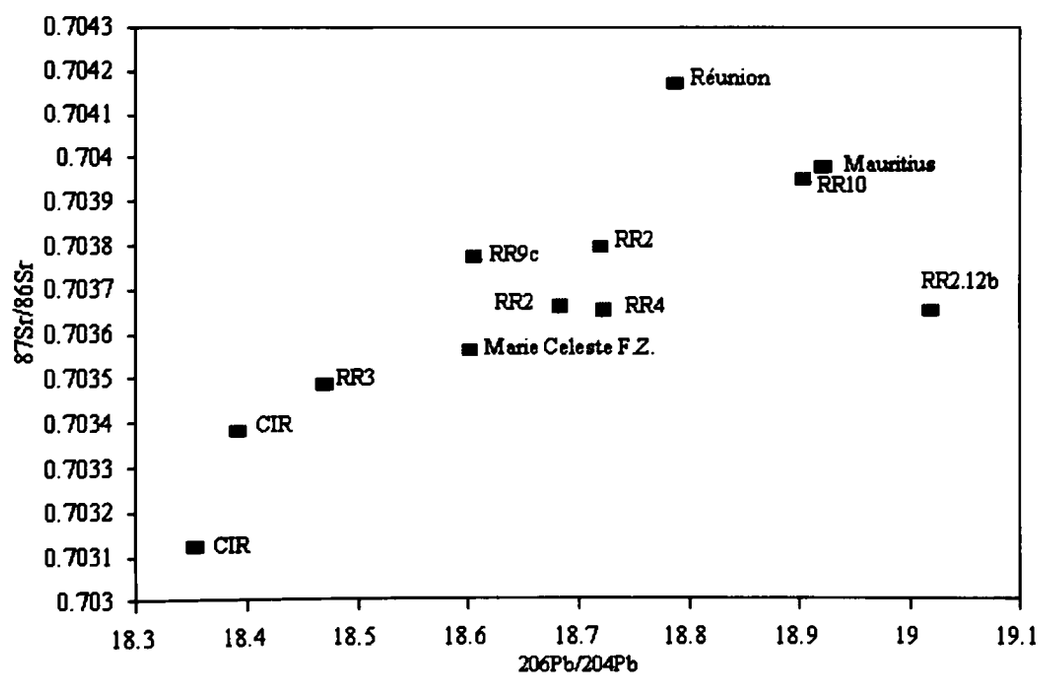

Sources of data: SWIR from Mahoney *et al.* (1989), Triple Junction from Price *et al.* (1986) all other data sources as in table 24b.

Figure 231b

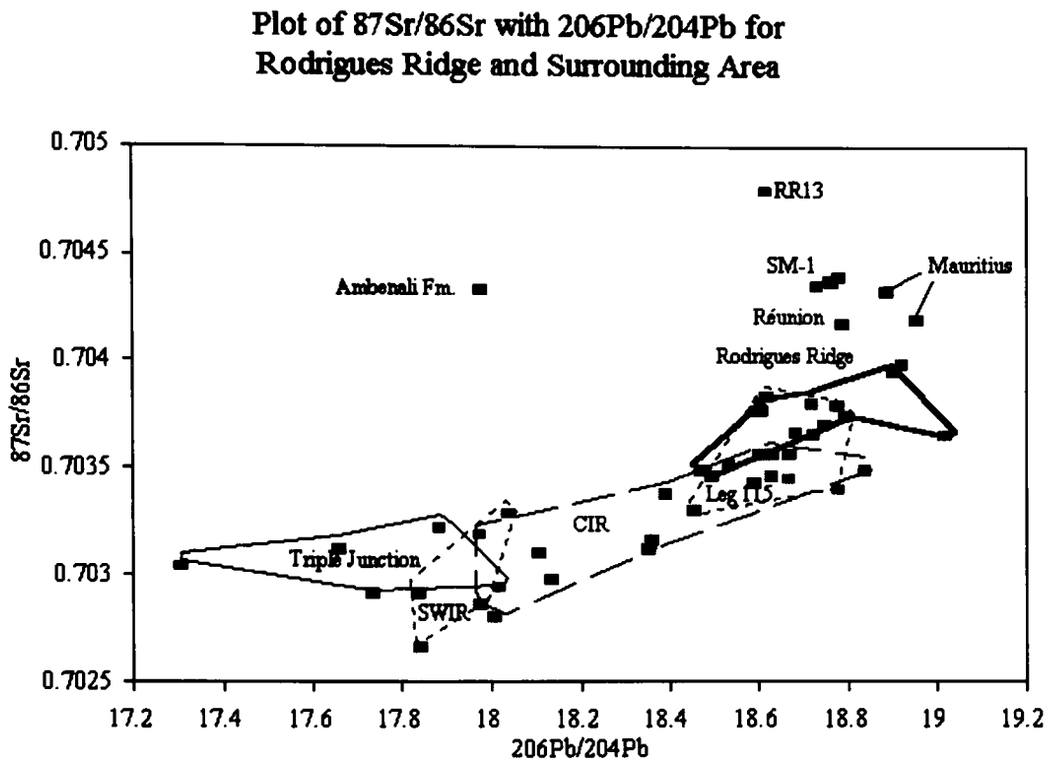

Figure 232a

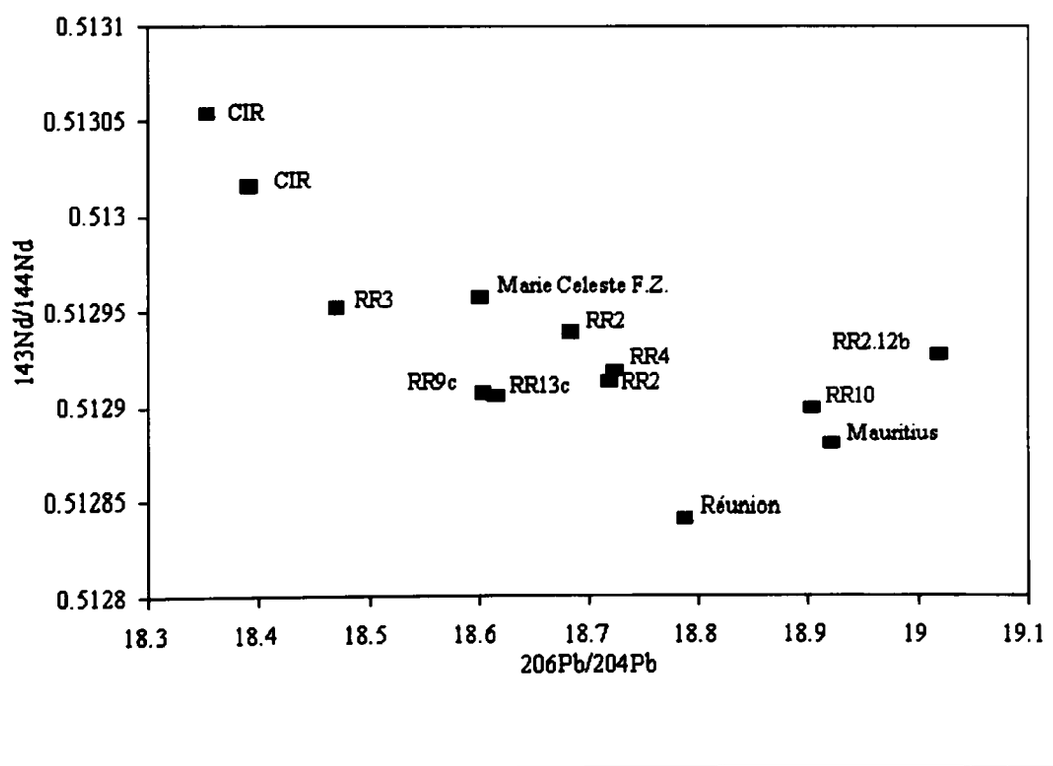

Sources of data: SWIR from Mahoney *et al.* (1989), Triple Junction from Price *et al.* (1986) all other data sources as in table 24b.

Figure 232b

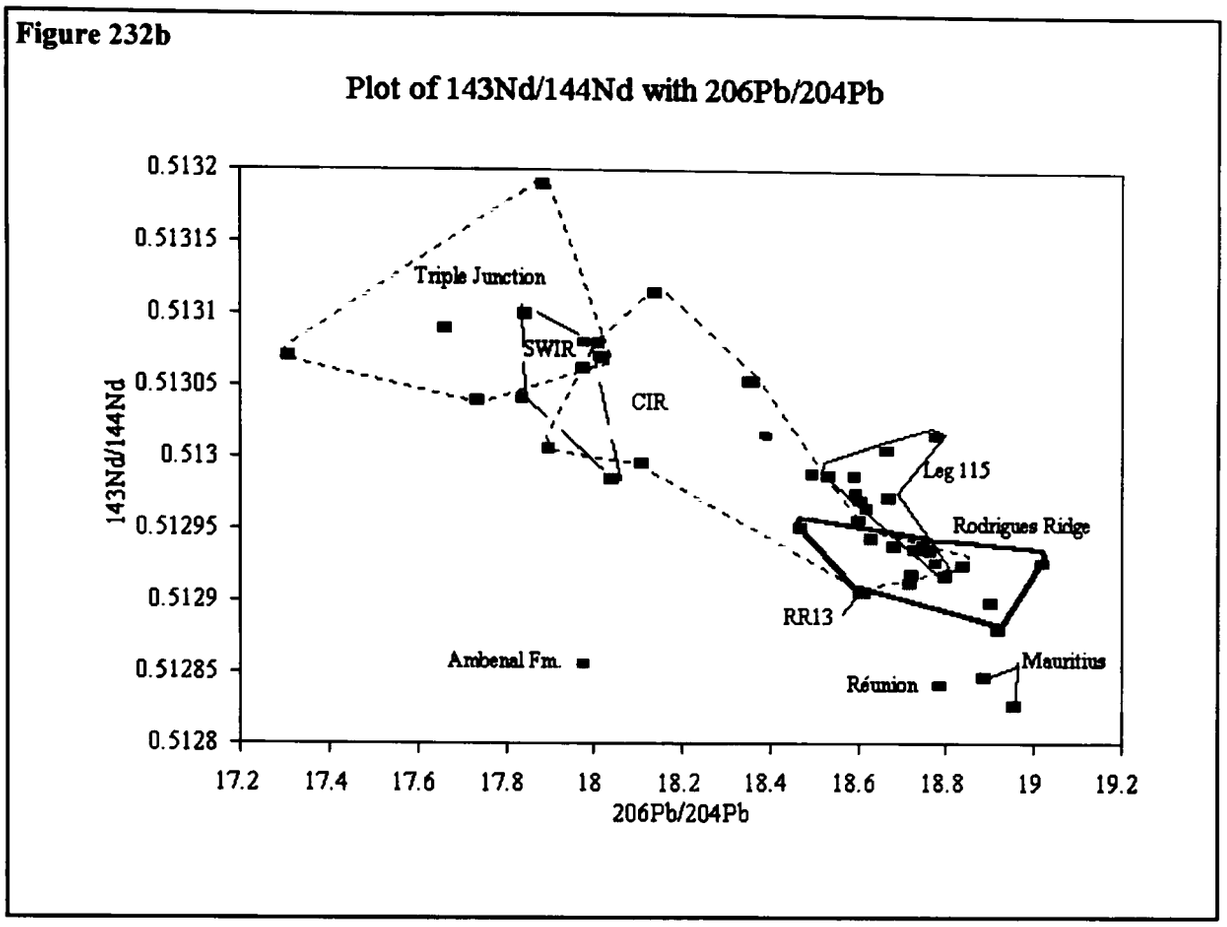

Sources of data: SWIR from Mahoney *et al.* (1989), Triple Junction from Price *et al.* (1986) all other data sources as in table 24b.

Ellam (1992) has suggested that the thickness of the oceanic lithosphere constrains the upper level at which melting may take place. As the lithosphere matures, the minimum depth at which melting can take place is driven down into the mantle, crossing from the stability fields of plagioclase and spinel into that of garnet. In this model the lithosphere thickens linearly to 80 km at an age of 50-70 Ma; about 80% of the thickness of mature oceanic lithosphere. After this the relationship breaks down and the lithosphere thickens more slowly to about 125 km. According to Ellam's model, the older the basement, the greater the minimum depth at which melting can take place. The transition between plagioclase and spinel lherzolite in the upper mantle is at 20-30 km and between spinel and garnet lherzolite at 60-80 km (Ellam, 1992). These different mantle mineralogies may leave a characteristic geochemical signatures on lavas derived from their partial melting. The Rodrigues Ridge should be an ideal area to test Ellam's model since all the lavas are of the same age, but the structure spans a region from close to the CIR (about 8 Ma) out to 33 my (Dyment 1999 pers. comm.) with increasingly thicker oceanic lithosphere. This should drive the upper limit of the melting zone down from the plagioclase stability field, through that of spinel towards that of garnet. Garnet will retain the HREE and Y, which are compatible in it, and hence the LREE will become increasingly enriched relative to the HREE in melts derived exclusively from deeper levels. Thus the ratio Ce/Y should increase linearly from east to

west, if garnet is present as a residual phase. Furthermore, shallow level mantle has probably been subject to one (or more) melting episodes on the ocean ridge which will cause it to be depleted in all the incompatible elements. The ratios $^{87}Sr/^{86}Sr$, $^{206}Pb/^{204}Pb$, $^{207}Pb/^{204}Pb$ and $^{208}Pb/^{204}Pb$ may also increase while $^{143}Nd/^{144}Nd$ decreases (figs. 233-234 and 223-227). This is a consequence of the greater contribution made by the partial melting of deeper (more fertile) mantle with a Réunion signature. Although the Rodrigues Ridge lavas broadly fulfil the above criteria, closer examination shows critical differences. (1) The radiogenic isotopes of Pb show only a weak correlation with longitude. (2) On plots of both $^{87}Sr/^{86}Sr$ and $^{143}Nd/^{144}Nd$ with longitude (figs. 223-224) some sites do not plot on the line described by the rest. (3) On the paired isotope plots, some sites do not plot in their geographic sequence between the CIR and Mauritius (figs. 236-238). (4) Several sites plot significantly off the trend described by the rest for Ce/Y (or Ce/Yb) with longitude (221 and 233). These discrepancies suggest that the model proposed by Ellam (1992) is an over-simplification of the processes that have been active during the formation of the Rodrigues Ridge. If, however, the lavas are variably sampling two sources; one deep (OIB-like) the other shallow (MORB-like), then slight perturbations could be superimposed on Ellam's model. Variable amounts of melting of the two sources could produce the effects seen and explain the anomalies. In the east, (sites RR2 and RR3) the lithosphere is thinner and hence the depleted MORB source may have provided a greater contribution to the melt. At RR2, however, greater amounts of deep melting may have also occurred giving the lavas a more enriched character than their neighbours at RR3. In the far west the source is principally the deeper enriched

Figure 233

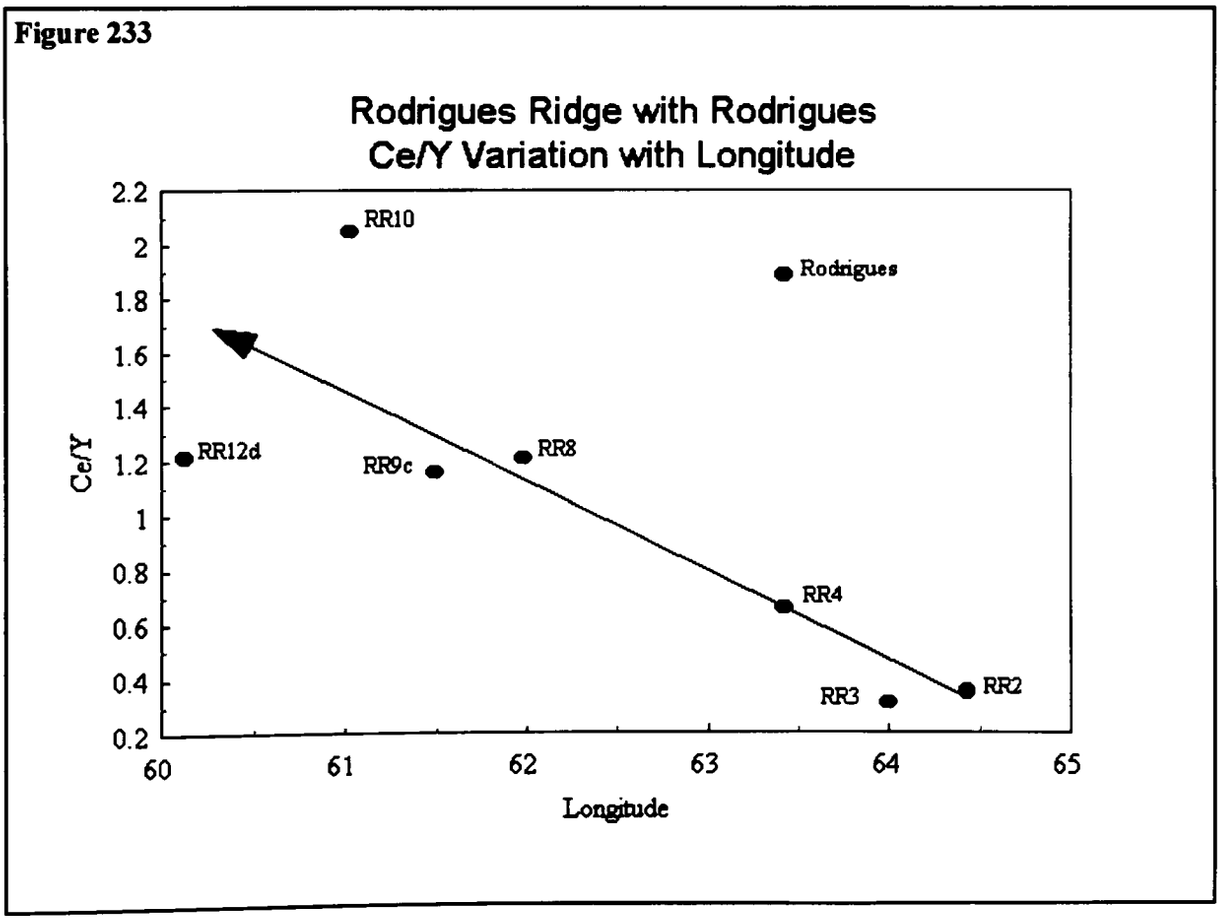

Figure 234

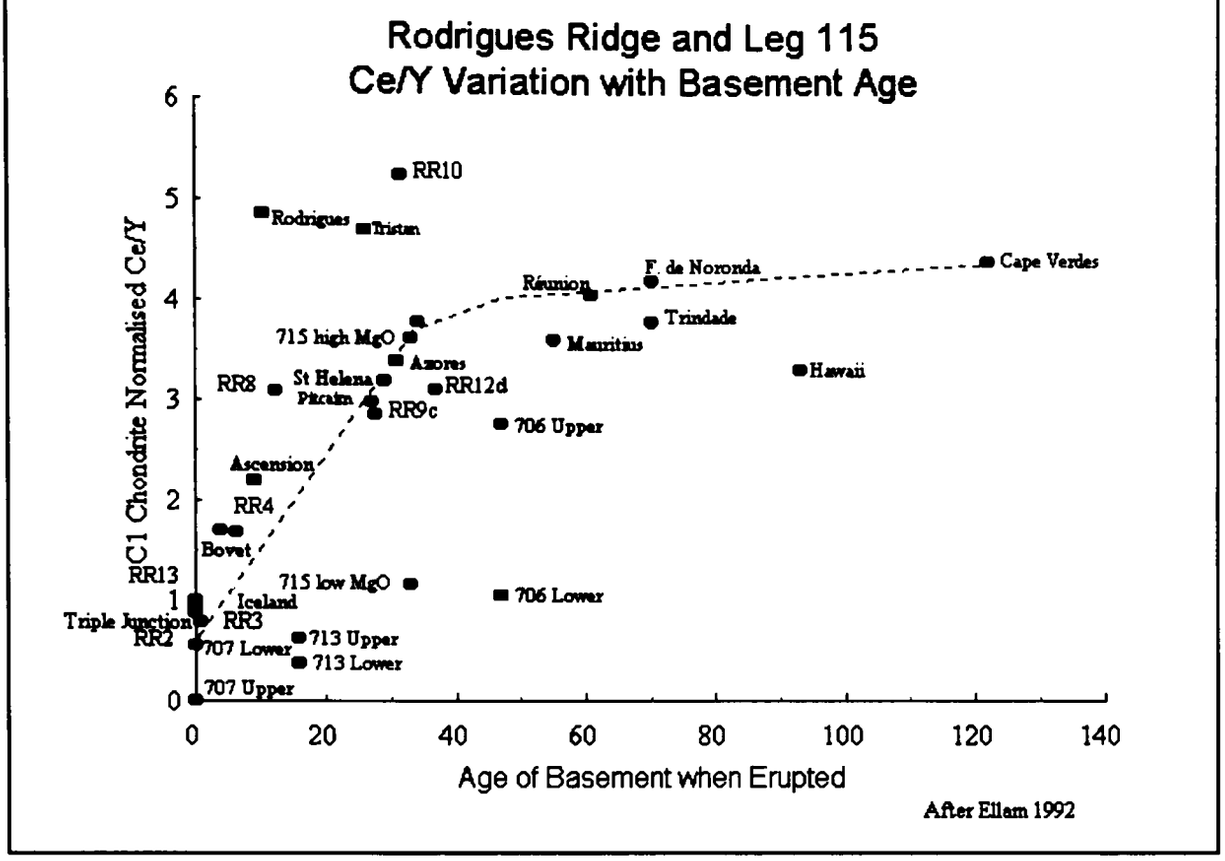

Sources: Rodrigues Island from Baxter *et al.*, 1985, Mauritius from Baxter 1990, Réunion from Fisk *et al*, 1988, Leg 115 from Backman *et al.*, 1988 all other islands from Ellam 1992.

mantle, *i.e.* a Réunion source, and hence the western lavas have a Réunion type character.

A number of oceanic mantle sources have been recognised, enriched mantle 1 (EMI), enriched mantle 2 (EMII), high in mantle uranium (HIMU), mid-ocean ridge (MORB), depleted mantle (DM) and prevalent mantle (PREMA) (Sun & McDonough, 1989, Rollinson, 1993). In addition to these, a mantle source similar to bulk silicate earth (BSE *i.e.*. bulk earth without the core) may also exist though no author has been able to confirm this (Rollinson, 1993). Rollinson presents plots of $^{143}Nd/^{144}Nd$ and $^{87}Sr/^{86}Sr$ against $^{206}Pb/^{204}Pb$ displaying the fields of these sources. On these diagrams (figs. 239-40) the Rodrigues Ridge suite plots close to the field of PREMA at the CIR end. The suite forms a trend between PREMA (and/or MORB) and a region between HIMU and EMII. This implies that as many three or even four mantle sources have combined to produce these lavas. Similar complexity in the origin of ocean island basalts was observed by Hoernle *et al.* (1991) among the post Miocene lavas of Grand Canaria. Stecher *et al.* (1999) have demonstrated that the lavas from Iceland (and other oceanic islands) display trends trailing away from a line between DMM (depleted MORB mantle) and HIMU, towards either EMI or EMII. While the Rodrigues Ridge lavas display similar behaviour, they seem to trail off towards a region to the HIMU side of EMII (figs. 239-240).

Unlike the Réunion hotspot trail, where there is a significant change in the age of the samples, the Rodrigues Ridge is all about the same age (table 1), yet it displays significant isotopic variation.

Figure 235

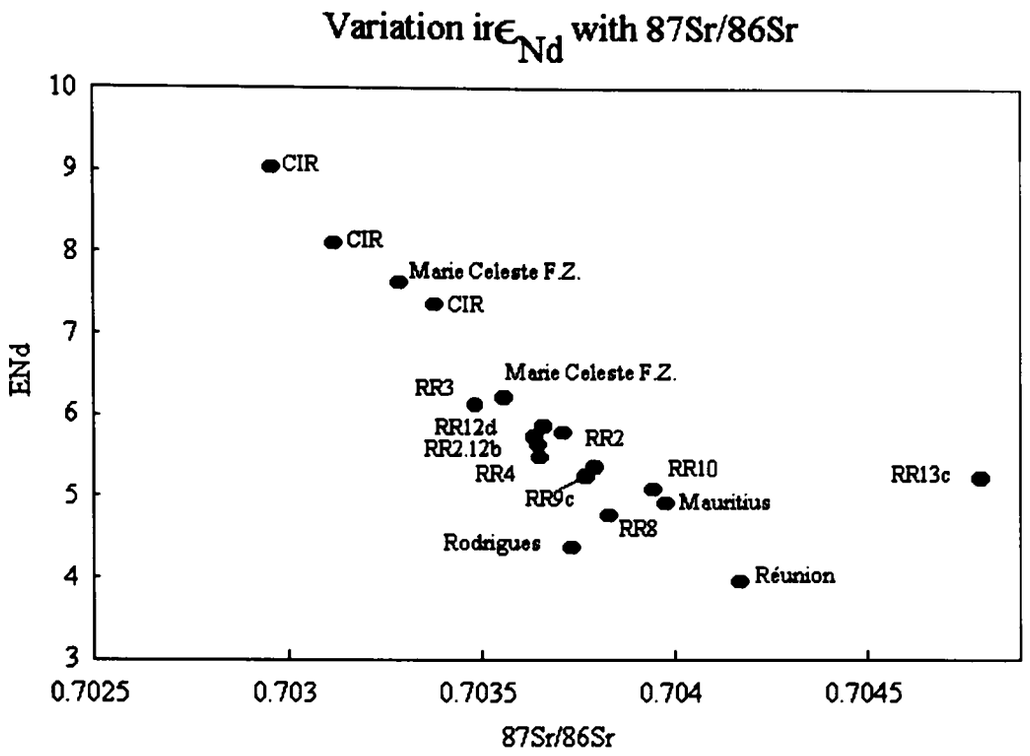

Figure 236

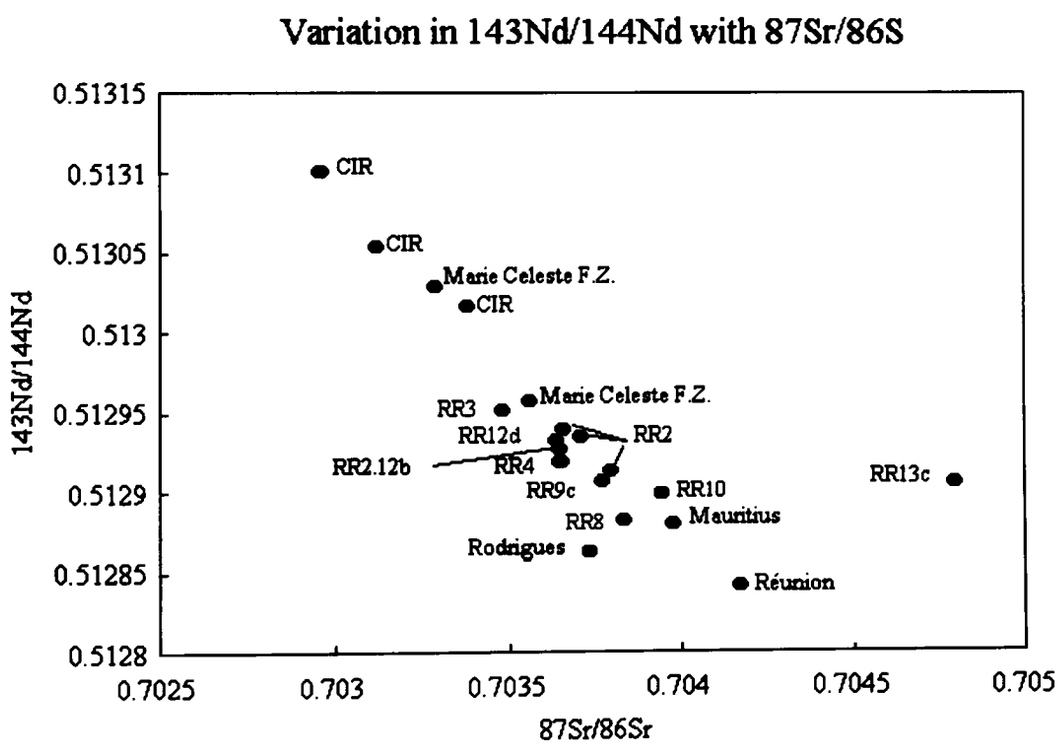

Sources of information for figs. 235-238 are given in notes to table 24b.

Figure 237

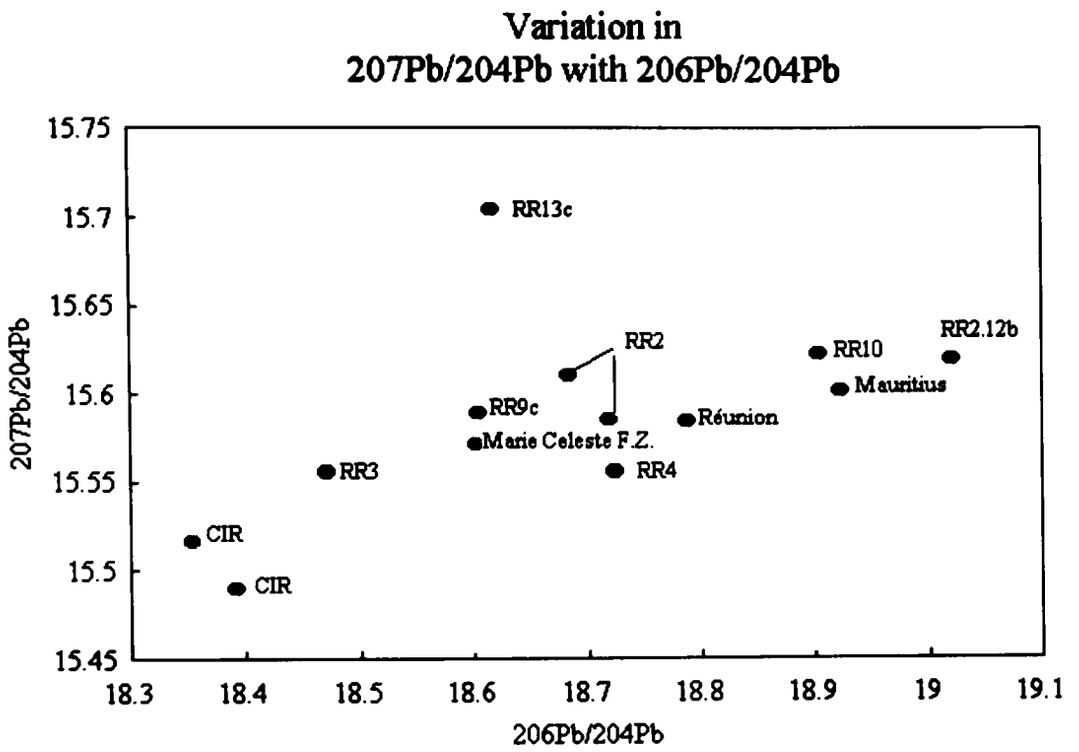

Figure 238

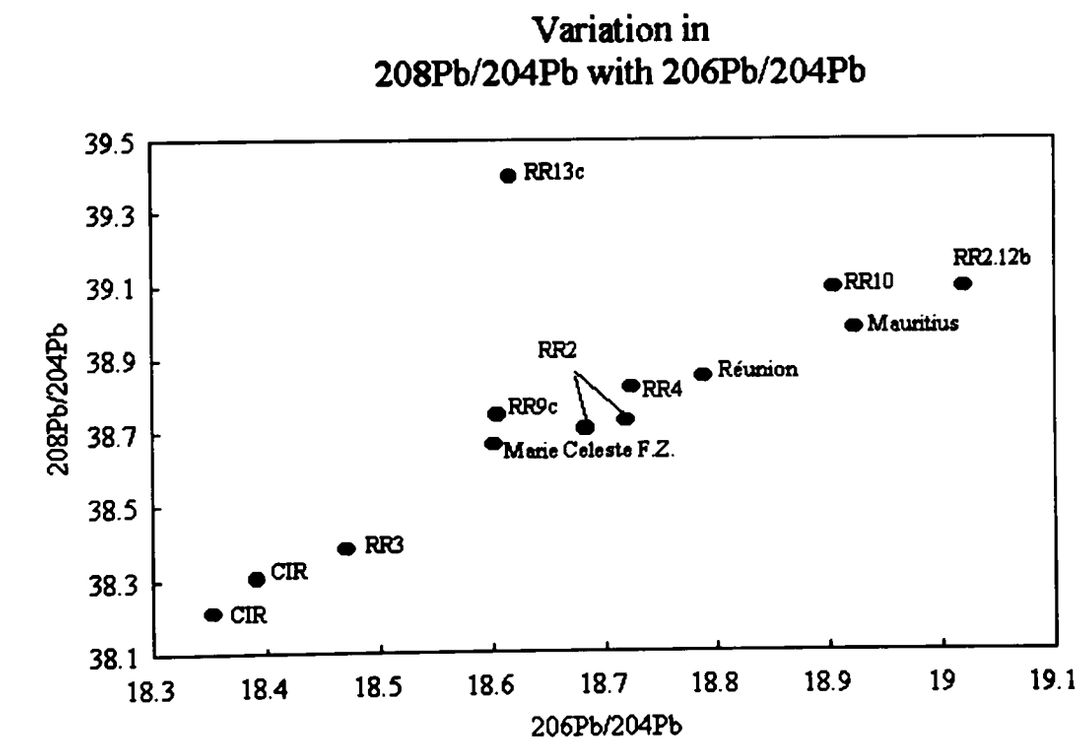

Figure 239

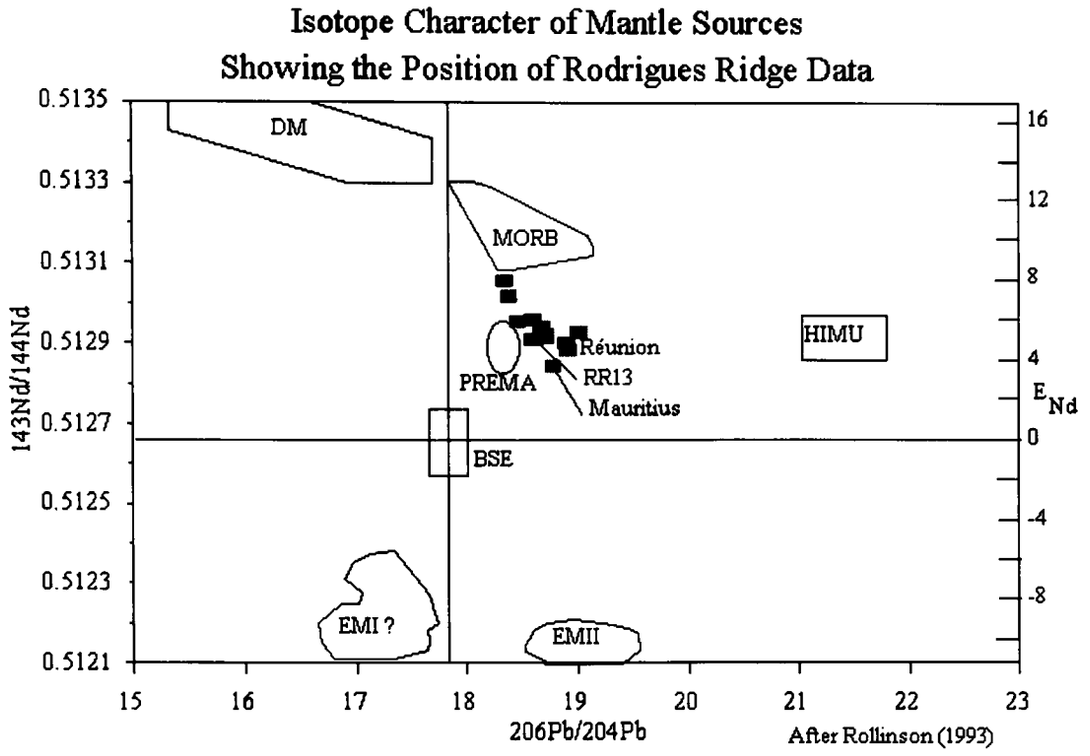

Figure 240

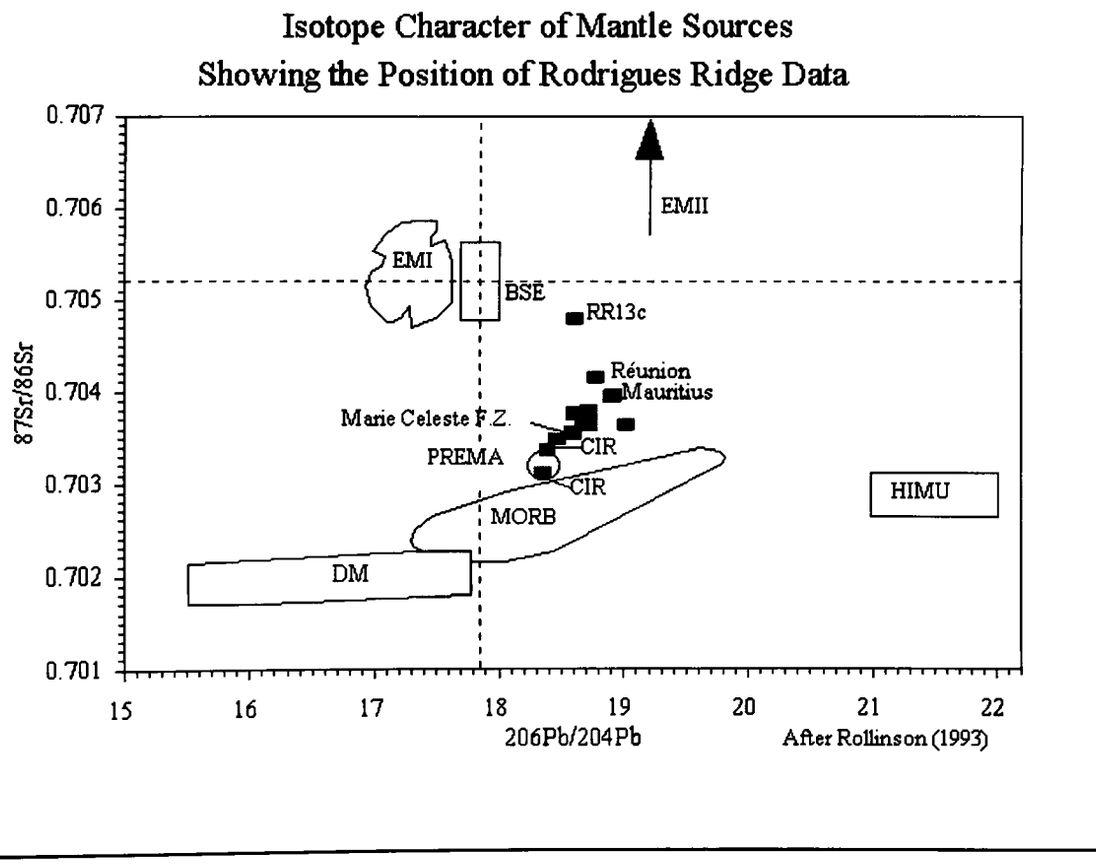

Sources as in table 24b

During the formation of the Mascarene Plateau by the Réunion plume, the volume of material involved in melting is believed to have reduced and the isotopic signature has become less depleted over time (White *et al.,* 1990). For the Rodrigues Ridge, the variations observed can only be explained by methods which permit the (near) simultaneous eruption of lavas with different isotopic signatures. Such variation can only be attained if the lavas have different sources or different amounts of material from at least two sources are mixed together. Varying the contributions of two or more sources would produce the greatest variety of compositions without requiring a prohibitively large number of independent sources.

5.7 Conclusions

The primary conclusion drawn from the isotopic data is that the Rodrigues Ridge lavas appear to have been derived as a result of melting of a mixed mantle source comprising at least three and possibly four sources. Within this heterogenous source, two components can be defined; one an enriched OIB-type source (HIMU + EMII) and the second a depleted MORB-type source (PREMA ± MORB). The variation in isotopic compositions observed are consistent with linear mixing of these two components along the Rodrigues Ridge. This conclusion is entirely consistent with the observations made in chapter 4, that the major and trace element chemistry show a linear progression from depleted (MORB) lavas in the east to enriched (OIB) lavas in the west. These lavas can be described as having been derived from the partial melting of upper mantle followed by the polybaric fractionation between 1 atm and 10 Kb involving olivine + spinel ± plagioclase ± clinopyroxene. The partial melting took place over a range of depths and was controlled by the thickness of the overlying lithosphere. The deep mantle source was an enriched (in trace elements) OIB-type source (HIMU + EMII), while the shallower source was depleted MORB-type source (PREMA ± MORB). Furthermore it is evident that the amount of melting which took place was constrained by the phase boundary Ol - En - Di - Sp + melt ⇌ Ol - En - Sp + melt.

Chapter 6

6. Petrogenesis

6.1 Introduction

To recap, MgO variation diagrams for the Rodrigues Ridge as a whole are scattered, lacking clear coherent trends as demonstrated by fig. 241. This reinforces the observation made in chapter 1, that the Ridge evolved by the coalescence of several volcanic centres, each fractionating independently of the others. At individual sites, MgO variation diagrams show trends indicative of olivine, plagioclase and clinopyroxene fractionation (see chapter 4). The phenocryst mineralogy of these lavas is olivine + plagioclase at sites RR1-RR10 and olivine (mostly pseudomorphed) + plagioclase + titanaugite at RR12d. At all sites there is also some evidence of accessory chrome spinel phenocrysts.

Figure 241

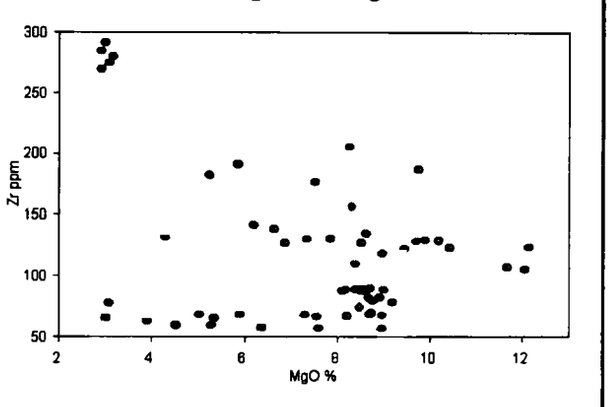

Collectively the mineralogical, petrographical and geochemical observations obtained for each of the Rodrigues Ridge sites can be used to develop a quantitative (or at least semi-quantitative) model for the formation and evolution of these lavas. In order to achieve this it is necessary to differentiate between the various processes which acted on these lavas. These processes may operate at crustal (*eg*... fractionation of phenocryst phases such as olivine and plagioclase), intermediate (*eg*... fractionation occurring during the ascent of the melt), or mantle depths (*eg*... melting processes and the reactions between the melt and coexisting mineral assemblages). Since the high-level processes over-print the effects of any deeper processes, these need to be addressed first. At each site the major element variation has been modelled using the empirical linear regression modelling technique described by Wright and Doherty (1970). The results of this have then been applied to modelling the trace element geochemistry, initially assuming simple Rayleigh-type fractionation. Following this, incompatible element ratios have been employed to examine both the role of partial melting, and that of source heterogeneity, in controlling the geochemical signature of the lavas. The radiogenic isotopes of Sr, Pb and Nd have been used to characterise the mantle sources and to consider the possible effects of source mixing on the geochemistry of the lavas. Finally, CMAS diagrams are used to investigate the polybaric history of the lavas.

6.2 Major Element Modelling

The linear regression modelling technique of Wright & Doherty (1970) was applied to the suite of lavas from each site, and to each group at RR2. This technique is based on a series of simultaneous equations of the general form:-

$$X = \sum_{i=1}^{n} x_i y_i$$

Where X is the analysed constituents of the rock given as weight % oxide recalculated to 100%
x_i = weight % of constituent X in mineral i,
y_i = weight % of mineral i in the rock where
$\sum y_i = 100\%$

To calculate the parent from the daughter composition:-

$$X_{parent} = \sum_{i=1}^{n} x_i y_i + y_n X_{daughter}$$

In this equation the daughter composition $X_{daughter}$ is put in as the n^{th} mineral constituent.

Or: Parent = $\sum$minerals + daughter

In the computer program, the compositions of parent and daughter are recalculated to 100% volatile free. The simultaneous equations are solved for each of 10 elements (SiO_2, TiO_2, Al_2O_3, FeO^*, MgO, CaO, MnO, Na_2O, K_2O, P_2O_5), with the residual errors being reduced to a minimum.

In each case the most mafic lava was used as the parent and (unless otherwise stated) the least mafic as the daughter, although, as will be seen later, this assumption may not be valid. At each site the fractionating phases were assumed to have the same composition as the phenocryst cores or as the crystals included within the phenocrysts. At many of the sites, solutions requiring the fractionation of olivine or olivine + plagioclase only had high residual errors. These residual errors were often substantially reduced by including clinopyroxene in the fractionating suite, although no phenocryst clinopyroxene has been found at any site other than RR12. CMAS plots (chapter 4) suggest that the lavas plot between the 1 atm. cotectic for olivine, plagioclase and clinopyroxene and the 10 Kb cotectics for olivine, clinopyroxene, spinel and in some cases plagioclase. This implies at least that clinopyroxene was a potential fractionating phase, albeit at *ca.* 10 Kb *i.e. ca.* 30 km depth.

RR2

In chapter 4 it was observed that the two groups at RR2 could not be related by simple high-level fractionation. Some relationship between the two groups can be seen on plots of CaO, Al_2O_3, Ni and Sr (figs. 64, 62, 73 and 75), but the clear separation between the two can be seen on plots of TiO_2, Nb, Sc, Y and Zr with MgO (figs. 61, 72, 74, 77 and 78). Attempts to derive the low MgO group lavas from mafic members of the high MgO group failed to reproduce observed behaviour and compositions. The

results for the geochemical modelling of each individual group are given in tables 25 & 26. Olivine and plagioclase phenocryst core compositions from the respective groups (tables 10-11) were used as compositions for the fractionating minerals. The best solution for the high MgO group required 4.0% fractionation of olivine and plagioclase in the proportions 63:37 (table 26). The best solution for the low MgO group required 17.6% fractionation of olivine and plagioclase in the proportions 53:47 (table 25). These extracts are much higher in olivine than the observed phenocryst assemblages which have olivine and plagioclase in the proportions 29:71 and 11:89 respectively in the high and low MgO groups. Xenoliths, which could have helped constrain the mineralogy of any extract, were not found at any of the Rodrigues Ridge sites.

Table 25 **Low MgO Group**

	Daughter Lava RR2.16	Ol.	Pl.	Parent Lava RR2.4	Calculated Parent Lava	Diff.
SiO_2	47.34	38.94	49.23	47.73	47.07	0.26
TiO_2	1.12	0.13	0.08	1.02	0.95	0.07
Al_2O_3	20.00	0.00	29.79	18.22	19.07	-0.42
MgO	4.02	45.45	0.00	7.61	7.66	-0.05
FeO^*	11.31	12.59	0.98	10.47	10.63	-0.15
Na_2O	3.23	0.31	3.69	2.95	3.01	-0.06
CaO	12.49	0.27	13.48	11.60	11.50	0.10
K_2O	0.08	0.04	0.00	0.16	0.07	0.09
MnO	0.17	0.41	0.04	0.15	0.18	-0.03
P_2O_5	0.24	0.00	0.01	0.26	0.20	-0.12
Solution	82.4	9.3%	8.3%			

Sum of the squares of the residuals = 0.318

Table 26 **High MgO Group**

	Daughter Lava RR2.2	Ol.	Pl.	Parent Lava RR2.11	Calculated Parent Lava	Diff.
SiO_2	47.67	39.41	49.53	47.79	47.50	0.12
TiO_2	1.30	0.00	0.22	1.25	1.25	0.01
Al_2O_3	17.29	0.36	30.05	16.89	17.06	-0.08
MgO	8.21	46.26	0.54	9.03	9.06	-0.03
FeO*	10.95	11.93	0.52	10.78	10.82	-0.04
Na_2O	2.99	0.03	3.44	2.98	2.92	0.06
CaO	11.19	0.07	13.63	10.85	10.95	-0.10
K_2O	0.11	0.00	0.00	0.12	0.11	0.01
MnO	0.18	0.11	0.03	0.20	0.18	0.02
P_2O_5	0.11	0.00	0.43	0.09	0.11	-0.02
Solution	96.0%	2.5%	1.4%			

Sum of the squares of the residuals = 0.038

The error in these solutions is expressed as the sum of the squares of the residuals (SSR). The SSR for the low MgO group is somewhat higher than that of the high MgO group. Most of this residual error is accounted for by SiO_2, FeO and Al_2O_3. Modelling the behaviour of the low MgO group lavas using olivine as the sole fractionating phase produces a better result for Al_2O_3, with a worse result for FeO and SiO_2.

The SSR for the high MgO group lavas is very low, suggesting that the model is able to reproduce the behaviour of these lavas well. The high MgO group is made up of a scattered group of lavas, with a limited range of MgO (8.17-9.00%). Modelling of these lavas required only 4% fractionation of olivine and plagioclase and had SSR = 0.038. However, a second solution was also obtained for these lavas requiring 2.1% fractionation of olivine only (see appendix 5) (SSR = 0.063) demonstrating that, for small amounts of fractionation, there is no unique solution. Furthermore, the arguments, concerning the difficulties of identifying fractionation where there is a limited range of MgO, presented in the trace element section on RR12d, are also true for this group.

RR3

Table 27

	Daughter Lava RR3.11	Ol.	Pl.	Parent Lava RR3.5	Calculated Parent Lava	Diff.
SiO_2	47.22	39.31	47.09	45.52	46.15	-0.25
TiO_2	1.19	0.15	0.24	1.00	1.04	-0.04
Al_2O_3	20.88	0.31	31.44	19.42	18.48	0.47
MgO	3.19	45.27	0.31	8.43	8.39	0.03
FeO^*	11.21	12.99	0.31	11.38	11.19	0.18
Na_2O	3.44	0.00	2.70	2.94	2.99	-0.04
CaO	12.32	0.43	14.86	10.68	10.86	-0.18
K_2O	0.09	0.00	0.00	0.08	0.08	0.00
MnO	0.17	0.21	0.00	0.13	0.17	-0.04
P_2O_5	0.29	0.00	0.21	0.42	0.25	0.17
Solution	85.5%	12.4%	2.0%			

Sum of squares of residuals = 0.380

Major element modelling required 14.5% fractionation of olivine and plagioclase in the proportions 86:14 to produce the most evolved lava (RR3.11) from the most primitive (RR3.5). The results of this linear regression modelling are given in table 27. The SSR for this model is 0.380, the majority of which is accounted for by SiO_2, Al_2O_3, FeO, CaO and P_2O_5. An extract made up of olivine, plagioclase and chrome spinel in the proportions 75:12:13 produced a lower residual error (SSR =0.034 see appendix 5). Chrome spinel is found included in the olivine phenocrysts, hence its inclusion in the fractionating suite would not seem unreasonable. The observed phenocryst proportions of olivine, plagioclase and chrome spinel are 14:84:2 respectively. In both models discussed the amounts of olivine (and chrome spinel) in the extract are greater than these observed phenocryst proportions.

RR4

Table 28

	Daughter Lava RR4.6	Ol.	Pl.	Parent Lava RR4.1	Calculated Parent Lava	Diff.
SiO_2	48.48	39.07	48.44	47.84	48.71	-0.35
TiO_2	1.83	0.06	0.02	0.87	1.45	-0.58
Al_2O_3	17.13	0.40	32.94	17.77	18.84	-0.53
MgO	7.60	44.43	0.00	9.08	9.08	-0.00
FeO^*	10.82	14.61	0.26	9.96	9.57	0.39
Na_2O	3.52	0.47	2.31	2.87	3.17	-0.30
CaO	9.54	0.29	16.23	11.15	10.15	1.00
K_2O	0.64	0.02	0.00	0.23	0.50	-0.28
MnO	0.19	0.27	0.00	0.16	0.17	-0.00
P_2O_5	0.25	0.12	0.26	0.07	0.25	-0.18
Solution	77.2%	6.9%	16.0%			

Sum of the squares of the residuals = 2.085

Like the RR2-high MgO group, the lavas of RR4 have a very limited range of MgO (7.52-8.97%). This is associated with somewhat scattered distributions on the variation diagrams and is further compounded by one sample (RR4.6) having 7.52% MgO, while all the others are between 8.48-8.97%. These problems combine to make a major element solution for this site rather unsatisfactory. The results obtained by modelling major element variation at this site are given in table 28. The best solution required 22.8% fractionation of the phenocryst phases olivine and plagioclase, in the proportions 30:70 to produce the most evolved lava (RR4.6) from the most primitive (RR4.1). The proportions of plagioclase required in this solution are somewhat higher than those at previously discussed sites. However the modelled fractionating suite is higher in olivine than the observed phenocryst proportions of 15:85.

The SSR for this model was 2.085, which is considerably greater than that observed at previous sites. One striking feature of the major element solution obtained for RR4 is the high absolute amount of fractionation required despite the limited range of MgO. The incorporation of clinopyroxene into the fractionating assemblage for this site substantially reduces the SSR to 0.468. This model required *ca.* 50% fractionation of olivine, plagioclase and clinopyroxene in the proportions 21:48:31 and is listed in appendix 5. The substantial improvement in the SSR and the improvements observed between the

calculated and observed parents for each element, suggest that clinopyroxene may well have been present during the fractionation of these lavas. However this solution, like that presented in table 28, requires large absolute amounts of fractionation as well as requiring clinopyroxene which is not observed as a phenocryst in the lavas. It is not uncommon to find lava suites which require clinopyroxene to form part of the fractionating assemblage, even though there is no clinopyroxene present within the phenocryst assemblage (Green pers. comm.).

RR8

Table 29

	Daughter Lava RR8.5	Ol.	Pl.	Parent Lava RR8.2	Calculated Parent Lava	Diff.
SiO_2	49.79	38.17	48.95	46.36	47.85	-0.60
TiO_2	1.56	0.00	0.22	1.45	1.24	0.21
Al_2O_3	18.00	0.00	31.81	15.41	15.45	-0.02
MgO	6.37	41.12	0.06	12.30	12.23	0.07
FeO^*	9.24	19.11	0.33	10.94	10.63	0.31
Na_2O	3.12	0.22	2.80	2.68	2.60	0.07
CaO	10.56	0.43	14.90	9.76	8.99	0.78
K_2O	0.89	0.00	0.16	0.67	0.71	-0.03
MnO	0.08	0.18	0.06	0.17	0.10	0.08
P_2O_5	0.39	0.00	0.00	0.24	0.30	-0.06
Solution	78.6%	17.4%	4.0%			

Sum of the squares of the residuals = 1.124

The scattered trends observed for many of the major, trace and rare earth elements, together with the limited data set, leaves the modelling carried out at this site less well constrained than at RR2, RR3 and RR9c. The model required 21.4% fractionation of olivine and plagioclase in the proportions 81:19 to produce the most evolved composition (RR8.5) from the most primitive (RR8.2) (table 29). The SSR for this solution was 1.124 with most of the residual error being accounted for by SiO_2, FeO, CaO and TiO_2. The residual errors for SiO_2, CaO and FeO could potentially be accounted for by compositional mismatch between the plagioclase and olivine phenocrysts used in the model, and the true fractionating phases.

RR9c

Table 30

	Daughter Lava RR9c.20	Ol.	Parent Lava RR9c.15	Calculated Parent Lava	Diff.
SiO_2	49.43	39.11	48.22	48.23	-0.00
TiO_2	1.57	0.00	1.45	1.38	0.08
Al_2O_3	18.35	0.30	15.86	16.17	-0.15
MgO	6.33	43.09	10.61	10.83	-0.22
FeO*	9.16	16.48	10.66	10.07	0.60
Na_2O	3.26	0.09	3.07	2.88	0.19
CaO	10.55	0.33	9.01	9.31	-0.31
K_2O	0.88	0.00	0.76	0.78	-0.02
MnO	0.08	0.26	0.16	0.11	0.05
P_2O_5	0.38	0.00	0.21	0.34	-0.13
Solution	87.9%	12.2%			

Sum of the squares of residuals = 0.583

The results of the major element modelling at RR9c are given in table 30. The best solution using the observed phenocryst phases, required 14.1% fractionation of olivine alone to derive the least magnesian lava (RR9c.20) from the most magnesian (RR9c.15). The SSR for this solution was 0.583, most of which is accounted for by differences between the calculated and the observed values for FeO, CaO, MgO, Na_2O, Al_2O_3 and P_2O_5. During this analysis it was noted that a more fayalitic (FeO rich) olivine produced a better match with the observed compositions (SSR = 0.321). However such fayalitic compositions were only observed around the edge of the phenocrysts or as matrix olivines, indicating that they were only in equilibrium with the final melts to crystallise. An alternative explanation is that clinopyroxene has also fractionated, as has been suggested at RR4 and RR8. This would be consistent with the CMAS plots which show the lavas plotting close to the 10 Kb cotectic within the field of clinopyroxene. A major element solution requiring 12.5% fractionation of olivine and clinopyroxene in the proportions 70:30 is presented in appendix 5. This model had an SSR of 0.533 which is slightly better than the model using olivine only.

RR10

At RR10 seawater alteration has modified the chemistry markedly, causing extremely low SiO_2 and highly variable K_2O and Na_2O contents. These effects render the application of the modelling process meaningless, and hence it was not carried out for this site.

RR12d

Table 31

	Daughter Lava RR12d.4	Ol.	CPX.	Pl.	Parent Lava RR12d.2	Calculated Parent Lava	Diff.
SiO_2	48.66	31.29	44.41	51.54	48.13	48.40	-0.11
TiO_2	2.00	0.87	3.46	0.01	1.94	1.96	-0.02
Al_2O_3	18.56	0.96	6.09	29.33	18.59	18.46	0.06
MgO	3.06	22.98	11.23	0.22	3.29	3.24	0.05
FeO^*	11.56	40.54	9.68	0.82	11.41	11.41	-0.01
Na_2O	4.51	0.91	0.97	4.32	4.56	4.41	0.15
CaO	8.66	0.93	20.68	12.46	8.92	8.87	0.05
K_2O	1.57	0.02	0.06	0.07	1.46	1.49	-0.03
MnO	0.27	0.62	0.25	0.06	0.22	0.27	-0.04
P_2O_5	1.16	0.69	0.35	0.12	1.48	1.11	0.37
Solution	94.8%	0.7%	1.6%	2.6%			

Sum of the squares of the residuals = 0.182

As was observed at RR2, a limited range of MgO (2.91-4.30%) severely hampers any attempts to derive a unique model of the major element variation. This is further compounded by the severe alteration state of RR12d.8 (with 4.3% MgO) which was not used, for this reason. The remaining samples have a range in MgO of 2.91-3.18%. This required just 5.2% fractionation of olivine, clinopyroxene and plagioclase in the proportions 14:33:53 to produce the least magnesian (RR12d.4) from the most magnesian lava (RR12d.2). The results of the major element modelling for RR12d can be found in table 30. Unlike the other Rodrigues Ridge sites the RR12d lavas contain some phenocryst clinopyroxene which has been used along with the phenocryst plagioclase and olivine in the modelling at this site. Olivine at this site is some-what scarce, having been largely pseudomorphed by iddingsite.

Several attempted analyses of these olivines were carried out, but all had characteristically low totals as a result of their alteration state. The olivine composition used in this model has therefore been normalised to 100%.

6.3 Conclusion

Major element modelling for sites RR2-RR8 and RR12d on the Rodrigues Ridge were generally unsatisfactory. The models, which sought to reproduce the observed fractionation trends using the composition of the observed phenocrysts, tended to have large residual errors or/and could not be applied satisfactorily to the trace elements (see section 6.4). However, the modelling techniques used were able to reproduce the observed behaviour at RR9c. This is emphasised by the effectiveness of the Rayleigh model used for the trace elements, which uses the same amounts and proportions of fractionating phases. At sites RR2 (high MgO group), RR4 and RR12d the limited range in MgO values among the lavas severely limits the usefulness of fractionation modelling.

6.4 Trace Element Modelling

The results of the major element modelling were used to develop models of the trace element behaviour. The amounts of fractionation and proportions of each phase calculated were used to provide initial constraints on the bulk distribution coefficients. These were calculated from the acceptable range of partition coefficients for each of the fractionating minerals, listed in appendix 1. This gave a range of 'acceptable' bulk distribution coefficients which are listed along with the models for each site. Initially the observed trace element variation was evaluated against a Rayleigh fractionation model provided in the *tracemod* program of Hagen & Neumann (1990). Rayleigh models take the form:

$$C_l = \frac{C_0(1 - DF)}{1 - F}$$

Where C_0 = the initial concentration, C_l = the final concentration, F = degree of fractionation and D = the bulk distribution coefficient

In this model it assumed that, once formed, the crystals are instantly removed and do not interact any further with the melt. This model also takes no account of any interaction between the wall rock and the melt and assumes that no melt is either added or subtracted during the fractionation process. Clearly this must be an over simplification. Although many other (open system) models exist which consider all of these aspects of the fractionation process the simple model was chosen for the following reasons; 1. The Rodrigues Ridge lava suite contains no xenoliths, which might have enabled an assessment of the wall rock composition and thus allowed the consideration of assimilation in the model. 2. No lavas from the Rodrigues Ridge have compositions typical of pristine melts; indeed all

appear to have been fractionated, and all contain phenocrysts. This leaves no information on initial melt compositions or on any subsequent injections of melt. Open system models require compositional information on the parental melt, any subsequent melt injected in to the magma chamber (replenishing melt) and on the composition of any assimilant. Using the parental composition as both the assimilant and the replenishing melt failed to produce improvements on any of the models presented here. Assimilation of small amounts of wall rock would produce a rise in the incompatible elements. If these wall rocks were altered, an increase in contaminants might be observed and the Sr isotopic signature would change markedly. The differences between the observed and modelled chemistry do not take this form, suggesting that assimilation alone is not the explanation for the observed differences (see section 6.6 with reference to RR3). Incremental batch melting, where the same source is used to produce several batches of melt, will be identical to the Rayleigh model for the first batch. Subsequent batches will, however, be increasingly depleted in the most incompatible elements relative to the less incompatible ones. For example; $D_{Ce} < D_{Yb}$, hence the ratio in the source region Ce/Yb must be lower than in the melt derived from it. In the case of a typical MORB Ce/Yb is 2.47 whereas typical (C1) chondrite Ce/Yb is 3.60 (Sun & McDonough 1989). Clearly if chondrite is analogous to pristine mantle, Ce should be more strongly concentrated in the melt (MORB) than Yb, thus the ratio Ce/Yb should increase. Thus in must be concluded that the source region for MORB has been subject to previous cycles of melting and is therefore depleted in incompatible elements relative to chondrite. In the case of the Rodrigues Ridge, the Ce/Yb ratio at sites RR2 and RR3 is lower than chondrite, indicating that these lavas had a depleted source.

For the purposes of modelling the evolution of the melt, batch melting models allow melts increasingly depleted in the most incompatible elements to be introduced into the magma chamber during the fractionation process. Since the magma chamber is not likely to get bigger, the model also allows for the eruption of some melt periodically to maintain the balance. Such models do not show the massive increases in the most incompatible elements that the Rayleigh model shows; however since not all the source melts, ratios such as Ce/Yb, will always increase with respect to the source. Models in which replenishment, fractional crystallisation and assimilation are continuous processes occurring simultaneously, and where eruption occurs periodically, show similar increases in ratios such as Ce/Yb. This last model probably best describes a natural system but it requires more information about the melt than is available for the Rodrigues Ridge, as mentioned at the beginning of this section. It was tested using the parent as both the assimilant and the replenishing melt but this failed to produce a significant improvement in the models described below.

In all the models presented below the partition coefficients used for each element in each mineral are presented in appendix 1. For most elements there are a range of partition coefficient values presented by several authors derived either experimentally or from natural basaltic or andesitic systems, (the details of the experimental or natural systems are give in the notes to appendix 1). For the purpose of this work all values within this range were considered acceptable. Bulk distribution coefficients were calculated using the same minerals and proportions as the major element models. This produced a

range of 'acceptable values' presented with each model. In many cases the highest or lowest 'acceptable value' produced the closest match, but still could not match the observed daughter. In these cases it is clear that this simple model is inadequate. The degree of fractionation used in these models was always the same as the major element model as all the elements must have experienced the same conditions. However, the trace elements are the most likely to differentiate between the simple Rayleigh model used and the more sophisticated open system models described above. One other possible cause of variation from a given model is the fundamental assumption that Henry's Law is applicable to elements whose concentration is below about 1% (Cox *et al.*, 1987), both in the melt and the mineral, and thus that the partition coefficient (K_D) can be defined as:

$$\frac{\text{Concentration in mineral}}{\text{Concentration in melt}} = K_D$$

Hagen & Neumann (1990) indicate that experiments to test this assumption have produced conflicting results. Furthermore, as they point out elements such as Cr, which is a stoichiometric constituent in chrome spinel, will not follow Henry's Law. Thus, while Cr is modelled for some sites here, if chrome spinel has fractionated (even in small quantities), the model will not predict its behaviour adequately. Accessory chrome spinel is noted in chapter 3 as being present at all sites, although the major element models suggest it did not contribute to the fractionation process.

The results of the trace element models are tabulated below for each site and summarised in table 45. These results are also shown graphically on the variation diagrams in chapter 4.

RR2

The trace element variation in both the high and low MgO groups at this site was modelled. The results are given in tables 32 and 33, while the bulk distribution coefficients used, together with the acceptable upper and lower limits, are given in table 34.

Table 32

High MgO Group. 4.0% Fractionation of Olivine and Plagioclase in the Proportions 63.3:36.7

Element ppm	Parent RR2.11	Calculated Daughter	RR2.2
Cr[#]	368.2	376.037	366.5
Nb	1.352	1.408	1.374
Ni	247.86	217.730	217.73
Sc	34.81	35.880	35.59
Sr	148.75	152.472	150.9
U	0.064	0.067	0.082
V	205.80	214.244	222.6
Y	28.508	29.689	30.60[*]
Zr	88.50	92.150	88.8
La	2.122	2.206	1.037
Ce	10.521	10.941	8.833
Eu	1.215	1.263	1.126
Yb	3.460	3.604	3.366
Lu	0.421	0.438	0.384

[*] Estimate for Y value is based on the observed trend, [#] XRF Cr values were preferred here.

Table 33 Low MgO Group.

17.6% Fractionation of Olivine and Plagioclase in the Proportions 52.9:47.1

Element ppm	Parent RR2.4	Calculated Daughter	RR2.16
Cr	291.3	346.004	355.0*
Nb	0.829	1.005	1.731
Ni	188.755	83.196	83.19
Sc	31.05	36.069	34.09
Sr	152.00	167.254	173.14
U	0.510	0.616	0.660
V	202.3	244.750	280.0*
Y	20.089	24.347	26.6
Zr	57.100	69.162	63.095
La	1.690	2.027	4.441
Ce	6.169	7.412	11.0*
Eu	0.803	0.962	1.076
Yb	2.119	2.569	3.190
Lu	0.288	0.349	0.340

* Estimates for Cr, V and Ce used here were derived from projections of the observed trend at 3.92% MgO.

Table 34

Bulk Distribution Coefficients

	Low MgO Group			High MgO Group		
	D used	Minimum	Maximum	D used	Minimum	Maximum
Cr	0.111	0.111	1.549	0.497	0.130	1.852
Nb	0.005	0.005	0.021	0.004	0.004	0.023
Ni	5.232	2.158	12.609	4.175	2.580	15.080
Sc	0.226	0.082	0.226	0.258	0.095	0.258
Sr	0.506	0.506	2.186	0.395	0.395	1.707
U	0.024	0.024	0.203	0.019	0.019	0.176
V	0.016	0.016	0.042	0.015	0.015	0.043
Y	0.007	0.007	0.033	0.006	0.006	0.032
Zr	0.010	0.005	0.010	0.010	0.004	0.010
La	0.061	0.061	0.132	0.048	0.048	0.103
Ce	0.052	0.052	0.106	0.040	0.040	0.085
Eu	0.066	0.066	0.356	0.052	0.052	0.282
Yb	0.005	0.005	0.062	0.004	0.004	0.061
Lu	0.013	0.013	0.040	0.010	0.010	0.032

The High MgO Group

Only the Ni values could be reproduced satisfactorily using Rayleigh modelling for the high MgO group . The results of this modelling of 4% fractionation of olivine and plagioclase are given in table 32. These suggest that a greater amount of fractionation (than 4%) is required to model Sc, U, V and Y. This would not significantly affect the Ni results as the range of acceptable partition coefficients for this element are quite large. Zr, however, seems to require trace amounts of another phase with a much higher distribution coefficient, to be on the liquidus. No such phase has been observed in any of the Rodrigues Ridge lavas, but several sites show more extreme anomalous behaviour of this type notably RR3. Alternative explanations for the observed behaviour are that the high MgO group lavas are not following simple Rayleigh fractionation, or that the limited range of MgO shows insufficient variation for accurate modelling *ie.* the errors inherent in the model exceed the amount of observed variation.

The high MgO group fails to show clearly defined fractionation trends for Ba, Cr, Cu, Nb, Rb, Sr, Th, Zn, La, Eu, and Yb with MgO. Such a limited amount of fractionation is unlikely to be able to overprint any pre-existing variation between the samples (see the discussion for RR12d, where similarly small amounts of fractionation were observed). Furthermore Ba, Rb, Th and U are sensitive

to seawater alteration, hence the scatter observed among these elements may reflect these processes rather than any pre-eruptive process. Cu and Zn display rather scattered behaviour with MgO, possibly as a consequence of their being preferentially taken up by trace amounts of sulphide-bearing minerals (see chapter 4).

The Low MgO Group

The low MgO group, unlike the high MgO group, has a broad (3.92-7.60%) range of MgO, with most trace elements showing tightly constrained fractionation trends. Despite this only Ni, with its wide range of acceptable partition coefficients, can be modelled well using the observed phenocryst phases (table 33). The calculated daughter is lower in Cr, Nb, Sr, V, Y, La, Ce, Eu and Yb than RR2.16, but higher in Zr and Sc. The modelled solutions are displayed graphically on the variation diagrams in chapter 4 (figs. 67-80), showing the mismatch between the model solution and the observed trends. Other fractionation models such as the open system described by O'Hara (1977) and O'Hara & Mathews (1981) enable much greater enrichment of incompatible elements (like Eu) compared with compatible elements like Ni. In an open system, new batches of melt are periodically introduced, fractionation and assimilation are continuous, and eruption is periodic. However, models using the parent composition as the assimilant were still unable to reproduce the observed behaviour. For most elements, the model required greater, but inconsistent, amounts of fractionation, while Sc and Zr were enriched more rapidly than is observed in the lavas.

It was observed that a solution requiring *ca.* 30% fractionation of olivine, plagioclase and clinopyroxene in the proportions 26:25:49 produced a better match for both the major and trace element behaviour (see appendix 5). In this model Sc is accommodated within the lattice of clinopyroxene, while the greater incompatibility of Eu and Sr in clinopyroxene, compared with plagioclase, results in greater enrichment of these elements in the daughter. Other incompatible elements, notably Y, are also enriched in the daughter due to the greater amounts of fractionation required by this model. Neither the olivine-plagioclase model or the olivine-plagioclase-clinopyroxene model were able to reproduce the behaviour of Cr, Nb, U, V or Zr. As was observed in the high MgO group, Zr is buffered, while Cr, Nb and V are all higher in RR2.16 than either model predicted. For Zr, in the low MgO group, a bulk distribution coefficient of $D_{Zr} = 0.484$ was required to reproduce the observed trend whereas acceptable values for the modelled fractionating assemblage were between 0.005-0.010. The olivine-plagioclase-clinopyroxene model is able to reproduce the observed value of U found in RR2.16, however other RR2-low MgO group rocks plot significantly below the straight line joining RR2.4 with RR2.16 (the parent and daughter lavas).

RR3

The results of Rayleigh modelling of trace elements are given in table 35 while the bulk distribution coefficients used are given in table 36. Major difficulties were experienced in modelling the trace element behaviour at this site. Rayleigh fractionation modelling using 14.5 % fractionation of olivine and plagioclase only produced satisfactory results for Ni and Sc.

Cr and V can be modelled if spinel is included in the fractionating suite (appendix. 5, table 35a). Chrome spinel is found as a minor phase, often included in the olivine phenocrysts. This major element model required 15.5% fractionation of olivine, plagioclase and chrome spinel in the proportions 75:12:13. This is substantially different to the observed phenocryst suite of 14% olivine, 84% plagioclase and 2% chrome spinel. This discrepancy may be explained by the dense spinel and olivine crystals sinking out of the melt prior to eruption. 15.5% fractionation of a suite of minerals which includes 13% spinel containing *ca.* 20% Cr_2O_3 (table 12) would remove *ca.* 2800 ppm Cr from the melt (assuming that all the Cr was contained within the spinel). This is considerably more than that observed in (RR3.5) the parent (544.5 ppm), hence this model would seem unsatisfactory.

The remaining trace elements (U, Y, Zn, Zr and the REE) show diffuse trends (U & Zn) and/or show trends which are buffered (Zr & Sm) or decrease with decreasing MgO *i.e.* they have the opposite sense to that which might be expected for incompatible elements in the common basaltic minerals (U, Y and most REE). U may have been subject to oxidation during weathering resulting in its enrichment relative to Th, producing the observed scatter. However oxidation cannot explain the decrease with MgO. To examine the curious behaviour of Y, Zr and the REE further, the bulk distribution coefficients which would be required to reproduce these trends during Rayleigh fractionation are presented in table 36. These bulk distribution coefficients were established simply by trial and error using the modelling program *tracemod.*

Table 35 14.5% Fractionation of Olivine and Plagioclase in the Proportions 86.0:14.0

Element ppm	Parent RR3.5	Calculated Daughter	Average Daughter*	RR3.1	RR3.11
Cr	544.53	429.649	240.99	243.5	238.48
Ni	302.73	135.851	135.85	138.40	133.3
Sc	33.12	37.855	37.853	32.68	37.853
TiO_2 %	0.977	1.131	1.073	0.992	1.154
U	2.636	3.027	0.669	0.312	1.026
V	232.31	269.714	257.00	224.10	289.9
Y	25.507	29.681	24.711	24.165	25.256
Zn	120.3	123.779	95.875	74.235	117.515
Zr	67.475	78.795	71.70	65.60	77.80
La	4.999	5.811	4.406	4.770	4.041
Ce	7.622	8.862	7.365	7.236	7.493
Pr	0.799	0.930	0.713	0.578	0.847
Nd	7.507	8.734	6.589	10.991	6.589
Sm	1.886	2.191	1.950	1.950	2.508
Eu	0.922	1.058	0.917	0.870	0.964
Gd	3.476	4.036	2.934	3.015	2.853
Tb	0.470	0.546	0.460	0.440	0.480
Dy	4.080	4.740	3.625	4.127	3.122
Ho	0.873	1.015	0.839	0.823	0.854
Er	2.523	2.928	2.449	2.439	2.458
Yb	2.875	3.333	2.312	2.380	2.244
Lu	0.348	0.406	0.341	0.303	0.379

* The average daughter was the mean of RR3.1 and RR3.11, except for Sc and Nd where RR3.11 was used and Sm where RR3.1 was used as the other value was significantly off the observed trend.

Table 36 **Bulk Distribution Coefficients**

	Maximum	Minimum	D used	D required
Cr	2.513	0.173	2.513	6.203
Ni	20.474	3.502	6.115	6.115
Ti	0.068	0.018	0.068	0.400
Sc	0.327	0.123	0.147	0.147
U	0.117	0.007	0.117	9.750
V	0.048*	0.013	0.048	0.355
Y	0.033	0.004	0.033	1.202
Zn	0.818	0.818	0.818	2.449
Zr	0.010	0.002	0.010	0.612
La	0.040	0.018	0.040	1.806
Ce	0.038	0.015	0.038	1.219
Pr	0.032	0.014	0.032	1.725
Nd	0.033	0.009	0.033	1.833
Sm	0.043	0.008	0.043	0.786
Eu	0.122	0.020	0.122	1.035
Gd	0.046	0.011	0.046	2.082
Tb	0.039	0.007	0.039	1.140
Dy	0.042	0.005	0.042	1.755
Ho	0.039	0.008	0.039	1.250
Er	0.050	0.003	0.050	1.190
Yb	0.057	0.002	0.057	2.390
Lu	0.015	0.005	0.015	1.125

* The partition coefficient recommended by Ringwood (1970) for vanadium in olivine is $D_V^{Ol} = 1.3$ this was achieved in lunar samples at very low oxygen fugacities appropriate to lunar conditions. This would give a partition coefficient of $D_V^{Ol} = 1.122$. Other authors (see appendix 1) suggest that the partition coefficient of V in olivine is much lower.

Assuming that the unusual behaviour of these elements has been caused by the fractionation of an accessory phase representing 0.1 or 1% of the fractionating assemblage, the partition coefficient for each element in this accessory phase can be estimated (table 37) from the bulk distribution coefficients. Before considering the possible accessory phases which may be causing this behaviour, it should be noted that P_2O_5 is enriched (fig. 53 p. 105) and shows anomalous behaviour similar to U at this and other Rodrigues Ridge sites. Furthermore Y shows a buffered trend in the lavas of Rodrigues island (Baxter *et al.*, 1985), while anomalous behaviour similar to that observed at this site is also observed at RR2, RR8 and possibly RR9c.

Table 37

Fractionating assemblage;

1. 85.91% Ol + 13.99% Plag + 0.1% X

2. 85.15% Ol + 13.86% Plag + 1% X

Element	$D^{X}_{(0.1)}$	$D^{X}_{(1)}$
Y	1169-1198	117-120
Zr	602-610	60-61
Ti	376	37.6
La	1766-1788	177-179
Ce	1181-1204	118-120
Pr	1693-1711	169-171
Nd	1800-1824	180-182
Sm	743-778	74-78
Eu	913-1015	91-101
Gd	2036-2071	204-206
Tb	1101-1133	110-113
Dy	1713-1750	171-175
Ho	1211-1242	121-124
Er	1140-1188	114-119
Yb	2333-2388	233-239
Lu	1110-1120	111-112

Table 38 **Partition coefficients (where known) for Apatite, Sphene, Allanite and Zircon.**

Element	Apatite	Zircon	Sphene	Allanite	References
P	Essential	*			6.
Nb	0.1	*	4.65		5, 6, 7.
Ti	0.1 20	*			3, 6.
Y	40	300 (Interp.)			1, 4.
Zr	8	Essential			3.
La	9-35	4.18-16.6 *	2	820.0-2594.5	3, 7, 6, 7.
Ce	10(I) 21.1-34.7	2.5-16.75		635.0-2278.5	3, 2, 7.
Pr	12	*			6.
Nd	12-63	4.29-13.3 *		463.0-1620.0	7, 6, 7.
Sm	11-60	3-14.4	10	205.0-866.5	3, 2, 7.
Eu	10 25.5-30.4	8-16.0		81.0-111.0	3, 2, 7.
Gd	43.9-56.3	6.56-12.0 *		130.0	7, 6, 7.
Tb	8 (Interp.)	37.0 *		71.0-273.0	3, 7, 6, 7.
Dy	7(I) 34.8-50.7	47.4-101.5 *		136.5	3, 7, 6, 7.
Ho	6 (Interp.)	*	10		3, 6, 7.
Er	4-25	99.8-135.0 *			3, 7, 6.
Yb	3.5-23.9	270-300		30.8-8.9	3, 2, 7.
Lu	13.8-20.2	264.5-641.5 *	6	7.7-33.0	7, 6, 7.

References for table 37. 1. - Pearce & Norry (1979), 2. - Cox *et al.* (1987), 3. - Irving (1978), 4. - Hanson (1980), 5. - Deer *et al.* (1967), 6. - Deer *et al.* (1982) 7. - Rollinson (1993) * REE, P, Ti and Nb in appreciable quantities have been reported in zircon

To reproduce the observed trends would require the fractionation of small amounts of an accessory phase (X in table 37) such as apatite, zircon, sphene or allanite in which P, Zr, Y, (U), REE and possibly Ti are compatible. Accessory apatite or zircon would, however, deplete the all the REE, since they are strongly partitioned into both of these phases (Hanson 1980). LREE have higher partition coefficients than HREE in apatite (table 38), hence the overall effect of small amounts of apatite fractionation would be LREE depletion associated with an overall absolute decrease in total REE content.

Several fundamental difficulties exist with the suggested involvement of any of these accessory phases;-

1. The lavas of RR3 are insufficiently evolved for zircon, apatite, sphene or allanite to be on

the liquidus.

2. No phenocrysts/megacrysts of any of these minerals have been found in any member of the Rodrigues Ridge lava suite, although some apatite megacrysts were found in evolved lavas on Rodrigues Island.

3. The accessory phases mentioned would have profound effect on the absolute concentrations of REE within the lavas, over-printing any source variations to produce lavas strongly depleted in the REE and other partitioned elements.

It is clear from the above analysis that no satisfactory explanation involving high-level fractionation processes can be found for the unusual behaviour of Y, Zr, (U, P) and REE with declining MgO content. The clear relationship between decreasing MgO and Y, Zr and REE suggests that the processes responsible for buffering or reducing the Y, Zr and REE are concurrent with the fractionation process at high-level. Clearly if a high-level process is acting on these elements, then it may be impossible to draw satisfactory conclusions about the earlier history of these lavas (see later).

RR4

The range of MgO is narrow (7.52-8.97%) and many trace elements show poorly defined trends at this site. These two factors limit the quality of the models used.

The results of trace element modelling can be found in table 39, while table 40 lists the bulk distribution coefficients used. Using the major element derived solution of 22.8% fractionation of olivine and plagioclase in the proportions 30:70 proved unsatisfactory. Using this extract, Rayleigh fractionation modelling was unable to predict the behaviour of Cr, Eu, Y, Sr, Th, Zr and Cu; satisfactory results were obtained for Ni and V. However, since all elements have been subject to the same process(es), a good model solution should be able to predict the behaviour of most, if not all, elements. Using the above extract, 66% fractionation was required to reproduce the observed behaviour of Eu, and Sr. With this amount of fractionation V, and Y were higher in the calculated daughter than in RR4.6 but Th and Zr remained low. Reasonable solutions for Cr and Ni could still be attained with this level of fractionation due to their large range of acceptable partition coefficients in olivine. Clearly such high levels of fractionation are inconsistent with the major elements chemistry, particularly MgO. No olivine-plagioclase model could describe the observed trend of Cu, which decreases with decreasing MgO, suggesting that it is being partitioned by a fractionating mineral. Trace amounts of Cu-bearing sulphides such as pyrites could cause this effect. The apparent need for such large amounts of fractionation among lavas with a limited range of MgO, implies that the olivine-plagioclase (Rayleigh) model being used is inadequate for this site. An open system model, such as that describe for the low MgO group at RR2 (see also section 6.4), did not resolve the difficulties. Once again the discussion at RR12d and RR2 (high MgO group) concerning the difficulties of

modelling limited ranges of MgO, must be borne in mind.

Table 39 22.8% Fractionation of Olivine and Plagioclase in the Proportions 30.0:70.0

Element ppm	Parent RR4.1/10	Calculated Daughter	RR4.6
Cr	232.13	240.150	171.1
Cu	96.8	114.957	70.49
Ni	200.12	171.732	171.73
Sr	189.0	201.662	233.9
Th	0.464	0.587	1.322
TiO_2 %	0.861	1.108	1.814
V	175.65	225.335	230.11
Y	19.208	24.831	36.705
Zr	57.281	74.098	176.5
Eu	0.753	0.951	1.611

The parent values used were either those of RR4.1 (Eu, Sr, Y, Ti and Th) or RR4.10. Both of which had very similar MgO contents (8.97% and 8.95% respectively) thus the lava which plotted closest to the apparent trend described by the data was selected.

Table 40 Bulk Distribution Coefficients

Element	Maximum	Minimum	D used
Cr	0.883	0.067	0.883
Cu	0.337	0.109	0.337
Ni	7.168	1.228	1.590
Sr	3.239	0.750	0.750
Th	0.141	0.091	0.091
Ti	0.061	0.029	0.029
V	0.037	0.019	0.019
Y	0.031	0.010	0.010
Zr	0.010	0.007	0.007
Eu	0.518	0.098	0.098

RR8

The lavas of RR8 display a broad range of MgO (6.21-12.13%). Despite this, many elements display substantial scatter, and fractionation patterns are often poorly defined. The results of the trace element modelling are given in table 41. The bulk distribution coefficients used are given in table 42. This model was able to predict the observed behaviour of Cr only. Eu, Sc, Sr and Y all show a decrease with decreasing MgO similar to the behaviour observed at RR3 and RR2, suggesting that they are being partitioned by an accessory phase. As has been observed at RR3, the REE also show unusual behaviour suggesting that their bulk distribution coefficient is substantially larger than that calculated from the recommended values for the fractionating suite of olivine and plagioclase. In addition to the above elements, Nb and Zr are apparently buffered, having more modest increases with MgO than the model requires.

A model including clinopyroxene in the extract was considered since this mineral is known to partition Sc, and the minor element Ti which is also buffered. The results of this model can be found in appendix 5. This model required 41.1% fractionation of olivine, plagioclase and clinopyroxene (a matrix composition was used) in the proportions 44:34:22. The trace element solution for this model produced a good match for Cr and Sr but not for Sc and TiO_2 or any of the other elements.

Table 41 21.4% Fractionation of Olivine and Plagioclase in the Proportions 81.0:19.0

Element ppm	Parent RR8.2	Calculated Daughter	RR8.5
Cr	587.3	668.533	668.5
Nb	15.984	20.255	16.653
Sc	27.65	32.627	25.742
Sr	341.69	351.437	302.50
Th	1.160	1.467	2.027
Y	23.506	29.673	21.853
Zn	94.2	99.492	196.035
Zr	123.4	156.620	141.6
Eu	1.308	1.603	1.150*

* The Eu value for RR8.5 is 1.003. This was some what lower than the trend apparent in the remaining data hence 1.15 was used as the observed daughter.

Neither model was capable of representing the behaviour of Zn, which is clearly incompatible, as shown in fig. 143. Little partitioning information for Zn is available, and that given in appendix 1

suggests that the element is only slightly incompatible in olivine. Despite this, both Doe (1994) and Clague *et al.* (1981) suggest that the element is incompatible in oceanic basalts, a conclusion also reached here.

From the above discussion it can only be concluded that, with the limited data set and the scatter of points within that set, no satisfactory trace element model can be found.

Table 42

Bulk Distribution Coefficients

	Maximum	Minimum	D used
Cr	2.373	0.164	0.462
Nb	0.017	0.002	0.017
Sc	0.313	0.117	0.313
Sr	0.883	0.204	0.883
Th	0.058	0.025	0.024
Ti	0.068	0.019	0.068
Y	0.032	0.002	0.032
Zn	0.773	0.773	0.773
Zr	0.010	0.004	0.010
Eu	0.156	0.027	0.156

RR9c

The major element model at this site required olivine as the sole fractionating phase. Using this result to model the trace element behaviour produced a good match with the observed data. The results of the trace element model are given in table 43. The bulk distribution coefficients used in both models are given in table 44. As with other models the bulk distribution coefficient used was that which provided the closest match with the observed daughter lava.

The results of this modelling are shown graphically on the variation diagrams in chapter 4 (figs. 158-168 pages 132-134). These figures show clearly that the model is able to accurately predict the behaviour of Cr, Nb, Ni, Sc, Th, U, V, Y, and Zr. The variations between the model and the observed values for Sr, Eu and Yb are sufficiently small to be accounted for by the scatter in the observed data. Alternatively the REE may be showing traces of the anomalous behaviour seen at RR3.

Table 43 **14.1% Fractionation of Olivine Only**

Element ppm	Parent RR9c.15	Calculated Daughter	Observed Daughter
Cr	458.900	498.192	498.20
Nb	12.134	13.801	13.80
Ni	331.830	219.398	219.40
Sc	26.970	29.461	29.46
Sr	326.500	371.301	410.00
Th	0.988	1.124	1.12
U	0.285	0.324	0.34
V	192.000	218.120	220.00
Y	22.114	25.152	25.50
Zr	123.0	139.751	138.40
Eu	1.223	1.387	1.26
Yb	2.325	2.626	2.40

The observed daughter was estimated from the trends described by most of the lavas at this site where RR9c.20 plots significantly off the general trend.

Table 44 **Ranges of Acceptable Values for the Bulk Distribution Coefficient at RR9c**

Element	Maximum	Minimum	D used
Cr	2.920	0.200	0.363
Nb	0.010	0.000	0.002
Ni	23.800	4.070	4.208
Sc	0.370	0.140	0.315
Sr	0.018	0.003	0.003
Th	0.027	0.000	0.000
U	0.081	0.000	0.000
V	0.081	0.001	0.011
Y	0.033	0.002	0.002
Zr	0.010	0.001	0.010
Eu	0.023	0.001	0.023
Yb	0.055	0.002	0.055

It is not clear why Rayleigh fractionation modelling at this site should be able to predict the observed trends well, when at other sites it is less successful. That the modelling at this site was successful indicates that modelling **can** work and that something other than simple high-level fractionation of the observed phenocrysts must be controlling the trends. There are a greater number of samples available at this site with a wide range of MgO values resulting in clear trends on most of the variation diagrams. This reduces the risk of placing too much emphasis on any single value. Limited sample size and/or MgO range have undoubtably restricted the usefulness of the models at sites RR2 (high MgO group), RR4, RR8, and RR12d. Sample size limitations, however, cannot be used to explain the anomalies observed at RR2 (low MgO group) and RR3.

RR12d

The lavas of RR12d do not show clear trends with MgO. The solution derived from major element modelling suggests 5.2% fractionation of olivine, plagioclase, clinopyroxene has occurred. Ni, which has a bulk distribution coefficient of $D_{Ni}^{extract} = 1.227\text{-}9.753$, would only be expected to show a clearly declining trend with decreasing MgO if the distribution coefficient was towards the higher end of this range. Other trace elements are incompatible (in this extract) and, as such, are unlikely to show substantial change during Rayleigh fractionation as a result of the removal of 5.2% of this extract from the RR12d.2 parent. For example:- if there is 100 ppm of an incompatible element ($D_{elm}^{extract} \approx 0$) in the parent, after 5.2% fractionation there would be 105.5 ppm in the derivative. This small variation (5.5%) is approaching the limits of precision of the instrumentation (see tables 49-50 appendix 3).

6.5 Conclusion

Major element models requiring the fractionation of olivine ± plagioclase ± clinopyroxene were considered at each of the Rodrigues Ridge sites. Sites RR2-RR8 required the fractionation of olivine + plagioclase to produce the most evolved lavas from the most primitive (table 45). Site RR9c required the fractionation of olivine alone, while RR12d required olivine + plagioclase + clinopyroxene. At each of sites RR2-RR9c, phenocrysts/microphenocrysts of olivine and plagioclase were observed in the lavas, while at RR12d clinopyroxene microphenocrysts were also observed. A summary of the fractionation models presented in this chapter is given in table 45.

The degree of alteration of most of these samples was not thought to have significantly affected the major element chemistry, except at RR10. No modelling was attempted at RR10 for this reason.

Table 45

Site	Suite	Amount %	Proportions
RR2 Low MgO	ol + pl	18	53:47
RR2 High MgO	ol + pl	4	63:37
RR3	ol + pl	15	86:14
RR4	ol + pl	23	30:70
RR8	ol + pl	21	81:19
RR9c	ol	14	100
RR12d	ol + pl + cpx	5	14:33:53

The trace element modelling at RR2, RR4 and RR8 was able to reproduce the sense of the observed trends with decreasing MgO for most elements, but in many cases not the absolute values. *i.e.* trace element modelling at RR2, RR4 and RR8 could predict if an element would be enriched or depleted in the melt, but not the amount of this enrichment or depletion.

At RR2 (high MgO group), RR4 and RR12d, the range of MgO between the most magnesian and the least magnesian samples was limited, leaving any modelling at best only poorly constrained. At RR2 (low MgO group) clear fractionation trends exist although the Rayleigh model solution is not always able to match them. At RR8 scatter of the data leaves the modelling poorly constrained.

The trace element solution for RR9c produced a good match for all the elements modelled, with the model being able to predict the concentration of all elements (modelled) in the daughter to within 10%. The larger number of analyses at this site clearly defines the fractionation trend, despite some scatter of individual points.

At RR3 trace element modelling was not able to reproduce the observed trends well. Several elements, notably the REE, Y and Zr, show unusual behaviour suggesting that they are being partitioned by one of the fractionating mineral phases. Principally these elements show buffered or declining trends with decreasing MgO, behaviour which is inconsistent with mantle-derived trends. No phase capable of partitioning these elements was observed in these or any other Rodrigues Ridge lavas, although RR2, RR8 and possibly RR9c show buffered REE patterns like those of RR3. Since no likely fractionating phase can be identified it must be concluded that the observations are the result of another process such as melting and melt-rock reaction (see section 6.8). It was noted that all lavas showing this unusual behaviour also show enrichment in U compared with Th (figs. 51, 53, 55 and 56a pages 104-106) and where U enrichment is severe they also display enrichment of P. Oxidation of the lavas may explain the enrichment of U compared with Th but it cannot explain the REE behaviour. Lavas with the greatest U enrichment have Th/U ratio less than 1 whereas unaffected samples show values of 3-4.

6.6 Incompatible Element Ratios

Ratios of the highly incompatible elements (*ca.* D≤ 0.01) generally reflect source variations rather than large-scale partial melting and/or fractionation processes (Floyd 1989, Fisk *et al.*, 1989 and Baxter 1990). However many of the most incompatible elements, such as the Large Ion Lithophile Elements (LILE) (K, Ba, Rb and Sr), are potentially susceptible to sea water alteration. The High Field Strength (HFS) elements (*i.e.* Zr, Y, Nb, Ti *etc.*.), however, are largely unaffected by these processes (Pearce & Cann 1973, Baxter 1990 and Fisk *et al.*, 1989) and as such these were preferred when interpreting these lavas to avoid possible alteration effects, which are known to occur. It was noted that at several of the Rodrigues Ridge sites the HFS elements (notably Y, Zr) displayed distinctly anomalous behaviour (see section 6.4). Trace element ratios are used to examine the source(s) of the lavas and to look at how partial melting processes have affected the chemistry of the melts (section 6.8). As far as possible the ratios were selected from lavas for which isotope data had been obtained, *i.e.* with around 8% MgO.

Ratios of a highly incompatible element to a moderately incompatible element such as Zr/Y are useful as an indicator of the degree of partial melting and mantle composition (Pearce & Norry 1979). For example, high ratios of a LREE/HREE (or Y) in basaltic rocks can reflect the presence of garnet in the source and hence indicate the depth of melting. Since HREE and Y are strongly partitioned into garnet, as the depth of melting increases, partial melting in the presence of garnet becomes more likely. The resulting lavas will show greater Ce/Y ratios the deeper they originated, as long as garnet remains within the residue. In the absence of garnet Y has a greater bulk partition coefficient than Ce (principally controlled by clinopyroxene); so reducing the degree of partial melting will therefore, also result in a rise in the Ce/Y ratios (Ellam 1992).

Table 46 (page 206) shows mean incompatible element ratios for Rodrigues Ridge basalts with between 7-9% MgO, in comparison to other geographically related areas (see fig. 1 and table 3). [Table 3 (page 14) shows the same data for *all* the Rodrigues Ridge lavas irrespective of their MgO content]. In tables 3 and 46 it can be seen that both the low MgO and high MgO groups of RR2 display characteristics similar to N-Type MORB. MORB samples from RR13 and the Triple Junction have very similar ratios with the exception of the Ba/Y and Ba/TiO_2 at RR13 which is enriched in Ba as a consequence of alteration. Between RR2 and RR9c (*i.e.* westwards along the Ridge) there is a steady increase in all ratios to values similar to those of Réunion *i.e.* to OIB values (fig. 242). Including samples from the Mascarene Islands, the CIR and the Marie Celeste F.Z. emphasises this trend on fig. 242 (and figs. 244-247). Two localities show aberrantly high values: Rodrigues Island and the unusual and altered lavas of RR10. Between RR9c and RR12d the increase with longitude continues for Ba/TiO_2 only. All other ratios except Zr/Ti show RR10 as having the highest values. Zr/Ti at RR10 is lower than at all other sites apart from RR2 reflecting the high values of TiO_2 found at RR10. Zr/Y, Ba/Y, Ba/TiO_2, Nb/Y, Nb/Zr and Ce/Y at RR10 all show values greater than those found on Réunion,

but not as high as those quoted for OIB (Sun & McDonough 1989). In general the lavas of RR10 are enriched in the most incompatible elements (LREE, Nb, K_2O, Th, U and Rb) compared to Y and the HREE. At RR12d all the incompatible elements are enriched, especially the highly incompatible elements. This enrichment has resulted in a decrease in the trace element ratios mentioned above. Where source variation can be ruled out as a cause, high ratios of highly incompatible to moderately incompatible elements (*e.g.* Zr/Y) are considered indicative of small degree partial melts (Rollinson 1993). The ratio of two similarly (highly) incompatible elements (*e.g.* Zr/Ti) reflect source variations except where the amounts of partial melting are small. RR10 has high Zr/Y associated with Zr/Ti similar to those found at the eastern sites. This together with enrichment in the immobile highly incompatible elements suggests that the lavas are the product of a lower degree of partial melting than the other Rodrigues Ridge sites.

Figure 242

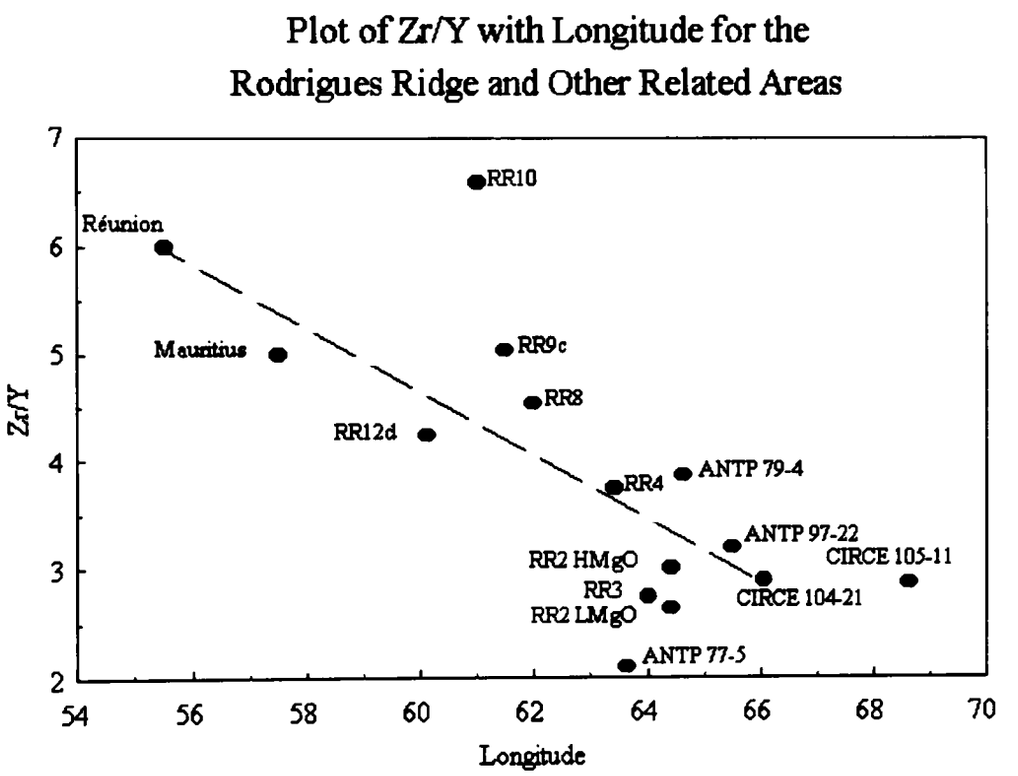

Sources of data: CIR data from Mahoney *et al* (1989) all other sources as in table 46.

Table 46 Incompatible Element Ratios for the Indian Ocean, Deccan Traps and Rodrigues Ridge Values for 8% MgO

Lava Group	Zr/Y	Ba/Y	Zr/Ti	Ba/TiO_2	Nb/Y	Nb/Zr	Ce/Y
Leg 115							
706C Upper	5.5	2.7	0.0128	38	0.50	0.0909	1.084
706C Lower	2.6	1.9	0.0092	42	0.26	0.1031	0.417
707C Upper	1.42	0.72	0.0069	21	0.10	0.0833	0.005
707C Lower	2.39	0.99	0.0094	23	0.18	0.0714	0.220
713 Upper	2.50	1.35	0.0109	35	0.17	0.0714	0.251
713 Lower	2.10	1.03	0.0087	26	0.15	0.0714	0.147
715 low MgO	3.3	3.4	0.0100	62	0.39	0.1205	0.458
715 high MgO	3.0	3.4	0.0095	64	0.40	0.1333	0.407
General MORB	3	0.5	0.0125	20	0.06	0.0200	N/D
N-Type MORB	2.6	0.23	0.0097	5	0.08	0.0314	0.268
E-Type MORB	3.3	2.59	0.0122	57	0.38	0.1136	0.682
CIR							
Triple Junction	3.56	0.78	0.0133	19	0.09	0.0224	0.429
RR13	2.69	2.01	0.0117	49	0.11	0.0452	0.391
238 Argo FZ	1.2	0.18	0.0090	6	N/D	N/D	N/D
OIB	9.7	12.07	0.0164	122	1.66	0.1724	2.759
Seychelles	3.23	15.41	0.0078	227	0.45	0.0789	1.088
Réunion	6	5.6	0.0122	70	0.87	0.1333	1.582
Mauritius	5	8	0.0119	95	0.65	0.1351	--
Rodrigues	6.0	18.01	0.0161	312	1.48	0.2439	1.889
Rodrigues Ridge:							
RR2 High MgO	3.01	0.62	0.0116	15	0.01	0.0020	0.347
Low MgO	2.94	0.44	0.0128	11	0.01	0.0049	0.318
RR3	2.64	1.32	0.0116	34	0.10	0.0367	0.336
RR4	3.75	3.83	0.0131	81	0.01	0.0024	0.659
RR8	3.95	2.01	0.0098	30	0.02	0.0051	0.640
RR9c	5.05	5.37	0.0139	88	0.02	0.0044	1.119
RR10	6.02	11.04	0.0113	125	0.10	0.0172	1.868
RR12*	4.25	6.36	0.0218	197	0.59	0.1398	1.212
Deccan:							
Poladpur	4.0	3.9	0.0118	69	0.28	0.0714	N/D
Ambenali	3.8	2.0	0.0099	32	0.29	0.0833	N/D
Mahabaleshwar	4.5	4.3	0.0105	59	0.49	0.1075	N/D

Sources of data; Leg 24 lavas from Engel *et al.*, 1974, Rodrigues Island from Baxter *et al.*, 1985, Mauritius and general MORB from Baxter 1990, Réunion from Upton & Wadsworth 1972 and Fisk *et al.*, 1988, Deccan lavas from Cox & Hawkesworth 1985, Seychelles from Devey & Stephens (1991) and Devey & Stephens (1992), E-type and N-type MORB and OIB from Sun & McDonough 1989, Triple Junction lavas from Price *et al.*, 1986 and leg 115 lavas from Backman *et al.*, 1988.

* No analyses of RR12d basalt with 7-9% MgO are available, this value is an average for the site.

Locations for samples given in table 46 can be found in fig. 1.

Figure 243

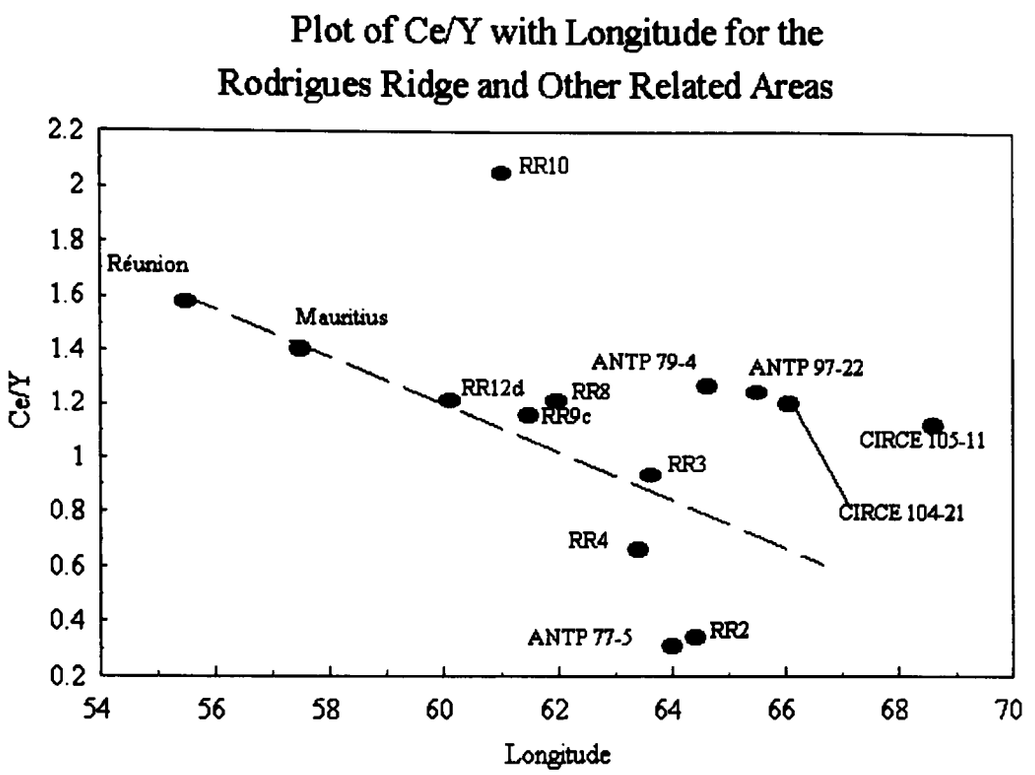

Figure 244

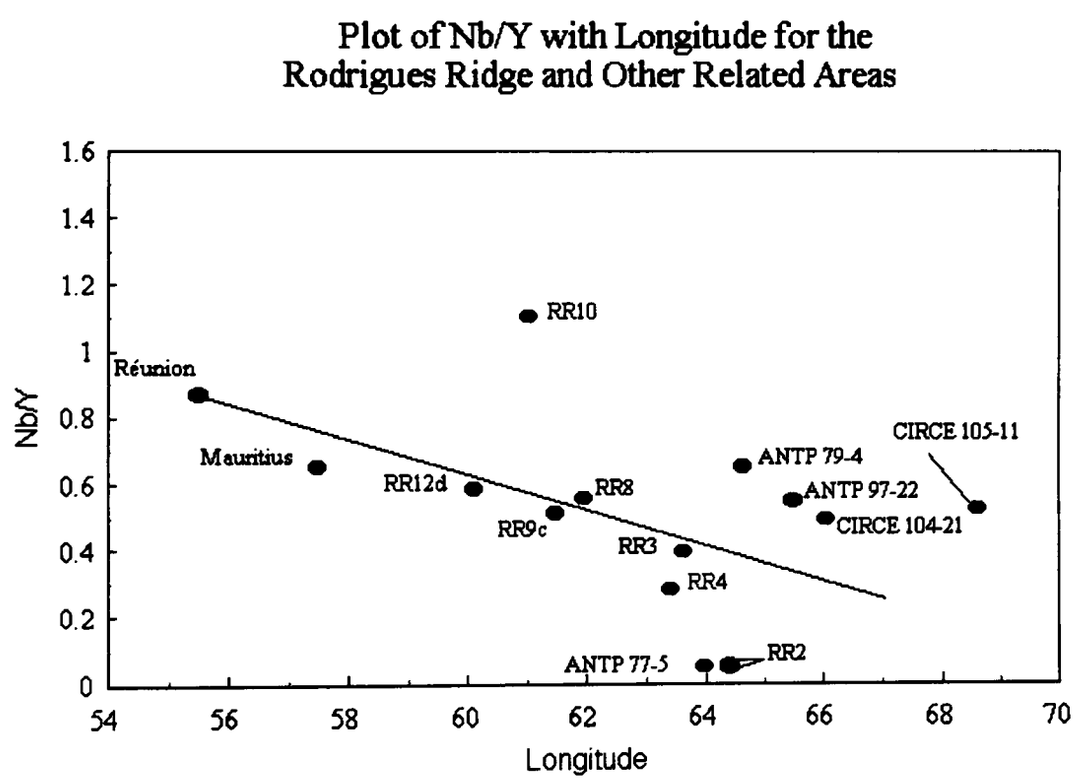

Sources of data: CIR from Mahoney *et al.* (1989) all other sources as in table 46.

Figure 245

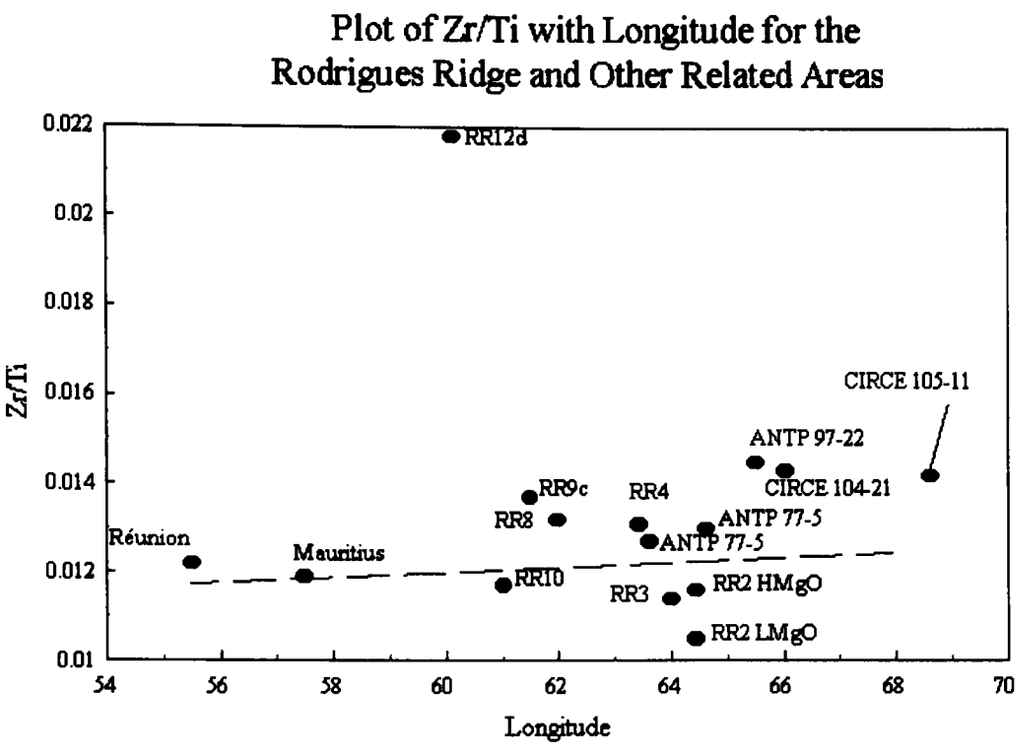

Figure 246

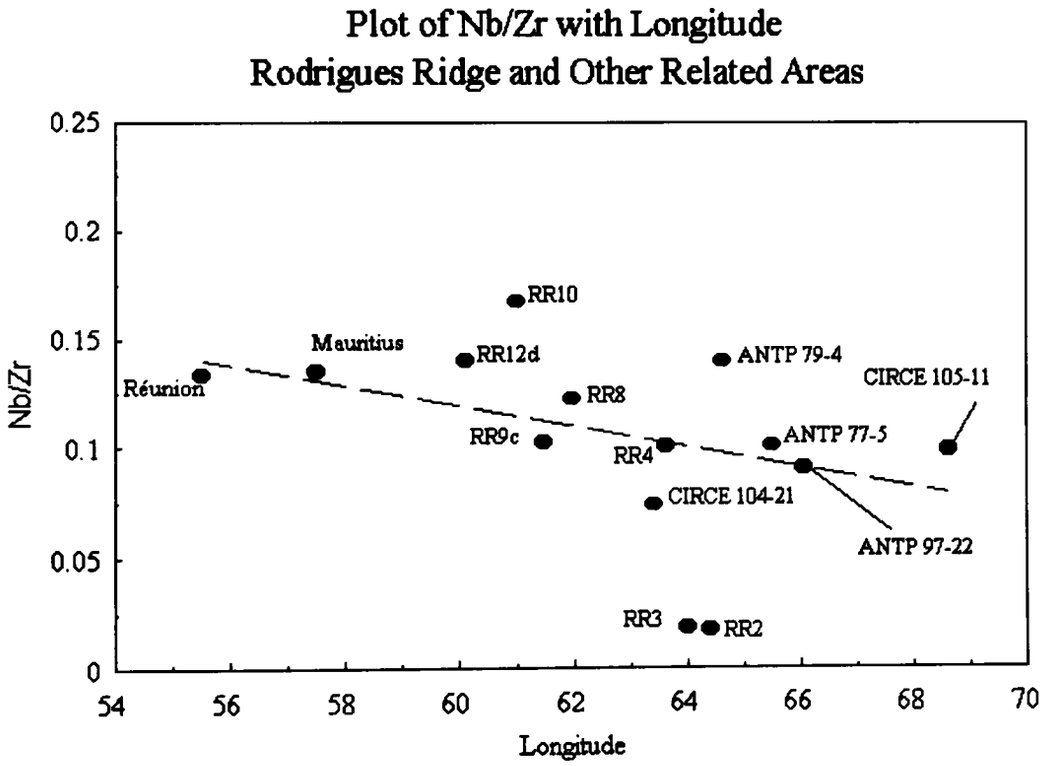

Sources of data: CIR from Mahoney *et al.* (1989) all other sources as in table 46.

Plots of Zr/Y and Zr/Ti with MgO for RR2

Figure 247

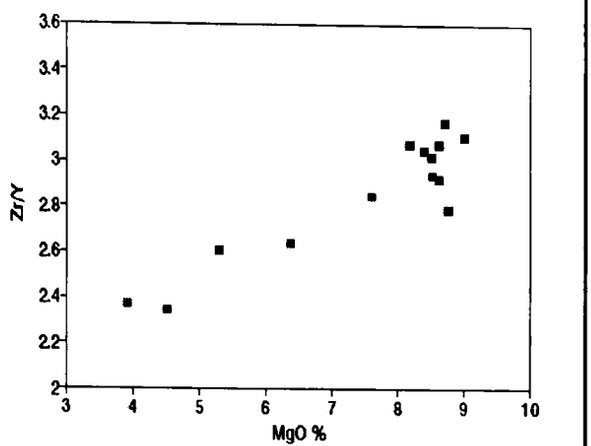

Figure 248

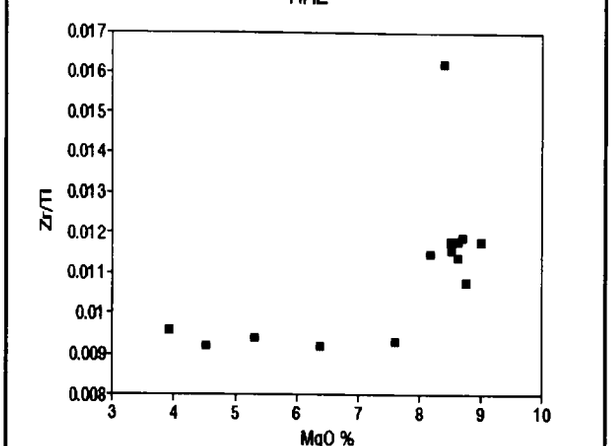

Plots of Zr/Y with MgO for RR3 and RR4

Figure 249

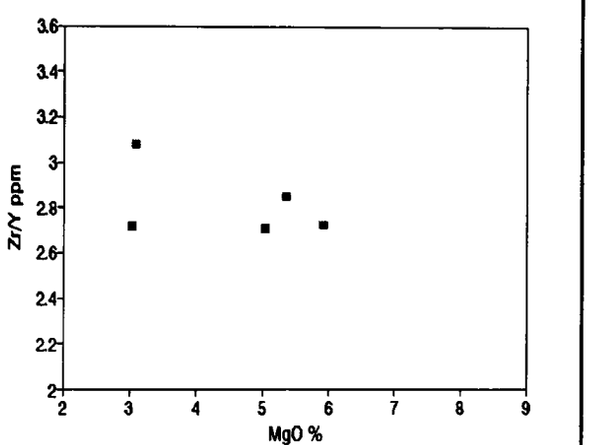

Figure 250

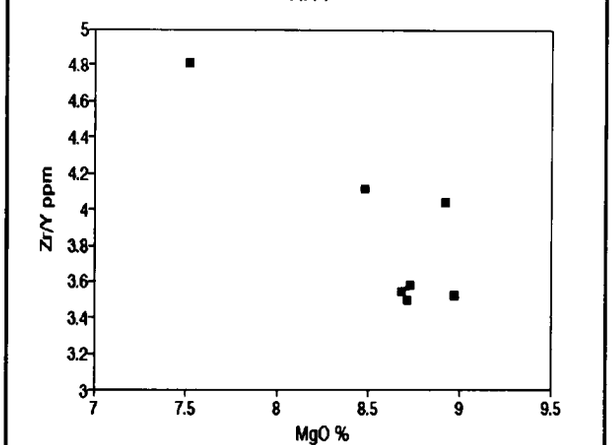

While ratios of two similarly highly incompatible elements reflect source variations, ratios of a highly incompatible and a moderately incompatible element (*eg.* Zr/Y) are also influenced by variations in partial melting. At RR2 and RR3 the Zr/Y ratios are the lowest of all the Rodrigues Ridge sites (2.343-3.104 and 2.711-3.080 respectively) (figs. 248 and 250) suggesting that these sites experienced either the greatest degree of partial melting or that the source had the lowest Zr/Y ratio of the Rodrigues Ridge sites. Typically MORB has Zr/Y values in the range 2.6-3.3 (Sun & McDonough 1989). Using only samples with 7-9% MgO (table 46) does not affect this observation, but should reduce the effects of apparent fractionation of either of these elements. At these sites however, a relationship between

Zr/Y and MgO was observed, suggesting that the ratio may have been influenced by the same process responsible for the aberrant behaviour of the REE, Y and Zr. There is a decrease in Zr/Y with MgO at RR2 which is difficult to explain since the bulk partition coefficient for Y is similar or higher, if clinopyroxene is on the liquidus, than that of Zr (appendix 1). The significance of both the high MgO and low MgO groups plotting along a continuous trend, controlled by buffering of Zr, is not clear (figs. 248 & 249). One possibility is that both groups were derived from a parental melt whose composition was similar to that of RR2.12b *i.e.* Zr *ca.* 89 ppm, Y *ca.* 29 ppm, TiO_2 *ca.* 0.9%. The two groups were either separated physically, for example by being injected into different magma chambers, or by time, for example by being injected into a single high-level magma chamber at different times. The high MgO group showing limited fractionation of olivine and plagioclase, while the low MgO group fractionated olivine + plagioclase ± clinopyroxene. Coincident with fractionation the melts were subject to an increase in the oxygen fugacity, possibly as a result of percolating fluids, resulting in the enrichment of U (± P_2O_5). There is little information available on the effects of increased oxygen fugacity on the partition coefficients of Zr and the REE, but Irving (1978) suggests that decreasing oxygen fugacity brings about a systematic decrease in the partition coefficients of the REE. If the converse is also true and the partition coefficients of the REE increase with increasing oxygen fugacity then this may help to explain the buffering of the REE and possibly of the incompatible elements like Zr at RR2.

Plots of Zr/Y with MgO for RR8 and RR9c

Figure 251

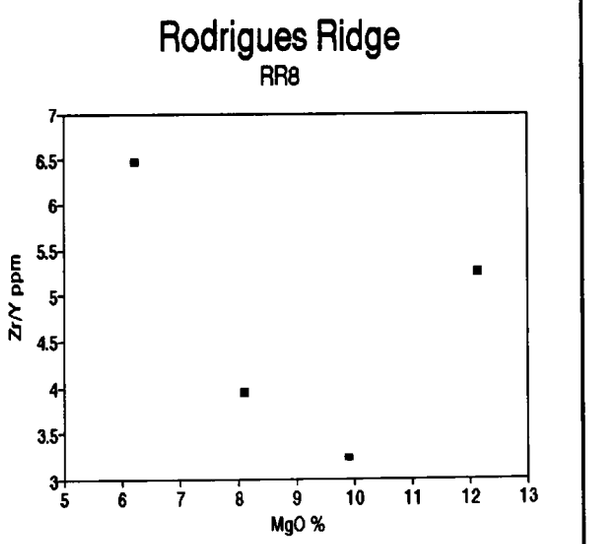

Figure 252

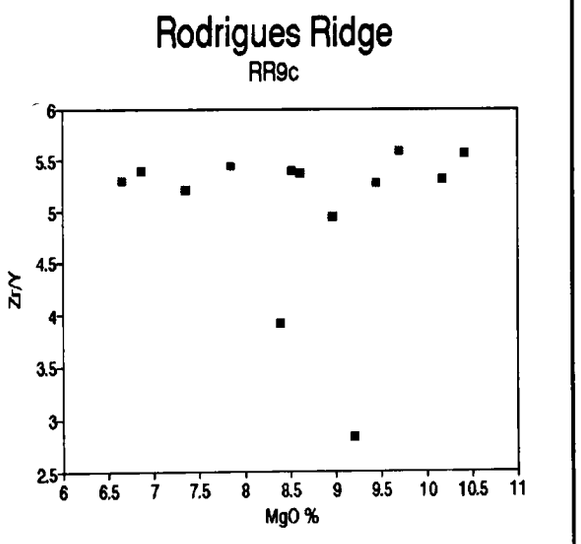

An alternative explanation for the high levels of P and U in these lavas is that they have assimilated a small amount (*ca.* 5%) of altered MORB. Fig. 255 shows the effect of adding 1 and 5% of RR13b.(8)a (a severely altered MORB sample from the flank of the Mauritius fracture zone). At 5% assimilation

Plots of Zr/Y with MgO for RR10 and RR12d

Figure 253

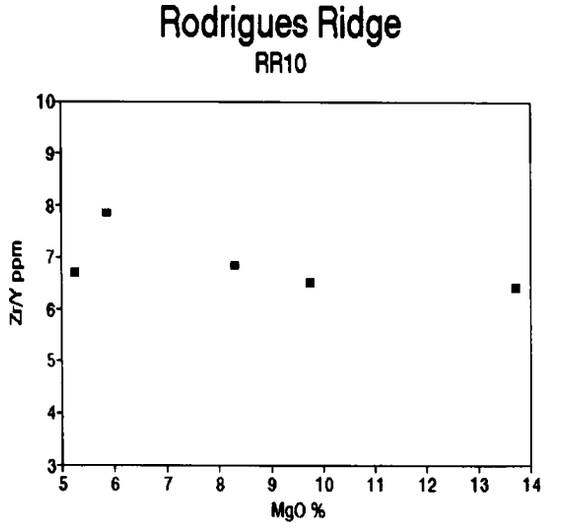

Figure 254

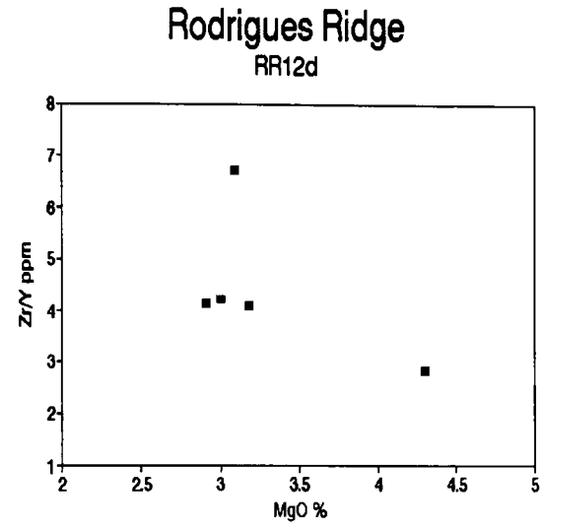

of altered MORB a high MgO group lava from RR2 develops a signature similar to that of the RR3 lavas. However, the isotope signature for such a lava would differ substantially from that found at RR3.

At RR3 and RR10 both Zr and Y show strongly buffered trends (figs. 249 and 253), resulting in the gentle increase in the ratio with decreasing MgO. Zr and Y are both incompatible in the mineral phases present (olivine, plagioclase and chrome spinel). The uniformity of Zr/Y (fig. 253) with MgO at RR9c, reflects the similar partition coefficients of both elements in olivine. The possible fractionating phases which could cause the buffering of Y, Zr and REE have already been discussed under the section on RR3. Of the remaining minerals which commonly influence basalt geochemistry only garnet could cause the buffering of Y, Zr and the REE observed at RR3. (Clinopyroxene could cause buffering in some of these elements but it is not capable of partitioning the REE except at mantle temperatures and pressures see section 6.8). Garnet is a high pressure mineral which would not fractionate from a low pressure MORB-like melt. Equally it is unlikely that residual garnet was present within the source region for the RR3 lavas since they are depleted in the LREE. Residual garnet in the mantle results in the enrichment of the LREE relative to the HREE. Source heterogeneity influences Zr/Y, but this cannot explain the linear trends with MgO which are observed at RR2, RR3, RR4, RR9c and RR10 (figs. 248, 250, 251, 253 and 254) but not at RR8 and RR12d (figs. 251 and 254). The Zr/Y ratio at RR4 is significantly higher than at the more easterly sites, 3.525-4.809. Here (fig. 251) it increases sharply with decreasing MgO reflecting the greater incompatibility of Zr compared to Y (appendix 1). There is no evidence of the buffering of Zr, (REE) or Y which is observed at RR3 and to a lesser degree at RR2.

At RR10, Zr/Y is the highest of all the Rodrigues Ridge sites (fig. 254), possibly as a result of reduced partial melting close to the end of the main body of the Rodrigues Ridge. Reduced partial melting is

Figure 255a

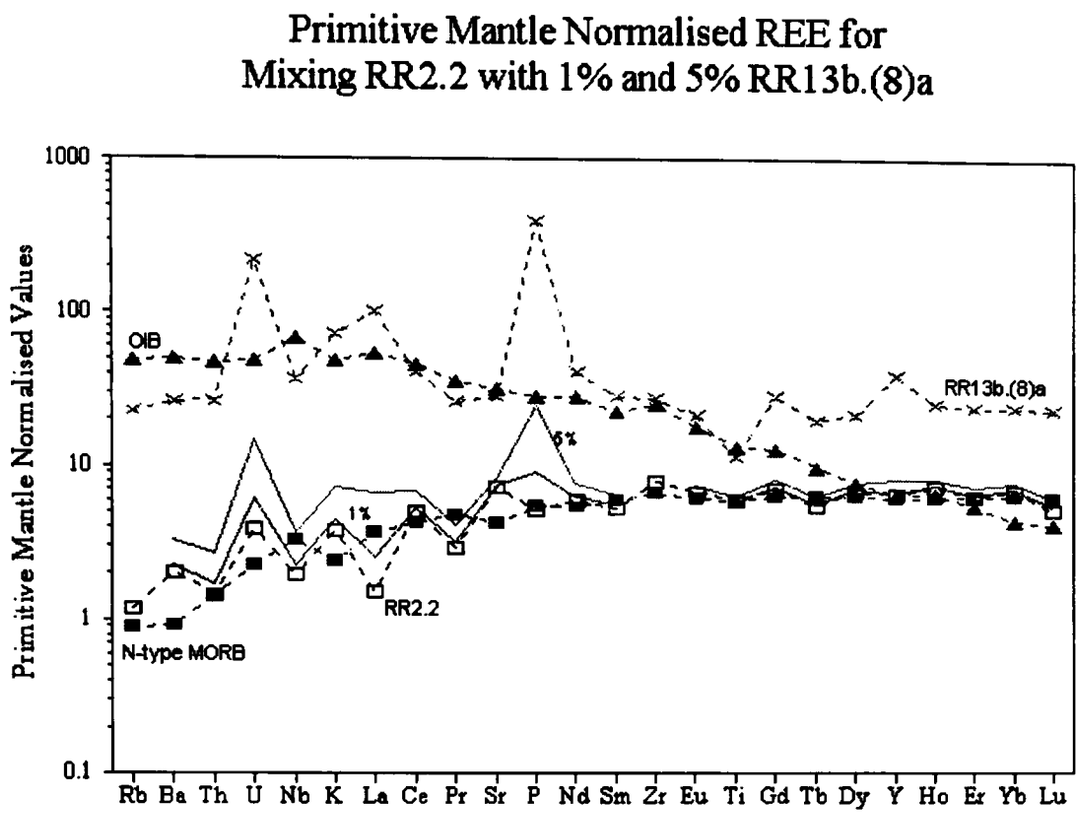

Figure 255b

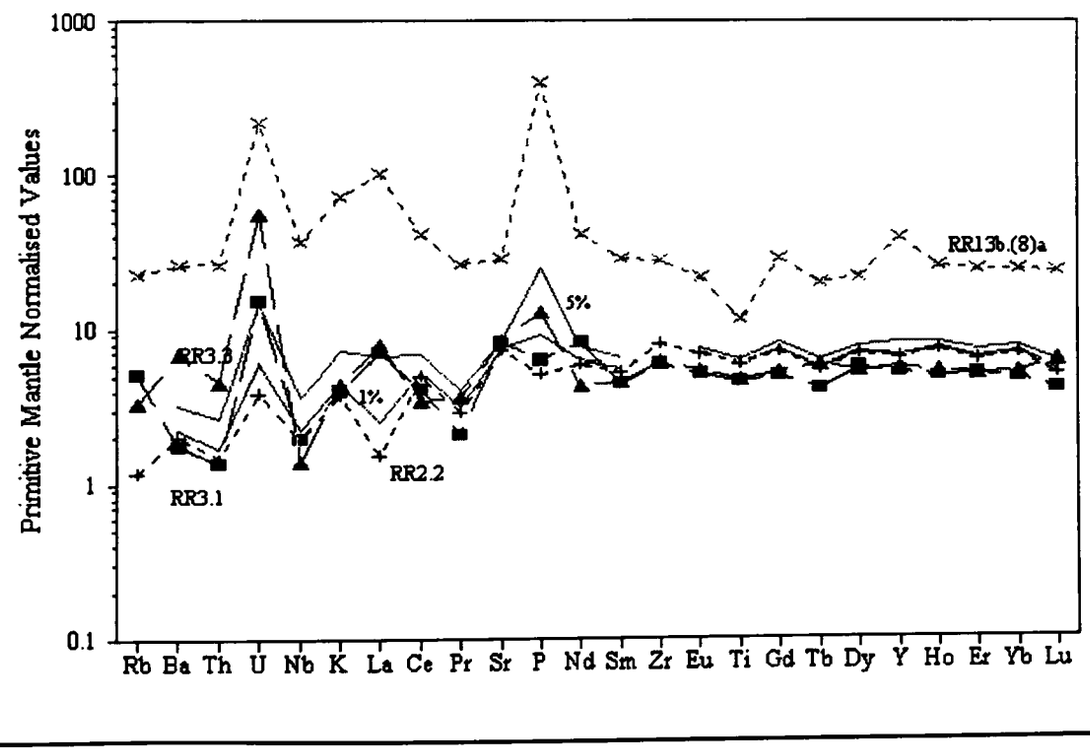

also observed on mid-ocean ridges close to major fracture zones (Langmuir 1990). Just west of RR10 the Rodrigues Ridge is cut by a major fracture zone (A) which may well be acting as a barrier to magma migration along the ridge, as do fracture zones on mid-ocean ridges (Rabinowicz *et al.*, 1993),. This produces basalts which are enriched in TiO_2 and K_2O, and tend to show higher FeO/MgO ratios than MORB recovered from areas of the spreading ridge away from fracture zones (Bryan 1979). Despite the high levels of many trace elements, reduced partial melting effects are not recognised at RR12 where the lavas are far more evolved than those at RR10.

Similar to Zr/Y, Ti/Zr shows buffered trends at RR2 (low MgO) and RR9c, steeply declining trends (with MgO) at RR3 and RR10 and no clear trends at the other sites. These steeply declining trends are counter to what might be expected from a basaltic melt, fractionating olivine, plagioclase, clinopyroxene and chrome spinel. In these minerals both Ti and Zr are incompatible, though mineral analyses conducted on these lavas suggests that Ti is only slightly incompatible in chrome spinel ($D_{Ti}^{Sp} = 0.46$). If magnetite ($D_{Ti}^{Mt} = 7.5\text{-}23.0$) appeared on the liquidus, the bulk distribution coefficient of Ti would increase dramatically. In this circumstance the observed, slightly buffered, trends would be expected. Although neither the trace element or major element models require magnetite on the liquidus, chrome spinel may be present at some sites.

6.7 Isotope-Trace Element Ratios

Ratios of the radiogenic isotopes of Pb, Sr and Nd were plotted against those trace element pairs which are resistant to the effects of seawater alteration. These radiogenic isotope ratios are not affected by the processes of melting and fractionation, hence plots of a radiogenic isotope ratio with a trace element ratio should differentiate whether, or to what degree, partial melting and fractionation are responsible for the variations observed in these lavas. Figs. 257-268 show a selection of radiogenic isotopes plotted against Zr/Y, Ce/Yb, La/Nb, Ti/Zr and Nb/Zr. On each diagram arrows indicate the direction in which the lavas would be driven with either increasing amounts of fractionation or increasing the degree of partial melting. There is no clear pattern of behaviour which affects all the ratios. Two of the trace element pairs (Ce/Yb and Zr/Y) show the samples falling into two groups: 1). RR2, RR3, RR4, CIR Marie Celeste F. Z. and RR13c; 2). RR8, RR9c, Mauritius and Rodrigues Island, Réunion, RR10 and RR12d. These two groups may represent a change from spinel to garnet lherzolite within the source region. The first group sampling spinel lherzolite, the second group garnet lherzolite. Equally the first group may represent the products of melting of a shallow depleted source, while the second represents an plume derived enriched source. The lavas tend towards enriched isotopic signatures further west, generally associated with an increase in the absolute concentrations of the most incompatible elements. Collectively the Rodrigues Ridge lavas form a gradual geochemical progression lying between lavas from the CIR (MORB basalts) and those from Réunion (OIB).

Figure 256

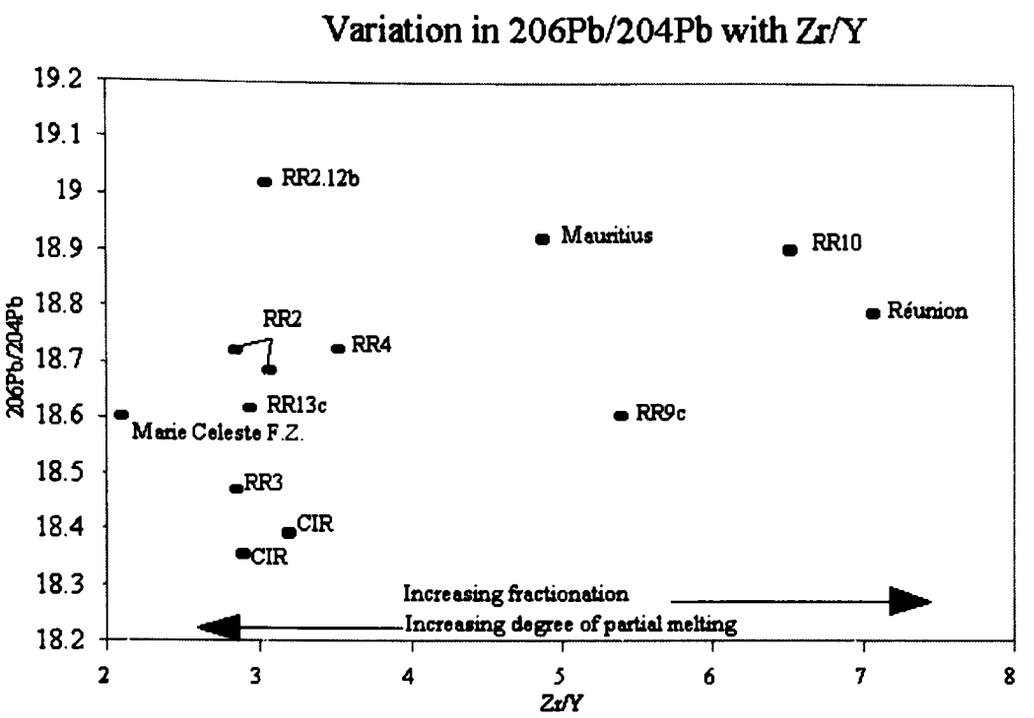

Figure 257

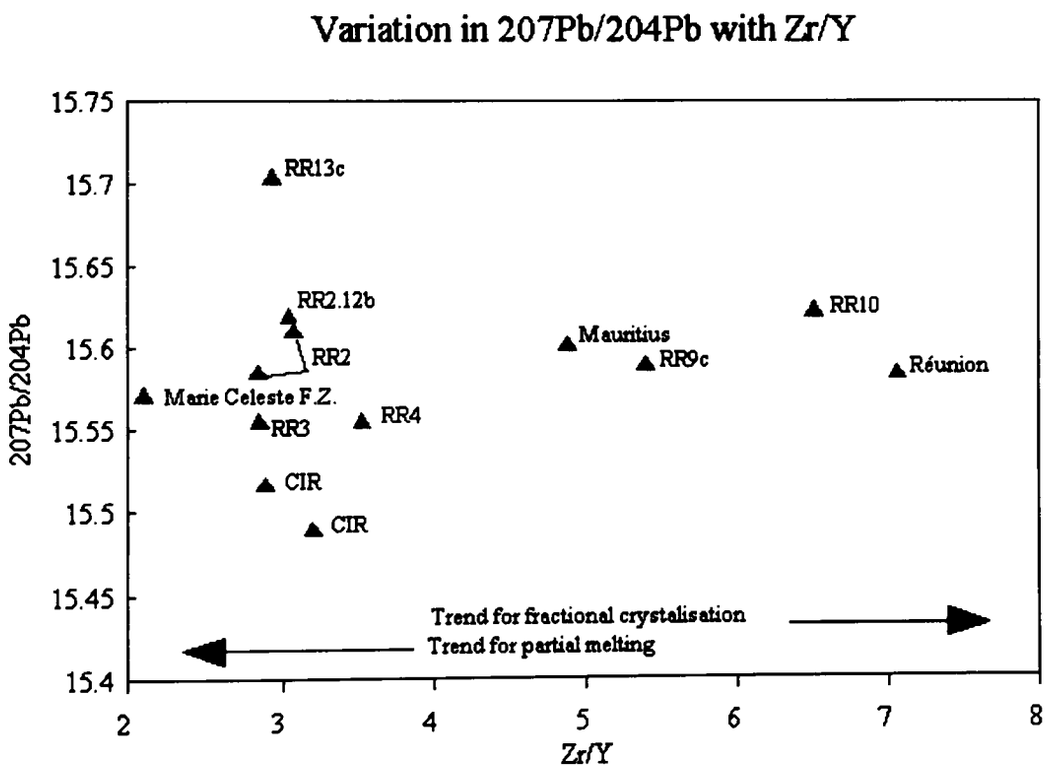

Sources of data: CIR from Mahoney *et al.* (1989) all other sources as in table 46.

Figure 258

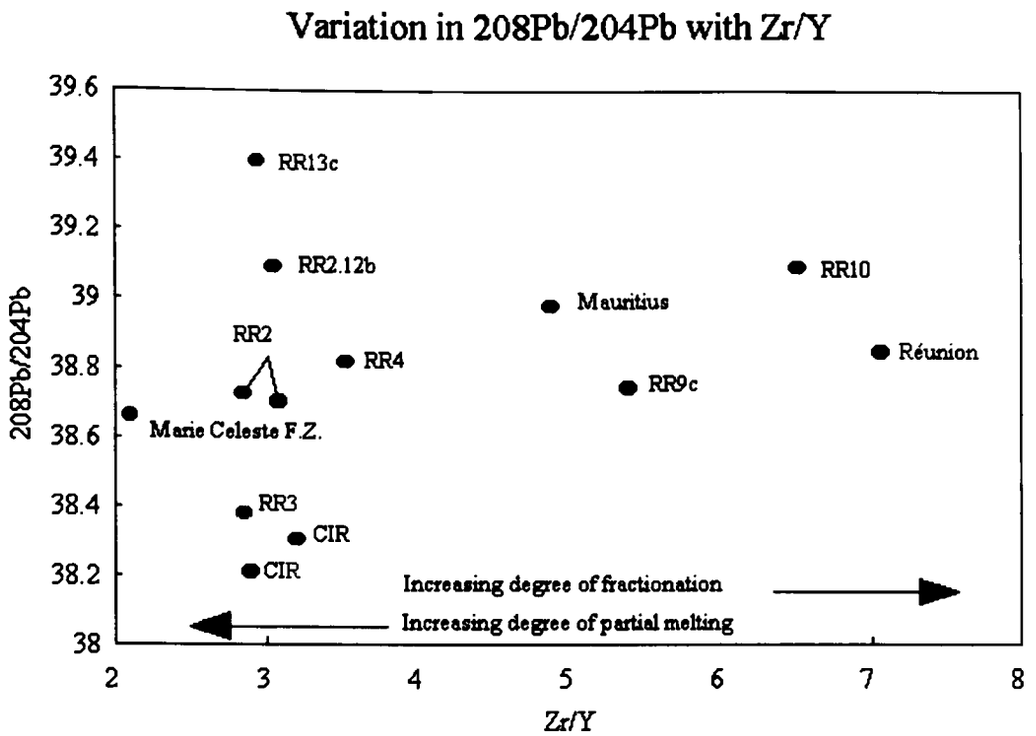

Figure 259

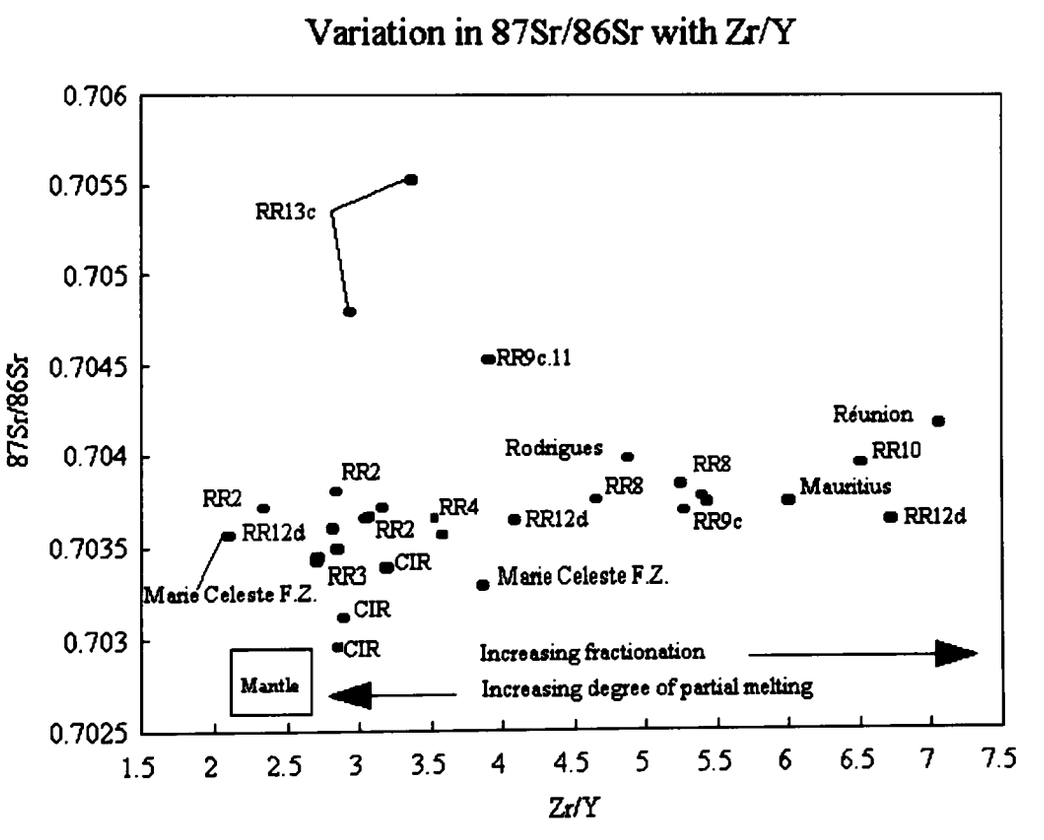

Sources of data: CIR from Mahoney *et al.* (1989) all other sources as in table 46.

Figure 260

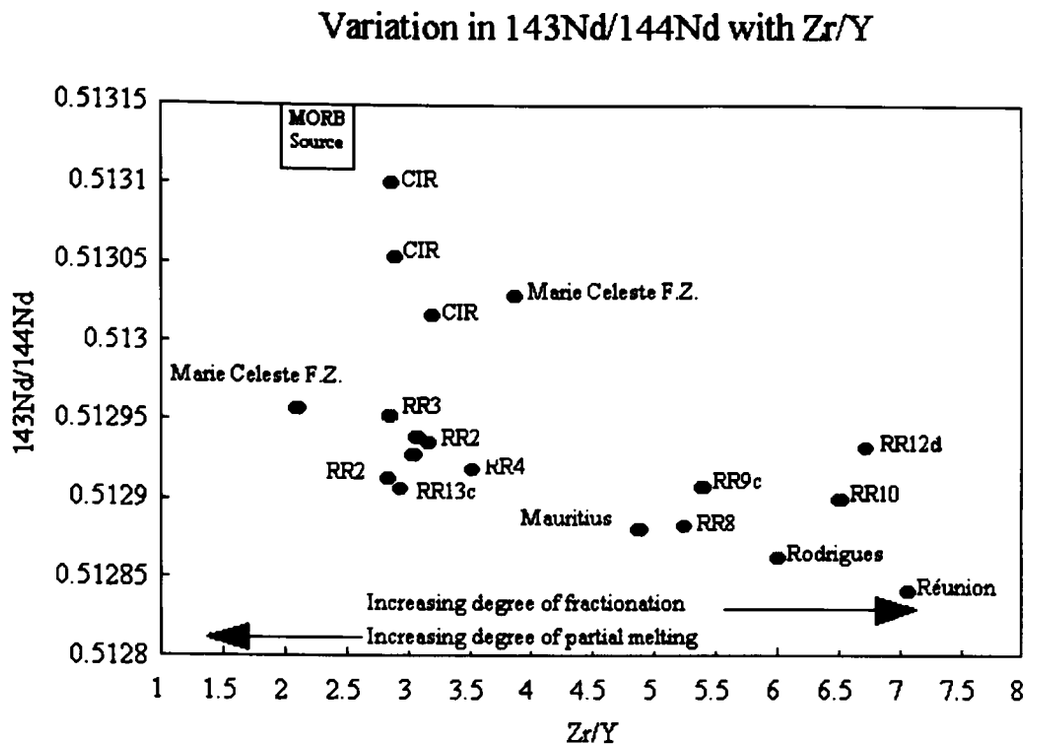

Figure 261

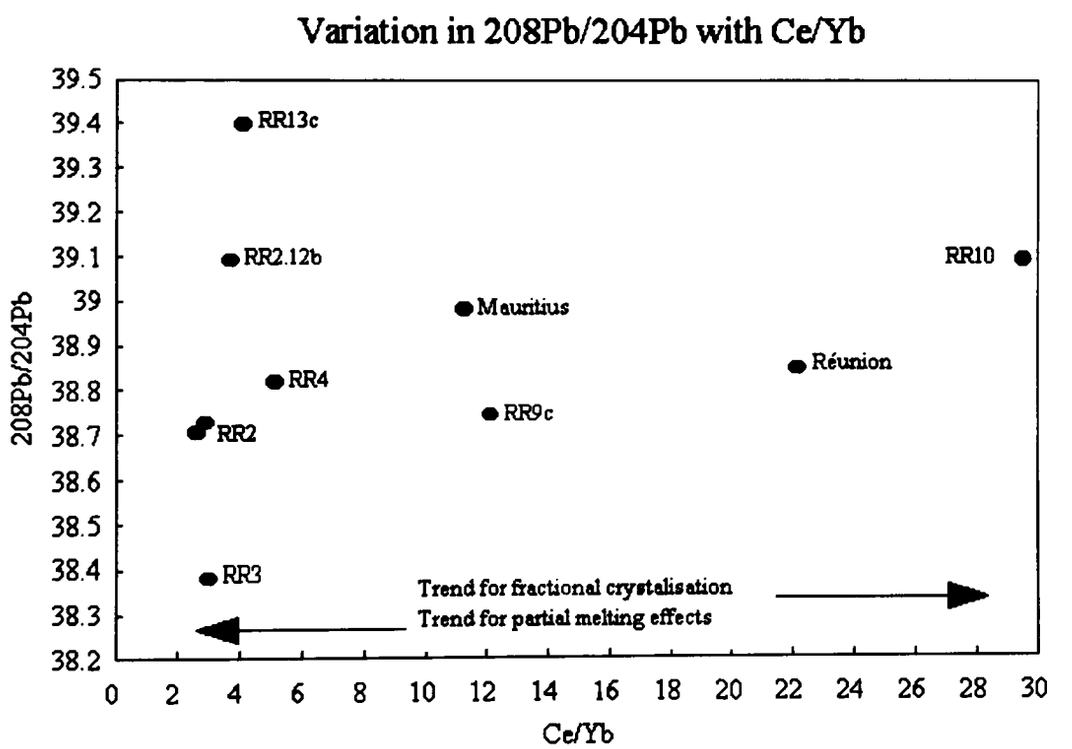

Sources as in table 46.

Figure 262

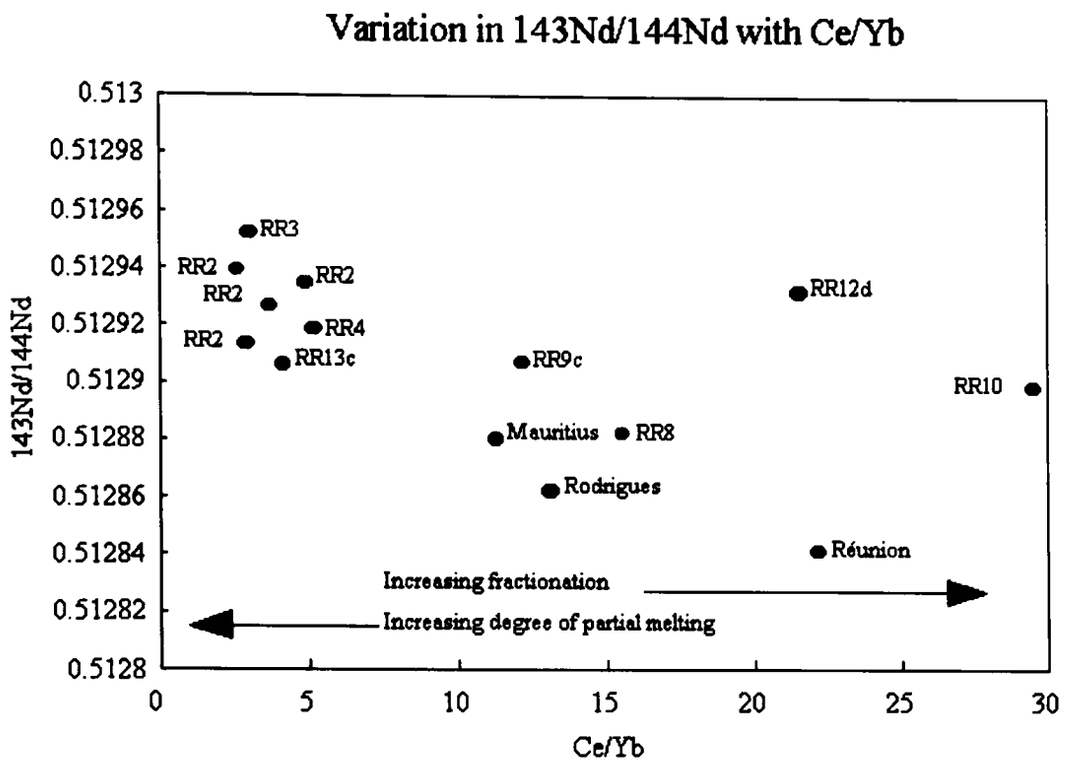

Figure 263

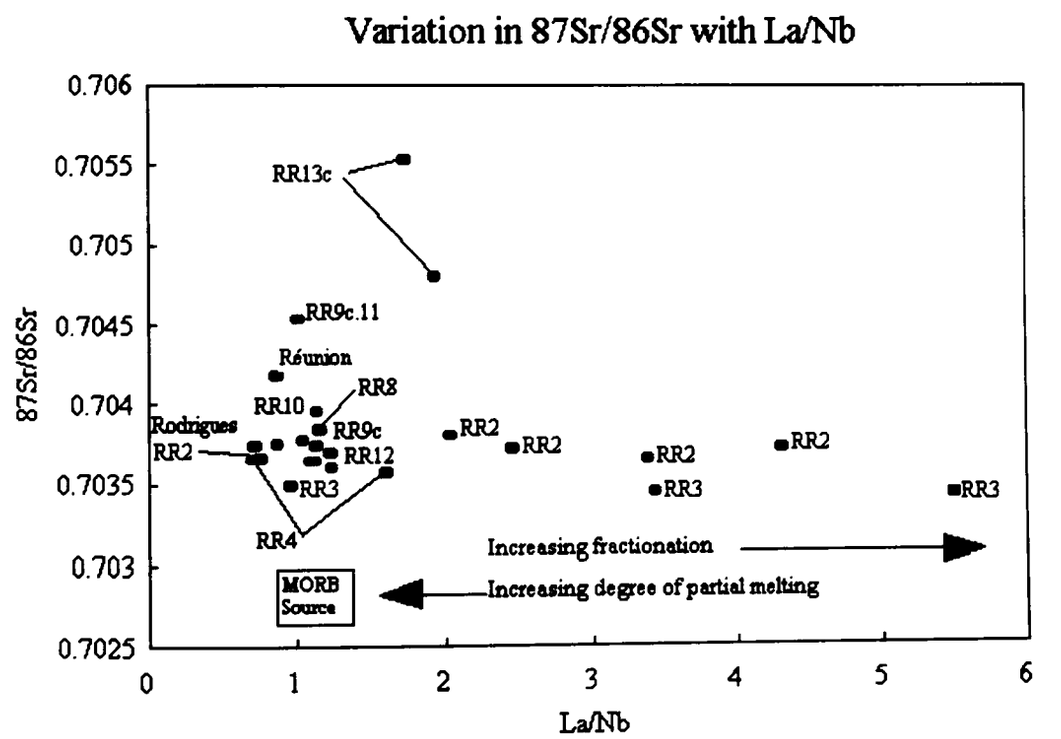

Sources as in table 46.

Figure 264

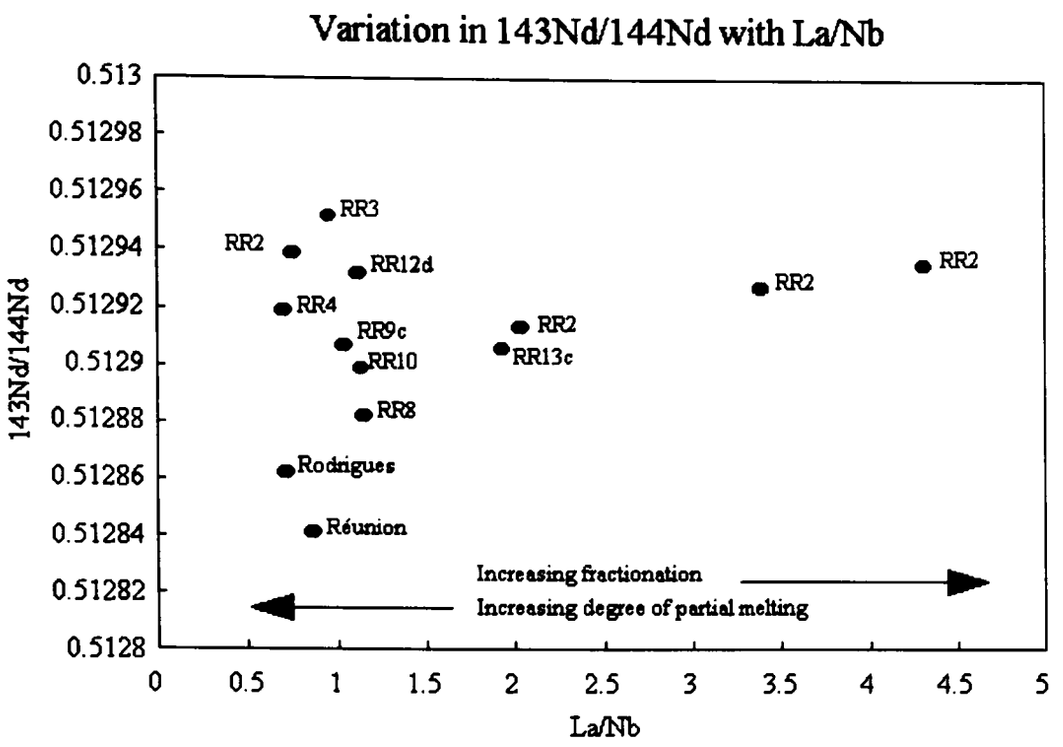

Figure 265

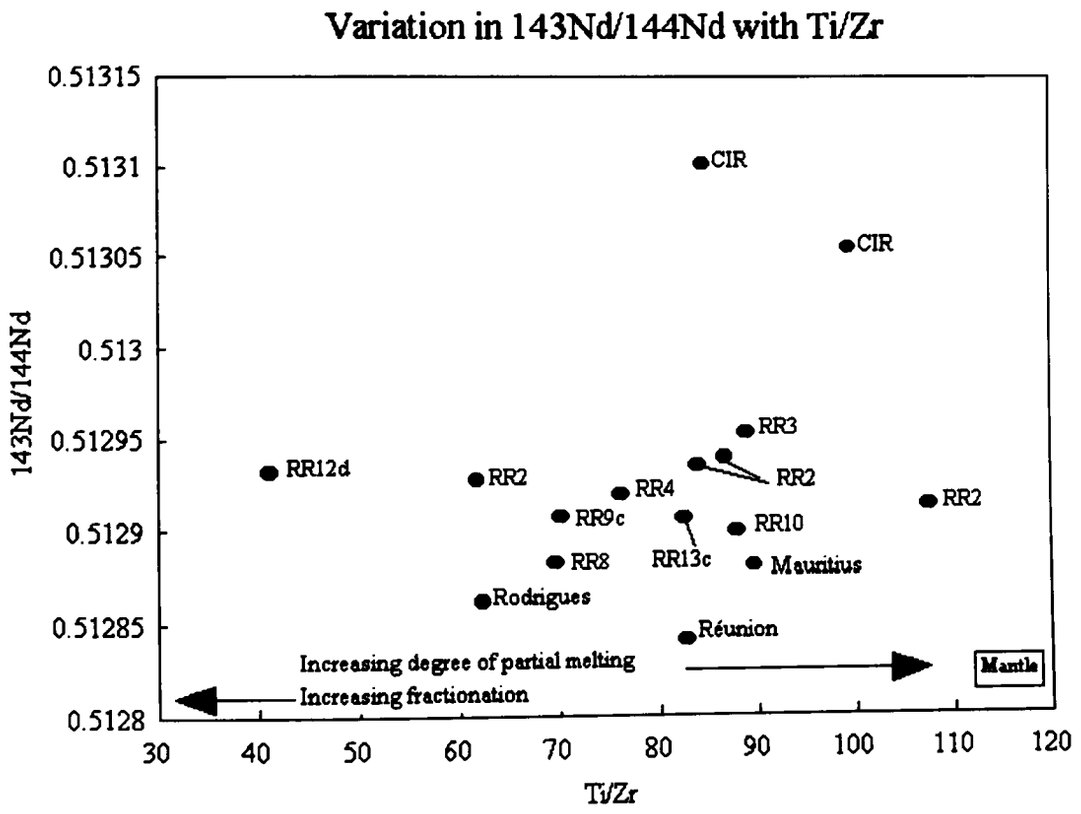

Sources as in table 46.

Figure 266

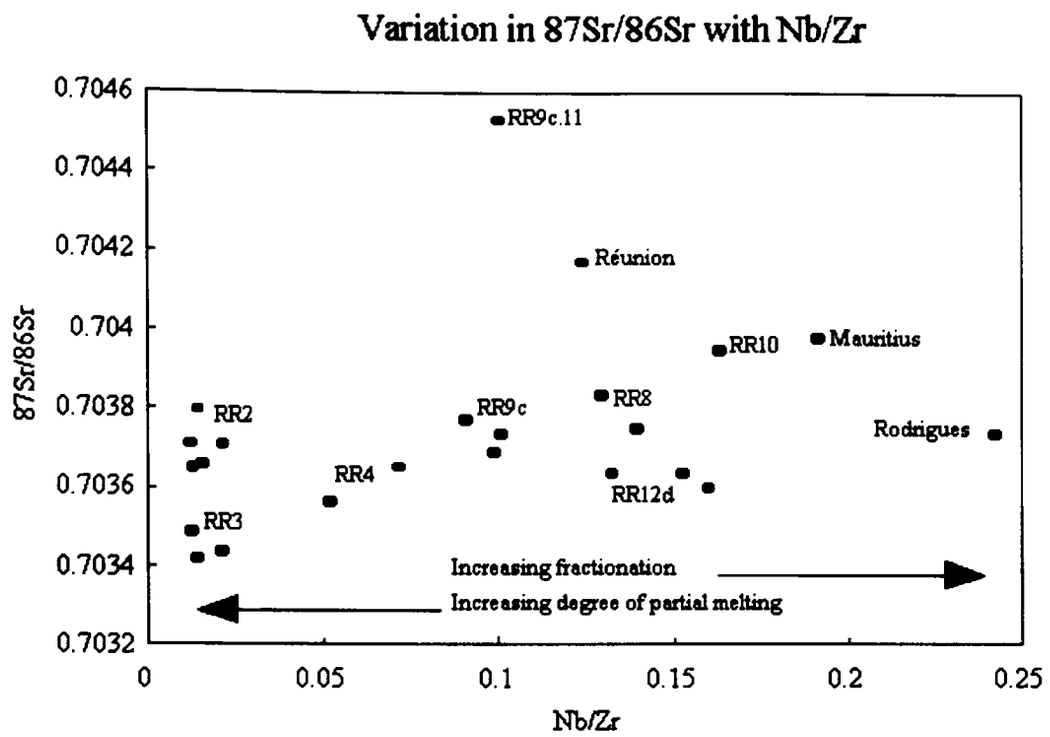

Figure 267

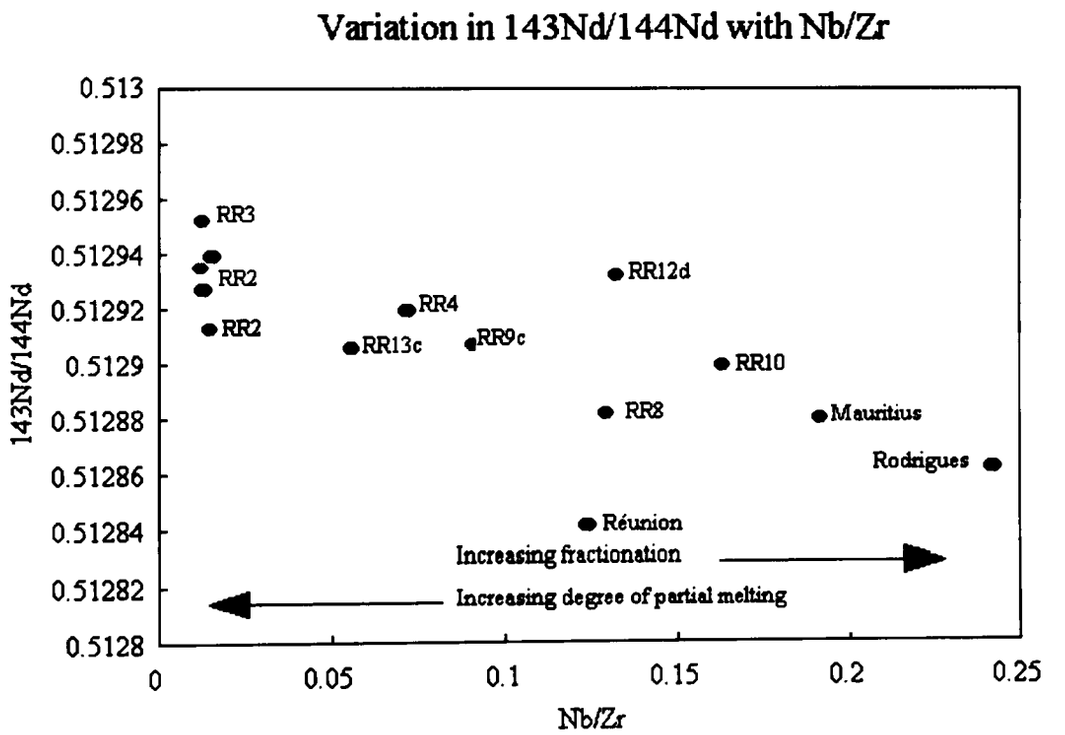

Sources as in table 46.

Figure 268

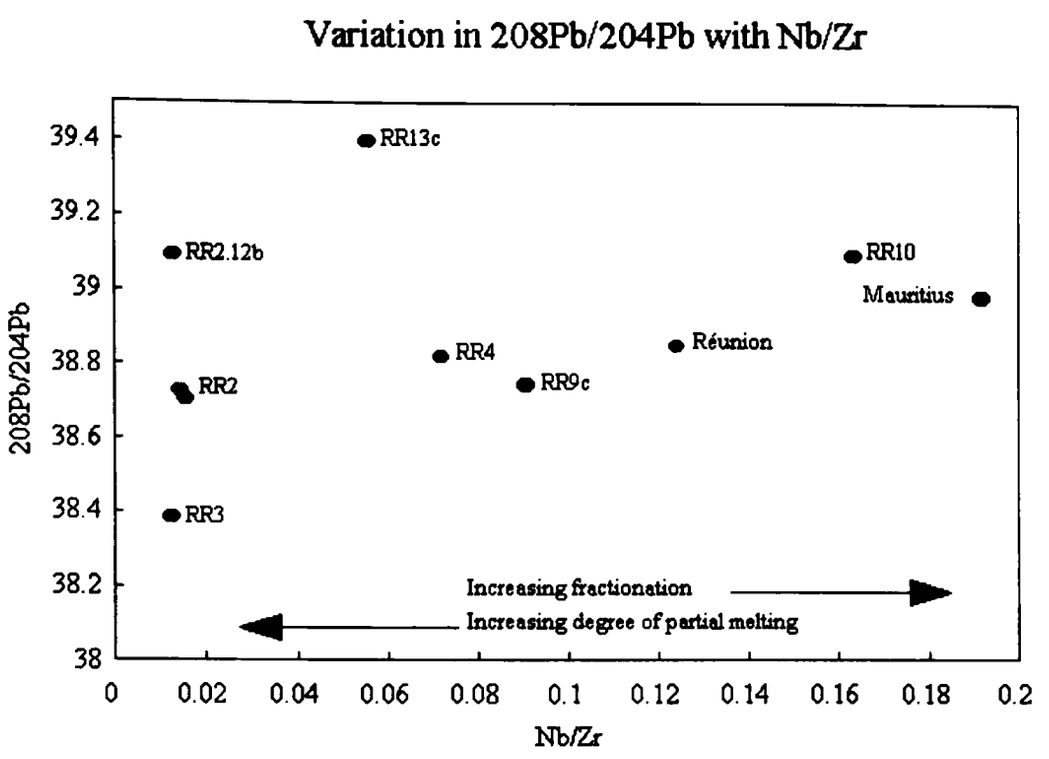

Sources as in table 46.

6.8 Melting Models

Many highly incompatible trace elements are susceptible to alteration. Individual samples at any one site display substantial variation due to both alteration and to variations in the partial melting history. Fractionation tends not to affect the ratios of these elements because their bulk partition coefficients are so low they always accumulate in the melt. In basaltic lavas, such those of the Rodrigues Ridge, K can be considered to be strongly incompatible as it does not readily enter any of the minerals present. It should be noted that K has a partition coefficient of 0.07-0.20 in plagioclase and Zr has a partition coefficient of 0.1-0.21 in clinopyroxene. The compatibility of K in plagioclase was not thought to be significant as the variation diagrams show steep increases in K_2O with declining MgO, indicating its incompatibility. As discussed later in this section, the partition coefficient of Zr in clinopyroxene may be even greater at mantle depths, suggesting that this may not be strongly incompatible in these lavas. Averaging the data for highly incompatible elements such as K reduces the effect that a few variably altered samples have at that site. Fig. 269 shows the linear relationship that is formed (after averaging) by plotting the ratios Nb/K against Nb/Zr. Although no Nb data are available for the CIR and Marie Celeste samples used in the isotope plots, a clear trend is present between RR2 and RR3 through to RR10 and Mauritius. On fig. 269 modelled batch melting lines are shown for primitive and depleted

mantle whose composition is that of a garnet or spinel lherzolite. The liquid concentrations, C_l in the batch melting models were calculated from the relationship:

$$\frac{C_l}{C_0} = \frac{1}{F + K_D - FK_D}$$

Where C_0 = the unmelted source concentration, F = the melt fraction and K_D = the bulk distribution coefficient.

The modelled batch melting lines have been drawn for 0.1%, 1%, 5%, 10% and 30% melting. Fig. 270 shows a similar plot for the ratios Zr/Y and Nb/Zr. Both of these figures clearly show that the compositions used are adequate to model the development of the MORB-like lavas at the eastern end of the Rodrigues Ridge, but not the Réunion-like lavas at the western end. These lavas are enriched in Nb/Zr and Nb/K, but depleted in Zr/Y when compared to the modelled trend produced by varying the degree of partial melting of a primitive mantle source. [The primitive mantle composition used for this model is that given by Sun & McDonough (1989) and the depleted mantle is that given by Wood (1979)]. It is, however, clear that the model involving garnet lherzolite has a much greater potential for modelling the observed behaviour at the western sites. The model is a simple Rayleigh melting model in which the melt is removed from the source once it is formed. In reality the melt will take sometime before it escapes the source region, during which it may react further with the surrounding solid phases. In this case the strongly incompatible trace elements will be preferentially enriched relative to the less incompatible ones, and to the major elements. In such models Zr, Ti and REE, and ratios like

Figure 269

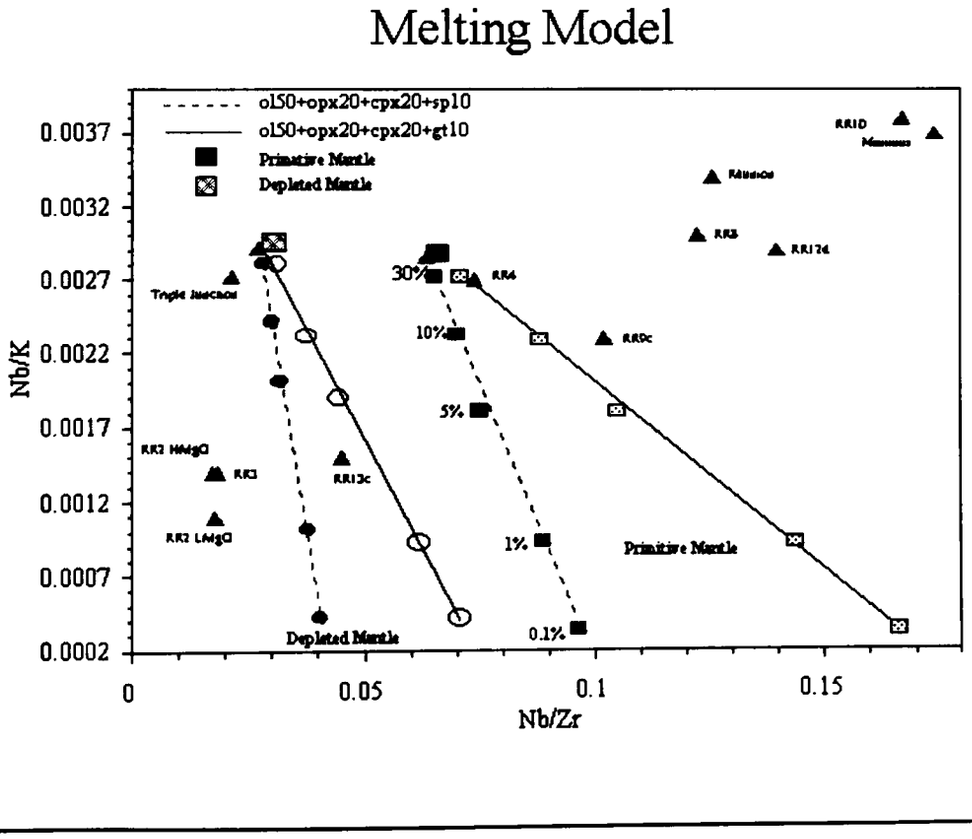

Sources: Sun & McDonough (1989), Wood (1979), other sources as in table 46.

Figure 270

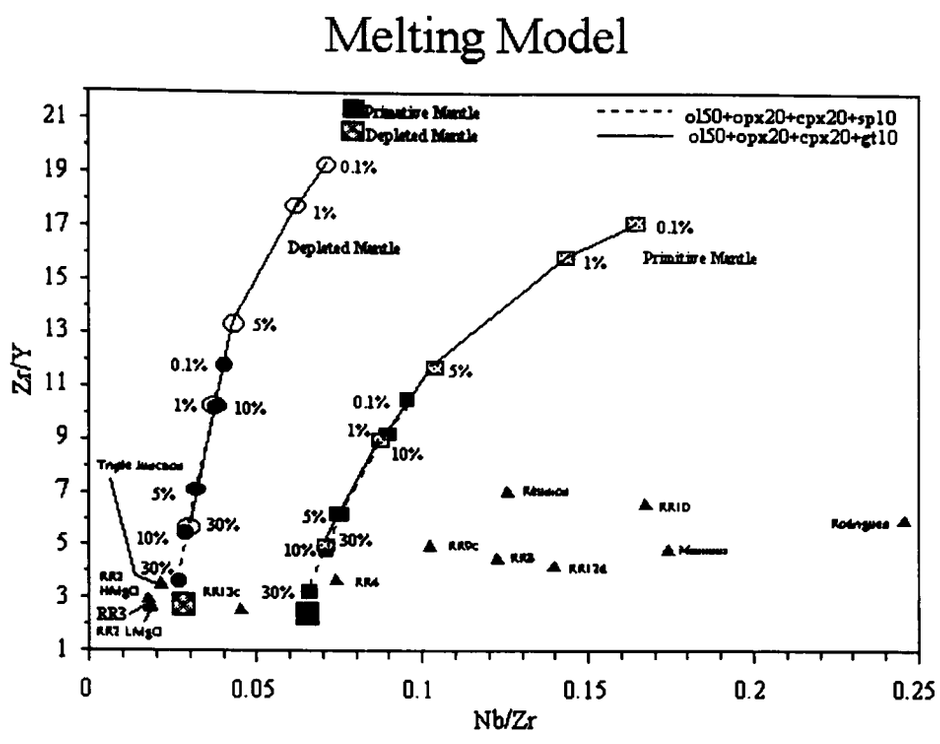

Sources: Figure 270 Sun & McDonough (1989), Wood (1979), other sources as in table 46. Figure 271 as for table 46.

Figure 271

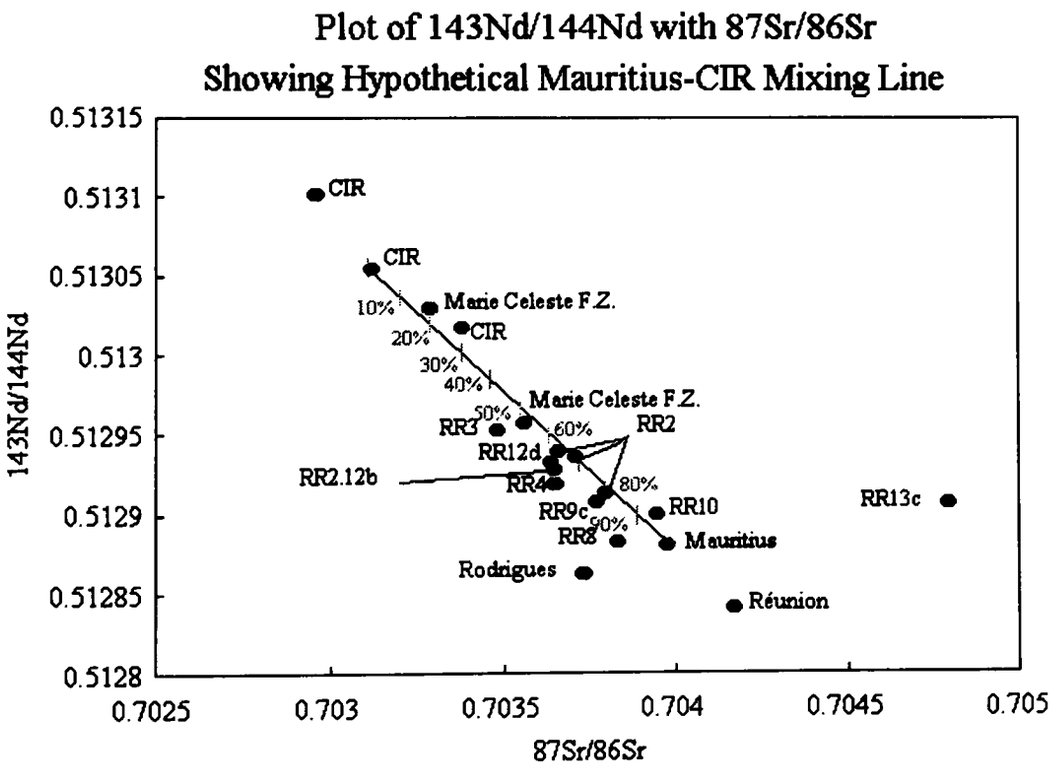

Figure 272

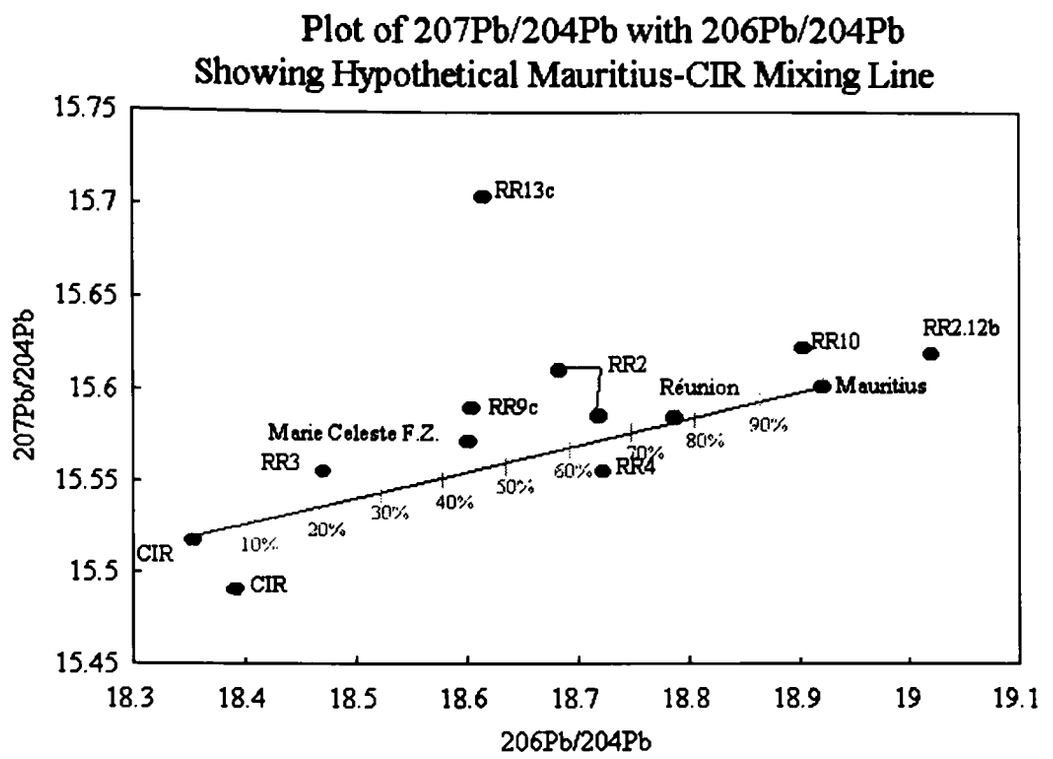

Figure 273

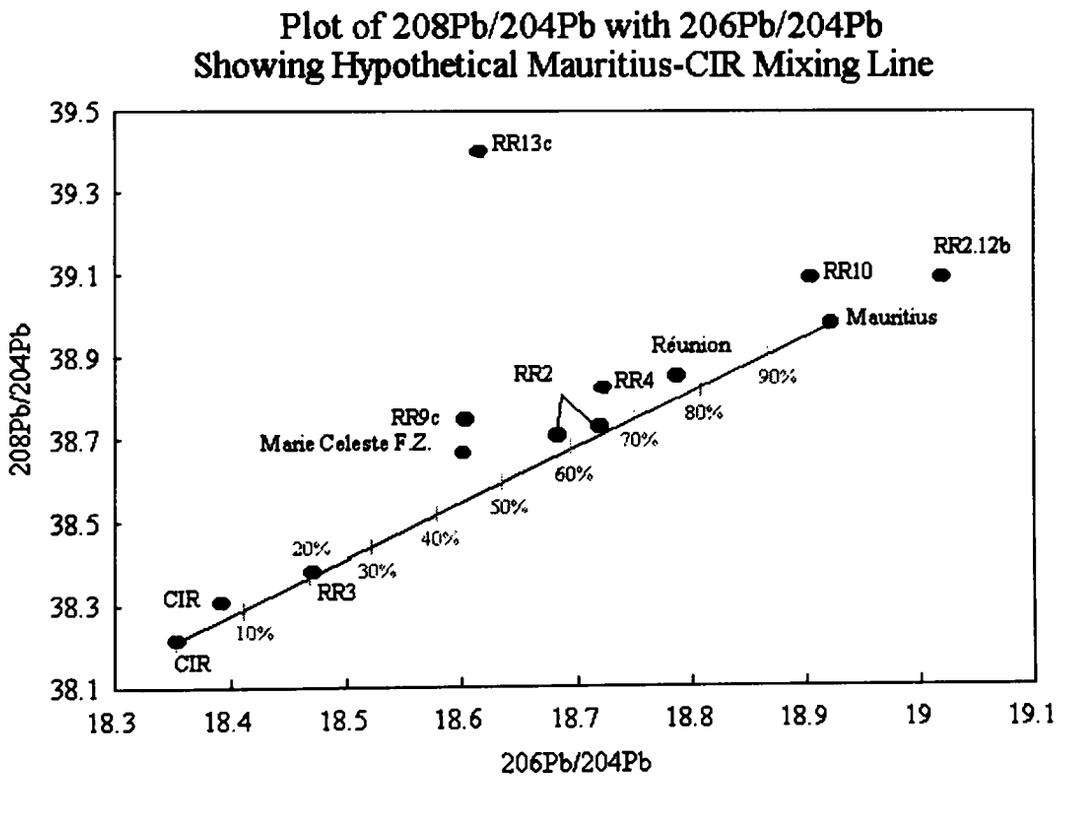

Sources: CIR from Mahoney *et al.* (1989), other sources as in table 46.

Ce/Yb display large variations for near constant Mg# (Keleman *et al.*, 1995, Keleman *et al.*, 1990). Such behaviour could help to explain the observed variation seen at the Rodrigues Ridge sites, in particular the unusual trace element behaviour observed at RR3. The east-west variation along the Rodrigues Ridge would, however, appear to require the mixing of either sources or melts, since no one source would be likely to supply the observed compositional range of melt.

Mixing the isotopic composition of CIR lava CIRCE 104-21 with an average composition for Mauritius produces the lines shown on figs. 271-273. These mixing lines produce a good match for the trend displayed by the Rodrigues Ridge lavas (percentages shown on the mixing lines are for the plume component). But the percentages of the proposed sources vary between the isotope plots and the REE plots (fig. 274a-c). According to the isotopic plots, RR2 requires between 60-70% Mauritian source and 30-40% CIR source. RR3 requires 20-50% Mauritian source, RR4 65-70%, RR8 90%, RR9c 50-80%, RR10 92-100% and RR12d 64% on the isotopic plots (figs. 271-273). On the REE plots (figs. 274a-c), the required amounts of mixing are; RR2: 5% Mauritian source (95% CIR), RR3: 10%, RR4: 20% RR8: 30%, RR9c: 50%, RR10: 80% and RR12d: 100% (not shown). From this it is clear that different factors are influencing the REE chemistry and the isotopic signatures of these lavas. As already discussed, the upper limit of the melting zone is constrained by the lithospheric thickness. This in turn governs the REE signature since residual garnet (after melting) will result in depletion of the HREE compared with the LREE. Such melts will also sample mantle less depleted by previous melting episodes. Thus the REE variation is reflecting the minimum depth of melting and not the source chemistry. However the REE signatures of lavas from all the sites show a greater level of enrichment

Figure 274a

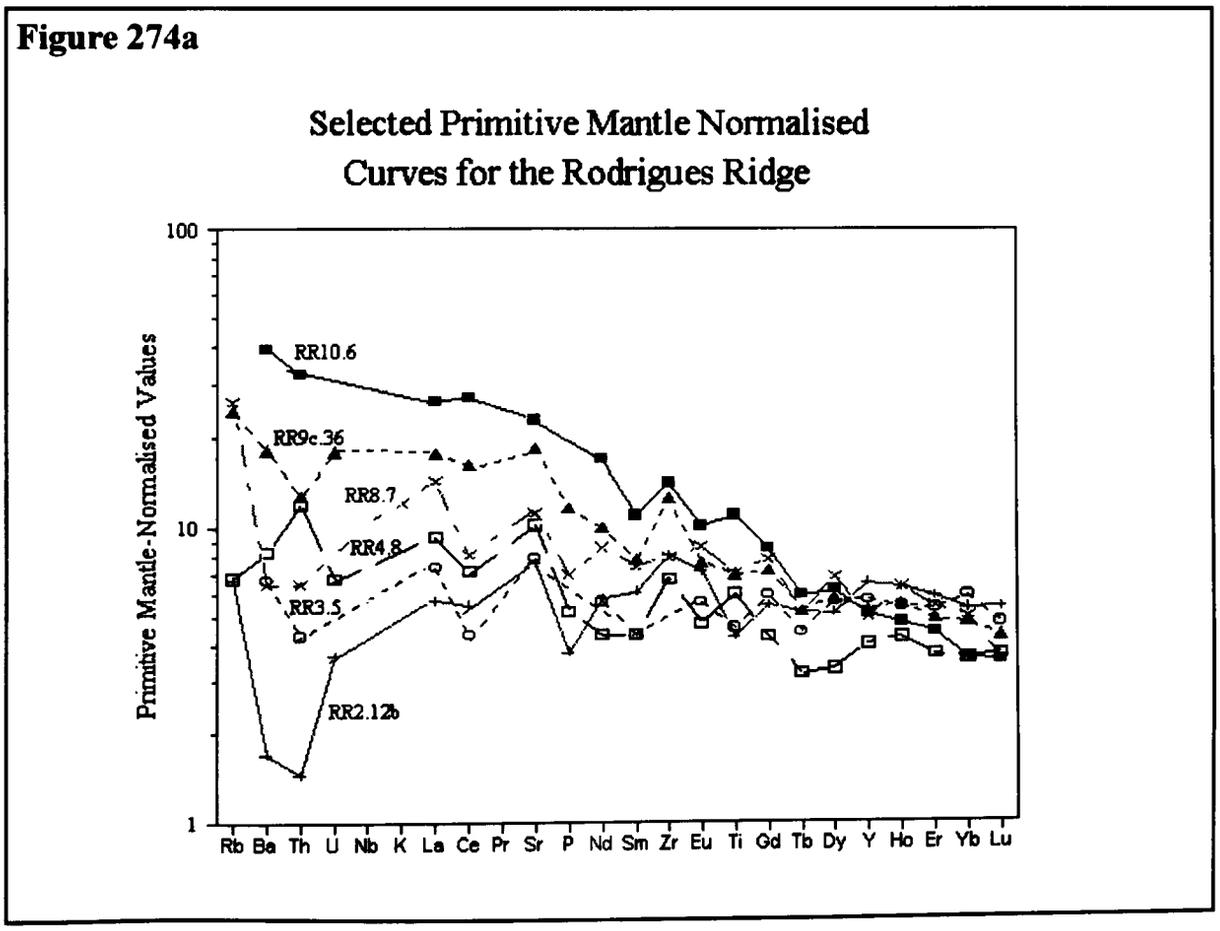

Figure 274b

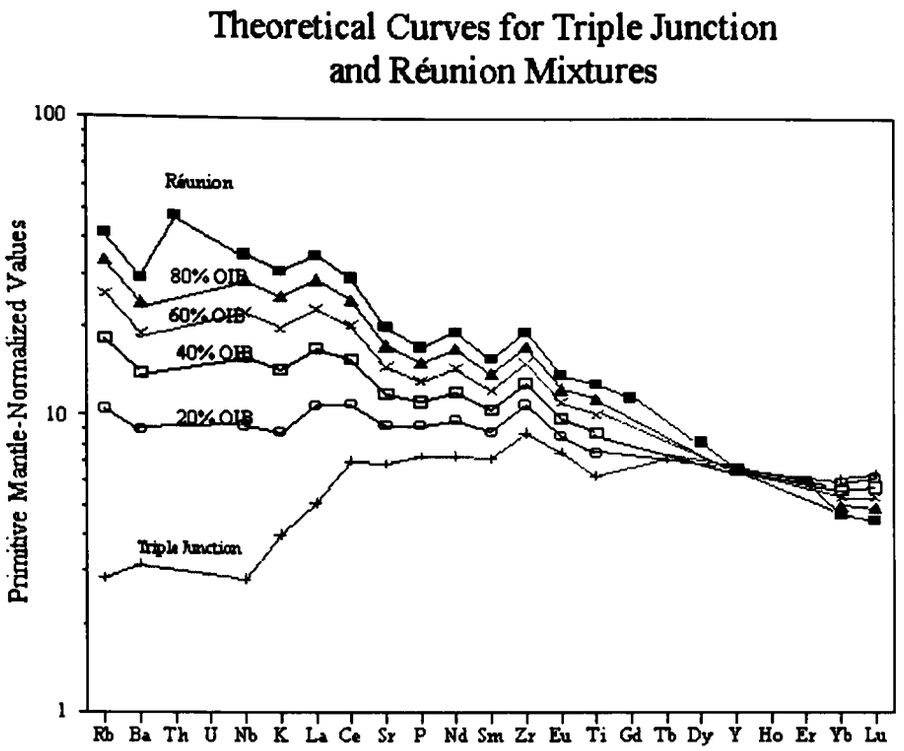

Figure 274c

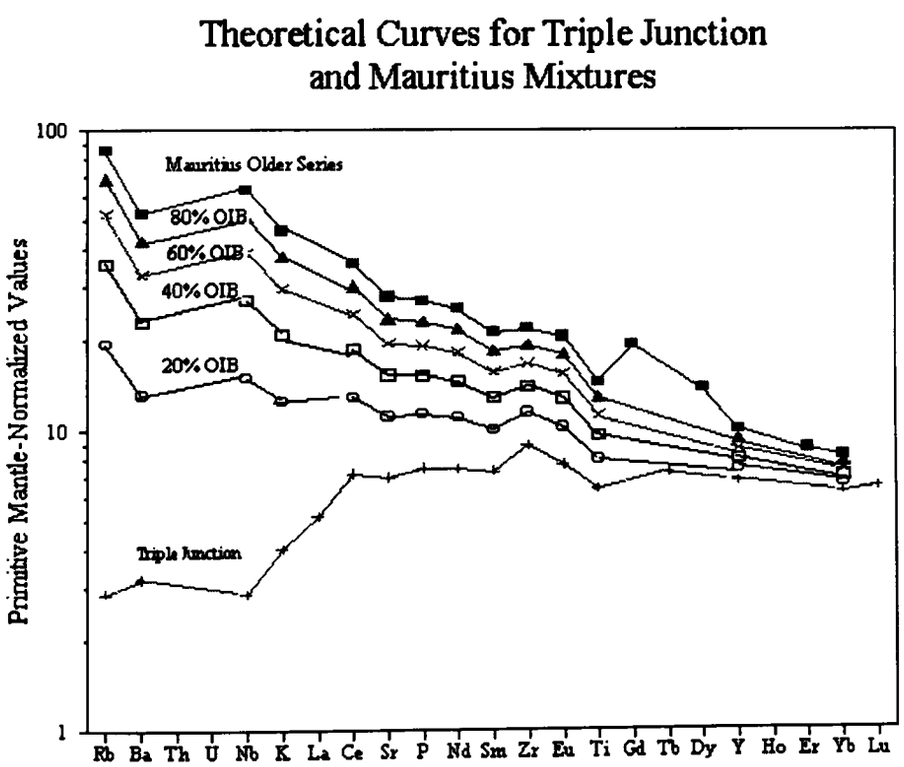

Figure 275

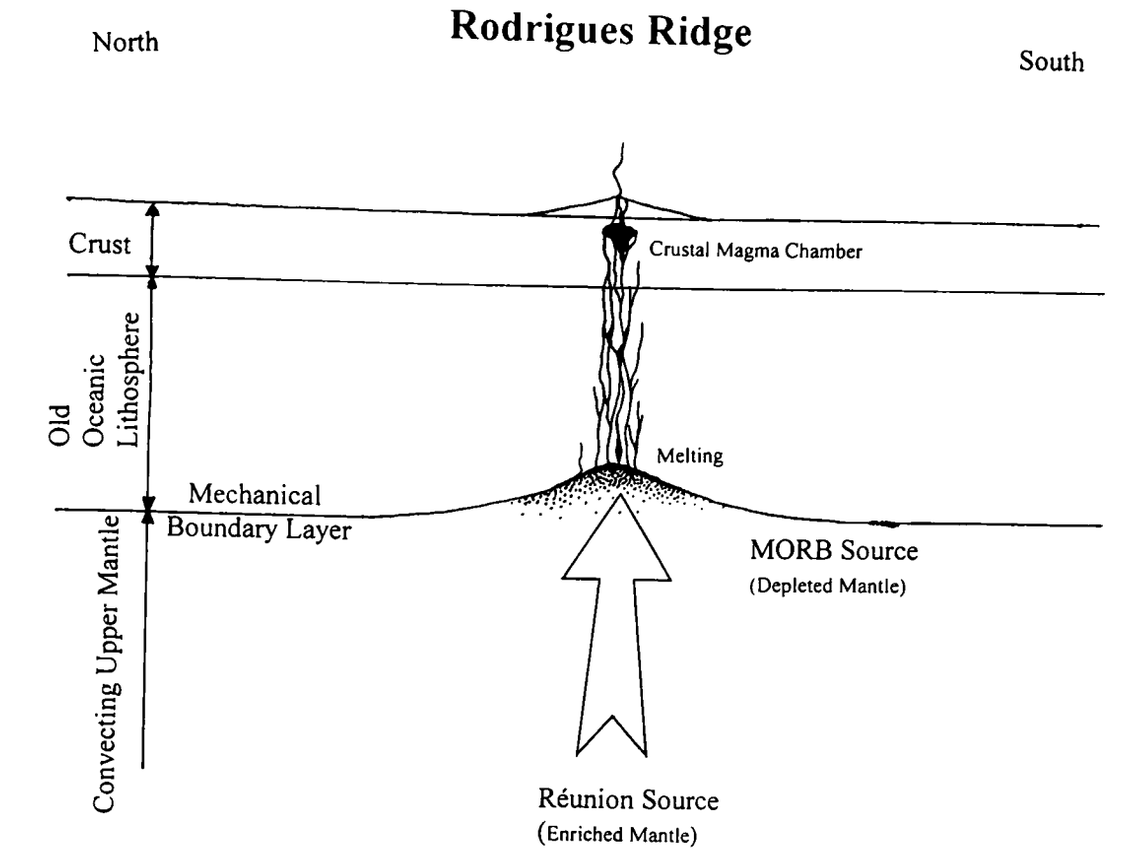

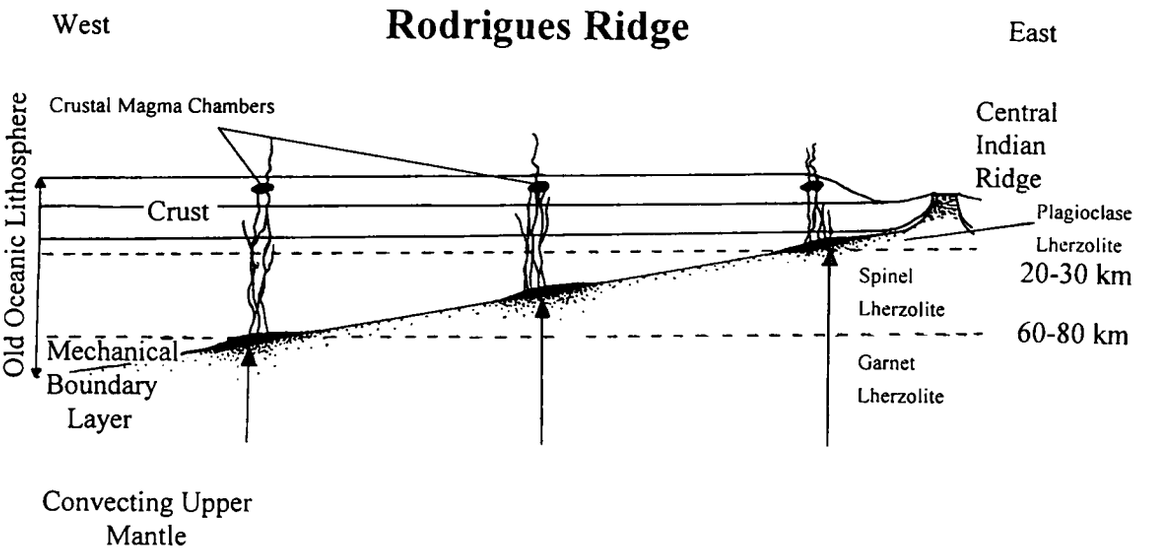

Sketch showing the three dimensional structure beneath the Rodrigues Ridge at the time of its formation. Melting of the upper mantle over a range of depths produces a mixed melt which locally melts the base of the (amphibole bearing) lithosphere. Fractionation occurs over a range of depths culminating in the fractionation of olivine ± plagioclase ± spinel ± clinopyroxene in a high-level magma chamber. With increasing lithospheric thickness away from the CIR, the upper limit of melting is driven down through spinel lherzolite into the garnet lherzolite, resulting in increasing LREE enriched lavas in the west.

in the LREE than the depth of the base of the lithosphere would suggest. For example, the lithosphere at RR2 would have been about 20 km thick when it formed and about 55 km thick at RR12d. These depths are shallower than the spinel-garnet transition at 60-80 km (Ellam 1992), thus for garnet to have influenced the chemistry of any Rodrigues Ridge melts, melting must have occurred over a substantial depth range. This is not unreasonable in the light of the isotopic variation which shows how the lavas at each site are derived by the mixing of a deep Réunion plume source (such as was active on Mauritius at the same time) and a shallow CIR source. However, the isotopic constraints indicate different amounts of deep melt to the REE chemistry. Blundy *et al.* (1998) have demonstrated that, under near-solidus melting conditions of spinel lherzolite in the upper mantle, HREE are compatible in clinopyroxene (D_{yb}^{Cpx} =1.43 see note 2 to appendix 1). Further support for this view was found by Vannucci *et al.* (1998) who looked at upper mantle xenoliths and associated glass inclusions in veins from La Palma (Canary Islands). Using clinopyroxene glass pairs, they demonstrated that MREE, HREE, Y and possibly Zr had partition coefficients which were greater than unity (D_{elm}^{Cpx} >1)(see note 2 to appendix 1). If this is the case beneath the Rodrigues Ridge it could, in conjunction with an increasing role for garnet, explain the REE behaviour along the Ridge, without contradicting the isotopic evidence. Furthermore, melt-rock reaction between RR3 melts and the underlying mantle (including clinopyroxene) could produce the associated drop in MgO and in HREE as ascending melts are believed to precipitate olivine while exchanging compatible and incompatible elements with the surrounding mantle rocks (Kelemen *et al.*, 1995). During decompression melting (near fractional melting), the melting of clinopyroxene, orthopyroxene and spinel and the precipitation of olivine occur according to the reaction aCpx + bOpx + cSp = dOl + melt; where a, b, c and d are the amounts of clinopyroxene, orthopyroxene, spinel and olivine respectively (Niu 1997). Below 25 Kb a < b *i.e.* Othopyroxene contributes more to the melt than clinopyroxene (Niu 1997). Thus, residual clinopyroxene is likely to exert a greater influence on the melt than orthopyroxene. In this model the lavas of RR3 may not have experienced high level fractionation but developed their characteristics at mantle depths instead. At other Rodrigues Ridge sites evidence of melt rock reactions may be masked by high level processes to a greater or lesser degree.

Fig 275 shows a summary of the processes involved in the formation of the Rodrigues Ridge. In cross-section (north-south) this is very similar to the model proposed by Class *et al.* (1998) for Grand Comore. On this island Class *et al.* (1998) were able to demonstrate that the lavas from the northern volcanic centre, La Grille, were derived from a lithospheric melt while lavas from Karthala were plume derived. In this model plume derived melts form the majority of the edifice with melting of the base of the lithosphere providing the final melts to be erupted at La Grille. These final melts are depleted in K/Nb indicating that amphibole was residual in the melting zone. On the Rodrigues Ridge similar

effects are seen (fig. 276) although the total range of K/Nb is much greater. Increased K/Nb is the result of low Nb rather than increased K as a result of the observed alteration. At RR2 (low MgO group) the highest K/Nb is observed. Alteration effects are the most likely explanation for two errant values from RR10 which have high K/Nb and high Nb, whereas the gentle decrease in K/Nb with increasing Nb (decreasing longitude) may represent the contribution made by reduced partial melting of lithospheric material (with residual amphibole) to the total melt. Equally, greater quantities of amphibole within the residue of the RR2 high MgO group than in the low group may explain some of the differences between these two. Plotting K_2O against P_2O_5, which are both similarly incompatible in basaltic minerals, shows that despite the high K/Nb, RR2 and RR3 show a very low K_2O, consistent with a residual K-bearing phase in the mantle (fig. 277). Two arrows are shown on this plot; the upper one indicates enrichment of both elements during fractional crystallisation, the lower indicates the depletion of K_2O shown in RR2 and RR3. Similar behaviour is observed if Nd is used instead of P_2O_5, indicating that this is not just the result of P_2O_5 enrichment at these sites.

Figure 276

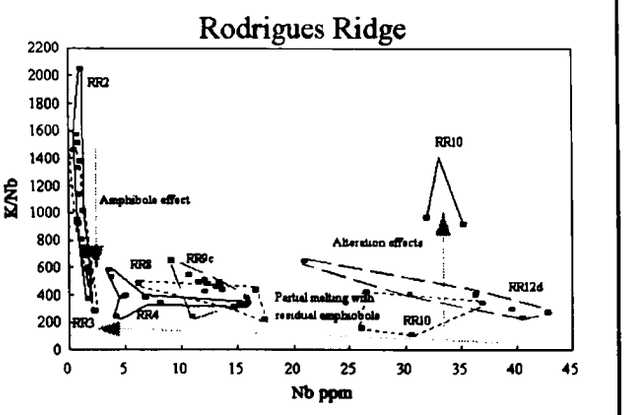

Figure 277

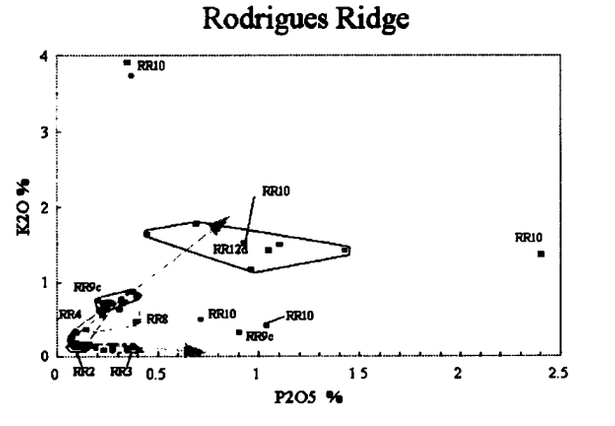

6.9 Rodrigues

The island of Rodrigues formed about 1.5 my (McDougall *et al.*, 1965) and represents a young phase of magmatic activity unrelated to the underlying structure. Only a limited set of isotope and trace element data are available for this island. The geochemistry was examined by Baxter *et al.* (1985), who found the lavas to be transitional alkali basalts like those of the underlying ridge. The relationship between Rodrigues and the Rodrigues Ridge is some what enigmatic as on most plots it shows chemistry more like Réunion, situated close to RR4. Some lavas from the island show LREE enrichment (45-120 x chondrite compared with 7-12 x chondrite for the HREE in the same samples) or,

in some cases, extreme HREE enrichment producing level trends (*circa* 90 x chondrite)(Baxter *et al.*, 1985). As with the Rodrigues Ridge, Y among the island basalts is buffered, suggesting that it has a bulk distribution coefficient of $K_{DY} = 0.65$. This would require an improbably high distribution coefficient for Y in clinopyroxene of $D_Y^{CPX} = 4$; alternatively it would require the fractionation of an accessory phase capable of strongly partitioning Y (*opp. cit.*). Such a phase is likely to also partition the REE, particularly the HREE, in much the same way as the unknown phase evident at RR3 and other Rodrigues Ridge sites. Equally the assimilation of wall rocks containing such a phase beneath Rodrigues Island may offer a possible explanation for the HREE behaviour observed on the island. Unfortunately, as with the Rodrigues Ridge, no suitable phase has been identified, despite a substantial megacryst suite being present. The presence of this behaviour on the island does at least demonstrate some link between the island and the older underlying structure.

6.10 Conclusion

Major and trace element modelling for the Rodrigues Ridge lava suite failed, at the majority of sites, to reproduce the observed fractionation trends. RR9c was the only site where the modelled and observed trends match closely. At this site the data set spans a broad range of MgO values and the number of analyses is larger, providing tighter constraints on the modelling. At RR2, RR3 and RR8, the REE, Zr, Y, (U), Ti and Nb all show buffered or decreasing trends with MgO, for which no satisfactory explanation exists, although reaction between the melt and source rocks may offer some explanation as this allows the development of a wide range of incompatible element values without affecting the Mg# of the melt. This behaviour occurs in conjunction with elevated (primitive mantle) normalised U ± P values. While these samples show clear petrographic and geochemical evidence for oxidation, they do not show the elevated $^{87}Sr/^{86}Sr$ which is associated with seawater alteration. Indeed the lavas of RR3 which display the most extreme anomalous REE (Y and Zr) behaviour, also show the lowest $^{87}Sr/^{86}Sr$ ratios. Assimilation of altered MORB may be one way in which these lavas could develop the elevated P and U; however this would also be expected to affect the Sr isotopic concentration, producing much higher values.

The radiogenic isotopes and the incompatible element ratios within the Rodrigues Ridge lava suite as a whole, show clear evidence of mixing between a CIR-type source and a Réunion type source. A progression in the trace element and isotopic composition of the lavas exists along the Rodrigues Ridge, from CIR-like in the east, to Réunion-like in the west. While this observation is broadly true, some individual sites have isotopic signatures more like Réunion than their geographic position would suggest, indicating that the sources are not uniformly mixed. Variable sampling of a deep Réunion source and a shallow CIR source could produce the observed effects (fig. 275). The zone of influence of the Réunion plume is widely believed to stretch to the CIR immediately north of the Rodrigues Ridge

(Schilling 1991, Mahoney *et al.,* 1989). Overlying this is a depleted upper mantle region (the source region of the CIR). In this model there is no need for channelling of melt as described by Morgan (1978) as the two sources are separated by depth and not distance. This is an important conclusion as two distinct melts migrating in from either end of the Rodrigues Ridge along a narrow conduit *circa* 50 km long, would be unable to mix effectively (Oldenburg *et al.,* 1989) (see sections 1.8 and 5.6). In such a circumstance a sharp change in composition over no more than about 50 km would be observed with lavas whose chemistry was essentially that of a single source on either side.

The evolutionary history of the Rodrigues Ridge lavas is summarised below:

Partial Melting

1. Clinopyroxene remains with in the residue at all sites.
2. Amphibole remains in the residue at sites RR2 and RR3 and may be residual at sites RR4-RR9c and RR12d. Since amphibole is not stable under upper mantle conditions, this indicates that some lithospheric melting has occurred at these sites. At RR10, alteration makes amphibole difficult to detect, but it is likely that it is present in the residue at this site also.
3. RR10 lavas are the products of lower degree partial melting than other Rodrigues Ridge sites, although alteration makes this difficult to quantify. This may be a fracture zone effect, as is observed on mid-ocean ridges *(e.g.* Bryan 1979).
4. The upper limit for the depth of melting is constrained by the thickness of the lithosphere beneath the particular site (fig. 275).
5. High distribution coefficients for HREE in clinopyroxene, and the spinel lherzolite - garnet lherzolite transition within the upper mantle, are controlling much of the trace element variation with longitude.
6. Unexpected buffering of the REE, Zr, Y and possibly Nb is observed at some sites. This behaviour is difficult to explain, although melt-rock reaction has been suggested as described by Keleman *et al.* (1995, 1990). This in conjunction with high distribution coefficients for REE and other elements in clinopyroxene could explain this behaviour. It also offers a mechanism by which a large variation in incompatible elements can be produced for little or no change in Mg#.

Sources

7. Melts are derived from the mixing of Réunion plume and CIR sources.
8. Linear mixing between the two sources is influencing the Rodrigues Ridge and the CIR between the Rodrigues Ridge and the Marie Celeste F.Z. Fracture zones on ocean ridges are the surface manifestations of boundaries between magma chambers. Thus the Marie Celeste F. Z. is able to act as an effective barrier to magma migration, resulting in an absence of melts contaminated with Rodrigues Ridge material being observed to the north of it (Mahoney *et al.,* 1989).

9. Numerical models for the contamination of the upper mantle by hotspot plumes, suggest that mature hotspots plumes are drawn towards adjacent spreading ridges; one such model is that described by Schilling (1991). In this case the Réunion plume's zone of influence would tend to bend towards the CIR as the crust passed over it. This 'contaminated' mantle could then mix with the depleted upper mantle left after the formation of ocean floor on the CIR. At the formation of the Rodrigues Ridge, at about 10 my, it was able to simultaneously sample mantle which became increasingly 'contaminated' both with depth and decreasing longitude (distance from plume).

Fractionation

10. In the suite as a whole there is evidence for polybaric fractionation between 30 Kb and 1 atm, culminating in the high-level fractionation of olivine ± plagioclase ± spinel ± clinopyroxene.
11. Rayleigh modelling of high-level fractionation was unsuccessful for most sites with only RR9c producing a good match for the observed behaviour.

Post-eruptive history

12. The lavas have collectively been subject to incipient seawater alteration resulting in palagonitisation of the matrices of most lavas. This occurs in conjunction with the replacement of the ferromagnesian minerals at some sites by serpentine and iddingsite. At some sites, notably RR3, there is evidence of oxidation bringing about the enrichment of U and P, compared with Th and Nd, respectively.
13. Many lavas showed evidence of having been displaced by debris flows down the sides of the Rodrigues Ridge, *ie.* they were not collected in situ.

Chapter 7

7. Conclusion

7.1 Introduction

To recap, the primary aims of this project were;- 1. to provide a greater understanding of the geology, petrology, petrogenesis and geochemistry of the Rodrigues Ridge. 2. To explain the paradoxical relationship between the east-west trend of the Rodrigues Ridge and the underlying ocean floor which formed at the NNW-SSE trending Central Indian Ridge. 3. To examine the relationship between Rodrigues Island and the underlying Ridge. 4. To establish whether any relationship exists between the Rodrigues Ridge and other major volcanic features in the region, in particular the CIR and the Réunion hotspot. 5. To present an explanation of how and why the Rodrigues Ridge formed.

In this final chapter the conclusions will be reviewed and a model is presented for tectonic history of the structure offering some insight into why this structure formed when and where it did. The temporal and spacial relationships between each site will be considered and the relationship between the structure as a whole and other near by features will be considered.

7.2 The Petrology, Geochemistry and Petrogenesis.

The samples dredged from the Rodrigues Ridge are exclusively transitional alkali basalts with MgO between 2.9-13.7%, Al_2O_3 between 13.4-20.2%, CaO between 1.4 (altered)-15.1%, total Fe as Fe_2O_3 between 10.0-14.9% and TiO_2 between 0.87-2.92%. The trace elements display an equally wide range for oceanic basalts, for example: Ba 9.6-490.5 ppm, Ni 47.5-480.0 ppm, Sc 18.7-39.8 ppm, Sr 148.3-593.0 ppm (additionally one altered sample had 9487 ppm Sr), Y 18.1-39.8 ppm and Zr 57.1-291.4 ppm. Mineralogically, the lavas of RR2-RR9c are all olivine+plagioclase-phyric, with either an altered glassy matrix or a microcrystalline matrix of clinopyroxene, plagioclase and iron oxides. Many of the lavas carry traces of chrome spinel, mostly, but not exclusively, within the phenocryst olivine.

At RR2, two groups unrelated by high-level fractionation are recognised; one termed the high MgO group with high TiO_2, MgO, Cr, Sc, Y, Zr and Zr/Y, Th/U and K/U, but low Ti/Zr and P/Nd, the other the low MgO group with low values of these elements and ratios. Some overlap exists between these two groups with one sample showing the major and minor element chemistry of the low MgO group and the trace and REE chemistry of the high MgO group.

All seven sites studied show clear evidence for the fractionation of olivine ± plagioclase ± clinopyroxene ± spinel. Major element modelling was carried out for six out of the seven sites, confirming the fractionation. The remaining site (RR10) displayed substantial modification of the

original chemistry as a result of alteration and the consequent growth of alteration minerals, principally zeolites. The fractionating suites vary between the sites in terms of their mineralogy, the proportions of fractionating phases present and the amounts of fractionation necessary to produce the most evolved lava from the most primitive lava. Some problems were experienced modelling the lavas using just the observed phenocryst phases. Table 47 gives a summary of the modelled fractionation suites for the six sites studied.

Table 47 **Summary of Modelling Results**

Site	Fractionating Minerals	% Fractionation	Respective Proportions of Minerals
RR2 Low MgO	ol + pl	18	53:47
	Or		
RR2 Low MgO	ol + pl + cpx	30	26:25:49
RR2 High MgO	ol + pl	4	63:37
	Or		
RR2 High MgO	ol	2	100
RR3	ol + pl	15	86:14
	Or		
RR3	ol + pl + sp	16	75:12:13
RR4	ol + pl	23	30:70
	Or		
RR4	ol + pl + cpx	50	21:48:31
RR8	ol + pl	21	81:19
	Or		
RR8	ol + pl + cpx	41	44:34:22
RR9c	ol	14	100
	Or		
RR9c	ol + cpx	13	70:30
RR12d	ol + pl + cpx	5	14:33:53

Alteration at RR10 manifested itself by high LOI, TiO_2, $Fe_2O_3^*$, P_2O_5 and U with low SiO_2 and a general scatter with declining MgO in Rb, Sr, Ba and K_2O. In general, alteration was found to influence K_2O, P_2O_5, H_2O, (CO_2), Rb, Ba, U and to a lesser degree Sr. The behaviour of these elements is consistent with the results of Verma (1992) and Hart *et al.* (1974), with the surprising exception that

H_2O seemed less mobile than K_2O or P_2O_5 under certain conditions which included oxidation. Further work on the alteration of these lavas is currently being undertaken by M. M. Hall.

7.3 The Relationships Between the Lavas Recovered from the Different Sites.

Along the Rodrigues Ridge there is a systematic change from MORB-like chemistry in the east, to OIB-like chemistry in the west. The basalts of RR2 and RR3 are depleted in incompatible elements and display chondrite-normalised REE patterns which are flat or LREE depleted. Typically these lavas show primitive mantle-normalised trace elements patterns only slightly higher in the most incompatible elements than typical N-type MORB, as given by Sun & McDonough (1989). Site RR4 most closely resembles E-type MORB in terms of its primitive mantle-normalised trace element chemistry. Sites RR8 and RR9c display similar mantle-normalised trace element patterns, between the E-type MORB and OIB traces of Sun & McDonough (1985). Despite the higher levels of alteration observed at RR10, the overall trace element signature of this site is like that of OIB. Basalts from site RR12d likewise, have OIB-like trace element signatures, but these more evolved lavas show enrichment of the HREE in addition to the LREE.

7.4 The Temporal and Spatial Relationship Between the Rodrigues Ridge and the Surrounding Area.

The role of the Réunion hotspot, and the geographically nearer CIR, in influencing the chemistry of the Rodrigues Ridge lavas is best demonstrated by the behaviour of the REE and the radiogenic isotopes of Pb, Sr and Nd. These clearly show a linear mixing between two mantle sources, one Réunion-like and the other CIR-like (figs. 271-274).

At 8-10 my the Réunion hotspot would have been situated under Mauritius some 300 km to the south of the Rodrigues Ridge (Patriat & Segoufin 1988, Hall 1986). Schilling *et al.* (1985) demonstrated that hotspots could modify the geochemistry of lavas extruded on ocean ridges some distance away (*ca.* 1000 km). This chemical influence was brought about by mantle convection displacing the plume (or a part thereof) towards the spreading ridge along a line parallel to the fracture zones. A passive asthenospheric tongue parallel to the spreading direction was speculated by Mahoney *et al.* (1989) to explain the Réunion-like isotopic signatures which they identified in the region of the Marie Celeste FZ. This tongue of plume material from the hotspot, then under Mauritius, would be available during the melting at the more western sites of the Rodrigues Ridge. Geochemically the lavas of the Rodrigues Ridge resemble those of the Older Series of Mauritius in the west and those of the CIR in

the east. These Mauritian lavas were erupted simultaneously or immediately after those of the Rodrigues Ridge (7.8-5.5 my compared to 9.8-7.5 for the Rodrigues Ridge). Although the present day Réunion lavas and the leg 115 samples from the Mascarene Plateau are quite distinct, there appears to be a geochemical relationship between the Older series lavas of Mauritius and the Rodrigues Ridge.

Despite their different chemistries and alteration states, the lavas of the Rodrigues Ridge are all approximately the same age (table 1). Only RR12 is significantly older than the more easterly sites. This site is situated on fractured oceanic crust, suggesting that initially the activity concentrated in the west before shifting to more easterly centres around longitude 62°45' and around Rodrigues Island. Although greater volumes of lava have been extruded around these two centres, activity must have occurred along a more or less continuous line from 60°45' to 64°45'. This activity has produced an edifice some 500 km long with distinct systematic variations in geochemistry from east to west. The most easterly site (RR2) is situated on 8-11 my crust (Patriat & Segoufin 1988) demonstrating that it must have formed very close to the CIR. There is no feature present on the east of the CIR, suggesting that the eastern end of the Rodrigues Ridge did not form on the CIR.

The above model demonstrates the likelihood of passive source mixing between the Réunion plume and the CIR. The presence of a Réunion tongue, immediately below the crust of the Rodrigues Ridge, provides a readily available source for incompatible elements. The greater thickness of crust in the west (than in the east) results in clear garnet signatures being manifested in the REE and trace element chemistry of the resulting lavas. In this model there is no need to look to a deep source (other than the Réunion plume), such as another hotspot, to explain the OIB chemistry.

In the vicinity of the Rodrigues Ridge the CIR is deflected to the west, with all the FZ's to the north having a dextral offset, while those to the south have a sinistral offset. This deflection is first observed at 42 my (anomaly 18) when the northern part of the CIR first began spreading. High heat flow was observed in this area by Fisher *et al.* (1967) and high ^{3}He was observed by Jean-Baptiste *et al.* (1992) indicating elevated hydrothermal activity. Additionally there is a gravitational high in this area (Briais pers. comm.) which together with the ^{3}He anomaly and the high heat flow is believed to be related to the Rodrigues Ridge - possibly a relict thermal anomaly.

7.5 The Reasons for the Formation of the Rodrigues Ridge.

Anomaly 5 spans 13 my, from 21 to 8 my, bracketing the formation of the Rodrigues Ridge. Fig. 278 shows the reconstructed Central Indian Ocean at the time of formation of the Rodrigues Ridge. Onto this diagram has been added σ^{1} (the maximum principal stress) and σ^{3} (the minimum principal stress) assuming that they are parallel and perpendicular, respectively, to the sum of spreading vectors for the CIR and SWIR (South West Indian Ridge). The present day stress regime is given on the "World

Stress Map" of Zoback & Burke (1993) which shows the principal stress in this area orientated along the Rodrigues Ridge. Prior to 10 my (and at the present day) the orientation of σ^1 was parallel to the Rodrigues Ridge. By anomaly 18 (42 my) the CIR had developed a marked deflection to the west which would eventually contribute to the formation of the Rodrigues Ridge. The precise reasons for this feature remains obscure, but the presence of high heat flow and the anomalously shallow nature of the CIR in this area suggest that there is still a greater level of magmatic activity in this area. Subject to a substantial compressive stress and probably elevated mantle temperatures, the young (thinner) crust east of the MFZ fractured with fissures opening parallel to σ^3. This localized fracturing resulted in the unloading of the asthenosphere and adiabatic decompression melting in situ. The Ridge developed in a manner akin to that of a tension gash. In the region of the MFZ and FZA in the west, the volcanism exploited the FZ's, resulting in the development of the seamount at RR12 and possibly the Soudan Bank, the neighbouring bank to the west and the bank at 59°20' 18°50'.

Volcanism along this structure would have been short-lived since the spreading direction changed (fig. 278) at 10 my (Patriat & Segoufin 1988) preventing further extension across the Ridge. Subsequent stress has been accommodated by strike-slip faulting in the region of the RR12 seamount and by fissuring, between 2-1 Ma, further east resulting in decompression melting and the formation of Rodrigues island. This may be related to the increased asymmetry of spreading between 1 and 2 my (Mitchell 1991) resulting in a change in the stress regime, and/or to isostatic compensation along the Rodrigues Ridge. In this model (isostatic compensation) the thermally domed crust cools as it moves away from the hotspot, and subsides under the weight of the accumulated lava pile. The higher flexural rigidity of the cooler crust results in fracturing which allows localized melting and extrusion of small volumes of more evolved melts (Ten Brink *et al.,* 1986 and Duncan 1990). In the case of the Rodrigues Ridge, low flexural rigidity identified by Bonneville *et al.* (1988), was related to its young age. The presence of the thermal anomaly identified on the CIR would delay the isostatic compensation of the Rodrigues Ridge, resulting in a delay in the eruption of the final stage melts (Rodrigues Island).

Initially movement along the strike-slip faults near RR12 occurred sinistrally along a series of Central Indian Ridge parallel faults (fig. 279). Subsequently it proceeded along the MFZ and at least two other parallel fracture zones (figs. 279 and 280). This movement rotated the RR12 seamount through 24° anticlockwise about 18 55°S 59 30°E. Although the motion is shown on one major NE-SW trending fault in fig. 3, several planes were recognised on the seismic profiles in this region, suggesting that this is an over simplification. A consequence of this rotation is that the oceanic lithosphere at 2. (fig. 3) would be thrust up over (or under) the Mascarene Plateau. While this apparently indicated by the presence of 48 my oceanic lithosphere west of the MFZ, forming the NE-SW trending ridge at site RR13 on the flank of the Mascarene Plateau, the crust immediately east of the MFZ is younger than this at 33 my (Dyment 1999 *pers. comm.*) suggesting that this material has been displaced from further south. This provides further evidence of the complex structural activity which has taken place in this region between RR10 and the MFZ.

Figure 278

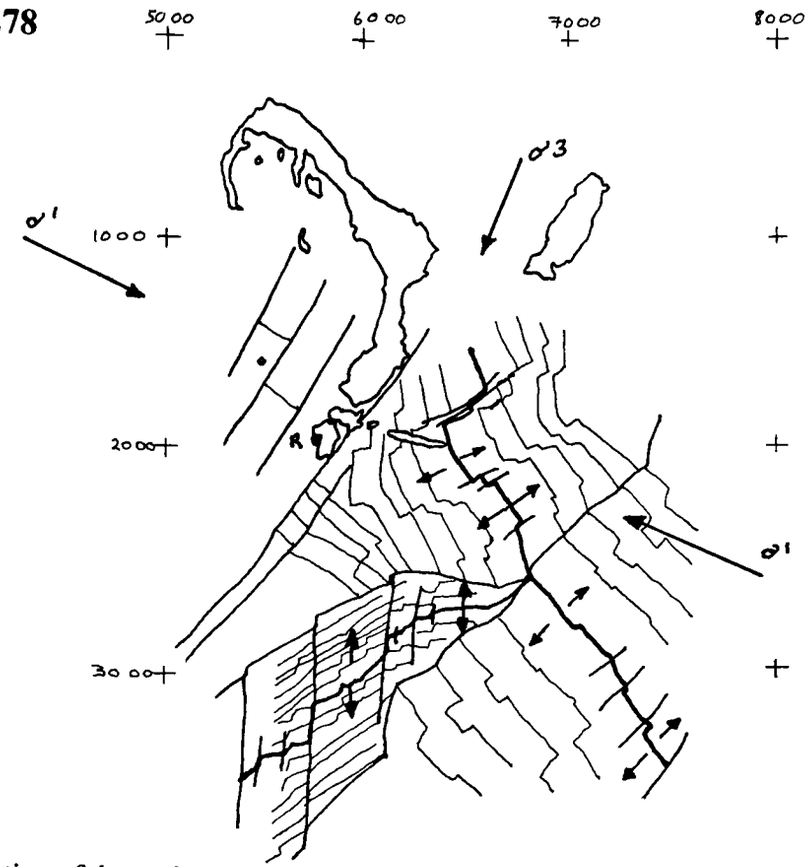

Reconstruction of the region at anomaly 5 showing the principle stress regime under which the Rodrigues Ridge was formed.

After Patriat & Ségoufin (1988).

Figure 279

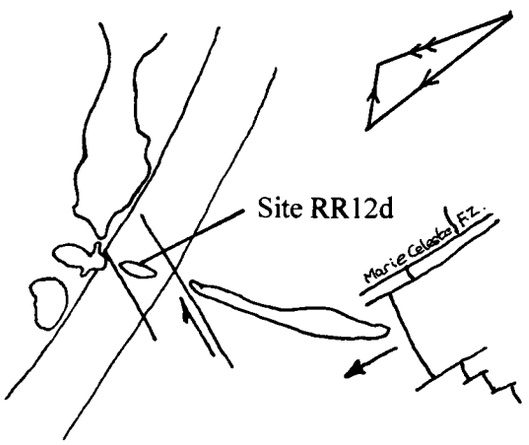

Detail showing the proposed initial fault movements in the region of RR12. Vectors show the principal stress direction derived from vector addition of the spreading for the CIR and the SWIR (Patriat & Ségoufin 1988). These are applicable for the last 10 my. Prior to this the principal stress direction σ^1 was orientated 114°N as shown on fig. 278.

Figure 280

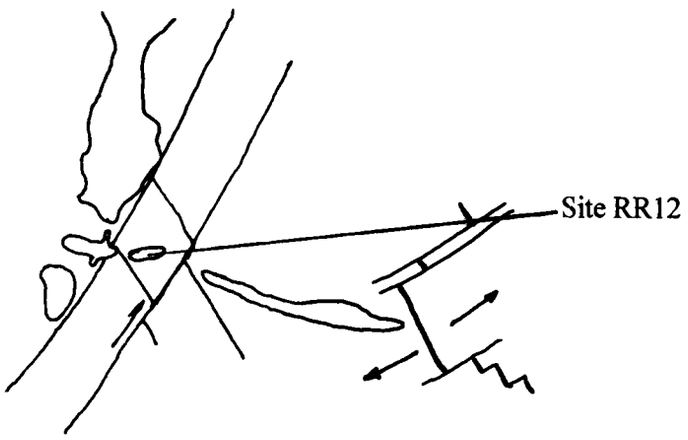

Detail showing later displacements in the region around site RR12.

Figure 281

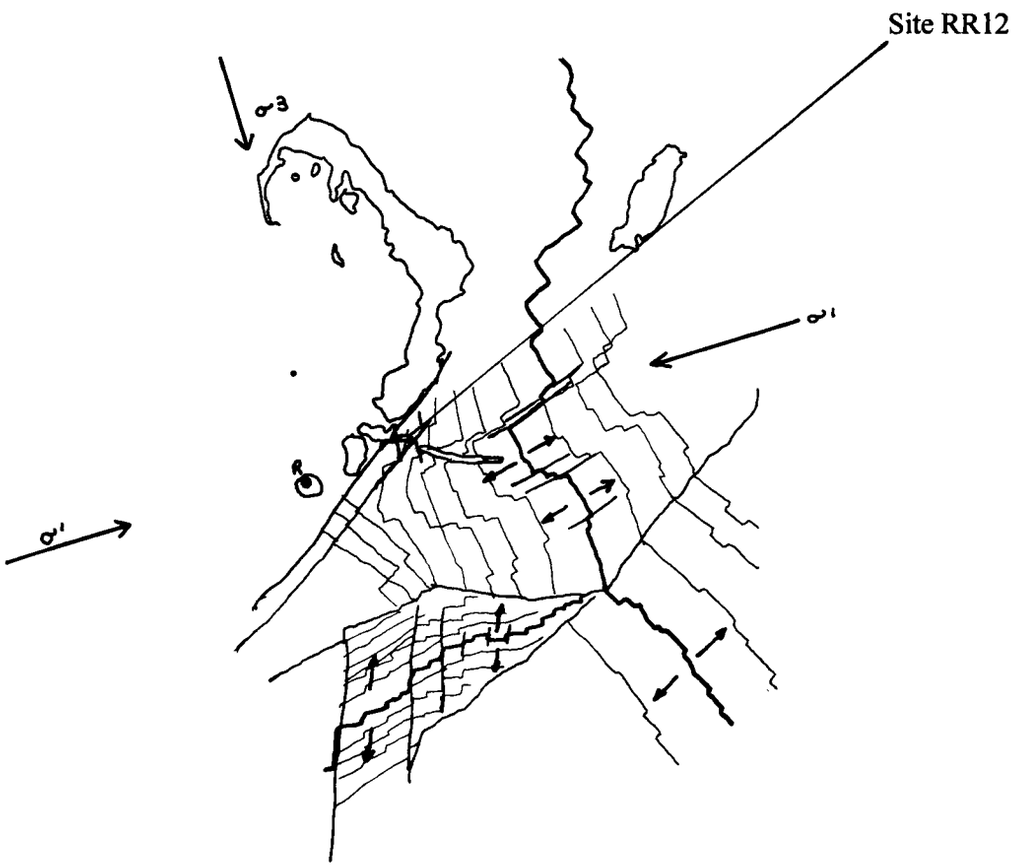

Reconstruction of the region at anomaly 1 showing the principal stress regime under which the seamount, on which RR12 is situated, rotated anticlockwise 24° to its present position.

After Patriat & Ségoufin (1988).

References

Backman J., Duncan R. A. *et al.,* 1988. Proc. ODP, Init. Repts., Vol 115, College Station TX (Ocean Drilling Program). 1085 pages.

Balfour I. B. 1879. Introductory Notes. In : The Collections from Rodriguez. Philos. Trans. Royal Soc. Vol.168 (extra volume) pp.289-92.

Baxter A. N. 1972. Magmatic Evolution of Mauritius, Western Indian Ocean. PhD Thesis University of Edinburgh. Unpublished.

Baxter A. N. 1975. Petrology of the Older Series Lavas from Mauritius, Indian Ocean. Geol. Soc. Am. Bull. Vol.86, pp.1449-1458.

Baxter A. N. 1976. Geochemistry and Petrogenesis of Primitive Alkali Basalts from Mauritius, Indian Ocean. Geol. Soc. Am. Bull. Vol. 87, pp.1028-1034.

Baxter A. N. 1990. Major and Trace Element Variations in Basalts from Leg 115. In: Duncan R. A., Backman J. & Peterson I. C. *et al.*, Proc. ODP, Sci. Results, Vol.115: College Station TX. (Ocean Drilling Program), pp.11-21.

Baxter A. N., Upton B. G. J. & White W. M. 1985. Petrology and Geochemistry of Rodrigues Island, Indian Ocean. Contrib. Min. & Petrol. Vol.89, pp.90-101.

Baxter A. N., Duncan R. A., Fisk M. R., Bussell M. A., Gale A. J., Pedley M., Heward G., Hall M. M. & Draper S. H. 1989. A Structural, Petrological and Sedimentological Investigation of the Rodrigues Ridge. Charles Darwin Scientific Report. Unpublished.

Beane J. E., Turner C. A., Hooper P. R., Subbarao K. V. & Walsh J. N. 1986. Stratigraphy, Composition and Form of the Deccan Basalts, Western Ghats, India. Bull. Volcanol. Vol.48, pp.61-83.

Belcher E. 1846. Cargados Carajos Shoals. Admiralty Chart 1881.

Безруков П. Л., Крылов А. Я., Чернышева В. И. 1966. Петрография и Абсолютный Возраст Базальтов со Дна Индийского Океана. Океанология т.VI, Вып.2, pp.261-66.

Bloomer S. H., Natland J. H. & Fisher R. L. 1989. Mineral Relationships in Gabbroic Rocks from Fracture Zones of Indian Ocean Ridges: Evidence for Extensive Fractionation, Parental Diversity and Boundary-Layer Recrystallization. In: Saunders A. D. and Norry M. J. Magmatism in the Ocean Basins. Geol. Soc. Special Publication No.42, pp.107-124.

Bloomer S. H. & Meyer P. 1992. Slimline Magma Chambers. Nature, Vol.357, pp.117-118.

Blundy J. D., Robinson J. A. C. and Wood B. J. 1998. Heavy REE are Compatible in Clinopyroxene on the Spinel Lherzolite Solidus. Earth. Planet. Sci. Lett. Vol. 160, pp.493-504.

Bonneville A., Barriot J. P. & Bayer R. 1988. Evidence from Geoid Data of a Hotspot Origin for the Southern Mascarene Plateau and Mascarene Islands (Indian Ocean). J. Geophys. Res. Vol.93, No. B5, pp.4199-4212.

Briais A. 1994. Pers. Comm.

Briais A. 1994. Unpubl. Structural Analysis of the Segmentation of the Central Indian Ridge between 25°30'S (Triple Junction) and 20°30'S.

Brooks C. K. 1976. The Fe_2O_3/FeO Ratio of Basalt Analysis: An Appeal for Standardized Procedure. Bull. Geol. Soc. Denmark. Vol.25, pp.117-120.

Bryan W. B. 1978. Regional Variation and Petrogenesis of Basalt Glasses from the FAMOUS Area, Mid-Atlantic Ridge. J. of Petrol. Vol. 20, No. 2, pp.293-325.

Cann J. R. 1970. Rb, Sr, Y, Zr and Nb in some Ocean Floor Basaltic Rocks. Earth and Planet. Sci. Lett. Vol.10, pp.7-11.

Carter D. J. T. 1980. Echo-Sounding Correction Tables. 3rd Edition. NP 139. M.O.D. Hydrographic Department. Taunton.

Clague D. A., Frey F. A., Thompson G. & Ringe S. 1981. Minor and Trace Element Geochemistry of Volcanic Rocks Dredged from the Galapagos Spreading Center. Role of Crystal Fractionation and Mantle Heterogeneity. J. Geophys. Res. Vol. 86, B10, pp. 9469-9482.

Class C., Goldstein S. L., Altherr R. & Bachèlery P. 1998. The Process of Plume-Lithosphere Interactions in the Ocean Basins - The Case of Grande Comore. J. of Petrol. Vol. 39, No. 5, pp.881-903

Couper A. (Ed.) 1989. The Times Atlas and Encyclopaedia of the Sea. Guild Publishing. London. 272 pages.

Courtillot V. 1990. Deccan Volcanism at the Cretaceous-Tertiary Boundary: Past Climatic Crises as a Key to the Future? Palaeogeog., Palaeoclim., Palaeoecol. (Global and Planet. Change Section) Vol.189 pp.291-299.

Cox K. G., Bell J. D. & Pankhurst R. J. 1987. The Interpretation of the Igneous Rocks. George Allen & Unwin. London. 450 pages.

Cox K. G. & Hawkesworth C. J. 1985. Geochemical Stratigraphy of the Deccan Traps at Mahabaleshwar, Western Ghats, India, with Implications for Open System Magmatic Processes. J. of Petrol. Vol.26, pp.355-377.

Deer W. A., Howie R. A. & Zussman J. 1982. Rock-Forming Minerals. Vol.1A, Orthosilicates. Longman. London. 919 pages.

Deer W. A., Howie R. A. & Zussman J. 1972. Rock-Forming Minerals. Vol. 5, Non-Silicates. Longmans. London. 371 pages.

Deer W. A., Howie R. A. & Zussman J. 1967. Rock-Forming Minerals. Vol. 1, Ortho- and Ring Silicates. Longmans. London. 333 pages.

Deer W. A., Howie R. A. & Zussman J. 1967. Rock-Forming Minerals. Vol. 2, Chain Silicates. Longmans. London. 379 pages.

Devey C. W. & Stephens W. E. 1991. Tholeiitic Dykes in the Seychelles and the Original Spatial Extent of the Deccan. J. Geol. Soc. London. Vol.148, pp.979-983.

Devey C. W. & Stephens W. E. 1992. Deccan-Related Magmatism West of the Seychelles-India Rift. In: Magmatism and the Causes of Continental Break-up. Eds. Storey B. C., Alabaster T. &

Pankhurst R. J. Geol. Soc. London Special Pub. No.68, pp.271-291.

De Ribet B. 1989. A Contribution to the Geophysical Study of the Northwest Indian Ocean. Characteristics of Indian-African Motion. PhD thesis University of Paris. Unpublished

Dick H. J. B. & Bullen T. 1984. Chromian Spinel as a Petrographic Indicator in Abyssal and Alpine-Type Peridotites and Spatially Associated Lavas. Contrib. Mineral. Petrol. Vol. 86, pp.54-76.

Din V. K. & Jones G. C. 1978. The Determination of Total Carbon and Combined Water in Silicates Using an Elemental Analyser. Chem. Geol. Vol. 23, pp 347-52.

Dmitriev L. V. 1974. Petrochemical Study of the Basaltic Basement of the Mid-Indian Ridge: Leg 24, Djibouti to Mauritius. In: Initial Reports of the Deep Sea Drilling Project, Vol.24. pp.767-779.

Doe B. R. 1994. Zinc, Copper and Lead in Mid-Ocean Ridge Basalts and the Source Rock Control on Zn/Pb in Ocean-Ridge Hydrothermal Deposits. Geochim. et Cosmochim. Acta. Vol. 58, pp.2215-2223.

Drake M. J. 1975. The Oxidation State of Europium as an Indicator of Oxygen Fugacity. Geochim. et Cosmochim. Acta. Vol.39, pp.55-64.

Draper S. H. 1988. The Geotechnical Properties of Carbonate Oozes from the Rodrigues Ridge, Indian Ocean. MSc. thesis Unpublished. 178 pages. University College of North Wales.

Duncan R. A. 1989. Pers. Comm.

Duncan R. A. 1990. The Volcanic Record of the Reunion Hotspot. In: Duncan R. A., Backman J. & Peterson I. C. *et al.*, Proc. ODP, Sci. Results. Vol.115, College Station TX (Ocean Drilling Program) pp.3-10.

Duncan R. A. & Hargraves R. B. 1990. $^{40}Ar/^{39}Ar$ Geochronology of Basement Rocks from the Mascarene Plateau, the Chagos Bank, and the Maldives Ridge. In: Duncan R. A., Backman J. & Peterson I. C. *et al.*, Proc. ODP, Sci. Results. Vol.115, College Station TX (Ocean Drilling Program) pp.43-51.

Duncan R. A. & Pyle D. G. 1988. Rapid Eruption of the Deccan Flood Basalts, Western India. In: Deccan Flood Basalts. (Ed.) Subbarao K. V. Geol. Soc. India. pp.1-9.

Duncan R. A. & Richards M. A. 1991. Hotspots, Mantle Plumes, Flood Basalts and True Polar Wander. Reviews in Geophysics. Vol.29, pp.31-50

Ellam R. M. 1992. Lithospheric Thickness as a Control on Basalt Geochemistry. Geology. Vol.20, pp.153-156.

Engel C. G., Bingham E. & Fisher R. L. 1974. Trace Element Composition of Leg 24 Basalts and One Diabase. In: Initial Reports of the Deep Sea Drilling Program. Vol.24, pp.781-786.

Erlank A. J. & Reed D. L. 1974. Geochemistry, Mineralogy and Petrology of Basalts, Leg 25, Deep Sea Drilling Project. In: Initial Reports of the Deep Sea Drilling Project Vol. 25. pp.543-551.

Faure G. 1977. Principles of Isotope Geology. John Wiley & Sons, New York. 464 pages.

Fisher R. L. 1983. Unpublished

Fisher R. L., Johnson G. L. & Heezen B. C. 1967. Mascarene Plateau, Western Indian Ocean. Geol. Soc. Am. Bull. Vol. 78, pp.1247-1266.

Fisher R. L. Sclater J. G. & McKenzie D. P. 1971. Evolution of the Central Indian Ridge, Western Indian Ocean. Geol. Soc. Am. Bull. Vol. 82, pp.553-562.

Fisk M. Upton B. G. J., Ford C. E. & White W. M. 1988. Geochemical and Experimental Study of the Genesis of Magmas of Reunion Island, Indian Ocean. J. Geophys. Res. Vol.93, No. B5, pp.4933-4950.

Fisk M. R., Duncan R. A., Baxter A. N.,Greenough J. D., Hargraves R. B., Tatsumi Y. and Shipboard Scientific Party 1989. Reunion Hotspot Magma Chemistry Over the Past 65 my: Results from Leg 115 of the Ocean Drilling Program. Geology. Vol.17, pp.934-937.

Fisk M. R. & Howard K. J. 1990. Primary Mineralogy of Leg 115 Basalts. In: Duncan R. A., Backman J. & Peterson I. C. *et al.,* Proc. ODP, Sci. Results. Vol.115, College Station TX (Ocean Drilling Program) pp.23-42.

Fitton J. G., Saunders A. D., Larsen L. M., Hardarson B. S. and Norry M. J. 1998. Volcanic Rocks from the Southeast Greenland Margin at 63°N: Composition, Petrogenesis, and Mantle Sources. In: Saunders A. D., Larsen L. M. and Wise S. W. (Eds.) Proc. ODP, Sci. Results. Vol.152, College Station TX (Ocean Drilling Program), pp.331-350.

Flower M. F. J. 1973. Evolution of Basaltic and Differentiated Lavas from Anjouan, Comores Archipelago. Contrib. Mineral. Petrol. Vol.38, pp.237-260.

Floyd P. A. 1989. Geochemical Features of Intraplate Oceanic Plateau Basalt. In: Magmatism in the Ocean Basins. Eds. Saunders A. D. & Norry M. J. Geol. Soc. London Special Publication. pp.215-230.

Green D. 1998 Pers. Comm.

Griffiths D. H. & King R. F. 1983. Applied Geophysics for Geologists and Engineers. 2nd Ed. Pergamon Press. Oxford. 230 pages.

Hagen H. & Neumann E. R. 1990. Modelling of Trace-Element Distribution in Magma Chambers Using Open-System Models. Computers & Geosciences Vol.16, No.4, pp.549-586.

Hall G. P. D. 1986. Chagos Archipelago to Madagasikara. Admiralty Chart No. 4702. New Edition.

Hall G. P. D. 1974. Chagos Archipelago to Madagasikara. Admiralty Chart No. 4702.

Hanson G. N. 1980. Rare Earth Elements in Petrogenetic Studies of Igneous Systems. Ann. Rev. Earth Planet. Sci. Vol.8, pp.371-406.

Hart S. R., Erlank A. J. & Kable J. D. 1974. Sea Floor Basalt Alteration: Some Chemical and Sr Isotopic Effects. Contrib. Mineral. and Petrol. Vol.44, pp.219-230.

Heezen B. C. & Tharp M. 1964. A Physiographic Diagram of the Indian Ocean. Geol. Soc. Am. Special Publication.

Heezen B. C. & Tharp M. 1965. Tectonic Fabric of the Atlantic and Indian Oceans and Continental Drift. Philos. Trans. R. Soc. Series A. Vol. 258, pp.90-108.

Heezen B. C. & Tharp M. 1966. Physiography of the Indian Ocean. Philos. Trans.R. Soc. Series A. Vol.259, pp.137-149.

Hékinian R. 1982. Petrology of the Ocean Floor. Elsevier Oceanographic Series, 33. Elsevier

Scientific Publishing Company. Amsterdam. 393 pages.

Heward G. 1989. Pers. Comm.

Higgin E. 1848. Remarks on the Country, Products, and Appearance of the Island of Rodriguez, with Opinions as to its Future Colonization. Geographical Journal. Vol.19, pp.17-20.

Hoernle K. A., Tilton G. and Schmincke H.-U. 1991. Sr-Nd-Pb isotopic evolution of Gran Canaria: Evidence for Shallow Enriched Mantle beneath the Canary Islands. Earth. Planet. Sci. Lett. Vol. 106, pp.44-63.

Irving A. J. 1978. A Review of Experimental Studies of Crystal/Liquid Trace Element Partitioning. Geochim. et Cosmochim. Acta. Vol.42, pp.743-770.

James D. E. 1996. The Geochemistry of Feldspar-Free Volcanic Rocks. Unpubl. PhD. Thesis The Open University.

Jarvis I. & Jarvis K. E. 1985. Rare Earth Element Geochemistry of Standard Sediments: A Study Using Plasma Spectrometry. Chem. Geol. Vol. 53, pp.335-44.

Jean-Baptiste P., Mantisi F., Pauwells H., Grimaud D. & Patriat P. 1992. Hydrothermal ^{3}He and Manganese Plumes at 19°29'S on the Central Indian Ridge. Geophys. Res. Lett. Vol.19, pp.1787-1790.

Kelemen P. B., Johnson K. T. M.., Kinzler R. J. & Irving A. J. 1990. High-Field Strength Element Depletions in Arc Basalts due to Mantle-Magma Interaction. Nature. Vol. 345, pp.521-524.

Kelemen P. B., Shimizu N. & Salters V. J. M. 1995. Extraction of Mid-Ocean-Ridge Basalt from the Upwelling Mantle by Focused Flow of Melt in Dunite Channels. Nature. Vol. 375, pp.747-753.

Kent P. E. 1974. Continental Margin of East Africa-A Region of Vertical Movements. In: The Geology of Continental Margins. Eds. Drake C. A. and Drake C. L. Springer. New York. pp.313-320.

Kolla V., Sullivan L., Streeter S. S. and Langseth M. G. 1976. Spreading of Antarctic Bottom Water and its Effect on the Indian Ocean Inferred from Bottom Water Potential Temperature, Turbidity and Sea Floor Photography. Mar. Geol. Vol. 21, pp.171-189.

Krishnan M. S. 1953. The Structural and Tectonic History of India. Mem. Geol. Surv. India. Vol.81, pp.1-109.

Langmuir C. H. 1990. Ocean Ridges Spring Surprises. Nature Vol.344. pp.585-586.

Langmuir C. H. & Bender J. F. 1984. The Geochemistry of Oceanic Basalts in the Vicinity of Transform Faults: Observations and Implications. Earth and Planet. Sci. Lett. Vol.69, pp.107-127.

Latin D. & Waters F. G. 1991. Melt Generation During Rifting in the North Sea. Nature. Vol.351, pp.559-562.

le Pichon X. and Heirtzler J. R. 1968. Magnetic Anomalies in the Indian Ocean and Sea-Floor Spreading. J. Geophys. Res. Vol.73, pp.2101-2117.

le Roex A. P., Dick H. J. B. and Watkins R. T. 1992. Petrogenesis of Anomalous K-Enriched MORB from the Southwest Indian Ridge: 11°53'E to 14°38'E. Contribs. Min. and Petrol. Vol.110, pp.253-268.

Lightfoot P. C., Hawkesworth C. J. Devey C. W., Rogers N. W. and Van Calstern P. W. C. 1990. Source and Differentiation of Deccan Trap Lavas: Implications of Geochemical and Mineral Chemical Variations. J. of Petrol. Vol.31, pp.1165-1200.

Lindstrom D. J. 1976. Experimental Study of the Partitioning of the Transition Metals between Clinopyroxene and Coexisting Silicate Liquids. PhD thesis unpublished University of Oregon.

Macdonald G. A. and Katsura T. 1964. Chemical Composition of Hawaiian Lavas. J. of Petrol. Vol.5, pp.82-133.

Macdonald R., McGarvie D. W., Pinkerton H., Smith R. L. & Palacz Z. A. 1990. Petrogenetic Evolution of the Torfajökull Volcanic Complex, Iceland I. Relationship Between the Magma Types. J. of Petrol. Vol.31, pp.429-459.

Mahoney J. J., Natland J. H., White W. M., Poreda R., Bloomer S. H., Fisher R. L. & Baxter A. N. 1989. Isotopic and Geochemical Provinces of the Western Indian Ocean Spreading Centers. J. Geophys. Res. Vol. 94, No. B4, pp.4033-4052.

Mart Y. 1988. The Tectonic Setting of the Seychelles, Mascarene and Amirante Plateaus in the Western Equatorial Indian Ocean. Marine Geology. Vol.79, pp.261-274.

Maskelyne N. S. 1879. Petrology. In : The Collections from Rodriguez. Philos. Trans. Royal Soc. Vol.168 (extra volume) pp.296-301.

McDougall I. 1971. The Geochronology and Evolution of the Young Volcanic Island of Réunion, Indian Ocean. Geochim. et Cosmochim. Acta. Vol.35, pp.261-288.

McDougall I. & Chamalaun F. H. 1969. Isotopic Dating and Geomagnetic Polarity Studies on Volcanic Rocks form Mauritius, Indian Ocean. Geol. Soc. Am. Bull. Vol.80, pp.1419-1442.

McDougall I., Upton B. G. J. & Wadsworth W. J. 1965. A Geological Reconnaissance of Rodriguez Island, Indian Ocean. Nature Vol.206, pp.26-27.

McKenzie D. & O'Nions R. K. 1991. Partial melt Distributions from Inversion of Rare Earth Element Concentrations. J. of Petrology. Vol.32, pp.1021-1091.

McKenzie D. P. & Sclater J. G. 1971. The Evolution of the Indian Ocean since Late Cretaceous. Geophys. J. R. astr. Soc. Vol.25, pp.437-528.

Mitchell N. C. 1991. An Evolving Ridge System Around the Indian ocean Triple Junction. Mar. Geophys. Res. Vol.13, pp.173-201.

Morgan W. J. 1971. Convective Plumes in the Lower Mantle. Nature Vol.230, pp.42-43.

Morgan W. J. 1978. Rodriguez, Darwin, Amsterdam,.., A Second Type of Hotspot Island. J. Geophys. Res. Vol.83, No. B11, pp.5355-5360.

Morgan W. J. 1981. Hotspot Tracks and the Opening of the Atlantic and Indian Oceans. In: The Sea, Ideas and Observations on Progress in the Study of the Sea. Volume VII; The Oceanic Lithosphere. Ed. Emiliani C. John Wiley & Sons. New York. 1738 pages.

Morgan W. J. 1982. Convection Plumes in the Lower Mantle. Nature. Vol. 230, pp.42-43.

Müller R. D., Royer J-Y. & Lawver L. A. 1993. Revised Plate Motions Relative to the Hotspots from Combined Atlantic and Indian Ocean Hotspot Tracks. Geology. Vol.21, pp.275-278.

Natland J. 1991. Indian Ocean Crust. Ch. 12. In: Oceanic Basalts. Ed. P. A. Floyd. Blackie. pp.289-310.

Nayudu Y. R. 1972. Geologic Implications of Microfossils in Submarine Volcanics. Bull. Volcanol. Vol.35, pp.402-23.

Niu Y. 1997. Mantle Melting and Melt Extraction Processes Beneath Ocean Ridges: Evidence from Abyssal Peridotites. J. of Petrol. Vol.38, No.8, pp.1047-1074

Norry M. J. 1973. A Geochemical Study of some Selected Lavas from Mauritius, Western Indian Ocean. Chapter 3. PhD Thesis. University of Oxford. Unpublished.

Norton I. O. & Sclater J. G. 1979. A Model for the Evolution of the Indian Ocean and the Breakup of Gondwanaland. J. Geophys. Res. Vol.84, No. B12, pp.6803-6830.

O'Hara M. J. 1968. The Bearing of Phase Equilibria Studies in Synthetic and Natural Systems on the Origin and Evolution of basic and Ultrabasic Rocks. Earth Sci. Reviews. Vol.4, pp.69-133.

O'Hara M. J. 1977. Geochemical Evolution During Fractional Crystallisation of a Periodically Refilled Magma Chamber. Nature Vol.266, pp.503-507.

O'Hara M. J. & Mathews R. E. 1981. Geochemical Evolution in a Advancing, Periodically Replenished, Periodically Tapped, Continuously Fractionated Magma Chamber. J. Geol. Soc. London. Vol.138, pp.237-277.

Oldenburg C. M., Spera F. J., Yuen D. A. & Sewell G. 1989. Dynamic Mixing in Magma Bodies: Theory, Simulations, and Implications. J. Geophys. Res. Vol. 94, No. B7, pp.9215-9236.

Olson P. & Singer H. 1985. Creeping Plumes. J. Fluid Mech. Vol.158, pp.511-531.

Oversby V. M. 1972. Genetic Relations Among the Volcanic Rocks of Réunion: Chemical and Lead Isotopic Evidence. Geochim. et Cosmochim. Acta. Vol.36, pp.1167-1179.

Parsons B. & McKenzie D. P. 1978. Mantle Convection and the Thermal Structure of the Plates. J. Geophys. Res. Vol.83, pp.4485-4496.

Parsons L. M., Patriat P., Searle R. C. and Briais A. R. 1993. Segmentation of the Central Indian Ridge Between 12°12'S and the Indian Ocean Triple Junction. Marine Geophysic. Res. Vol.15, pp.265-282.

Patriat P. & Ségoufin J. 1988. Reconstruction of the Central Indian Ocean. Tectonophysics. Vol.155, pp.211-234.

Paul D. K., Potts P. J., Rex D. C. & Beckinsale R. D. 1977. Geochemical and Petrogenetic Study of the Girnar Igneous Complex, Deccan Volcanic Province, India. Geol. Soc. Am. Bull. Vol.88, pp.227-234.

Pearce J. A. & Cann J. R. 1973. Tectonic Setting of Basic Volcanic Rocks Determined Using Trace Element Analyses. Earth & Planet. Sci. Lett. Vol.19, pp.290-300.

Pearce J. A. & Norry M. J. 1979. Petrogenetic Implications of Ti, Zr, Y, and Nb Variations in Volcanic Rocks. Contrib. Min. & Petrol. Vol.69, pp.33-47.

Peng Z. X. & Mahoney J. J. 1995. Drillhole lavas from the Northwestern Deccan Traps, and the Evolution of Réunion Hotspot Mantle. Earth. Planet. Sci. Lett. Vol.134, pp.169-185.

Perfit M. R. & Fornari D. J. 1983. Geochemical Studies of Abyssal lavas Recovered by DSRV Alvin from Eastern Galapagos Rift, Inca Transform, & Ecuador Rift. 2. Phase Chemistry & Crystallization History. J. Geophys. Res. Vol.88, No. B12, pp.10,530-10,550.

Perroud B. 1982. Etude Volcano Structurale des iles Maurice et Rodrigue (Ocean Indien Occidental). Origine du Volcanisme. unpublished PhD thesis. Grenoble.

Price R. C., Kennedy A. K., Riggs-Sneeringer M. & Frey F. A. 1986. Geochemistry of Basalts from the Indian Ocean Triple Junction: Implications for the Generation and Evolution of Indian Ocean Basalts. Earth and Planet. Sci. Lett. Vol.78, pp.379-396.

Rabinowicz M., Rouzo S., Sempere J.-C. & Rosemberg C. 1993. Three-Dimensional Mantle Flow Beneath Mid-Ocean Ridges. J. of Geophys. Res. Vol.98, No. B5, pp.7851-7869.

Rampone E., Piccardo G. B., Vannucci R., Bottazzi P. and Ottolini L. 1993. Subsolidus Reactions Monitored by trace Element Partitioning: The Spinel-to Plagioclase-Facies Transition in Mantle Peridotites. Contrib. Mineral. Petrol. Vol.115, pp.1-17.

Richards M. A., Duncan R. A. & Courtillot V. E. 1989. Flood Basalts and Hot-Spot Tracks: Plume Heads and Tails. Science Vol.246, pp.103-107.

Ringwood A. E. 1970. Petrogenesis of Apollo 11 Basalts and Implications for Lunar Origin. J. Geophys. Res. Vol.75, No.32, pp.6453-6479.

Robinson P. T., Von Herzen R., *et al.,* 1989. Proc. ODP, Initial Reports. Vol.118, College Station, TX (Ocean Drilling Program). 826 pages.

Rollinson H. R. 1993. Using Geochemical Data: Evaluation, Presentation, Interpretation. Longman Scientific & Technical. New York. 352 pages.

Schilling J. G., Thompson G., Kingsley R. & Humphris S. 1985. Hotspot-migrating Ridge Interaction in the South Atlantic. Nature. Vol. 313, pp.187-191.

Schilling J. G. 1991. Fluxes and Excess Temperatures of Mantle Plumes Inferred from their Interaction with Migrating Mid-Ocean Ridges. Nature. Vol.352, pp.397-403.

Schlich R. 1982. Aseismic Ridges, Spreading Centres and Basins. In: The Ocean Basins and Margins. Eds. Nairn A. E. M. and Stehli F. G. Vol.6 The Indian Ocean. 776 pages.

Ségoufin J. 1978. Anomalies Magnétiques Mésozoiques dans le Bassin de Mozambique. Computes Rendu Acad. Sci. Vol.287D, pp.109-112.

Sigurdson H. & Brown G. M. 1970. An Unusual Enstatite-Forsterite Basalt from Kolbeinsey Island, North of Iceland. J. of Petrol. Vol.11, pp.205-220.

Sleep N. H. 1990. Hotspots and Mantle Plumes: Some Phenomenology. J. Geophys. Res. Vol.95, No. B5, pp.6715-6736.

Snell H. J. & Tams W. H. T. 1920. The Natural History of the Island of Rodrigues. Trans. Cambridge Philos. Soc. Vol.19, pp.283-292.

Staudigel H & Hart S. R. 1983. Alteration of Basaltic Glass: Mechanisms and Significance for the Oceanic Crust-Seawater Budget. Geochim. et Cosmochim. Acta. Vol.47, pp.337-350.

Stecher O., Carlson R. W. and Gunnarsson B. 1999. Torfajökull: A Radiogenic End-Member of the

Iceland Pb-Isotopic Array. Earth. Planet. Sci. Lett. Vol. 165, pp.117-127.

Stommel H and Arons A. B. 1958. The Abyssal Circulation. Deep Sea Res. Vol. 5, pp 80-82.

Stommel H and Arons A. B. 1960a. On the Abyssal Circulation of the World Ocean I. Stationary Planetary Flow Patterns on a Sphere. Deep Sea Res. Vol.6, pp.140-154.

Stommel H and Arons A. B. 1960b. On the Abyssal Circulation of the World Ocean II. An Idealized Model of the Circulation Pattern and Amplitude in the Ocean Basins. Deep Sea Res. Vol.6, pp.217-233.

Strong D. F. 1972a. Petrology of the Island of Moheli, Western Indian Ocean. Geol. Soc. Am. Bull. Vol.83, pp.389-406.

Strong D. F. 1972b. The Petrology of the Lavas of Grande Comore. J. of Petrol. Vol.13, pp.181-217.

Sun S. -S. & McDonough W. F.1989. Chemical and Isotopic Systematics of Oceanic Basalts: Implications for Mantle Composition and Processes. In: Magmatism in the Ocean Basins. Eds. Saunders A. D. & Norry M. J. Geol. Soc. London Special Publication No.42, pp.313-345.

Ten Brink U. S., Brocher T. M. and Watts A. B. 1986. The Nature of the Crust-Mantle Transition under the Flexural Moats Flanking Hawaii. EOS. Vol.67, p.371 (Abstract).

Thompson M. & Walsh J. N. 1989. Handbook of Inductively Coupled Plasma Spectrometry. 2nd Ed. Blackie. Glasgow. 316 pages.

Tlig S. 1991. Rare Earth Element Redistribution During Secondary Mineral Formation: Examples from Reef Carbonate Karst (Jebel Stah, Tunisia) and from Oceanic Basalts (Site 417A, Northern Atlantic). J. African Earth Sci. Vol.1, pp.173-182.

Udintsev G. B. 1975. Geological-Geophysical Atlas of the Indian Ocean. International Indian Ocean Expedition. Pergamon Press. Oxford. 115 pages.

Upton B. G. J. 1982. Oceanic Islands. In: The Ocean Basins and Margins. Vol.6, The Indian Ocean. Eds. Nairn A. E. M. & Stehli F. G. Ch.13, pp.585-648.

Upton B. G. J. & Wadsworth W. J. 1965. Geology of Réunion Island, Indian Ocean. Nature Vol.207, pp.131-154.

Upton B. G. J. & Wadsworth W. J. 1966. The Basalts of Réunion Island, Indian Ocean. Bull. Volcanologique. Vol.29, pp.7-24.

Upton B. G. J. & Wadsworth W. J. 1969. Early Volcanic Rocks of Réunion and Their Significance. Bull. Volcanologique Vol.33, pp.1246-1268.

Upton B. G. J. & Wadsworth W. J. 1972. Aspects of Magmatic Evolution on Reunion Island. Philos. Trans. R. Soc. London. Series A, Vol.271, pp.105-130.

Upton B. G. J., Wadsworth W. J. & Newman T. C. 1967. The Petrology of Rodriguez Island, Indian Ocean. Geol. Soc. Am. Bull. Vol.78, pp.1495-1506.

Upton B. G. J. 1997. Pers. Comm.

Vandamme D. & Courtillot V. 1990. Latitudinal Evolution of the Reunion Hotspot Deduced from Paleomagnetic Results of Leg 115. Geophys. Res. Lett. Vol.17, pp.1105-1108.

Vannucci R., Bottazzi P., Wulff-Pedersen E. and Neumann E.-R. 1998. Partitioning of REE, Y, Sr, Zr,

and Ti Between Clinopyroxene and Silicate Melts in the Upper Mantle Under La Palma (Canary Islands): Implications for the Nature of the Metasomatic Agents. Earth. Planet. Sci. Lett. Vol.158, pp.39-51.

Verma S. P. 1992. Seawater Alteration Effects on REE, K, Rb, Cs, Sr, U, Th, Pb, and Sr-Nd-Pb Isotope Systematics of Mid-Ocean Ridge Basalt. Geochemical Journal. Vol.26, pp.159-177.

Von Herzen R. P. & Vacquier V. 1966. Heat Flow and Magnetic Profiles on the Mid-Indian Ocean Ridge. Philos. Trans. R. Soc. London. Series A, Vol. 259, pp.262-270.

Walsh J. N., Buckley F. & Barker J. 1981. The Simultaneous Determination of the Rare-Earth Elements in Rocks Using Inductively Coupled Plasma Source Spectrometry. Chem. Geol. Vol.33, pp.141-53.

White, W. M., Cheatham M. M. & Duncan R. A. 1990. Isotope Geochemistry of Leg 115 Basalts and Inferences on the History of the Réunion Mantle Plume. In: Duncan R. A., Backman J. & Peterson I. C. *et al.*, Proc. ODP, Sci. Results. Vol.115, College Station TX (Ocean Drilling Program) pp.53-61.

Whitehead J. A. & Luther D. S. 1975. Dynamics of Laboratory Diapir and Plume Models. J. Geophys. Res. Vol.80, No.5, pp.705-717.

Wood D. A., Gibson I. L. & Thompson R. N. 1976. Elemental Mobility During Zeolite Facies Metamorphism of the Basalts of Eastern Iceland. Contrib. Mineral. Petrol. Vol.55, pp.241-254.

Wood D. A. 1979. A Variably Veined Suboceanic Upper Mantle - Genetic Significance for Mid-Ocean Ridge Basalts from Geochemical Evidence. Geology. Vol.7, pp.499-503.

Wright T. L. & Doherty P. C. 1970. A Linear Programming and Least Squares Computer Method for Solving Petrologic Mixing Problems. Geol. Soc. Am. Bull. Vol.81, pp.1995-2008.

Yoder Jr. H. S. & Tilley C. E. 1962. Origin of Basalt Magmas: An Experimental Study of Natural and Synthetic Rock Systems. J. of Petrol. Vol.3, pp.342-532.

Zielinski R. A. 1975. Trace Element Evaluation of a Suite of Rocks from Reunion Island, Indian Ocean. Geochim. et Cosmochim. Acta. Vol.39, pp.713-734.

Zoback M. L. & Burke K. 1993. Lithospheric Stress Patterns: A Global View. EOS Trans. A.G.U. Vol.74, No.52, pp.609, 615, 618.

References for Appendix 1

1. Baxter A. N., Upton B. G. J. & White W. M. 1985. Petrology and Geochemistry of Rodrigues Island, Indian Ocean. Contrib. Mineral. Petrol. Vol. 89, pp.90-101.
2. Benjamin T., Heuser W. R., Burnett D. S. & Seitz M. G. 1980. Actinide Crystal-Liquid Partitioning for Clinopyroxene and $Ca_3(PO_4)_2$. Geochimica et Cosmochim. Acta. Vol.44, pp.1251-264.
3. Bird M. L. 1971. Distribution of Trace Elements in Olivines and Pyroxenes an Experimental Study. Phd Thesis, University of Missouri, Rolla.

39. Blundy J. D., Robinson J. A. C. and Wood B. J. 1998. Heavy REE are Compatible in Clinopyroxene on the Spinel Lherzolite Solidus. Earth. Planet. Sci. Lett. Vol. 160, pp.493-504.

4. Clague D. A. & Beeson M. H. 1980. Trace Element Geochemistry of the East Molokai Volcanic Series, Hawaii. Am. J. Sci. Vol. 280A, pp.820-844.

26. Cox K. G., Bell J. D. & Pankhurst R. J. 1987. The Interpretation of the Igneous Rocks. George Allen and Unwin. London. 450 pages.

5. Drake M. J. 1975. The Oxidation State of Europium as an Indicator of Oxygen Fugacity. Geochim. et Cosmochim. Acta. Vol.39, pp.55-64.
6. Duke J. M. 1976. Distribution of the Period Four Transition Elements Among Olivine, Calcic Clinopyroxene and Mafic Silicate Liquid: Experimental Results. J. of Petrol. Vol.17, Pt.4, pp.499-521.
7. Dunn T. & Sen C. 1994. Mineral Matrix Partition Coefficients for Othopyroxene, Plagioclase and Olivine in Basaltic to Andesitic Systems: A Combined Analytical and Experimental Study. Geochim. et Cosmochim. Acta. Vol.58, No. 2, pp.717-733.

29. Ewart A., Bryan W. B. and Gill J. B. 1973. Mineralogy and Geochemistry of the Younger Volcanic Islands of Tonga, S.W. Pacific. J. of Petrol. Vol.14, Pt.3, pp.429-465.

8. Frey F. A., Green D. H. & Roy S. D. 1978. Integrated Models of Basalt Petrogenesis: A Study of Quartz Tholeiites to Olivine Melilites from South Eastern Australia Utilizing Geochemical and Experimental Petrological Data. J. of Petrol. Vol.19, Pt.3, pp.463-513.

36. Gill J. B. 1978. Role of Trace Element Partition Coefficients in Models of Andesite Genesis. Geochim. et Cosmochim. Acta. Vol.42, pp.709-724.

9. Grutzeck M., Kridelbaugh S. & Weill D. 1974. The Distribution of Sr and REE Between Diopside and Silicate Liquid. Geophys. Res. Lett. Vol.1, No.6, pp.273-275.
10. Gunn B. M. 1971. Trace Element Partition During Olivine Fractionation of Hawaiian Basalts. Chem. Geol. Vol.8, pp.1-13.
11. Hanson G. N. 1980. Rare Earth Elements in Petrogenetic Studies of Igneous Systems. Ann. Rev. Earth Planet. Sci. Vol.8, pp.371-406.
12. Irving A. J. 1978a. A Review of Experimental Studies of Crystal/Liquid Trace Element Partitioning. Geochim. et Cosmochim. Acta. Vol.42, pp.743-770.

35. Irving A. J. 1978b. The Distribution of Trace Elements between Garnet Megacrysts and Volcanic Liquids of Kimberlitic to Rhyolitic Composition. Geochim. et Cosmochim. Acta. Vol.42, pp.743-770.

28. Jenner G. A., Foley S. F., Jackson S. E., Green T. H., Freyer B. J. and Longerich H. P. 1993. Determination of Partition Coefficients for Trace Elements in High Pressure-Temperature Experimental Run Products by Laser Ablation Microprobe-Inductively Coupled Plasma-Mass Spectrometry (LAM-ICP-MS). Geochim. Cosmochim. Acta. Vol.57, No.23/24, pp.5099-5103.

30. Kay R. W. & Gast P. W. 1973. The Rare Earth Content and Origin of Alkali-Rich Basalts. J. of Geol. Vol.81, pp.653-682.

13. Kelemen P. B., Shimizu N. and Dunn T. 1993. Relative Depletion of Niobium in some Arc Magmas and the Continental Crust: Partitioning of K, Nb, La and Ce During Melt/Rock Reaction in the Upper Mantle. Earth and Planet. Sci. Lett. Vol.120, pp.111-134.

27. LaTourrette T. Z., Kennedy A. K. & Wasserburg G. J. 1993. Thorium-Uranium Fractionation by Garnet: Evidence for a Deep Source and Rapid Rise of Oceanic Basalts. Science Vol. 261, pp.739-742.

14. Leeman W. P. and Scheidegger K. F. 1977. Olivine/Liquid Distribution Coefficients and a test for Crystal-Liquid Equlibrium. Earth and Planet. Sci. Lett. Vol.35, pp.247-257.

34. Lindstrom D. J. 1976. Experimental Study of the Partitioning of the Transition Metals Between Clinopyroxene and Coexisting Liquids. Phd Thesis unpublished. University of Oregon.

37. Lindstrom W. P. and Weill D. F. 1978. Partitioning of Transition Metals between Diopside and Coexisting Silicate Liquids. I. Nickel, Cobalt, and Manganese. Geochim. et Cosmochim. Acta. Vol.42, pp.743-770.

15. McKenzie D. & O'Nions R. K. 1991. Partial Melt Distributions from Inversion of Rare Earth Element Concentrations. J. of Petrol. Vol.32, Pt.5, pp.1012-1091.

16. Nagasawa H. 1973. Rare Earth Distribution in Alkali Rocks from Oki-Dogo Island, Japan. Contrib. Mineral. and Petrol. Vol.39, pp.301-308.

32. Nagasawa H. & Wakita H. 1968 Partition of Uranium and Thorium between augite and Host Lavas. Geochim. et Cosmochim. Acta. Vol.32, pp.917-921.

17. Pearce J. A. & Norry M. J. 1979. Petrogenetic Implications of Ti, Zr, Y, and Nb Variations in Volcanic Rocks. Contrib. Mineral. and Petrol. Vol.69, pp.33-47.

31. Peters M. T., Shaffer E. E. Brnett D. S. 1994. Temperature and Time Marking of Crystal Growth During Crystal-Liquid Partitioning Experiments: A New Technique and Application to Anorthite-Liquid Partitioning. Mineral. Mag. Vol.58, pp.713-714.

18. Rampone E., Piccardo G. B., Vannucci R., Bottazzi P. and Ottolini L. 1993. Subsolidus Reactions Monitored by trace Element Partitioning: The Spinel-to Plagioclase-Facies Transition in Mantle Peridotites. Contrib. Mineral. Petrol. Vol.115, pp.1-17.

33. Ringwood A. E. 1970. Petrogenesis of Apollo 11 Basalts and Implications for Lunar Origin. J. Geophys. Res. Vol.75, No.32, pp.6453-6479.

41. Salters V. J. M. and Longhi J. 1999. Trace Element Partitioning During the Initial Stages of Melting Beneath Mid-Ocean Ridges. Earth. Planet. Sci. Lett. Vol.166, pp.15-30.

19. Schnetzler C. C. & Philpotts J. A. 1970. Partition Coefficients of Rare-Earth Elements Between Igneous Matrix Material and Rock-Forming Mineral Phenocrysts- II. Geochim. et Cosmochim. Acta. Vol.34, pp.331-340.

38. Schock H. H. 1979. Distribution of Rare-Earth and Other Trace Elements in Magnetites. Chem. Geol. Vol.26, pp.119-133.

40. Schosnig M. and Hoffer E. 1998. Compositional Dependence of REE Partitioning Between Diopside and Melt at 1 Athmosphere. Contrib. Mineral. And Petrol. Vol.133, pp.205-216.

20. Seward T. M. 1971. The Distribution of transition Elements in the System $CaMgSi_2O_6$-$Na_2Si_2O_5$-H_2O at 1,000 bars Pressure. Chem. Geol. Vol.7, pp.73-95.

21. Shilling J.-G., Bergeron M. B. and Evans R. 1980. Halogens in the Mantle Beneath the North Atlantic. Philos. Trans. R. Soc. London. Series A. Vol.297, pp.147-178.

22. Shimizu N. 1974. An Experimental Study of the Partitioning of K, Rb, Cs, Sr and Ba Between Clinopyroxene and Liquid at High Pressures. Geochim. et Cosmochim. Acta. Vol.38, pp.1789-1798.

23. Shimizu N., & Kushiro I. 1975. The Partitioning of Rare Earth Elements Between Garnet and Liquid at High Pressures: Preliminary Experiments. Geophys. Res. Lett. Vol.2, No.10, pp.413-415.

24. Sun S.-S. & Hanson G. N. 1976. Rare Earth Element Evidence for Differentiation of McMurdo Volcanics, Ross Island, Antarctica. Contrib. Mineral. Petrol. Vol.54, pp.139-155.

25. Sun C.-O., Williams R. J. & Sun S.-S. 1974. Distribution Coefficients of Eu and Sr for Plagioclase-Liquid and Clinopyroxene Liquid Equilibria in Oceanic Ridge Basalt: an Experimental Study. Geochim. et Cosmochim. Acta. Vol.38, pp.1415-1433.

42. Vannucci R., Bottazzi P., Wulff-Pedersen E. and Neumann E.-R. 1998. Partitioning of REE, Y, Sr, Zr, and Ti Between Clinopyroxene and Silicate Melts in the Mantle Under La Palma (Canary Islands): Implications for the Nature of the Metasomatic Agents. Earth. Planet. Sci. Lett. Vol.158, pp.39-51

Appendix 1

Mineral Partition Coefficients

In this appendix a collated list of trace element partition coefficients is presented for olivine, orthopyroxene, clinopyroxene, plagioclase, garnet, spinel and magnetite in basaltic and basaltic-andesite compositions. Three basic methods have been employed to determine these values; 1. experimental results, 2. Natural systems and 3. Interpolation between previously published values.

1. Experimental results are either derived on artificial systems of using natural basalts. In either case samples are heated under controlled conditions and the compositions of both crystals and melt are subsequently measured.

2. Compositions of coexisting mineral/glass pairs are analysed in naturally occurring basalts, as has been done in this study for Cr, K, Mn, P and Ti in olivine, K, Mn, P and Ti in plagioclase and spinel (values underlined on table 48). Partition coefficients derived in this way probably provide a better idea of behaviour in natural basalts, but the exact detail of the prevailing conditions remains unknown. Furthermore values derived in this way assume that the crystals are at equilibrium with the coexisting melt, something that not be the case for many basalt systems. For example some zoning has been observed among the phenocrysts in the Rodrigues Ridge lavas indicating that the melt was evolving rapidly and that only the outer most layer of such crystals was in equilibrium with the surrounding melt. Despite the difficulties this is often the best source of partition coefficients for a given suite of lavas.

3. Where no published information is available some authors has used data for chemically similar elements to estimate partition coefficients. This technique is particularly common for partition coefficients of REE. Where the partition coefficients for the neighbouring elements are well constrained this technique is also well constrained but in some cases previous estimates have been used to estimate other element partition coefficients which must ultimately lead to poorly constrained results. In the notes to this appendix the sources are listed and summaries of the conditions under which the data were obtained.

Table 48 **Mineral Partition Coefficients**

	ol	opx	cpx	plag	gt	sp	mt
Ba	0.0001-0.005	0.0006-0.011	0.00078-0.0309	0.12-1.47	0.001-0.002	0.01	
Ce	0.00001-0.009	0.0009-0.038	0.04-0.12	0.11-0.215	0.0033-0.348	0.0006-0.08	1.3-3
Cr	0.2-2.92 0.78	1.96-36	1.5-76.0	0.01	0.06-17.5	10-750	64-620
Cu	0.2-0.47	0.13-0.18	0.09-2.6	0.07-0.28			1.7
Dy	0.0017-0.034	0.022-0.40	0.33-0.37	0.024-0.094	1.06-28.6	0.0015-0.109	
Er	0.0015-0.045	0.030-0.65	0.30-0.37	0.015-0.078	2.00-42.8	0.003-0.118	
Eu	0.00095-0.023	0.0036-0.086	0.273-0.36	0.14-0.73	0.1333-1.5	0.0006-0.055	0.6-1.5
Gd	0.0015-0.033	0.016-0.24	0.08-0.53	0.066-0.127	0.498-10.5	0.0006-0.077	
Ho	0.0016-0.037	0.0089-0.52	0.195-0.31	0.048	1.083-13.2	0.1	
K	1 x 10^{-9}-0.007 0.08	0.00001-0.0025	0.0014-0.0072	0.07-0.20 0.32	0.00001-0.001	0-0.01 0.17	
La	0.00007-0.0005	0.0005-0.002	0.02-0.11	0.13-0.280	0.001-0.026	0.0006-0.01	1.5-3
Lu	0.0015-0.0048	0.038-1.4	0.11-0.55	0.025-0.080	5.01-41	0.02-0.091	0.9-1.5
Mn	0.58-1.67 1.33	0.62-2.2	0.3-1.8	0.05 0.25	2.0	1.40	1.4-1.81
Nb	0.0001-0.01	0.003-0.15	0.004-0.1	0.01-0.045	0.004-0.1	0.01	0.4
Nd	0.00007-0.011	0.0019-0.058	0.09-0.24	0.066-0.170	0.0184-0.525	0.0006-0.037	1-3
Ni	4.07-23.8	1.67-13	2.0-12.0	0.01-0.04	0.4-5.1	4.43-53	4-77
P	0.043 0.23	0.014	0.009-0.025	0.51	0.15	0.08	
Pr	0.0008-0.0098	0.0034-0.0059	0.15	0.096-0.17	0.054	0.01-0.03	1.5-2.3
Rb	0.0011-0.017	0.0006-0.001	0.0010-0.0041	0.056-0.07	0.0007-0.001	0.01	
Sc	0.14-*0.37*	0.53-1.8	1.42-3.2	0.017-0.065	2.6-27.6	0.048	0.80-3.3
Sm	0.0007-0.028	0.0028-0.100	0.11-0.61	0.053-0.135	0.074-2.66	0.0006-0.052	1.1-2.2
Sr	0.003-0.018	0.009-0.018	0.054-0.196	1.07-4.62	0.001-0.015	0.01	
Tb	0.0015-0.035	0.0059-0.32	0.19-0.31	0.040-0.061	0.2568-4.1	0.0075	1-2
Th	0.0001-0.027	0.0001-0.01	0.0019-0.0033	0.13-0.19	0.0001-0.017		
Ti	0.015-0.07 0.02	0.1-0.2	0.19-2.4	0.035-0.057 0.05	0.3-1.0	0.15 0.46	7.5-23
U	0.0001-0.081	0.0013-0.008	0.0019-0.0047	0.051-0.34	0.0001-0.044		
V	0.011-0.05 1.3*	0.06-2.8	0.64-10.4	0.022-0.032	0.2-3.75	(38*) or 0.1	5-30
Y	0.002-0.033	0.19-0.54	0.07-0.72	0.013-0.03	2.0-7.1		0.2
Yb	0.0015-0.055	0.0286-0.92	0.11-0.53	0.0079-0.07	4.0-39.9	0.0045-0.111	0.9-1.8
Zn	0.95			0.01			10-20
Zr	0.0005-0.01	0.014-0.03	0.1-0.21	0.01	0.3-1.027	0.07	0.1

Appendix 1 cont... **Numbers of References Used to Construct table 48**

	Olivine	Orthopyroxene	Clinopyroxene	Plagioclase	Garnet	Spinel	Magnetite
Ba	21-12 26	21-12 26	22-16 21, 26	29-24 16,7,4,33,36	21-26.	26.	
Ce	13-19 8, 11, 26, 7	13/8-19 11, 26, 7	8-9/40, 19, 11, 28, 26	7-24 11	8-19 13,11,23,26,35,41	13-26 30, 15	38-38
Cr	26-14 6,3,33 This Work	3-29 26	4-20 6, 26, 29, 33	12	35-12 21, 26	26-3, 33	36-12, 29.
Cu	3-12	29-29	29-20 12	29-29 4			29.
Dy	7/11-7 19, 13	11-7 19, 13	11/9-19	7-24 11	11/23-19 13	13-30 15, 1	
Er	11-7 19, 13	11-7 19, 13	11/9-19	7-24 11	11/23-19 13, 41	13-30 15	
Eu	13-7 11, 19, 8, 26	8-7 19 11, 13, 26	19-9, 8,19,25,11,26	5-15 25, 7, 36	8-19 13, 11, 23, 26, 35	13-30 15, 26	38-38
Gd	11-7 19, 13	11-7 19, 13	40-40, 11, 9 19	11-24	11/23-19 13, 35	13-30 15	
Ho	15-7 8	8-7 15	8-15	15	8-35 15	Interpolated-12	
K	13-4 21, 26 This work	13-21	22-13 21	29-12 36 This work	13-26	13-26 This work	
La	13-8	13/8-15 7	8-40 9, 15	7-24 15	13/8-35 15, 21	13-15	38-38
Lu	15-8	8-7 19	40-40, 8, 9, 15	15	41-35 15, 19, 8	12-30 15	38-38
Mn	3-14 6,10,21 This work	3-29	20-29 6, 21, 37	12 This work	21	This work	29-12
Nb	13-17 7	13-17 7	28-17 13	17-7	41-17 13, 28	13	17
Nd	13-7 19, 8, 11	8-19 11, 13, 7	8-9 19, 11	7-24 11	8-19 13, 11, 23, 41	13-30 15	38-38
Ni	3-14 6, 26, 10, 21	3-29 26, 21, 12	20-20 26, 20, 6, 29	26-12	26-12	3-12, 26	4-12 29
P	21 This work	21	21-2	This work	21	This work	
Pr	15-7	7-7 15.	15	7-15	15	15-1	
Rb	7-7 8, 26	15-26 21	26/22-22.	7-36 24	15-26 21	26	
Sc	14-12	12-29 21	28-29 21 12, 8	12	35-12 21, 28	12	12-12,36,29,38
Sm	13-7 19,11,7,8,21,14,26	8-19,11,13,21,26,7	40-40,8, 9,19,11,26	7-24 11 36	8-19,13,11,21,23,26-28,35,41	13-30 26, 15	38-38
Sr	12-7 26	12-12 21, 26, 7	22-25 9,16,21,28,26,40	31-24,7,25,5,16,29,33,36	26-21 28	26	
Tb	15-7 8	8-7 15	8-15	7-7 15	8-35 15	12	38-38
Th	15-7	15-7	2-2, 32	7-7	15-41, 27		
Ti	13-6 17 This work	17-29 13, 21	29-20 6, 28, 17	31-7 17 This work	17-28 13	13, This work	17-29
U	15-7	7-12	2-2, 32	7-7	15-41, 27		
V	12-6/33	12-12 21, 7, 29	29-20 28,12,6,33,34	7-7	21-28 8	33 see also 18	12-36
Y	8-7 17	7-7 17	40-40, 8, 28 17	7-17	17-28 41		17
Yb	11-7 13, 21, 19, 26, 8	8-7,19,11,13,21	40-40,8,15,19,11,21	7-36, 24, 11	26/21/13/8-19,23,11,35,41	13-30 15, 26	38-38
Zn	10			4			38-38
Zr	13-17/4	13-17	17-28	17	13/17-41 28	13	17

Appendix 1 cont...

Notes on Information Sources Used in Table 48

Original references:
Gunn-10
Drake-5
Seward-20
Frey-8 REE's
Benjamin-2

Dunn-7

Jenner-28

Hanson-11 for ol.
Grutzeck-9

Leeman-14
Sun-25
Schnetzler-19
Bird-3
Shimizu-23
Shimizu-22
Nagasawa-16
Pearce-17
Cox-26 for Ni and Cr in ol. Also cpx, gt and plag.
Ewart-29
Duke-6
(Rampone-18)
Sun-24
LaTourrette-27
Peters-31
Nagasawa-32
Ringwood-33
Lindstrom-34
Irving-35
Lindstrom-37
Schock-38
Kelemen-13 for ol, K, Nb, La, Ce, Zr in opx, & gt, K in sp.
Blundy -39 for Ti, Sr, Y, La, Ce and Nd in plag.
Schosnig-40
Salters-41
Values underlined this work

Compilations: with sources where known
Irving-12
Clague-4; 8, 10, 12 and Arth (1976)
Frey-8 for trace elements; 10, 22, and others
Shilling-21
McKenzie-15; 11 or interpolated for 11 for REE's 12, 17 and others
Kelemen-13 for cpx, Nd, Sm, Eu, Gd, Ti, Dy, Er and Yb in opx and gt. All sp except K.
Hanson-11 for cpx, opx, gt and plag. Sources;- 9, 23, 19 and Philpotts et al. (1972).
Baxter-1
Cox-26; Hanson 1977 for K, Rb, Sr, Ba, Ce, Sm, Eu and Yb for ol and opx.
Gill-36

Appendix 1. cont... Notes

1. All the data presented in appendix 1 are for basalt or basaltic andesites at low pressures unless otherwise stated. Sources: **20.** Seward (1971) experimentally derived for the system $CaMgSi_2O_6$-$Na_2Si_2O_5$-H_2O at temperatures between 830-1080°C, 1 kb, low oxygen fugacity such that values are for Cr^{+3} and V^{+3} although small amounts of V^{+4} were probably present. Seward (1971) found a pronounced decrease from 10.4 to 5 for V in cpx with increasing temperature. **10.** Gunn (1971) data derived for the 1959 Kilauea Iki eruption. **17.** Pearce & Norry (1979) these are recommenced values based on numerous sources (see Pearce & Norry 1979 for further details). **11.** Hanson (1980) values for ol are estimated based on work of Grutzeck *et al.* (1974) for the cpx-ol system while opx values are estimated based these data and on those of Philpotts *et al.* (1972) for the cpx-opx system (see Hanson 1980 for details). **15.** McKenzie & O'Nions (1991) Ho, Pr and Tb are interpolated based on the data presented by Hanson (1980). The source of the Lu and La values presented by McKenzie & O'Nions (1991) is not given. **24.** Sun & Hanson (1976) values for plag in trachybasalt data derived from phenocryst-bulk rock data from the McMurdo Volcanics, Ross Island, Antarctica. They also give the partition coefficient of Eu as 1.10, substantially more than 0.20 which was recommended by Irving (1978a) for an oxygen fugacity of 10^{-7} [the value suggested by Drake (1975)]. **25.** Sun *et al.* (1974), experimentally derived data for ocean ridge basalts at 1150°C and an oxygen fugacity of $10^{-7\,95}$ at atmospheric pressure. **8.** Frey *et al.* (1978) values are derived from studies of phenocryst-melt systems for Auckland Island olivine basalts (see Frey *et al.*, 1978 for further details). **16.** Nagasawa (1973) based on phenocryst-ground mass ratios for Oki-Dogo Island, Japan. **6.** Duke (1976) experimentally derived at 1125-1250°C, 1 bar, only the mean for the data is used here. Data in italics are from **12.** Irving's (1978a) review of data then available, all values quoted are for 1 bar and 1025-1400°C unless otherwise stated, for oxygen fugacities see Irving (1978a). Nb and V in opx decrease with increasing oxygen fugacity. K and Rb for cpx is given for 15-30 kb, Sc and Cr for gt are given for 30 kb while Ni in gt is given for 20 kb. The higher values for Ni in sp are achieved for higher oxygen fugacities. Cr (higher value) in opx is for 1200-1350°C no pressure is given, values are quoted for an oxygen fugacity of 10^{-7} as suggested by Drake (1975) for terrestrial basalts. **2.** Benjamin *et al.* (1980) data derived for 1375-1390°C, 20 kb, low oxygen fugacity ($10^{-8\,5}$). **19.** Schnetzler & Philpotts (1970) for basaltic-andesitic compositions. **9.** Grutzeck *et al.* (1974) for the system $NaAlSi_3O_8$-$CaAl_2Si_2O_8$-$CaMgSi_2O_6$ in air (at oxygen fugacities of $10^{-9\,5}$ and $10^{-12\,5}$ x atmospheric pressure) and 1265°C, no pressure values are given but it is probable that these experiments were carried out at atmospheric pressure. **23.** Shimizu and Kushiro (1975) derived from experiments using the system diopside-pyrope-water at 30 Kb and 1275°C in air. **14.** Leeman & Scheidegger (1977) derived for the Kilauea Iki eruption in 1959. **22.** Shimizu (1974) in the system diopside-anorthite-albite-water at 15-30 Kb and 1100-1200°C, no oxygen fugacity is given, but the experiments were on geological compositions under hydrous, but not saturated conditions. **3.** Bird (1971) experiments using the system forsterite-anorthite-silica for 1300-1400°C at 1 atm. Bird also notes that the partition coefficients of trace elements (Mn, Ni, Co and Cr were studied) increase with decreasing temperature. **26.** Cox *et al.* (1987) from phenocryst-glass ratios for volcanic rocks. **13.** Kelemen *et al.* (1993) for high pressures (mantle pressures) and basaltic melts. **18.** Rampone *et al.* (1993) suggest that V is incompatible in spinel, under mantle conditions. Irving (1978) shows that V compatibility increases with decreasing oxygen fugacity in magnetite, this also seems likely to be true in spinel as the value of 38 was obtained for lunar samples by Ringwood.* **33.** Ringwood (1970) V in ol and sp. Data are for lunar basalts at lunar oxygen fugacities. Partition coefficients exceed other results presented for olivine suggesting that the low oxygen content has resulted in higher values. Rampone suggests D_V^{Sp} should be nearer 0.1. **34.** Lindstrom (1976) shows that D_V^{Mt} is sensitive to the oxygen fugacity, varying over 2 orders of magnitude between log f_{O2} - log f_{O2}(Fe/Wü) = -4 to +12 **4.** Clague & Beeson (1980) give an estimate for Cu in plag. Eu values were calculated from the experimental results of **5.** Drake (1975) for the system $NaAlSi_3O_8$-$CaAl_2Si_2O_8$-$CaMgSi_2O_6$ for oxygen fugacities of the order 10^{-7} and 1290°C and 1 atm. **1.** Baxter *et al.* (1985) Pr in sp, interpolated from the REE data of **8.** Frey *et al.* (1978). **7.** Dunn & Sen (1994) most data are for basaltic compositions only, but V, Th and U in plag are for basaltic to andesitic compositions. All the lavas used in their experiments are from Mt. Adams Washington USA at 1100-1200°C 0.1 MPa and oxygen fugacity controlled at the Qz-Fa-Mt buffer. **21.** Shilling *et al.* (1980) P in ol, opx and gt, no information is available about these. **30.** Kay & Gast (1973) analytical data for spinel used to calculate mineral/host rock partition coefficients for an alkali basalt from Armidale, New South Wales. **27.** LaTourrette *et al.* (1993) experimental data using garnets and coexisting glass at 27 Kb, 1355°C and oxygen fugacity of 6.3 x 10^{-8}. **29.** Ewart (1973) data derived from phenocryst/matrix ratios in basaltic andesites from Tonga (SW Pacific). **28.** Jenner *et al.* (1994) data derived from coexisting mineral/glass pairs in a Norfolk Island basalt. **31.** Peters *et al.* (1994). Experimental results derived for a CaO-MgO-Al_2O_3-SiO_2-TiO_2 bulk composition at 1300°C and 1 atm. no oxygen fugacity is given. Underlined values were estimated from the phenocryst/glass compositions presented in this work (see appendix 4). Ho in spinel interpolated from data presented by Irving (1978a). **35.** Irving 1978b La, Ce, Sm, Eu, Gd, Tb, Ho, Yb, Lu, Sc, Cr in gt for olivine basalt and hawaiite. **36.** Gill (1978) Cr in mt. **37.** Lindstrom (1978) Mn in cpx between 1110-1360°C, 1 atmosphere and log $_{fO2}$ from -0.7 to -10.0. **38.** Schock (1979) REE (La, Ce, Nd, Sm, Eu, Tb, Yb and Lu) data for MORB's and Zn in mt. **32.** Nagasawa (1968) Th and U in augite only. **40.** Schosnig & Hoffer (1998) REE, Y and Sr in cpx using eutectic compositions in the system anorthite-diopside-titanite starting 50-70 °C above the melting temperature and cooled steadily over 36-56 hours. **41.** Salters & Longhi (1999) REE, Y, Zr, Nb Th and U in gt using various MORB compositions, between 1375-1570 °C and 1.0-2.8 Gpa.

2. **39.** Blundy *et al.* (1998) investigated near solidus melting of spinel lherzolite at 1.5 Gpa and 1255°C to ensure clinopyroxene crystallisation. In this experiment there is a high content of Ca-Tschermak's molecule within the clinopyroxene as would be expected in upper mantle conditions. Under these conditions the following results were obtained $D_{Sc}^{Cpx} = 3.20 \pm 0.15$, $D_U^{Cpx} = 0.71 \pm 0.03$, $D_V^{Cpx} = 5.1 \pm 0.9$, $D_{Sr}^{Cpx} = 0.062 \pm 0.004$, $D_Y^{Cpx} = 1.27 \pm 0.06$, $D_{Zr}^{Cpx} = 0.27 \pm 0.03$, $D_{Nb}^{Cpx} = 0.020 \pm 0.007$, $D_{La}^{Cpx} = 0.089 \pm 0.021$, $D_{Ce}^{Cpx} = 0.160 \pm 0.018$, $D_{Nd}^{Cpx} = 0.36 \pm 0.02$, $D_{Sm}^{Cpx} = 0.67 \pm 0.03$, $D_{Eu}^{Cpx} = 0.38 \pm 0.05$, $D_{Gd}^{Cpx} = 0.99 \pm 0.04$, $D_{Er}^{Cpx} = 1.44 \pm 0.09$, $D_{Yb}^{Cpx} = 1.43 \pm 0.29$ and $D_{Lu}^{Cpx} = 1.48 \pm 0.12$. Clearly this could have a profound effect on the melting and melt-rock reactions of basaltic melts derived from above the garnet stability field within the upper mantle. For plagioclase their results are similar to those listed in table 48 except for the HREE which tend to be slightly lower, and Eu which is higher than listed here probably as a consequence of the low oxygen fugacity. **42.** Vannucci *et al.* (1998) recognised similarly high values in coexisting glass and clinopyroxene in dunite from La Palma (Canary Islands): $D_{La}^{Cpx} = 0.14$-0.51, $D_{Ce}^{Cpx} = 0.24$-0.82, $D_{Nd}^{Cpx} = 0.46$-1.69, $D_{Sm}^{Cpx} = 0.64$-2.62, $D_{Eu}^{Cpx} = 0.68$-3.65, $D_{Gd}^{Cpx} = 0.59$-3.69, $D_{Dy}^{Cpx} = 0.65$-2.37, $D_{Er}^{Cpx} = 0.56$-1.43, $D_{Yb}^{Cpx} = 0.65$-3.37 and $D_Y^{Cpx} = 0.65$-2.95, $D_{Ti}^{Cpx} = 0.12$-0.64, $D_{Zr}^{Cpx} = 0.27$-1.01 and $D_{Sr}^{Cpx} = 0.11$-0.56.

Appendix 2

Seismic Interpretation

Seismic sections are plots of the time the seismic signal takes to reach the sedimentary reflector and return to the ship (two-way travel time) against the pulse time on the abscissa. The pulse time is constant irrespective of the velocity of the ship. A typical speed for the ship was 5 knots, approximately 2.5 ms^{-1}. While the pulse duration was 18 seconds, the speed of sound in seawater is about 1500 ms^{-1}, which increases through sediment and is about 2500-3000 ms^{-1} in limestone or basalt (Griffiths & King 1983). Hence in 3 km of water, the pulse theoretically could (if it was not attenuated) attain a depth of 20 km below the seabed while the ship had travelled just 27 m. This effect results in substantial vertical exaggeration on seismic records. Furthermore, because the pulse is omnidirectional the first signal to return is always from the nearest object which may not be the shallowest object directly beneath the ship. This relationship is demonstrated graphically in fig. 282 and can be expressed by;-

$$\tan \Theta = \sin \alpha \quad - 1.$$

where α = the slope of the seabed and Θ = the recorded slope.

As a consequence of equation 1, recorded slopes (Θ), after correction for vertical exaggeration, never exceed 45° (see fig. 282). To correct for vertical exaggeration requires an understanding of the sound speed in the sediment and rock through which the pulse is travelling. This can only be obtained by seismic refraction profiling of the region, which was not attempted. Some interpretation can still be undertaken using standard (recommended) values for seismic velocities in seawater, sediment, limestone, basalt and gabbro. Before this detailed interpretation is undertaken it is necessary to process the data to filter out spurious signals caused by reflections from the sea surface and multiple reflections from the sea bed as well as extraneous high and low frequency noise.

Figure 282

Sea Bed Profile.

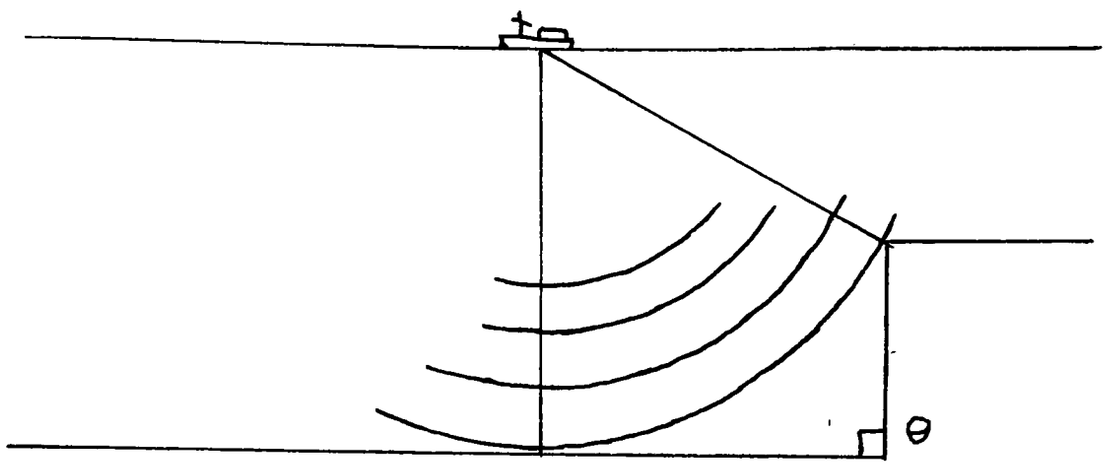

Seismic Record After Correction for Vertical Exaggeration.

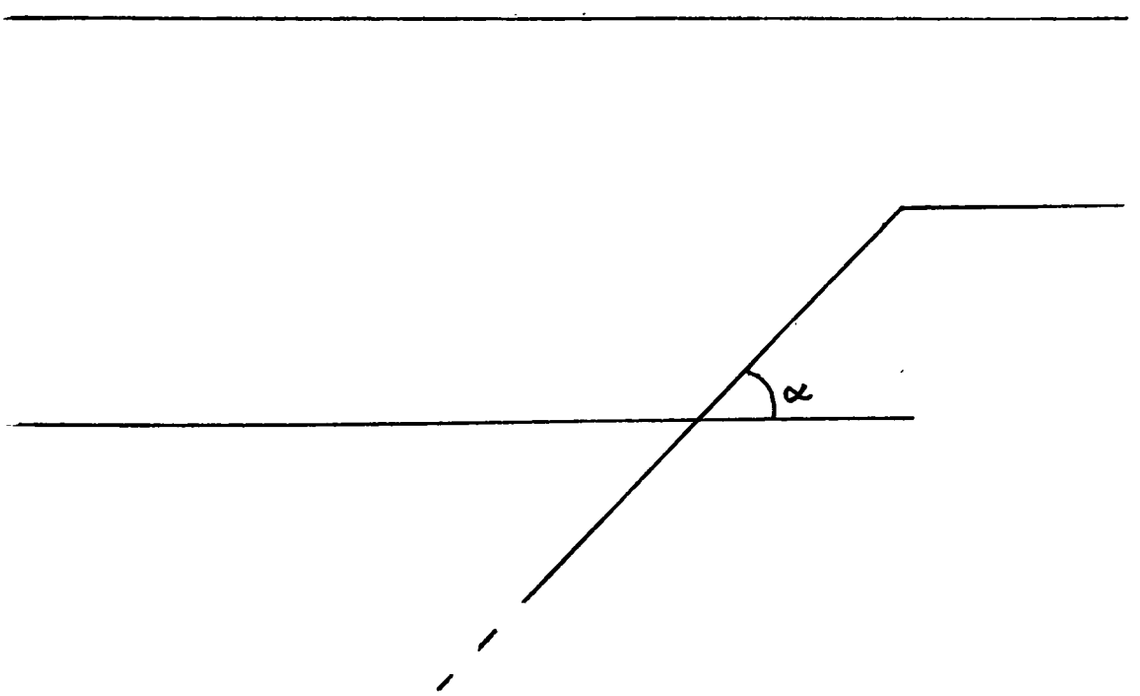

Appendix 3

Experimental Methods

A3.1 Introduction

The dredged material was sorted, on the ship, into sedimentary and igneous rocks. The igneous material was the further separated into intrusive rocks, basalts and tuffs. The latter two groups form the basis of this work.

The samples were air dried, then placed into plastic bags with a label indicating the dredge number (*ie.*. RR2) and, if there was more than one dredge at the location, a letter was added to the dredge number (*eg.*. RR12d). Finally a sample number was assigned to each specimen (*eg.*. RR2.2). A total of 99 polished thin sections or polished blocks (and thin sections, which proved easier to make) were made from the samples. Thin section preparation was hampered by the presence of soft secondary minerals and harder primary minerals which made it difficult to section without the polishing and grinding process plucking out the softer minerals. The above problems have resulted in many of the samples from RR10 and some from RR12 having a spongy texture where the original degree of vesiculation is difficult to assess. Voids reached 20% in the lavas, while in the single tuff studied they compose 65% of the volume. This high level of voids and hydrous phases such as zeolites caused further problems in the preparation of thin sections. Some sections shrank, probably as a consequence of dehydration, others failed to adhere to the epoxy resin, while others polished unpredictably.

Samples were selected for analysis on the basis of their fresh appearance and in some cases their mineralogy. A section of the specimen was then cut using a diamant-boart-saw, the outer rinds were then removed either by cutting (from the large samples) or grinding to leave at least 12 g of clean fresh rock. In a few cases it was necessary to try to pick the sediment from the vesicles to reduce potential calcium carbonate contamination. (The sediments were found to contain 96-98% carbonate in the form of microfossil tests). Contamination from this source is only likely to seriously affect CaO and CO_2.

The cut samples were cleaned in petroleum ether for an hour using a sonic bath, after which they were dried and rinsed with distilled deionised water and stored in clean plastic bags. Samples were crushed to <100 μm using either the jaw crusher (for the larger samples) or a hammer (for the smaller samples) and then a carborundum tema for 2 minutes (or more if required).

Two samples were split and handled as two or more separate samples (RR13a.1 and RR2.11) to examine the analytical precision which might be introduced at this or later stages.

After crushing, all the samples were stored in glass sample jars and dried in the oven at 105°C for at least 16 hours, to remove any adsorbed water.

Table 49 **Comparison of Trace Element Data Achieved by XRF and ICP-AES or ICP-MS**

Sample	Ba ppm	Ce ppm	Cr ppm	Cu ppm	La ppm	Nb ppm	Nd ppm	Ni ppm	Rb ppm	Sc ppm	Sr ppm	Th ppm	V ppm	Y ppm	Zn ppm	Zr ppm
RR2.2	14.15	8.83	425.9	78.87	1.04	1.37	8.09	217.7	0.74	35.59	150.9	0.12	222.6	27.47	104.91	118.8
	-2.5	6.7	366.5	81.3	-3.0	0.4	8.9	204.4	1.2	44.3	160.7	2.9	222.5	31.7	108.9	88.8
RR2.3	13.31	11.85	264.2	105.89	3.19	1.30	8.56	152.4	2.91	33.56	165.8	0.08	241.3	25.61	104.30	66.4
	-2.6	9.7	337.0	115.4	-1.3	0.6	8.5	148.0	3.1	46.1	170.6	2.4	250.2	23.9	100.4	60.0
RR2.4	9.64	6.17	361.3	114.21	1.69	0.83	5.33	188.8	3.04	31.05	152.0	0.28	202.3	20.09	117.99	82.0
	-2.3	11.5	291.3	113.8	-1.5	-0.0	6.4	189.1	3.3	39.2	159.7	2.2	202.0	22.1	81.6	57.1
RR2.5	15.28	9.10	249.6	122.13	3.50	0.87	6.27	145.4	3.65	32.86	161.6	0.17	230.9	22.80	84.31	72.7
	-1.7	4.0	316.9	117.4	-2.9	1.4	5.1	157.5	3.2	38.9	171.9	2.7	242.1	22.9	99.3	59.4
RR2.6	14.23	6.16	235.9	102.12	4.85	0.93	11.17	171.1	1.45	32.80	159.5	0.17	221.6	21.73	78.09	63.2
	-1.0	1.4	294.0	107.1	-3.2	0.2	5.9	173.1	1.3	36.0	169.7	1.6	235.2	22.7	88.5	57.4
RR2.7	19.85	8.43	401.7	83.80	2.90	1.76	8.05	214.0	2.46	34.78	158.2	0.18	217.0	30.03	87.30	66.0
	-7.8	12.9	385.8	91.2	-2.0	1.2	9.6	210.1	1.3	42.7	158.7	3.4	214.7	30.7	99.9	88.2
RR2.8	24.02	8.34	388.4	82.90	5.86	1.66	13.77	211.3	4.94	34.81	158.7	0.08	218.9	29.55	84.30	80.8
	-11.0	11.2	400.2	87.1	3.0	0.6	3.9	214.5	1.1	40.0	157.8	1.4	216.3	30.8	97.7	89.1
RR2.9	17.49	12.61	325.0	82.32	4.67	1.08	7.97	246.3	1.11	35.85	--	0.24	285.6	28.33	116.93	73.7
	25.5	16.8	359.2	85.8	2.9	1.8	9.9	237.4	2.3	40.2	162.7	1.0	224.0	29.7	102.1	89.8
RR2.10	28.81	9.68	387.8	75.80	2.20	--	8.35	215.8	--	35.43	160.4	0.16	217.6	39.84	98.20	144.7
	-9.5	14.8	397.5	81.5	-1.0	0.3	8.6	216.4	1.3	41.3	158.9	2.1	215.5	30.4	101.2	87.2
RR2.11	13.90	10.52	384.2	97.26	2.12	1.35	8.75	247.9	1.83	34.81	148.8	0.24	205.8	28.51	94.71	113.3
	-5.5	7.8	368.4	87.2	4.2	-0.1	9.6	236.2	1.4	34.4	157.2	1.8	192.9	30.3	96.4	88.5

Table 49 cont... **Comparison of Trace Element Data Achieved by XRF and ICP-AES or ICP-MS**

Sample	Ba ppm	Ce ppm	Cr ppm	Cu ppm	La ppm	Nb ppm	Nd ppm	Ni ppm	Rb ppm	Sc ppm	Sr ppm	Th ppm	V ppm	Y ppm	Zn ppm	Zr ppm
RR2.12b	11.88	9.61	370.0	104.68	3.86	1.14	7.68	245.2	4.23	39.85	--	0.12	379.2	29.24	134.19	88.7
	14.2	9.8	396.3	92.2	0.7	1.5	6.4	209.0	1.5	41.7	158.6	1.5	236.2	30.5	108.3	89.1
RR2.18	12.76	9.49	296.0	85.11	2.65	--	7.57	221.3	--	34.68	148.3	0.21	216.2	29.00	109.35	94.2
	-11.9	7.9	400.3	87.7	-1.1	0.5	7.3	215.3	1.5	42.3	159.4	2.2	217.3	30.4	119.4	89.1
RR3.1	12.35	7.24	243.5	124.61	4.77	1.39	10.99	127.6	3.30	32.68	171.9	0.19	224.1	24.17	71.17	75.8
	4.3	9.2	299.4	132.9	0.2	0.8	5.6	138.4	1.7	39.0	184.8	2.9	238.6	26.1	77.3	65.6
RR3.2	27.83	7.23	562.1	122.85	0.78	0.82	6.05	295.8	0.90	34.91	160.5	0.92	240.2	22.93	83.64	65.8
	6.5	5.3	618.0	132.0	-7.4	1.3	5.2	297.0	1.6	44.1	168.0	2.0	258.5	26.0	93.2	65.4
RR3.3	47.79	6.09	300.2	122.90	5.38	0.98	5.79	205.0	2.12	35.40	177.2	0.39	248.3	25.30	102.10	46.7
	35.2	5.6	459.7	131.0	0.1	1.7	3.7	206.0	2.2	41.8	172.4	1.1	272.9	25.9	102.6	68.6
RR3.6	56.15	7.85	520.0	116.80	7.41	1.94	6.08	211.6	6.40	35.78	162.3	0.43	244.0	25.12	101.40	59.4
	-0.3	13.0	509.9	124.8	9.8	1.4	8.4	216.1	1.1	42.7	160.6	2.4	250.2	26.4	105.7	68.5
RR3.11	17.67	7.49	238.5	114.50	4.04	0.81	6.59	138.8	2.35	37.85	--	0.07	264.2	25.26	123.83	66.1
	22.4	9.2	335.6	132.5	2.4	1.1	3.3	133.3	1.0	46.6	186.7	2.4	289.9	28.0	111.2	77.8
RR4.1	52.41	11.40	256.6	89.26	3.42	4.86	6.22	199.0	4.87	29.72	189.0	0.46	180.6	19.21	71.00	81.2
	44.0	14.2	267.5	84.8	1.8	5.3	6.8	196.1	4.4	29.2	197.5	2.4	160.1	20.6	71.5	67.7
RR4.2	57.78	9.40	220.5	103.82	4.30	5.12	5.46	194.7	10.07	29.95	188.1	0.63	173.2	19.72	64.64	72.7
	47.1	11.8	266.4	100.2	2.1	5.4	7.1	199.6	5.2	29.9	196.6	2.5	169.5	21.1	76.3	68.9

Table 49 cont... **Comparison of Trace Element Data Achieved by XRF and ICP-AES or ICP-MS**

Sample	Ba ppm	Ce ppm	Cr ppm	Cu ppm	La ppm	Nb ppm	Nd ppm	Ni ppm	Rb ppm	Sc ppm	Sr ppm	Th ppm	V ppm	Y ppm	Zn ppm	Zr ppm
RR4.3	97.80	17.23	252.0	92.31	7.39	6.83	9.25	192.0	11.79	30.00	210.8	0.58	177.6	23.24	72.85	67.5
	62.8	13.9	238.8	100.8	-0.6	7.6	12.5	188.3	7.4	31.1	210.1	2.7	168.3	22.8	79.1	82.4
RR4.4	69.41	13.40	216.7	95.21	7.21	8.14	6.44	210.5	7.96	30.55	--	1.16	264.2	20.45	94.81	79.1
	70.5	11.9	242.2	97.0	2.1	8.6	8.7	189.0	7.2	30.3	213.9	2.0	178.2	24.2	99.9	82.6
RR4.6	292.6	36.12	171.1	70.49	13.17	15.79	18.49	171.7	12.95	29.34	233.9	1.32	230.1	36.71	93.60	165.3
	89.4	34.7	258.4	73.6	14.3	20.0	18.6	162.7	14.0	32.0	235.8	4.1	211.9	38.4	103.4	176.5
RR4.8	57.88	12.55	268.3	83.18	6.36	4.20	5.80	189.0	4.29	28.59	--	1.02	256.2	18.06	92.92	66.3
	61.0	8.9	242.2	89.8	1.1	7.4	8.2	188.2	6.3	24.7	214.0	3.1	187.8	20.0	75.6	74.4
RR4.12	49.51	10.81	187.4	96.79	5.77	3.07	5.55	203.9	3.11	30.66	--	1.07	257.4	19.40	96.50	62.3
	53.1	11.5	250.6	99.6	8.5	5.2	5.8	188.8	5.7	31.7	197.5	2.0	177.2	20.5	75.1	69.5
RR8.2	193.10	35.17	481.4	77.70	18.47	15.98	19.15	367.9	12.62	27.65	341.7	1.16	206.9	23.51	88.90	106.4
	165.0	33.3	587.3	81.7	17.3	21.5	14.8	374.2	13.7	31.5	352.0	2.9	212.3	24.0	99.5	123.4
RR8.3	152.93	37.66	624.3	90.93	21.75	17.43	18.61	348.8	11.64	29.52	--	2.56	344.3	39.77	169.72	121.8
	154.4	44.8	608.1	102.2	22.5	22.0	23.6	341.4	6.7	33.7	357.6	2.9	326.3	43.2	161.4	128.9
RR8.5	115.22	31.69	550.5	171.23	14.23	16.65	13.06	480.0	12.87	25.74	--	2.03	272.1	21.86	236.47	125.4
	117.1	38.0	668.5	78.8	15.5	19.6	15.6	436.9	9.9	29.9	302.5	5.0	202.2	23.3	155.6	141.6
RR8.7	44.61	14.24	491.7	58.08	9.82	6.19	11.43	202.3	16.62	24.30	234.3	0.54	179.9	22.25	117.60	91.8
	39.8	11.5	613.1	69.0	3.7	5.9	11.8	208.6	4.9	31.1	243.5	2.8	198.9	22.2	129.7	87.9

Table 49 cont... **Comparison of Trace Element Data Achieved by XRF and ICP-AES or ICP-MS**

Sample	Ba ppm	Ce ppm	Cr ppm	Cu ppm	La ppm	Nb ppm	Nd ppm	Ni ppm	Rb ppm	Sc ppm	Sr ppm	Th ppm	V ppm	Y ppm	Zn ppm	Zr ppm
RR9c.6	171.45	28.03	481.9	91.34	9.44	13.66	13.82	340.8	13.67	26.80	334.7	1.43	189.8	22.96	91.27	159.8
	90.8	26.2	468.4	93.1	9.0	17.7	13.4	333.7	14.9	30.8	338.5	3.3	190.3	24.6	101.8	128.2
RR9c.11	112.53	26.26	343.3	83.03	11.11	11.01	12.74	325.3	3.11	29.01	411.2	0.87	242.4	28.03	117.00	92.7
	66.0	29.4	615.2	95.9	12.5	13.2	13.3	329.3	3.1	34.6	424.2	3.8	255.8	29.2	131.5	109.7
RR9c.15	144.50	29.36	431.6	78.10	12.03	12.13	13.53	331.8	13.99	26.97	326.5	0.99	192.0	22.11	77.80	147.1
	98.5	31.2	458.9	85.4	8.1	16.9	15.9	344.2	17.1	29.2	336.4	4.5	177.9	24.I	89.2	123.0
RR9c.18	148.27	29.85	410.6	78.87	14.85	13.14	17.87	291.3	15.29	27.99	403.0	1.04	209.8	23.99	94.00	164.8
	123.0	31.8	465.2	92.9	12.8	17.8	19.3	308.0	19.2	30.2	409.1	4.8	205.7	25.5	97.5	130.4
RR9c.21	--	--	--	--	--	15.82	--	--	21.89	--	--	--	--	--	--	--
	127.5	31.1	471.7	81.7	13.7	17.7	21.7	322.6	17.1	30.1	340.5	3.2	199.9	24.2	99.9	128.7
RR9c.32	175.30	28.61	440.5	78.70	13.03	--	14.48	300.1	--	27.98	362.2	1.56	201.4	25.01	98.80	115.9
	102.2	36.7	469.3	85.0	7.5	18.5	19.4	312.9	18.3	34.8	362.3	3.3	196.1	27.9	107.1	134.4
RR9c.33	110.80	26.53	476.9	90.40	11.29	12.34	12.91	311.6	19.35	28.22	322.3	0.98	202.2	23.88	97.40	109.7
	73.3	28.8	495.0	89.9	11.9	16.6	12.4	322.5	19.7	32.1	325.2	3.0	195.7	25.4	106.4	118.1
RR9c.35	136.47	31.68	242.1	90.44	13.55	10.69	15.41	186.3	18.03	29.53	368.0	1.30	216.5	26.09	88.14	150.4
	91.0	31.8	349.3	92.7	16.9	19.0	16.6	193.6	20.7	34.9	377.4	4.2	204.3	27.7	98.3	138.4
RR9c.36	125.84	28.32	297.4	86.38	12.02	11.55	13.43	326.3	15.42	27.70	383.I	1.08	206.1	23.56	83.17	144.9
	94.5	26.5	465.6	87.6	9.8	17.8	14.9	322.9	19.0	30.6	387.0	3.0	201.8	25.1	92.0	127.2
RR9c.37	148.47	26.03	418.6	78.87	14.80	12.09	19.14	382.3	11.07	27.17	364.0	0.96	195.9	23.17	76.19	155.3
	118.7	30.8	458.9	85.5	15.7	17.0	13.2	368.6	11.4	28.6	369.6	3.8	193.3	24.1	84.8	122.3

Table 49 cont... **Comparison of Trace Element Data Achieved by XRF and ICP-AES or ICP-MS**

Sample	Ba ppm	Ce ppm	Cr ppm	Cu ppm	La ppm	Nb ppm	Nd ppm	Ni ppm	Rb ppm	Sc ppm	Sr ppm	Th ppm	V ppm	Y ppm	Zn ppm	Zr ppm
RR9c.38	125.14	26.82	348.2	83.03	11.96	13.51	13.18	285.3	23.46	28.62	364.0	1.05	220.3	24.95	105.90	143.2
	84.5	28.3	475.2	92.9	8.7	18.4	18.4	273.8	25.4	33.9	364.5	3.5	204.2	26.8	107.7	129.9
RR9c.39	151.18	27.52	418.5	82.33	14.80	13.44	17.98	262.3	21.17	27.84	400.3	1.13	212.1	23.56	82.54	165.3
	112.7	24.6	498.0	86.8	11.8	17.9	16.9	288.0	23.7	30.85	397.7	3.9	193.9	25.4	105.9	127.2
RR10.1	294.06	83.79	549.3	72.63	34.73	30.56	38.61	333.4	3.70	22.12	529.4	2.02	289.0	28.72	94.04	235.5
	244.3	60.7	586.7	85.1	28.6	41.3	29.2	358.6	4.6	23.1	526.1	4.2	280.5	26.3	113.1	187.1
RR10.6	274.90	47.70	352.4	61.57	17.88	26.07	22.50	316.6	4.80	22.07	475.1	2.72	261.0	22.80	108.10	147.0
	241.0	48.5	506.8	86.8	26.0	33.6	25.8	366.6	5.2	13.8	484.3	4.0	261.7	25.0	103.5	156.3
RR10.7	153.18	40.42	304.0	79.88	31.77	26.51	27.63	390.5	15.03	18.72	(6975)*	2.57	169.5	31.39	119.42	87.4
	231.2	62.1	427.8	123.6	35.4	30.5	42.0	481.0	15.0	32.9	9487.1	5.3	142.2	35.7	145.9	201.5
RR10.8	274.18	59.47	585.6	115.23	27.04	35.28	25.82	365.3	44.97	24.23	--	4.48	147.5	24.28	185.90	80.0
	278.3	68.0	541.5	115.6	23.2	39.7	29.6	44.0	44.0	25.9	189.2	6.0	147.5	24.3	149.3	191.0
RR10.19	306.61	51.87	593.8	110.49	24.44	31.99	22.48	325.5	43.22	22.73	--	4.66	167.5	27.10	214.24	112.0
	316.3	64.7	499.7	99.4	29.7	36.0	28.4	305.5	44.2	26.7	208.2	4.9	162.5	25.8	145.2	181.9
RR12d.1	413.61	84.15	297.2	81.25	50.64	39.59	38.72	91.2	17.41	21.28	569.3	6.37	332.7	68.87	178.83	271.1
	419.3	92.5	348.8	80.0	55.3	49.6	42.1	84.8	20.1	20.5	569.3	7.0	279.8	74.8	155.7	291.4
RR12d.2	388.75	71.85	304.7	72.58	46.60	42.79	34.40	69.3	19.19	20.07	--	5.94	304.6	68.52	160.71	235.5
	395.6	87.6	338.7	74.3	50.1	47.4	37.8	61.4	18.3	27.3	593.0	7.8	256.2	75.5	147.8	280.1

Table 49 cont... **Comparison of Trace Element Data Achieved by XRF and ICP-AES or ICP-MS**

Sample	Ba ppm	Ce ppm	Cr ppm	Cu ppm	La ppm	Nb ppm	Nd ppm	Ni ppm	Rb ppm	Sc ppm	Sr ppm	Th ppm	V ppm	Y ppm	Zn ppm	Zr ppm
RR12d.4	442.41	73.90	292.7	80.95	41.38	30.44	32.99	63.8	19.38	20.70	540.8	3.41	236.6	68.55	146.10	391.8
	397.2	83.9	335.6	83.7	51.4	46.9	37.9	64.7	23.2	20.1	560.7	6.9	264.1	72.1	159.5	284.3
RR12d.5	383.90	75.09	330.7	84.26	40.82	36.36	33.33	47.5	34.70	21.17	512.1	3.17	243.9	40.86	147.55	256.3
	365.9	73.0	337.8	87.6	32.6	43.4	32.6	43.2	35.6	22.9	512.7	7.2	265.0	39.6	145.7	274.8
RR12d.8	198.22	35.87	358.6	127.02	25.99	21.05	23.65	142.8	26.73	29.66	--	2.30	338.9	46.64	190.23	127.9
	201.5	47.4	337.9	135.6	27.8	22.3	27.9	140.8	21.5	37.4	405.7	3.2	338.9	50.8	157.6	131.6

* This value was well outside the calibrated range of the instrument and as such can only serve to re-enforce the XRF Sr value for this sample

The upper value in each row was achieved by ICP-AES or ICP-MS while the lower value was achieved by XRF.

A comprehensive list of the analytical data used in this thesis may be found in table 16 in chapter 4.

A3.2 Analytical Techniques

Major Elements

The major elements (excluding H_2O and CO_2) in all samples except RR12d.9 were analysed by X-ray Fluorescence Spectrometer (XRF) in the Kings Buildings, University of Edinburgh. Pressed glass discs were prepared for major element analyses using a 5:1 ratio of flux (lithium tetraborate, lithium carbonate, lanthanum oxide) to sample. The dry sample was ignited in the furnace at 800°C for 20 minutes to calculate LOI, before being fused over a burner and cast into a disc. This is a standard technique used in many establishments and discussed further by Couture *et al.* (1993), James (1996) and Fitton *et al.*, 1998. Where the amount of powder permitted, pressed powder discs were prepared and analysed on the XRF. Table 49 shows these results for trace elements.

Volatiles

Water and carbon dioxide were analysed using a Carlo Erba Strumentazione Elemental Analyzer, Model 1106. 50 μg of sample were weighed in a tin boat which was then crimped and loaded into the auto-sampler. About thirty samples could be analysed before it was necessary to clean out the furnace. The instrument was kept on for the period of the analysis (about 6 days) to prevent the problems of variable instrumental stability. Some analyses were repeated on different days to assess the repeatability and the stability. This technique is described by Din & Jones (1978). Instrument calibration was achieved by including a standard every 7 runs and by calibrating on the same sample at the start of the day.

Trace Elements

0.5 g of powder was weighed out and digested with HF-$HClO_3$ according to the method described by Walsh *et al.* (1981) and Thompson & Walsh (1989). The resulting solutions were then analysed for trace elements using an ARL 3510 Inductively Coupled Plasma Emission Spectrometer (ICP-AES). Standard rocks:- MRG-1, NIM-D, JB-1, BE-N, NIM-N and SY-2 were prepared using the same technique. These were used, together with a blank prepared in the same way, to produce the calibration curve for the subsequent analysis. Intensities used for the calibration were measured in triplicate while the analysis was carried out in duplicate or triplicate depending on the amount of available solution. Before being introduced into the ICP-AES the solutions were randomised to reduce any systematic errors resulting from the preparation order or from the order of analysis. Instrumental drift was monitored by the analysis of a standard or a previously analysed sample at regular intervals, usually either every tenth sample or every hour whichever was sooner. Further control on analytical technique

was attained by preparing more than one solution from a particular powder. Other solutions were subject to repeated analysis on different days.

U, Th, Hf, Rb, Pr, Tb and Lu were analysed by Inductively Coupled Plasma Mass Spectrometer (ICP-MS), as were the full range of trace and REE for the last batch of samples (see table 16, chapter 4). The sample preparation techniques for this instrument are the same as those give for the ICP-AES except that samples are taken back into solution using 5M HNO_3, and are subject to a further ten fold dilution prior to analysis. Detection limits are given in table 50.

Cr, Rb and Zr were analysed with the other trace elements by XRF or ICP-MS. In general Cr, Zr and Rb obtained by ICP-MS compared favourably with that obtained on the same samples by XRF (table 47).

The small size of RR12d.9 prevented this samples being analysed by XRF. Major elements for this sample were achieved using the fusion technique described by Walsh *et al.* (1981) and Thompson & Walsh (1989). Rubidium and potassium in RR12d.9 were analysed by Atomic Emission Spectrometry (AES) or Absorption Spectrometry (AAS) respectively, using a Pye-Unicam SP 1900 Atomic Absorption Spectrophotometer. For potassium a solution of 10% CsCl was added as an ionization suppressant.

Rare Earth Elements

Rare earth elements were prepared using the technique described by Jarvis & Jarvis (1985). It was found necessary to dissolve the dried rare earth solutions in 5 ml of 10% HNO_3 and 1 ml of conc HCl, then returning them to dryness before taking them up in 10% HNO_3 for aspiration into the ICP-AES. For those samples which did not dissolve in the 10% HNO_3 alone, it was necessary to repeat this process up to three times. Those which still failed to dissolve were re-prepared. Additionally some samples were prepared more than once to improve control on the analytical errors (see tables 51 and 52).

A blank, together with standard rocks JB-1, BE-N, MRG-1 and sample RR2.4, were analysed with each batch of 20 samples. Standards for rare earth analysis were artificial standards prepared from the solutions of single rare earths produced by Aldrich Chemical Company. Chemical interferences from major elements such as Ba, Y, Ti, Ca and Zr, which are not stripped off fully by the ion exchange columns, were examined by:- 1. analysing each single element solution of each of these for REE. 2, scanning each single element solution to look for potential interference peaks on the spectrum, (see Jarvis & Jarvis 1985 for further details of these problems), and 3. by scanning a selection of unknown solutions to allow the careful selection of background correction points to eliminate the potential interference.

Isotopes

21 samples were analysed for Sr, 10 for Nd, and 7 for Pb isotopes, using a VG354 Mass Spectrometry at Royal Holloway and Bedford New College. Prior to digestion all samples were leached using 6 M HCl for 30-45 minutes in a sealed capsule at 150°C. For Sr, samples were digested in HF-HNO_3 for at least 3 hours, then dried; 6 M HCl was added and evaporated to ensure complete removal of Hf. Samples were them taken up in 2 ml HCl and centrifuged, then passed through an ion exchange column to separate the Sr, before being loaded on to Ta beads for analysis on the mass spectrometer. The standard used was SRM 987; recommended $^{87}Sr/^{86}Sr = 0.710239 \pm 12$. The analysed results were $^{87}Sr/^{86}Sr = 0.710259 \pm 9$ for run 1 and $^{87}Sr/^{86}Sr = 0.710280 \pm 0.000011$ for run 2). For Pb and Nd, UHQ (ultra high quality) reagents were used (in house preparations). Samples were leached in 6 M HCl for 30-45 minutes, washed, and digested in HNO_3 -HF for 2 days. After drying, a further 2 ml of conc. HNO_3 was added and evaporated off, followed by 6 M HCl to remove any remaining HF. The blank was spiked with 0.4 ppm ^{208}Pb prior to digestion. The samples were then taken up in 1 M HBr and passed through new ion exchange columns. The elutant was then loaded on to Nd ion exchange columns. Samples were eluted using orange cocktail (1500 ml SB methanol + 102 ml SB HOAC + 64 ml SB HNO_3 + 334 ml UHQ water) and yellow cocktail (1500 ml SB methanol + 102 ml SB HOAC + 32 ml SB HNO_3 + 366 ml UHQ water). Samples were collected using 5 ml 0.05 M HNO_3 and then passed back through the columns before being collected using 26 ml yellow cocktail. A third stage column was then employed to complete the separation. Samples were finally collected using 0.05 M HNO_3. Recommended standard value for $^{143}Nd/^{144}Nd = 0.511420$ while analysed results were $^{143}Nd/^{144}Nd = 0.511425 \pm 5$, 0.511423 ± 6 and 0.511428 ± 5.

Pb samples were passed through the ion exchange columns a second time before collection in a few drops of 6 M HCl. Both Pb an Nd samples were loaded on to Re beads for analysis using silica gel and H_3PO_4 (0.25 M). Dilute Aldrich solution ($^{143}Nd/^{144}Nd = 0.511423 \pm 6$) was used as a Nd standard while SRN 981 was used for Pb (recommended $^{206}Pb/^{204}Pb = 16.937$, analysed $^{206}Pb/^{204}Pb = 16.939$, recommended $^{207}Pb/^{204}Pb = 15.491$, analysed $^{207}Pb/^{204}Pb = 15.496$, recommended $^{208}Pb/^{204}Pb = 36.720$, analysed $^{208}Pb/^{204}Pb = 36.713$).

All techniques use are conventional separation techniques to concentrate the isotopes for analysis.

ϵ_{Nd} is defined as:

$$\epsilon_{Nd} = \left[\frac{^{143}Nd/^{144}Nd_{sample}}{^{143}Nd/^{144}Nd_{chondrite}} - 1 \right] \times 10^4$$

where $^{143}Nd/^{144}Nd_{chondrite} = 0.512638$

A3.3 Analytical Quality

Three issues need to be considered when reviewing analytical quality; 1. detection limits, 2. precision and 3. accuracy. Detection limits are a measure of how much of a given element needs to be present in order for the instrument to recognise and quantify it. The detection limit of an instrument is defined as 10 x σ + blank, where σ = the standard deviation of the blank. The detection limits for the ICP-AES and ICP-MS are given in table 50.

Precision is a measure of the ability of the analyst and instrument to produce repeatable analyses. Two samples were split at the crushing stage and treated separately in the subsequent preparation and analysis. Tables 51 and 52 show the results achieved for the two samples which were split at the cutting stage to study reproducibility and any potential contamination introduced by the techniques. (Sample RR2.11 was divided into three a, b, and x and RR13a.1 was divided into two x and y). It should be noted here that samples RR2.11a and RR2.11b may have been contaminated by small amounts of epoxy resin. Such contamination should not adversely affect elements other than the volatile components of the sample, hence only RR2.11x has been used (the precision of the volatile analysis is discussed later). In table 51 La has a value of 7.40 for σ_n/x % (standard deviation/mean) when the ICP data for RR2.11x is ignored. As most REE are low in this preparation it would seem likely that this solution has been diluted during its preparation. In general Y was noted to be slightly lower when analysed on the concentrated solutions from the ion exchange column technique. Comparing tables 51 and 52 shows that, for most of the trace elements, the ICP has better reproducibility than the XRF. Table 53 gives results obtained for standard rocks for both ICP techniques used, together with the recommended values (as recommended at the time of the analyses for ICP-AES which relies on standard rocks for it's calibration).

Accuracy is a measure of how close to the real value the resulting analysis is. This can be difficult to quantify, but recommended values for international standards are used for comparison with the results obtained for the same standards 'in house'. Table 53 lists the recommended values for standards used in ICP-AES and ICP-MS analyses.

Full details of the accuracy and precision of the XRF are given in James (1996) and in Fitton *et al.*, 1998 together with details of the preparation and analytical techniques used.

Table 50

Detection Limits for Different Analytical Techniques in ppm

	ICP-AES	ICP-MS	AES
Ba	0.31	0.75	--
Cr	27.24	2.43	--
Cu	13.31	0.21	7.41
Hf	--	0.03	--
Nb	0.71	0.27	--
Ni	8.65	2.59	--
Rb	--	0.19	5.50
Sc	0.27	0.13	--
Sr	0.24	0.70	--
Th	--	<0.03	--
U	--	<0.03	--
V	3.35	9.63	--
Y	0.57	0.04	--
Zn	10.39	12.02	--
Zr	21.47	0.28	--
La	0.21	1.21	--
Ce	1.37	1.20	--
Pr	--	<0.30	--
Nd	0.81	<0.74	--
Sm	0.32	0.23	--
Eu	0.01	0.04	--
Gd	0.62	0.09	--
Tb	--	<0.08	--
Dy	0.08	0.07	--
Ho	0.09	0.05	--
Er	0.11	<0.04	--
Yb	0.08	0.09	--
Lu	0.22	0.03	--

All values are quoted in ppm in rock. Detection limits are defined by 10σ+blank, where σ = the standard deviation of the blank. XRF data are those suggested by Dodie James

Table 51 **Comparison of Analytical Precision for RR2.11**

	RR2.11a	RR2.11b	RR2.11x	RR2.11x*	σ_n ICP	σ_n	σ_n/x %
SiO_2 %	--	--	--	47.61	--	--	--
TiO_2 %	1.265	1.335	1.399	1.248	0.055	0.060	4.57
Al_2O_3 %	16.34	16.20	17.07	16.83	0.381	0.354	2.13
FeO* %	10.77	10.73	11.46	10.10	0.335	0.481	4.47
FeO %	10.089	10.052	10.736	9.458	0.314	0.452	4.48
Fe_2O_3 %	1.513	1.508	1.610	1.419	0.047	0.068	4.47
MgO %	8.935	9.286	9.026	9.00	0.149	0.134	1.47
MnO %	0.162	0.198	0.196	0.203	0.017	0.016	8.55
CaO %	10.87	11.26	12.06	10.81	0.495	0.499	4.43
Na_2O %	3.311	3.352	3.670	2.97	0.160	0.248	7.46
K_2O %	0.090	0.100	0.090	0.121	0.005	0.013	12.62
P_2O_5 %	0.103	0.088	0.108	0.092	0.008	0.008	8.26
H_2O %	--	--	0.476	--	0.319	--	--
CO_2 %	--	--	0.147	--	1.210	--	--
Total %♦	100.29	100.99	103.58	99.76			
Total %	100.90	101.61	104.20	100.38			

Table 51 cont... **Comparison of Analytical Precision for RR2.11**

All values are in ppm.

	RR2.11a	RR2.11b	RR2.11x	RR2.11x^{rpt}	RR2.11x*	σ_n ICP	σ_n	σ_n/x %
Ba	10.55	11.46	13.83	13.90	-5.5	1.466	8.154	*13.61*
Cr	374.1	494.8	393.3	384.2	368.4	48.513	46.706	11.59
Cu	97.58	101.74	92.46	97.76	87.2	3.294	5.077	*3.38*
Nb	--	--	--	1.352	-0.1	--	--	--
Ni	224.57	239.57	224.67	247.86	236.2	9.987	8.970	3.82
Rb	--	--	1.830	1.376	1.4	0.227	0.209	13.59
Sc	34.74	33.80	34.87	34.81	34.4	0.438	0.397	1.15
Sr	148.9	136.3	148.60	148.75	157.2	5.392	6.682	*3.70*
Th	0.253	0.279	0.12	0.235	1.8	0.061	0.634	*27.41*
U	0.049	0.103	0.058	0.064	--	0.021	--	*30.10*
V	210.6	197.6	209.2	205.8	192.9	5.046	6.855	*2.45*
Y	29.38	29.10	29.61	28.1	30.3	0.576	0.715	*0.20*
Zn	86	86.87	71.34	94.708	96.4	8.442	8.877	*9.96*
Zr	98.31	116.12	110.38	113.25	88.5	6.780	10.365	*6.19*
				Average				
La	3.621	--	0.622	2.122	4.2	1.500	1.568	55.72
Ce	12.414	--	8.628	10.521	7.8	1.893	2.009	*17.99*
Pr	0.773	0.731	0.798	0.767	--	0.028	--	*3.60*
Nd	9.930	--	7.560	8.745	9.6	1.185	1.048	11.61
Sm	2.893	--	2.146	2.152	--	0.374	--	*14.82*
Eu	1.400	--	1.030	1.215	--	0.185	--	*15.23*
Gd	5.525	--	3.572	4.549	--	0.977	--	*21.47*
Tb	0.623	0.635	0.787	0.682	--	0.075	--	*10.95*
Ho	1.385	--	0.601	0.993	--	0.392	--	*39.48*
Dy	6.093	--	4.397	5.245	--	0.848	--	*16.17*
Er	3.851	--	2.649	3.250	--	0.601	--	*18.49*
Yb	3.977	--	2.943	3.460	--	0.517	--	*14.94*
Lu	0.418	0.408	0.436	0.421	--	0.012	--	*2.75*
Y^+	34.45	--	21.75	--	--	4.067	3.751	12.89

* Data achieved by XRF. Y^+ was achieved using the ion exchange column technique used for the REE's. For RR2.11a and RR2.11b Cu was achieved by AES. RR2.11x^{rpt} was a second preparation of this powder and was eventually used in table 16 for the trace elements. The averaged ICP REE values were used in table 16 and are given column 5 here. The σ_n (standard deviation) is given for all techniques used, under Y^+ and for the trace element technique alone under Y. ♦ Total without volatiles. σ_n ICP applies to ICP data only. x = mean. Values in italics are ICP data only.

Table 52 **Comparison of Analytical Precision for RR13a.1**

	RR13a.1x	RR13a.1y	RR13a.1*	σ_n ICP	σ_n	σ_n/x %
SiO_2 %	--	--	46.25	--	--	--
TiO_2 %	1.340	1.232	1.363	0.076	0.070	5.33
Al_2O_3 %	13.23	11.98	14.67	0.884	1.346	10.13
FeO* %	11.37	9.68	11.25	1.195	0.943	8.76
FeO %	10.018	8.529	9.91	1.053	0.830	8.75
Fe_2O_3 %	1.503	1.279	1.487	0.158	0.125	8.78
MgO %	7.728	6.880	8.68	0.600	0.901	11.60
MnO %	0.186	0.159	0.218	0.019	0.030	15.74
CaO %	10.60	10.87	11.09	0.191	0.245	2.26
Na_2O %	2.520	2.423	2.45	0.069	0.050	2.03
K_2O %	0.270	0.290	0.341	0.014	0.037	12.19
P_2O_5 %	0.140	0.124	0.111	0.011	0.015	11.62
H_2O %	2.301	2.381	--	0.057	--	2.42
CO_2 %	0.256	0.403	--	0.104	--	31.55
Total %♦	93.634	89.888	96.423			
Total %	96.191	92.672	99.094			
Ba ppm	25.45	38.45	18.2	9.192	10.260	*28.77*
Cr ppm	244.8	256.0	338.9	7.920	51.401	18.36
Cu ppm	45.61	45.61	56.8	0	6.461	13.09
Nb ppm	28.48	25.65	2.5	2.001	14.243	*7.39*
Ni ppm	84.04	89.45	98.5	3.825	7.306	8.06
Rb ppm	10.4	10.4	6.2	0	2.425	26.94
Sc ppm	54.97	54.20	61.5	0.544	0.414	*1.00*
Sr ppm	94.5	96.4	103.6	1.344	4.800	4.89
Th ppm	0.098	0.157	1.9	0.042	1.024	*32.72*
U ppm	0.181	0.211	--	0.021	--	*10.82*
V ppm	363.4	343.1	381.0	14.354	18.966	5.23
Y ppm	31.97	30.62	32.3	0.955	0.890	2.81
Zn ppm	89	88	95.2	0.707	3.900	4.30
Zr ppm	89.63	72.42	79.6	12.169	8.644	10.73

Table 52 cont... **Comparison of Analytical Precision for RR13a.1**

All values in ppm

	RR13a.1x	RR13a.1y	*RR13a.1	σ_n ICP	σ_n	σ_n/x %
La	3.880	12.49	1.2	6.088	5.899	*74.38*
Ce	9.832	9.091	9.1	0.524	0.425	4.55
Pr	0.595	0.784	--	0.134	--	*19.38*
Nd	8.761	7.673	9.2	0.769	0.786	9.20
Sm	3.247	2.553	--	0.491	--	*16.92*
Eu	1.292	1.150	--	0.100	--	*8.22*
Gd	5.053	4.284	--	0.544	--	*11.65*
Tb	0.551	0.658	--	0.076	--	*12.52*
Dy	6.047	5.337	--	0.502	--	*8.82*
Ho	1.385	1.231	--	0.109	--	*8.33*
Er	3.587	3.200	--	0.274	--	*8.06*
Yb	3.718	3.422	--	0.209	--	*5.86*
Lu	0.367	0.440	--	0.052	--	*12.79*
Y^+	32.435	26.96	--	2.480	2.294	7.44

* Data achieved by XRF. Y^+ was achieved using the ion exchange column technique used for the REE's, the σ_n (standard deviation) is given for all techniques used under Y^+ and for the trace element technique alone under Y. ♦ Total without volatiles. σ_n ICP applies to ICP data only. x = mean. Values in italics were achieved using ICP data only. FeO and Fe_2O_3 were calculated from the total Fe assuming $Fe_2O_3/FeO = 0.15$.

Table 53 **Standard Rock Analysis**

ICP AES

	BE-N Recommended	BE-N Analysed	MRG-I Recommended	MRG-1 Analysed	JB-1 Recommended	JB-1 Analysed
Ba	1025	1083	50	50.26	490	505.5
Cr	360	344.3	450	448.1	405	406.6
Cu	72	71.74	135	137.1	56	54.06
Ni	267	272.0	195	184.3	139	139.7
Sc	22	21.47	48	52.36	27.4	26.71
Sr	1370	1357	260	263.4	435	435.1
V	235	227.7	520	521.4	210	206.4
Y	30	29.02	14	--	25.5	23.93
Zn	120	117.1	190	184.3	84	85.22
La	82	77.12	9.8	8.713	38	35.87
Ce	152	154.6	26	28.90	67	67.31
Nd	70	63.93	19.2	19.42	27	25.96
Sm	12	11.84	4.5	4.476	5.0	4.964
Eu	3.6	3.471	1.39	1.507	1.52	1.428
Gd	9.5	9.916	4	4.408	4.7	4.750
Dy	6.4	6.439	2.9	3.237	4	4.139
Ho	1.1	0.967	0.49	0.553	0.7	0.828
Er	2.5	2.280	1.12	1.384	2.2	2.152
Yb	1.8	1.887	0.6	0.965	2.1	2.160
Y	30	25.16	14	12.51	24	20.24

	NIM-D Recommended	NIM-D Analysed	NIM-N Recommended	NIM-N Analysed	SY-2 Recommended	SY-2 Analysed
Ba	10	5.920	100	95.82	460	484.1
Cr	2900	2910	30	34.11	12	11.06
Cu	10	--	14	--	5.0	--
Ni	2050	2065	120	121.6	10	8.041
Sc	7	--	38	38.07	7	6.630
Sr	3.0	3.070	260	256.3	275	273.6
V	40	46.49	220	222.4	52	53.22
Y	--	--	7.0	6.799	130	145.2
Zn	90	98.25	68	62.83	250	253.5

Table 53 cont... **Standard Rock Analysis**

ICP-MS

	NIM-D Recommended	NIM-D Analysed	NIM-N Recommended	NIM-N Analysed	SY-2 Recommended	SY-2 Analysed
Lu		0.005		0.140		

ICP-MS

	BE-N Recommended	BE-N Analysed	MRG-1 Recommended	MRG-1 Analysed	JB-1 Recommended	JB-1 Analysed
Ba	1025	892.3	61	47.23	490	518.1
Cu	72	94.43	134	111.8	56.3	61.55
Hf	5.4	5.060	3.76	1.543	3.4	3.111
Nb	100	106.0	20	0.295	34.5	34.80
Ni	267	282.7	193	211.3	139	283.7
Rb	47	48.06	8.5	7.806	41.2	42.32
Sc	22	21.44	55	54.05	27.4	28.22
Th	11	11.17	0.93	0.991	9.2	10.78
U	2.4	2.495	0.24	0.182	1.7	1.831
Y	30	24.78	14	12.03	24	21.34
Zn	120	157.3	191	187.2	83	104.2
La	82	82.38	9.8	10.01	38	36.93
Ce	152	151.6	26	25.55	67	64.11
Pr	--	14.67	3.4	2.897	7.5	5.710
Nd	70	64.46	19.2	17.24	27	24.49
Sm	12	11.45	4.5	4.191	5.0	4.748
Eu	3.6	3.739	1.39	1.378	1.52	1.454
Gd	9.5	10.69	4	3.813	4.7	4.968
Tb	1.3	1.227	0.51	0.475	0.76	0.582
Dy	6.4	5.091	2.9	2.311	4.0	3.135
Ho	1.1	1.056	0.49	0.511	0.7	0.774
Er	2.5	2.424	1.12	1.138	2.2	1.907
Yb	1.8	1.643	0.6	0.763	2.1	1.793
Lu	0.24	0.237	0.12	0.119	0.31	0.299

Volatiles

In general the reproducibility for both CO_2 and H_2O is within about 10%. This is only exceeded by one sample in table 54 (RR12d.9 CO_2) which has values within 10 x detection limits. The detection limits were calculated as 0.149% CO_2 and 0.071% H_2O. As with the trace element analyses, values below about 10 x detection limits can only be considered qualitative. For H_2O most samples are above this level with only sites RR4 and RR2 having samples with lower H_2O levels. CO_2 has a higher detection limit and is generally lower in the samples, hence many of the samples are below the quantitative/qualitative boundary.

Table 54

	CO_2			H_2O		
Date	4/9/90	5/9/90	10/9/90	4/9/90	5/9/90	10/9/90
RR12d.9	0.513	0.623	--	1.825	1.984	--
RR9c.39	1.319	--	1.392	I.508	--	1.667
RR13b.(7)a	--	0.586	--	--	7.777	--
	--	0.513	--	--	8.174	--
RR2.16	--	0.330	--	--	1.032	--
	--	0.366	--	--	1.111	--

A3.4 The Electron Microprobe

The mineral analyses were obtained using a JEOL JSM-35C Scanning Electron Microscope. The initial preparation involved making polished thin sections or blocks (polished to ¼ μm). These were then coated with carbon using a Nannotech High Vacuum Sputter Coater. The edges of the sections were then hand painted with carbon paint to improve the conductivity. The samples were analysed using the energy dispersive system, with an accelerating voltage of 15 KeV and a spot size of 3 μm. Each sample had a counting time of 100 secs. The instrument was calibrated using a cobalt standard prior to the start of the analysis and at regular intervals thereafter. The sum total of the oxides was used as an indicator as to the quality of the analysis. It was noted that the best surfaces and the highest counts were obtained from chrome spinel. This resulted in totals which were typically in the range 99.5-101%. Olivine produced similarly good results, although in general the surfaces achieved on olivine were not as good. In general the quality of surfaces produced on plagioclase were not as good and this is reflected in their slightly lower totals, typically 97-99%. The surfaces achieved on unaltered glass were similar to those obtained for plagioclase. Of the other minerals analysed the alteration minerals (and mineraloids) principally iddingsite, serpentine, zeolites and palagonite often had very poor surfaces primarily because these 'minerals' are soft. Achieving satisfactory totals for these

minerals were hampered by their tendency to incorporate volatiles into their lattice (totals were in the range 60-90%). Consequently the analyses for these can only be considered as qualitative. Alkali loss was also reported for these 'minerals' by M. M. Hall. Clinopyroxene, where present, often occurred as very small matrix crystals (<3 μm) which could not be analysed. At sites RR10 and RR12 clinopyroxene was larger and some analyses were attempted. In these totals were around 85-97%, reflecting the size of the crystals and the quality of the polish which was attained. Detection limits for the electron microprobe have been calculated as 10σ + blank where σ = standard deviation of the blank. The choice of a suitable blank was problematic as the Co standard used for calibration purposes was found to contain detectable levels of iron and possibly silicon. Epoxy resin (used in mounting the slides) was found to contain detectable Cl and possibly S (table 55). An alternative approach was to analyse those elements which were strongly incompatible in a given mineral, for example SiO_2 in Chrome spinel or MgO in plagioclase. Only those values within two standard deviations of the instrumental blank were used. Using this method an upper limit for the detection limits was obtained (table 56), in most cases these values are better than those obtained from the Co standard. It should be stressed that these values represent the upper limits for detection limits and in the cases of FeO^*, Al_2O_3 and Na_2O the two epoxy resin analyses suggest that the detection limits may be some what lower (table 55).

To test the quality and reproducibility of the results, three analyses of orthoclase standard 249 are presented in table 57, together with the recommended values for this standard. In table 57 the silica values are up to 2% higher than the reported values, whereas Al_2O_3 are nearly 7% lower than those reported. Other elements are closer to the reported values and vary in a less consistent manner.

Table 55 **Electron Microprobe Blank Analysis**

	Co	Co	Co	Co	Co	Detect Lt	Resin	Resin
SiO_2	0.500	0.793	0.843	0.365	0.460	2.494	0.131	0.626
TiO_2	0.000	0.000	0.000	0.000	0.000	<0.002	0.000	0.000
Al_2O_3	0.137	0.167	0.263	0.000	0.015	1.099	0.010	0.121
MgO	0.099	0.150	0.119	0.000	0.373	1.379	0.000	0.000
FeO^*	0.950	1.003	0.892	0.716	1.084	2.167	0.090	0.077
Na_2O	0.000	0.000	0.018	0.000	0.386	1.608	0.101	0.009
CaO	0.000	0.000	0.078	0.005	0.000	0.324	0.072	0.470
K_2O	0.000	0.156	0.000	0.000	0.000	0.655	0.000	0.000
MnO	0.300	0.623	0.381	0.292	0.218	1.763	0.066	0.044
P_2O_5	0.000	0.000	0.000	0.000	0.161	0.676	0.000	0.000
Cl	0.000	0.043	0.000	0.051	0.065	0.301	2.076	2.348
Cr_2O_3	0.000	0.000	0.000	0.000	0.000	<0.002	0.099	0.000
S	0.084	0.000	0.051	0.000	0.000	0.374	0.102	0.355

Detect Lt = Detection limit calculated from Co 'blank' values

Table 56 **Electron Microprobe Detection Limits**

	Detection Limit	Number of Analyses	Minerals Used
SiO_2	0.647	13	Spinel, Calcite
TiO_2	0.608	72	Plagioclase, Olivine, Calcite, Resin
Al_2O_3	1.235	73	Olivine, Calcite, Magnetite, Resin
MgO	0.829	73	Plagioclase, Quartz, Illite, Resin, Co standard
FeO^*	1.050	43	Plagioclase, Calcite, Quartz, Zeolite, Resin, Orthoclase
Na_2O	1.341	71	Spinel, Olivine, Calcite, Resin
CaO	0.499	70	Spinel, Quartz, Magnetite, Resin, Co standard
K_2O	0.325	71	Plagioclase, Spinel, Olivine, Calcite, Magnetite
MnO	0.496	72	Plagioclase, Calcite, Quartz, Sphene, Illite, Resin
P_2O_5	0.620	73	Spinel, Olivine, Calcite, Magnetite
Cl	0.327	71	Plagioclase, Spinel, Olivine, Clinopyroxene, Calcite
Cr_2O_3	0.732	72	Plagioclase, Calcite, Quartz, Illite, Resin, Co standard
S	0.289	73	Plagioclase, Spinel, Olivine, Clinopyroxene, Magnetite

Table 57 **Analyses of Orthoclase Standard 249**

	Orthoclase 249	Orthoclase 249	Orthoclase 249	Recommended
SiO_2	65.458	64.864	65.325	64.3
TiO_2	0.000	0.034	0.000	--
Al_2O_3	18.545	18.884	18.745	19.9
MgO	0.000	0.000	0.000	--
FeO^*	0.036	0.022	0.086	--
Na_2O	3.868	3.617	3.597	3.7
CaO	0.277	0.294	0.172	0.24
K_2O	11.032	11.043	11.626	11.4
MnO	0.000	0.164	0.010	--
P_2O_5	0.265	0.301	0.000	--
Cl	0.000	0.030	0.128	--
Cr_2O_3	0.133	0.000	0.017	--
S	0.000	0.012	0.089	--
Total %	99.614	99.265	99.795	99.54

Appendix 4

Partition Coefficients for Rodrigues Ridge Minerals

Introduction

Partition coefficients are an essential tool in understanding how melts form and how minerals fractionate. Consequently it is important to select the most appropriate values for the rock being studied. One way of doing this, if analytical information is available for both minerals and melt, is to calculate the partition coefficients from the minerals themselves. These can then be compared with the values obtained by other authors using other techniques. The available partition coefficient data is presented in appendix 1 for the minerals olivine, plagioclase, clinopyroxene, othopyroxene, garnet, spinel and magnetite, in basaltic or basaltic andesite compositions. Calculations are presented below for phenocrysts with the Rodrigues Ridge lavas, based on electron microprobe analyses of mineral - glass pairs. It is inevitable that the analytical quality governs the reliability of this data; the reader is directed to appendix 3 for further details.

The Calculation of Partition Coefficients

Assuming that the crystal is equilibrium with the surrounding melt and that the concentration of the element in both the mineral and the melt does not exceed about 1%, Henry's law can be applied to obtain the partition coefficient (K_D) from the following relationship:-

$$\frac{\text{Concentration in the mineral}}{\text{Concentration in the liquid}} = K_D$$

Since most the crystals within these rocks show some evidence of chemical zoning, the initial assumption of equilibrium may not be strictly true. Furthermore, most of these crystals show skeletal forms or other features consistent with their having formed in a rapidly cooling environment where both pressure and oxygen fugacity may also have been in flux. Since these three are the primary controls on partitioning (Irving 1978), the data presented here can only be considered applicable to these rocks. Nevertheless taking average values for both glass and mineral analyses should give a bulk analysis for each. *In all cases the limiting factor is the quantitative detection limits of the instrument, estimated values for which are given in table 56.* The results highlighted below were calculated for glasses where the result was below 0.1% oxide in rock. In almost all cases (except Ti in Cr spinel), some of the individual mineral analyses fell below this limit, thus these results can be considered as a qualitative upper limit.

Table 58 **Estimates of partition coefficients**

Cr spinel	RR2.11	RR2.18	RR4.3	RR4.6	RR8.4
K_{DP}	0.09	**0.17**	0.00	0.06	0.04
K_{DMn}	0.86	0.86	**1.98**	0.50	1.40
K_{DTi}	0.25	0.42	0.81	0.57	0.23
K_{DK}	**0.36**	**0.61**	0.46	0.02	0.01
Olivine					
K_{DP}	--	**0.41**	0.43	0.02	0.02
K_{DMn}	--	0.94	**1.26**	1.34	1.58
K_{DTi}	--	0.01	0.00	0.02	0.00
K_{DCr}	--	**1.96**	**0.25**	**0.74**	0.32
K_{DK}	--	**0.20**	0.07	0.04	0.13
Plagioclase					
K_{DP}	--	**0.39**	0.34	0.00	0.00
K_{DMn}	--	0.21	**0.15**	0.45	0.13
K_{DTi}	--	0.06	0.04	0.03	0.03
K_{DK}	--	**0.15**	0.22	0.12	1.19

Number of analyses averaged

	RR2.11	RR2.18	RR4.3	RR4.6	RR8.4
Glass	2	10	2	1	1
Spinel	1	7	1	3	5
Olivine	0	8	7	12	3
Plagioclase	0	11	4	4	5

	RR9c.6	RR9c.14	RR9c.15	RR9c.32	RR9c.38	Average
Cr spinel						
K_{DP}	0.00	**0.27**	0.03	--	0.00	0.08
K_{DMn}	**3.15**	0.88	2.41	--	0.54	1.40
K_{DTi}	0.35	0.52	0.45	--	0.52	0.46
K_{DK}	0.00	0.02	0.04	--	0.02	0.17
Olivine						
K_{DP}	0.16	**0.17**	0.20	0.34	0.40	0.23
K_{DMn}	**3.45**	0.68	1.48	0.50	0.75	1.33
K_{DTi}	0.04	0.02	0.02	0.00	0.02	0.01
K_{DCr}	**0.52**	**1.43**	0.57	**0.00**	**1.25**	0.78
K_{DK}	0.02	0.01	0.16	0.19	0.03	0.08

Table 58 cont....

Plagioclase

K_{DP}	RR9c.6	RR9c.14	RR9c.15	RR9c.32	RR9c.38	Average
K_{DMn}	0.39	**0.17**	2.18	--	0.62	0.51
K_{DTi}	**0.57**	0.11	0.31	--	0.07	0.25
K_{DK}	0.07	0.09	0.04	--	0.06	0.05
	0.17	0.12	0.33	--	0.24	0.32

Number of analyses averaged

	RR9c.6	RR9c.14	RR9c.15	RR9c.32	RR9c.38
Glass	2	3	2	4	3
Cr Spinel	2	3	3	--	3
Olivine	3	3	1	1	9
Plagioclase	3	6	2	--	6

Comparing the results which are given in table 58 (underlined in table 48 appendix 1) with published data (appendix 1), it is notable that K_{DTi} for Cr Spinel is significantly higher than the published value, probably due to the presence of titanomagnetite coatings around some Cr spinel crystals. In all cases where edge and centre compositions are given in tables A3, A7, A11, A15, A19, A23 and A25, the edge is seen to be more titaniferous. K_{DMn} for plagioclase, K_{DP} for plagioclase and olivine and K_{DK} for olivine also seem high, probably reflecting the difficulty in quantitatively detecting very low levels of these elements in the minerals. K_{DK} for plagioclase is high but this is likely to be the result of slight sea water alteration replacing Na in the plagioclase lattice with K.

Appendix 5

Major and Trace Element Models

To further explore the high-level fractionation history of these lavas, models which included other minerals such as clinopyroxene and spinel were considered. At sites RR2 (low MgO group), RR4, RR8 and RR9c, including clinopyroxene in the extract during fractionation was noted to reduce the residual error (SSR). The tables presented here show the results of these major element models together with the trace element models achieved using these results.

In addition to olivine + clinopyroxene ± plagioclase models for the above sites, an olivine model for the high MgO group at RR2 is listed here, as is an olivine + plagioclase + chrome spinel model for RR3. For further discussion of these models see chapter 6.

RR2

Major elements

For the low MgO group 30% fractionation of olivine + plagioclase + clinopyroxene in the proportions 26:25:49 was required, while for the high MgO group 2% fractionation of olivine only produced a good match with observed trends. The results of this major element modelling are given in tables 25a and 26a. In the low MgO group the SSR for this model is very low (SSR = 0.049 compared with 0.318 for the model involving olivine and plagioclase only), suggesting that clinopyroxene was on the liquidus for at least some of the fractionating history of these lavas. This is consistent with the conclusion that the lavas have experienced high pressure fractionation of clinopyroxene based on CAMS plots (see chapter 4). The fact that the residual error for the high MgO group is not substantially greater for this model involving olivine only (SSR = 0.063 compared with 0.038 if plagioclase is included in the model) demonstrates how very small amounts of fractionation and associated limited MgO values make major element models unreliable and leave no unambiguous solutions.

Trace Elements

For five elements (Eu, Ni, Sc, Sr and Y) from the low MgO group, the simple Rayleigh model of 30% fractionation of olivine, plagioclase and clinopyroxene produces satisfactory results (table 33a). Nb, Cr and V all increase more steeply with decreasing MgO than the model predicts. Zr is buffered, as was observed in the high MgO group. The distribution coefficients for these models are given in table 34a.

Table 25a **Low MgO Group**

	Daughter Lava RR2.16	Ol.	Pl.	CPX.	Parent Lava RR2.4	Calculated Parent Lava	Diff.
SiO_2	47.34	39.29	49.79	50.30	47.73	47.60	0.05
TiO_2	1.12	0.00	0.08	1.99	1.02	1.09	-0.07
Al_2O_3	20.00	0.47	29.79	13.17	18.22	18.28	-0.03
MgO	4.02	45.48	0.00	7.98	7.61	7.63	-0.02
FeO^*	11.31	12.77	0.98	9.61	10.47	10.47	0.00
Na_2O	3.23	0.36	3.69	2.88	2.95	2.98	-0.03
CaO	12.49	0.37	13.48	12.34	11.60	11.64	-0.03
K_2O	0.08	0.04	0.00	0.16	0.16	0.08	0.08
MnO	0.17	0.10	0.04	0.18	0.15	0.17	-0.02
P_2O_5	0.24	0.05	0.01	0.56	0.08	0.26	-0.18
Solution	70.3%	7.9%	7.5%	14.6%			

Sum of the squares of the residuals = 0.049

Table 26a **RR2 High MgO Group**

	Daughter Lava RR2.2	Ol.	Parent Lava RR2.11	Calculated Parent Lava	Diff.
SiO_2	47.67	39.633	47.79	47.55	0.14
TiO_2	1.30	0.00	1.25	1.27	-0.01
Al_2O_3	17.29	0.420	16.89	16.94	-0.00
MgO	8.21	45.876	9.03	9.06	-0.00
FeO^*	10.95	12.490	10.78	10.80	-0.18
Na_2O	2.99	0.032	2.98	2.91	0.06
CaO	11.19	0.235	10.85	10.98	-0.08
K_2O	0.11	0.000	0.12	0.11	0.01
MnO	0.18	0.308	0.20	0.18	0.02
P_2O_5	0.11	0.093	0.09	0.12	-0.02
Solution	97.9%	2.1%			

Sum of the squares of the residuals = 0.063

Table 32a **High MgO Group.**

Element ppm	Parent RR2.11	Calculated Daughter	RR2.2
Cr	368.4	366.497	366.5
Nb	1.352	1.381	1.374
Ni	247.86	217.729	217.73
Sc	34.81	35.451	35.59
Sr	148.75	151.883	150.9
U	0.064	0.065	0.082
V	205.80	210.165	222.6
Y	28.508	29.118	30.60*
Zr	88.50	90.379	88.8
La	2.122	2.157	1.037
Ce	10.521	10.746	8.833
Eu	1.215	1.240	1.126
Yb	3.460	3.530	3.366
Lu	0.421	0.430	0.384

* Estimate for Y value is based on the observed trend.

Table 33a **Low MgO Group.**

Element ppm	Parent RR2.4	Calculated Daughter	RR2.16
Cr	291.3	314.306	355.0*
Nb	0.829	1.177	1.731
Ni	188.755	83.190	83.19
Sc	31.05	34.089	34.09
Sr	152.00	173.108	173.14
U	0.510	0.698	0.660
V	202.3	257.133	280.0*
Y	20.089	26.603	26.6
Zr	57.100	78.212	63.095
La	1.690	2.368	4.441
Ce	6.169	8.631	11.0*
Eu	0.803	1.076	1.076
Yb	2.119	2.910	3.190
Lu	0.288	0.378	0.340

* The Cr, V and Ce values for RR2.16 deviate significantly from the trend observed among the other samples from this group. Hence estimates for Cr and V at 3.92% MgO are presented here.

For the high MgO group, table 32a shows that the model is able to reproduce the observed trends for Cr, Nb, Ni, Sc, Sr, Y and Zr, although the absolute values of the incompatible trace elements (Nb, Sc, Sr, Y and Zr) show some deviation from the observed values. For La, Ce Eu, Yb and Lu, the observed trend is in the opposite sense to that which the model predicts. In short these elements are behaving as though they are compatible in these lavas. U and V show a much greater increase in concentration between the parent and daughter than the model would suggest.

Table 34a **Distribution Coefficients**

	Low MgO Group			High MgO Group		
	D used	Minimum	Maximum	D used	Minimum	Maximum
Cr	0.784	0.784	37.709	1.244	0.200	2.920
Nb	0.004	0.004	0.062	0.010	0.0001	0.010
Ni	3.325	2.049	12.125	7.107	4.070	23.800
Sc	0.735	0.731	1.669	0.140	0.140	0.370
Sr	0.631	0.295	1.255	0.018	0.003	0.018
U	0.109	0.014	0.109	0.0001	0.0001	0.081
V	0.319	0.319	5.076	0.011	0.011	0.050
Y	0.203	0.101	0.366	0.002	0.002	0.033
Zr	0.107	0.051	0.107	0.010	0.0005	0.010
La	0.042	0.042	0.116	0.0005	0.00007	0.0005
Ce	0.047	0.047	0.114	0.005	0.00001	0.005
Eu	0.170	0.168	0.364	0.023	0.00095	0.023
Yb	0.100	0.100	0.168	0.055	0.0015	0.055
Lu	0.225	0.099	0.225	0.048	0.0015	0.048

RR3

Major Elements

Table 27a shows a major element model which includes chrome spinel among the fractionating phases. In this model 15.5% fractionation of olivine + plagioclase + spinel in the proportions 74:12:13 is required to reproduce the observed trends. In this model the SSR is 0.034, an order of magnitude less than the SSR of 0.380 obtained using olivine and plagioclase alone. Although spinel is observed as an accessory phase it never exceeds 1 % by volume, substantially lower than required in the cumulate by this model. Further evidence to suggest that spinel is among the fractionating phases can be seen in the trace element model which, without spinel, could not reproduce the observed Cr behaviour.

Table 27a

	Daughter Lava RR3.11	Ol.	Cr Sp.*	Pl.	Parent Lava RR3.5	Calculated Parent Lava	Diff
SiO_2	47.22	39.31	0.65	49.24	45.52	45.45	0.03
TiO_2	1.19	0.15	0.46	0.07	1.00	1.04	-0.03
Al_2O_3	20.88	0.31	46.28	30.40	19.42	19.41	0.01
MgO	3.19	45.27	18.30	0.07	8.43	8.44	-0.01
FeO*	11.21	12.99	14.73	0.57	11.38	11.37	0.01
Na_2O	3.44	0.00	0.50	3.50	2.94	2.98	-0.04
CaO	12.32	0.43	0.17	13.98	10.68	10.73	-0.04
K_2O	0.09	0.00	0.00	0.00	0.08	0.08	0.00
MnO	0.17	0.21	0.00	0.00	0.13	0.17	-0.04
P_2O_5	0.29	0.00	0.12	0.37	0.42	0.25	0.16
Solution	84.5%	11.5%	2.0%	1.9%			

Sum of squares of residuals = 0.034

* Contains 18.39% Cr_2O_3

Trace Elements

The results of Rayleigh modelling of trace elements are given in table 35a; the bulk distribution coefficients used are given in table 36a. Major difficulties were experienced in modelling the trace element behaviour at this site. Rayleigh fractionation modelling using 15.5 % fractionation of olivine, plagioclase and chrome spinel was successful in describing the behaviour of Cr, Ni, Sc and V (see foot-note to table 36a). As already observed, the remaining trace elements (REE, Y, Zn, Zr and U) show diffuse trends (U & Zn) and/or show trends which are buffered (Zr & Sm) or decrease with decreasing MgO (U, Y and most REE). U may have been subject to oxidation resulting in its enrichment relative to Th. To examine the curious behaviour of the REE, Y and Zr further, the distribution coefficients which would be required to reproduce these trends during Rayleigh fractionation were calculated (table 36a). Using these bulk distribution coefficients, estimates of the partition coefficients for REE, Y, and Zr have been made assuming that the unusual behaviour of these elements has been caused by the fractionation of an accessory phase representing either 0.1 or 1% of the fractionating assemblage (table 37a).

Table 35a

15.5% fractionation of 74.7% olivine, 12.2% plagioclase and 13.1% chrome spinel

Element ppm	Parent RR3.5	Calculated Daughter	Average Daughter*	RR3.1	RR3.11
Cr	544.53	240.991	240.99	243.5	238.48
Ni	302.73	135.851	135.85	138.40	133.3
Sc	33.12	37.852	37.853	32.68	37.853
V	232.31	257.004	257.00	224.10	289.9
Y	25.507	29.910	24.711	24.165	25.256
Zn	120.3	126.302	95.875	74.235	117.515
Zr	67.475	79.612	71.70	65.60	77.80
U	2.636	3.066	0.669	0.312	1.026
La	4.999	5.880	4.406	4.770	4.041
Ce	7.622	8.954	7.365	7.236	7.493
Pr	0.799	0.940	0.713	0.578	0.847
Nd	7.507	8.834	6.589	10.991	6.589
Sm	1.886	2.215	1.950	1.950	2.508
Eu	0.922	1.070	0.917	0.870	0.964
Gd	3.476	4.079	2.934	3.015	2.853
Tb	0.470	0.553	0.460	0.440	0.480
Dy	4.080	4.787	3.625	4.127	3.122
Ho	0.873	1.025	0.839	0.823	0.854
Er	2.523	2.956	2.449	2.439	2.458
Yb	2.875	3.366	2.312	2.380	2.244
Lu	0.348	0.410	0.341	0.303	0.379

* The average daughter was the average of RR3.1 and RR3.11 except for Sm and Nd where RR3.11 was used and Sm where RR3.1 was used as the other value was significantly off the observed trend.

Table 36a **Bulk Distribution Coefficient**

	Maximum	Minimum	D used	D required
Cr	100.443	1.472	5.840	5.840
Ni	24.726	3.622	5.758	5.758
Sc	0.291	0.113	0.207	0.207
V	5.019*	0.024	0.400	0.400
Y	0.055	0.029	0.055	1.188
Zn	0.711	0.711	0.711	2.347
Zr	0.018	0.011	0.018	0.639
U	0.102	0.006	0.102	9.140
La	0.036	0.016	0.036	1.750
Ce	0.043	0.014	0.043	1.204
Pr	0.032	0.014	0.032	1.680
Nd	0.034	0.008	0.034	1.775
Sm	0.044	0.007	0.044	0.801
Eu	0.113	0.018	0.113	1.035
Gd	0.050	0.009	0.050	2.006
Tb	0.035	0.007	0.035	1.130
Dy	0.051	0.004	0.051	1.702
Ho	0.047	0.020	0.047	1.239
Er	0.059	0.003	0.059	1.177
Yb	0.064	0.003	0.064	2.294
Lu	0.025	0.007	0.025	1.120

* The recommended partition coefficient for vanadium in spinel is $D_V^{Sp} = 38$ (Ringwood 1970), which was achieved using lunar samples at appropriate oxygen fugacities. Lindstrom (1976) has pointed out that V in magnetite (and presumably spinel) is very sensitive to the oxygen fugacity. He suggests that the partition coefficient of V in magnetite may increase by two orders of magnitude at low oxygen fugacities, thus the value of 0.1 suggested by Rampone et al. (1993) is probably near the true value for terrestrial melts. $D_V^{Sp} = 0.1$ gives a bulk distribution coefficient of 0.024. A value of 0.400 for the bulk distribution coefficient of vanadium produced the best match with the observations. Assuming that the fractionating mineral suite is indeed olivine, chrome spinel and plagioclase in the proportions mentioned this would imply a partition coefficient $D_V^{Sp} = 2.7\text{-}3.0$.

Table 37a

Estimated Partition Coefficients for Unknown Accessory Phase

Fractionating assemblage;

1. 74.63% Ol + 12.19% Plag + 13.09% Cr Sp + 0.1% X
2. 73.95% Ol + 12.08% + Plag + 12.97% Cr Sp + 1% X

Element	$X_{(0.1)}$	$X_{(1)}$
Y	1134	113.4
Zr	621	62.1
La	1714	171.5
Ce	1161	116.I
Pr	1648	164.8
Nd	1741	174.2
Sm	757	75.7
Eu	922	92.3
Gd	1956	195.6
Tb	1095	109.6
Dy	1651	165.1
Ho	1192	119.3
Er	1118	111.9
Yb	2230	223.0
Lu	1095	109.5

RR4

Major Elements

A model was considered using a matrix clinopyroxene which had a residual error SSR of 0.495 but also required a higher degree of fractionation to produce the major element model. Despite this, the residual error in this model is substantially less than observed using only olivine and plagioclase in the model (SSR = 2.085). In this model 50% fractionation of olivine, plagioclase, clinopyroxene and chrome spinel was required, in the proportions 20.1:46.6:32.3:1.0 respectively (table 28a).

Table 28a

RR4

	Daughter Lava RR4.6	Ol.	Pl.	CPX.	Cr..Sp.*	Parent Lava RR4.1	Calculated Parent Lava	Diff.
SiO_2	48.48	39.39	48.72	47.67	4.35	47.84	47.74	0.04
TiO_2	1.83	0.07	0.00	3.42	1.00	0.87	1.49	-0.62
Al_2O_3	17.13	0.60	32.22	8.44	35.61	17.77	17.90	-0.06
MgO	7.60	44.75	0.06	3.69	13.65	9.08	9.12	-0.05
FeO*	10.82	13.50	0.49	17.00	20.83	9.96	9.85	0.11
Na_2O	3.52	0.27	2.82	2.14	0.59	2.87	2.81	0.06
CaO	9.54	0.34	15.46	16.23	0.51	11.15	11.15	0.00
K_2O	0.64	0.00	0.04	0.74	0.15	0.23	0.45	-0.22
MnO	0.19	0.14	0.00	0.20	0.31	0.16	0.14	0.02
P_2O_5	0.25	0.18	0.02	0.63	0.00	0.07	0.25	-0.18
Solution	50.0%	10.2%	23.7%	16.5%	0.5%			

Sum of the squares of the residuals = 0.495

* contains 23.29% Cr_2O_3

Trace Elements

The trace element model produced using these results was able to match the observed data for Cr, Sr, V and Y (table 39a). The remaining elements required at least 60% fractionation, but were largely inconsistent with each other.

The range of acceptable values for the bulk distribution coefficients are given in table 40a.

Table 39a

50% Fractionation

Extract:-20.1% olivine, 46.6% plagioclase, 32.3% clinopyroxene, 1.0% chrome spinel.

Element	Calculated	RR4.6	Parent
ppm	Daughter		
Cr	171.080	171.1	232.13
Cu	89.893	70.49	96.8
Ni	140.237	171.73	200.12
Sr	233.899	233.9	189.0
Th	0.889	1.322	0.464
V	230.107	230.11	175.65
Y	36.518	36.705	19.208
Zr	112.184	176.5	57.281
Eu	1.354	1.611	0.753

Table 40a

Bulk Distribution Coefficients

	D Max	D Min	D
Cr	32.640	0.629	1.263
Cu	1.107	0.144	1.107
Ni	9.208	1.513	1.513
Sr	2.220	0.517	0.692
Th	0.095	0.061	0.061
V	3.385	0.220	0.610
Y	0.255	0.073	0.073
Zr	0.075	0.038	0.038
Eu	0.462	0.154	0.154

RR8

Major Elements

A model requiring 41% fractionation of olivine, plagioclase and clinopyroxene in the proportions 44:34:22 (table 29a) had a lower SSR = 0.228 than the model presented in chapter 6 using only olivine and plagioclase (SSR = 1.124). In this major element model, Na_2O was the principle source of the residual error. There was more Na_2O in RR8.5 than in the modelled daughter, suggesting either that there has been some post eruptive Na_2O addition, or that the matrix clinopyroxene used contained more Al_2O_3, with less TiO_2 and Na_2O than that actually involved.

Table 29a

	Daughter Lava RR8.5	Ol.	Pl.	CPX.	Parent Lava RR8.2	Calculated Parent Lava	Diff.
SiO_2	49.79	38.17	48.95	38.47	46.36	46.59	-0.09
TiO_2	1.56	0.00	0.22	3.15	1.45	1.25	0.21
Al_2O_3	18.00	0.00	31.81	6.35	15.41	15.60	-0.09
MgO	6.37	41.12	0.06	11.18	12.30	12.23	0.07
FeO^*	9.24	19.11	0.33	22.46	10.94	11.04	-0.09
Na_2O	3.12	0.22	2.80	0.79	2.68	2.34	0.34
CaO	10.56	0.43	14.90	13.36	9.76	9.61	0.15
K_2O	0.89	0.00	0.16	0.51	0.67	0.59	0.08
MnO	0.08	0.18	0.06	0.34	0.17	0.12	0.05
P_2O_5	0.39	0.00	0.00	0.92	0.24	0.31	-0.07
Solution	58.9%	17.9%	13.8%	9.1%			

Sum of the squares of the residuals = 0.228

Trace Elements

The major element solution required 41% fractionation of olivine, plagioclase and clinopyroxene. Table 41a shows the results of trace element modelling. The bulk distribution coefficients used are given in table 42a.

Table 41a

Element ppm	Parent RR8.2	Model Daughter	RR8.5
Cr	587.3	668.518	668.5
Nb	15.984	26.541	16.653
Sc	27.65	29.136	25.742
Sr	341.69	302.507	302.50
Th	1.160	1.924	2.027
Y	23.506	36.168	21.853
Zn	94.2	121.945	196.035
Zr	123.4	203.518	141.6
Eu	I.308	1.858	1.150*

* The Eu value for RR8.5 is 1.003. This was some what lower than the trend apparent in the remaining data hence 1.15 was used as the observed daughter.

Table 42a **Bulk Distribution Coefficients**

	Max	Min	D used
Cr	18.309	0.427	0.755
Nb	0.042	0.004	0.042
Sc	0.901	0.385	0.901
Sr	1.609	0.374	1.230
Th	0.077	0.044	0.044
Y	0.186	0.050	0.186
Zn	0.512	0.512	0.512
Zr	0.055	0.026	0.055
Eu	0.337	0.109	0.337

Of the two solutions considered only this model was able to reproduce the observed behaviour for any of the trace elements. Here satisfactory solutions were obtained for the elements Sr and Cr, but not for any of the other elements.

RR9c

Major Elements

At this site the trace element model described in chapter 6 is able to reproduce the observed trace element trends satisfactorily. The major elements have been modelled using clinopyroxene (table 30a) but since a satisfactory result has already been obtained for the trace elements no further modelling of these elements has been attempted. The addition of clinopyroxene to the model at RR9c produced only a modest change in the residual error (SSR = 0.533 compared with 0.583 for olivine alone).

Table 30a

	Daughter Lava RR9c.20	Ol.	Cpx.	Parent Lava RR9c.15	Calculated Parent Lava	Diff.
SiO_2	49.43	39.59	44.28	48.22	47.95	0.11
TiO_2	1.57	0.02	4.74	1.45	1.54	-0.09
Al_2O_3	18.35	0.57	8.44	15.86	15.79	0.03
MgO	6.33	44.35	8.51	10.61	10.79	-0.18
FeO*	9.16	15.53	17.23	10.66	10.27	0.40
Na_2O	3.26	0.43	2.05	3.07	2.87	0.20
CaO	10.55	0.16	14.26	9.01	9.52	-0.51
K_2O	0.88	0.05	0.44	0.76	0.76	0.03
MnO	0.08	0.33	0.43	0.16	0.13	-0.01
P_2O_5	0.38	0.11	0.73	0.21	0.37	-0.16
Solution	83.5	11.6%	4.9%			

Sum of squares of residuals = 0.533

Summary

Including clinopyroxene and/or chrome spinel produces some improvements in the residual errors observed at RR2 low MgO group, RR3, RR4 and RR8 and in general improves the trace element models. Trace element models at all these sites still fail to reproduce the observed trends for a number of incompatible elements, notably the REE and Zr and also Y, at all sites except RR4 where the observed trend was reproduced adequately by this model.